

Pertanika Journal of

SCIENCE &

TECHNOLOGY

JST

VOL. 33 (2) MAR. 2025



PERTANIKA
JOURNALS

A scientific journal published by Universiti Putra Malaysia Press

PERTANIKA JOURNAL OF SCIENCE & TECHNOLOGY

About the Journal

Overview

Pertanika Journal of Science & Technology is an official journal of Universiti Putra Malaysia. It is an open-access online scientific journal. It publishes original scientific outputs. It neither accepts nor commissions third party content.

Recognised internationally as the leading peer-reviewed interdisciplinary journal devoted to the publication of original papers, it serves as a forum for practical approaches to improve quality on issues pertaining to science and engineering and its related fields.

Pertanika Journal of Science & Technology currently publishes 6 issues a year (*January, March, April, July, August, and October*). It is considered for publication of original articles as per its scope. The journal publishes in **English** and it is open for submission by authors from all over the world.

The journal is available world-wide.

Aims and scope

Pertanika Journal of Science & Technology aims to provide a forum for high quality research related to science and engineering research. Areas relevant to the scope of the journal include: bioinformatics, bioscience, biotechnology and bio-molecular sciences, chemistry, computer science, ecology, engineering, engineering design, environmental control and management, mathematics and statistics, medicine and health sciences, nanotechnology, physics, safety and emergency management, and related fields of study.

History

Pertanika Journal of Science & Technology was founded in 1993 and focuses on research in science and engineering and its related fields.

Vision

To publish a journal of international repute.

Mission

Our goal is to bring the highest quality research to the widest possible audience.

Quality

We aim for excellence, sustained by a responsible and professional approach to journal publishing. Submissions can expect to receive a decision within 90 days. The elapsed time from submission to publication for the articles averages 180 days. We are working towards decreasing the processing time with the help of our editors and the reviewers.

Abstracting and indexing of Pertanika

Pertanika Journal of Science & Technology is now over 32 years old; this accumulated knowledge and experience has resulted the journal being abstracted and indexed in SCOPUS (Elsevier), Journal Citation Reports (JCR-Clarivate), EBSCO, ASEAN CITATION INDEX, Microsoft Academic, Google Scholar, and MyCite.

Citing journal articles

The abbreviation for Pertanika Journal of Science & Technology is *Pertanika J. Sci. & Technol.*

Publication policy

Pertanika policy prohibits an author from submitting the same manuscript for concurrent consideration by two or more publications. It prohibits as well publication of any manuscript that has already been published either in whole or substantial part elsewhere. It also does not permit publication of manuscript that has been published in full in proceedings.

Code of Ethics

The *Pertanika* journals and Universiti Putra Malaysia take seriously the responsibility of all of its journal publications to reflect the highest in publication ethics. Thus, all journals and journal editors are expected to abide by the journal's codes of ethics. Refer to *Pertanika's Code of Ethics* for full details, or visit the journal's web link at http://www.pertanika.upm.edu.my/code_of_ethics.php

Originality

The author must ensure that when a manuscript is submitted to *Pertanika*, the manuscript must be an original work. The author should check the manuscript for any possible plagiarism using any program such as Turn-It-In or any other software before submitting the manuscripts to the *Pertanika* Editorial Office, Journal Division.

All submitted manuscripts must be in the journal's acceptable similarity index range:
≤ 20% – PASS; > 20% – REJECT.

International Standard Serial Number (ISSN)

An ISSN is an 8-digit code used to identify periodicals such as journals of all kinds and on all media—print and electronic.

Pertanika Journal of Science & Technology: e-ISSN 2231-8526 (Online).

Lag time

A decision on acceptance or rejection of a manuscript is reached in 90 days (average). The elapsed time from submission to publication for the articles averages 180 days.

Authorship

Authors are not permitted to add or remove any names from the authorship provided at the time of initial submission without the consent of the journal's Chief Executive Editor.

Manuscript preparation

For manuscript preparation, authors may refer to *Pertanika*'s **INSTRUCTION TO AUTHORS**, available on the official website of *Pertanika*.

Editorial process

Authors who complete any submission are notified with an acknowledgement containing a manuscript ID on receipt of a manuscript, and upon the editorial decision regarding publication.

Pertanika follows a **double-blind peer-review** process. Manuscripts deemed suitable for publication are sent to reviewers. Authors are encouraged to suggest names of at least 3 potential reviewers at the time of submission of their manuscripts to *Pertanika*, but the editors will make the final selection and are not, however, bound by these suggestions.

Notification of the editorial decision is usually provided within 90 days from the receipt of manuscript. Publication of solicited manuscripts is not guaranteed. In most cases, manuscripts are accepted conditionally, pending an author's revision of the material.

The journal's peer review

In the peer-review process, 2 to 3 referees independently evaluate the scientific quality of the submitted manuscripts. At least 2 referee reports are required to help make a decision.

Peer reviewers are experts chosen by journal editors to provide written assessment of the **strengths and weaknesses** of written research, with the aim of improving the reporting of research and identifying the most appropriate and highest quality material for the journal.

Operating and review process

What happens to a manuscript once it is submitted to *Pertanika*? Typically, there are 7 steps to the editorial review process:

1. The journal's Chief Executive Editor and the Editor-in-Chief examine the paper to determine whether it is relevance to journal needs in terms of novelty, impact, design, procedure, language as well as presentation and allow it to proceed to the reviewing process. If not appropriate, the manuscript is rejected outright and the author is informed.
2. The Chief Executive Editor sends the article-identifying information having been removed, to 2 to 3 reviewers. They are specialists in the subject matter of the article. The Chief Executive Editor requests that they complete the review within 3 weeks.

Comments to authors are about the appropriateness and adequacy of the theoretical or conceptual framework, literature review, method, results and discussion, and conclusions. Reviewers often include suggestions for strengthening of the manuscript. Comments to the editor are in the nature of the significance of the work and its potential contribution to the research field.

3. The Editor-in-Chief examines the review reports and decides whether to accept or reject the manuscript, invite the authors to revise and resubmit the manuscript, or seek additional review reports. In rare instances, the manuscript is accepted with almost no revision. Almost without exception, reviewers' comments (to the authors) are forwarded to the authors. If a revision is indicated, the editor provides guidelines for attending to the reviewers' suggestions and perhaps additional advice about revising the manuscript.
4. The authors decide whether and how to address the reviewers' comments and criticisms and the editor's concerns. The authors return a revised version of the paper to the Chief Executive Editor along with specific information describing how they have addressed the concerns of the reviewers and the editor, usually in a tabular form. The authors may also submit a rebuttal if there is a need especially when the authors disagree with certain comments provided by reviewers.
5. The Chief Executive Editor sends the revised manuscript out for re-review. Typically, at least 1 of the original reviewers will be asked to examine the article.
6. When the reviewers have completed their work, the Editor-in-Chief examines their comments and decides whether the manuscript is ready to be published, needs another round of revisions, or should be rejected. If the decision is to accept, the Chief Executive Editor is notified.
7. The Chief Executive Editor reserves the final right to accept or reject any material for publication, if the processing of a particular manuscript is deemed not to be in compliance with the S.O.P. of *Pertanika*. An acceptance letter is sent to all the authors.

The editorial office ensures that the manuscript adheres to the correct style (in-text citations, the reference list, and tables are typical areas of concern, clarity, and grammar). The authors are asked to respond to any minor queries by the editorial office. Following these corrections, page proofs are mailed to the corresponding authors for their final approval. At this point, **only essential changes are accepted**. Finally, the manuscript appears in the pages of the journal and is posted on-line.

Pertanika Journal of
**SCIENCE
& TECHNOLOGY**

Vol. 33 (2) Mar. 2025



A scientific journal published by Universiti Putra Malaysia Press

UNIVERSITY PUBLICATIONS COMMITTEE

CHAIRMAN
Zamberi Sekawi

EDITOR-IN-CHIEF
Luqman Chuah Abdullah
Chemical Engineering

EDITORIAL STAFF

Journal Officers:
Ellyianur Puteri Zainal
Kanagamalar Silvarajoo
Siti Zuhaila Abd Wahid

Editorial Assistants:
Siti Juridah Mat Arip
Zulinaardawati Kamarudin

English Editor:
Norhanizah Ismail

PRODUCTION STAFF

Pre-press Officers:
Ku Ida Mastura Ku Baharom
Nur Farrah Dila Ismail

WEBMASTER

IT Officer:
Kiran Raj Kaneswaran

EDITORIAL OFFICE

JOURNAL DIVISION
Putra Science Park
1st Floor, IDEA Tower II
UPM-MTDC Technology Centre
Universiti Putra Malaysia
43400 Serdang, Selangor Malaysia.

General Enquiry
Tel. No: +603 9769 1622
E-mail:
executive_editor.pertanika@upm.edu.my
URL: <http://www.pertanika.upm.edu.my>

PUBLISHER

UPM Press
Universiti Putra Malaysia
43400 UPM, Serdang, Selangor, Malaysia.
Tel: +603 9769 8855
E-mail: dir.penerbit@upm.edu.my
URL: <http://penerbit.upm.edu.my>



ASSOCIATE EDITOR

2024-2026

Miss Laiha Mat Kiah
Security Services Sn: Digital Forensic, Steganography, Network Security, Information Security, Communication Protocols, Security Protocols
Universiti Malaysia, Malaysia

Saidur Rahman
Renewable Energy, Nanofluids, Energy Efficiency, Heat Transfer, Energy Policy
Sunway University, Malaysia

EDITORIAL BOARD

2024-2026

Abdul Latif Ahmad
Chemical Engineering
Universiti Sains Malaysia, Malaysia

Hsiu-Po Kuo
Chemical Engineering
National Taiwan University, Taiwan

Mohd. Ali Hassan
Bioprocess Engineering, Environmental Biotechnology
Universiti Putra Malaysia, Malaysia

Ahmad Zaharin Aris
Hydrochemistry, Environmental Chemistry, Environmental Forensics, Heavy Metals
Universiti Putra Malaysia, Malaysia

Ivan D. Rukhlenko
Nonlinear Optics, Silicon Photonics, Plasmonics and Nanotechnology
The University of Sydney, Australia

Nor Azah Yusof
Biosensors, Chemical Sensor, Functional Material
Universiti Putra Malaysia, Malaysia

Azlina Harun@Kamaruddin
Enzyme Technology, Fermentation Technology
Universiti Sains Malaysia, Malaysia

Lee Keat Teong
Energy Environment, Reaction Engineering, Waste Utilization, Renewable Energy
Universiti Sains Malaysia, Malaysia

Norbahiah Misran
Communication Engineering
Universiti Kebangsaan Malaysia, Malaysia

Bassim H. Hameed
Chemical Engineering: Reaction Engineering, Environmental Catalysis & Adsorption
Qatar University, Qatar

Mohamed Othman
Communication Technology and Network, Scientific Computing
Universiti Putra Malaysia, Malaysia

Roslan Abd-Shukor
Physics & Materials Physics, Superconducting Materials
Universiti Kebangsaan Malaysia, Malaysia

Biswajeet Pradhan
Digital image processing, Geographical Information System (GIS), Remote Sensing
University of Technology Sydney, Australia

Mohd Shukry Abdul Majid
Polymer Composites, Composite Pipes, Natural Fibre Composites, Biodegradable Composites, Bio-Composites
Universiti Malaysia Perlis, Malaysia

Sodeifan Gholamhossein
Supercritical technology, Optimization, nanoparticles, Polymer nanocomposites
University of Kashan, Iran

Ho Yuh-Shan
Water research, Chemical Engineering and Environmental Studies
Asia University, Taiwan

Mohd Zulkifly Abdullah
Fluid Mechanics, Heat Transfer, Computational Fluid Dynamics (CFD)
Universiti Sains Malaysia, Malaysia

Wing Keong Ng
Aquaculture, Aquatic Animal Nutrition, Aqua Feed Technology
Universiti Sains Malaysia, Malaysia

INTERNATIONAL ADVISORY BOARD

2024-2027

Hiroshi Uyama
Polymer Chemistry, Organic Compounds, Coating, Chemical Engineering
Osaka University, Japan

Mohini Sain
Material Science, Biocomposites, Biomaterials
University of Toronto, Canada

Mohamed Pourkashanian
Mechanical Engineering, Energy, CFD and Combustion Processes
Sheffield University, United Kingdom

Yulong Ding
Particle Science & Thermal Engineering
University of Birmingham, United Kingdom

ABSTRACTING AND INDEXING OF PERTANIKA JOURNALS

Pertanika Journal of Science & Technology is indexed in Journal Citation Reports (JCR-Clarivate), SCOPUS (Elsevier), EBSCO, ASEAN Citation Index, Microsoft Academic, Google Scholar and MyCite.

The publisher of Pertanika will not be responsible for the statements made by the authors in any articles published in the journal. Under no circumstances will the publisher of this publication be liable for any loss or damage caused by your reliance on the advice, opinion or information obtained either explicitly or implied through the contents of this publication. All rights of reproduction are reserved in respect of all papers, articles, illustrations, etc., published in Pertanika. Pertanika provides free access to the full text of research articles for anyone, worldwide. It does not charge either its authors or author-institution for refereeing/publishing outgoing articles or user-institution for accessing incoming articles. No material published in Pertanika may be reproduced or stored on microfilm or in electronic, optical or magnetic form without the written authorization of the Publisher.

Copyright ©2021 Universiti Putra Malaysia Press. All Rights Reserved.

Pertanika Journal of Science & Technology
Vol. 33 (2) Mar. 2025

Contents

Foreword	i
<i>Luqman Chuah Abdullah</i>	
A Study of Different Antenna Models on the Performance of UAV-Based LoRa Communication Network Using Taguchi and ANOVA Methods	557
<i>Mohamad Hazwan Mohd Ghazali, Kelvin Teoh and Wan Rahiman</i>	
Numerical Analysis of Solar Pavement Collector for Malaysian Environment	579
<i>Nurul Aqilah Razeman, Zarina Itam, Salmia Beddu, Muhammad Imran Najeeb, Nazirul Mubin Zahari, Daud Mohammad, Mohd Hafiz Zawawi, Agusril Syamsir and Norizham Abdul Razak</i>	
Determination of Optimal Water Requirement for Sweet Corn Crop Based on Meteorological Data and Plant Growth Parameters	599
<i>Noorellimia Mat Toridi, Muhammad Maleq Isqandar Nor Jalal, Aimrun Wayayok and Mohamed Azwan Mohamed Zawawi</i>	
A Study on the Impact of Chamber Size, Configuration, Environmental Factors and Maximum Power Point Tracking (MPPT) Integration on Microbial Fuel Cell Voltage	625
<i>Siti Kudnie Sahari, Nashley Ursula Mundi Ujai, Thommy Thomas, Ibrahim Yakub, Marini Sawawi, Lilik Hasanah, Abdul Rahman Kram, Zaidi Embong, Kasumawati Lias, Annie Joseph, Kho Lee Chin and Sharifah Masniah Wan Masra</i>	
Simulation of Solar Charge Controller Module with Current Backflow Protection	639
<i>Aimi Dalila Azhar, Weng Ho Yew, Akmal Zaini Arsad, Azrul Ghazali, Fazrena Azlee Hamid and Ahmad Wafi Mahmood Zuhdi</i>	
Leveraging Computational Model Approach in Understanding Infectious Disease: A Case Study in Sabah, Malaysia	653
<i>Siti Sarah Mohd Isnan, Ahmad Fikri Abdullah, Abdul Rashid Mohamed Shariff, Iskandar Ishak, Sharifah Norkhadijah Syed Ismail, Doria Tai and Maheshwara Rao Appanan</i>	

Performance of High-volume Carbide Lime Mortar Under Accelerated <i>CO₂ Curing Followed by Postconditioning Treatments</i> <i>Adrina Rosseira A. Talip, Nur Hafizah A. Khalid and Abdul Rahman Mohd Sam</i>	677
<i>Review Article</i>	
An Overview of the 5G Patent Landscape <i>Mohammad Sadegh Naghipour and Zulhasni Abdul Rahim</i>	693
Effective Vibration-Based Anomaly Detection in Water Pump Operation Using Arduino Microcontroller <i>Azahar Mohd, Khairil Anas Md Rezali, Sharafiz Abdul Rahim, Mohammad Yazdi Harmin, Abdul Murad Zainal Abidin and Mohamad Fikri Mohamad Yunus</i>	725
Temperature-corrected Performance Ratio of Grid-Connected Photovoltaic System: Tropical versus Continental Climate <i>Siti Nor Nakhirah Ibrahim, Hedzlin Zainuddin and Shahril Irwan Sulaiman</i>	745
<i>Review Article</i>	
Machine Learning Applications in Multiplayer Online Battle Arena Esports—A Systematic Review <i>Ahmad Alif Kamal, Mohd. Asyraf Mansor, Liyana Truna, Norhunaini Mohd. Shaipullah and Nor Hafizie Habib Sultan</i>	765
Estimation of Mangrove Gross Primary Productivity Using Sentinel-2 Imagery Data: A Case Study in Ujung Pangkah East Java, Indonesia <i>Zainul Hidayah, Abd Rahman As-Syakur, Herlambang Aulia Rachman, Linda Sri Rahayu Romadhoni and Martiwi Diah Setiawati</i>	799
Stock Trend Prediction Using Multi-attention Network on Domain- specific and Domain-general Features in News Headline <i>Phaik Ching Soon, Tien-Ping Tan, Huah Yong Chan and Keng Hoon Gan</i>	823
<i>Review Article</i>	
Recent Advances in Nickel Catalysts for Deoxygenation of Triglycerides and Fatty Acids: A Review <i>Syazwani Mahmud Puzi, Khairuddin Md Isa, Farizul Hafiz Kasim, Tuan Amran Tuan Abdullah, Mohd. Aizudin Abd. Aziz and Nur Amira Fatimah Bashari</i>	845
Better Network Optimization Through Batch Normalization in Left Ventricle Chamber Classification <i>Dayang Suhaida Awang Damit, Siti Noraini Sulaiman, Muhammad Khusairi Osman, Noor Khairiah A Karim and Samsul Setumin</i>	875

Physical Parameters Optimization of Bacterial Cellulose from <i>Komagataeibacter sucrofermentans</i> <i>Siti Noorfathiah Mohd Razin, Siti Nurbaya Oslan and Noor Dina Muhd Noor</i>	893
Investigation of Partial Discharge Characteristics in Mineral Oil Induced by Dibenzyl Disulfide <i>Amran Mohd Selva, Norhafiz Azis, Muhammad Umair Tariq, Mohd Zainal Abidin Ab Kadir, Jasronita Jasni and Hidayat Zainuddin</i>	913
<i>Review Article</i>	
Fulfilling Feed Demands: Industrial Production of <i>Saccharomyces cerevisiae</i> as Key Protein Source for Aquaculture, Poultry and Livestock <i>Zahra Safdari, Mohd Khairol Anuar Ariffin, Eris Elianddy Supeni and Mohamed Thariq Hameed Sultan</i>	939
Virus Particle Dispersion and Infection Risk Assessment in Aircraft Cabins: A CFD Approach <i>Mohd Syakirin Rusdi, Di Fey Way, Mohd Sharizal Abdul Aziz, Farzad Ismail and Mohammad Hafifi Hafiz Ishak</i>	969
Public Awareness and Performance Assessment of Communal Grease Traps in Klang Valley, Malaysia <i>Theban Arumugam, Priyadarshini Ravindran, Shafreeza Sobri, Salmiaton Ali and Mus'ab Abdul Razak</i>	987
Hydrogenolysis of Glycerol to Propanediols over Ni supported on MgO Catalyst <i>Maryam Shakur, Maryum Irshad and Muhammad Sajjad Haider</i>	1007
Selected papers from The 11th International Conference on Multidisciplinary Research 2023 (iCMR 2023)	
Random Forest Model for Software Build Time Prediction on CI/CD Pipeline <i>Wen Han Seow, Chia Yean Lim and Sau Loong Ang</i>	1031
A Novel Approach to Evaluating HEMA Polymer Gel Dosimeters Using Molecular Vibrational Features <i>Muhammad Alhassan, Azhar Abdul Rahman, Iskandar Shahrin Mustafa, Mohd Zahri Abdul Aziz, Mohd Zakir Kassim, Mohammed Salem Abdullah Bagahezel, Habib Ahmad Ibrahim and Kabiru Alhaji Bala</i>	1049

The Impact of Hydrocarbon R290 Refrigerant on Air Conditioner
Performance and Environmental Sustainability 1069

Ferdinand Ng Siek Khai and Nurul Sabihah Zakaria

**Selected paper from The 9th International Conference and Exhibition on
Sustainable Energy and Advanced Material 2023 (ICE-SEAM 2023)**

Dynamic Vibration Absorber (DVA) Using Combined Piecewise and
Magnetic Stiffness Mechanism 1089

*Wan Muhammad Amir, Roszaidi Ramlan, Mohd Nazim Abdul Rahman,
Azma Putra Azis, Abd Rahman Dullah and Kok Swee Leong*

Foreword

Welcome to the second issue of 2025 for the *Pertanika Journal of Science and Technology (PJST)*!

PJST is an open-access journal for studies in Science and Technology published by Universiti Putra Malaysia Press. It is independently owned and managed by the university for the benefit of the world-wide science community.

This issue contains 25 articles: four review articles; and the rest are regular articles. The authors of these articles come from different countries namely Australia, Bangladesh, Indonesia, Japan, Malaysia, Nigeria and Pakistan.

A review article that we wish to highlight is on the 5G patent landscape by Mohammad Sadegh Naghipour and Zulhasni Abdul Rahim from Universiti Teknologi Malaysia. The fifth generation of mobile networks (5G) is a crucial development in cellular technology, and 5G patents play a key role in helping telecommunications companies remain competitive and maintain their market position. This review analyzes the 5G patent landscape, considering technological, scientific, and financial aspects. The analysis uses Questel's Orbit Insight software to identify key patterns in patent applications, major industry players, and implications for technological standards and market competition. 5G patents are expected to continue driving innovation, influencing market dynamics, shaping industrial competitiveness and setting technological standards. Understanding patent strategies is essential for businesses and legislators to navigate the rapidly evolving 5G ecosystem. Future research could investigate the effects of emerging technologies and legislative changes on patent portfolios while monitoring trends in 5G patents and their impact on the industry. The detailed information of this study is available on page 693.

Another review article titled "Machine Learning (ML) Applications in Multiplayer Online Battle Arena (MOBA) Esports" was presented by Ahmad Alif Kamal et al. from Malaysia. ML has gained significant attention in esports, particularly in MOBA games like *Defence of the Ancients 2 (DotA 2)* and *League of Legends (LoL)*, which generate abundant data. The application of ML in MOBA is a promising area for research, with the esports industry growing rapidly and stakeholders seeking innovative studies. A systematic review was conducted using the PRISMA method by searching databases such as Scopus, Web of Science, PubMed, ScienceDirect, and Google Scholar. A total of 35 peer-reviewed studies were analyzed, focusing on ML applications for MOBA. These studies primarily used algorithms like random forests, decision trees, and neural networks to predict various aspects of gameplay using player data. The results showed strong performance of ML models and highlighted potential future research in mobile-based MOBA, commercialization opportunities, and addressing challenges related to data access and regional differences. The detailed information of this study is available on page 765.

The next article investigates the virus particle dispersion and infection risk assessment in aircraft cabins using the computational fluid dynamics (CFD) approach. It investigated the effects of virus source location and particle size on particle dynamics and infection risk, focusing on particle deposition on surfaces such as passenger bodies and seats. The study revealed that airflow in the cabin was nearly symmetric around the aisle, with slight asymmetry due to the location of a coughing passenger. Most particles were either deposited on surfaces or removed through the ventilation system within 10 minutes. The source location and particle size influenced particle deposition and removal dynamics, with larger particles being affected by gravity. The particles primarily spread within the row of the source and the two rows ahead. The infection risk assessment showed a higher risk for passengers seated directly in front of the virus source and those seated on the same side of the aisle. The detailed information of this study is available on page 969.

We anticipate that you will find the evidence presented in this issue to be intriguing, thought-provoking and useful in reaching new milestones in your own research. Please recommend the journal to your colleagues and students to make this endeavour meaningful.

All the papers published in this edition underwent Pertanika's stringent peer-review process involving a minimum of two reviewers comprising internal as well as external referees. This was to ensure that the quality of the papers justified the high ranking of the journal, which is renowned as a heavily-cited journal not only by authors and researchers in Malaysia but by those in other countries around the world as well.

We would also like to express our gratitude to all the contributors, namely the authors, reviewers and Editorial Board Members of PJST, who have made this issue possible.

PJST is currently accepting manuscripts for upcoming issues based on original qualitative or quantitative research that opens new areas of inquiry and investigation.

Editor-in-Chief

Luqman Chuah Abdullah

A Study of Different Antenna Models on the Performance of UAV-Based LoRa Communication Network Using Taguchi and ANOVA Methods

Mohamad Hazwan Mohd Ghazali¹, Kelvin Teoh¹ and Wan Rahiman^{1,2,3*}

¹*School of Electric & Electronic Engineering, Universiti Sains Malaysia Engineering Campus, 14300 Nibong Tebal, Pulau Pinang, Malaysia*

²*Cluster of Smart Port and Logistics Technology (COSPALT), Universiti Sains Malaysia Engineering Campus, 14300 Nibong Tebal, Pulau Pinang, Malaysia*

³*Daffodil Robotics Lab, Department of Computer Science and Engineering, Daffodil International University, Dhaka, Bangladesh*

ABSTRACT

In a UAV-based LoRa communication network, one critical aspect that requires careful consideration is the weight applied to the UAV, which can be affected by the choice of antenna and the size of the power source utilized to operate the LoRa device. Therefore, in this study, the effects of different antenna models, transmitting powers (TP), and surrounding temperatures on the performance of LoRa are investigated under varying conditions. The other contributions of the paper include investigating the optimum LoRa configuration under different test scenarios and the correlation between TP and power consumption. Based on the Taguchi and ANOVA analysis, the optimum LoRa configuration in terms of packet delivery rate (PDR) for a 1 km direct line-of-sight scenario is TP = 15 dBm, antenna model = 5 dBi antenna, and surrounding temperature = 34°C. With the optimum setting, the power consumption was reduced to approximately 168.4 mW, and 3789 times more data transmission can be achieved compared to the default parameter. Therefore, a smaller power source can prolong the UAV flight time.

Keywords: Antenna, drone, LoRa, power consumption, wireless communication

ARTICLE INFO

Article history:

Received: 11 December 2023

Accepted: 16 April 2024

Published: 21 February 2025

DOI: <https://doi.org/10.47836/pjst.33.2.01>

E-mail addresses:

hazwan_ghazali@yahoo.com (Mohamad Hazwan Mohd Ghazali)

ttk.kelvin@gmail.com (Kelvin Teoh)

wanrahiman@usm.my (Wan Rahiman)

*Corresponding author

INTRODUCTION

LoRa has been increasingly utilized worldwide, where the number of countries deploying long-range wide-area networks (LoRaWAN) is nearly 150 (Edward et al., 2020). The commercial growth of LoRa is

due to its advantages, which include offering long-range (at the scale of kilometers), low power, and secure data transmission for Internet of Things (IoT) applications. However, LoRa requires a trade-off between communication range and data rates. The data rate has to be reduced to achieve a higher communication range and vice versa. LoRa is based on chirp spread spectrum (CSS) modulation, where chirps are signals that have a fluctuating frequency over time. This modulation spreads the data along the bandwidth using a Spreading Factor (SF), which will generate a signal resilient against noise and other interference.

Using UAVs can expand the potential of LoRa in data collection and transmission, and this UAV-based LoRa can be classified into LoRa node and LoRa gateway (Ghazali et al., 2021). It is made possible thanks to the high maneuverability, customizability, and pervasiveness of UAVs (Wang et al., 2021). For instance, a UAV equipped with relevant sensors and a LoRa device can act as a LoRa node and be deployed in locations with difficult access to monitor the quality of the air or traffic and transmit the information to the base station (J. Liu et al., 2020; S. Liu et al., 2020; Trasvina-Moreno et al., 2017). As a LoRa gateway, in some of the precision agriculture and livestock farming applications, a UAV carrying a LoRa device will fly above the LoRa nodes on the ground to collect the data and relay it to the base station (Caruso et al., 2021; Vlasceanu et al., 2019; Behjati et al., 2021; Zorbas & O'Flynn, 2019). Other advantages of UAV-based LoRa communication include its high flexibility, line-of-sight transmission, and reduced computing pressures and computation delay (Lu et al., 2022; Ding et al., 2022). However, there is a trade-off between communication rate and bit rate, in which increasing the bit rate will reduce the communication range—also, the higher the bit rate, the longer the duration of data transmission. LoRa's communication performance also depends on tuning several PHY settings, such as the coding rate (CR), SF, bandwidth (BW), and transmit power (TP).

Many researchers have conducted various studies to evaluate the performance of the LoRa communication network. Faber et al. (2020) and Sanchez-Iborra et al. (2018) assessed the reliability of LoRa in terms of packet error rate (PER) and packet delivery rate (PDR), respectively, under urban and suburban scenarios. Meanwhile, different PHY settings (CR, BW, and SF) have been utilized by Yim et al. (2018) to determine their effects on the LoRa's RSSI and PDR. By applying the LoRa shield based on the Semtech SX1276 chip that works on the 915 MHz band, they also studied the influence of different antenna placements on the LoRa performance. It was discovered that BW had the lowest impact on the LoRa performance compared to CR and SF, and raising the antenna from 0 to 1 m can drastically improve the LoRa signal. Similar work has been conducted by Cattani et al. (2017), utilizing the HopeRF RFM95 LoRa device that operates in the 868 MHz band. Additionally, they investigated the impacts of surrounding temperatures on the LoRa's packet reception rate (PRR). The worst PRR was registered at a temperature of 60°C.

Regarding the TP setting, few researchers have conducted a comprehensive study on this matter. Liang et al. (2020) analyzed the effects of different TPs (20, 17, 14, 10 dBm) and payload length on the LoRa performance in terms of PDR and round-trip time in an indoor environment. A LoRa module based on the Semtech SX1278 chip with a 433 MHz band was used in this study. Experimental results showed that the different TPs had minimal effects on the RTT, and using the lowest setting (10 dBm) could still yield satisfactory PDR. Similarly, (Wang et al., 2017) an investigation was conducted to determine the correlation between different TPs (20, 11, 2 dBm) and the LoRa's packet loss rate. The PLR increased from 0% to 68% when the TP was changed from 20 dBm to 2 dBm. Petajajarvi et al. (2017) evaluated the performance of LoRa in terms of PDR and RSSI using the TP of 14 dBm. Experimental results demonstrated that 60% of the packets could be successfully delivered at a 30 km communication range using the highest spreading factor of 12 and TP of 12 dBm.

As observed in the reviewed works, most of the previous literature analyzed the influence of several PHY settings on the LoRa performance in terms of RSSI, PLR, and PDR parameters. The experimental works have been conducted in various environments, ranging from urban to rural areas. It is commonly understood that UAVs have a limited operational time. Therefore, in a UAV-based LoRa communication network, selecting the best LoRa configuration is crucial to achieving the optimum results without excessively compromising power consumption and flight time. This is what motivates us to perform this study. The key advantage of this work is that, to the best of our knowledge, no literature investigates the impact of different antenna models on LoRa's performance. In addition, compared to existing studies, this work analyzes the correlation between TP and power consumption. The main contributions of this study are as follows:

1. The effects of different antenna models, TPs, and surrounding temperatures on the LoRa RSSI and PDR are investigated.
2. The reliability of LoRa under different test scenarios is presented.
3. The correlation between TP and power consumption is analyzed.
4. The optimized LoRa's configuration for different test scenarios is identified and discussed.

METHODOLOGY

Taguchi Method

Careful planning of the experiment is vital if the full benefits of the experimental methods are to be realized. The Taguchi approach is one of the very useful DOE methods for determining the optimized configuration of different parameters for the best performance. Opposite to other DOE techniques, such as full factorial analysis and response surface

methodology (RSM), the Taguchi approach minimizes the number of experimental runs to a reasonable one in terms of cost and time, using orthogonal arrays (Davis & Pretesh, 2018). Although the number of experiments is reduced, the output still contains the most information. While the RSM method also reduces the number of experiments, the Taguchi method requires fewer experiments than the RSM method to obtain optimum findings (Said et al., 2013). The Taguchi method is also more robust than the RSM technique. This study applied the Taguchi technique to determine the optimized LoRa configuration on the PDR and RSSI and obtain the contribution ratios and order of importance for each parameter.

The factors and levels used in the Taguchi analysis are listed in Table 1. The TP parameter has more levels than other factors due to its high selection choice. Out of the 19 different values (5 to 23 dBm), it is not convincing to select only three levels to determine the optimum TP. Besides, there is limited information regarding the TP used in previous studies. The antenna chosen is based on the widely used ones and must be light enough for the drone to carry. Three different surrounding temperatures represent three distinct environments at the test location. Specifically, a temperature of 27°C indicates the morning period from 8 am to 10 am, a temperature of 31°C indicates the evening period from 5 pm to 7 pm, and a temperature of 34°C indicates the afternoon period from 12 pm to 2 pm. In this research, the L18 Taguchi orthogonal array is chosen and presented in the experimental setup.

Table 1
Factors and levels used in the experiment

Factor	Level 1	Level 2	Level 3	Level 4	Level 5	Level 6
TP (A)	5 dBm	10 dBm	15 dBm	18 dBm	20 dBm	23 dBm
Antenna model (B)	2 dBi	5 dBi	8 dBi			
Surrounding temperature (C)	27°C	31°C	34°C			

The Taguchi analysis utilizes the signal-to-noise (S/N) ratio as a performance indicator to optimize the response variable against variations in noise factors. S/N ratio can be defined as the ratio of the mean (signal) to the standard deviation (noise) (Ginting & Tambunan, 2018). Taguchi has suggested many S/N ratios, but the three most commonly used are smallest-is-best (SB), largest-is-best (LB), and nominal-is-best (NB). This study selected the SB and LB S/N ratios because minimum RSSI and maximum PDR were desired. In practical application, a minimum RSSI is desired, where an RSSI of close to 0 means the received signal is of high quality. However, in Taguchi analysis, the response data cannot be negative; thus, the RSSI obtained from every transmission will be converted to a positive value. Hence, the SB S/N ratio is selected for RSSI response. Therefore, the S/N ratios are defined using the following Equations 1 and 2 (Bademlioglu et al., 2018):

$$\text{For SB, } S/N = -10\log\left(\frac{1}{n}\sum_{i=1}^n y_i^2\right) \quad [1]$$

$$\text{For LB, } S/N = -10\log\left(\frac{1}{n}\left(\frac{1}{\sum_{i=1}^n y_i^2}\right)\right) \quad [2]$$

where n represents the number of experimental trials, and y_i is the resulting value for the i th performance characteristics, which in this study is the PDR or average RSSI for each case.

Analysis of Variance (ANOVA)

After conducting the Taguchi analysis, the ANOVA analysis was carried out to determine the impact ratios of each parameter and to verify the results obtained from the Taguchi method. ANOVA is a statistical technique used to analyze variability in data measured under conditions defined by discrete factors. ANOVA has been widely used in various fields, such as psychology, biology, economics, and engineering, to name a few. In this study, the ANOVA analysis is adopted to analyze the effect level of each parameter on the LoRa's PDR and RSSI (Bademlioglu et al., 2018). In the ANOVA analysis, the sum of squares (SS), degrees of freedom (DOF), F values, mean of squares (MS), and parameters' impact ratios are computed as following Equations 3 to 7:

$$SS_{factor} = \frac{\beta_{factor,i}^2}{N} - \frac{(\sum \beta_i)^2}{n} \quad [3]$$

$$DOF_{factor} = k - 1 \quad [4]$$

$$V_{factor} = \frac{SS_{factor}}{DOF_{error}} \quad [5]$$

$$F_{factor} = \frac{V_{factor}}{V_{error}} \quad [6]$$

$$MS_{factor} = \frac{SS_{factor}}{DOF_{factor}} \quad [7]$$

The SS_{factor} represents the sums of squares due to factor, whereas β_i and $\beta_{factor,i}$ are the S/N ratio at the i th level of the factor and its sum, respectively (Equation 3). In Equation 4, the DOF_{factor} is the number of factors' DOF, and k represents the number of levels of the factor. The V_{factor} in Equation 5 represents the variance of the factor. For Equations 6 and 7, the F_{factor} is the factor's test value, V_{error} is the variance of the error, and MS_{factor} is the ratio of the SS values of each parameter to the DOF of each parameter. The most significant parameter and the parameter ranking obtained from the ANOVA analysis will be compared with the results from the Taguchi analysis.

EXPERIMENTAL SETUP

Hardware

Three omnidirectional antennas are used in this study, as shown in Figure 1, and their technical specifications are listed in Table 2. This study focuses exclusively on omnidirectional antennas, excluding horn and beam antennas from consideration due to their heavier weight, which renders them unsuitable for implementation with UAVs. These antennas are installed on the RFM LoRa shield, which integrates the RFM95W LoRa module. The LoRa shield is then attached to the Arduino UNO as a transmitter and powered

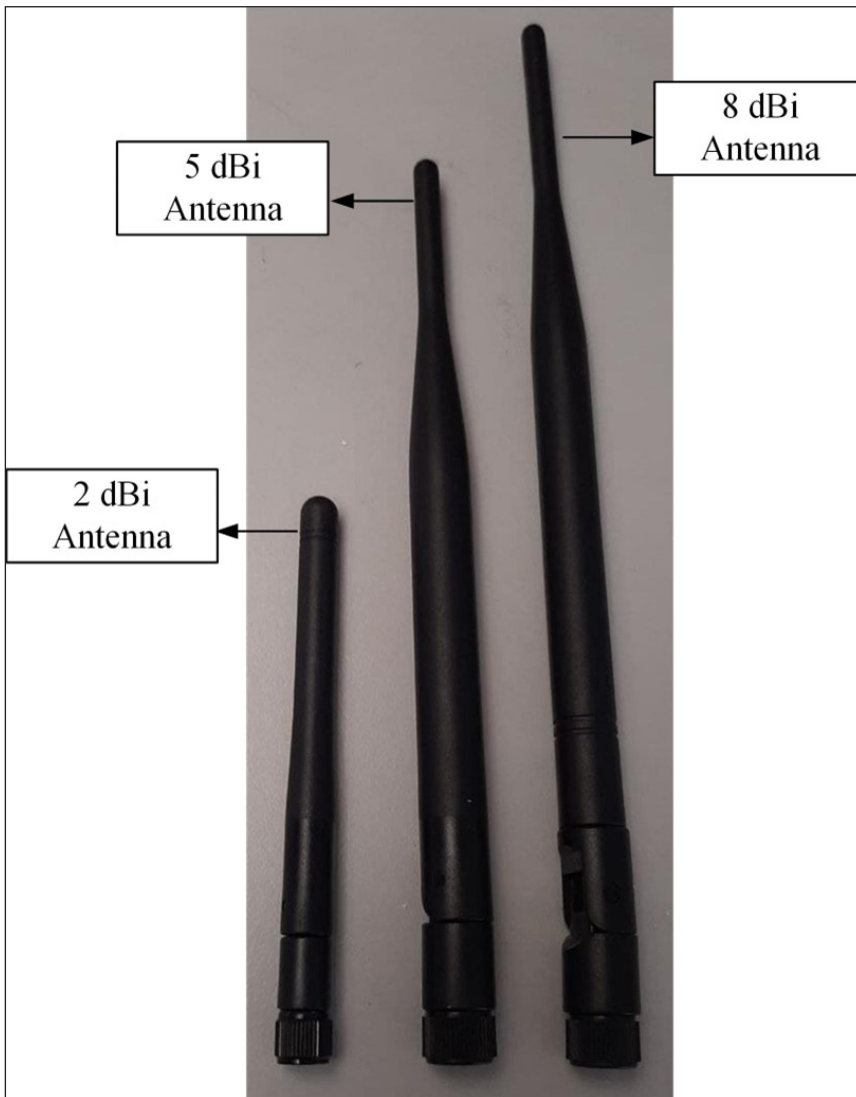


Figure 1. Three omni-directional antennas with different antenna gains used in this experiment

by a 5000 mAh power bank (Figure 2). The UAV's center of gravity needs to be considered while mounting the antenna so that the UAV's stability is not disrupted during flying. The UAV used to carry the setup is the Storm Drone 8, an octocopter-type UAV with a maximum payload of 600 g, excluding the battery. The overall weight of the LoRa communication setup is approximately 168 g (8 dBi antenna = 19 g, LoRa shield = 25 g, Arduino UNO = 25 g, and power bank = 99 g), which is below the maximum payload of Storm Drone 8. Thus, the drone can deploy this experimental setup in the outdoor environment. For each LoRa configuration, the drone will fly with the LoRa transmitter up to approximately 3 m and transmit random integers to the LoRa receiver every 2.5 seconds. For each packet sent, we computed the PDR and RSSI.

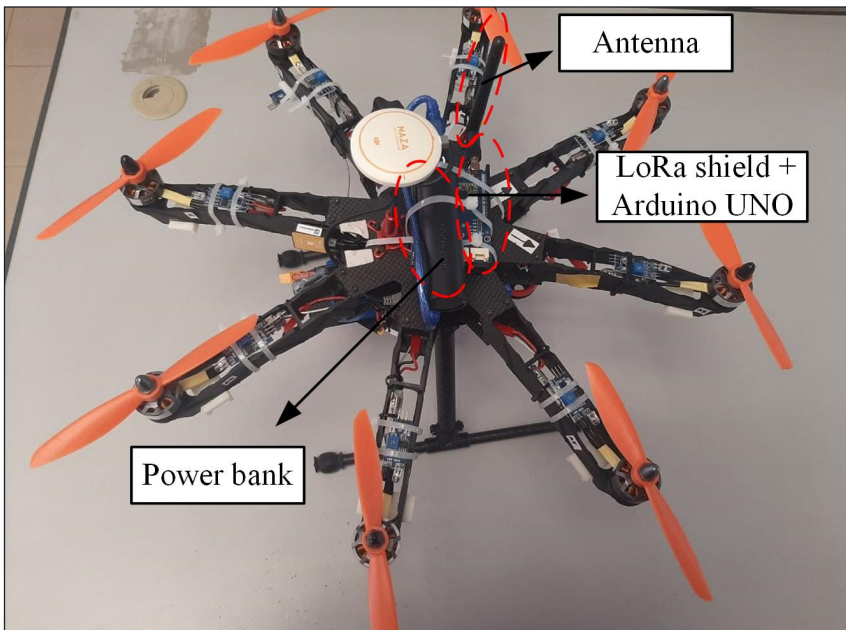


Figure 2. The experimental setup to evaluate the performance of UAV-based LoRa Communication

Table 2
 Technical specifications of three antennas used in this experiment

Specification	Antenna 1	Antenna 2	Antenna 3
Gain	2 dBi	5 dBi	8 dBi
Input Impedance	50 Ω	50 Ω	50 Ω
Antenna Length	10.9 cm	20 cm	24 cm
Frequency	915 MHz	915 MHz	915 MHz
Weight	10 g	16 g	19 g

Test Location

The experimental works are conducted in two different test locations, marked as Location A and B. Ban Pecah, located in Parit Buntar, Perak, Malaysia, is chosen as Location A because it can cater to the 1 km direct line-of-sight feature, as depicted in Figure 3(a). The areas inside Universiti Sains Malaysia, Penang, Malaysia, are chosen as Location B, as

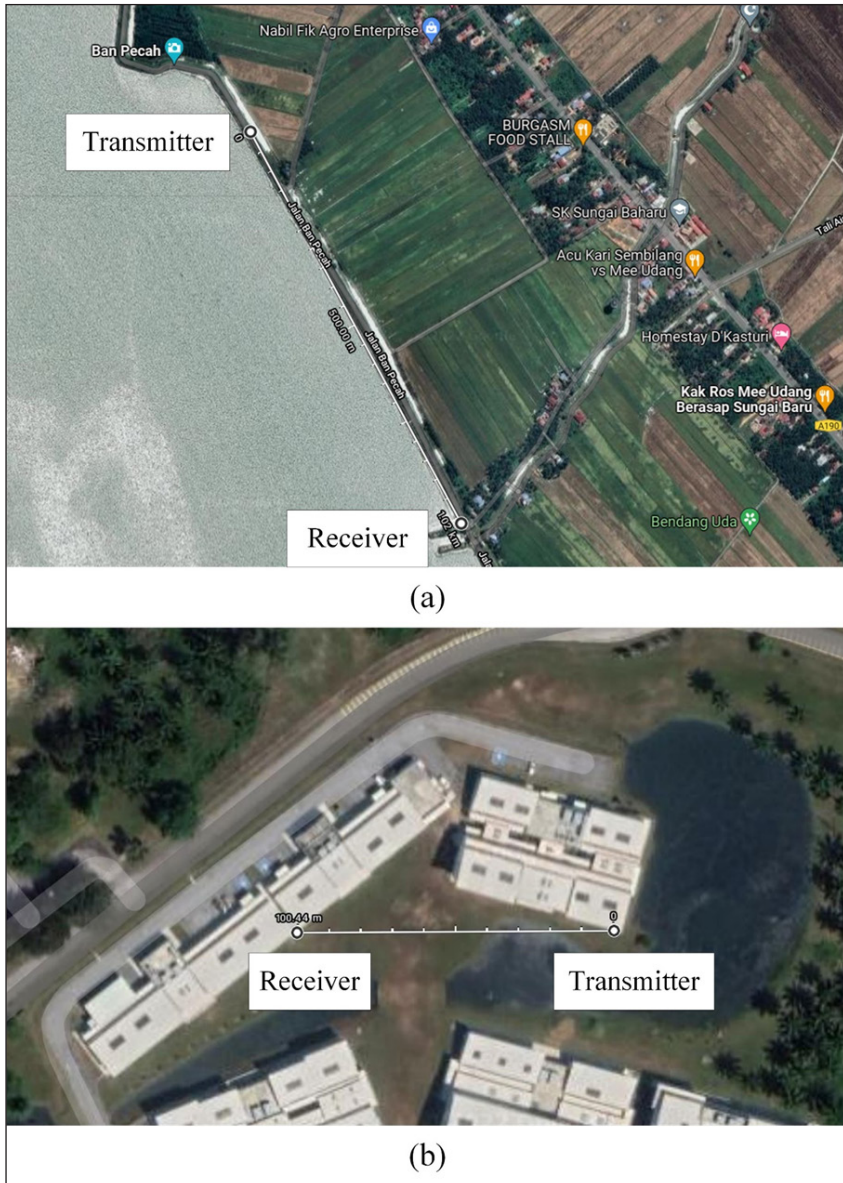


Figure 3. The experimental locations used to conduct the study: (a) Location A in the Ban Pecah Area and (b) Location B in the University Area

shown in Figure 3(b), specifically for the 100 m direct line-of-sight scenario. Two different communication ranges are chosen because we want to determine whether the outputs behave the same in a short and long-range environment or not. As mentioned earlier, the optimum parameters for both communication ranges have been determined.

The correlation between TP and power consumption can be described based on the following Equation 8:

$$P_{mW} = 1 \text{ mW} \left(10^{\frac{P_{dBm}}{10}} \right) \quad [8]$$

where P_{mW} is the power in milliwatts (mW), and P_{dBm} represents the power in Decibel-milliwatts. The current drawn for each data transmission has to be calculated using Equation 9 to determine the number of packets that can be transmitted for a specific capacity of a power supply:

$$I = \sqrt{\frac{P_{mW}}{R}} \quad [9]$$

where I is the current drawn in milliampere (mA), and R is the resistance. Depending on the capacity of the power supply, the current value obtained will be used as a ratio to determine the maximum number of data transmissions.

RESULTS AND DISCUSSION

Tables 3 and 4 show the statistical analyses performed via the Taguchi technique for the 1 km and 100 m experimental scenarios. When data transmission is unsuccessful, the PDR is 0%. However, for the sake of Taguchi analysis, we computed the 0% PDR as 0.001%. We also assumed the worst possible RSSI, which is -146 dBm (according to the RFM LoRa Shield datasheet), for every unsuccessful LoRa communication. It can be seen that there are 18 cases with different levels of parameters (Tables 3 and 4). For instance, the PDR recorded for Trial 1 (Table 3) is 0.001% for a TP of 5 dBm, 2 dBi antenna model, and a surrounding temperature of 27°C. The higher the TP, the higher the tendency for successful LoRa communication (Figure 4). However, for the 2 dBi antenna model, the data can be transmitted only when the TP is set to 15 dBm. Also, Figures 4, 5 and Table 3 demonstrate that in the 1 km direct line-of-sight environment, the UAV-based LoRa communication is unsuccessful at all TPs and temperatures when the 8 dBi antenna model is applied. It might be due to an error in adjusting the position of the UAV to face the receiver, in which the UAV's position does not fall within the effective coverage angle of the 8 dBi antenna (Figure 6).

Table 3
PDRs and S/N ratios for the L18 orthogonal array in a 1 km test scenario

Trial	Parameters			Results		S/N Ratio	
	A Level	B Level	C Level	PDR	Average RSSI	PDR	Average RSSI
1	5 dBm	2 dBi	27°C	0.001% (0%)	146 dBm (-146 dBm)	60	-43.287
2	5 dBm	5 dBi	31°C	25%	98 dBm (-98 dBm)	27.959	-39.825
3	5 dBm	8 dBi	34°C	0.001% (0%)	146 dBm (-146 dBm)	60	-43.287
4	10 dBm	2 dBi	27°C	0.001% (0%)	146 dBm (-146 dBm)	60	-43.287
5	10 dBm	5 dBi	31°C	75%	92 dBm (-92 dBm)	37.5	-39.276
6	10 dBm	8 dBi	34°C	0.001% (0%)	146 dBm (-146 dBm)	60	-43.287
7	15 dBm	2 dBi	31°C	85%	93 dBm (-93 dBm)	38.588	-39.37
8	15 dBm	5 dBi	34°C	100%	90 dBm (-90 dBm)	40	-39.085
9	15 dBm	8 dBi	27°C	0.001% (0%)	146 dBm (-146 dBm)	60	-43.287
10	18 dBm	2 dBi	34°C	90%	88 dBm (-88 dBm)	39.085	-38.89
11	18 dBm	5 dBi	27°C	99%	88 dBm (-88 dBm)	39.554	-38.89
12	18 dBm	8 dBi	31°C	0.001% (0%)	146 dBm (-146 dBm)	60	-43.287
13	20 dBm	2 dBi	31°C	100%	88 dBm (-88 dBm)	40	-38.89
14	20 dBm	5 dBi	34°C	100%	89 dBm (-89 dBm)	40	-38.99
15	20 dBm	8 dBi	27°C	0.001% (0%)	146 dBm (-146 dBm)	60	-43.287
16	23 dBm	2 dBi	34°C	100%	91 dBm (-91 dBm)	40	-39.181
17	23 dBm	5 dBi	27°C	100%	89 dBm (-89 dBm)	40	-38.99
18	23 dBm	8 dBi	31°C	0.001% (0%)	146 dBm (-146 dBm)	60	-43.287

Table 4

PDRs and S/N ratios for the L18 orthogonal array in a 100 m test scenario

Trial	Parameters			Results		S/N Ratio	
	A Level	B Level	C Level	PDR	Average RSSI	PDR	Average RSSI
1	5 dBm	2 dBi	27°C	100%	72 dBm (-72 dBm)	40	-37.147
2	5 dBm	5 dBi	31°C	100%	66 dBm (-66 dBm)	40	-36.391
3	5 dBm	8 dBi	34°C	82%	95 dBm (-95 dBm)	38.276	-39.554
4	10 dBm	2 dBi	27°C	100%	66 dBm (66 dBm)	40	-36.391
5	10 dBm	5 dBi	31°C	100%	62 dBm (-62 dBm)	40	-35.848
6	10 dBm	8 dBi	34°C	93%	90 dBm (-90 dBm)	39.37	-39.085
7	15 dBm	2 dBi	31°C	100%	53 dBm (-53 dBm)	40	-34.486
8	15 dBm	5 dBi	34°C	100%	53 dBm (-53 dBm)	40	-34.486
9	15 dBm	8 dBi	27°C	96%	90 dBm (-90 dBm)	39.645	-39.085
10	18 dBm	2 dBi	34°C	100%	52 dBm (-52 dBm)	40	-34.32
11	18 dBm	5 dBi	27°C	100%	50 dBm (-50 dBm)	40	-33.979
12	18 dBm	8 dBi	31°C	100%	88 dBm (88 dBm)	40	-38.89
13	20 dBm	2 dBi	31°C	100%	50 dBm (-50 dBm)	40	-33.979
14	20 dBm	5 dBi	34°C	100%	48 dBm (-48 dBm)	40	-33.625
15	20 dBm	8 dBi	27°C	100%	85 dBm (-85 dBm)	40	-38.588
16	23 dBm	2 dBi	34°C	100%	50 dBm (-50 dBm)	40	-33.979
17	23 dBm	5 dBi	27°C	100%	46 dBm (-46 dBm)	40	-33.255
18	23 dBm	8 dBi	21°C	100%	83 dBm (-83 dBm)	40	-38.382

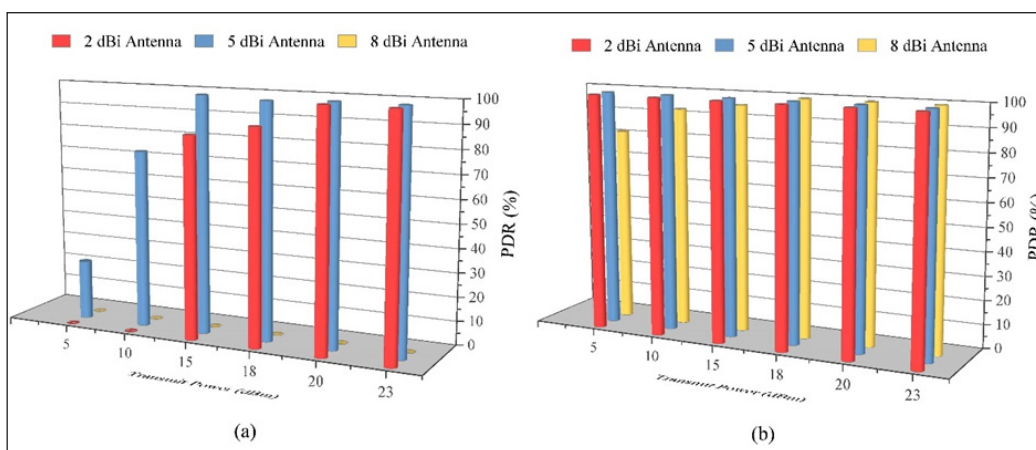


Figure 4. The PDRs computed at different TPs for 2 dBi, 5 dBi, and 8 dBi antennas in (a) a 1 km direct line-of-sight environment and (b) a 100 m direct line-of-sight environment

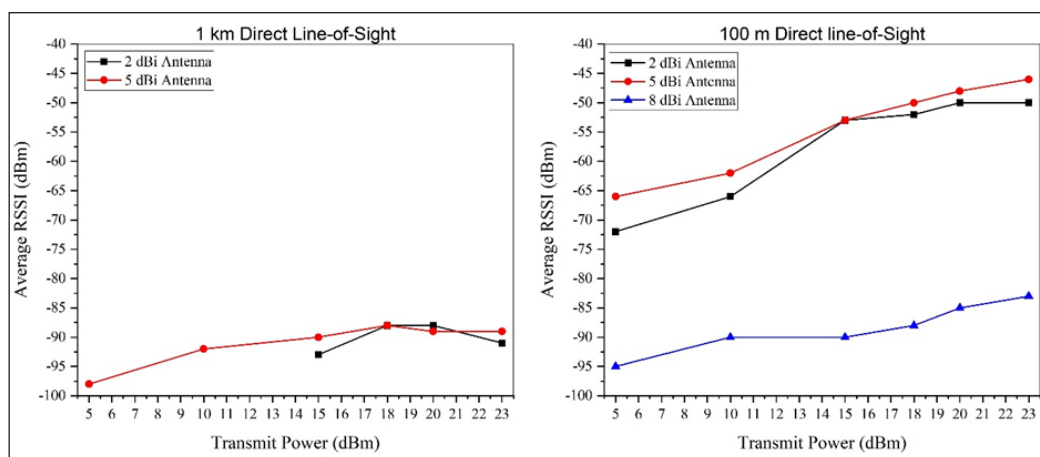


Figure 5. The average RSSIs computed at different TPs for 2 dBi, 5 dBi, and 8 dBi antennas in 1 km and 100 m environments

In contrast to the 8 dBi antenna, the UAV-based LoRa communication with the 5 dBi antenna is successful at all experimental trials, though there are packet losses at the minimum TP. The LoRa communication using the 8 dBi antenna produced the worst PDR and average RSSI in 1 km and 100 m test scenarios, as depicted in Figures 3 and 4. The reason behind this is the narrow effective angle coverage of an 8 dBi antenna, compared to 2 dBi and 5 dBi antennas. The 2 dBi antennas can cover all 360 coverage angles, whereas 5 dBi antennas have a range of 40. As for the 8 dBi antenna, the effective coverage angle is between 25° and 30°. Thus, during the data collection process using the 8 dBi antenna, although the UAV that carried the LoRa transmitter was hovering, the effective angle

coverage was not static due to the slight movement of the UAV, which led to poor PDR and RSSI recorded. However, if the UAV's position is properly facing the 8 dBi receiver, the outcome could vary, and the 8 dBi antenna could potentially perform similarly or even better than the 5 dBi antenna.

For the 100 m direct line-of-sight test scenario, the LoRa communication is successful at every TP for all antenna models. However, for a 100% PDR, the TP must be set to 18 dBm if the 8 dBi antennas are used. The same results can be obtained for the 2 dBi and 5 dBi antennas, even if the minimum TP (5 dBm) is applied. In terms of RSSI, the 5 dBi antenna is the best choice for LoRa communication in the 100 m range, whereas if maximum PDR is desired, the 2 dBi antenna is sufficient.

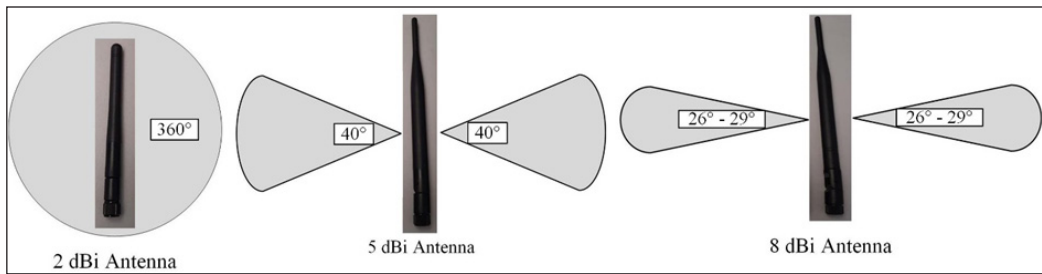


Figure 6. Effective coverage angles of each LoRa antenna

Average S/N ratios, contribution ratios, and parameter ranking on the PDR and average RSSI are computed using the Taguchi technique (Tables 5, 6, 7, and 8). The parameters are ranked based on the magnitude of the effect on PDR and average RSSI. It can be observed from Tables 5 to 8 that the antenna model is the most significant parameter on the PDR and average RSSI for both test scenarios. In contrast, the least significant parameter is

Table 5
Average S/N ratio and ranking of parameters for the PDR in a 1 km direct line-of-sight scenario

Level	Parameters		
	A	B	C
1	-30.68	6.279	-14.411
2	-27.5	37.502	4.008
3	30.856	-47.67	6.514
4	6.213		
5	6.667		
6	6.667		
Delta	61.536	85.173	20.925
Contribution Ratio	36.71%	50.81%	12.48%
Rank	2	1	3

Table 6
Average S/N Ratio and ranking of parameters for the average RSSI in a 1 km direct line-of-sight scenario

Level	Parameters		
	A	B	C
1	-42.13	-40.48	-41.84
2	-41.95	-39.13	-40.66
3	-40.58	-43.29	-40.40
4	-40.36		
5	-40.29		
6	-40.29		
Delta	1.84	4.16	1.43
Contribution Ratio	24.76%	55.99%	19.25%
Rank	2	1	3

Table 7
Average S/N ratio and ranking of parameters for the PDR in a 100 m direct line-of-sight scenario

Level	Parameters		
	A	B	C
1	39.43	40	39.94
2	39.79	40	40
3	39.88	39.55	39.61
4	40		
5	40		
6	40		
Delta	0.57	0.45	0.59
Contribution Ratio	40.4%	31.9%	27.7%
Rank	1	2	3

Table 8
Average S/N ratio and ranking of parameters for the average RSSI in a 100 m direct line-of-sight scenario

Level	Parameters		
	A	B	C
1	-37.7	-35.05	-36.48
2	-37.11	-34.66	-36.40
3	-36.08	-39.01	-35.84
4	-35.73		
5	-35.36		
6	-35.46		
Delta	2.33	4.35	0.64
Contribution Ratio	31.8%	59.4%	8.8%
Rank	2	1	3

the surrounding temperature. Thus, the ranking orders of the impact of parameters on the average RSSI for both test scenarios are the same, which are antenna model > TP > surrounding temperature. For PDR, the ranking orders are determined as follows: antenna model > TP > surrounding temperature (for 1 km environment) and TP > antenna model > surrounding temperature (for 100 m environment).

Figures 7 and 8 demonstrate each parameter's effect on the PDR and average RSSI. The parameter is considered to strongly influence the output if there is a huge discrepancy between the maximum and minimum S/N ratios. Parameters that produce the highest S/N ratio will contribute to the desired optimum UAV-based LoRa configuration. Therefore, based on the Taguchi analysis, TP = 15 dBm, antenna model = 5 dBi antenna, and surrounding temperature = 34°C are determined as an optimum UAV-based LoRa configuration for maximum PDR (100%) in a 1 km direct line-of-sight scenario. As for the best average RSSI, the optimum configurations are TP = 20 dBm, antenna model = 5 dBi antenna, and surrounding temperature = 34°C. In addition, the worst LoRa configuration was found to be the TP = 5 dBm, antenna model = 8 dBi antenna, and surrounding temperature = 27°C, where LoRa communication was unsuccessful. As for the 100 m test scenario, the optimum LoRa configuration suggested by the Taguchi analysis is TP = 18 dBm, antenna model = 2 dBi antenna, and surrounding temperature = 31°C for the best PDR. However, from the experimental works, the minimum TP (5 dBm) can still yield 100% PDR when applied to the 2 dBi and 5 dBi antennas. For the best RSSI, the

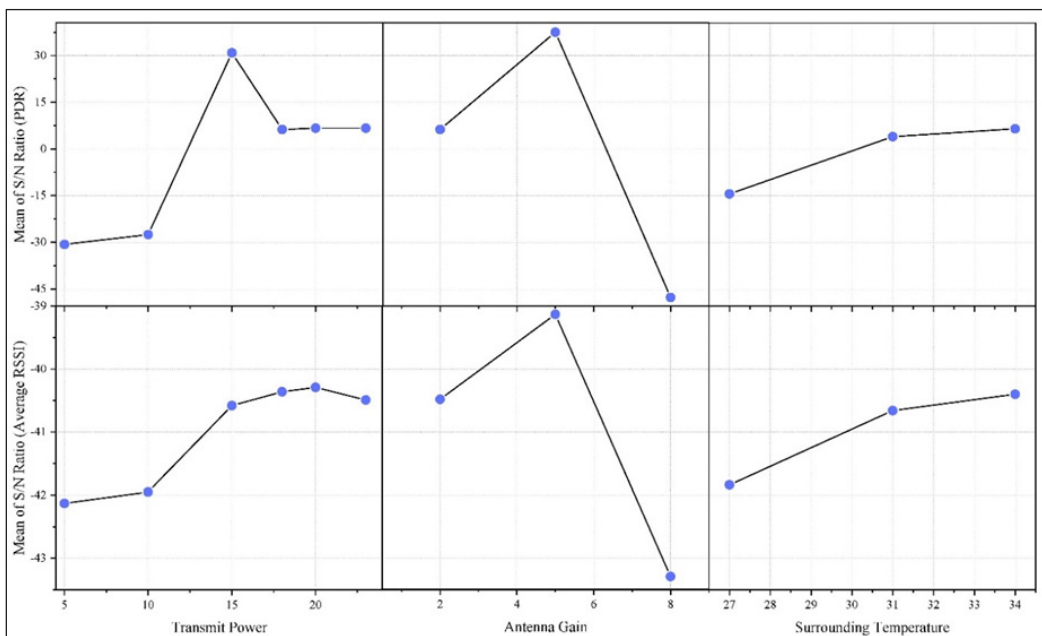


Figure 7. Effective of each parameter on the PDR and average RSSI in a 1 km direct line-of-sight scenario

optimum LoRa configuration is determined as follows: TP = 20 dBm, antenna model = 5 dBi antenna, and surrounding temperature = 34°C. Minimum PDR and average RSSI are obtained under the following LoRa configuration: TP = 5 dBm, antenna model = 8 dBi antenna, and surrounding temperature = 34°C (for PDR) and 27°C (for average RSSI).

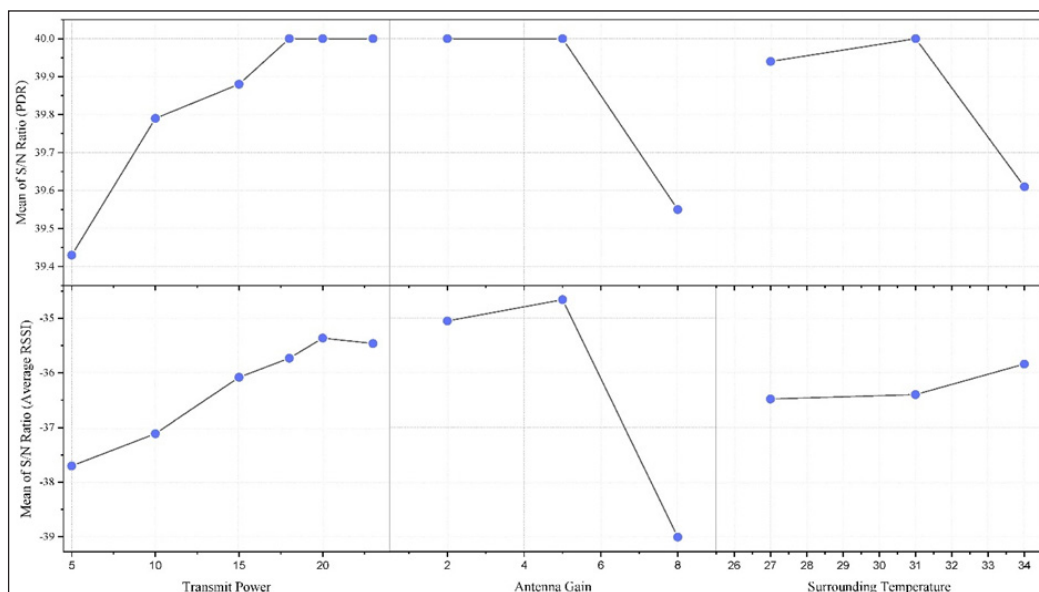


Figure 8. Effective of each parameter on the PDR and average RSSI in a 100 m direct line-of-sight scenario

The ANOVA analysis was applied, and the outputs were obtained to verify the results of the Taguchi analysis (Tables 9, 10, 11, and 12). Based on the ANOVA tables, it can be seen that the most significant parameter on the PDR and average RSSI for 1 km test scenarios is the antenna gain, with an impact ratio of 75.96% and 82.92%, respectively. The order of importance of the parameters for the PDR and average RSSI is determined as antenna model > TP > surrounding temperature. These results are in agreement with the

Table 9
ANOVA table for PDR in a 1 km direct line-of-sight scenario

Parameters	DOF	SS	MS	F	Contribution
TP	5	9657	1931.4	4.21	13.49%
AG	2	21744	10872	23.70	75.96%
ST	2	3019	1509.7	3.29	10.54%
Error	8	3669	458.7		
Total	17	38090			100%

TP = Transmit power, AG = Antenna gain, and ST = Surrounding temperature

results obtained from the Taguchi analysis. Although the contribution ratios computed from both analyses are slightly different, the ranking order of the parameters is still the same.

Table 10

ANOVA table for average RSSI in a 1 km direct line-of-sight scenario

Parameters	DOF	SS	MS	F	Contribution
TP	5	1270	634.9	4.08	10.96%
AG	2	9608	4804.1	30.87	82.92%
ST	2	1772	354.5	2.28	6.12%
Error	8	1245	155.6		
Total	17	13895			100%

TP = Transmit power, AG = Antenna gain, and ST = Surrounding temperature

Table 11

ANOVA table for PDR in a 100 m direct line-of-sight scenario

Parameters	DOF	SS	MS	F	Contribution
TP	5	82.94	16.59	1.25	17.7%
AG	2	93.44	46.72	3.53	50.1%
ST	2	60.11	30.06	2.27	32.2%
Error	8	105.78	13.22		
Total	17	342.28			100%

TP = Transmit power, AG = Antenna gain, and ST = Surrounding temperature

Table 12

ANOVA table for average RSSI in a 100 m direct line-of-sight scenario

Parameters	DOF	SS	MS	F	Contribution
TP	5	686.67	137.33	14.27	5.7%
AG	2	4510.33	2255.17	234.3	93.2%
ST	2	52	26	2.7	1.1%
Error	8	77	9.63		
Total	17	5326			100%

TP = Transmit power, AG = Antenna gain, and ST = Surrounding temperature

In a 100 m direct line-of-sight environment, the most significant parameter that affects the PDR and average RSSI is the antenna gain, with an impact ratio of 50.1% and 93.2%, respectively. However, the ranking parameters are different compared to the 1 km one. In terms of PDR, the ranking order is determined as antenna model > surrounding temperature > TP, whereas for the average RSSI, antenna model > TP > surrounding temperature is the

ranking order. There is a conflict in terms of the ranking order of the parameters obtained from the Taguchi and ANOVA analysis. The reason behind this might be the 100 m communication range, which is considered insufficient in distinguishing and analyzing the performance of 2 dBi and 5 dBi antennas. As shown in Table 4 and Figure 4(b), the PDRs acquired from the 2 dBi and 5 dBi antennas at all experimental trials are the same, and the difference in terms of the average RSSI is also very small. Therefore, it is recommended that the reliability of LoRa communication be tested at a longer communication range, such as 500 m, to properly determine the order of the importance of parameters. However, findings obtained from experimental work in a 100 m environment are still useful. It was discovered that the minimum TP (5 dBm) for the 2 dBi antenna yields the same PDR as the 5 dBi antenna, regardless of the surrounding temperature.

Based on the Taguchi and ANOVA analysis performed, it was discovered that the TP could be reduced to as low as 15 dBm for a maximum PDR in a 1 km direct line-of-sight environment if the 5 dBi antenna is used. Therefore, by applying Equations 8 and 9, the LoRa power consumption can be reduced by approximately 168.4 mW, and the maximum number of data transmissions is increased to 6289 times, which is more than double the data that can be transmitted using the default TP (2500 times). For the 100 m direct line-of-sight scenario, applying the lowest TP (5 dBm) on the 2 dBi antenna can still yield maximum PDR while at the same time reducing the power consumption by up to 196.8 mW and transmitting about 17388 more data compared to default TP. Although it was discovered that the 5 dBi performs better in terms of PDR and average RSSI, in most UAV applications, the UAV will perform more than hovering and most likely not stay in the effective coverage angle of the 5 dBi antenna. Thus, it is recommended that the 2 dBi antenna be applied in UAV-based LoRa applications as the antenna has a 360° coverage angle, making the UAV not limited by maneuverability.

In the future, additional parameters such as BW, SF, and CR can be included in the Taguchi and ANOVA analysis to determine the optimum LoRa configuration for further minimizing the power consumption. Also, the performance of a 3.5 dBi antenna model can be evaluated, and the surrounding temperature can be further varied by introducing a colder (less than 10°C) and hotter environment (more than 40°C). Further analysis can be conducted to examine the impact of other factors on the performance of UAV-based LoRa communication, such as antenna gain, weight, and coverage capability. Additional experiments will also be conducted to assess the performance of each antenna at intermediate distances between 100 m and 1000 m.

CONCLUSION

The application of UAVs can increase LoRa's potential, especially in monitoring and precision agriculture. Many parameters can affect the performance of the UAV-based

LoRa communication network, such as TP, BW, SF, CR, and surrounding temperature. The main contribution of this study is the investigation of the optimum LoRa configuration, which consists of TP, antenna model, and the surrounding temperature. It aims to achieve maximum PDR and RSSI with less power consumption. Two different statistical methods (Taguchi and ANOVA) are applied to determine the ranking order of these parameters. In a 1 km direct line-of-sight environment, results from both Taguchi and ANOVA analysis are in agreement that the most significant parameter is the antenna model, followed by TP and surrounding temperature. The optimum LoRa configuration for the best PDR is TP = 15 dBm, antenna model = 5 dBi antenna, and surrounding temperature = 34°C, reducing the power consumption by approximately 168.4 mW. For a 100 m communication range, the TP can be set to as low as 5 dBm on the 2 dBi antenna, reducing the power consumption by up to 196.8 mW and transmitting 17388 times more data compared to the default configuration. Meanwhile, in a 1 km communication range, the proposed work's efficacy in the maximum number of data transmissions is approximately 151.56% higher than that of the default setting. Minimizing power consumption is essential so that a lighter power supply can be equipped, prolonging the flight time of the UAV. In the future, the reflection signal from the UAV that will affect the antenna performance can be calculated and investigated.

ACKNOWLEDGEMENT

This work was supported by Collaborative Research in Engineering, Science, and Technology (CREST) with grant no. 304/PELECT/6050424/C121.

REFERENCES

- Bademlioglu, A. H., Canbolat, A. S., Yamankaradeniz, N., & Kaynakli, O. (2018). Investigation of parameters affecting Organic Rankine Cycle efficiency by using Taguchi and ANOVA methods. *Applied Thermal Engineering*, 145(1), 221–228. <https://doi.org/10.1016/j.applthermaleng.2018.09.032>
- Behjati, M., Noh, Y., Alobaidy, H. A. H., Zulkifley, M. A., Nordin, R., & Abdullah, N. F. (2021). LoRa communications as an enabler for internet of drones towards large-scale livestock monitoring in rural farms. *Sensors*, 21(15), 5044–5071. <https://doi.org/10.3390/s21155044>
- Caruso, M., Boano, C. A., & Romer, K. (2021). Collection of data with drones in precision agriculture: Analytical model and LoRa case study. *IEEE Internet of Things Journal*, 8(22), 16692–16704. <https://doi.org/10.1109/JIOT.2021.3075561>
- Cattani, A., Chessa, S., Escolar, S., Barba, J., & Lopez, J. C. (2017). An experimental evaluation of the reliability of lora long-range low-power wireless communication. *Journal of Sensors and Actuator Networks*, 6(2), 7–26. <https://doi.org/10.3390/jsan6020007>
- Davis, R., & Pretesh, J. (2018). Application of Taguchi-based design of experiments for industrial chemical processes. In V. Silva (Ed.), *Statistical Approaches With Emphasis on Design of Experiments Applied to Chemical Processes* (pp. 137-156). IntechOpen. <http://dx.doi.org/10.5772/intechopen.69501>

- Ding, Y., Feng, Y., Lu, W., Zheng, S., Zhao, N., Meng, L., Nallanathan, A., & Yang, X. (2022). Online edge learning offloading and resource management for UAV-assisted MEC secure communications. *IEEE Journal of Selected Topics in Signal Processing*, 17(1), 54–65. <https://doi.org/10.1109/JSTSP.2022.3222910>
- Edward, P., El-Aasser, M., Ashour, M., & Elshabrawy, T. (2020). Interleaved chirp spreading LoRa as a parallel network to enhance LoRa capacity. *IEEE Internet of Things Journal*, 8(5), 3864–3874. <https://doi.org/10.1109/JIOT.2020.3027100>
- Faber, M. J., van der Zwaag, K. M., dos Santos, W. G. V., de O Rocha, H. R., Segatto, M. E. V., & Silva, J. A. L. (2020). A theoretical and experimental evaluation on the performance of LoRa technology. *IEEE Sensors Journal*, 20(16), 9480–9489. [10.1109/JSEN.2020.2987776](https://doi.org/10.1109/JSEN.2020.2987776)
- Ghazali, M. H. M., Teoh, K., & Rahiman, W. (2021). A systematic review of real-time deployments of UAV-based LoRa communication network. *IEEE Access*, 9, 124817–124830. <https://doi.org/10.1109/ACCESS.2021.3110872>
- Ginting, E., & Tambunan, M. M. (2018). Selection of optimal factor level from process parameters in palm oil industry. In *IOP Conference Series: Materials Science and Engineering* (Vol. 288, No. 1, p. 012056). IOP Publishing. <https://doi.org/10.1088/1757-899X/288/1/012056>
- Liang, R., Zhao, L., & Wang, P. (2020). Performance evaluations of LoRa wireless communication in building environments. *Sensors*, 20(14), 3828–3847. <https://doi.org/10.3390/s20143828>
- Liu, J., Wu, J., & Liu, M. (2020). UAV monitoring and forecasting model in intelligent traffic oriented applications. *Computer Communications*, 153, 499–506. <https://doi.org/10.1016/j.comcom.2020.02.009>
- Liu, S., Yang, X., & Zhou, Z. (2020). Development of a low-cost UAV-based system for CH₄ monitoring over oil fields. *Environmental Technology*, 42(20), 3154–3163. <https://doi.org/10.1080/09593330.2020.1724199>
- Lu, W., Yandan, M., Feng, Y., Gao, Y., Zhao, N., Wu, Y., & Moose, P. H. (2022). Secure transmission for multi-UAV-assisted mobile edge computing based on reinforcement learning. *IEEE Transactions on Network Science and Engineering*, 10(3), 1270–1282. <https://doi.org/10.1109/TNSE.2022.3185130>
- Petajajarvi, J., Mikhaylov, K., Pettisalo M., Janhunen, J., & Inatti, J. (2017). Performance of a low-power wide-area network based on LoRa technology: Doppler, robustness, scalability, and coverage. *International Journal of Distributed Sensor Networks*, 13(3), 1–16. <https://doi.org/10.1177/1550147717699412>
- Said, M. S. M., Ghani, J. A., Kassim, M. S., Tomadi, S. H., & Haron, C. H. C. (2013). Comparison between Taguchi method and response surface methodology (RSM) in optimizing machining condition. In *Proceeding of 1st International Conference on Robust Quality Engineering* (pp. 60-68). UTM Razak School.
- Sanchez-Iborra, R., Sanchez-Gomez, J., Ballesta-Vinas, J., Maria-Dolores, C., & Skarmeta, A. F. (2018). Performance evaluation of LoRa considering scenario conditions. *Sensors*, 18(3), 772–791. <https://doi.org/10.3390/s18030772>
- Trasvina-Moreno, C. A., Blasco, R., Marco, A., Casas, R., & Trasvina-Castro, A. (2017). Unmanned aerial vehicle based wireless sensor network for marine coastal environment monitoring. *Sensors*, 17(3), 460–482. <https://doi.org/10.3390/s17030460>

- Vlasceanu, E., Dima, M., Popescu, D., & Ichim, L. (2019). Sensor and communication considerations in UAV-WSN based system for precision agriculture. In *2019 IEEE International Conference on Cybernetics and Intelligent Systems (CIS) and IEEE Conference on Robotics, Automation and Mechatronics (RAM)* (pp. 281-286). IEEE Publishing. <https://doi.org/10.1109/CIS-RAM47153.2019.9095823>
- Wang, S. Y., Chen, Y. R., Chen, T. Y., Chang, C. H., Cheng, Y. H., Hsu, C. C., & Lin, Y. B. (2017). Performance of LoRa-based IoT applications on campus. In *2017 IEEE 86th vehicular technology conference (VTC-Fall)* (pp. 1-6). IEEE Publishing. <https://doi.org/10.1109/VTCFall.2017.8288154>
- Wang, Z., Wen, M., Dang, S., Yu, L., & Wang, Y. (2021). Trajectory design and resource allocation for UAV energy minimization in a rotary-wing UAV-enabled WPCN. *Alexandria Engineering Journal*, *60*(1), 1787–1796. <https://doi.org/10.1016/j.aej.2020.11.027>
- Yim, D., Chung, J., Cho, Y., Song, H., Jin, D., Kim, S., Ko, S., Smith, A., & Riegsecker, A. (2018). An experimental LoRa performance evaluation in tree farm. In *2018 IEEE sensors applications Symposium (SAS)* (pp. 1-6). IEEE Publishing. <https://doi.org/10.1109/SAS.2018.8336764>
- Zorbas, D., & O'Flynn, B. (2019). A network architecture for high volume data collection in agricultural applications. In *2019 15th International Conference on Distributed Computing in Sensor Systems (DCOSS)* (pp. 578-583). IEEE Publishing. <https://doi.org/10.1109/DCOSS.2019.00107>

Numerical Analysis of Solar Pavement Collector for Malaysian Environment

Nurul Aqilah Razeman¹, Zarina Itam^{2*}, Salmia Beddu²,
Muhammad Imran Najeeb², Nazirul Mubin Zahari², Daud Mohammad²,
Mohd Hafiz Zawawi², Agusril Syamsir² and Norizham Abdul Razak³

¹College of Graduate School, Universiti Tenaga Nasional, Jalan IKRAM - UNITEN, 43000 Kajang, Selangor, Malaysia

²Institute of Energy Infrastructure, Universiti Tenaga Nasional, Jalan IKRAM - UNITEN, 43000 Kajang, Selangor, Malaysia

³School of Aerospace Engineering, Universiti Sains Malaysia, Engineering Campus, 14300 Nibong Tebal, Pulau Pinang, Malaysia

ABSTRACT

Tapping into solar renewable energy can accelerate Malaysia's energy economy, and one of the ways to achieve this is through solar pavement technology. Solar pavement technology is an emerging field, and Malaysia, through its green policies, welcomes such innovations to promote environmental sustainability. This research investigates the use of conductive pipes for thermal energy harvesting in solar pavement collectors. Design software, Solidworks 2020, and simulation software, Ansys Fluent 19.2, were utilised to optimise the design parameters of the solar pavement collector. These parameters included the pipe materials (copper, stainless steel, and aluminium), pipe depths (30, 40, 50, 60, 70, and 80mm), and pipe spacing (70, 80, 100, 130, and 150mm). Results show that

a serpentine configuration with copper piping exhibited the highest heat efficiency, producing an outlet temperature of 54.21°C at a pipe depth of 50 mm and a centre-to-centre spacing of 80 mm. Additionally, the water flow rate of the optimised pipe design reached an acceptable value of 1.562 m/s. Stainless steel, arranged in a serpentine pattern, achieved a maximum temperature of 54.92 °C, 1.3% higher than copper in the same configuration. However, aluminium in a serpentine pattern showed a 2.9% decrease compared to stainless steel. The generated warm water has potential for household use, reducing reliance on conventional electricity

ARTICLE INFO

Article history:

Received: 13 February 2024

Accepted: 9 May 2024

Published: 21 February 2025

DOI: <https://doi.org/10.47836/pjst.33.2.02>

E-mail addresses:

aqilahrazeman@gmail.com (Nurul Aqilah Razeman)

iZarina@uniten.edu.my (Zarina Itam)

Salmia@uniten.edu.my (Salmia Beddu)

imran.najeeb@uniten.edu.my (Muhammad Imran Najeeb)

Nazirul@uniten.edu.my (Nazirul Mubin Zahari)

Daud@uniten.edu.my (Daud Mohammad)

Mhafiz@uniten.edu.my (Mohd Hafiz Zawawi)

Agusril@uniten.edu.my (Agusril Syamsir)

norizham@usm.my (Norizham Abdul Razak)

*Corresponding author

and contributing to a reduction in carbon footprint, given Malaysia's heavy reliance on fossil fuels for electricity generation.

Keywords: Outlet temperature; simulation; solar pavement collector; thermal energy harness

INTRODUCTION

Most countries rely heavily on fossil fuels, accounting for over 50% of their electricity generation. The by-products of this power generation process are greenhouse gases that form a blanket around the Earth's atmosphere, trapping the sun's heat and contributing to global warming. To mitigate dependence on fossil fuels, especially in Malaysia, embracing green renewable energy, such as solar power, emerges as the optimal solution due to its widespread accessibility. Solar energy is easily accessible across most regions in Malaysia, and the heat produced can be harnessed efficiently through innovative technologies like pavement solar collectors. A pavement solar collector extracts heat from the sun's rays and surroundings to generate electricity. The extensive coverage of roads on Earth's surface provides immense potential for embedding such heat-harvesting technologies. This approach aligns seamlessly with various aspects of global research initiatives, exemplified by The World in 2050 (TWI2050) and the United Nations Sustainable Development Goals (Figure 1).

One heat-harvesting technology is the implementation of thermoelectric generators (TEGs). These devices can be seamlessly integrated into road pavements to capture the temperature difference between the surface and subsurface. The heat gradient generated by the sun's rays and ambient heat can be efficiently converted into electricity through TEGs, contributing to sustainable energy generation. Additionally, another viable technology for harnessing heat is the use of phase-change materials (PCMs). These materials leverage latent heat, causing the bitumen in the road pavement to release or harness heat energy. Embedding PCMs in road pavement serves as thermal energy storage during the day. This stored energy can be utilised at night, balancing temperatures and serving as a source for cooling or heating in the surrounding environment. This dual functionality demonstrates the versatility and potential of incorporating innovative technologies like TEGs and PCMs into road pavements for sustainable energy solutions. In addition to harnessing heat, heat harness technology also serves to extend the life of road pavement. Studies have shown that asphalt roads experience permanent damage when temperatures exceed 70°C (Bobes-Jesus et al., 2013).

Furthermore, recent work has focused on enhancing conventional photovoltaic (PV) systems, particularly through the implementation of concentrated photovoltaic thermal (CPVT) technology (Sheikholeslami & Khalili, 2024a). For instance, Sheikholeslami (2023) utilised flat plate mirror concentrators to concentrate sunlight more effectively,

augmenting solar energy capture by incorporating multi-walled carbon nanotube (MWCNT) nanoparticles. Moreover, the author has refined the design of PV-thermal (PVT) systems through hybridisation with a thermoelectric generator (TEG). Multiple cooling system designs of PVT-TEG were developed and simulated using the finite volume method to optimise energy conversion efficiency (Sheikholeslami & Khalili, 2024b).

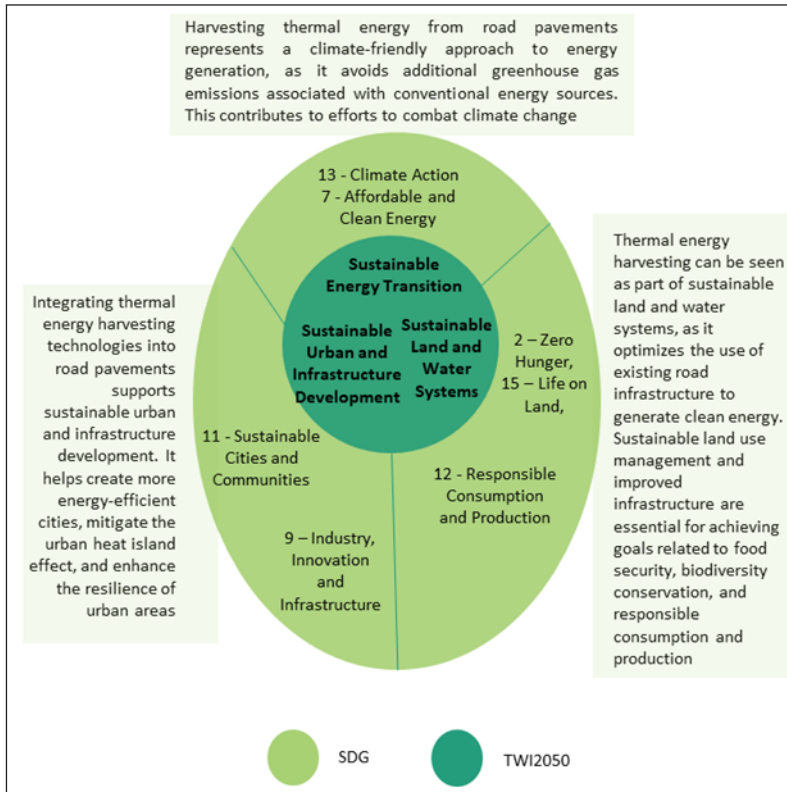


Figure 1. Solar pavement collector align with TWI2050 and SDGs

Pavement solar collectors (PSCs) represent a method of harvesting solar energy and converting it to thermal energy. Zaim et al. (2020) discovered that PSCs consist of a succession of metallic or nonmetallic pipes (such as stainless steel, copper, polyethylene, and rubber pipes) embedded in paving slabs, with an active fluid moving and accumulating thermal energy from the hot pavements. The pipes are systematically implanted in asphalt and can extract thermal energy via fluids, such as water. The asphalt transmits heat to compensate for the lower temperature of the fluid. Therefore, cool fluid is introduced while hot fluid is removed from the system.

The energy balance of an asphalt solar collector includes the following components and environments: asphalt pavement, pipes, the atmosphere, and fluids moving through

the pipe network (Vizzari et al., 2021). Heat exchange systems distribute the energy evenly across the full pavement-atmosphere interaction. Asphalt absorbs heat from the sun, transfers some heat to the surrounding air by convection and emits some of its heat into space. The heat flow causes the road's surface to heat up before its interior, a process known as conduction. Initially, conduction occurs at the asphalt-pipe junction, then convection occurs at the asphalt-fluid contact. Asphalt solar collectors have advanced further than any other road energy collection system, becoming a commonplace technology with a variety of practical uses. For instance, ICAX built a system of pipes to circulate water for heat transfer (Vizzari et al., 2021). A heat storage system is buried beneath the insulated floors of nearby buildings to store thermal energy.

Further studies were conducted by Talib et al. (2016) to investigate piping depths at different burial depths using steel piping. Six physical-model mixtures of asphalt pavement were prepared. Three models were mounted with empty steel pipes, while the others were mounted with steel pipes filled with ethylene glycol to act as heat exchanger fluid. The heat exchanger pipes were placed into the asphalt pavement at different depths. The prototypes were installed outdoors, exposed to sunlight, and connected to a data logger to determine the temperature difference within the asphalt layer. The maximum pavement depth was 150 mm, and the steel pipe was 20 mm in diameter. The findings indicated that ethylene glycol extracted the most heat at a depth of 150 mm, reaching 51.2°C.

Johnsson and Adl-Zarrabi (2020) found that altering the albedo, fluid flow rate, and pipe spacing impacted the pavement solar collectors (PSCs). The authors concluded that efficiency was raised by up to 49% by altering the albedo and flow rate. Placing pipes closely together introduces additional constraints. For instance, the bending radius of pipes cannot be excessively small, as this causes damage to the pipes due to stresses. Additionally, if multiple pipes are placed in the pavement, the load-bearing capability of the pavement could be diminished. In general, a deeper position and closer spacing between pipes result in a greater amount of generated electricity. The measured harvested energy was 245 kWh/m², with a solar efficiency of 42% (Johnsson & Adl-Zarrabi, 2020).

The thermoelectric generators (TEGs), phase change materials (PCMs), photovoltaic-thermal (PVT), and pavement solar collector (PSC) technologies mentioned possess their respective advantages and disadvantages, yet all offer significant positive aspects. Ultimately, the suitability of adopting these technologies depends largely on the specific location and environmental conditions. By carefully assessing factors such as solar irradiance levels, climate, available space, and local regulations, stakeholders can determine the most appropriate technology for maximising energy generation and addressing local needs effectively.

Based on the literature review, it is evident that the effectiveness of pipe arrangements in heat dynamics and pavement solar collector performance has not been given much

consideration. The current work involves conducting experimental and numerical analyses to determine the crucial technical specifications of the built Pavement Solar Collector (PSC) thermal performance based on temperature measurements taken in Malaysia. This work extends the experimental work done by Ahmad et al. (2018), which primarily focused on the materials of pipes using copper and rubber materials. The experimental data were used to validate the numerical modelling presented in this paper. Subsequently, the validated numerical model was employed to optimise the design parameters of the solar pavement collector. These design parameters included the choice of pipe materials (copper, stainless steel, and aluminium), varying pipe depths (ranging from 30 to 80mm) and adjusting the spaces between pipes (ranging from 70 to 150mm).

METHODOLOGY

The software used for the numerical simulation work was Ansys Fluent 19.2 and Solidworks 2020. Two models have been developed: a control sample (no embedded piping) and an asphalt pavement model with various types of piping positioned at varying depths. Figure 2 illustrates the schematic representation of the asphalt pavement model. Both types have identical dimensions of 400mm × 400mm × 100mm, and the pipes possess a diameter of 20mm. Water was employed as the fluid in the pipes, and it remained stationary throughout the simulations.

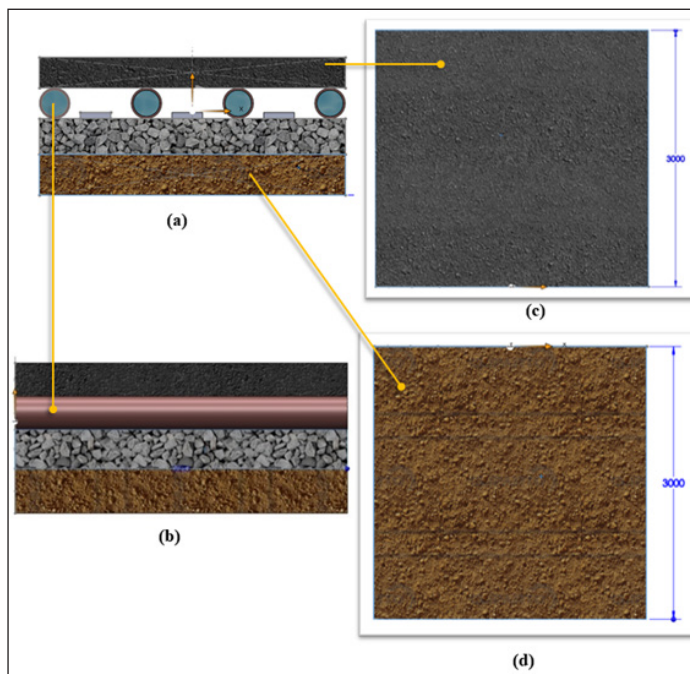


Figure 2. Asphalt pavement layer: (a) Frontal view, (b) Profile view, (c) Top course, (d) Sub-base course

The study employed the model arrangement illustrated in Figure 3. The asphalt pavement layer has been designed to have uniform properties in all directions and evaluated using the finite element method (FEM) to study the effect of temperature distribution on different surfaces of the pavement. The pipe was located at depths varying from 30 mm to 80 mm below the surface of the asphalt pavement. Two contact zones have been created: contact region 1, between the pavement and pipes, and contact region 2, between the pipes and fluid flow. Boundary conditions were established using data on material properties. Figure 3 (a–b) depicts the model with a solitary serpentine pipe, while Figure 3 (c–d) displays the model with several pipes stacked consecutively.

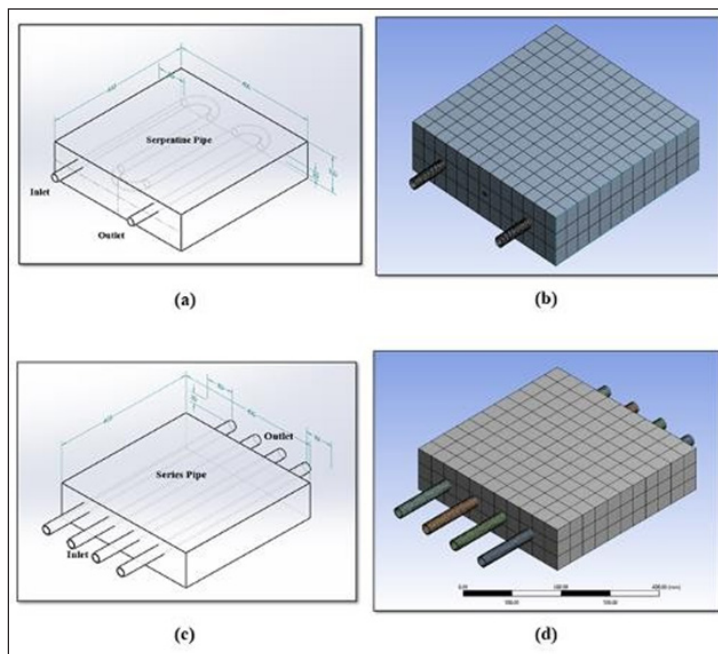


Figure 3. (a) Serpentine pipe configuration (b) Serpentine pipe mesh (c) Series pipe configuration (d) Series pipe mesh

The model was configured to account for energy, materials (fluid and solid), temperature distribution, wall shear stress between the asphalt pavement and fluid, and velocity profiles. Table 1 presents the parameters inputted into Ansys Fluent Workbench 19.2 for running the simulation.

Ahmad et al. (2018) validated the simulation setup using experimental work. According to their research, the highest temperature recorded at the outflow of the serpentine pipe was 53.5°C at a depth of 50 mm. In comparison to the current simulation results, the data shows a temperature of 54.21°C with a minimal error of 1.33%. This validation step confirms that the percentage of errors falls within an acceptable range (Adenan et al., 2023).

Table 1
Properties of pipes and concrete

Item	Parameter	Value
Copper pipe	Inlet Temperature, K (°C)	314.15 (41.00)
Stainless steel pipe	Inlet Temperature, K (°C)	317.35 (44.20)
Aluminium pipe	Inlet Temperature, K (°C)	42.90 (316.05)
	Bulk Density (kg/m ³)	2297.17
Asphalt concrete	Thermal Conductivity (W/m.K)	2.19
	Specific Heat Capacity (J/kg/K)	782.04
Normal flow	Velocity (m/s)	0.0205
Peak flow	Velocity (m/s)	0.0409

RESULTS

The investigation into thermal energy harvesting included studying each type of pipe material at various depths (30–80 mm) and pipe spacings (70–150 mm) for both serpentine and series piping configurations.

Numerical Simulation of Thermal Energy Harvesting in Serpentine Piping Systems at Various Depths

Figure 4 illustrates the relationship between the depth of embedded copper pipes, ranging from 30 mm to 80 mm below the surface pavement, and the temperature distribution. Meanwhile, Table 2 presents the different types of piping materials (copper, stainless steel, and aluminium) along with the corresponding outlet temperatures for pipe depths ranging from 30 mm to 80 mm. Figure 4(c) shows that the copper pipe located at a depth of 50 mm has the highest temperature at the outlet pipe, measuring 327.36K (54.21°C). Conversely, the lowest temperature of 326.23K (53.08°C) is observed from the pipe at a depth of 80 mm, as depicted in Figure 4(f).

Table 2
Outlet temperature of serpentine pipes at different depths and materials

Pipe material	Inlet Temperature, K (°C)	Outlet Temperature, K (°C)					
		30 mm	40 mm	50 mm	60 mm	70 mm	80 mm
Copper	315.15 (41.00)	326.33	326.80	327.36	326.55	326.71	326.23
		(53.18)	(53.65)	(54.21)	(54.21)	(53.56)	(53.08)
Stainless steel	317.35 (44.20)	326.72	327.21	328.07	327.57	326.62	326.43
		(53.57)	(54.06)	(54.92)	(54.41)	(53.47)	(53.28)
Aluminium	316.05 (42.90)	325.95	326.11	326.35	327.57	326.49	326.44
		(52.80)	(52.96)	(53.20)	(54.41)	(53.39)	(53.29)

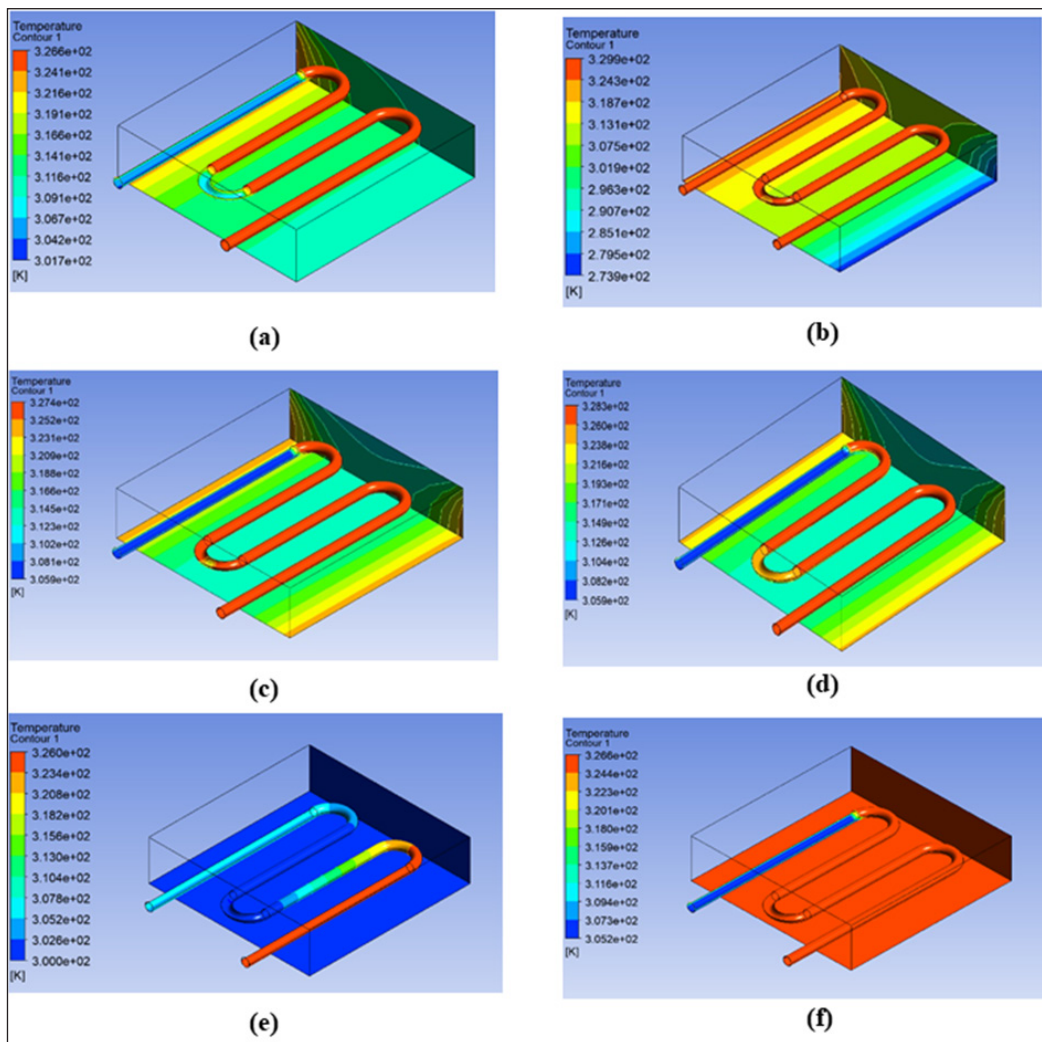


Figure 4. Simulation analysis of serpentine copper pipes at various burial depths: (a) 30 mm, (b) 40 mm, (c) 50 mm, (d) 60 mm, (e) 70 mm, and (f) 80 mm

These findings align with the previous study conducted by Ahmad et al. (2018), which determined that the upper portion of the asphalt pavement collects the most solar energy until the centre depth, while the lower portion collects less. Placing copper pipes in a serpentine arrangement, embedded 50 mm deep in the asphalt pavement, has the potential to reach a maximum temperature of 53.5°C at the outlet pipe (Ahmad et al., 2018).

Figure 5 illustrates the serpentine configuration of stainless-steel pipes positioned at depths ranging from 30 mm to 80 mm below the top surface of the pavement. Similar to copper piping, the findings indicate that the highest heat extraction from the outlet pipe was 328.07K (54.92°C) at a pipe depth of 50 mm (Figure 5(c)), while the lowest was

326.43K (53.28°C) at a depth of 80 mm, as shown in Figure 5(f). Field monitoring of six asphalt slab samples with stainless steel pipes placed at depths of 50 mm, 100 mm, and 150 mm revealed that the highest heat extraction occurred at 50 mm, reaching a temperature of 53.2°C. Increasing the heat applied to the asphalt surface can significantly raise the temperature. As the asphalt pavement's ability to absorb radiant heat increases, it results in a greater accumulation of heat in the thermal block.

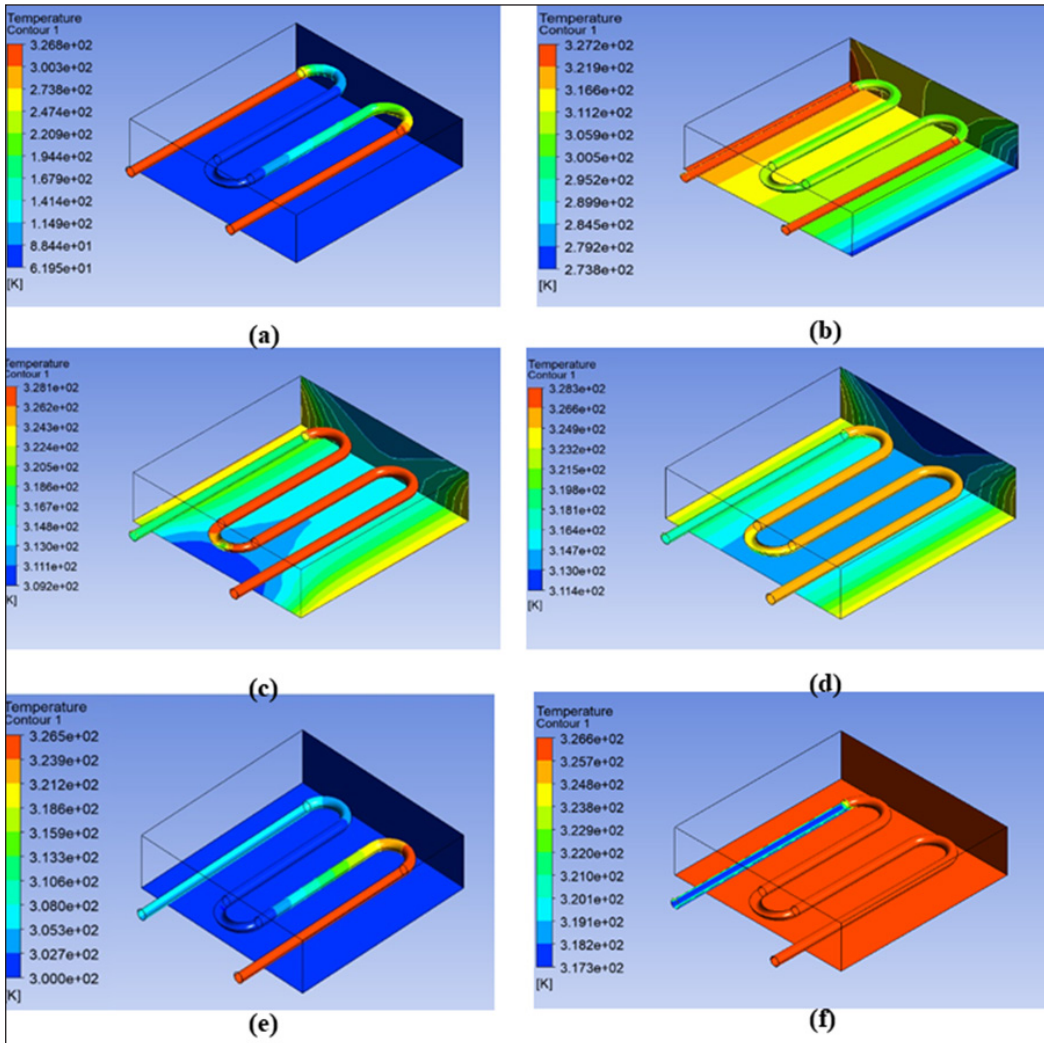


Figure 5. Simulation analysis of serpentine stainless-steel pipes at various burial depths: (a) 30 mm, (b) 40 mm, (c) 50 mm, (d) 60 mm, (e) 70 mm, and (f) 80 mm

Figure 6 presents an analysis of the serpentine configuration of aluminium pipes, with pipe depths comparable to those of copper and stainless steel pipes. Figure 6(e) illustrates

that the aluminium pipe achieved the highest heat extraction from the outlet at a depth of 70 mm, with a temperature of 326.54K (53.39°C). Aluminium reached its lowest outlet temperature of 325.95K (52.80°C) at a depth of 30 mm, as depicted in Figure 6(a). The hot air is expelled through the central aluminium pipe in the top channel of the design model. Temperature measurements of incoming and exiting air were conducted using a thermocouple. The highest recorded outlet temperature was 55°C, while the minimum recorded during morning observations was 42°C.

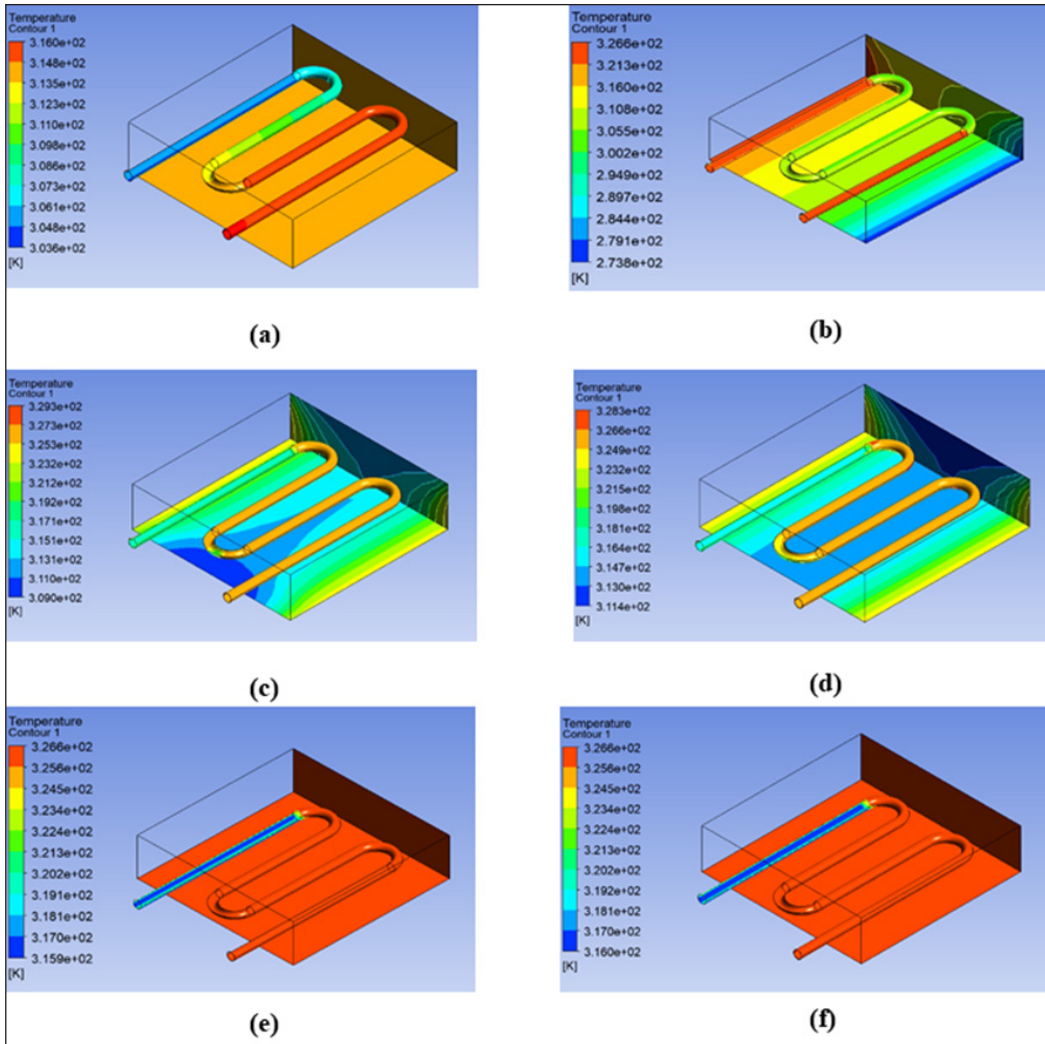


Figure 6. Simulation analysis of serpentine aluminium pipes at various burial depths: (a) 30 mm, (b) 40 mm, (c) 50 mm, (d) 60 mm, (e) 70 mm, and (f) 80 mm

Figure 7 presents tabulated data for the outlet temperature of the serpentine piping system with various materials versus piping depth in graphical form. The graph

demonstrates an increasing outlet temperature at intermediate piping depths, followed by a decrease at the deepest piping depths for all materials. As depicted in Figure 7, the aluminium pipe at a depth of 30 mm exhibits the lowest outlet temperature at 325.95K (52.80°C). In comparison, the stainless-steel pipe shows the highest outlet temperature at 328.07K (54.92°C) at a depth of 50 mm. The results indicate that aluminium pipes show the lowest outlet temperature at a depth of 50 mm compared to copper and stainless steel pipes, with temperatures of 327.36K (54.21°C) and 328.07K (54.92°C), respectively.

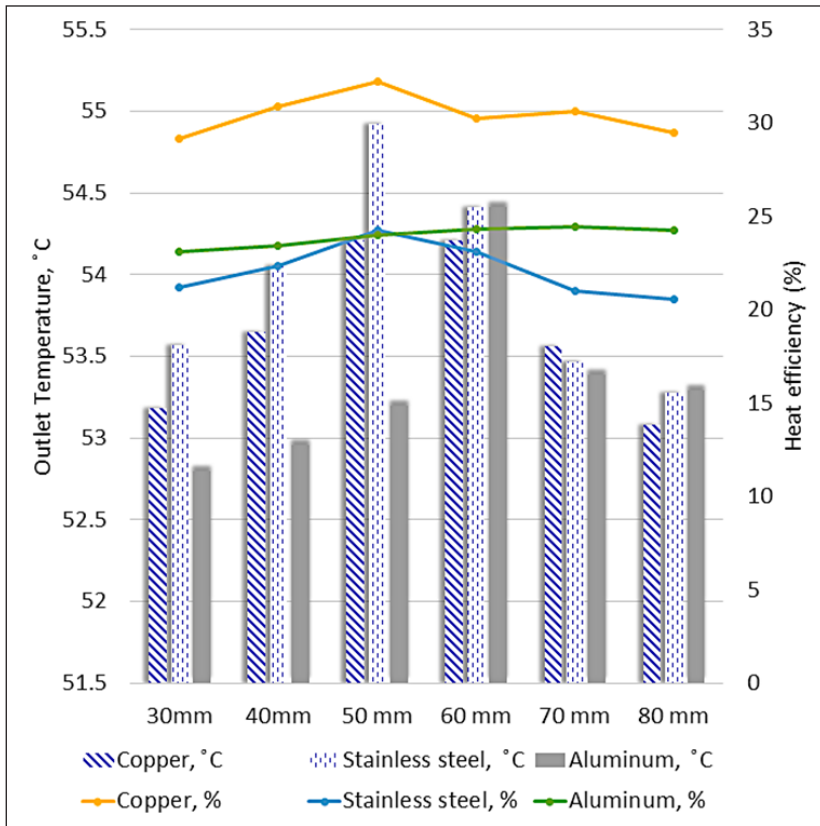


Figure 7. Outlet temperature and heat efficiency of various serpentine pipe materials at different burial depths

Furthermore, Figure 7 illustrates the graphical representation of tabulated data comparing the heat efficiency of serpentine pipes at different depths. Copper pipes achieved the highest heat efficiency of 32.22% at a depth of 50 mm, whereas stainless steel pipes had the lowest heat efficiency of 20.54% at a depth of 80 mm. Notably, the thermal efficiency of even the most optimal heat systems typically ranges around 50% (Vizzari et al., 2021). Therefore, in this study, copper pipes located at a depth of 50 mm were selected as the material for the piping system due to their demonstrated maximum

heat efficiency. Additionally, copper pipes possess exceptional thermal conductivity, which ensures efficient heat transfer in both the liquid and gas phases. Their passive operation further contributes to their reliability, making them an integral and dependable component of the thermal management system.

Numerical Simulation of Thermal Energy Harvesting in Series-arrangement Piping Systems at Various Depths

Figures 8, 9 and 10 illustrate the relationship between the depths of copper, stainless steel, and aluminium pipes buried in the surface pavement, ranging from 30 mm to 80 mm, and

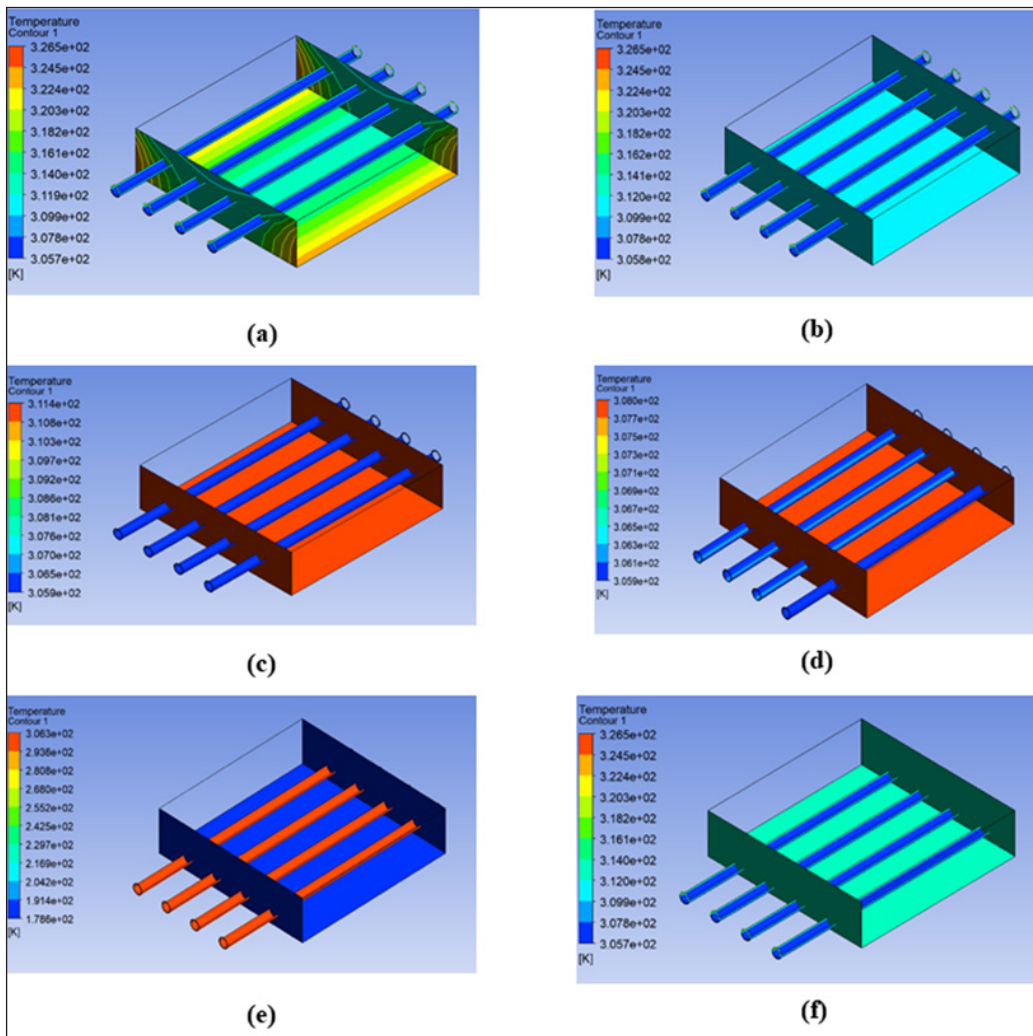


Figure 8. Simulation analysis of series copper pipes at various burial depths: (a) 30 mm, (b) 40 mm, (c) 50 mm, (d) 60 mm, (e) 70 mm, and (f) 80 mm

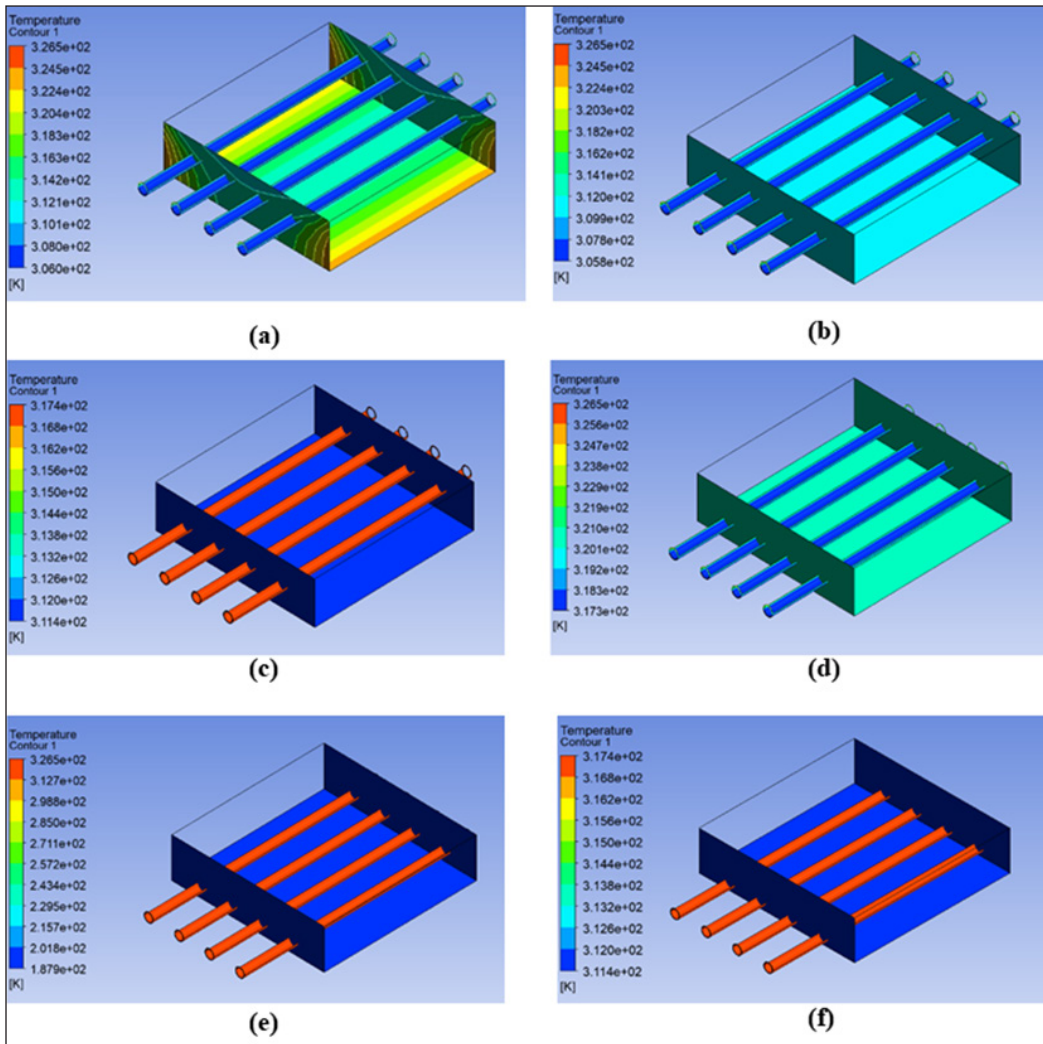


Figure 9. Simulation analysis of a series of stainless-steel pipes at various burial depths: (a) 30 mm, (b) 40 mm, (c) 50 mm, (d) 60 mm, (e) 70 mm, and (f) 80 mm

the temperature distribution. Table 3 provides a concise overview of temperatures at the inlet and outlet points for various depths of piping materials. Stainless steel pipes exhibited the highest heat extraction at the outlet pipe, measuring 317.62K (44.47°C) at a depth of 70 mm. In contrast, copper pipes showed the lowest heat extraction, with the outlet temperature measuring 305.94K (32.79°C) at a depth of 50 mm. The arrangement of pipes has a significant impact on the heat temperature at the outlet of the pavement solar collector.

Table 3
Outlet temperatures for series pipes at varying depths and materials

Pipe material	Inlet Temperature, K (°C)	Outlet Temperature, K (°C)					
		30 mm	40 mm	50 mm	60 mm	70 mm	80 mm
Copper	314.15 (41.00)	305.95 (32.80)	305.95 (32.80)	305.94 (32.79)	306.15 (33.00)	306.34 (33.19)	305.95 (32.80)
Stainless steel	317.35 (44.20)	317.35 (44.20)	317.36 (44.21)	317.37 (44.22)	317.43 (44.28)	317.62 (44.47)	317.35 (44.20)
Aluminium	316.05 (42.90)	316.05 (42.90)	316.05 (42.90)	316.06 (42.91)	316.46 (43.31)	316.33 (43.18)	316.05 (42.90)

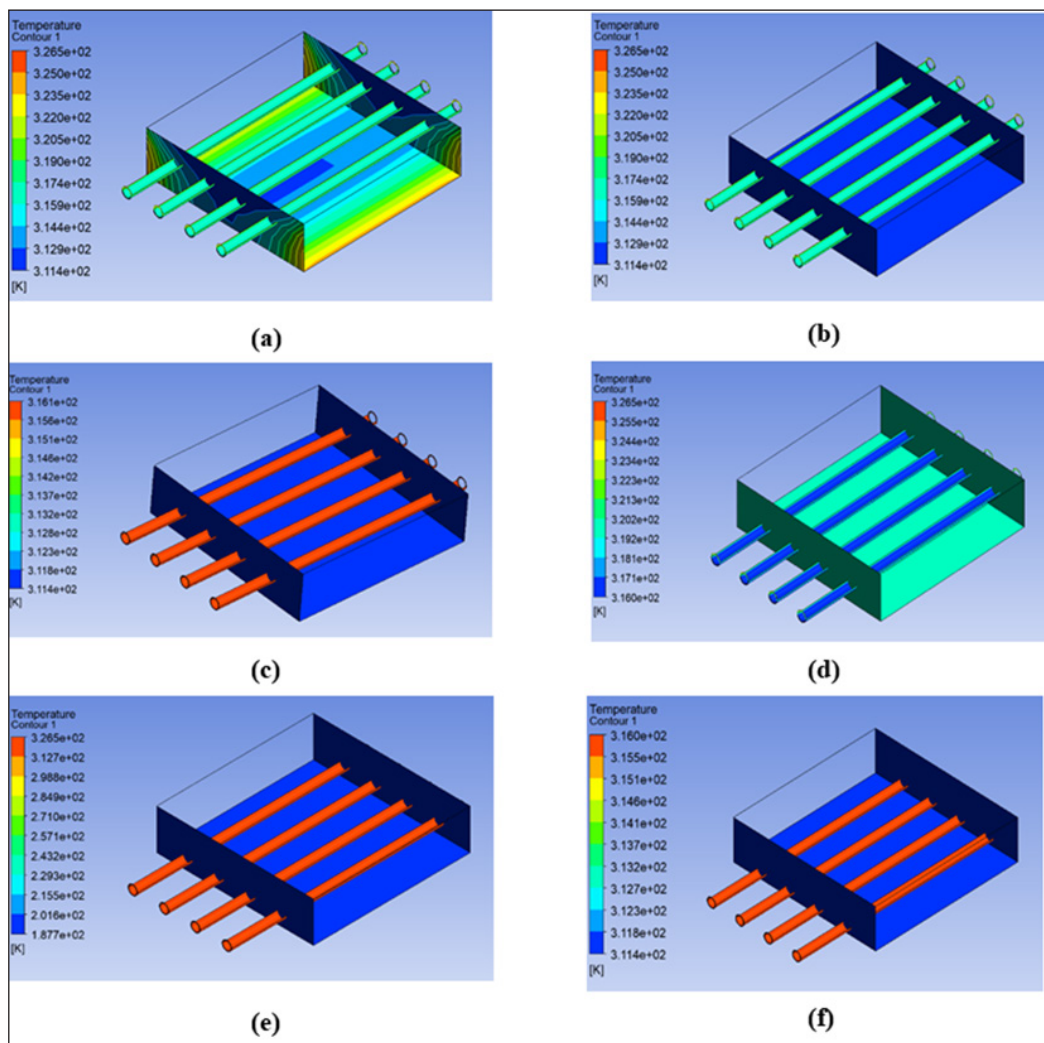


Figure 10. Simulation analysis of a series of aluminium pipes at various burial depths: (a) 30 mm, (b) 40 mm, (c) 50 mm, (d) 60 mm, (e) 70 mm, and (f) 80 mm

Figure 11 presents a visual representation of the temperature outlet of the series piping system at various piping depths. According to the data in Table 3, the analysis reveals that the stainless-steel pipe consistently exhibits the maximum outlet temperature for each depth. In contrast, the copper pipe consistently shows the lowest outlet temperature. Pipes are widely recognised as a cost-effective method for fluid transportation and are commonly used for water, fuel, and other substances. However, in the case of the series pipe arrangement studied here, the temperature at the outlet pipe closely approximated the inlet temperature, except for the copper pipe.

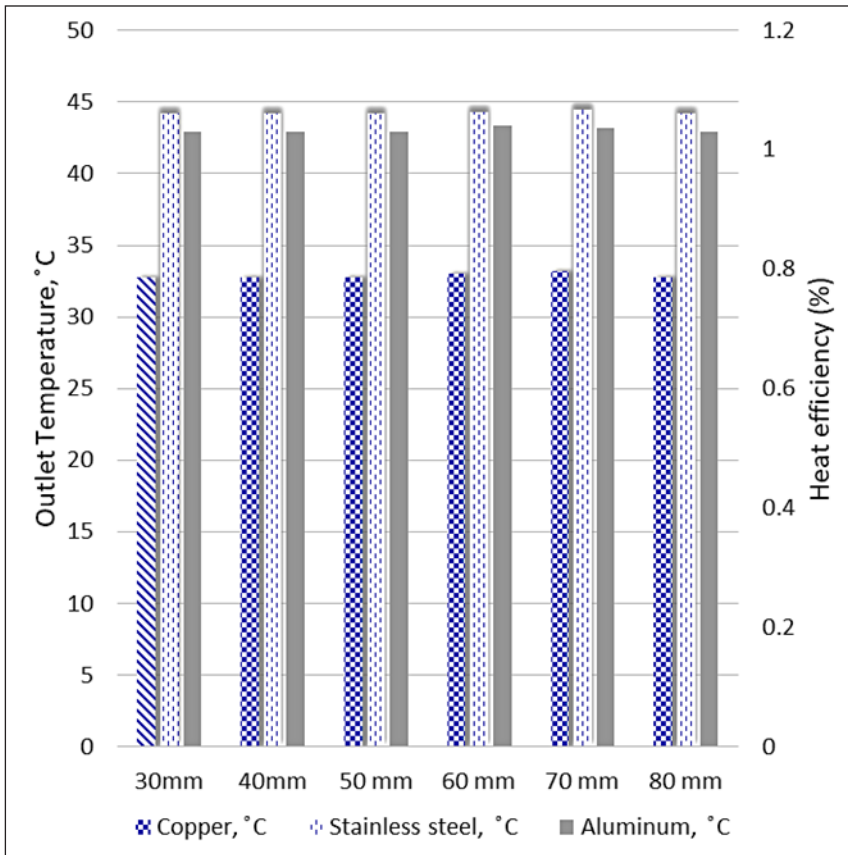


Figure 11. Outlet temperature and heat efficiency of various series pipe materials at different burial depths

A study by Santos-Ruiz et al. (2020) investigates head loss coefficients for local losses, fittings, valves, and friction coefficients for distributed losses along the pipe. The research has indicated the friction caused by the pipe's interior wall (Santos-Ruiz et al., 2020). In contrast to the serpentine pipe, the series pipe did not exhibit a heat efficiency value below 50%, which is typically considered optimal (Pietzonka & Seifert, 2018). Therefore, based on the comparison between the serpentine and series pipes, it can be inferred that the

serpentine arrangement is the optimal choice for thermal energy harvesting on pavements. It has achieved the highest temperature outlet, with the copper pipe reaching 54.21°C at a depth of 50 mm and the stainless-steel pipe reaching 44.47°C at a depth of 70 mm.

DISCUSSION

Discussion on Optimising Depth, Spacing, and Pipe Arrangement

Figure 12 compares the outlet temperatures between serpentine and series pipes for three different materials: copper, stainless steel, and aluminium. The results consistently show that the serpentine pipe achieves higher output temperatures compared to the series pipe

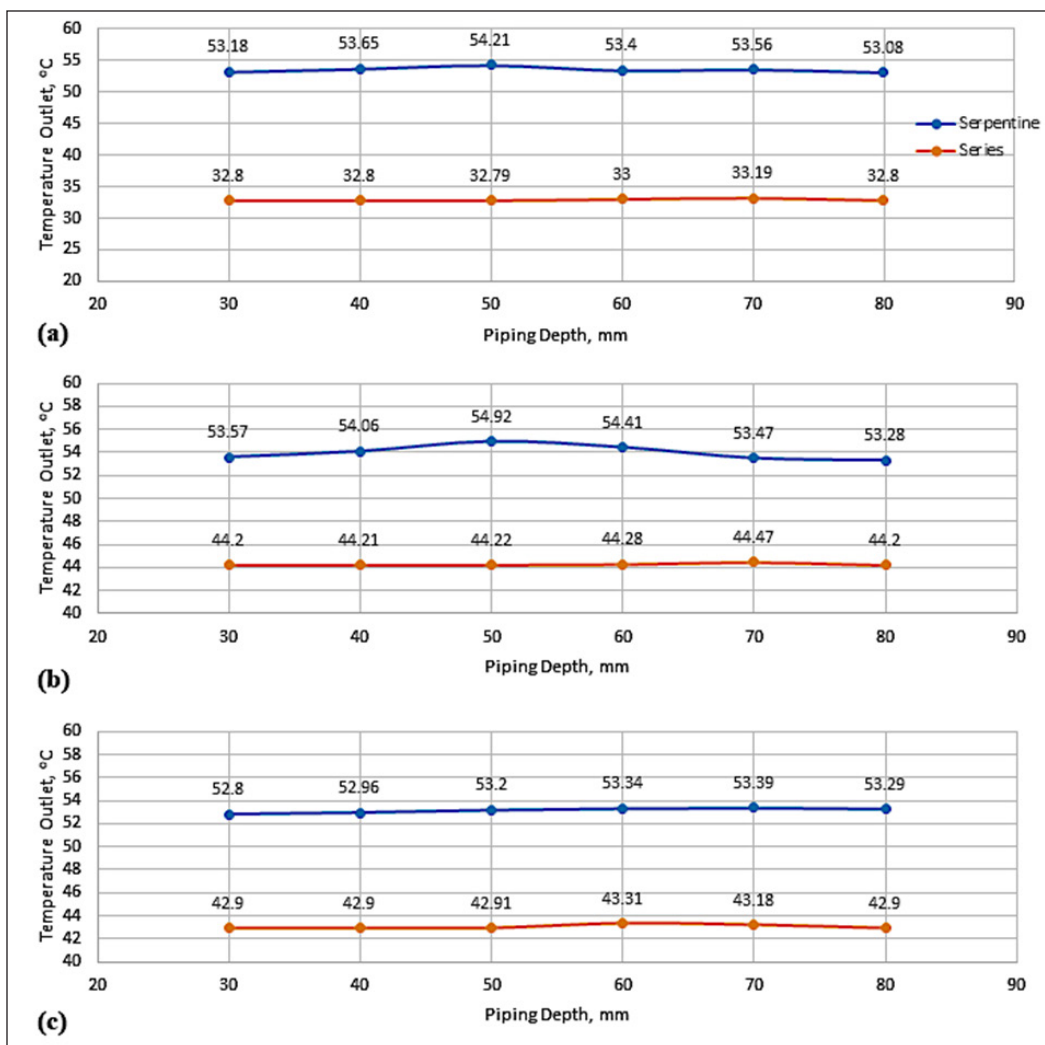


Figure 12. Serpentine and series pipe outlet temperatures for (a) copper pipe, (b) stainless steel pipe, (c) aluminium pipe

for all types of piping materials. While stainless steel pipes exhibit the highest temperatures among the materials tested and are widely used in various industries due to their superior corrosion resistance, formability, and weldability, their use may be limited by factors such as low hardness, poor tribological characteristics, and susceptibility to localised corrosion under certain conditions (Pietzonka & Seifert, 2018).

Furthermore, Figure 12 compares the highest temperature readings at the outlets for both piping systems. The serpentine pipe layout consistently shows higher outlet temperatures for all piping materials compared to the series pipe arrangement (aluminium at 23.27%, stainless steel at 23.5%, and copper at 64.27%). The maximum temperature of 54.92 °C is achieved by stainless steel in a serpentine pattern, 1.3% higher than copper's second-highest temperature of 54.21 °C in the same arrangement. In contrast, aluminium in a serpentine pattern exhibits a 2.9% decrease compared to stainless steel.

Using a serpentine copper pipe at a depth of 50 mm results in the highest heat extraction value from the outlet pipe. Figure 13 presents the data and graphical trends of pipe spacing versus outlet temperature for copper pipes arranged in a serpentine pattern at a depth of 50 mm. The results highlight that serpentine copper pipes positioned 50 mm below the

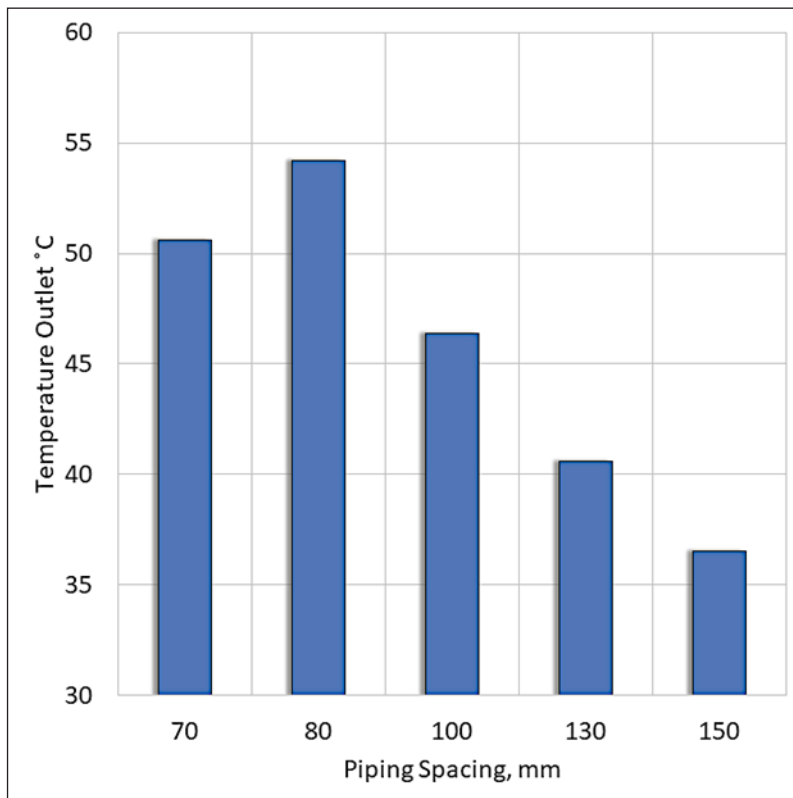


Figure 13. Relationship between outlet temperature and pipe spacing

surface show excellent thermal harvesting potential by achieving the highest heat efficiency. Additionally, it was determined that the optimal pipe spacing is 80 mm, resulting in an outlet temperature of 327.36K (54.21°C). The investigation of the new multi-control heating system emphasised the crucial role of pipe spacing in determining heat loss and transfer efficiency between pipes (Xu et al., 2021).

Further examination of the optimal pipe configuration presented in this study is essential to verifying the water flow rate inside the pipe, as depicted in Figure 14. The velocity at the inlet pipe was adjusted to 0.0409 m/s, following established guidelines for domestic usage. The velocity at the outlet pipe was measured at 1.562 m/s, with the outlet temperature recorded at 327.36K (54.21 °C). This velocity range falls within the acceptable guideline range of 1 to 2 m/s for pipe flow rates (Michael Smith Engineers, 2024).

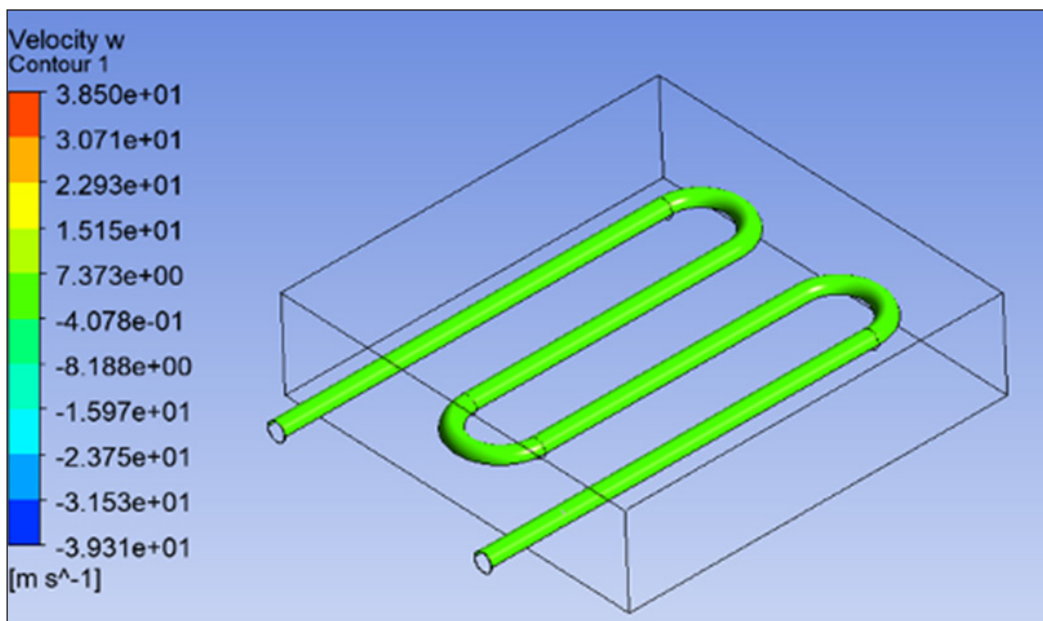


Figure 14. Uniform flow rate in an optimised serpentine pipe

CONCLUSION

The study examined thermal performance using different pipe materials (copper, stainless steel, and aluminium) embedded at various depths (30 mm to 80 mm) beneath the surface pavement. Different pipe spacings (70 mm to 150 mm centre-to-centre) were also analysed. Results show copper piping in a serpentine pattern as the optimal choice for thermal energy harvesting in pavement, achieving the highest heat efficiency (32.22%) and outlet temperature (327.35K or 54.21°C). This arrangement's superior performance is attributed to its larger surface area, which enables greater heat absorption compared to

other configurations. For optimal performance, pipes should be placed 50 mm below the pavement surface and spaced 80 mm apart. The achieved flow rate of 1.562 m/s for water circulation meets household demands, with the inlet pipe's flow rate set at 0.0409 m/s. These findings underscore the potential for reducing reliance on fossil fuels, emphasising environmental and economic benefits. Implementing pavement solar collectors can significantly enhance sustainability and economic viability in Malaysia, promoting innovation for a greener future.

ACKNOWLEDGEMENTS

The authors would like to extend their gratitude to the Innovation & Research Management Centre of Universiti Tenaga Nasional for supporting this research, FRGS 2020-1 Grant No. FRGS/1/2020/TK0/UNITEN/02/18 for providing the necessary funding, and BOLD HICOE Grant No. J510050002/HICOE05 for covering the journal publication fees. Special thanks are also given to all the contributors involved in this project.

REFERENCES

- Adenan, M. S., Prajadhiana, K. P., Mat, M. F., Manurung, Y. H. P., Ishak, D. P., Adesta, E. T., Colditz, P., Dizon, J. R. C., Mohamed, M. A., & Jamaludin, M. F. (2023). Chained simulation of the welding-forming process in analysing press force and geometrical deformation using non-linear numerical computation with experimental validation. *The International Journal of Advanced Manufacturing Technology*, 125(9–10), 4631–4646. <https://doi.org/10.1007/s00170-023-11069-x>
- Ahmad, M., Itam, Z. B., Beddu, S., Alanimi, F. B. I., & Soanathan, S. A. P. (2018). A determination of solar heat collection in serpentine copper and rubber pipe embedded in asphalt pavement using finite element method. *Journal of Engineering and Applied Sciences*, 13(1), 181–189. <https://doi.org/10.3923/jeasci.2018.181.189>
- Bobes-Jesus, V., Pascual-Muñoz, P., Castro-Fresno, D., & Rodriguez-Hernandez, J. (2013). Asphalt solar collectors: A literature review. *Applied Energy*, 102, 962–970. <https://doi.org/10.1016/j.apenergy.2012.08.050>
- Johnsson, J., & Adl-Zarrabi, B. (2020). A numerical and experimental study of a pavement solar collector for the northern hemisphere. *Applied Energy*, 260, Article 114286. <https://doi.org/10.1016/j.apenergy.2019.114286>
- Michael Smith Engineers. (2024). *Useful information on pipe velocity*. <https://www.michael-smith-engineers.co.uk/resources/useful-info/pipe-velocity>
- Pietzonka, P., & Seifert, U. (2018). Universal trade-off between power, efficiency, and constancy in steady-state heat engines. *Physical Review Letters*, 120(19), Article 190602. <https://doi.org/10.1103/PhysRevLett.120.190602>
- Santos-Ruiz, I., López-Estrada, F. R., Puig, V., & Valencia-Palomo, G. (2020). Simultaneous optimal estimation of roughness and minor loss coefficients in a pipeline. *Mathematical and Computational Applications*, 25(3), Article 56. <https://doi.org/10.3390/mca25030056>

- Sheikholeslami, M. (2023). Numerical investigation for concentrated photovoltaic solar system in existence of paraffin equipped with MWCNT nanoparticles. *Sustainable Cities and Society*, 99, Article 104901. <https://doi.org/10.1016/j.scs.2023.104901>
- Sheikholeslami, M., & Khalili, Z. (2024a). Energy management of a concentrated photovoltaic–thermal unit utilizing nanofluid jet impingement in existence of thermoelectric module. *Engineering Applications of Computational Fluid Mechanics*, 18(1), Article 2297044. <https://doi.org/10.1080/19942060.2023.2297044>
- Sheikholeslami, M., & Khalili, Z. (2024b). Environmental and energy analysis for photovoltaic-thermoelectric solar unit in existence of nanofluid cooling reporting CO₂ emission reduction. *Journal of the Taiwan Institute of Chemical Engineers*, 156, Article 105341. <https://doi.org/10.1016/j.jtice.2023.105341>
- Talib, S. H. A., Hashim, S. I. N. S., Beddu, S., Maidin, A. F., & Abustan, M. S. (2017). Heat lump in different pavement layer using ethylene glycol as a solar heat collector. In *MATEC Web of Conferences* (Vol. 87, p. 01015). EDP Sciences. <https://doi.org/10.1051/mateconf/20178701015>
- Vizzari, D., Genesseeaux, E., Lavaud, S., Bouron, S., & Chailleux, E. (2021). Pavement energy harvesting technologies: A critical review. *RILEM Technical Letters*, 6, 93–104. <https://doi.org/10.21809/rilemtechlett.2021.131>
- Xu, Q., Wang, K., Zou, Z., Zhong, L., Akkurt, N., Feng, J., Xiong, Y., Han, J., Wang, J., & Du, Y. (2021). A new type of two-supply, one-return, triple pipe-structured heat loss model based on a low temperature district heating system. *Energy*, 218, Article 119569. <https://doi.org/10.1016/j.energy.2020.119569>
- Zaim, E. H., Farzan, H., & Ameri, M. (2020). Assessment of pipe configurations on heat dynamics and performance of pavement solar collectors: An experimental and numerical study. *Sustainable Energy Technologies and Assessments*, 37, Article 100635. <https://doi.org/10.1016/j.seta.2020.100635>

Determination of Optimal Water Requirement for Sweet Corn Crop Based on Meteorological Data and Plant Growth Parameters

Noorellimia Mat Toridi^{1,2*}, Muhammad Maleq Isqandar Nor Jalal¹,
Aimrun Wayayok^{1,2} and Mohamed Azwan Mohamed Zawawi^{1,2}

¹Department of Biological and Agricultural Engineering, Faculty of Engineering, Universiti Putra Malaysia, 43400 UPM, Serdang, Selangor, Malaysia

²Smart Farming Technology Research Centre, Faculty of Engineering, Universiti Putra Malaysia, 43400 UPM, Serdang, Selangor, Malaysia

ABSTRACT

Maize (*Zea mays* L.), or corn, is the world's leading cereal crop and ranks third in importance after rice and wheat. It is a primary food source for humans and livestock and a raw material in various industries. To reduce dependence on corn imports, Malaysia has initiated large-scale local cultivation. However, the maize industry faces challenges from waterlogging and water scarcity due to the tropical climate, which causes droughts and floods, impacting maize production. This study aims to improve crop water requirement (CWR) estimations for maize using CROPWAT, considering growth stages and soil variability, and validate irrigation management strategies. Based on 30 years of climatic data from MetMalaysia, evapotranspiration (ET_c) was estimated using CROPWAT V8. Experimental plots with four irrigation water application (IWA) treatments were used to validate ET_c : T1 (50% ET_c), T2 (75% ET_c), T3 (100% ET_c), and T4 (125% ET_c). Crop growth parameters were assessed at four growth stages: plant height, stem diameter, shoot fresh weight, and kernel moisture. Results showed T4 (451.07 mm/season) had the highest growth rate and met all hybrid corn growth standards set by the Department of Agriculture, Ministry of Agricultural and Food Security (MAFS). In contrast, T3 (100% ET_c) was insufficient for sweet corn, failing to meet several standards. Thus, T4 (125% ET_c) proved the most effective IWA practice, particularly for areas within a 30 km radius of the Subang weather station.

ARTICLE INFO

Article history:

Received: 1 March 2024

Accepted: 7 October 2024

Published: 21 February 2025

DOI: <https://doi.org/10.47836/pjst.33.2.03>

E-mail addresses:

noorellimia@upm.edu.my (Noorellimia Mat Toridi)

maleqisqandar@gmail.com (Muhammad Maleq Isqandar Nor Jalal)

aimrun@upm.edu.my (Aimrun Wayayok)

mohdazwan@upm.edu.my (Mohamed Azwan Mohamed Zawawi)

*Corresponding author

Keywords: Corn, crop water requirement, CROPWAT, evapotranspiration, growth parameters

INTRODUCTION

According to information from the Malaysia Department of Agriculture, the production

cost of maize in Malaysia was \$84.00 per ton in 2012. While global demand for maize was on the rise, there was uncertainty about whether a future supply could meet the growing demand. Increasing imported maize prices raised economic concerns in Malaysia, as highlighted by Soleymani and Shahrajabian (2018). The government acknowledged the difficulties faced by the industry, including constraints such as limited arable land, unfavorable weather conditions for corn cultivation and water scarcity. The high water requirements, along with susceptibility to drought and heat, were negatively impacting corn productivity.

In Malaysia, both droughts and floods further complicate agricultural production. Droughts, often associated with the Southwest Monsoon, exacerbate water scarcity, while floods, particularly during the Northeast Monsoon, can damage crops and disrupt farming. These weather extremes, driven by Malaysia's tropical climate, are making it increasingly difficult to maintain stable maize production.

Water scarcity, exacerbated by climate change and competition from various sectors, was a significant barrier to maize cultivation in non-irrigated areas (Song et al., 2010). This scarcity restricted agricultural growth and reliability. It became crucial to accurately determine crop water requirements to mitigate these issues. However, the current estimation methods pose challenges for water utilities' distribution systems, leading to uncertainty and the potential need for unnecessary infrastructure expansion.

Crop Water Requirement (CWR), also known as crop evapotranspiration (ET_c), is the amount of water a specific crop needs over its entire growing season to meet its evaporation and transpiration needs. The reference evapotranspiration (ET_o) is often used as a basis, and crop coefficients (K_c) are applied to adjust ET_o for specific crops and their growth stages. These coefficients play a crucial role in accommodating the diverse water requirements of different crops throughout their growth cycles. In their study, Gamal et al. (2022) utilize an energy balance approach to estimate ET, where latent heat exhibits a similar pattern to daily ET observed at research stations. Concurrently, the determination of crop coefficients (K_c) through unmanned aerial vehicle (UAV) remote sensing, as exemplified in the study by Parmar et al. (2023) and machine learning (ML) techniques, as discussed by Shao et al. (2023), has proven to be a viable approach for estimating cumulative evapotranspiration (ET) at various growth stages.

Various methods exist for estimating crop evapotranspiration (ET_c). In the study by Hong et al. (2022), the evapotranspiration of tomatoes was determined using the water balance method (ET_c), which includes irrigation as part of the water balance. Jie et al. (2022) provide a quantitative analysis of agricultural water requirements under different probabilities, employing a Copula function–Monte Carlo method (CFMC). Meanwhile, the SIMDual K_c model, introduced by Xuan et al. (2021), computes daily crop evapotranspiration (ET_c) by incorporating soil evaporation (E_s) and transpiration (Tr),

employing a soil water balance approach and a dual K_c method, introduced the SIMDual K_c model, which calculates daily crop ET_c by taking into account both E_s and T_r , using the soil water balance and a dual K_c method.

Recent research has brought into focus the intricate and interconnected nature of estimating crop water requirements (CWR) through tools like CROPWAT. Ruan et al. (2020) illustrated how the diminishing water resources in the basin have exacerbated water stress in the SDB, while sensitivity analysis emphasized that fluctuations in CWR are primarily linked to climate change, a point reinforced by both Nie et al. (2023) and Saeed et al. (2021). They emphasize the necessity of implementing adaptable irrigation approaches that respond effectively to changing climatic conditions, with CROPWAT as a versatile tool for managing water resources. Furthermore, (Wang et al., 2020) have highlighted the geographical disparities in CWR, wherein ET_c exhibited distinctive patterns compared to effective rainfall in specific geographic regions.

Meanwhile, Feng et al. (2023) have highlighted the significance of soil structure in determining crop water requirements. This finding underscores the need for CROPWAT users to integrate soil properties into their models and irrigation plans, recognizing that soil type plays a crucial role in influencing CWR. On the other hand, Gabr (2022) provides insights into irrigation efficiency when water resources are available. Integrating knowledge about soil properties and selecting appropriate irrigation methods can lead to more accurate CWR estimation and irrigation planning.

Although there has been considerable effort to determine crop water requirements using models like CROPWAT, more effective water management practices are needed for maize due to its high water needs and sensitivity to drought and heat, which reduce productivity. Current methods, such as crop evapotranspiration (ET_c), often have difficulty accurately predicting water needs across various growth stages and conditions. While advancements in remote sensing, machine learning, and models like SIMDual K_c and CROPWAT have improved estimations by accounting for factors like soil evaporation, transpiration, soil properties, and climate, these methods have not yet been fully applied to practical irrigation management, especially considering geographic and soil differences.

Therefore, the objectives of this study are (1) to improve the accuracy of CWR estimations for maize by integrating CROPWAT to account for variability in growth stages and soil properties and (2) to validate practical irrigation management strategies that utilize the refined CWR estimations through the experimental site.

MATERIALS AND METHODS

Overview of Methodology

Our primary goal is to improve the accuracy of CWR estimations for maize by integrating CROPWAT to account for variability in growth stages and soil properties. Based on

extensive prior research and comparative analysis, one of the most effective methods for estimating this requirement is utilizing FAO-CROPWAT 8.0. This process necessitates the inclusion of vital parameters, including climatic data, crop specifics and soil information. Concerning climatic data, these crucial values were sourced from the nearest weather station situated in Subang, Petaling, Selangor.

Simultaneously, crop-related data, such as crop coefficient at various growth stages, growth rates and yield reduction percentages, were obtained from secondary sources via an extensive literature review. Furthermore, soil data, encompassing soil texture type, were gathered through soil sampling analysis employing the sieve method. Upon the completion of this extensive data collection, the crop water requirement (ET_c) was calculated using the Penman-Monteith method within the CROPWAT 8.0 framework.

The second objective is to validate practical irrigation management strategies that utilize the refined CWR estimations through the experimental site. To achieve this, we conducted a Randomized Complete Block Design (RCBD) experiment at the Ladang 15 nursery greenhouse within the Faculty of Agriculture, UPM. Based on the estimated crop water requirement determined by CROPWAT, four different IWA (Irrigation Water Application) designs were applied to seven replicates of sweet corn, resulting in a total of 28 replications. These IWA treatments were designated as follows: T1 = 50% of the simulated ET_c , T2 = 75% of the simulated ET_c , T3 = 100% of the simulated ET_c and T4 = 125% of the simulated ET_c .

Throughout the growth period from March to June, various plant growth parameters such as the number of leaves, leaf length, plant height, stem diameter and the size or weight of the yield produced were meticulously recorded to analyze growth rates under different treatment conditions. Finally, the growth parameters for each distinct treatment were subjected to analysis using IBM SPSS Statistics (Version 23) via one-way analysis of variance (ANOVA) and Tukey post hoc test to ascertain the relationship between the quantity of IWA and the observed growth parameters. The study's flowchart in Figure 1 illustrates the research process.

Study Area

The experiment took place during a single growing season, starting in March 2023, at the Ladang 15 greenhouse in the Faculty of Agriculture at Universiti Putra Malaysia, situated in Selangor, Malaysia (Figure 2). The geographic coordinates of the location are approximately 2°59'11"N latitude and 101°44'13"E longitude. As per the 2023 climate data for Selangor, Malaysia, the area experiences tropical humid conditions. Selangor is known for its warm climate, with an average daily high temperature of 33°C throughout the year, providing favorable conditions for outdoor activities with an average water temperature of 29°C. The region receives most of its precipitation between April and December.

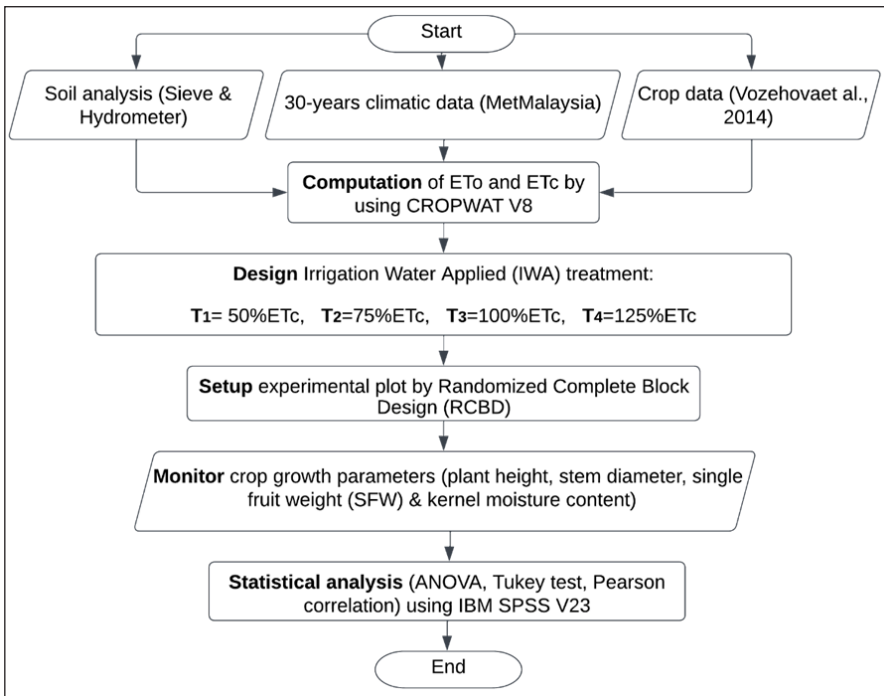


Figure 1. The flowchart of the study

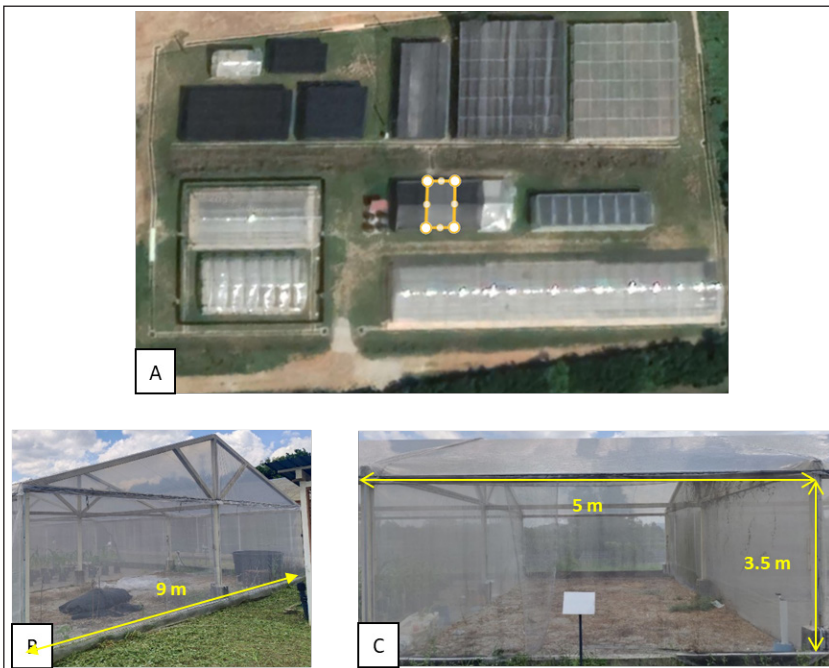


Figure 2. The greenhouse at Nursery of Ladang 15, Faculty of Agriculture, UPM. The top view of the greenhouse was obtained from Google Earth (A). The side and front view with dimensions (B, C)

Determination of Crop Water Requirement

The utilization of water by crops exhibited a direct connection to crop evapotranspiration, commonly referred to as ET_c . The crop's water use, ET_c , could be determined by multiplying the reference ET_o by a crop coefficient, K_c . The CROPWAT 8.0 model had the capacity to calculate daily ET_c , provided that the necessary climatic, soil and crop data were also available.

It includes climatic data, such as temperature, rainfall, wind speed and humidity, which are crucial for calculating reference evapotranspiration (ET_o). Additionally, crop-specific data is required, such as the type of crop, planting dates, growth stages, crop coefficients and potential yield. Soil data, encompassing soil type, texture, infiltration rates and root zone depth, is also necessary to account for the soil's water-holding capacity.

Climatic Data

In the estimation of crop water requirements within CROPWAT, the software considers vital climatic data. It encompasses essential meteorological parameters such as temperature, precipitation, wind speed and humidity. These climatic factors play a fundamental role in the calculation of reference evapotranspiration (ET_o), a key component in determining a crop's water needs. Data on precipitation, maximum and minimum temperatures, relative humidity, wind speed and sunshine duration, as displayed in Table 1, were gathered from the Subang Jaya weather station during the period spanning from 1993 to 2022.

Table 1

Average climate characteristics from 1993–2022 recorded by Subang Jaya weather, Department of Meteorology Malaysia (MetMalaysia)

Month	Min. Temp. (°C)	Max. Temp. (°C)	Humidity (%)	Wind speed (km/day)	Sunshine (hours)
January	24.0	32.6	78	120	6.1
February	24.1	33.4	77	129	6.6
March	24.6	33.7	78	137	6.7
April	24.8	33.7	80	136	6.6
May	25.1	33.6	78	140	6.7
June	24.8	33.3	77	145	6.2
July	24.6	32.8	76	151	6.3
August	24.5	32.8	76	153	6.1
September	24.3	32.7	78	145	5.5
October	24.3	32.7	79	149	5.6
November	24.2	32.3	82	132	5.0
December	24.1	32.0	82	127	5.1
Average	24.4	33.0	78.5	138.7	6.0

ET_0 was computed through the FAO Penman-Monteith method, incorporated into the CROPWAT program and denoted as Equation 1.

$$ET_0 = \frac{0.408\Delta(R_n - G) + \gamma \frac{900}{T_a + 273} u_2 (e_s - e_a)}{\Delta + \gamma(1 + 0.34u_2)} \quad [1]$$

Where: ET_0 is reference evapotranspiration (mm day^{-1}), T , G and R_n are daily mean temperature $^{\circ}\text{C}$ at 2 m height, soil heat flux density ($\text{MJ m}^{-2} \text{day}^{-1}$) and net radiation value at crop surface ($\text{MJ m}^{-2} \text{day}^{-1}$), respectively. Also, U_2 , $e_s e_a$, $(e_s - e_a)$, Δ and γ represent wind speed at 2 m height (m s^{-1}), saturated vapor pressure at the given temperature (kPa), actual vapor pressure (kPa), saturation vapor pressure deficit (kPa), slope of the saturation vapor pressure curve ($\text{Pa}/^{\circ}\text{C}$) and psychrometric constant ($\text{kPa}/^{\circ}\text{C}$), respectively (Halimi & Tefera, 2019).

Crop Data

CROPWAT relies on the integration of crucial crop-specific information to estimate crop water requirements. It includes details about the type of crop being cultivated, planting dates, various developmental stages of the crop, crop coefficients representing its water needs at different growth phases and potential yield expectations. These crop-specific parameters are crucial for CROPWAT to calculate the reference evapotranspiration (ET_0) and subsequently determine the crop's water requirement (ET_c) throughout its growth cycle.

Sweet corn typically undergoes four discernible growth stages: initial, development, middle and late. Each stage has a specific duration of 15, 20, 25 and 15 days, respectively, with a total growing period of 75 days. Fortunately, CROPWAT software provides valuable crop data for sweet corn, including crop coefficients, maximum root depth, depletion fraction and yield response factors for each stage, as detailed in Table 2.

Table 2

Details of the crop data stored in the CROPWAT 8.0 software (Adapted from Ushkarenko et al., 2014)

Crop	Stage	Duration (Days)	Crop Coefficient	Maximum Root Depth (M)	Depletion Fraction	Yield Response Factor
Sweet corn	Initial	15	0.30	0.3	0.50	0.4
	Development	20	0.30-1.15		-	0.4
	Mid-season	25	1.15	0.5	0.50	1.3
	Late season	15	0.40		0.75	0.5

Significantly, there was an increase in the crop coefficient from the initial to the mid-stage, followed by a decrease from the mid to late stages. Although the change in K_c was slight, it did not remain a consistent value within any growth stage, indicating the dynamic nature of seasonal crop water requirements. Furthermore, the ET_c values were observed to be relatively low at the beginning and end of the growth cycle, registering at 0.3 and 0.4, respectively, when the crops were in their early and late productive stages. In contrast, they were notably higher during the mid-stage at 1.08.

Soil Data

The CROPWAT system evaluates soil type and texture to determine water-holding capacity, affecting crop water availability. A sieve analysis (Figure 3a) uses multiple sieves to assess particle size distribution in granular soils, involving sieves with mesh sizes from 4.75 mm to 0.075 mm, a mechanical shaker, and other tools (Fomin et al., 2019). The hydrometer test (Figure 3b) determines particle size distribution in fine-grained soils (Alade, 2018). Data from these analyses are used to plot a particle size distribution curve, which helps classify soil type using the U.S.D.A Soil Textural Triangle. Additional soil information, such as field capacity, wilting point, and available water holding capacity, is obtained from secondary data within CROPWAT.

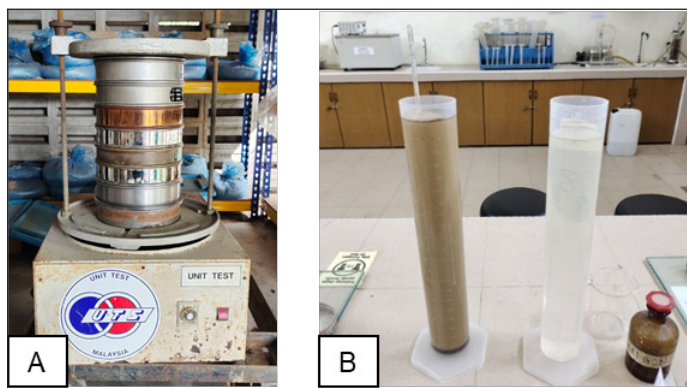


Figure 3. Figure 3a demonstrates the sieve analysis, while Figure 3b illustrates the hydrometer test

Experimental Design

The planting media, with a 3:2:1 ratio of topsoil, peat, and sand, was used to fill polybags to a height of 30 cm, with each polybag weighing approximately 10–15 kg. F1 Hybrida 301 sweet corn seeds were initially sown in plastic trays and nurtured for 10 days until fully developed leaves emerged. Subsequently, these 10-day-old, fully germinated seedlings were individually transplanted into polybags pre-treated with insecticide or nematicide to prevent insect disturbances.

The treatments were categorized into four levels of irrigation water application (IWA). The IWA was determined as a percentage of the crop evapotranspiration (ET_c) as shown in Equation 2 by considering 70% irrigation efficiency since the plants were cultivated individually in a polybag with a radius of 17.5 mm and an area of 96,211.28 mm². The specific IWA levels were defined as follows: $T_1 = 50\%$ of the simulated ET_c , $T_2 = 75\%$ of the simulated ET_c , $T_3 = 100\%$ of the simulated ET_c and $T_4 = 125\%$ of the simulated ET_c .

$$IWA = (ET_c \times T\% \times A) / (I_e \times 1000) \quad [2]$$

Where: IWA is Irrigation water applied for a particular treatment and stage (ml), ET_c , A, I_e are Crop evapotranspiration (mm), 96211.28 mm² and Irrigation Efficiency, 70%. Also, $T\%$ is 50%, 75%, 100% or 125% of simulated ET_c .

The study was conducted within a greenhouse with a measurement of 9 meters by 5 meters, with a polycarbonate roof. Each treatment consisted of 7 replicates, leading to 28 experimental units. The experiment adhered to a Randomized Complete Block Design (RCBD), where 28 polybags containing different treatments were fully randomized, as shown in Figure 4. The experimental plot covered an area measuring 6.2 meters long by 2.45 meters in row width, totaling 15.19 square meters, with pots spaced approximately 0.7 meters by 0.3 meters apart. The plants were manually irrigated with a measuring cylinder following their designated IWA levels, starting one week after full germination and continuing until the harvest throughout the entire growing season from March to June.

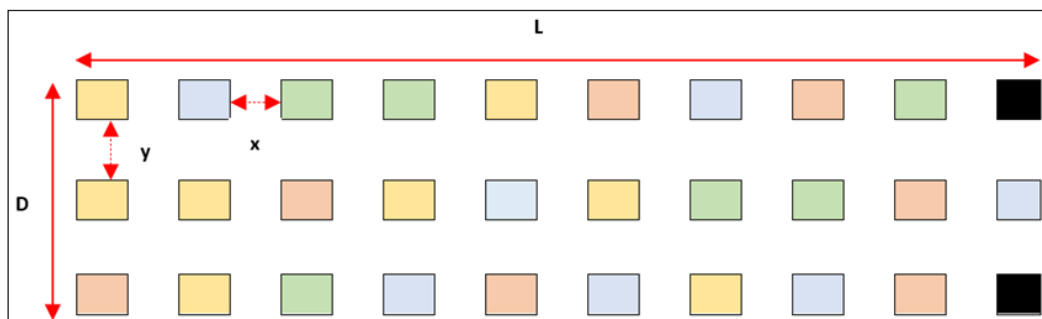


Figure 4. Polybag plots arrangement. $L = 620$ cm, $D = 245$ cm, $x = 30$ cm and $y = 70$ cm

Plant Growth Monitoring and Measurement

The monitoring and measurement of plant growth involved continuous evaluation and tracking of the progress and development of plants. This procedure necessitated regular measurements of essential plant characteristics, such as leaf count, leaf length, leaf width, plant height, stem diameter and the eventual yield size or weight. These measurements were employed in this study to investigate the relationship between irrigation and the growth

and development of plants. Consequently, plant growth parameters were recorded every two weeks throughout the entire growing season, extending until the harvest.

Plant Height

Plant height was measured from the soil surface to the highest point of the arch created by the uppermost leaf, specifically when its tip was pointing downward. Figure 5 illustrates the process for measuring the height of a corn plant using a measuring tape.

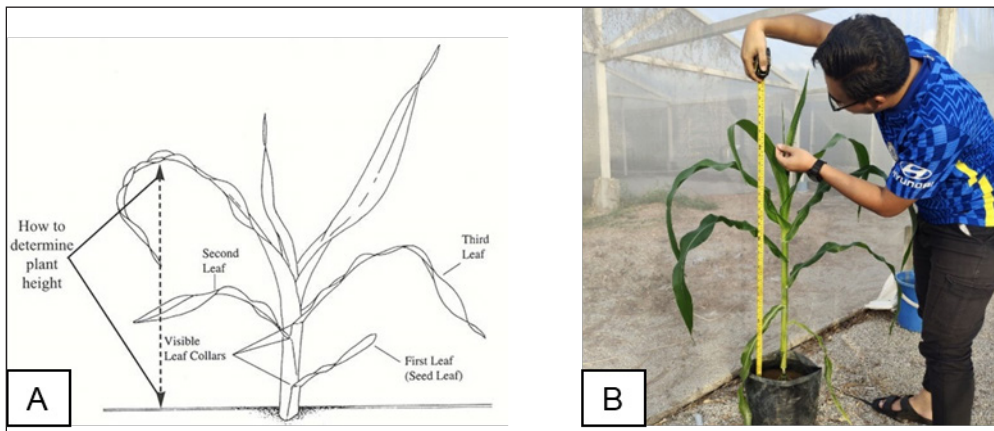


Figure 5. The determination of plant height (A). Plant measurements were taken at the study site (B)

Stem Diameter

The stem diameter was assessed using an electronic steel caliper vernier positioned 10 cm from the stem base, as illustrated in Figure 6. Alternatively, the second stem node of the

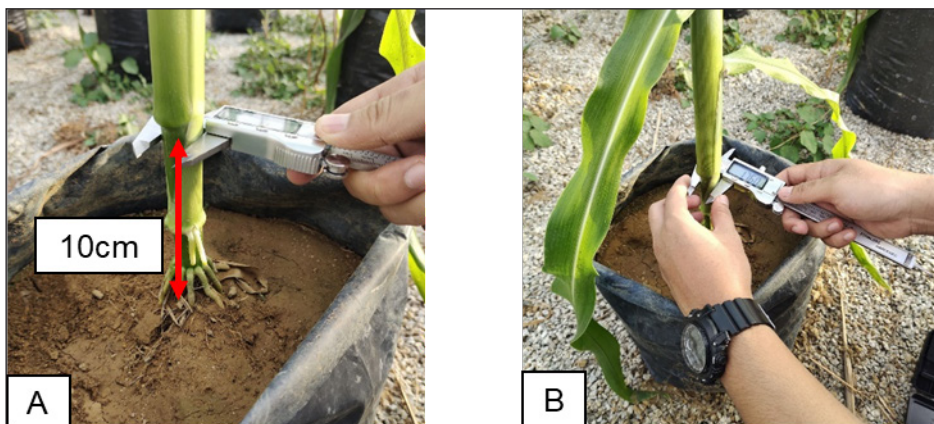


Figure 6. The stem diameter was 10 cm from the soil surface (A). Stem diameter was measured using an electronic vernier caliper (B)

maize could also serve as the area of interest, following agronomists' recommendations. The vernier caliper featured an LCD digital display with a high precision of 0.01 mm and a tolerance of 0.02 mm.

Single Fruit Weight

The sweet corn ears (mature cobs of sweet corn plants containing edible kernels) were harvested and weighed, and the average values were calculated to represent the yield for each treatment. The single fruit weight (SFW) was measured using an electronic scale with a sensitivity of 0.01 g. At the end of the fruiting stage, fruits with uniform maturity and color were randomly selected for quality assessment.

Kernel Moisture Content

Kernel biomass measurement reveals corn plant water content, including kernel moisture (Gambín et al., 2007). Sweet corn, harvested at the "milk stage" (75–80 days after sowing), was processed by separating grains from different parts of the cob (Figure 7A, 7B). A 10 g kernel sample was weighed initially (Figure 7C, 7D) and dried for 24 hours at 110°C according to ISO 6540 and BS 4317. After drying, the sample's weight was recorded, and the moisture content percentage was calculated.

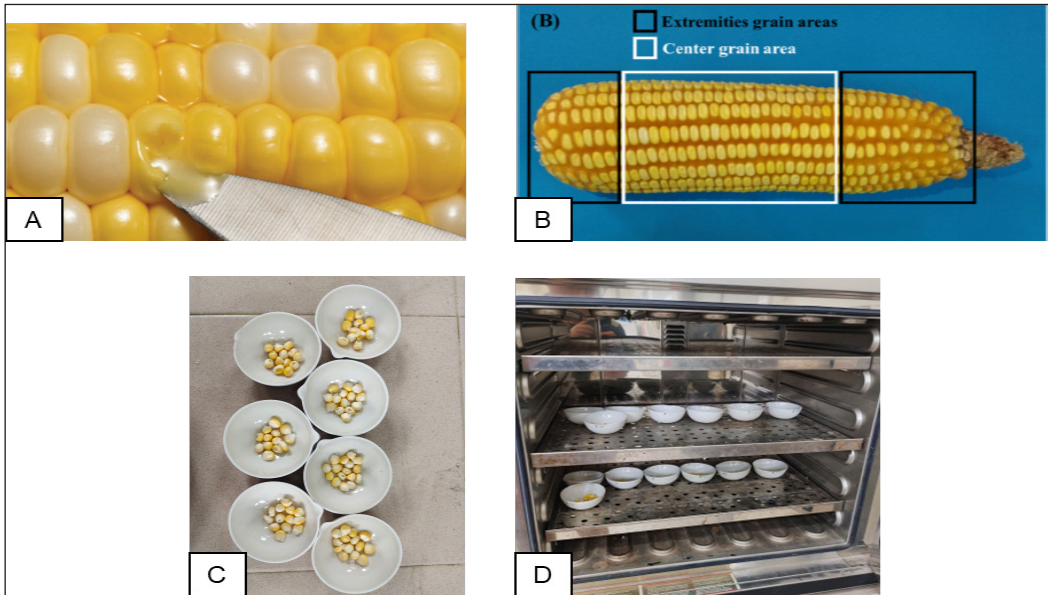


Figure 7. The kernels were tested by pinching them until “milk” liquid came out, which shows that they were ready and good to be harvested (A) Definition of corncob grain area (B) Sample preparation collected from center and extremities of the corncob (da Silva Timm et al., 2023) (C) Sample was placed into the drying oven (D)

Statistical Analysis

Plant growth data were analyzed using IBM SPSS Version 23. Levene's test checked if variances among irrigation treatments were equal, followed by ANOVA to find significant differences between treatment means. If ANOVA showed significant differences, Tukey's Honestly Significant Difference (HSD) test and Duncan's Multiple Range Test were used to identify specific pairwise differences. All post hoc and Pearson correlation tests were conducted at significant $P \leq 0.05$ and $P \leq 0.01$, respectively.

RESULT AND DISCUSSIONS

Water Requirements

Properties of Planting Soil

The soil's particle size distribution was assessed using mechanical sieve and hydrometer tests, resulting in a grain size distribution graph, as shown in Figure 8. Based on USDA standards, the soil is composed of 36.97% silt, 5.31% clay, and 57.72% sand, classifying it as sandy loam. Key parameters such as permanent wilting point (PWP), field capacity (FC), rainfall infiltration rate, maximum rooting depth, and soil moisture were obtained from CROPWAT 8.0 and literature, with PWP at 140 mm/meter, FC at 30 mm/day, maximum rooting depth at 300 cm, and initial moisture values at 0% and 140 mm/meter, respectively.

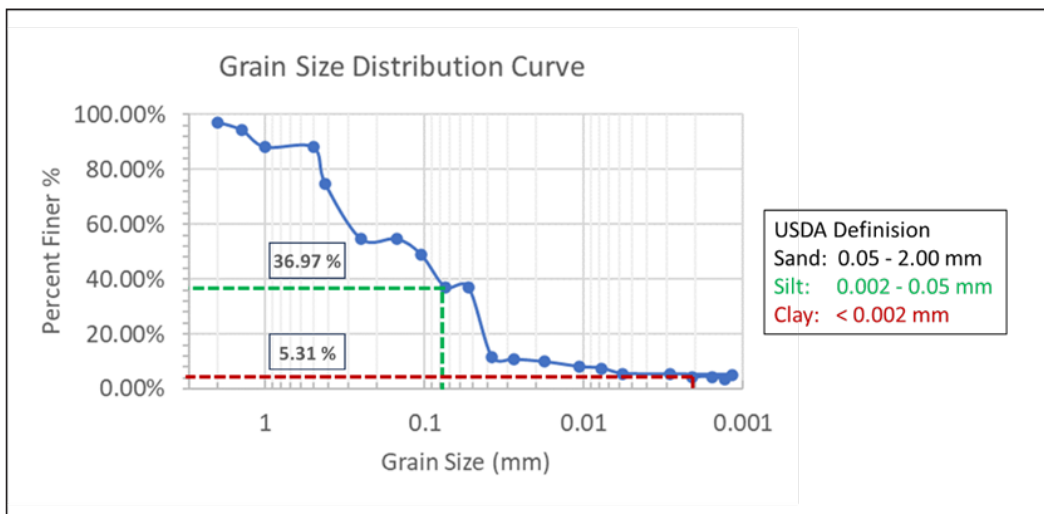


Figure 8. The grain size distribution curve is based on sieve and hydrometer analysis of the planting soil

Reference Evapotranspiration

In March, elevated temperatures, low relative humidity and strong winds significantly elevated radiation and evapotranspiration, recording 19.9 MJ/m²/day and 4.65 mm/day.

Conversely, lower temperatures, high relative humidity and weak winds significantly reduced radiation and evapotranspiration in December, registering values of 16 MJ/m²/day and 3.65 mm/day.

The higher solar radiation levels resulted in increased evaporation rates, leading to elevated ET_o values, as illustrated in Figure 9. Throughout the corn's growth period, which spans from March to June, there was a noticeable reduction in both radiation and ET_o, with radiation declining from 19.90 MJ/m²/day to 17.5016 MJ/m²/day and ET_o decreasing from 4.65 mm/day to 4.22 mm/day.

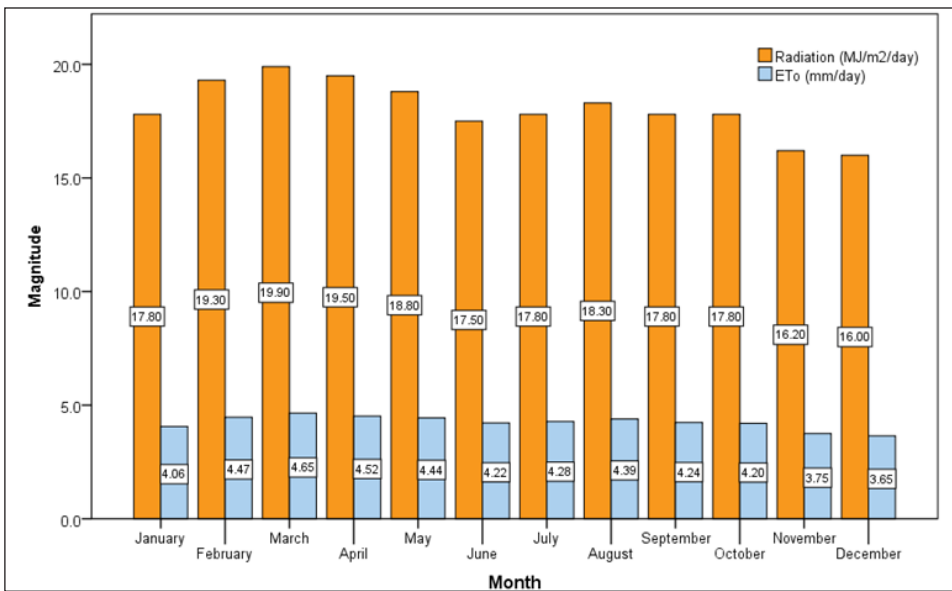


Figure 9. The effect of climatic parameters on radiation and reference evapotranspiration, ET_o.

Crop Evapotranspiration

ET_c exhibited an increase during the early to mid-growth stages (Initial-Mid) but showed a slight decrease in the later stages (Mid-Late). These fluctuations could be attributed to the changing crop coefficient, which increased from the Initial to Mid stages but decreased from the Mid to Late stages. Notably, effective rainfall was not factored in, as the plants were cultivated within a greenhouse and received tap water exclusively. Consequently, the results indicated no rainfall during the entire experimental period, resulting in net irrigation requirements (NIR) equal to the total crop evapotranspiration, amounting to 251.1 mm. Due to the cultivation method in polybags, water losses such as runoff, seepage, evaporation and percolation during irrigation application were negligible. Figure 10 provides a visualization of the crop water requirement at specific intervals, accounting for a 70% irrigation efficiency.

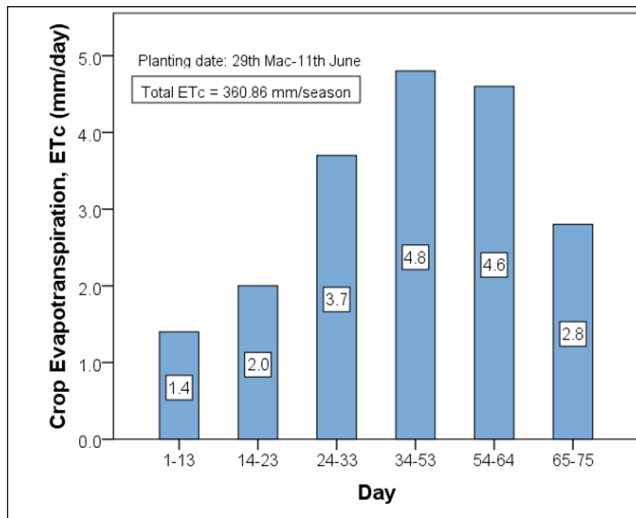


Figure 10. Crop water requirement, ET_c for sweet corn based on the reference evapotranspiration with the respective crop coefficient by considering 70% irrigation efficiency

Irrigation Water Applied

According to Equation 2, the IWA (Irrigation Water Amount) is expected to be slightly higher than the ET_c (Crop Evapotranspiration), taking into account 70% irrigation efficiency. Furthermore, the quantities of IWA varied based on the different assigned treatments, which were 50%, 75%, 100% and 125% of ET_c for T1, T2, T3 and T4, respectively, as illustrated in Figure 11 below. The water supply pattern followed the same trend shown in Figure 11, increasing from 1 to 53 DAS (Days After Sowing) but decreasing from 54 to 75 DAS due to changes in crop coefficients (K_c).

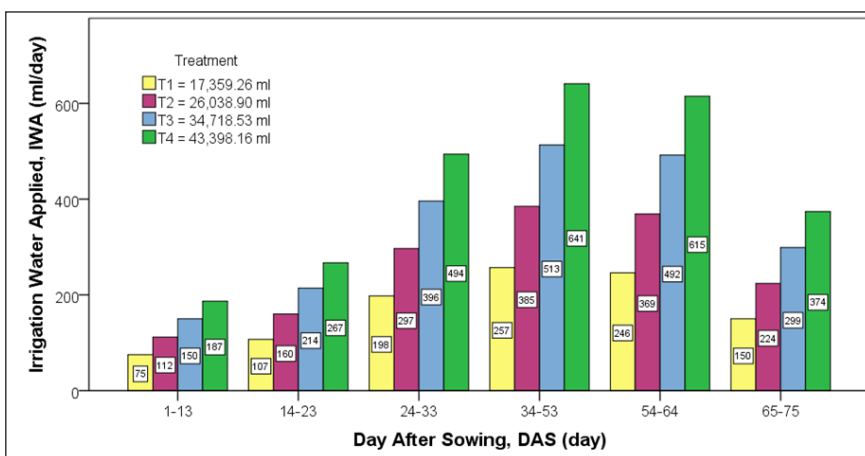


Figure 11. IWA in milliliter (ml) was applied to the experimental plot for each treatment at specific DAS intervals

Plant Growth Assessment

Individual phytomers were closely examined from planting to harvest to assess how plants responded to the water supplied. While all plants displayed a high survival rate for approximately 2.5 months, the notable distinction lay in their growth rates, as depicted in Figure 12. Furthermore, variations among treatments became apparent in terms of plant height, stem diameter, single fruit weight (SFW) and kernel moisture content. These differences were subjected to statistical analysis using tests for homogeneity of variance, ANOVA (Analysis of Variance) and Tukey tests to ascertain the p-value and establish the significance of the disparities between treatments.

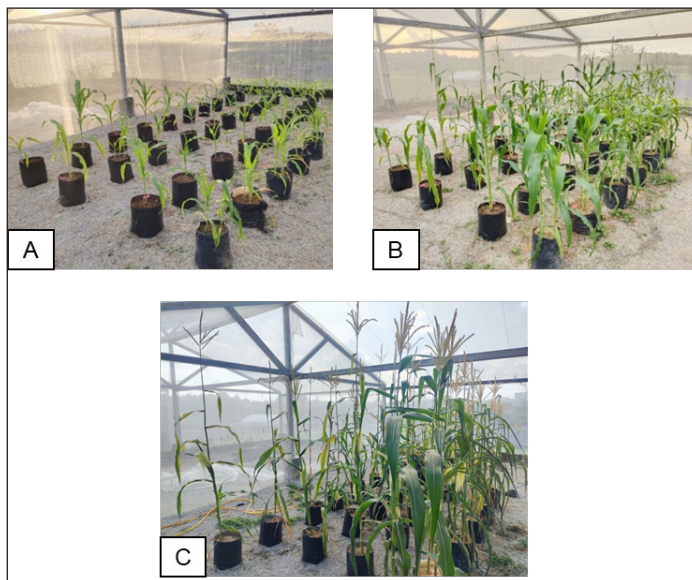


Figure 12. The growth of plants at the study site at 15 DAS (A), 30 DAS (B) and 75 DAS (C)

Plant Height

The study showed significant variation in plant height across different stages. During 15 Days After Sowing (DAS), early growth focused on root and leaf development. ANOVA results indicated significant differences between treatments T1 and T3, T4, and T2 and T4, with p-values under 0.05 (Figure 13). From 16 to 30 DAS, plant height increased rapidly for all treatments without significant differences. During 31 to 60 DAS, growth slowed, and differences between treatments were not significant (Figure 14). Plant height stabilized from 61 to 75 DAS, with significant differences found between T1, T2, and T3, T4, though height remained stable (Figure 14). Overall, T4 consistently showed the highest growth rate compared to the other treatments.

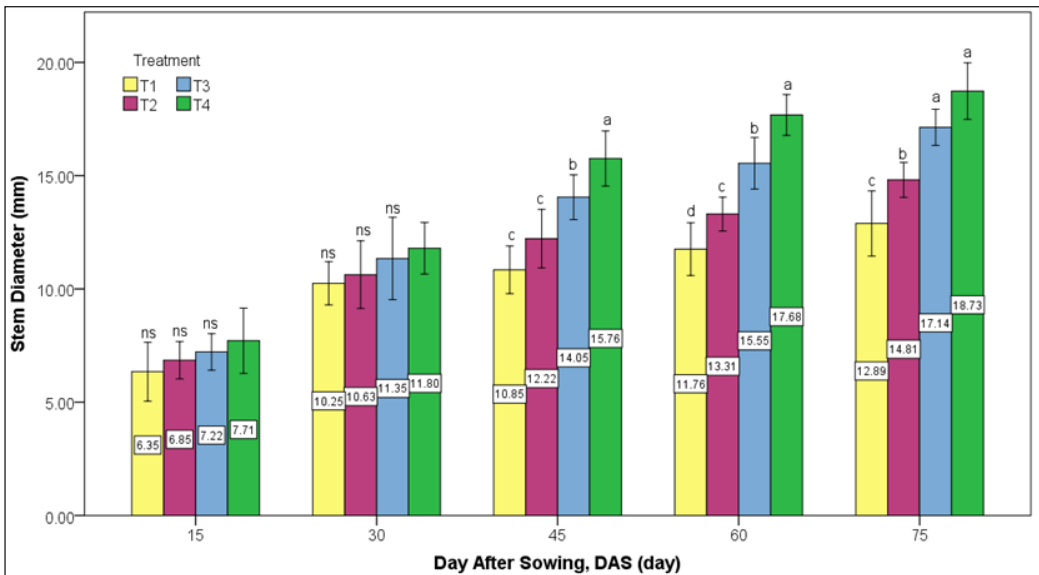


Figure 13. The effect of different amounts of IWA on stem diameter over time. Data represents the mean \pm error bars of standard deviation (± 1) of all replicates at a particular DAS. Different lowercase letters indicate significant differences among treatments at $P < 0.05$ level

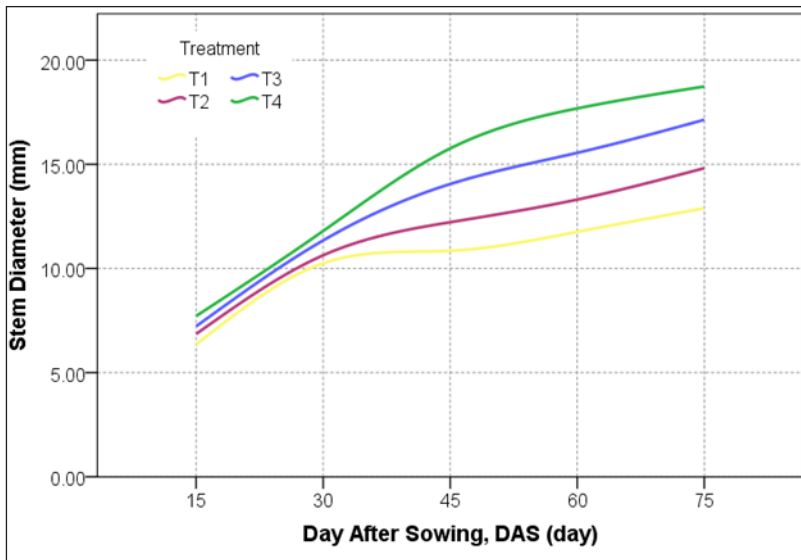


Figure 14. The growth curve of sweet corn in terms of stem diameter at specific DAS for each treatment

Single Fruit Weight

The study investigated how irrigation quantity (IWA) impacted sweet corn quality, focusing on Single Fruit Weight (SFW). Figure 15 shows that higher irrigation levels resulted in

significantly higher SFW, with T3 and T4 yielding the largest fruits. ANOVA revealed substantial differences among treatments ($P < 3.9161E-12$), with SFW values of 96.65 g, 152.87 g, 217.21 g, and 278.13 g for T1 through T4, respectively. Lower irrigation (T1 and T2) reduced ear diameter and weight due to decreased photosynthesis and assimilate production, affecting final yield. Water deficit stress was linked to poor flower development and lower yield (Sah et al., 2020).

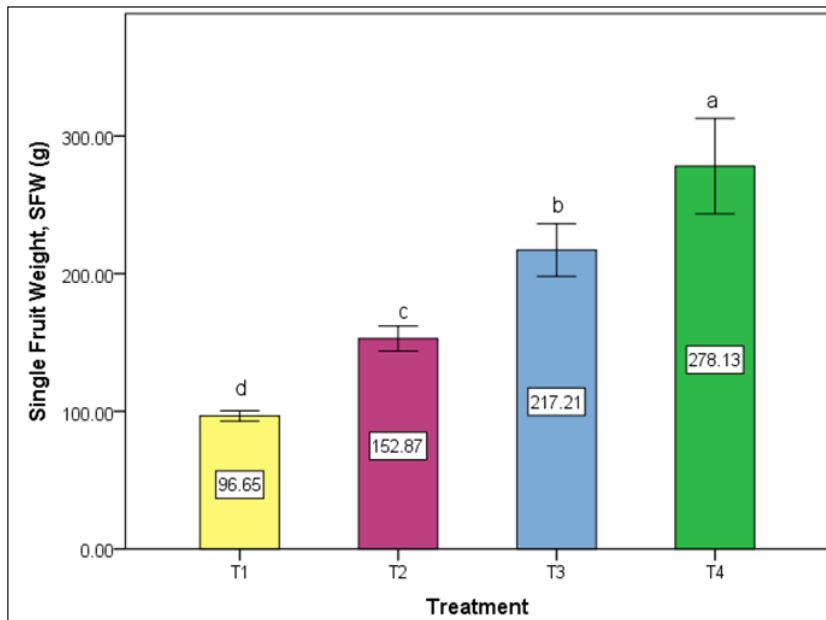


Figure 15. The effect of different amounts of IWA on SFW right after harvesting. Data represents the mean \pm error bars of standard deviation (± 1) of all replicates at a particular DAS. Different lowercase letters indicate significant differences among treatments at $P < 0.05$ level

Kernel Moisture Content

Sweet corn growers and processors aim to achieve kernels with specific qualities, such as a tender pericarp, creamy texture, high sugar content in the endosperm, low starch content and high water content (Ha, 2017). The results of ANOVA indicated a significant effect of different irrigation water amounts (IWA) on kernel moisture content (MC), as demonstrated in Figure 16. The Tukey test revealed that both T1 and T2 were not significantly different but significantly different from T3 and T4. In contrast, T3 and T4 showed significant differences from the other treatments. T4 had the highest MC at 78.20%, followed by T3 at 76.05%, T2 at 72.29%, and T1 the lowest at 71.65%. Upon comparing means, it became apparent that grain yield showed a significant increase under optimal irrigation treatments, T3 and T4, in contrast to the suboptimal treatments, T1 and T2.

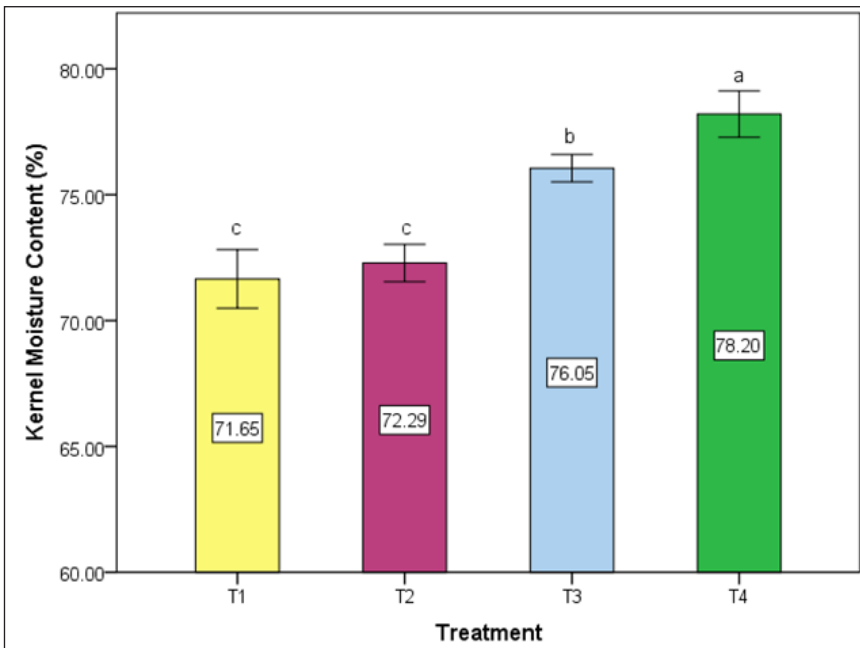


Figure 16. Different amounts of IWA affect kernel moisture content right after harvest. Data represents the mean \pm error bars of standard deviation (± 1) of all replicates at a particular DAS. Different lowercase letters indicate significant differences among treatments at $P < 0.05$ level

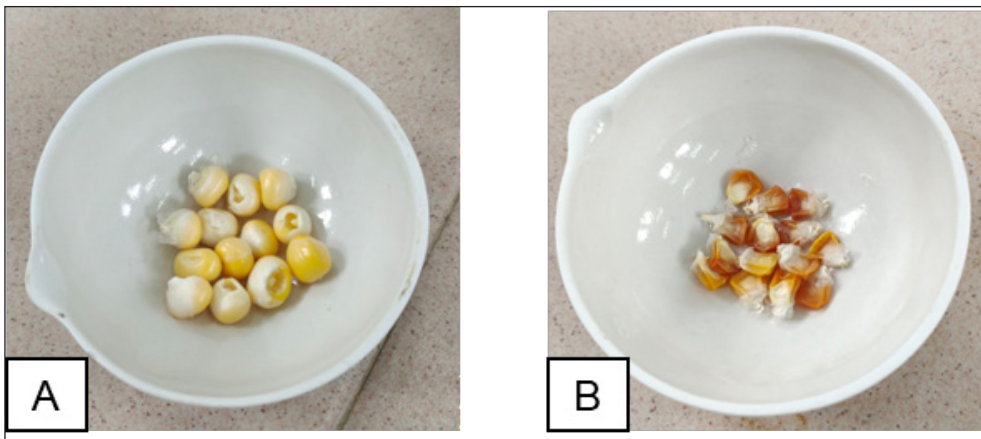


Figure 17. Physical appearance of corn kernel before (A) and after (B) the oven drying process

Persistent water stress caused by deficit irrigation in T1 and T2 could lead to kernel desiccation (Figure 17). Desiccation refers to the drying out of kernels due to inadequate water supply. Prolonged water stress can significantly decrease kernel moisture content, reducing kernel weight and potentially lowering overall yield (Figure 18).



Figure 18. The difference in corn cob size for each treatment (A) and desiccation of corn kernel (B) by T₁

Optimal Water Requirement

Table 3 summarizes plant growth parameters 75 days after sowing (DAS), showing significant differences in moisture content, Single Fruit Weight (SFW), stem diameter, and plant height between treatments. Table 4 indicates strong correlations among these parameters ($p < 0.001$).

The "Pakej Teknologi Jagung Manis" booklet recommends plant heights of 165 cm to 215 cm, which are only T₃ (170.71 cm) and T₄ (180 cm). None of the treatments achieved the 20 mm minimum stem diameter, though T₄ (18 mm) was the closest. The stem diameter measurements at 75 DAS may differ from other studies due to varying stages or conditions. However, T₄ still showed healthy growth and good yield quality, indicating minimal impact on overall performance.

Only T₄ met the recommended SFW range of 250 g to 325 g, with an average of 278.13 g. T₃ and T₄ also met the optimal moisture content of 76%–79%, while T₁ and T₂ did not. Based on these results, T₄ was the best irrigation practice for achieving optimal growth and quality in Malaysian sweet corn, outperforming T₃ in plant height, stem diameter, SFW, and moisture content.

Table 3
Average parameters growth readings for each treatment at 75 DAS

Treatment	Total IWA (mm)	Plant Height (cm) N = 7	Stem Diameter (mm) N = 7	SFW (g) N = 5	Moisture Content (%) N = 5
T ₁	140.36	138.29 ± 12.74 b	12.89 ± 1.44 c	96.65 ± 3.73 d	71.65 ± 1.16 c
T ₂	210.50	155.14 ± 8.99 ab	14.81 ± 0.77 b	152.87 ± 9.10 c	72.29 ± 0.75 c
T ₃	280.67	170.71 ± 21.52 ab	17.14 ± 0.80 a	217.21 ± 19.13 b	76.05 ± 0.55 b
T ₄	350.83	180.00 ± 17.87 a	18.73 ± 1.25 a	278.13 ± 34.72 a	78.20 ± 0.92 a

Note: Data represent the mean ± standard deviation on four growth parameters of 7 replicates. Different lowercase letters indicate significant differences among treatments at $P < 0.05$ level

Table 4
Pearson correlation of parameters at 75 DAS

	Growth Parameters	SFW	Moisture Content	Plant Height	Stem Diameter
SFW	Pearson Correlation	1	0.890**	0.698**	0.891**
	Sig. (2-tailed)		0.000	0.000	0.000
	N	26	26	26	26
Moisture Content	Pearson Correlation	0.890**	1	0.653**	0.867**
	Sig. (2-tailed)	.000		.000	.000
	N	26	26	26	26
Plant Height	Pearson Correlation	0.698**	0.653**	1	0.748**
	Sig. (2-tailed)	0.000	0.000		0.000
	N	26	26	26	26
Stem Diameter	Pearson Correlation	0.891**	0.867**	0.748**	1
	Sig. (2-tailed)	0.000	0.000	0.000	
	N	26	26	26	26

** . Correlation is significant at p-value 0.01 level (2-tailed)

Comparison with Other Studies

This study shared similarities with other studies with its aim to optimize water use in agriculture and in its use of climatic data to estimate water requirements (Table 5). Like the other studies, it evaluated different irrigation levels to determine the most effective crop growth and yield practices. However, it differed in its focus on sweet corn under local Malaysian conditions, using long-term climatic data and specific irrigation treatments. In contrast, the study by Shaw et al. (2023) covered various crops in an arid region, and Hong et al. (2022) focused on tomatoes in a greenhouse setting in China. Ray et al. (2023) offered a broader, global perspective on maize irrigation strategies, while Mirhashemi and Panahi (2021) examined maize water requirements in a specific region of Iran using environmental factors. The studies used different methods; this study employed CROPWAT software for ET_c estimation and experimental validation, while others used various models and algorithms based on their specific environmental and crop contexts. Thus, all studies aimed to improve irrigation efficiency differed in scope, methodology, and regional applicability.

Table 5
Comparison of studies on crop water requirements and irrigation practices

Aspect	This study	Shaw et al. (2023)	Hong et al. (2022)	Ray et al. (2023)	Mirhashemi & Panahi (2021)
Objective	Determine the optimal water requirement for sweet corn using ET_c and validate it with different irrigation treatments.	Optimize furrow irrigation design for various crops in arid conditions.	Identify optimal water requirement for tomatoes in a greenhouse to improve yield and Water Use Efficiency (WUE).	Review strategies to enhance maize water productivity under different irrigation methods.	Predict maize water requirements at different growth stages under natural factors.
Water Requirement Estimation	Based on 30-year climatic data and ET_c estimated with CROPWAT V8, four irrigation treatments (50%, 75%, 100%, and 125% ET_c) were tested.	ET_c estimated with Penman-Monteith equation and CROPWAT 8.0; calculated CWR, Net Irrigation Requirement (NIR), and Gross Irrigation Requirement (GIR) for multiple crops.	Calculated using root distribution, soil moisture, and wetted percentage for five irrigation levels (60%, 80%, 100%, 120%, 140% medium irrigation quota).	Discusses water requirements for maize with furrow and drip methods; ranges from 425–789 mm (furrow) and 351–685 mm (drip).	Estimated using algorithms (C5.0, CART, CHAID, QUISST) based on factors like humidity, precipitation, air temperature, and wind speed.
Growth Parameters and Yield	Assessed plant height, stem diameter, shoot fresh weight, and kernel moisture content; T4 (125% ET_c) optimal.	Focused on maximizing dry yield; detailed NIR values for crops including maize.	Studied tomato yield, WUE, and fruit quality; 120% Ia optimal for balancing yield and efficiency.	Discusses yield improvement under different irrigation methods; drip irrigation boosts yield by 28%.	Analyzed growth stages and natural factors affecting water requirements; key influences include precipitation, temperature, and wind speed.
Environmental and Soil Conditions	Conducted in Malaysia with data from Subang weather station; focused on local sweet corn cultivation.	Conducted in Kurmool District, India; considered various soil types and arid conditions.	Conducted in a solar greenhouse in the Taklimakan Desert, China.	It covers global conditions and discusses irrigation methods in various climates and soil types.	Conducted in the Qazvin plain, Iran; findings influenced by local natural factors.

Table 5 (continue)

Aspect	This study	Shaw et al. (2023)	Hong et al. (2022)	Ray et al. (2023)	Mirhashemi & Panahi (2021)
Methodology	ET _c estimation using CROPWAT V8; experimental validation with different irrigation treatments.	Penman-Monteith equation, CROPWAT 8.0, and FURDEV were used and compared the models for accuracy.	The TOPSIS method was used to determine optimal irrigation for yield and WUE.	Reviewed global irrigation strategies (furrow, drip, mulching) for maize.	Algorithms (C5.0, CART, CHAID, QUIST) and Apriori were used to predict water requirements and analyze association rules.
Challenges and Limitations	Specific to Malaysian conditions, it may not generalize to other climates or soils.	Tailored to arid conditions and specific soils; limited generalizability.	Results are specific to greenhouse conditions.	The broad review may lack specific details for certain regions.	Local factors influence findings and have limited broader applicability.

CONCLUSION

In conclusion, this study included a variety of activities, such as lab experiments, fieldwork, software analysis, collaboration with external agencies, and statistical data analysis, to improve the accuracy of CWR estimations for sweet corn. Using the Penman-Monteith method from FAO 56 guidelines and the CROPWAT 8 software, we calculated reference evapotranspiration (ET_0), crop evapotranspiration (ET_c), and irrigation requirements based on 30 years of climatic data from MetMalaysia. Although ET_0 slightly declined from March to June, it did not significantly affect ET_c due to varying crop coefficients (K_c) at different growth stages.

The total water requirement for sweet corn was estimated at 251.1 mm/day or 360.86 mm/season, assuming a 70% irrigation efficiency. A field study at the Greenhouse, Ladang 15, Faculty of Agriculture, UPM, tested different irrigation levels (50%, 75%, 100%, and 125% of ET_c) to validate practical irrigation management strategies that utilize the refined CWR estimations through the experimental site. Key growth parameters such as plant height, stem diameter, single fruit weight, and kernel moisture content were recorded.

Results showed that plants receiving irrigation water application T4 at 125% ET_c had better growth and higher survival rates compared to other treatments. Statistical analysis confirmed that higher irrigation levels significantly improved plant growth ($P < 0.05$). It was concluded that the estimated irrigation based on T3 at 100% ET_c was insufficient, and T4 at 125% ET_c was most suitable for optimal sweet corn growth in Malaysia. The study demonstrated that optimizing irrigation to 125% of the estimated crop water requirement (based on ET_c) significantly improved sweet corn growth and survival, validating refined CWR estimations and highlighting the necessity of adjusting irrigation strategies to achieve optimal crop productivity.

ACKNOWLEDGEMENT

The authors express their gratitude to the Ladang 15 Office, Faculty of Agriculture, UPM, for giving us the opportunity to conduct our research and for all the resources and support they provided. The authors also extend their appreciation to the anonymous reviewer for their valuable feedback, which greatly contributed to enhancing the quality of the paper.

REFERENCE

- Alade, S. M. (2018). Correlation of unified and AASHTO soil classification systems for soils classification. *Journal of Earth Sciences and Geotechnical Engineering*, 8(1), 39-50.
- da Silva Timm, N., Coradi, P. C., Cañizares, L. D. C. C., Jappe, S. N., Ferreira, C. D., & Lutz, É. (2023). Effects of the storage temperature and time of corn from the center and extremities of corncob on quality parameters. *Journal of Cereal Science*, 110, Article 103645. <https://doi.org/10.1016/j.jcs.2023.103645>

- Feng, Z., Miao, Q., Shi, H., Feng, W., Li, X., Yan, J., Liu, M., Sun, W., Dai, L., & Liu, J. (2023). Simulation of water balance and irrigation strategy of typical sand-layered farmland in the Hetao Irrigation District, China. *Agricultural Water Management*, 280, Article 108236. <https://doi.org/10.1016/j.agwat.2023.108236>
- Fomin, D. S., Valdes-Korovkin, I. A., Holub, A. P., & Yudina, A. V. (2019). Dry sieving analysis of soil by vibratory sieve shaker: modification and optimization. *Bulleten' Pochvennogo Instituta Imeni V.V. Dokuchaeva*, 96, 149–177. <https://doi.org/10.19047/0136-1694-2019-96-149-177>
- Gabr, M. E. S. (2022). Management of irrigation requirements using FAO-CROPWAT 8.0 model: A case study of Egypt. *Modeling Earth Systems and Environment*, 8(3), 3127–3142. <https://doi.org/10.1007/s40808-021-01268-4>
- Gamal, R., El-Shirbeny, M., Abou-Hadid, A., Swelam, A., El-Gindy, A. G., Arafa, Y., & Nangia, V. (2022). Identification and quantification of actual evapotranspiration using integrated satellite data for sustainable water management in dry areas. *Agronomy*, 12(9), Article 2143. <https://doi.org/10.3390/agronomy12092143>
- Gambín, B. L., Borrás, L., & Otegui, M. E. (2007). Kernel water relations and duration of grain filling in maize temperate hybrids. *Field Crops Research*, 101(1), 1–9. <https://doi.org/10.1016/j.fcr.2006.09.001>
- Ha, B. M. (2017). A review of growth stage deficit irrigation affecting sticky maize production. *GeoScience Engineering*, 2017(2), 13-18.
- Halimi, A. H., & Tefera, A. H. (2019). Application of cropwat model for estimation of irrigation scheduling of tomato in changing climate of Eastern Europe: The case study of Godollo, Hungary. *SSRG International Journal of Agriculture & Environmental Science*, 6(1), 1–11.
- Hong, M., Zhang, Z., Fu, Q., & Liu, Y. (2022). Water requirement of solar greenhouse tomatoes with drip irrigation under mulch in the southwest of the Taklimakan Desert. *Water*, 14(19), Article 3050. <https://doi.org/10.3390/w14193050>
- Jie, F., Fei, L., Li, S., Hao, K., Liu, L., & Peng, Y. (2022). Effects on net irrigation water requirement of joint distribution of precipitation and reference evapotranspiration. *Agriculture*, 12(6), Article 0801. <https://doi.org/10.3390/agriculture12060801>
- Mirhashemi, S. H., & Panahi, M. (2021). Investigation and prediction of maize water requirements in four growth stages under the influence of natural factors (Case study: Qazvin plain, Iran). *Environmental Technology & Innovation*, 24, Article 102062. <https://doi.org/10.1016/j.eti.2021.102062>
- Nie, T., Gong, Z., Zhang, Z., Wang, T., Sun, N., Tang, Y., Chen, P., Li, T., Yin, S., Zhang, M., & Jiang, S. (2023). Irrigation scheduling for maize under different hydrological years in Heilongjiang Province, China. *Plants*, 12(8), Article 1676. <https://doi.org/10.3390/plants12081676>
- Parmar, S. H., Patel, G. R., & Tiwari, M. K. (2023). Assessment of crop water requirement of maize using remote sensing and GIS. *Smart Agricultural Technology*, 4, Article 100186. <https://doi.org/10.1016/j.atech.2023.100186>
- Ray, L. I., Smith, J. A., & Kumar, S. (2023). Strategies for water productivity enhancement in maize - A comprehensive review. *Agricultural Water Management*, 271, Article 107789. <https://doi.org/10.1016/j.agwat.2023.107789>

- Ruan, H., Yu, J., Wang, P., & Wang, T. (2020). Increased crop water requirements have exacerbated water stress in the arid transboundary rivers of Central Asia. *Science of the Total Environment*, 713, Article 136585. <https://doi.org/10.1016/j.scitotenv.2020.136585>
- Saeed, F. H., Al-Khafaji, M. S., & Mahmood Al-Faraj, F. A. (2021). Sensitivity of irrigation water requirement to climate change in arid and semi-arid regions towards sustainable management of water resources. *Sustainability*, 13(24), Article 13608. <https://doi.org/10.3390/su132413608>
- Sah, R. P., Chakraborty, M., Prasad, K., Pandit, M., Tudu, V. K., Chakravarty, M. K., Narayan, S. C., Rana, M., & Moharana, D. (2020). Impact of water deficit stress in maize: Phenology and yield components. *Scientific Reports*, 10(1), Article 2944. <https://doi.org/10.1038/s41598-020-59689-7>
- Shao, G., Han, W., Zhang, H., Zhang, L., Wang, Y., & Zhang, Y. (2023). Prediction of maize crop coefficient from UAV multisensor remote sensing using machine learning methods. *Agricultural Water Management*, 276, Article 108064. <https://doi.org/10.1016/j.agwat.2022.108064>
- Shaw, S. K., Sharma, A., Khatua, K. K., & Oliveto, G. (2023). An integrated approach to evaluating crop water requirements and irrigation schedule for optimizing furrow irrigation design parameters in Kurnool District, India. *Water*, 15(10), Article 1801. <https://doi.org/10.3390/w15101801>
- Soleymani, A., & Shahrajabian, M. H. (2018). Assessment of ET-HS model for estimating crop water demand and its effects on yield and yield components of barley and wheat in semi-arid region of Iran. *Cercetari Agronomice in Moldova*, 50(4), 37–49. <https://doi.org/10.1515/cerce-2017-0034>
- Song, Y., Birch, C., Qu, S., Doherty, A., & Hanan, J. (2010). Analysis and modelling of the effects of water stress on maize growth and yield in dryland conditions. *Plant Production Science*, 13(2), 199–208. <https://doi.org/10.1626/pp.s.13.199>
- Ushkarenko, V., Vozhehova, R., Pavlik, N., & Hordienko, I. (2014). Assessment of the CROPWAT 8.0 software reliability for determining the water balance of crops. *Journal of Water and Land Development*, (23), 27–33.
- Wang, T., Du, C., Nie, T., Sun, Z., Zhu, S., Feng, C., Dai, C., Chu, L., Liu, Y., & Liang, Q. (2020). Spatiotemporal analysis of maize water requirement in the Heilongjiang province of China during 1960-2015. *Water*, 12(9), Article 2472. <https://doi.org/10.3390/w12092472>
- Xuan, C., Ding, R., Shao, J., & Liu, Y. (2021). Evapotranspiration and quantitative partitioning of spring maize with drip irrigation under mulch in an arid region of northwestern China. *Water*, 13(22), Article 3169. <https://doi.org/10.3390/w13223169>

A Study on the Impact of Chamber Size, Configuration, Environmental Factors and Maximum Power Point Tracking (MPPT) Integration on Microbial Fuel Cell Voltage

Siti Kudnie Sahari^{1*}, Nashley Ursula Mundi Ujai¹, Thommy Thomas¹, Ibrahim Yakub¹, Marini Sawawi¹, Lilik Hasanah², Abdul Rahman Kram¹, Zaidi Embong³, Kasumawati Lias¹, Annie Joseph¹, Kho Lee Chin¹ and Sharifah Masniah Wan Masra¹

¹Faculty of Engineering, Universiti Malaysia Sarawak, 94300 Kota Samarahan, Sarawak, Malaysia

²Faculty of Mathematics and Sciences Education, Indonesia University of Education, Bandung, Jawa Barat 40154, Indonesia

³Faculty of Applied Science and Technology, Universiti Tun Hussein Onn Malaysia, 84600 Muar Johor, Malaysia

ABSTRACT

The study examines the effect of chamber size, Microbial Fuel Cell (MFC) arrangement, environmental conditions on voltage production, and the influence of connecting Power Management System (PMS) with MFC. A 6-unit single-chamber MFC device was built using soil as a catalyst and coconut leaves as a substrate. It was then connected to a PMS. The study showed that a 350

ml MFC unit arranged in series produced a greater voltage of 457 mV compared to a 700 ml container. The smaller chamber was connected in series and integrated with a PMS consisting of a charge pump, DC-DC boost converter, and Maximum Power Point Tracking (MPPT), which led to a maximum stable voltage of 10.56 V. It highlights the possibility of increasing voltage consistently by using smaller MFC chambers, dirt as a catalyst, coconut leaves as a substrate, and aluminum as an electrode, together with a thorough PMS setup.

Keywords: Boost converter, charge pump, microbial fuel cell, power management system, soil microbial fuel cell (SMFC), zinc

ARTICLE INFO

Article history:

Received: 30 March 2024

Accepted: 1 October 2024

Published: 21 February 2025

DOI: <https://doi.org/10.47836/pjst.33.2.04>

E-mail addresses:

sskudnie@unimas.my (Siti Kudnie Sahari)
nashleyujai@gmail.com (Nashley Ursula Mundi Ujai)
t5thommy@gmail.com (Thommy Thomas)
yibrahim@unimas.my (Ibrahim Yakub)
smarini@unimas.my (Marini Sawawi)
lilikhasanah@upi.edu (Lilik Hasanah)
karahman@unimas.my (Abdul Rahman Kram)
zembong@gmail.com (Zaidi Embong)
lkasumawati@unimas.my (Kasumawati Lias)
jannie@unimas.my (Annie Joseph)
lckho@unimas.my (Kho Lee Chin)
wmmasniah@unimas.my (Sharifah Masniah Wan Masra)

*Corresponding author

INTRODUCTION

The yearly rise in global electricity usage poses a significant environmental threat. The utilization of traditional fuel sources such as gas, coal and oil for power production has led to a rise in greenhouse gas (GHG) emissions, which in turn has contributed to the negative impacts of climate change (Chen et al., 2023). This alarming trend is worsened by the consumption of limited non-renewable resources and the rapid expansion of the energy sector's economy and industry. Numerous developing countries have extensively explored alternative and sustainable energy sources to adjust their strategic approaches to addressing the environmental challenges posed by traditional energy practices (Kabeyi & Olanrewaju, 2022).

Various renewable energy sources have been developed to meet the increasing need for energy. An emerging technology that is currently being developed is the MFCs. Employing MFC helps minimize the emission of dangerous chemicals, such as carbon dioxide and wastewater, produced by major companies, which can jeopardize human health and the ecosystem. MFC functions as a bio-electrochemical system, wherein organic chemicals undergo chemical reactions that are converted into electrical energy through the catalytic activities of bacteria within a biofilm (Santoro et al., 2017). The bacteria's end-product produces electrons, which move from an anode chamber (where oxidation occurs) to a cathode chamber (where reduction occurs) (Rabaey & Verstraete, 2005). MFCs have attracted interest due to their capacity to produce electricity ecologically and sustainably. Nevertheless, the reduced voltage output of MFC has become a noteworthy issue. As a result, many research endeavors have been undertaken to examine each element of MFC, particularly the substrate. Various substances, ranging from simple ones like glucose and acetate to more complicated ones like starch, sludge, cellulose waste, and sediments found in seas and rivers, can all be used as substrates in MFC (Lu et al., 2009; Rahimejad et al., 2011; Zhu et al., 2015; Nitorisavut & Regmi, 2017). Biomass substrates are becoming increasingly important because of their high lignocellulosic content, a great resource for nourishing bacteria in the MFC. These materials, used as substrates for energy generation and storage, are highly sought after because they are easy to get, quickly replenishable, and have minimum carbon dioxide emissions.

The coconut leaf, known for its high lignocellulosic content, plays a vital role in generating power in MFC. Our previous study has shown that using coconut waste as a substrate for MFCs resulted in the highest power density of $230 \mu\text{W}/\text{m}^2$, surpassing that of rice husk and bamboo waste (Ujai et al., 2023). It highlights the considerable potential of coconut-derived materials in improving MFC performance. The palm tree, scientifically named *Cocos nucifera* L., plays an essential role in the economy of many Pacific Islands, making a substantial contribution to their prosperity. The palm produces clusters of nuts monthly (Henrietta et al., 2022). Each nut consists of a kernel surrounded by a strong wooden shell and covered by a thick fibrous husk. The palm frond displays a sequence of

leaves organized along a petiole or a strong wooden midrib. The appropriateness of coconut leaves as a substrate for MFC arises from various crucial features. As a permanent crop, coconuts eliminate the need for frequent land preparation and additional work post-planting. Furthermore, the fact that coconut leaves are not limited to specific seasons guarantees their steady and constant availability every month. It makes coconut leaves an excellent and environmentally friendly option for MFC substrate material.

The complexities associated with the lignocellulosic composition pose challenges for bacteria, which potentially cause a decrease in the voltage generation by the MFC (Sahari et al., 2023). Additionally, the unpredictability of MFC electricity production must be considered. Therefore, developing a power management system specifically designed to tackle these challenges is of the utmost importance. A previous inquiry focused on a soil-based single-chamber Microbial Fuel Cell (SMFC) and integrating a DC-DC boost converter into the SMFC led to an extraordinary 150% increase in voltage (Sahari et al., 2022). Nevertheless, the voltage that was produced displayed a lack of stability. To tackle this issue, we put forth an innovative methodology that draws inspiration from Maximum Power Point Tracking (MPPT) systems implemented in solar energy systems. According to our hypothesis, the enhancement and stabilization of the voltage output of MFCs can be achieved by integrating a charge pump, DC-DC converter, and MPPT.

The present study utilized a substrate made of coconut leaf, an aluminum electrode, and a soil catalyst to construct the MFC. The power management system (PMS) integrated with the MFC comprised an MPPT, charge pump, and DC-DC converter. Two distinct dimensions of MFC compartments connected in the series were evaluated.

METHODOLOGY

Design Stage: Construction of Microbial Fuel Cell (MFC)

Preparation of MFC's Electrode

This research employed aluminum foil electrodes measuring 7.35 cm in diameter, maintaining consistency across all MFC units. A small hole was created for wire insertion, which was then secured with solder. Subsequently, the electrode was inserted into a hole in the plastic container, with its connection secured using a hot glue gun to prevent water leakage. The electrode strip was pressed down to ensure maximum contact with the soil to enhance electron transfer rates. Figure 1 shows the visual depiction of the aluminum electrode strip.



Figure 1. Aluminum foil electrode



Figure 2. 700 ml and 350 ml MFC chambers

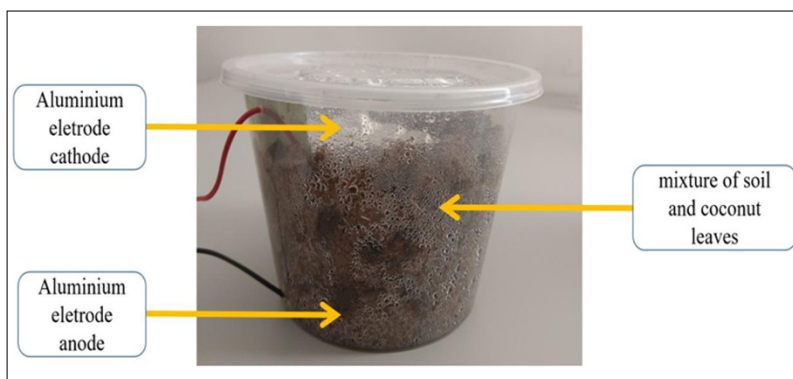


Figure 3. Arrangement of components for the MFC chamber

Construction of MFC Chamber

The small MFC units were assembled using 350 ml plastic containers for the chambers, as depicted in Figure 2, with a hole drilled on one side for accessibility. Two additional holes were made in the lower and upper sections for wire connections to the electrode strip. Soil was sourced from the backyard, while coconut palm leaves were obtained from the garden and shredded using garden shredders. A 5 g of shredded coconut palm leaves and 345 g of soil were mixed in the plastic container by hand or with a stick. Another MFC unit was prepared using 10 g of shredded coconut palm leaves and 695 g of soil for a larger unit, totaling six units. Subsequently, a thin layer of the soil mixture was poured, and the electrode was placed atop it. The container was then filled, and the electrode was positioned on top, as illustrated in Figure 3, detailing the MFC chamber's component arrangement.

Proposed Power Management System (PMS)

A charge pump, a DC-DC converter and the MPPT system were integrated into the PMS to establish a connection between the output and the MFC. Figure 4 depicts the block diagram that is proposed to represent this system. The block diagram depicts the MFC producing

an exceedingly low voltage, measuring around millivolts. As a result, the charge pump is connected to the MFC's output to extract a negligible amount of current from the MFC, thereby enabling the conversion of voltage magnitude and the subsequent charging of a capacitor or supercapacitor. The charged capacitor assists in activating the boost converter upon reaching the required voltage level, owing to the insufficient MFC voltage necessary for starting this basic electronic device. Hence, the incorporation of a charge pump into the PMS fulfills three fundamental objectives: (1) expedite the initiation of the boost converter; (2) extract power that is in closer proximity to the maximum achievable power of the MFCs through the consumption of low current from the MFCs; and (3) aid in the advancement of a power-efficient PMS. MPPT requires that the voltage from the charge pump be increased to a predetermined level by means of the DC-DC boost converter. MPPT becomes imperative in systems reliant on MFCs due to their nonlinear properties. MPPT techniques, often utilized in solar photovoltaic (PV) systems, play a vital role in monitoring and managing the energy transfer from the PV panel to the consumer's load. The details of the charge pump circuit and DC-DC boost converter are shown in Figures 5 and 6, respectively.

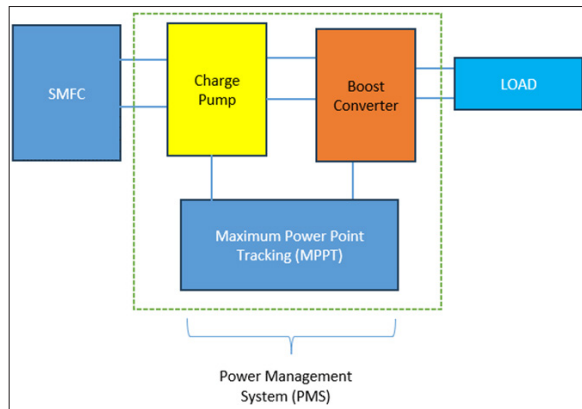


Figure 4. Proposed block diagram of power management system

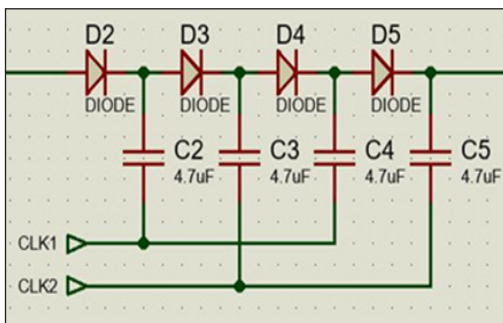


Figure 5. Design of Charge Pump

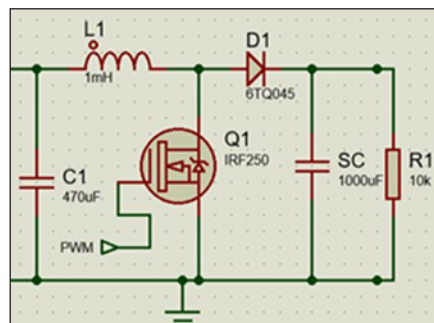


Figure 6. Design of DC-DC Boost Converter

Researchers globally incorporated various MPPT algorithms into their PMS configurations to track the Maximum Power Point (MPP) produced by the MFC. These existing MPPT algorithms include Perturb and Observe (P&O), Incremental Conductance (INC), Fuzzy Logic Control (FLC), Particle Swarm Optimization (PSO) and Model Predictive Control (MPC). In this study, the P&O MPPT algorithm is implemented, considering its simplicity and cost-effectiveness compared to other existing algorithms. The P&O algorithm operates by extracting the maximum allowable fuel cell power, where it periodically perturbs the duty cycle controlling the array and comparing the PV output power with that of the previous perturbation cycle, i.e., $I(i)$ is perturbed periodically until the change in its output power, $P(i)$ is equivalent to zero. The subsequent perturbation is made in the same direction if it leads to an increase; otherwise, it is made in the opposite direction (Eltamaly, 2018). Figure 7 shows the flowchart on the P&O algorithm operation.

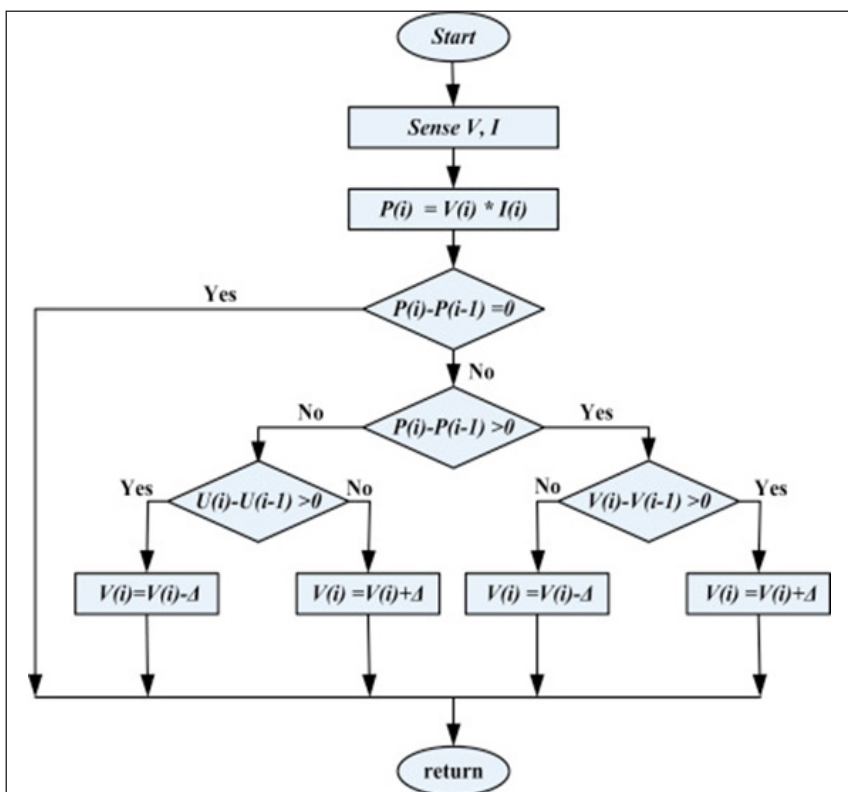


Figure 7. P&O algorithm flowchart (Eltamaly, 2018)

Electrical Measurement

A multimeter was used to measure voltage output from MFCs and compare the outcomes of smaller and larger MFC chambers.

RESULTS AND DISCUSSION

The Effect of Different Sizes of MFC Chambers on Voltage Production

This study examined the influence of chamber size variation on MFCs. Figure 8 demonstrates the voltage generation patterns in larger and smaller MFC chambers. The larger chamber showed almost little voltage for the first 6 days, in contrast to the smaller chamber of MFC. After 7 days of substrate fermentation, the voltage suddenly increased to 280mV, then remained stable at roughly 150mV from 9 to 12. On the other hand, the smaller chamber consistently showed greater voltages without a stable phase. Table 1 displays the average performance of both chamber sizes, showing that the smaller chamber produced around 50% more voltage than the bigger one. The difference in voltage production and stability between smaller and larger chambers in MFCs is influenced by several factors. Smaller chambers, with their higher surface area to volume ratio, enhance microorganism-electrode interactions, leading to higher voltage production (Fathima et al., 2024). Additionally, the confinement within smaller compartments increases microbial density, subsequently enhancing metabolic activity. Its heightened metabolic activity contributes to a higher voltage output by accelerating the rate of electron generation and transfer (Garimella et al., 2024). Moreover, in more compact chambers, the reduced distance that electrons and protons need to travel

Table 1
Average voltage of small chamber versus large chamber for 21 days

Size of Chamber	Voltage (mV)
Small chamber	212
Large chamber	164

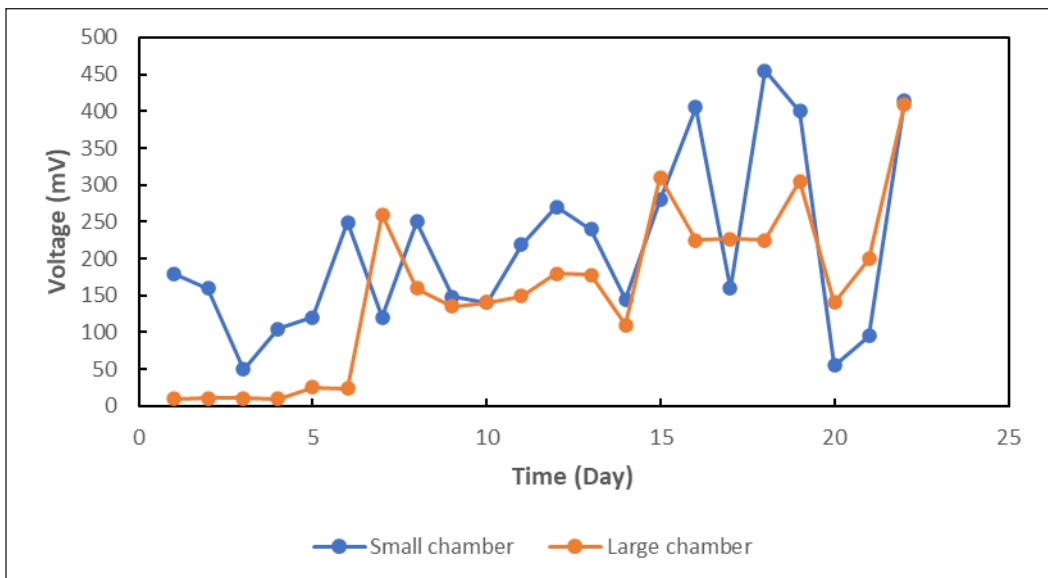


Figure 8. Voltage of small and large chambers of MFC

minimizes energy losses associated with diffusion, thereby increasing the efficiency of the electron transfer process and resulting in higher voltage output (Apollon, 2023). In contrast to the larger chambers, their lower surface area to volume ratio may produce lower voltage but offer greater stability due to their capacity to buffer against environmental fluctuations (Roy et al., 2023). Regardless of chamber size, voltage instability in both chamber types can be attributed to microbial activity and environmental conditions, such as nutrient availability, temperature, and pH, all of which influence the metabolic rates and electron transfer efficiency of microorganisms (Wani et al., 2022).-

The Effect of Different Configurations of MFC Chambers on Voltage Production

The configurations of MFC were compared without a Power Management System, specifically series versus parallel connections. The results indicate that the series configuration of MFC exhibits slightly higher voltage points compared to the parallel configuration, as in Figure 9. In the current study, we observed that in the series configuration, the voltage varied between 51 mV and 457 mV, while in contrast, in the parallel configuration, it spanned from 104 mV to 376 mV. Our findings indicate a notable disparity, suggesting that the series configuration consistently produces higher voltages compared to the parallel arrangement. Due to the additive effect of voltage, series MFCs have a higher voltage than parallel connections. The sum of the voltages of each MFC increases when MFCs are connected in series, leading to a greater overall voltage output. In parallel connections, however, the voltage across each MFC is constant; therefore, the sum of the currents determines the total current, not the voltage. As a result, series connections

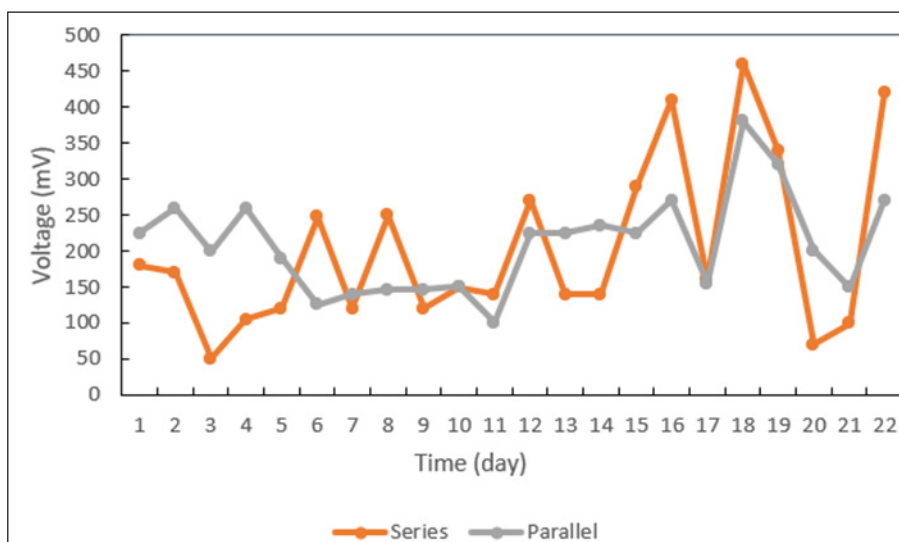


Figure 9 . Voltage from series and parallel configuration of MFC

exhibit greater efficacy in augmenting voltage output than parallel connections. The six chambers were connected in series to the power management system (Figure 10) to increase the voltage production. The voltage increased significantly by over 200% after integrating six series of MFCs connected with a charge pump, as illustrated in Table 2. Following the subsequent connection to a boost converter and MPPT, the voltage increased to 10.56 V, indicating a surge exceeding 500% compared to MFCs that were exclusively connected to a charge pump. The results of this study highlight the significant improvement in the performance of MFC that can be attributed to the effective integration of a charge pump, boost converter and MPPT into the PMS.

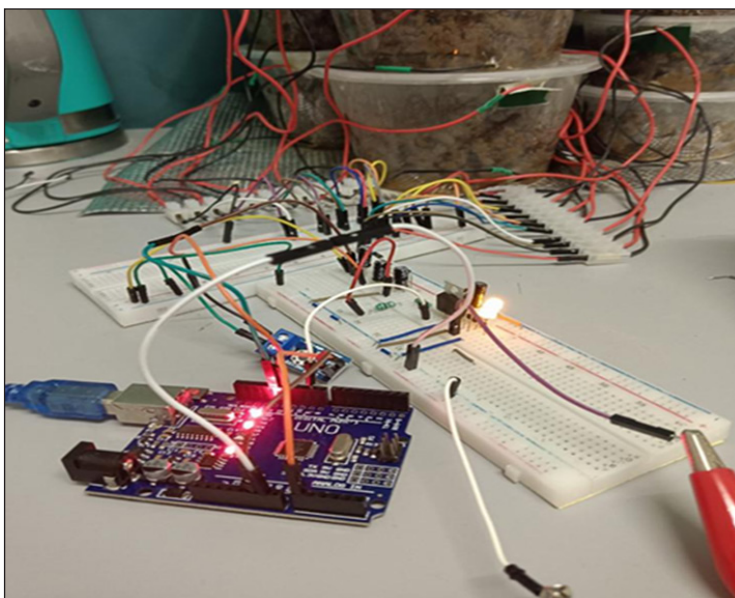


Figure 10. Series connection of 6 units MFC to the Power Management System (PMS)

Table 2

Comparison of electrical properties for different circuit configurations

Parameter	OVC 6 Series MFCs	OVC 6 Series MFCs + Charge Pump	OVC 6 Series MFCs + Charge Pump + Boost Converter + MPPT
Voltage (V)	0.134	2.5	10.56
Current (A)	0.216	0.015	0.036
Power (W)	0.028	0.125	0.038
Efficiency (%)	Initial value	94.64	98.73

We have conducted various experiments implementing different PMS approaches. Table 3 depicts the findings we obtained, illustrating the effect of implementing PMS on MFC.

The observed results indicate that the implementation of the DC-DC boost converter and charge pump with MPPT (Perturb and Observe algorithm) yielded a significantly higher and stable voltage, maintained consistently for 20 minutes.

Table 3
Comparison of voltages obtained from different PMS

Configuration	Voltage (V)	Power Density	Stability Time	Reference
Single-chamber MFC without PMS	-	230 μ W/m ²	N/A	Ujai et al., 2023
DC-DC boost converter without MPPT	1.722 (4 series of soil-based SMFC) 1.592 (4 series soil-based SMFC)	904 mW/m ² (graphite-activated carbon electrodes) 146 mW/m ² (copper-zinc electrodes)	N/A	Sahari et al., 2022
DC-DC boost converter, charge pump with MPPT (P&O algorithm)	10.56	-	20mins	*This study

Voltage Taken from Two Different Time Intervals and Room Conditions

The microbial fuel cell (MFC) voltages were measured at two specified times: from 7:00 to 8:00 in the morning and from 7:00 to 8:00 in the evening. The surroundings were dark in the morning, while it was brightly illuminated in the evening. Figure 11 illustrates a comparison of voltage levels observed during morning and evening measurements under

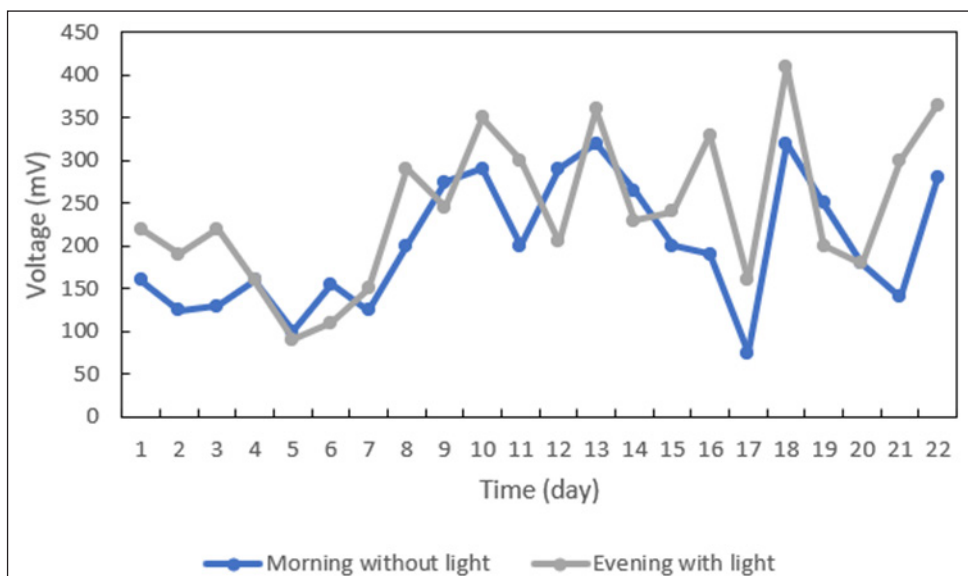


Figure 11. The voltage production from MFC at different room conditions

different room conditions. The microbial fuel cell (MFC) produces a higher voltage at night under bright conditions than in the morning when there is no light. The results indicate that the level of environmental brightness affects voltage generation in contrast to room temperature. This phenomenon could be explained by the photochemical alteration of organic substances caused by visible or ultraviolet light wavelengths, which have been proven to enhance bacterial proliferation in specific environments (Lindell et al., 1995).

COMPARISON OF PREVIOUS STUDIES

Table 4 illustrates the performance of various PMS configurations connected to the MFC. The results reveal that the voltage generated in this study aligns closely with values reported

Table 4
Comparison of MFC with PMS in the literature

Number of MFC	Type of MFC	Power Management System		Input Voltage (V)	Output Voltage (V)	Power (W)	Stability Time (minute)	Reference
		Circuit Topology	MPPT					
4	Single chamber	Boost converter	No	0.7	1.7	N/A	N/A	Sahari et al., 2022
2	Single chamber	Charge pump + boost converter	No	0.3	3.3	0.11	N/A	Umaz, 2020
1	Single chamber	Charge pump + boost converter	No	0.3	3.3	0.95	N/A	Meehan et al., 2011
1	Single chamber	Charge pump + transformer + boost converter	No	0.3-0.18	3.3	0.18	N/A	Zhang et al., 2012
1	Single chamber	MFC + charge pump + 2 boost converter	No	0.3	5	2.5	N/A	Donovan et al., 2011
1	Single chamber	MFC + charge pump + boost converter	Yes	0.3	3.3	N/A	3	Umaz, 2019
2	Single chamber	Charge pump	No	0.3	1.6-2.2	0.11	N/A	Carreon-Bautista et al., 2015
6	Single chamber	Charge pump	No	0.134	2.5	0.125	N/A	This study
6	Single chamber	Charge pump + boost converter + MPPT	Yes	0.134	10.56	0.038	20	This study

in previous literature. Moreover, our investigation demonstrates an enhancement in both voltage output and stability duration, reaching 20 minutes, attributable to the integration of MPPT within the PMS.

CONCLUSION

The study investigated how chamber size, MFC chamber configuration, and environmental factors affect MFC voltage. It was found that smaller MFC chambers yielded notably higher voltages than larger ones. Additionally, series connections resulted in higher voltages due to cumulative current effects. Interestingly, MFC brightness significantly influenced voltage, outweighing temperature effects. Furthermore, the study highlighted the crucial role of Maximum Power Point Tracking (MPPT) in Power Management System (PMS) setups. Integrating a charge pump, boost converter, and MPPT into a six-series PMS configuration significantly improved voltage output and stability. These findings underscore MPPT's effectiveness in optimizing MFC performance by ensuring consistent voltage output over time. The study provides compelling evidence supporting the integration of MPPT into MFC PMS for prolonged periods of reliable voltage production.

ACKNOWLEDGEMENT

A part of this work was supported by a Postgraduate Research Grant (UNI/F02/GRADUATES/86210/2024).

REFERENCES

- Apollon, W. (2023). An overview of microbial fuel cell technology for sustainable electricity production. *Membranes*, 13(11), Article 0884. <https://doi.org/10.3390/membranes13110884>
- Carreon-Bautista, S., Erbay, C., Han, A., & Sanchez-Sinencio, E. (2015). An inductorless DC–DC converter for an energy aware power management unit aimed at microbial fuel cell arrays. *IEEE Journal of Emerging and Selected Topics in Power Electronics*, 3(4), 1109–1121. <https://doi.org/10.1109/jestpe.2015.2398851>
- Chen, X. H., Tee, K., Elnahass, M., & Ahmed, R. (2023). Assessing the environmental impacts of renewable energy sources: A case study on air pollution and carbon emissions in China. *Journal of Environmental Management*, 345, Article 118525. <https://doi.org/10.1016/j.jenvman.2023.118525>
- Donovan, C., Dewan, A., Peng, H., Heo, D., & Beyenal, H. (2011). Power management system for a 2.5W remote sensor powered by a sediment microbial fuel cell. *Journal of Power Sources*, 196(3), 1171–1177. <https://doi.org/10.1016/j.jpowsour.2010.08.099>
- Eltamaly, A. M. (2018). Performance of MPPT techniques if photovoltaic systems under normal and partial shading conditions. In I. Yahyaoui (Ed.), *Advances in Renewable Energies and Power Technologies: Volume 1: Solar and Wind Energies* (pp. 115-161). Elsevier. <https://doi.org/10.1016/b978-0-12-812959-3.00004-6>

- Fathima, A., Ilankoon, I. M. S. K., Zhang, Y., & Chong, M. N. (2024). Scaling up of dual-chamber microbial electrochemical systems – An appraisal using systems design approach. *Science of The Total Environment*, 912, Article 169186. <https://doi.org/10.1016/j.scitotenv.2023.169186>.
- Garimella, S. S. S., Rachakonda, S. V., Pratapa, S. S., Mannem, G. D., & Mahidhara, G. (2024). From cells to power cells: Harnessing bacterial electron transport for microbial fuel cells (MFCs). *Annals of Microbiology*, 74, Article 19. <https://doi.org/10.1186/s13213-024-01761-y>
- Henrietta, H. M., Kalaiyarasi, K., & Raj, A. S. (2022). Coconut tree (*Cocos nucifera*) products: A review of global cultivation and its benefits. *Journal of Sustainability and Environmental Management*, 1(2), 257–264. <https://doi.org/10.3126/josem.v1i2.45377>
- Kabeyi, M. J., & Olanrewaju, O. A. (2022). Sustainable energy transition for renewable and low carbon grid electricity generation and supply. *Frontiers in Energy Research*, 9, Article 743114. <https://doi.org/10.3389/fenrg.2021.743114>
- Lindell, M. J., Granéli, W., & Tranvik, L. J. (1995). Enhanced bacterial growth in response to photochemical transformation of dissolved organic matter. *Limnology and Oceanography*, 40(1), 195–199. <https://doi.org/10.4319/lo.1995.40.1.0195>.
- Lu, N., Zhou, S., Zhuang, L., Zhang, J., & Ni, J. (2009). Electricity generation from starch processing wastewater using microbial fuel cell technology. *Biochemical Engineering Journal*, 43(3), 246–251. <https://doi.org/10.1016/j.bej.2008.10.005>
- Meehan, A., Gao, H., & Lewandowski, Z. (2011). Energy harvesting with microbial fuel cell and power management system. *IEEE Transactions on Power Electronics*, 26(1), 176–181. <https://doi.org/10.1109/tpe.2010.2054114>
- Nitorisavut, R., & Regmi, R. (2017). Plant Microbial Fuel Cells: A promising biosystems engineering. *Renewable and Sustainable Energy Reviews*, 76, 81–89. <https://doi.org/10.1016/j.rser.2017.03.064>
- Rabaey, K., & Verstraete, W. (2005). Microbial fuel cells: Novel biotechnology for energy generation. *Trends in Biotechnology*, 23(6), 291–298. <https://doi.org/10.1016/j.tibtech.2005.04.008>
- Rahimnejad, M., Najafpour, G. D., Ghoreyshi, A. A., Shakeri, M., & Zare, H. (2011). Methylene blue as electron promoters in microbial fuel cell. *International Journal of Hydrogen Energy*, 36(20), 13335–13341. <https://doi.org/10.1016/j.ijhydene.2011.07.059>
- Roy, H., Rahman, T. U., Tasnim, N., Arju, J., Rafid, M. M., Islam, M. R., Pervez, M. N., Cai, Y., Naddeo, V., & Islam, M. S. (2023). Microbial fuel cell construction features and application for sustainable wastewater treatment. *Membranes*, 13(5), Article 490. <https://doi.org/10.3390/membranes13050490>
- Sahari, S. K., Butit, A. M., Ngaini, Z., Arief, Y. Z., Kipli, K., Anyi, M., Awang, A., Muhammad Kashif, M. K., Mahmood, M. R., Embong, Z., Lilik Hasanah, L. H., Kram, A. R., & Sawawi, M. (2023). Bioelectricity generation from bamboo leaves waste in a double chambered microbial fuel cell. *Sains Malaysiana*, 52(6), 1855–1864. <https://doi.org/10.17576/jsm-2023-5206-20>
- Sahari, S. K., Rosli, M. Z. F., Butit, A. M., Kipli, K., Anyi, M., Awang, A., Sawawi, M., Mahmood, M. R., Hasanah, L., Kram, A. R., Embong, Z., & Nahrawi, H. (2022). Fabrication of single chamber microbial fuel cell (SMFC) using soil as a substrate. *Pertanika Journal of Science and Technology*, 30(2), 1103–1114. <https://doi.org/10.47836/pjst.30.2.14>

- Santoro, C., Arbizzani, C., Erable, B., & Ieropoulos, I. (2017). Microbial fuel cells: From fundamentals to applications. A Review. *Journal of Power Sources*, 356, 225–244. <https://doi.org/10.1016/j.jpowsour.2017.03.109>
- Ujai, N. U. M., Sahari, S. K., Sawawi, M., Kipli, K., Awang, A., Mahmood, M. R., Hasanah, L., Kram, A. R., & Ngaini, Z. (2023). The effect of nutrients in anodic chamber to the performance of microbial fuel cell (MFC). *Pertanika Journal of Science and Technology*, 32(1), 205–215. <https://doi.org/10.47836/pjst.32.1.12>
- Umaz, R. (2019). A two-stage power converter architecture with maximum power extraction for low-power energy sources. *Turkish Journal of Electrical Engineering & Computer Sciences*, 27(6), 4744–4755. <https://doi.org/10.3906/elk-1811-6>
- Umaz, R. (2020). A power management system for microbial fuel cells with 53.02% peak end-to-end efficiency. *IEEE Transactions on Circuits and Systems II: Express Briefs*, 67(11), 2592–2596. <https://doi.org/10.1109/tcsii.2019.2951810>
- Wani, A. K., Akhtar, N., Sher, F., Navarrete, A. A., & Américo-Pinheiro, J. H. P. (2022). Microbial adaptation to different environmental conditions: Molecular perspective of evolved genetic and cellular systems. *Archives of Microbiology*, 204(2), Article 144. <https://doi.org/10.1007/s00203-022-02757-5>
- Zhang, D., Yang, F., Shimotori, T., Wang, K. C., & Huang, Y. (2012). Performance evaluation of power management systems in microbial fuel cell-based energy harvesting applications for driving small electronic devices. *Journal of Power Sources*, 217, 65–71. <https://doi.org/10.1016/j.jpowsour.2012.06.013>
- Zhu, D., Wang, D. B., Song, T., Guo, T., Wei, P., Ouyang, P., & Xie, J. (2015). Enhancement of cellulose degradation in freshwater sediments by a sediment microbial fuel cell. *Biotechnology Letters*, 38(2), 271–277. <https://doi.org/10.1007/s10529-015-1985-z>

Simulation of Solar Charge Controller Module with Current Backflow Protection

Aimi Dalila Azhar^{1*}, Weng Ho Yew², Akmal Zaini Arsad², Azrul Ghazali¹,
Fazrena Azlee Hamid¹ and Ahmad Wafi Mahmood Zuhdi^{1,2}

¹College of Engineering, Universiti Tenaga Nasional (UNITEN), Kajang 43000, Selangor, Malaysia

²Institute of Sustainable Energy, Universiti Tenaga Nasional (UNITEN), Kajang 43000, Selangor, Malaysia

ABSTRACT

Solar energy is popular worldwide due to the escalating demand for renewable and clean energy solutions. The inherent low power conversion efficiency of solar panels highlights the indispensable role of a solar charge controller in optimizing the power transfers from the solar panel to a storage battery. Traditional buck converters are marred by considerable power losses due to freewheeling diodes, thus making a synchronous buck converter, which necessitates protection against the reverse current from the battery to the solar panel. During low irradiation, the solar panel voltage typically falls below the battery voltage, creating the potential for reverse current flow, which may cause damage to other system components. This study proposes an innovative current backflow protection circuit, effectively addressing reverse polarity risks, demonstrated through LTspice simulations. Utilizing an NMOS MOSFET, this circuit disrupts the connection whenever solar panel voltage falls beneath a predefined cutoff value, thereby preventing reverse current damage. The protective mechanism's efficacy is validated by monitoring the NMOS MOSFET's drain current, which remains at 0A below the cutoff voltage but transitions to negative values above it, indicating a reverse flow and underscoring the circuit's reliability in safeguarding solar energy systems.

Keywords: Current backflow, cutoff MOSFET, protection circuit, solar charge controller, undervoltage

ARTICLE INFO

Article history:

Received: 4 April 2024

Accepted: 1 October 2024

Published: 21 February 2025

DOI: <https://doi.org/10.47836/pjst.33.2.05>

E-mail addresses:

aimi.dalila@uniten.edu.my (Aimi Dalila Azhar)

whyew97@hotmail.com (Weng Ho Yew)

akmalzaini@uniten.edu.my (Akmal Zaini Arsad)

azrulg@uniten.edu.my (Azrul Ghazali)

Fazrena@uniten.edu.my (Fazrena Azlee Hamid)

Wafi@uniten.edu.my (Ahmad Wafi Mahmood Zuhdi)

*Corresponding author

INTRODUCTION

Solar energy is one of the abundant resources that can be harvested to meet energy demands following the sustainable energy solution. Solar photovoltaic (PV) systems have become an important component of renewable energy, generating electricity for

a wide array of applications, from residential rooftops to large-utility installations (Breyer et al., 2021). A solar charge controller (SCC) is responsible for ensuring that solar energy is optimally converted into electricity, increasing the efficiency of the system (Rokonuzzaman et al., 2020). Typically, a SCC uses buck converter topology to step down the voltage from the solar panel to the battery. Figure 1(a) presents a conventional buck converter consisting of a MOSFET, a freewheeling diode, an inductor, and a capacitor. The freewheeling diode has caused a significant loss from the voltage drop across it (Zomorodi & Nazari, 2022). A synchronous buck converter was used to replace the diode with an active component, such as a MOSFET, as shown in Figure 1(b), to address this issue.

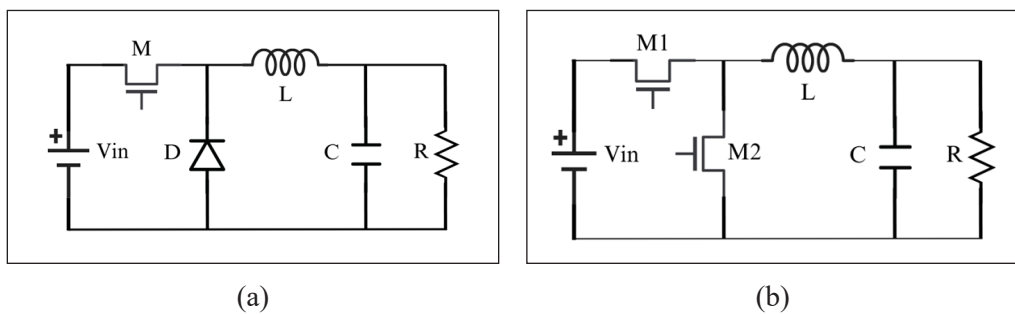


Figure 1. Circuit diagram of (a) conventional buck converter and (b) synchronous buck converter

The synchronous buck converter, however, has a few drawbacks. Switching losses occur during the switching of the MOSFETs depending on the frequency of the converter (Eraydin & Bakan, 2020). Lee et al. (2015) improved up to 7% efficiency by introducing a zero-voltage resonant-transition switching on a GaN-based synchronous buck converter. The resonant transition ensures the MOSFET is turned on and off when only the voltage across it is zero or nearly zero. Kumar et al. (2015) used a simple passive auxiliary circuit to reduce the stress caused by the switching action and can improve the efficiency of the synchronous buck converter. Therefore, proper gate driver circuitry and MOSFET selection are crucial to minimizing the switching losses.

On the other hand, a synchronous buck converter also requires circuit protection since the presence of passive components like an inductor and capacitor may create a potential for voltage spike and current surge (Muntaser et al., 2022). Wang et al. (2016) proposed a fast overcurrent detection method that limits the inductor peak current during short circuit cases. This applied method is able to protect the devices from any damage caused by the overcurrent. Guo et al. (2019) used a current-constraint controller to work with a disturbance observer to limit the inductor current whenever a disturbance occurred. A peak current detection with an in-built maximum current limiter was offered by Deo et al. (2022) again to limit the inductor's current. Hammerbauer and Stork (2021) acknowledged that an

overvoltage might happen during sudden load disconnects. They used a comparator after the inductor or simply a Zener diode to protect the transistor of the buck converter for a low-power converter application. Nevertheless, these overvoltage solutions only address the problems related to the load.

The inductor in the buck converter keeps charging and discharging while storing energy in the form of a magnetic field during the switching process. When energy is released during discharging, a reverse current may occur, which flows in the opposite direction (Marouchos, 2006). Besides, a reverse current might also happen during a lack of irradiation, in which the voltage extracted from the solar panel is lower than the voltage supplied to the battery. This phenomenon typically occurs in dual-active-bridge (DAB) converters, which reduces the converter's efficiency (Xu et al., 2022). Since the DAB converter is a dual-flow converter, the power backflow needs to be minimized instead of prevented. The reverse current that flows from the battery to the solar panel may cause damage to the components of the buck converter. Raghavendra and Padmavathi (2018) acknowledged that the reverse polarity of the battery may have caused this phenomenon. Hence, they used a transistor to detect the polarity of the battery and turn a MOSFET OFF when it is reversed. Kumar et al. (2018) utilized a MOSFET to block the current from the battery whenever the battery is fully charged, as indicated by an LED. Meanwhile, Gupta et al. (2022) implemented a relay to disconnect the battery from the system.

To the best of our knowledge, no work has been conducted to overcome the problem of current backflow from the load to the solar panel specifically caused by under-voltage at the input side. Most of the literature discussed monitoring the status of the battery before disconnecting it, while current backflow might happen before the battery is fully charged, which is during low irradiation. Therefore, this paper addresses the issue of current backflow that typically occurs in synchronous buck converters due to a drop in the input voltage compared to the output. A 50W solar panel with a maximum voltage of 20V and a 12V lead acid battery is used. A predefined offset value of 15V is set as the minimum voltage of the solar panel before the protection circuit disconnects the solar panel from the whole system. MPPT algorithm is not the main focus of this study since the issue is on the current backflow.

MATERIALS AND METHODS

Buck Converter

From this discussion onwards, the input voltage term is used to mention voltage from the solar panel, while output voltage for voltage is supplied to the battery. A circuit diagram of a conventional buck converter is portrayed in Figure 1(a). It consists of a MOSFET (M), a freewheeling diode (D), an inductor (L), a capacitor (C), and a load (R). When MOSFET M1 is ON, the current will flow from the input voltage to the load through the

inductor. When it is OFF, the current will flow through the diode, and since a diode has a high voltage drop of around 0.7V, it will cause a conduction loss that will lead to efficiency reduction. A lower-side MOSFET, M2, is used to replace the diode in a synchronous buck converter, as displayed in Figure 1(b), which will reduce the drop typically around 0.3V or less, therefore increasing the power efficiency by 5% or higher (Eraydin & Bakan, 2020).

Current Backflow in Synchronous Buck Converter

During dawn, dusk, and night times, where low irradiance times and places, the voltage from the solar panel has the potential to be lower than the battery voltage, thus causing a current backflow from the battery to the panel. In a synchronous buck converter, a large reverse current flow might happen when the output voltage is higher than the input voltage, and the output capacitance is modeled as the battery is large (Wang et al., 2019). The reverse current from the inductor, $I_{L, reversed}$ during discharging, and the reverse current that flows through the body diode of M1, $I_{M1, reversed}$ during the OFF state, produced around three to four times the amount that flows through the inductor, as portrayed in Figure 2, therefore damaging the M2. Compared to a conventional buck converter, the current backflow is most unlikely to happen because of the presence of the freewheeling diode that blocks any current flow from the opposite direction.

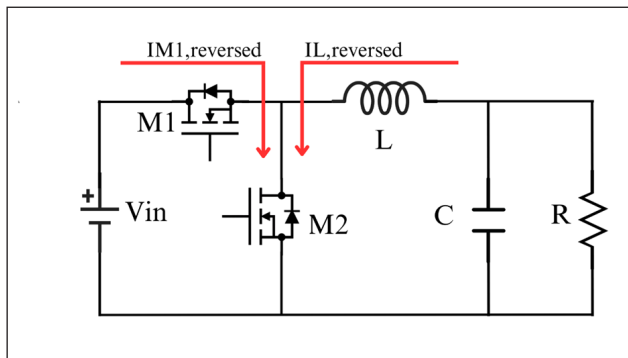


Figure 2. Reverse current is caused by reverse current from the inductor and transistor (M1) body diode

Current Backflow Protection Circuit

In this paper, a protection circuit is designed to address the issue of the current backflow in a synchronous buck converter. The circuit is placed between the input voltage and the buck converter, as shown in Figure 3. The buck converter circuit will be disconnected from the solar panel when the solar panel voltage falls below a predefined offset value. The offset value of 15V was chosen, as it is slightly higher than the maximum charging voltage of the battery, which is 14.8V. Simulation using LTSpice was conducted to analyze

the behavior of the circuits under various conditions, with components modeled based on real components to ensure circuit functionality.

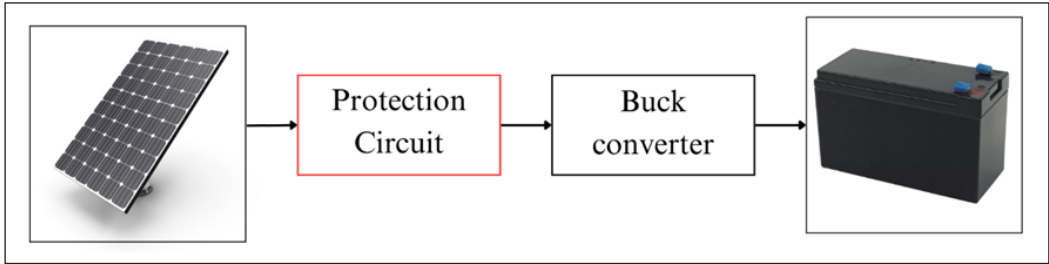


Figure 3. Block diagram of the proposed system

Figure 4 shows the circuit diagram of the protection circuit. V_{panel} represents the input voltage from the solar panel, while V_{buck} represents the voltage of the synchronous buck converter circuit. M3, on the other hand, is the cutoff NMOS MOSFET that will connect and disconnect the converter circuit. V_{cc} is set to 12V, while V_{pc} is voltage-dependent on the V_{panel} value. Besides, the gate voltage of M4, V_g and M4 depends on V_{pc} . In other words, the state of M4 depends on the value of V_{panel} .

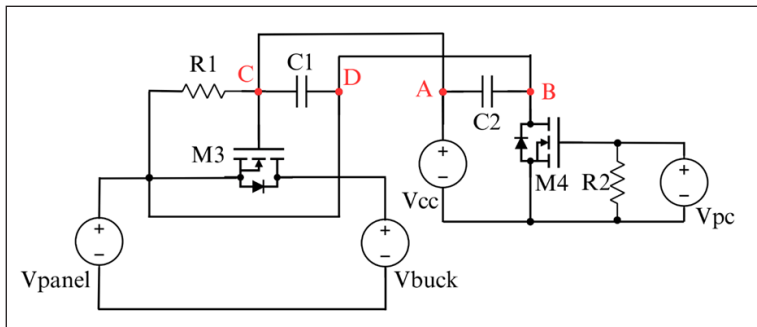


Figure 4. Current backflow protection circuit

For the first case where $V_{panel} \geq 15V$, M4 will be ON and shorted to ground, thus introducing a voltage difference between Node A and B. Since Node C is equal to Node A, while Node D is equal to Node B, they will have the same value. The voltage difference is good enough to make M3 ON and thus connect the solar panel from the buck converter. On the other hand, for the second case where $V_{panel} < 15V$, V_{pc} is inadequate to supply enough voltage to $V_{g, M4}$. M4 is OFF and causes the same voltage at Node A and B. The same voltage value is insufficient to make M3 ON, thus disconnecting the solar panel from the buck converter.

RESULTS AND DISCUSSION

Synchronous Buck Converter

A synchronous buck converter consists of two MOSFETs, an inductor, and a capacitor at the output, as shown in Figure 5. An NMOS (IRFZ44N, Infineon) with a threshold voltage, V_{th} of 4V, was selected because it has low on-state resistance and fast switching speed that are suitable for use by a switching converter. The gate signals are given a PWM signal with a 50% duty cycle driven by a gate driver that uses a push-pull configuration. The gate driver contains a bootstrap capacitor, C2, that will introduce a delay to produce a dead time to minimize the switching losses.

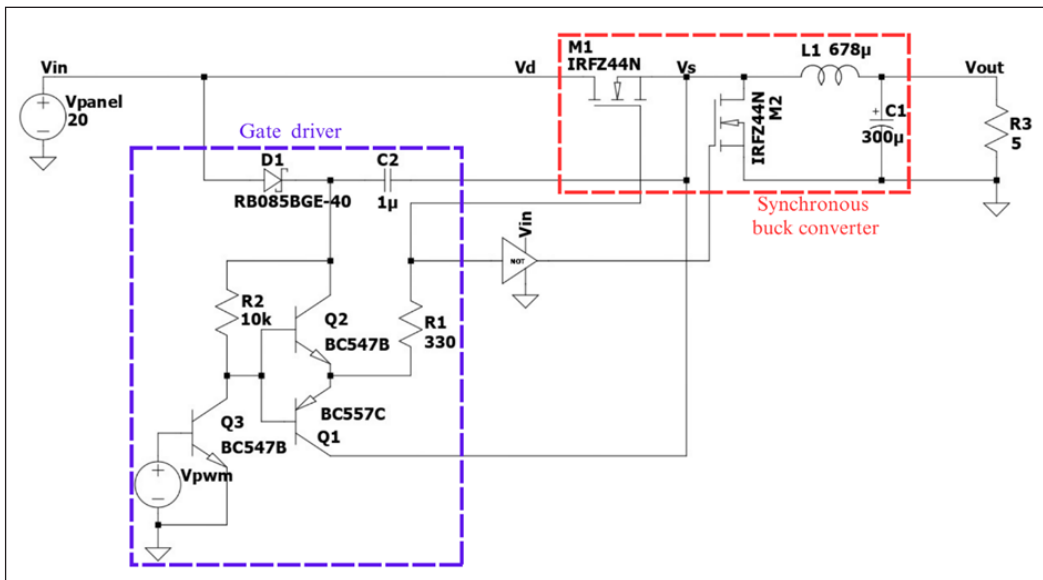


Figure 5. Synchronous buck converter circuit in LTspice

Figure 6(a) shows the voltage transfer function of the synchronous buck converter by sweeping the V_{panel} from 0V to 20V. The linear graph starts at 4V panel voltage, which indicates the need to exceed the V_{th} of the M1 to operate the converter. The same model is simulated again for a transient time of 30ms, and the V_{panel} is set to constant 20V. The output response (V_{out}) is shown in Figure 6(b). The graph shows that the circuit took around 9ms for the output voltage to achieve a steady state voltage of 9.43V. The slightly lower voltage from the estimated 50% duty cycle is due to conduction losses from the NMOS (Eraydin & Bakan, 2020). It shows that the synchronous buck converter has a small power drop with a power efficiency of 94.3%.

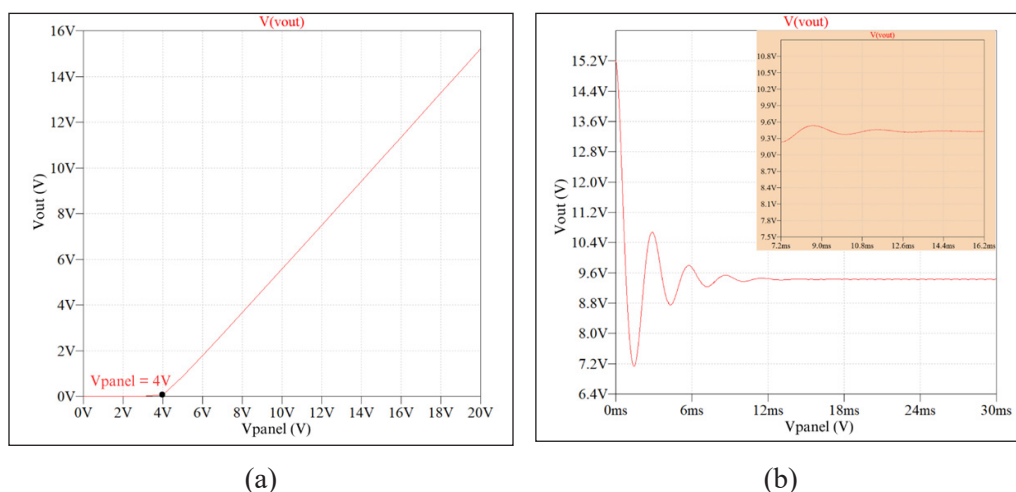


Figure 6. Output voltage of synchronous buck converter for (a) panel voltage from 0V to 20V, and (b) panel voltage at 20V in 30ms

Current Backflow Protection Circuit

The proposed protection circuit in Figure 4 was previously implemented in LTspice, as shown in Figure 7. M3 uses NMOS (CSD17506, Texas Instrument) with V_{TH} of 1.6V as the cutoff NMOS because it has the lowest drift in R_{DS} on over operating temperature range. M4 uses NMOS (Si2316DS, Vishay) with a threshold voltage, $V_{TH,M4}$ of 2.1V. When $V_{panel} < 15V$, the V2 will supply V_g , M4 is lower than $V_{TH,M4}$, and thus, M4 is turned OFF. An additional resistor, R2, is added in series with a voltage source to make it a current source from the solar panel for better analysis in LTspice.

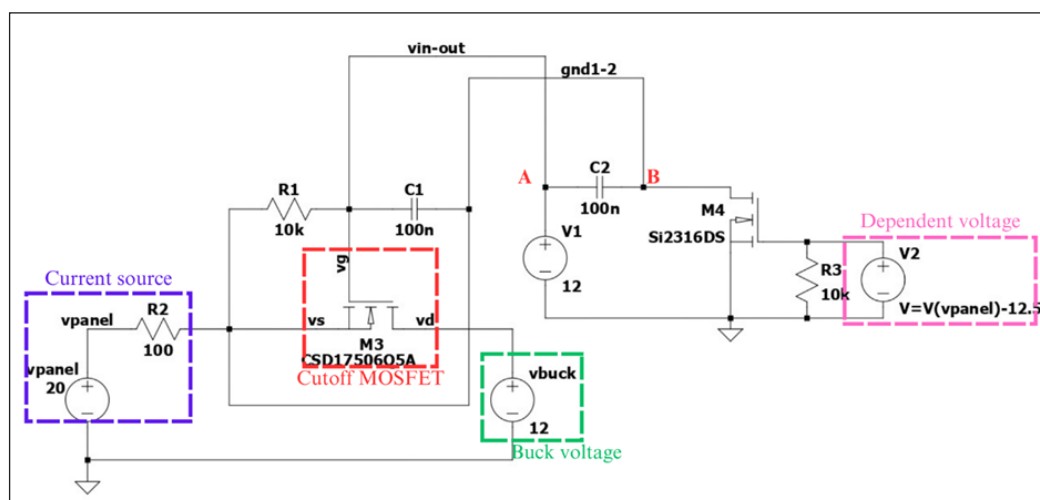


Figure 7. LTspice model of backflow current protection circuit

Figure 8(a) below shows the gate-to-source V_{GS} of M3 for panel voltage from 0V to 20V. At 15V V_{panel} , M3 is turned ON after V_{GS} reaches the $V_{TH,M3}$, which is 1.7V. The drain current I_D , meanwhile, is shown in Figure 8(b) for the same panel voltage. In the OFF region where the $V_{panel} < 15V$, no current flows out of the M3. At 15V V_{panel} , the M3 starts to ON, and the current starts to flow. This proves that the M3 is able to block the reverse current flowing from the buck converter to the solar panel in the OFF region.

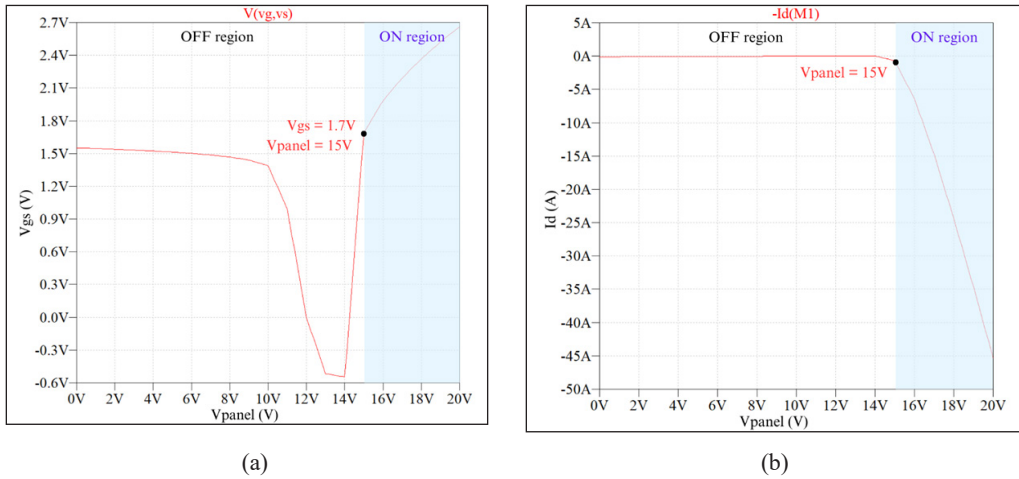


Figure 8. (a) VGS and (b) ID of M3 for backflow current protection circuit

Synchronous Buck Converter with Current Backflow Protection Circuit

Figure 9 shows the integration of the synchronous buck converter and backflow current protection circuit in LTspice. The protection circuit is located between the voltage source and the synchronous buck converter. Initially, the model is simulated without a battery model first. Figure 10(a) shows the I_D of M3 to monitor the ON/OFF state of the NMOS. M3 has a leakage current of $1\mu A$; therefore, M3 is assumed to be ON when I_D is more than $1\mu A$. From Figure 10(a), the M3 is ON when $V_{panel} < 15V$ while OFF when $V_{panel} > 15V$, which is supposedly ON only when the V_{panel} is more than 15V.

Therefore, a battery model is inserted as the load of the buck converter to force an almost constant 12 voltage. The I_D current is presented in Figure 10(b), showing the current is almost 0A for $V_{panel} < 15V$, indicating the OFF state of M3. Then, it decreases to almost -6A after the V_{panel} reaches 15V, indicating the ON state of M3. The ON and OFF regions with the additional battery model are now swapped (Figure 10). It shows that reverse current might not happen when there is no battery as the load. This battery introduced a voltage difference that led to a reverse current, as shown in Figure 10(b).

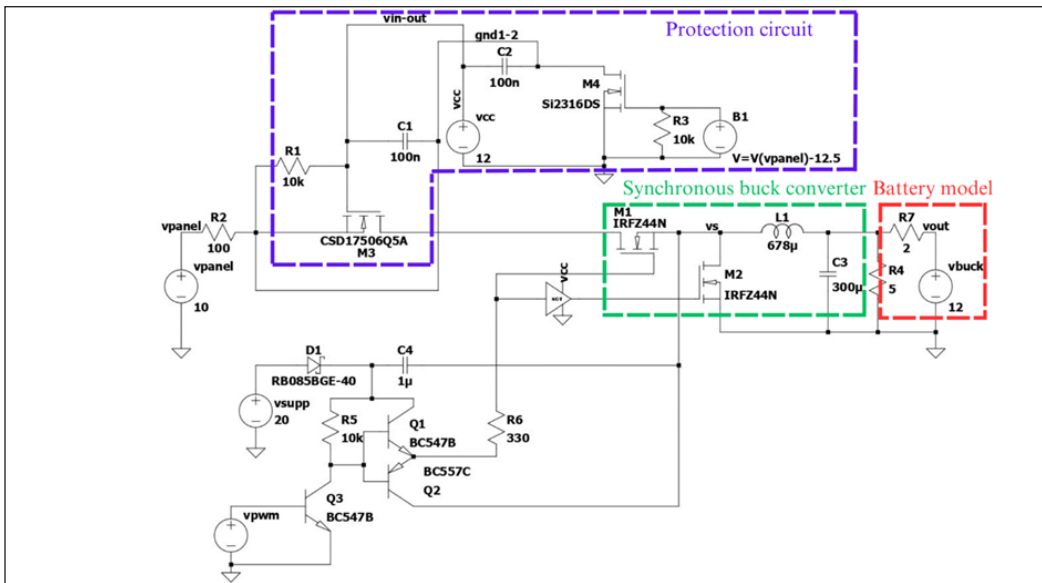


Figure 9. Synchronous buck converter with protection circuit in LTSpice

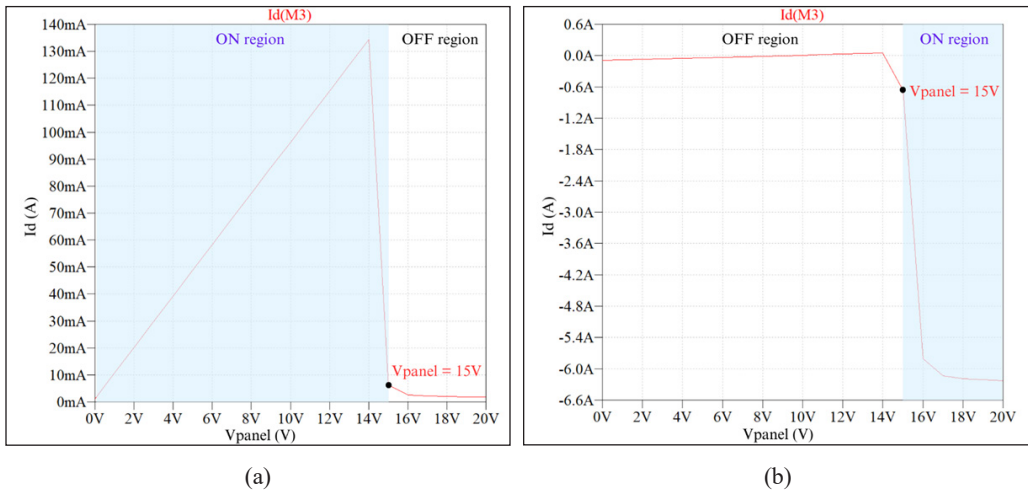


Figure 10. Drain current of M3 for a synchronous buck converter with protection circuit (a) without battery model, and (b) with battery model

Validation of the Results

Model validation was performed by inserting the current backflow protection circuit into a solar charge controller module prototype. The prototype was then tested under a controlled condition to replicate a low irradiance condition. Further testing under real operating conditions will be conducted and reported in a separate manuscript. Figure 11 shows the

response of the input current when the input voltage is beneath the predefined offset voltage during a period of low irradiation ($300\text{W}/\text{m}^2$). The input current fell to 0A when the input voltage started to drop towards 15V. The current was maintained at 0A until the voltage rose steadily beyond 15V.

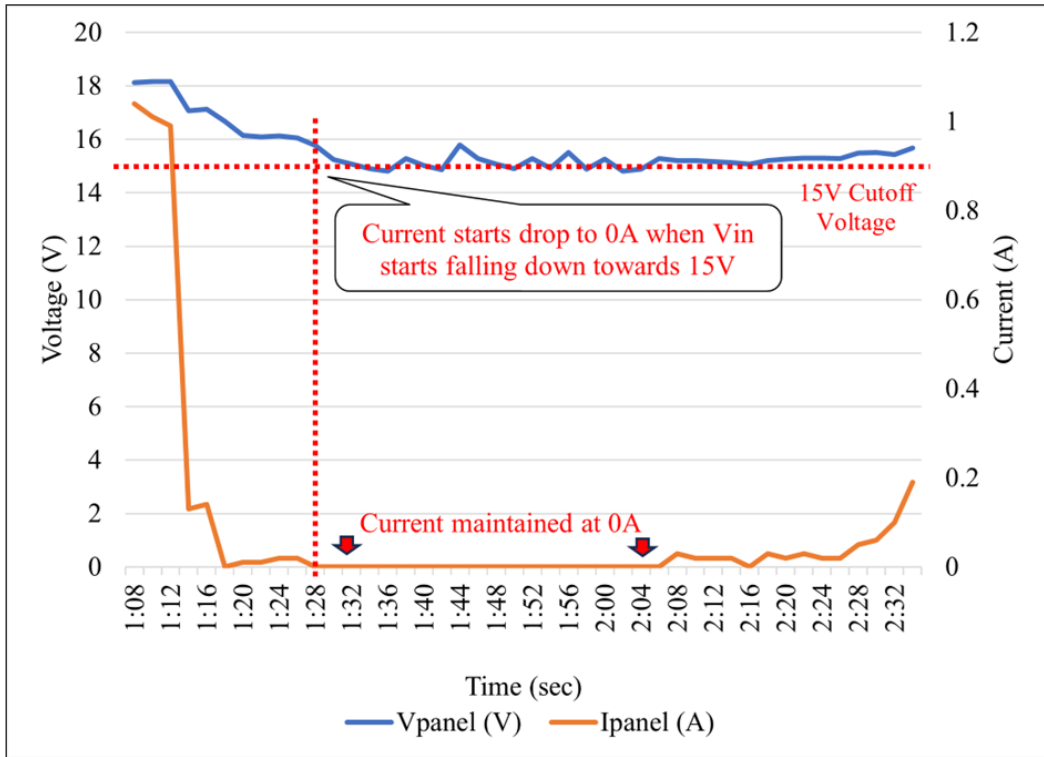


Figure 11. Input current response to the input voltage

Discussion of the Results

A synchronous buck converter was successfully simulated in LTspice. The output voltage gives a value once the input voltage exceeds the MOSFET's V_{TH} . The buck converter steps down the input voltage with an efficiency of 94.3%. A current source is used as the input to monitor the system's current flow. The current starts giving a value after the input voltage exceeds the predefined offset value of 15V. The current is in negative values, showing that the current is flowing in the opposite direction.

After passing the functionality test of the individual circuit, the protection circuit is integrated into the synchronous buck converter. At first, the converter seems to be ON for $0\text{V} < \text{input voltage} < 15\text{V}$. The voltage at Vd of M3 is no longer a 12V, as constructed in Figure 7, because it depends on the input voltage values. Consequently, a 12V battery model is inserted as the circuit's load to force a constant 12V at Vd. The converter is simulated

again and shows different behavior. The output current starts giving negative values after the input voltage achieves 15V. The proposed protection circuit can block the reverse current when the input voltage is below the predefined offset value of 15V.

Compared to the output voltage of the synchronous buck converter without circuit protection in Figure 6, the buck converter is operated when the panel voltage reaches the threshold voltage, which is 4V. Meanwhile, a protection circuit is introduced only to let the buck converter operate after the panel voltage reaches the predefined offset voltage of 15V, as shown in Figure 10. From Figure 10, the current is flowing in the reverse direction. Therefore, for $V_{\text{panel}} < 15\text{V}$, the protection circuit can block the reverse current by disconnecting the solar panel from the synchronous buck converter. In addition, the model was validated by using a prototype. The protection circuit was proven to disconnect the solar panel from the buck converter whenever the input voltage drops below 15V.

CONCLUSION

This paper introduces a protection circuit with a synchronous buck converter strategically designed to mitigate the challenges associated with current backflow during low irradiance and nighttime operation. The proposed circuit works by turning off the cutoff NMOS MOSFET M3 and consequently shutting down the converter when the panel voltage falls below the predefined offset voltage of 15V. This protective mechanism is achieved through the introduction of a specific potential difference at the gate and source of M3. The proposed protection circuit has been simulated using the LTspice software. Using the available market components in the simulation, the proposed model shows a promising result in preventing current backflow in synchronous buck converter. The design was also validated through a prototype, which proved the proof-of-concept of the protection circuit.

Using a highly efficient topology, a synchronous buck converter, brings many benefits to a solar charge controller application. However, timing plays a critical role in determining the operation of the converter. During the simulation, the timing of the upper-side and lower-side MOSFET (M1 and M2) can work synchronously, but not in the implementation. It comes with the role of the gate driver to ensure the MOSFETs switch quickly and efficiently. Other than that, having four MOSFETs in a controller will increase heat dissipation. Ineffective thermal management will cause higher temperatures and lead to higher losses, further damaging the components. Lastly, changing the type of MOSFETs (M3 and M4) might produce different results because the protection circuit depends on the V_{TH} value of the MOSFET. Different MOSFET has different V_{TH} values.

The next phase of the research involves establishing a hardware model to experimentally verify the robustness and real-world applicability of the proposed protection circuit. This validation process by using the hardware model is crucial for confirming the reliability and performance of the circuit in practical scenarios, considering factors such as

component tolerances, temperature variations, and transient conditions. Future work also could explore enhancing the circuit's efficiency, reducing power losses, or adapting it for specific application scenarios. Additionally, comprehensive testing under diverse operating conditions will contribute to a more thorough understanding of the circuit's behavior.

ACKNOWLEDGEMENT

The authors acknowledged the support of the Institute of Sustainable Energy (ISE) of Universiti Tenaga Nasional and UNITEN R&D Sdn. Bhd. for continuous support through the TNB Seeding fund U-TE-RD-18-01.

REFERENCES

- Breyer, C., Bogdanov, D., Khalili, S., & Keiner, D. (2021). Solar photovoltaics in 100% renewable energy systems. In Meyers, R. A. (Ed.), *Encyclopedia of Sustainability Science and Technology* (pp. 1-30). Springer. https://doi.org/10.1007/978-1-4939-2493-6_1071-1
- Deo, A., Maity, A., & Patra, A. (2022). A voltage-emulated peak current controlled buck converter for automotive applications with in-built over-current protection. *Microelectronics Journal*, 123, Article 105423. <https://doi.org/10.1016/J.MEJO.2022.105423>
- Eraydin, H., & Bakan, A. F. (2020). Efficiency comparison of asynchronous and synchronous buck converter. In *2020 6th International Conference on Electric Power and Energy Conversion Systems (EPECS)* (pp. 30-33). IEEE Publishing. <https://doi.org/10.1109/ICPERE.2012.6287236>
- Guo, T., Huang, S., & Wang, X. (2019). Overcurrent protection control design for DC-DC buck converter with disturbances. *IEEE Access*, 7, 90825–90833. <https://doi.org/10.1109/ACCESS.2019.2926985>
- Gupta, P. P., Kumar, N., & Nangia, U. (2022). Passive cell balancing and battery charge controller with CCCV topology. In *2022 3rd International Conference for Emerging Technology (INCET)* (pp. 1-5). IEEE Publishing. <https://doi.org/10.1109/INCET54531.2022.9825104>
- Hammerbauer, J., & Stork, M. (2021). Output overvoltage in DC-DC switching converters in case of sudden unloading. In *2021 International Conference on Applied Electronics (AE)* (pp. 1-4). IEEE Publishing. <https://doi.org/10.23919/AE51540.2021.9542875>
- Kumar, P., Sinha, P., Roy, C., & Basu, M. (2018). Design and implementation of solar charge controller for photovoltaic systems. *ADBU-Journal of Engineering Technology*, 7(1), 1-4.
- Kumar, S. S., Panda, A. K., & Ramesh, T. (2015). A ZVT-ZCT PWM synchronous buck converter with a simple passive auxiliary circuit for reduction of losses and efficiency enhancement. *Ain Shams Engineering Journal*, 6(2), 491–500. <https://doi.org/10.1016/J.ASEJ.2014.10.018>
- Lee, W., Han, D., Morris, C., & Sarlioglu, B. (2015). Minimizing switching losses in high switching frequency GaN-based synchronous buck converter with zero-voltage resonant-transition switching. In *2015 9th International Conference on Power Electronics and ECCE Asia (ICPE-ECCE Asia)* (pp. 233-239). IEEE Publishing. <https://doi.org/10.1109/ICPE.2015.7167792>

- Marouchos, C. C. (2006). The buck boost DC to DC converter. In *The Switching Function: Analysis of Power Electronic Circuits* (pp. 163–174). The Institution of Engineering and Technology. https://doi.org/10.1049/PBCS017E_CH11
- Muntaser, A., Ragb, H., & Elwrfalli, I. (2022). *DC Microgrid Based on Battery, Photovoltaic, and Fuel Cells: Design and Control*. arXiv Preprint. <https://doi.org/10.20944/preprints202212.0527.v1>
- Raghavendra, N. K., & Padmavathi, K. (2018). Solar charge controller for lithium-ion battery. In *2018 IEEE International Conference on Power Electronics, Drives and Energy Systems (PEDES)* (pp. 1-5). IEEE Publishing. <https://doi.org/10.1109/PEDES.2018.8707743>
- Rokonuzzaman, M., Shakeri, M., Hamid, F. A., Mishu, M. K., Pasupuleti, J., Rahman, K. S., Tiong, S. K., & Amin, N. (2020). IoT-enabled high efficiency smart solar charge controller with maximum power point tracking - Design, hardware implementation and performance testing. *Electronics*, *9*(8), 1–16. <https://doi.org/10.3390/electronics9081267>
- Wang, L. Y., Zhao, M. L., & Wu, X. B. (2016). A monolithic high-performance buck converter with enhanced current-mode control and advanced protection circuits. *IEEE Transactions on Power Electronics*, *31*(1), 793–805. <https://doi.org/10.1109/TPEL.2015.2405093>
- Wang, N., Hu, R., & Zhu, M. (2019). *Methods to Solve Reverse Current Caused Damage in Synchronous Buck Converter* (Application Report). Texas Instruments. https://www.ti.com/lit/an/slua962/slua962.pdf?ts=1736996669125&ref_url=https%253A%252F%252Fwww.google.com%252F
- Xu, F., Liu, J., & Dong, Z. (2022). Minimum backflow power and ZVS design for dual-active-bridge DC-DC converters. *IEEE Transactions on Industrial Electronics*, *70*(1), 474-484. <https://doi.org/10.1109/TIE.2022.3156159>
- Zomorodi, H., & Nazari, E. (2022). Design and simulation of synchronous buck converter in comparison with regular buck converter. *International Journal of Robotics and Control Systems*, *2*(1), 79–86. <https://doi.org/10.31763/ijrcs.v2i1.538>

Leveraging Computational Model Approach in Understanding Infectious Disease: A Case Study in Sabah, Malaysia

Siti Sarah Mohd Isnani^{1,2}, Ahmad Fikri Abdullah^{3*}, Abdul Rashid Mohamed Shariff¹, Iskandar Ishak⁴, Sharifah Norkhadijah Syed Ismail⁵, Doria Tai⁶ and Maheshwara Rao Appanan⁷

¹Faculty of Defence Science and Technology, Universiti Pertahanan Nasional Malaysia, 57000 Kem Sg Besi, Malaysia

²Department of Biological and Agricultural Engineering, Faculty of Engineering, University Putra Malaysia, 43400 UPM, Serdang, Selangor, Malaysia

³International Institute of Aquaculture and Aquatic Sciences (I-AQUAS), Universiti Putra Malaysia, Port Dickson 70150, Malaysia

⁴Department of Computer Science, Faculty of Computer Science and Information Technology, Universiti Putra Malaysia, 43400 UPM, Serdang, Selangor, Malaysia

⁵Department Environmental and Occupational Health, Faculty of Medicine and Health Sciences, University Putra Malaysia, 43400 UPM, Serdang, Selangor, Malaysia

⁶Sabah State Department, Floor 12-14, Block A, Sabah State Administrative Centre, Jalan Sulaiman, Teluk Likas, 88400 Kota Kinabalu, Sabah, Malaysia

⁷Ministry of Health Malaysia, 62000 Putrajaya, Malaysia

ABSTRACT

The COVID-19 pandemic due to the SARS-CoV-2 coronavirus has vastly impacted our national health and economic industries. Hence, the utilisation of big data simulation of the outbreak is essential to guide policymakers, government, and health authorities in better understanding the dynamics of the infectious disease. This paper integrates the Agent-Based-Model (ABM) and Susceptible, Exposed, Infectious and Recovered (SEIR) framework to understand the dynamic transmission of COVID-19 in Sabah, Malaysia. This study employed NetLogo software, which

includes parameters such as geographical distribution, population density, variant type, lockdown measures, and vaccination rates across 27 districts, to run the simulation and assess the potential impact of public health interventions. The methodology involves different scenario simulations using varying variant types, vaccination coverage, lockdown, and social distancing measures to determine the virus transmission level. The results indicate that higher vaccination coverage and strict adherence

ARTICLE INFO

Article history:

Received: 16 April 2024

Accepted: 19 August 2024

Published: 21 February 2025

DOI: <https://doi.org/10.47836/pjst.33.2.06>

E-mail addresses:

sarahmohdisnan@gmail.com (Siti Sarah Mohd Isnani)

ahmadfikri@upm.edu.my (Ahmad Fikri Abdullah)

rashidpls@upm.edu.my (Abdul Rashid Mohamed Shariff)

iskandar_i@upm.edu.my (Iskandar Ishak)

norkhadijah@upm.edu.my (Sharifah Norkhadijah Syed Ismail)

doria.tai@sabah.gov.my (Doria Tai)

mahesh@moh.gov.my (Maheshwara Rao Appanan)

* Corresponding author

to preventive measures can reduce the spread of the virus, especially in highly densely populated areas. Our simulation resulted in a 2.54% variance with the true data following the parameters and settings mentioned above. Additionally, this study also found that geographical structure and uneven distribution of healthcare across the Sabah district notably affect disease and disaster management and intervention policy and efficacy. These insights are crucial for Malaysian policymakers and health authorities, which need to tailor the public health responses considering geographical and demographic settings. Future recommendations include data of higher geographical resolution, immunisation records, and real-time mobility data to portray a more realistic simulation.

Keywords: ABM, big data, COVID-19, epidemiology, infectious disease, SEIR

INTRODUCTION

COVID-19 is caused by Severe Acute Respiratory Syndrome Coronavirus 2, known as SARS-CoV-2, which has affected countries worldwide since March 2020 (López & Rodó, 2021). The first case was reported in December 2019 in Wuhan, China, and it spread all over the world until WHO announced it as a pandemic in March 2020 (Shamil et al., 2021). By June 2023, the number of COVID-19 cases worldwide had exceeded 767 million, and deaths had reached almost 7 million (World Health Organization, 2023b). Governments around the world have implemented various measures to curb the spread of the virus, such as social distancing, travel restrictions, and widespread testing (Shah et al., 2020). Despite these efforts, the number of confirmed cases has continued to rise, and the pandemic has significantly impacted the country's economy, healthcare system and society (Gill et al., 2020). International research to aid policymakers in combatting the virus is crucial to avoid more loss, especially in economic industries (Cheng et al., 2020).

In Malaysia, the first COVID-19 case was reported in January 2020, followed by a total lockdown in March 2020, which has caused catastrophic effects on economic industries and other government and private sectors (Roslan et al., 2022). Sabah, particularly a state in Malaysia, has also experienced the devastating effects of the outbreak. A study by Azzeri et al. (2020) has proven that Sabah communities were experiencing significant health issues even before COVID-19 appeared. M. Goroh et al. (2020) have reported that Sabah is experiencing high cases of infectious diseases such as tuberculosis. Additionally, the Sabah citizens are experiencing difficulties in healthcare facilities and delivery due to the geographical location separating them from the main Peninsular of Malaysia. Tha et al. (2020) mentioned that the geographical features in Sabah, especially in rural areas, have further hindered the healthcare system accessibility there due to the steep hills and rivers.

Patients with COVID-19 have experienced difficulties accessing hospitals and clinics to get treated and get vaccinations (Yeo, 2020). Scholars such as Azhary et al. (2022) have demonstrated that the healthcare services in rural areas of Sabah are 48% lower than in Peninsular Malaysia, which is around 68% in terms of longer travel time and distance

to access healthcare facilities. Due to this, COVID-19 patients may not be able to be treated properly, causing morbidity and mortality rates to be high. As stated by Jafar et al. (2024), the vaccination rate of COVID-19 in Sabah is lower compared to Peninsular Malaysia; therefore, dynamic predictions in the Sabah area will provide valuable insights into determining the epidemiological characteristics, analysing the effects of interventions, and offering useful insights into the dynamics of the disease. They assist policymakers and public health professionals in making decisions about allocating resources and implementing efficient control measures. Among the various models and approaches used to predict the dynamics of COVID-19, the SEIR model is one of the famous methods for studying COVID-19 transmission (Thompson & Wattam, 2021). The SEIR model divides the population into four compartments: susceptible, exposed, infectious, and recovered (Qiu et al., 2022). SEIR model uses dynamic equations to detect the dynamics of COVID-19. Hence, the adaptive numerical method, introduced by Qureshi et al. (2023) and Hassan et al. (2023), is useful for increasing the accuracy of the simulations, especially when dealing with unpredictable and variable changes in COVID-19.

Most researchers incorporated and added new variables in their research. For example, Silva et al. (2020) used the SEIR model to simulate the dynamics of COVID-19 using a society of agents emulating people, businesses, and government in Brazil. Pandey et al. (2019) used the SEIR model and regression analysis to predict the dynamics and patterns of COVID-19, while Avinash et al. (2022) used optimisation to increase the effectiveness of the SEIR model in India. Kucharski et al. (2020) evaluated the effectiveness of isolation, testing, contact tracing, and physical distancing measures with different parameters using the SEIR model in the United Kingdom. Almeshal et al. (2020) and Zhao et al. (2022) combined logistic regression and the SEIR model to predict the COVID-19 cases in China and Kuwait. Paul et al. (2020) compared the effectiveness of the SEIR model in different regions of India and Brazil. Yang et al. (2020) modified the SEIR model by integrating the population variable into the mathematical model in China, while Mwalili et al. (2020) incorporated environment and social distancing in the compartment model in order to increase the efficiency of the model.

Agent-Based Model (ABM) is a model that can be used to better understand the dynamics of infectious disease, as it allows researchers to capture the heterogeneity of the disease by simulating a population of agents with varying characteristics and behaviours (Farheen et al., 2022). ABM also enables researchers to explore different scenarios and interventions to see how they might affect the spread of the disease, such as the effects of social distancing measures or vaccination campaigns (Dong et al., 2022). Additionally, ABM can account for spatial heterogeneity by simulating interactions between agents within geospatial data, which is able to help policymakers and public health officials make informed decisions about how to respond to infectious diseases (Thompson & Wattam, 2021).

Dong et al. (2022) utilised the agent-based model to simulate the COVID-19 cases using geographical data in China. However, Kim and Cho (2022) used the ABM model to investigate the effectiveness of control measures in order to control COVID-19 in a closed environment. Farheen et al. (2022), Hinch et al. (2021), and Shamil et al. (2021) used ABM to simulate the dynamics of COVID-19 in the USA, United Kingdom and Bangladesh. Hunter and Kelleher (2022) also used ABM to simulate the effect of crowdedness in Ireland. Compartmental models are useful for modelling disease transmission mechanisms. However, they require the assumption of complete mixing within compartments and ignore many other factors such as geography, population heterogeneity, individual contact vectors, social dynamics, governmental decisions (e.g., lockdown measures), and other human behaviour complexities (Kong et al., 2022). The COVID-19 pandemic has highlighted the need for accurate and reliable models to understand the spread of infectious diseases and develop effective strategies to control their transmission. While compartmental models such as SEIR have been widely used to study the transmission dynamics of COVID-19, they have several limitations, including the assumption of complete mixing within compartments and the lack of consideration for individual behaviours, population heterogeneity, and other factors that can influence the spread of the virus (Kong et al., 2022).

Hence, to overcome these limitations, scholars have tried to simulate infectious diseases using ABM, which is able to produce results of complex patterns (Dong et al., 2022). By integrating SEIR models with ABMs using big data, researchers can develop more accurate and realistic models to understand the dynamics of infectious disease outbreaks in specific contexts, such as the Malaysian population, with its unique cultural practices and available resources (Tang et al., 2017). As a result, this integration can offer a more thorough and precise understanding of the transmission of infectious illnesses as well as the efficacy of interventional measures. The architecture of the combined SEIR-ABM model involves simulating the behaviour of individual agents and their interactions with each other and their environment. It also incorporates the SEIR model to capture the spread of the disease.

In this context, the paper aims to develop an ABM combined with an SEIR model to better understand the patterns and dynamics of COVID-19 transmission in Sabah, Malaysia, by using big data and incorporating factors such as vaccination coverage, population mobility and the transmission rate which is able to simulate the spread of the virus and explore the impact of interventions such as vaccination and the development of herd immunity. The researcher chose Sabah as the study area due to its unique geographical distribution, which makes it a challenge for the accessibility of the healthcare system; hence, this study is important to yield insights both locally with similar geographical challenges (Balakrishnan et al., 2023; M. Goroh et al., 2020; M. M. D. Goroh et al., 2020; Onyechege et al., 2022; Tan et al., 2021). Figure 1 depicts the summary of the SEIR-ABM simulation.

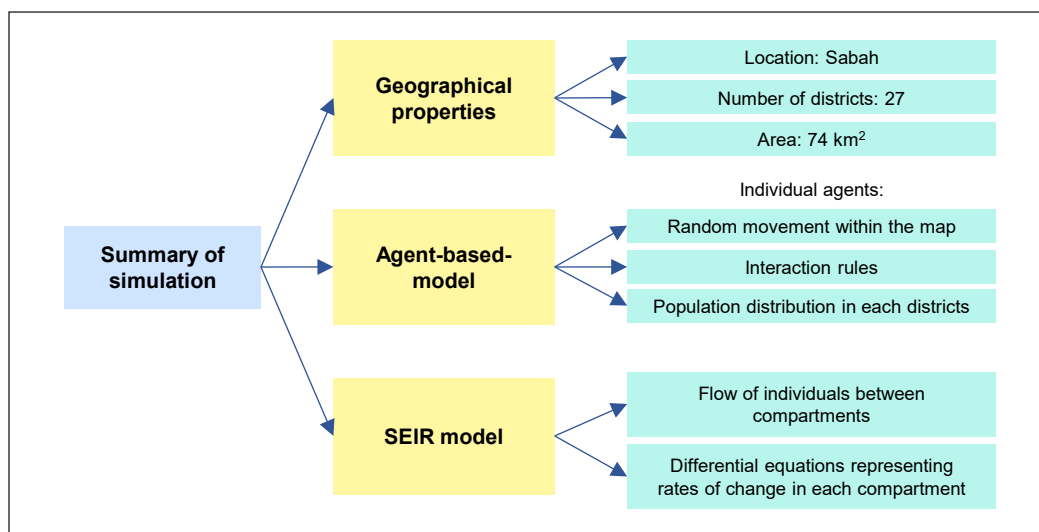


Figure 1. Summary of SEIR-ABM simulation

METHODS

This study focuses on Sabah, a state in Malaysia with a total area of 73,904 km² (M. M. D. Goroh et al., 2020). Sabah has 27 districts, which are Tawau, Papar, Lahad Datu, Tuaran, Putatan, Sipitang, Beaufort, Kota Belud, Kinabatangan, Kunak, Sandakan, Semporna, Ranau, Penampang, Tambunan, Keningau, Labuk Sugut, Kota Marudu, Pitas, Pensiangan, Kudat, Tongod, Telupid, Kuala Penyu, Tenom, Kalabakan and Kota Kinabalu as the capital city of Sabah, each population for each district is depicted as shown in Figure 2 (Azzeri et al., 2020). The average annual temperature of Sabah is around 24°C, which shows the humidity and tropical weather of Sabah throughout the year (Iderus et al., 2022). The annual rainfall is about 2102 mm yearly (Iderus et al., 2022). The geographical feature of Sabah is mostly covered with mountains and tropical rainforests with an altitude range of 4100m (Iderus et al., 2022). Kota Kinabalu, which is the capital of the Sabah, has gone through rapid urbanisation compared to other districts. The data acquisition resources for each variable are shown in Table 1.

Our dataset of 365,115 COVID-19-positive cases was extracted from the Sabah State Government. The dataset was derived from hospital reports in Sabah and sent to the Sabah State Government (Hashim et al., 2021). This data also included the collection of MySejahtera records, which is a mobile application developed by the Malaysian Government to monitor COVID-19 in Malaysia (<https://mysejahtera.moh.gov.my/ms/>). The data contains the district-level cases, confirmed cases, recovered cases, and death cases. Our population demographic data was obtained from the Department of Statistics, Malaysia, during the 2020 census. This data acts as a true representation of the population

in each district of Sabah. The data collection period covered the period of the outbreak from March 2020 until March 2022.

The attributes dataset, which includes rivers, buildings, mountains, forests, and roads, is downloaded from the Open Street Map website (Relation: Malaysia (2108121) | OpenStreetMap). After that, the Sabah district, rivers, roads, buildings, and mountains are imported into ArcMap 10.8 for checking. All these layers are aligned with each other using the Projected Coordinates of WGS 1984. The map of the Sabah in ArcMap is shown in

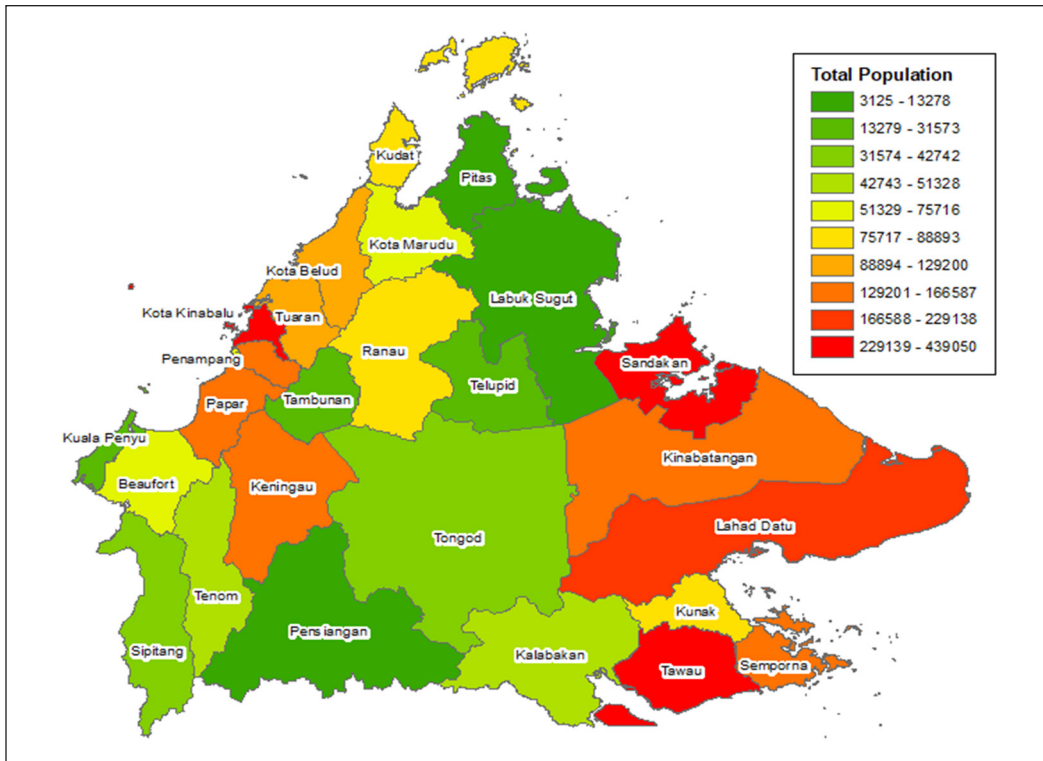


Figure 2. Map of Sabah districts and their total number of populations

Table 1
Data acquisition resources

Data	Source	Period/Year
District of Sabah Shapefile	Sabah State Government	2020
Buildings		2020
Roads		2020
Mountains and Forest	Open Street Map	2020
Rivers		2020
Number of populations by district in Sabah	Department of Statistics Sabah	Census data for the year 2020

Figures 3 and 4. We separated the geographical features into two different maps for better visualisation, as distinguishing different geographical features on a large map of Sabah is challenging due to the large scale of the Sabah area. However, a large number of attributes have caused ArcMap 10.8 to perform slower when loading various elements.

The simulation of the outbreak is performed in the NetLogo Software Version 6.4.0. All the geographical layers are imported in NetLogo, as shown in the code of Figure 5. As for this model, the agent or turtle is a person in every district of Sabah. The total number of people in each district depicted the total population. The researcher set the location and movement of each person at random, as this study does not exhibit the location and mobility data of each positive COVID-19 case. Hence, the assumptions of the models are:

1. Number of populations remains constant based on the data.
2. Random movement at rate 2.0 within the map.
3. Recovered people become immune; if they have already been infected and recovered, they will not be infected for the second time.

The SEIR model can be represented graphically using a set of differential equations (Equations 1 to 4), which describe the flow of individuals between compartments over time (https://docs.idmod.org/projects/emod-hiv/en/2.20_a/model-seir.html).

$$\frac{dS}{dt} = - \frac{\beta IS}{N} \quad [1]$$

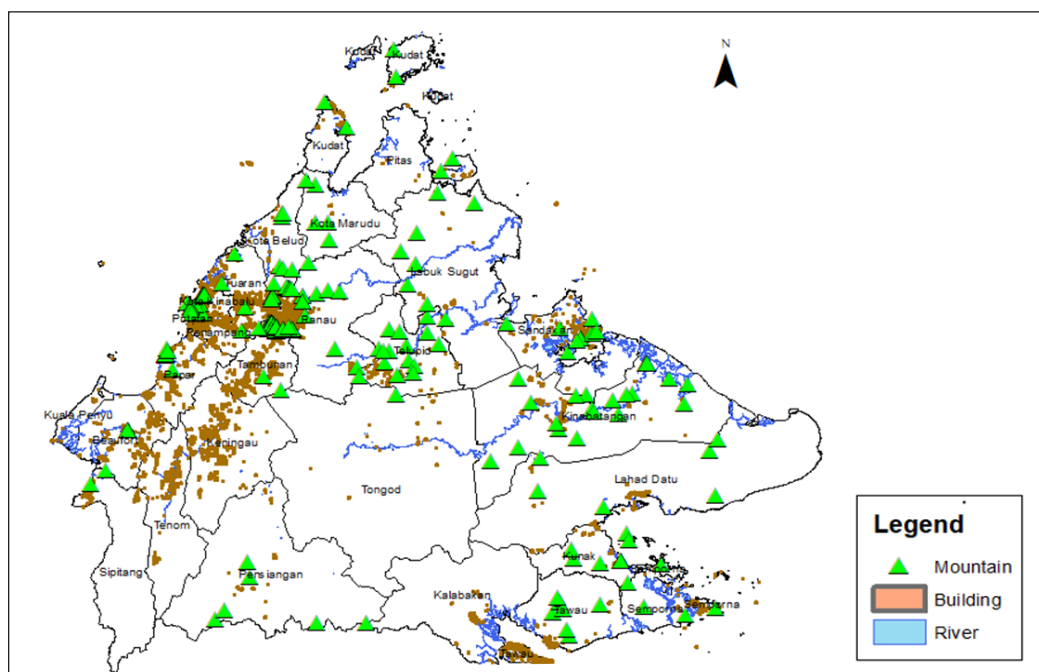


Figure 3. Distribution of buildings, rivers and mountains in Sabah

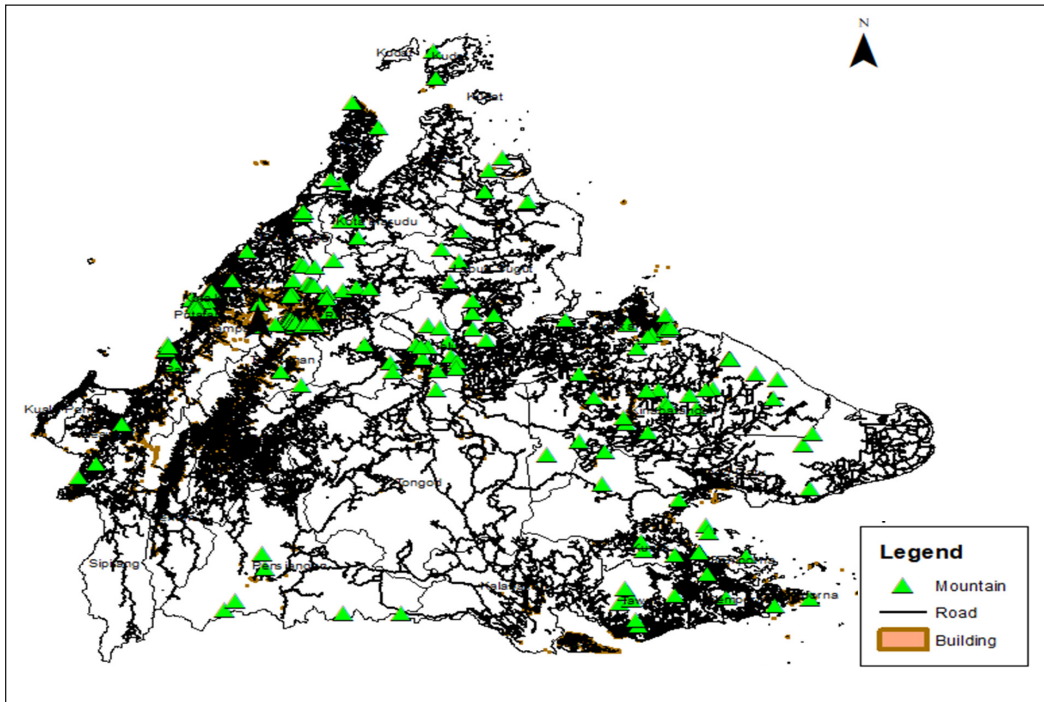


Figure 4. Distribution of roads, rivers and mountains in Sabah

$$\frac{dE}{dt} = -\frac{\beta IS}{N} - \sigma E \quad [2]$$

$$\frac{dI}{dt} = \sigma E - \gamma I \quad [3]$$

$$\frac{dR}{dt} = \gamma I \quad [4]$$

Where: dS/dt = the change in the number of susceptible individuals over time; dE/dt = the change in the number of exposed individuals over time; dI/dt = the change in the number of infectious individuals over time; dR/dt = the change in the number of recovered individuals over time; β = the disease transmission rate from infectious individuals to susceptible individuals; σ = the rate at which exposed individuals become infectious; γ = the rate at which infectious individuals recover or develop immunity.

Based on Equation 1, it depicted the rate of change of the susceptible over time. The total number of susceptible people is inversely proportional to the number of infected people; hence, it is indicated by the negative sign (He et al., 2020). The rate of change is directly proportional to the rate of transmission (β), the number of infected persons (I) and the remaining susceptible persons (S/N) (He et al., 2020). Equation 2 depicts the rate

of change of the exposed people over time. The negative sign indicated that the number of exposed people is inversely proportional over time as by the time they will recover and become infectious (He et al., 2020). The rate of change is directly proportional to the same state as the susceptible conditions and the rate at which the exposed persons become infectious (σ) (He et al., 2020). Equation 3 shows the rate of change of the infected persons over time. The rate at which people move from the exposed condition to the infected condition is represented by positive signs. However, the negative sign is represented by the rate at which people recover and move to the recovered condition (He et al., 2020). Equation 4 depicts the rate of change of recovered people over time, which shows the infected people recovered and moved to the recovered compartment represented by the positive sign (He et al., 2020).

The simulation started by creating a population of citizens, each with its characteristics, such as days after exposure and days of sickness. After that, the simulation will run a series of procedures to mimic the virus's spread among them. The simulation is divided into procedures, each of which simulates a distinct element of the outbreak. The setup process starts the simulation by loading a GIS shapefile and creating citizens within the shapefile's area. The population-list variable, which contains a list of population sizes for each district, determines the total number of citizens created in each district.

Each citizen is chosen at random to be infected with the virus. The go procedure is the simulation's primary loop. It begins by determining whether the simulation has ended, with all residents recovering or dying. If not, it performs the following procedures:

1. The moving procedure mimics citizen mobility by randomly rotating and moving citizens forward, with a check to see if the target patch is a valid path.
2. The transmission process mimics the virus spread among citizens, with carriers (citizens with the orange colour) spreading the virus to susceptible citizens within a 1-patch radius, as social distancing lower than 1 metre will increase the risk of infection (Badr et al., 2020).
3. The incubation process mimics the virus's incubation period, with carriers becoming infectious after a certain number of days (determined by the incubation period variable) and turning red. In the case of this simulation, we chose 6 days as the incubation period following a recommendation by the World Health Organisation (World Health Organization, 2023a)
4. The sickness process mimics the virus's period, with infectious citizens recovering or dying after a set number of days (determined by the mortality and recovery rates). The transmission rate is set at 75 and 100 to compare the effect of these two conditions and the mortality rate at 10.
5. The find-max-daily-cases procedure keeps track of the simulation's highest number of daily cases.

6. The mobility procedure keeps the movement of the citizens throughout the districts. The movement is set to 0.5 and 1.0 to compare the results.
7. Other processes in the simulation include vaccinating, which simulates vaccination by randomly selecting a certain proportion of susceptible citizens and changing their colour to blue to symbolise immunity.
8. A watch-an-infected-person process also highlights a randomly selected infected citizen for visualisation reasons.
9. The variant type provides how fast the COVID-19 virus spreads to another person. For example, the Omicron and Delta variants have a higher transmission rate.
10. The transmission rate indicates the speed of the transmission, which is denoted by the type of variant. A transmission rate of 80 for Omicron, 70 for Delta, and 40 for Alpha denotes a higher susceptibility of the variant (Umair, 2022).
11. The mountains, buildings, roads and rivers act as geographical features that allow the person to move more realistically. Roads facilitate faster transmission; however, mountains and rivers can be denoted as obstacles that limit movement and slow down the spread of the virus.

```
--
26
27 to setup
28   clear-all
29   set scale 30
30   set population-list [75716 48195 150927 143112 107243 371221 69528 23710 86410 88893 3125
31                       13278 3666 68811 85077 439050 166587 37828 31573 372615 29241 51328
32   set country gis:load-dataset "C:/Sabah_District_Boundary/district_no_sea.shp"
33   set rivers gis:load-dataset "C:/Shp/River/River.shp"
34   set roads gis:load-dataset "C:/Shp/Road/Road.shp"
35   set mountForest gis:load-dataset "C:/Shp/Mountain/Mountain.shp"
36   set building gis:load-dataset "C:/Shp/Building/Building.shp"
37   gis:set-world-envelope (gis:envelope-union-of (gis:envelope-of country)
38                                               (gis:envelope-of rivers)
39                                               (gis:envelope-of roads)
40                                               (gis:envelope-of mountForest)
41                                               (gis:envelope-of building))
42   display-country
43   if river? [draw-rivers]
44   if road? [draw-roads]
45   if building? [draw-building]
46   if mountain? [draw-mountForest]
47   create-paths
48   create-citizens-in-country
49   set susceptible count citizens with [color = yellow]
50   ;show susceptible
51   ;show count citizens
52   set died-citizen 0
53   set watching false
54   reset-ticks
55 end
56
57 ;-----
58
59 to display-country
60   gis:set-drawing-color brown
61   gis:draw country 1
62 end
```

Figure 5. Script to load geographical layers in Netlogo 6.4.0

12. The lockdown rate parameter also restricts mobility to reduce the spread of the virus (Dong et al., 2022).
13. Social distancing also indicates virus spread mitigation (López & Rodó, 2021).

RESULTS

The model begins with a human population comprised of susceptible (yellow-coloured) individuals, as in Figure 6. When a person exposed to the disease (orange colour) enters the community, he or she will spread the disease to one of the susceptible people nearby (within a radius of less than 1 metre) at the stated transmission rate as in Figure 7. After the specified incubation period, the exposed may develop ill (infectious red colour), as shown in Figures 8 and 9. The sick will be quarantined so that they do not infect others. The sick individuals will be hospitalised for 14 days. They either die (disappear from the model) on the 15th day of illness or recover and become immune to the sickness (blue colour), as in Figures 10 and 11. Each citizen is allocated a sex, colour, and size, with some being chosen at random to be disease carriers (orange colour). Citizens travel across the nation randomly, with mobility limited by areas of green pavement. The model also incorporates a vaccine mechanism that vaccinates citizens at random with a predetermined probability. The simulation is performed on a grid, with each cell representing a district in the region, and citizens are assigned to each cell based on the district's population density. The simulation terminates when there are no more citizens with the red colour, i.e., contagious citizens. During the simulation, the model maintains track of the number of residents who died as a result of the virus, together with the maximum number of daily cases.

The mobility movement is set to random as this study does not exhibit mobility data. More simulations will produce more accurate results because of the nature of the random

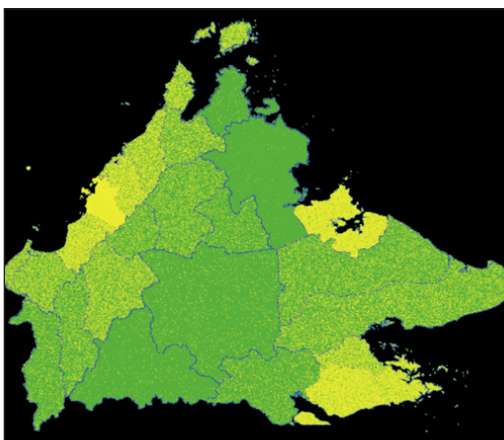


Figure 6. Susceptible person in yellow colour on day 1 during simulation one

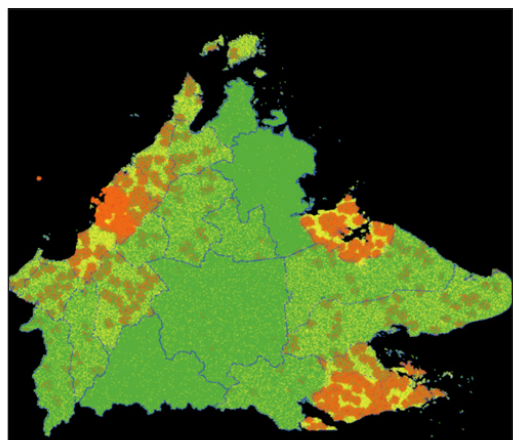


Figure 7. Exposed person in orange colour day 10 during simulation one

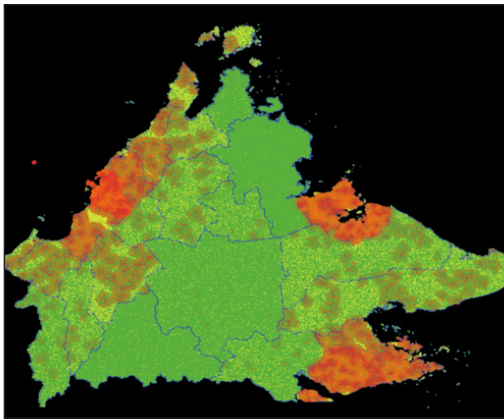


Figure 8. Infected person in red colour day 20 during simulation one

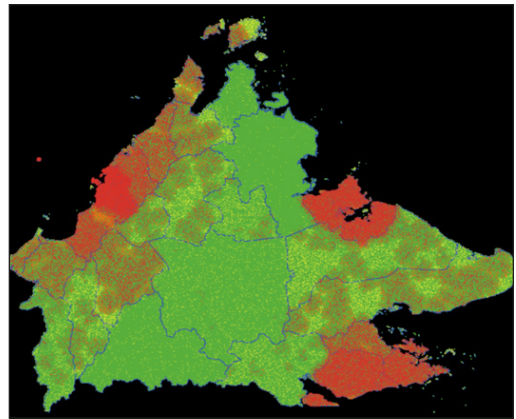


Figure 9. Simulation of Sabah map showing increasing of infected persons day 23 during simulation one

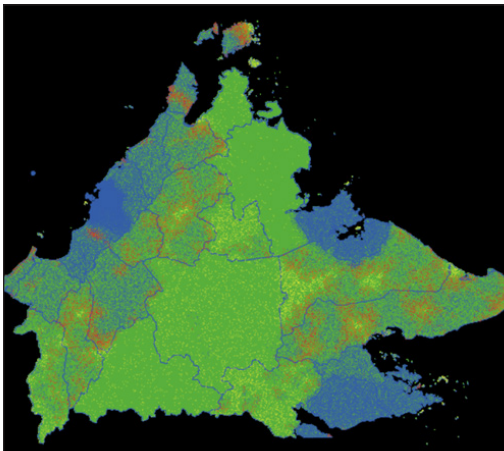


Figure 10. Recovered/vaccinated person in blue colour day 190 during simulation 1

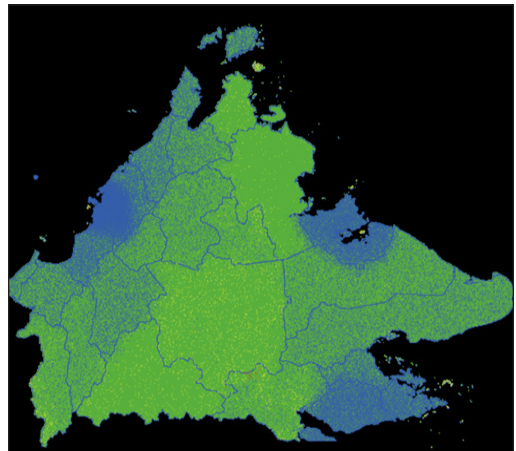


Figure 11. Sabah map showing infected person that has recovered day 210 during simulation one

movement (Motzev, 2019). Since the movement of the agent is set to random, the agent may sometimes move in a direction that is not optimal or may even move in the opposite direction of the target. In other words, running multiple simulations helps reduce the effect of randomness in the agent's movements, leading to more accurate and reliable results. By averaging the results from multiple simulations, the researcher can get a more representative sample of the agent's performance and reduce the impact of individual instances of suboptimal or random movements.

Fifteen simulations were run with the parameters in Table 2 to investigate the impact of different combinations of parameters on the spread of the disease. The simulations were designed to test the effectiveness of various interventions, such as vaccination rates, transmission rates, incubation periods, mobility, social distancing, lockdown, and

Table 2
Parameters setting for 15 simulations

Simulation	The initial number of infected cases	Vaccination rate	Transmission Rate	Mortality	Incubation Period	Mobility	Type of variant	Lockdown	Social Distancing
1	8	78	75	10	6	0.5	-	-	-
2	8	78	75	10	6	1	-	-	-
3	8	78	100	10	6	0.5	-	-	-
4	8	78	100	10	6	1	-	-	-
5	20	100	50	10	6	1	-	-	-
6	20	100	100	10	6	1	-	-	-
7	20	0	50	10	6	1	-	-	-
8	20	0	100	10	6	1	-	-	-
9	20	100	50	10	6	1	-	-	-
10	20	100	100	10	6	1	-	-	-
11	200	0	70	10	6	0.5	Delta	Yes	Yes
12	200	0	70	10	6	0.5	Delta	No	No
13	8	78	75	10	6	0.5	Delta	Yes	Yes
14	200	45	80	10	6	1	Omicron	Yes	Yes
15	200	60	80	10	6	1	Omicron	No	Yes

variant types, in controlling the spread of the disease. The simulations were conducted to gain a better understanding of the complex interactions between these variables and to make more informed decisions about how to control the spread of the disease (Kim & Cho, 2022; Gharakhanlou & Hooshangi, 2020; Nagori et al., 2020). Figure 12 shows the NetLogo interface to run the simulation, as stated in Table 1. All settings are stated in the methodology section. Figure 13 depicts the screenshot of the NetLogo 6.4 scripts to load geographical features of rivers, roads, mountains and buildings.

Figure 14 shows the Graph of Simulation One with a transmission rate of 75, mortality of 10, incubation period of 6 days and mobility rate of 0.5. Based on the graph, the number of infected cases reached around 1.60 million within 25 days, recovered cases reached around 2.5 million within 143 days and died cases of 293,640 cases within 199 days. This simulation took around 210 days for all the infected cases to be recovered, and no more infections were transmitted.

Simulation Two demonstrated a transmission rate of 75, mortality of 10, incubation period of 6 days and mobility rate of 1. Based on the results, infected cases reached 2.05 million within 23 days, recovered cases reached around 2.71 million within 143 days and died cases of 300,480 cases within 130 days. This simulation took around 143 days for all the infected cases to be recovered, and no more infections were transmitted.

Simulation Three demonstrated a transmission rate of 100, mortality of 10, incubation period of 6 days and mobility rate of 0.5. Based on the results, the infected cases reached around 1.76 million within 23 days, recovered cases reached around 2.65 million within

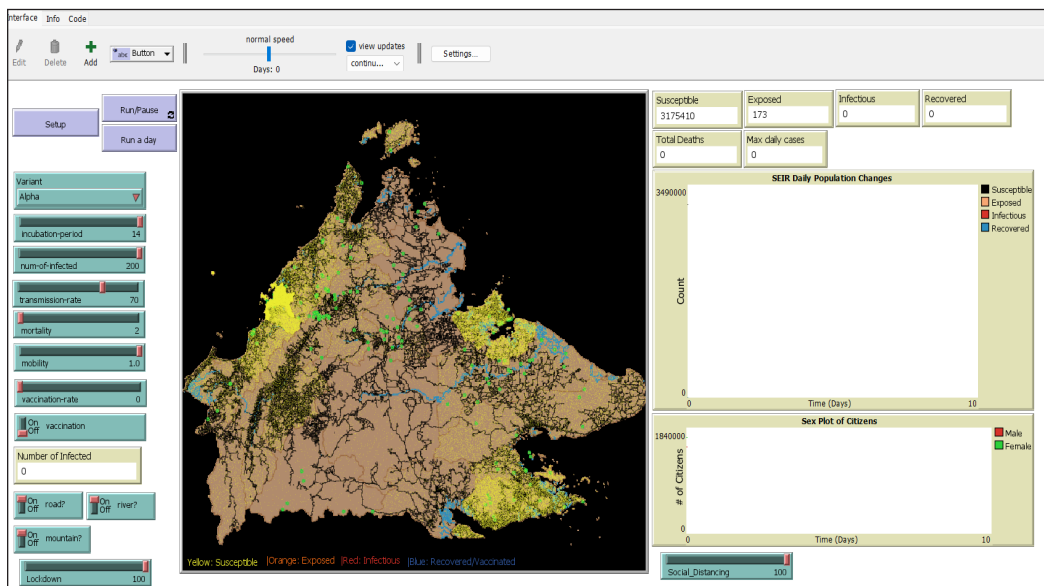


Figure 12. Table 1 lists the NetLogo interface to run the simulation. The methodology section states all settings

```

file Edit Tools Zoom Tabs Help
Interface Info Code
Find... Check Procedures Indent automatically Code Tab in separate window
]
10 ]
11
12 globals [
13   population-list
14   country
15   watching
16   max-daily-cases
17   susceptible
18   died-citizen
19   scale
20   forests-mountains
21   roads
22   buildings
23   rivers
24 ]
25
26
27 to setup
28   clear-all
29   set scale 30
30   set country gis:load-dataset "C:/Sabah_District_Boundary/district_no_sea.shp"
31   print "Country dataset loaded successfully."
32
33   set forests-mountains gis:load-dataset "C:/Shp/Mountain/Mountain.shp"
34   print "Mountains dataset loaded successfully."
35
36   set buildings gis:load-dataset "C:/Shp/LandUse/Landuse.shp"
37   print "Buildings dataset loaded successfully."
38
39   set rivers gis:load-dataset "C:/Shp/River/River.shp"
40   print "Rivers dataset loaded successfully."
41
42   set roads gis:load-dataset "C:/Shp/Road/Road.shp"
43   print "Roads dataset loaded successfully."
44
45   gis:set-world-envelope (gis:envelope-union-of (gis:envelope-of country))
46   display-country
47   create-paths
48   create-citizens-in-country
49   set susceptible count citizens with [color = yellow]
50   set died-citizen 0
51   set watching false

```

Figure 13. Screenshot of the NetLogo 6.4 scripts to load geographical features of rivers, roads, mountains and buildings

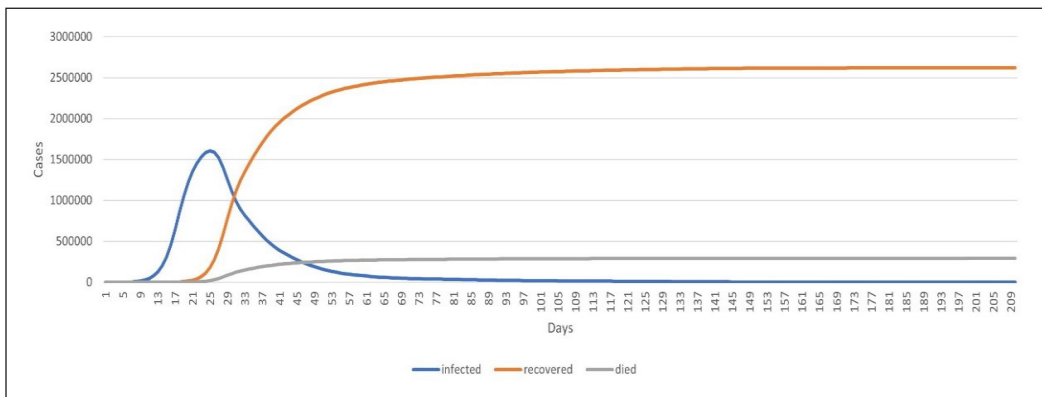


Figure 14. Graph of simulation one

211 days and dead cases 292,740 within 212 days. This simulation took around 212 days for all the infected cases to be recovered.

Simulation Four tested a transmission rate of 100, mortality of 10, incubation period of 6 days and mobility rate of 1. Based on the results, the graph of infected cases reached around 2.07 million within 23 days, recovered cases reached around 2.73 million within

207 days and died cases 292,740 within 207 days. This simulation took around 207 days for all the infected cases to be recovered.

Simulation Five demonstrated a transmission rate of 50, mortality of 10, incubation period of 6 days, vaccination rate of 100%, initial number of infected cases of 20 and mobility rate of 1. Based on the results, the infected cases reached around 14,400 within 8 days, recovered cases reached around 3.17 million within 19 days and died cases 1,620 within 19 days. This simulation took around 19 days for all the infected cases to be recovered.

Simulation Six tested a transmission rate of 100, a mortality of 10, an incubation period of 6 days, a vaccination rate of 100%, an initial number of infected cases of 20 and a mobility rate of 1. Based on the results, the infected cases reached around 15,300 within 7 days, recovered cases reached around 3.17 million within 19 days and died cases 1,620 within 19 days. This simulation took around 19 days for all the infected cases to be recovered.

Simulation Seven demonstrated a transmission rate of 50, a mortality of 10, an incubation period of 6 days, a vaccination rate of 0%, an initial number of infected cases of 20 and a mobility rate of 1. Based on the results, the infected cases reached around 21,450 within 7 days, recovered cases reached around 2.67 million within 161 days and died cases 294,900 within 161 days. This simulation took around 161 days for all the infected cases to be recovered.

Simulation Eight demonstrated a transmission rate of 100, a mortality of 10, an incubation period of 6 days, a vaccination rate of 0%, an initial number of infected cases of 20 and a mobility rate of 1. Based on the results, the infected cases reached around 28,560 within 8 days, recovered cases reached around 2.76 million within 143 days and died cases 303,330 within 143 days. This simulation took around 161 days for all the infected cases to be recovered.

Simulation Nine tested a transmission rate of 50, a mortality of 10, an incubation period of 6 days, a vaccination rate of 100%, an initial number of infected cases of 20 and a mobility rate of 1. Based on the results, the infected cases reached around 23,520 within 8 days, recovered cases reached around 3.17 million within 23 days and died cases 2880 within 23 days. This simulation took around 23 days for all the infected cases to be recovered.

Simulation Ten tested a transmission rate of 100, a mortality rate of 10, an incubation period of 6 days, a vaccination rate of 100%, an initial number of infected cases of 20 and a mobility rate of 1. Based on the results, the infected cases reached around 26,430 within 8 days, recovered cases reached around 3.17 million within 23 days and died cases reached 4,350 within 23 days. This simulation took around 23 days for all the infected cases to be recovered.

Simulation 11 demonstrated a transmission rate of 70, the Delta variant with 200 initial infected cases, no vaccination with a mobility rate of 0.5, and the implementation of lockdown and social distancing. Based on the results, the infected cases reached around 1,003 within 28 days, recovered cases reached around 973 within 200 days, and death cases reached around 30 within 40 days. The simulation took 200 days to complete.

Simulation 12 performed the same parameters as Simulation 11 but without lockdown and social distancing. The results of the initial infected cases are higher: 5,73 cases within 21 days, 5,625 recovered cases within 31 days and 48 death cases within 31 days. This simulation took 212 days to complete.

Simulation 13 demonstrated the same parameters as Simulation 1, with the added parameters of Delta variant, social distancing and lockdown, and an initial infected number of 8 cases. The results show that the number of infected cases is smaller than those in Simulation 1, which included 127 cases, 112 recovered cases, and six death cases within 197 days.

Simulation 14 demonstrated 200 initial infected cases with the Omicron variant at a 45% vaccination rate and an 80% transmission rate. The results showed that the infected cases became 5495, recovered 5148, and death cases 20 within 183 days consecutively.

The final simulation demonstrated a higher vaccination rate of 60% without lockdown intervention. The infected cases became 4193, the recovered cases 4441 and 17 deaths occurred within 171 days. Hence, Table 3 summarises the simulation results.

Table 3
Simulation results

Simulation	Infected cases	Day	Recovered cases	Day	Died Cases	Day	Days to complete
1	160	25	2,622,750	210	293,640	199	210
2	205	24	2,713,320	143	300,480	130	143
3	176	23	2,656,890	211	292,740	212	212
4	207	23	2,730,780	207	300,270	185	207
5	14,400	8	3178980	19	1620	19	19
6	15,030	8	3178980	19	1620	19	19
7	1994730	26	2665800	161	294900	147	161
8	2454750	21	2764920	143	303330	128	143
9	31560	12	3177690	23	2880	22	23
10	42330	12	3176220	23	4350	22	23
11	1003	28	973	200	30	40	200
12	5673	21	5625	212	48	31	212
13	127	19	112	197	6	27	197
14	5495	22	5148	183	20	28	183
15	4192	18	4441	171	17	19	171

DISCUSSION

The different parameters and interventions simulated using NetLogo provide dynamics transmission results in the case of COVID-19. Throughout this study, parameters such as vaccination rate, transmission rate, the initial number of infected cases, incubation period, mobility rate, social distancing, lockdown intervention, and geographical features play an important role in depicting the real-world situation, which highlights the nuanced interplay of these factors in disease outbreak management.

The initial number of infected cases proves to be one factor that leads to a higher number of cases, such as in Simulations 5 and 8. The higher the number of infected cases, the higher the susceptibility of the citizens to be exposed to the infected, causing the number of cases to spike faster (Balakrishnan et al., 2023). The higher vaccination rate, such as in Simulation 10, is effective in curbing the disease spread, which shows that the vaccination program is effective in controlling the severity effect of the infectious disease (Chen et al., 2022). The types of variants, especially Omicron and Delta, with higher transmission rates demonstrated that these variants are contagious and a higher vaccination rate is able to reduce mortality and higher mobility produced higher cases, especially in the absence of movement restrictions (lockdown) and social distancing rate (Chenchula et al., 2022).

The first case in Sabah was reported on 25 January 2020, but Sabah remained unaffected by this case until Sri Petaling tabligh cases appeared, which caused a massive wave in Malaysia, including Sabah (Balakrishnan et al., 2023). We compared the simulated cases with the real-world cases that occurred in Sabah from March 2020 until March 2022. Simulation 1 to Simulation 10 produced a high variance due to the discrepancies with the real-world conditions. However, simulation 11 until simulation 15, which considered the geographical features and obstacles, variant types, social distance, citing and lockdown measures, produced more robust and reliable results with the real-world data for infected and recovered. Simulations 12 and 14 depicted the least variation, about less than 10%, for recovered and infected cases compared to other simulations. However, the simulation of death cases is not successfully captured by the simulation due to the model representing different health states, and it handled the transition between each compartment (susceptible, carrier, infected and recovered) in deterministic modelling (Godio et al., 2020). Data such as different age groups is crucial to determine the death susceptibility as the older age groups may have more severe effects towards the outbreak (He et al., 2020). This comparative analysis demonstrated that simulations 12 and 14 are the most accurate and aligned with the true data in Sabah because the simulation added new parameters such as geographical obstacles, variant types, social distancing and lockdown intervention. The first simulation until simulation 10 shows a large variance with the true data due to significant real-world representation differences, especially in terms of variant differences and geographical features.

The infected cases in Sabah have spiked during August 2021 and February 2022. The emergence of the Delta variant and Omicron in Sabah has caused the number of infected cases to be high, especially without the lockdown intervention. The Delta variant, which arrived in Sabah in June 2021 has caused the COVID-19 cases to spike in August 2021 (3487 cases) (Balakrishnan et al., 2023), which is the same as our predicted cases, around 4192 (20% variance) cases in Simulation 15. The variance is most likely due to a lack of demographic data such as age, severity of the cases and distance of the patient to the nearest health facility (Jiee et al., 2021). Sabah Health Authority Department has taken the initiative to expedite the targeted groups in Sabah, especially those who live in rural areas, to take the vaccination dose to shrink the number of infected COVID-19 cases (Harizah, 2021). This condition is correlated with the study by Dollah et al. (2022), which highlighted that misinformation and information management have impacted youth vaccine hesitancy in Sabah. Moreover, the geographical features in Sabah have shown difficulties for the health authority in accessing and facilitating the distribution of vaccination programmes.

Due to the failure of the vaccination program in Sabah, it only reached less than 50% of the vaccination adult program during the end of 2021; the cases of COVID-19 reached their peak in January 2022 and reached 5565 cases due to the Omicron variant (Balakrishnan et al., 2023; Patrick, 2022). The Omicron variant has a higher transmission rate compared to the Delta variant due to its multiple mutation characteristics in the spike protein of the virus (Reeves et al., 2022). It increases the ability of this variant to bind with human cells and attack the human immune system (Ahasan et al., 2022). Our simulated data in Simulation 12 and 14 are almost identical to the third wave of COVID-19 during the Omicron spread in Sabah. The variance of the prediction with the true data is 2.54% for Simulation 14 and 5.86% for Simulation 12, which makes Simulation 14 more accurate to the actual number of cases. The recovered and death cases during the peak wave are 1708 and 14, respectively. Our prediction estimated around 183 recovered cases and 28 cases, respectively, which was underestimated due to insufficient demographic data.

The limitations of this study are that the simulation assumes a random movement pattern, linear mobility pattern, homogenous population and vaccination rates, which may not accurately reflect real-world mobility patterns. Additionally, Netlogo software is unstable if the dataset is too large, causing the map's performance and visualisation to become very slow to load. Hence, AnyLogic software can be used to overcome this problem.

CONCLUSION

Overall, the simulation is a deterministic and fundamental model that can provide important insights to the local health authority and government by developing an Agent-Based Model integrated with the SEIR model in areas with complex geography.

Simulation with geographical features, lockdown intervention, social distancing, variant types, and vaccine programmes have shown accurate results with a 2.54% variance from the true data. This model can be further tuned with the smaller scale of the granularity of geographical units, social isolation, immunisations and demographic variations. The findings highlight the necessity for efficient preventative strategies, early intervention, and precise statistics to support policy development.

ACKNOWLEDGEMENT

The authors acknowledged University Putra Malaysia for funding this project under IPS Grant Number 9738200.

REFERENCES

- Ahasan, R., Alam, M. S., Chakraborty, T., & Hossain, M. M. (2022). Applications of GIS and geospatial analyses in COVID-19 research: A systematic review. *F1000Research*, 9, 1–18. <https://doi.org/10.12688/f1000research.27544.2>
- Almeshal, A. M., Almazrouee, A. I., Alenizi, M. R., & Alhajeri, S. N. (2020). Forecasting the spread of COVID-19 in Kuwait using compartmental and logistic regression models. *Applied Sciences*, 10(10), Article 3402. <https://doi.org/10.3390/app10103402>
- Avinash, N., Xavier, G. B. A., Alsinai, A., Ahmed, H., Sherine, V. R., & Chellamani, P. (2022). Dynamics of COVID-19 using SEIQR epidemic model. *Journal of Mathematics*, 2022(1), Article 2138165. <https://doi.org/10.1155/2022/2138165>
- Azhary, J. M. K., Leng, L. K., Razali, N., Sulaiman, S., Wahab, A. V. A., Adlan, A. S. A., & Hassan, J. (2022). The prevalence of menstrual disorders and premenstrual syndrome among adolescent girls living in North Borneo, Malaysia: a questionnaire-based study. *BMC Women's Health*, 22(1), 1–9. <https://doi.org/10.1186/s12905-022-01929-1>
- Azzeri, A., Goh, H. C., Jaafar, H., Mohd Noor, M. I., Razi, N. A., Then, A. Y., Suhaimi, J., Kari, F., & Dahlui, M. (2020). A review of published literature regarding health issues of coastal communities in Sabah, Malaysia. *International Journal of Environmental Research and Public Health*, 17(5), Article 1533. <https://doi.org/10.3390/ijerph17051533>
- Badr, H. S., Du, H., Marshall, M., Dong, E., Squire, M. M., & Gardner, L. M. (2020). Association between mobility patterns and COVID-19 transmission in the USA: A mathematical modelling study. *The Lancet Infectious Diseases*, 20(11), 1247–1254. [https://doi.org/10.1016/S1473-3099\(20\)30553-3](https://doi.org/10.1016/S1473-3099(20)30553-3)
- Balakrishnan, K. N., Yew, C. W., Chong, E. T. J., Daim, S., Mohamad, N. E., Rodrigues, K., & Lee, P. C. (2023). Timeline of SARS-CoV-2 transmission in Sabah, Malaysia: Tracking the molecular evolution. *Pathogens*, 12(8), 1–17. <https://doi.org/10.3390/pathogens12081047>
- Chen, X., Huang, H., Ju, J., Sun, R., & Zhang, J. (2022). Impact of vaccination on the COVID-19 pandemic in U.S. states. *Scientific Reports*, 12(1), 1–10. <https://doi.org/10.1038/s41598-022-05498-z>

- Chenchula, S., Karunakaran, P., Sharma, S., & Chavan, M. (2022). Current evidence on efficacy of COVID-19 booster dose vaccination against the Omicron variant: A systematic review. *Journal of Medical Virology*, *94*(7), 2969–2976. <https://doi.org/10.1002/jmv.27697>
- Cheng, X., Han, Z., Abba, B., & Wang, H. (2020). Regional infectious risk prediction of COVID-19 based on geo-spatial data. *PeerJ*, *8*, 1–24. <https://doi.org/10.7717/peerj.10139>
- Dollah, R., Jafar, A., Joko, E. P., Sakke, N., Mapa, M. T., Atang, C., Hung, C. V., & George, F. (2022). Perception of youth in East Malaysia (Sabah) towards the Malaysia national COVID-19 immunisation programme (PICK). *Journal of Public Health and Development*, *20*(1), 203–217. <https://doi.org/10.55131/jphd/2022/200116>
- Dong, T., Dong, W., & Xu, Q. (2022). Agent simulation model of COVID-19 epidemic agent-based on GIS: A case study of Huangpu District, Shanghai. *International Journal of Environmental Research and Public Health*, *19*(16), Article 10242. <https://doi.org/10.3390/ijerph191610242>
- Farheen, F., Shamil, M. S., Rahman Jony, S. S., Ahmad, Z., Sojib, K. H., Chowdhury, A., Niaz Arifin, S. M., Sania, A., & Rahman, M. S. (2022). *An agent-based model for COVID-19 in Bangladesh*. MedRxiv. <https://doi.org/10.1101/2022.07.24.22277974>
- Gill, B. S., Jayaraj, V. J., Singh, S., Ghazali, S. M., Cheong, Y. L., Iderus, N. H. M., Sundram, B. M., Aris, T., Ibrahim, H. M., Hong, B. H., & Labadin, J. (2020). Modelling the effectiveness of epidemic control measures in preventing the transmis. *International Journal of Environmental Research and Public Health*, *17*(15), 1–13. <https://doi.org/10.3390/ijerph17155509>
- Goroh, M. M. D., Rajahram, G. S., Avoi, R., Van Den Boogaard, C. H., William, T., Ralph, A. P., & Lowbridge, C. (2020). Epidemiology of tuberculosis in Sabah, Malaysia, 2012–2018. *Infectious Diseases of Poverty*, *9*, 1-11. <https://doi.org/10.1186/s40249-020-00739-7>
- Goroh, M., Rajahram, G., Avoi, R., Cvd, B., William, T., Ralph, A. P., & Lowbridge, C. (2020). *An Epidemiological Review of Tuberculosis in Sabah, Malaysia, 2012-2018*. Research Square. <https://doi.org/10.21203/rs.3.rs-28071/v1>
- Godio, A., Pace, F., & Vergnano, A. (2020). SEIR Modeling of the Italian Epidemic of SARS-CoV-2 Using Computational Swarm Intelligence. *International Journal of Environmental Research and Public Health*, *17*(10), Article 3535. <https://doi.org/10.3390/ijerph17103535>
- Gharakhanlou, N. M., & Hooshangi, N. (2020). Spatio-temporal simulation of the novel coronavirus (COVID-19) outbreak using the agent-based modeling approach (case study: Urmia, Iran). *Informatics in Medicine Unlocked*, *20*, Article 100403. <https://doi.org/10.1016/j.imu.2020.100403>
- Harizah, K. (2021, August 27). Highest records to date at 24,599 cases, 393 deaths. *The Malaysian Reserve*. <https://themalaysianreserve.com/2021/08/27/highest-records-to-date-at-24599-cases-393-deaths/>
- Hashim, J. H., Adman, M. A., Hashim, Z., Radi, M. F. M., & Kwan, S. C. (2021). COVID-19 epidemic in Malaysia: Epidemic progression, challenges, and response. *Frontiers in Public Health*, *9*, 1–19. <https://doi.org/10.3389/fpubh.2021.560592>
- Hassan, A. M., Ramos, H., & Moaaz, O. (2023). Second-order dynamic equations with noncanonical operator: Oscillatory behavior. *Fractal and Fractional*, *7*(2), 1–17. <https://doi.org/10.3390/fractalfract7020134>

- He, S., Peng, Y., & Sun, K. (2020). SEIR modeling of the COVID-19 and its dynamics. *Nonlinear Dynamics*, 101(3), 1667–1680. <https://doi.org/10.1007/s11071-020-05743-y>
- Hinch, R., Probert, W. J. M., Nurtay, A., Kendall, M., Wymant, C., Hall, M., Lythgoe, K., Bulas Cruz, A., Zhao, L., Stewart, A., Ferretti, L., Montero, D., Warren, J., Mather, N., Abueg, M., Wu, N., Legat, O., Bentley, K., Mead, T., ... & Fraser, C. (2021). OpenABM-Covid19-An agent-based model for non-pharmaceutical interventions against COVID-19 including contact tracing. *PLoS Computational Biology*, 17(7), 1–26. <https://doi.org/10.1371/journal.pcbi.1009146>
- Hunter, E., & Kelleher, J. D. (2022). Validating and testing an agent-based model for the spread of COVID-19 in Ireland. *Algorithms*, 15(08), Article 0270. <https://doi.org/10.3390/a15080270>
- Iderus, N. H., Singh, S., Singh, L., Ghazali, S. M., Ling, C. Y., Vei, T. C., Syahmi, A., Zamri, S., Jaafar, N. A., Ruslan, Q., Huda, N., Jaghfir, A., & Gill, B. S. (2022). Correlation between population density and COVID-19 cases during the third wave in Malaysia: Effect of the Delta Variant. *International Journal of Environmental Research and Public Health*, 19(12), Article 7439. <https://doi.org/10.3390/ijerph19127439>
- Jafar, A., Dollah, R., Sakke, N., Mapa, M. T., Atang, C., Joko, E. P., Sarjono, F., Zakaria, N. S., George, F., & Hung, C. V. (2024). Public perception toward the Malaysian National COVID-19 Immunisation Programme (PICK) in the state of Sabah, Malaysia: A cross-sectional survey. *Disaster Medicine and Public Health Preparedness*, 18, Article e43. <https://doi.org/10.1017/dmp.2024.31>
- Jiee, S. F., Jantim, A., Mohamed, A. F., & Emirai, M. E. (2021). COVID-19 Pandemic: determinants of workplace preventive practice among primary healthcare workers in Sabah, Malaysia. *Journal of Preventive Medicine and Hygiene*, 62(3), Article E605. <https://doi.org/10.15167/2421-4248/jpmh2021.62.3.2031>
- Kim, Y., & Cho, N. (2022). A Simulation study on spread of disease and control measures in closed population using ABM. *Computation*, 10(01), Article 0002. <https://doi.org/10.3390/computation10010002>
- Kong, L., Duan, M., Shi, J., Hong, J., Chang, Z., & Zhang, Z. (2022). Compartmental structures used in modeling COVID-19: A scoping review. *Infectious Diseases of Poverty*, 11(1), 1–9. <https://doi.org/10.1186/s40249-022-01001-y>
- Kucharski, A. J., Klepac, P., Conlan, A. J. K., Kissler, S. M., Tang, M. L., Fry, H., Gog, J. R., Edmunds, W. J., Emery, J. C., Medley, G., Munday, J. D., Russell, T. W., Leclerc, Q. J., Diamond, C., Procter, S. R., Gimma, A., Sun, F. Y., Gibbs, H. P., Rosello, A., ... & Simons, D. (2020). Effectiveness of isolation, testing, contact tracing, and physical distancing on reducing transmission of SARS-CoV-2 in different settings: A mathematical modelling study. *The Lancet Infectious Diseases*, 20(10), 1151–1160. [https://doi.org/10.1016/S1473-3099\(20\)30457-6](https://doi.org/10.1016/S1473-3099(20)30457-6)
- López, L., & Rodó, X. (2021). A modified SEIR model to predict the COVID-19 outbreak in Spain and Italy: Simulating control scenarios and multi-scale epidemics. *Results in Physics*, 21, Article 103746. <https://doi.org/10.1016/j.rinp.2020.103746>
- Motzev, M. (2019). Prediction accuracy - A measure of simulation reality. *Vanguard Scientific Instruments in Management*, 15(1), 1–18. <https://doi.org/10.13140/RG.2.2.18743.75687>
- Mwalili, S., Kimathi, M., Ojiambo, V., Gathungu, D., & Mbogo, R. (2020). SEIR model for COVID-19 dynamics incorporating the environment and social distancing. *BMC Research Notes*, 13(1), 1–5. <https://doi.org/10.1186/s13104-020-05192-1>

- Nagori, A., Awasthi, R., Joshi, V., Vyalla, S. R., Jarodia, A., Gupta, C., Gulati, A., Bandhey, H., Guliani, K. K., Gill, M. S., Kumaraguru, P., & Sethi, T. (2020). *Less wrong COVID-19 projections with interactive assumptions*. medRxiv. <https://doi.org/10.1101/2020.06.06.20124495>
- Onyechege, D. C., Nor, N. M., & Omer, A. S. F. (2022). The indirect effect of coronavirus disease (COVID-19) pandemic on economic growth in Malaysia: Evidence from the ARDL approach. *International Journal of Economics and Management*, 16(S1), 99-115. <https://doi.org/10.47836/ijeamsi.16.1.007>
- Pandey, G., Chaudhary, P., Gupta, R., & Pal, S. (2019). *SEIR and Regression Model based COVID-19 outbreak predictions in India*. arXiv Preprint.
- Patrick, E. M. (2022, January 05). Sabah kesan Omicron pertama [Sabah the first Omicron effect]. *Astro Awani*. <https://www.astroawani.com/berita-malaysia/sabah-kesan-kes-omicron-pertama-340088>
- Paul, S., Mahata, A., Ghosh, U., & Roy, B. (2020). *Since January 2020 Elsevier has created a COVID-19 resource centre with free information in English and Mandarin on the novel coronavirus COVID- 19*. Elsevier.
- Qiu, Z., Sun, Y., He, X., Wei, J., Zhou, R., Bai, J., & Du, S. (2022). Application of genetic algorithm combined with improved SEIR model in predicting the epidemic trend of COVID-19, China. *Scientific Reports*, 12(1), 1–9. <https://doi.org/10.1038/s41598-022-12958-z>
- Qureshi, S., Akanbi, M. A., Shaikh, A. A., Wusu, A. S., Ogunlaran, O. M., Mahmoud, W., & Osman, M. S. (2023). A new adaptive nonlinear numerical method for singular and stiff differential problems. *Alexandria Engineering Journal*, 74, 585–597. <https://doi.org/10.1016/j.aej.2023.05.055>
- Reeves, K. D., Polk, C. M., Cox, L. A., Fairman, R. T., Hawkins, G. A., Passaretti, C. L., & Sampson, M. M. (2022). Severe acute respiratory coronavirus virus 2 (SARS-CoV-2) infections occurring in healthcare workers after booster vaccination: A comparison of delta versus omicron variants. *Antimicrobial Stewardship and Healthcare Epidemiology*, 2(1), 1–7. <https://doi.org/10.1017/ash.2022.239>
- Roslan, M. N. F., Ismail, W. I., Zamzuri, A. S., Ismail, N. F., & Abdul, N. A. N. (2022). Comorbidity status of deceased of Covid-19 patients in Malaysia. *International Journal of Academic Research in Business and Social Sciences*, 12(10), 2262-2268. <https://doi.org/10.6007/ijarbss/v12-i10/15465>
- Shah, A. U. M., Safri, S. N. A., Thevadas, R., Noordin, N. K., Rahman, A. A., Sekawi, Z., Ideris, A., & Sultan, M. T. H. (2020). COVID-19 outbreak in Malaysia: Actions taken by the Malaysian government. *International Journal of Infectious Diseases*, 97, 108–116. <https://doi.org/10.1016/j.ijid.2020.05.093>
- Shamil, S., Farheen, F., Ibtehaz, N., Mahmud, I., & Soheli, K. M. (2021). An agent-based modeling of COVID-19: Validation, analysis, and recommendations. In *Cognitive Computation* (pp. 1723–1734). Springer. <https://doi.org/10.1007/s12559-020-09801-w>
- Silva, P. C. L., Batista, P. V. C., Lima, H. S., Alves, M. A., Guimarães, F. G., & Silva, R. C. P. (2020). COVID-ABS: An agent-based model of COVID-19 epidemic to simulate health and economic effects of social distancing interventions. *Chaos, Solitons and Fractals*, 139, Article 110088. <https://doi.org/10.1016/j.chaos.2020.110088>
- Tan, C. S., Saim, L., Rao, Y., Kok, S. H., & Ming, L. C. (2021). Public and private sectors collective response to combat COVID-19 in Malaysia. *Journal of Pharmaceutical Policy and Practice*, 14(1), Article 40. <https://doi.org/10.1186/s40545-021-00322-x>

- Tang, X., Zhao, S., Chiu, A. P. Y., Ma, H., Xie, X., Mei, S., Kong, D., Qin, Y., Chen, Z., Wang, X., & He, D. (2017). Modelling the transmission and control strategies of varicella among school children in Shenzhen, China. *PLoS ONE*, *12*(5), 1–17. <https://doi.org/10.1371/journal.pone.0177514>
- Tha, N. O., Shoesmith, W. D., Tan, B. Y., Ibrahim, M. Y., & Hussein, S. S. (2020). Geographic accessibility of healthcare services and health seeking behaviours of rural communities in Kudat and Pitas areas of Sabah. *Borneo Epidemiology Journal*, *1*(1), 46-54. <https://doi.org/10.51200/bej.v1i1.2436>
- Thompson, J., & Wattam, S. (2021). Estimating the impact of interventions against COVID-19: From lockdown to vaccination. *PLoS ONE*, *16*, 1–54. <https://doi.org/10.1371/journal.pone.0261330>
- Umair, I. (2022, January 31). The science behind the omicron wave's sharp peak and rapid decline. *The Vox*. <https://www.vox.com/22905020/omicron-wave-surge-covid-19-cases-vaccines>
- World Health Organization. (2023a). *Covid-19*. World Health Organization. <https://www.who.int/emergencies/diseases/novel-coronavirus-2019/covid-19-policy-briefs>
- World Health Organization. (2023b). *WHO Coronavirus (COVID-19) Dashboard*. World Health Organization. <https://covid19.who.int/>
- Yang, Z., Zeng, Z., Wang, K., Wong, S. S., Liang, W., Zanin, M., Liu, P., Cao, X., Gao, Z., Mai, Z., Liang, J., Liu, X., Li, S., Li, Y., Ye, F., Guan, W., Yang, Y., Li, F., Luo, S., ... & He, J. (2020). Modified SEIR and AI prediction of the epidemics trend of COVID-19 in China under public health interventions. *Journal of Thoracic Disease*, *12*(3), 165–174. <https://doi.org/10.21037/jtd.2020.02.64>
- Yeo, A. (2020, October 31). Sabah perlu infrastruktur, sistem kesihatan lebih baik [Sabah needs better infrastructure and healthcare systems]. *Berita Harian*. <https://www.bharian.com.my/rencana/komentar/2020/10/748301/sabah-perlu-infrastruktur-sistem-kesihatan-lebih-baik>
- Zhao, W., Sun, Y., Li, Y., & Guan, W. (2022). Prediction of COVID-19 data using hybrid modeling approaches. *Frontiers in Public Health*, *10*, 1–13. <https://doi.org/10.3389/fpubh.2022.923978>

Performance of High-volume Carbide Lime Mortar Under Accelerated CO₂ Curing Followed by Postconditioning Treatments

Adrina Rosseira A. Talip^{1,2}, Nur Hafizah A. Khalid^{1*} and Abdul Rahman Mohd Sam¹

¹Faculty of Civil Engineering, Universiti Teknologi Malaysia, 81310 Johor Bahru, Johor, Malaysia

²Civil Engineering Studies, College of Engineering, Universiti Teknologi MARA Cawangan Johor, 81750 Masai, Johor, Malaysia

ABSTRACT

This study explores the potential of using calcium hydroxide (Ca(OH)₂) derived from Carbide Lime Waste (CLW) as a high-volume cement replacement (40%–70% by volume) in mortar. The mortar was subjected to accelerated carbon dioxide (CO₂) curing to enhance carbonation capture while maintaining the desired strength, promoting more sustainable construction practices. The optimum high-volume mortar was further analysed to examine its long-term properties under various postconditioning treatments, including water, wet gunny, and air curing, in terms of calcium carbonate (CaCO₃) formation and late-age strength. The physical properties, such as water absorption and mechanical properties, including compressive, flexural, and splitting tensile strengths, were evaluated. CO₂ capture performance was assessed through carbonation depth testing, and microstructural analysis was performed using Thermogravimetric analysis (TGA) and X-ray diffraction (XRD). Results showed that CLW₇₀ exhibited the best mix design, achieving 100% carbonation depth and 70% CaCO₃ formation within 7 days of accelerated CO₂ curing. Compressive strength increased from 2.62 MPa on day 1 to 17.01 MPa on day 7. XRD analysis indicated that air curing was the most effective postconditioning treatment, resulting in the highest CaCO₃ peaks. Accelerated CO₂ curing also reduced water absorption, and mechanical strength improved with curing age, demonstrating that the CaCO₃ formed during the carbonation process densified the CLW mortar after 7 days of curing.

ARTICLE INFO

Article history:

Received: 08 May 2024

Accepted: 24 December 2024

Published: 21 February 2025

DOI: <https://doi.org/10.47836/pjst.33.2.07>

E-mail addresses:

adrinarosseira@graduate.utm.my (Adrina Rosseira A. Talip)

nur_hafizah@utm.my (Nur Hafizah A. Khalid)

abdrahman@utm.my (Abdul Rahman Mohd Sam)

* Corresponding author

Keywords: Accelerated CO₂ curing, CaCO₃ precipitation, carbide lime waste, CO₂ capturing, postconditioning

INTRODUCTION

Concrete remains the dominant construction material worldwide, and ongoing efforts focus on finding environmentally friendly alternatives that maintain strength and durability. The choice of alternative materials often depends on the specific application. For example, supplementary cementitious materials (SCMs) rich in cementitious properties are beneficial because they produce secondary calcium silicate hydrates (CSH) gels, enhancing strength. In addition, SCMs can address environmental concerns such as CO₂ emissions. Accelerated carbonation curing (ACC) has been shown to improve initial strength and reduce porosity better than conventional water curing, leading to at least a 20% strength improvement across mixtures (Sharma & Goyal, 2018).

Previous research has extensively explored industrial waste materials, such as fly ash, slag, and recycled concrete aggregates, for mineral CO₂ sequestration in the concrete industry. These waste products often contain calcium-bearing phases that facilitate the formation of carbonate compounds, aiding in CO₂ sequestration. Early-stage carbonation curing can significantly affect the early and late-stage performance of cement-based composites. ACC treatment, in particular, shows promise for the precast concrete industry, which accounts for about 10% of global concrete consumption every year (Li & Wu, 2022).

There are several noteworthy benefits to using SCMs. First, early strength in SCM concrete can be enhanced by carbonation reactions. Second, carbonate precipitation can improve durability. Third, carbon emissions can be reduced by lowering cement usage and increasing CO₂ uptake during carbonation (Zhang et al., 2016).

One material gaining attention is carbide lime waste (CLW), a byproduct of acetylene gas production, which raises concerns about disposal and environmental impact (Adamu et al., 2021). The main component of CLW is calcium hydroxide (Ca(OH)₂), which has a high calcium oxide (CaO) content, making it a promising binder material (Lorca et al., 2014). Additionally, CLW has a strong potential for CO₂ capture.

Several factors influence the rate of carbonation, including CO₂ concentration, which plays a critical role in the carbonation process. A specific concentration of CO₂ in waste flue gases is preferred for effective carbonation treatment in concrete. Cement plants typically emit waste flue gas with a CO₂ concentration of 14%–33%, while iron and steel plants release gases with 20%–30% CO₂ concentration (Li & Wu, 2022). A higher CO₂ concentration, such as 20%, has been shown to enhance crystallinity and particle size compared to a lower concentration of 1% (Li & Ling, 2020).

Most earlier studies have used carbonation treatments for building materials at 20–80°C temperatures to achieve cost-effective CO₂ sequestration (Li & Wu, 2022). The water-to-cement ratio (w/c) also plays a crucial role in carbonation. A higher w/c can facilitate the separation of cement and limestone particles, promoting carbonation by creating a more aqueous environment. However, excess water in the pores of cementitious materials can

hinder CO₂ diffusion, limiting penetration depth (Li & Wu, 2022; Zhang et al., 2016). Therefore, preconditioning is necessary to remove excess moisture before CO₂ curing. A reduced w/c ratio can improve gas permeability, allowing CO₂ to diffuse more effectively into the material. This preconditioning not only affects the initial carbonation process but also has long-term positive implications for the durability and strength of the final product.

However, the carbonation through CO₂ curing is an exothermic process that can cause early water loss from the mixture. It can inhibit the further hydration of unreacted cement, particularly when combined with water removal during preconditioning. Water loss during carbonation may hinder future hydration, reducing compressive strength (Sharma & Goyal, 2018). It is especially important in regions where materials are exposed to varied climates and environmental pressures. Postconditioning, such as subsequent water curing, may be needed to replenish lost water, enhance hydration, improve microstructure, and promote further strength development (Liu & Meng, 2021).

Although the carbonation of cement-based materials has been extensively studied, limited research has focused on accelerated CO₂ curing, preconditioning, and postconditioning treatments specifically for lime-based materials. Furthermore, many previous studies have primarily investigated factors influencing CO₂ curing, such as CO₂ concentration, pressure, temperature and humidity (Li & Ling, 2020; Lu et al., 2022; Xu et al., 2022). However, there remains a gap in the research regarding curing regimes that optimise CO₂ capturing and mechanical strength properties. Addressing this gap could provide significant insights into curing optimisation, ultimately improving mortar performance.

It is also important to assess the tensile strength of mortar and concrete, as these materials are weak in tension but strong in compression. Applications such as unreinforced concrete roads and runways rely on their ability to bend, distributing concentrated loads over large areas (Gloria et al., 2017). This research aims to determine the mechanical properties of mortar, including compressive, flexural and splitting tensile strengths, to provide baseline data for unreinforced mortar applications. While many studies have investigated high-volume replacement (40% or more) of SCMs or alternative materials for Portland Cement (PC), few have focused on high-volume lime-based materials subjected to accelerated CO₂ curing and later strength development under postconditioning treatments. Other alternative materials that have been studied include fly ash, palm oil fuel ash and ground granulated blast furnace slag (Nwankwo et al., 2020).

This research consists of two stages. The optimal high-volume CLW mortar was determined in the first stage based on the highest carbonation rate at a desired strength for non-loadbearing applications. In the second stage, the CO₂ capture and mechanical properties of the optimal high-volume CLW mortar were examined under various postconditioning treatments. This study contributes valuable knowledge on the performance of high-volume lime-based materials in mortar under accelerated CO₂ curing, particularly in

terms of CO₂ uptakes and mechanical strength. It also provides insights into later strength performance under postconditioning treatments.

MATERIALS AND METHODS

Materials and Sample Preparation

Ordinary Portland Cement (OPC) and Carbide Lime Waste (CLW) were the primary materials used in this study. The fineness of both OPC (99.73%) and CLW (92%) passing a 45µm sieve size was used. CLW was ground using a ball mill to enhance its hydration potential, aligning it with OPC standards. The chemical composition of CLW was predominantly calcium oxide (96% CaO), as shown in Figure 1.

In the first stage, mortar mixes were prepared according to the mix proportions listed in Table 1. A constant water-cement ratio (w/c) of 0.6 and a cement-to-sand ratio (c/s) of 1:3 was maintained across all samples. Mortar samples were cast into 50 × 50 × 50 mm cubes,

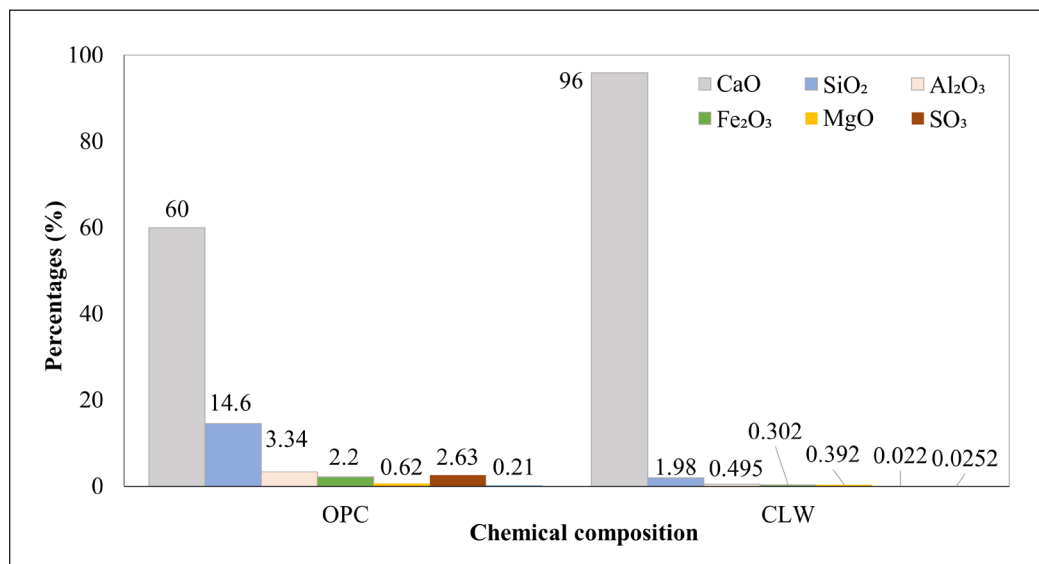


Figure 1. Chemical composition of OPC and CLW

Table 1
Mix design proportion

Types of mortar	CLW replacement (kg/m ³)	Cement (kg/m ³)	CLW (kg/m ³)	Sand (kg/m ³)	w/c (kg/m ³)
CLW ₄₀	40	300	200		
CLW ₅₀	50	250	250		
CLW ₆₀	60	200	300	1500	300
CLW ₇₀	70	150	350		

with each mould filled in two layers and subjected to vibration to ensure homogeneous distribution. After that, the mould was levelled, covered with a plastic sheet, and stored at room temperature. After 24 hours, the mortar samples were demoulded and placed in a CO₂ curing chamber at 60°C and a CO₂ concentration of 20% for 1, 3, and 7 days of accelerated curing.

The optimal mix based on CO₂ capture and strength was selected in the second stage for further analysis. The optimal mix was subjected to extended accelerated CO₂ curing for 3 and 7 days, followed by postconditioning treatments (air, wet gunny, and water curing) for up to 28 days. The design codes and curing conditions are summarised in Table 2.

Table 2
Sample code and its corresponding curing condition

Code	Description	Subsequent postconditioning (method)	Test age (days)
CLW ₄₀ CLW ₅₀ CLW ₆₀ CLW ₇₀	CLW mortar without preconditioning (numeric refers to the cement replacement proportion)	-	1, 3, 7
CLWpc ₇₀	CLW mortar with preconditioning treatment	-	
CLWpc _{70WG}	70% of CLW mortar with preconditioning treatment + postconditioning	Wet gunny	1, 3, 7, 28
CLWpc _{70WC}	70% of CLW mortar with preconditioning treatment + postconditioning	Water curing	1, 3, 7, 28
CLWpc _{70AC}	70% of CLW mortar with preconditioning treatment + postconditioning	Air curing	1, 3, 7, 28

Physical and Mechanical Properties

A series of tests were conducted to assess the performance of both control and CLW mortars, including compressive strength, flexural strength, splitting tensile strength, and water absorption. Three samples were used per test condition, and each property's average value was recorded. Compressive strength was evaluated at both stages, while flexural and splitting tensile tests were carried out after postconditioning.

Compressive Test

Compressive strength tests were performed on 50 x 50 x 50 mm cubes using a Universal Testing Machine (3000 kN capacity) with a load rate of 2000 N/s (ASTM C109/C109M-02, 2012).

Flexural Test

The three-point loading test was used to evaluate the flexural strength of mortar prisms (40 × 40 × 160 mm) subjected to postconditioning treatments. The test followed ASTM

C348-21 (2021) standards with a load rate of 40 N/s to ensure failure occurred between 30 s and 90 s without any sudden impact.

Splitting Tensile Test

Splitting tensile strength was measured on cylindrical samples (50 mm diameter by 100 mm height) using the same Universal Testing Machine as the compressive test, with a loading rate of 1mm/min (ASTM C109/C109M-02, 2012; Nwankwo et al., 2020). The compressive force was applied on the ends of the cylindrical mortar samples splitting along the central plane.

Water Absorption Test

Optimum mortar samples were dried in an oven at 105°C to a consistent weight before water absorption tests. After cooling, the initial mass (m_1 in g) was recorded, and samples were submerged in water for 24 hours. After that, the final mass (m_2 in g) was measured to calculate water absorption using Equation 1 (Luo et al., 2022).

$$WA (\%) = \frac{m_2 - m_1}{m_1} \times 100\% \quad [1]$$

CO₂ Capturing Properties and Visual Evaluation of Carbonation Depth

The carbonation depth of control and CLW mortars was evaluated using phenolphthalein spray after flexural testing. This was done in both stages to first determine the optimal mix and then examine the carbonation performance at a later age after various postconditioning treatments. The phenolphthalein spray turned the alkaline region purple, and the more acidic region was colourless (Roy et al., 1999). The carbonation depth was taken as the average of ten measurements across the cross-section of the sample (Liu et al., 2019).

CO₂ Sequestration by Thermogravimetric Analysis Test (TGA) Test

Thermogravimetric analysis (TGA) assessed CaCO₃ precipitation in the mortars during the first stage. To prepare the samples, the CLW pastes with the highest CO₂ capturing based on carbonation depth were immersed in acetone for 24 hours to stop hydration (Zhang et al., 2016). The pastes were then dried at 105°C for a day and then crushed to a powder with a particle size of less than 45 µm. About 5 to 10 mg of this powder was then heated at 10°C/min to reach 1000°C in the presence of flowing N₂ gas (Ma, 2014). The amount of Ca(OH)₂ and CaCO₃ was determined by measuring the mass loss using Equations 2 and 3.

$$Ca(OH)_2 (\%) = \left(\frac{M_{350} - M_{500}}{M_{350}} \right) * 100 \quad [2]$$

$$\text{CaCO}_3 (\%) = \left(\frac{M_{500} - M_{800}}{M_{500}} \right) * 100 \quad [3]$$

X-ray Diffraction (XRD) Test

X-ray diffraction (XRD) was used to identify mineral compositions, focusing on raw and carbonated samples. The samples were in powder form and crushed into particle sizes of less than 75 µm. The diffraction angle range used to scan the sample was from 10° to 90° within a 2θ range and at a speed of 1°/min (Wu et al., 2021).

RESULTS AND DISCUSSION

Optimisation of CLW Mortars Based on CO₂ Capture and Strength

Figure 2 shows the compressive strength of high-volume CLW mortars (40%–70%) at different curing ages. Two key trends emerge: first, a decrease in strength as CLW content increases, and second, a significant increase in strength with longer accelerated CO₂ curing durations. By day 7, CLW₆₀ and CLW₇₀ reached compressive strengths around 17 MPa. As a comparison, Luo et al. (2022) replaced 60% of cement with carbide slag (CS) at lower CO₂ concentrations. At 5% CO₂ concentration at 25°C, the study reported compressive and flexural strengths of 2.0–5.7 MPa and 9.9–19.3 MPa after 7 and 28 days of accelerated CO₂ curing. In contrast, after 7 days of accelerated CO₂ curing, CLW₆₀ demonstrated a compressive strength of 17.19 MPa—an 83% improvement. This strength enhancement highlights the significant influence of accelerated curing parameters, particularly the higher CO₂ concentration and temperature, on the early-age mechanical properties. Similarly, CLW₇₀ mortar achieved full carbonation (100%) with a compressive strength of 17.01 MPa after 7 days.

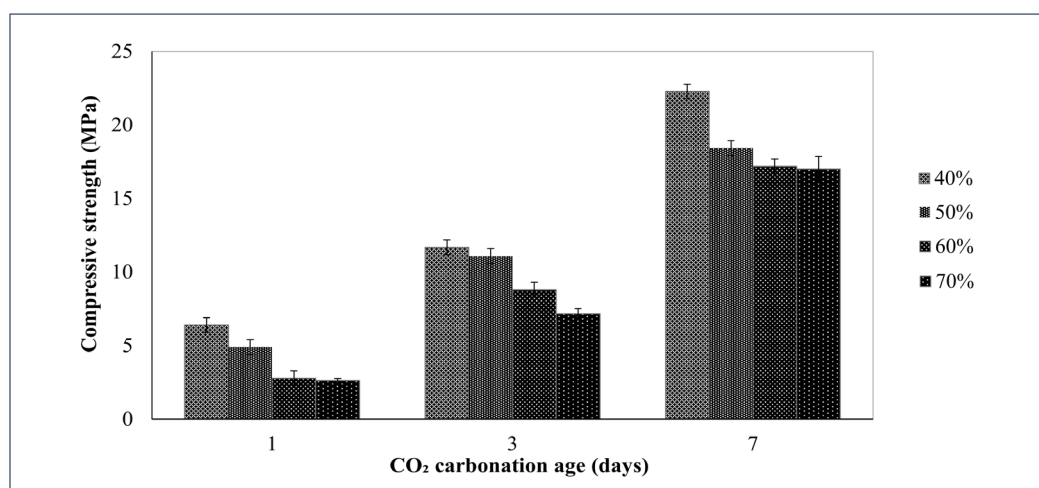


Figure 2. The compressive strength performance of CLW mortars at all ages

Figure 3 shows the carbonation depth for similar high-volume CLW mortars. The results indicated that all samples' carbonation depth increased with longer accelerated CO_2 curing durations. Additionally, there was a notable increase in carbonation depth as the proportion of CLW increased. Since CLW primarily consists of $\text{Ca}(\text{OH})_2$, the higher its content, the more CaCO_3 would be formed under accelerated CO_2 curing conditions as the curing time increased. It suggests that the high CLW content, the high concentration of CO_2 , and the elevated curing temperature significantly enhanced the carbonation rate. In traditional cement, calcium derives mainly from hydrated products like $\text{Ca}(\text{OH})_2$ and CSH, while in CLW mortars, $\text{Ca}(\text{OH})_2$ directly reacts with CO_2 gas during accelerated curing. As a result, carbonation reduces the amount of $\text{Ca}(\text{OH})_2$ in both the cement and CLW, leading to the precipitation of CaCO_3 . Moreover, higher curing temperatures and water content can further enhance carbonation (Li & Wu, 2022).

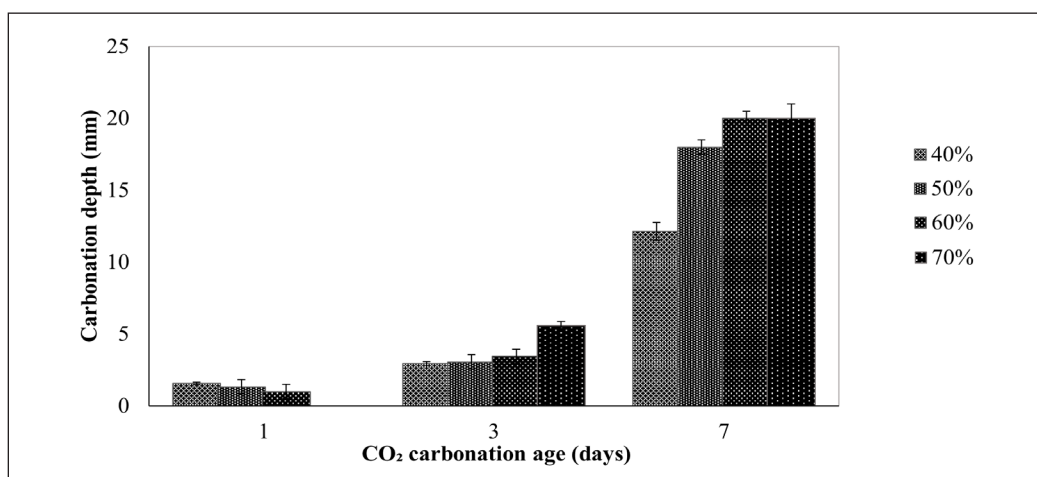


Figure 3. The carbonation depth performance of CLW mortars at all ages

Physical, Mechanical and CO_2 Capture Performance of Optimum CLW Mortars

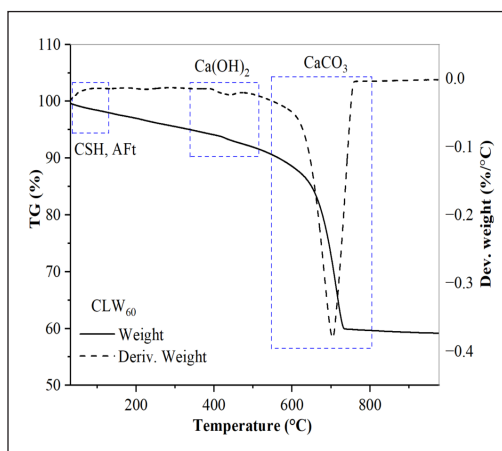
The optimum mix was selected based on its CO_2 capture performance. Figure 4 shows that CLW_{60} and CLW_{70} exhibited similar carbonation depths, leading to further investigation. The DTG curves from TGA revealed three distinct peaks of mass loss between 30–400°C. The main reason is due to the dehydration of CSH gels, monosulfate (AF_m), and ettringite (AF_t) (Zhang et al., 2023). According to Luo et al. (2022), the major mass loss at 100°C is due to the dehydration of CSH gels formed by the hydration of silicate phases. The loss of $\text{Ca}(\text{OH})_2$ due to dehydroxylation occurs between 350–450°C, while the decomposition of CaCO_3 takes place at temperatures above 600°C (Cizer et al., 2012).

After 7 days of accelerated CO_2 curing, as shown in Figures 4(a) and 4(b), CLW_{60} exhibited 1.11% of $\text{Ca}(\text{OH})_2$ and 65.41% of CaCO_3 precipitation, while CLW_{70} showed

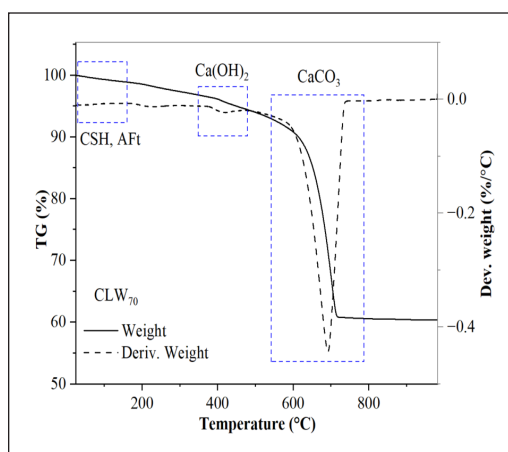
slightly higher CO₂ capture with less than 1% of Ca(OH)₂ and 70% of CaCO₃ as shown in Figure 4(c). These findings suggest that CLW₇₀ achieved greater CaCO₃ formation. Since this study aimed to identify the optimum mix based on CO₂ capture and desired strength, CLW₇₀ was selected for further evaluation under various postconditioning treatments to investigate its later-age strength.

To verify the effectiveness of accelerated CO₂ curing, Figure 4(c) compares mortar subjected to conventional curing (non-CO₂ curing). The uncarbonated CLW₇₀ mortars showed only 41.40% Ca(OH)₂ and 17.86% CaCO₃. The 98.41% reduction in Ca(OH)₂ after accelerated CO₂ curing confirms the significant role of this process in promoting CaCO₃ precipitation. These findings demonstrate that CLW is highly effective in capturing CO₂ and efficiently converts portlandite into calcite through accelerated CO₂ curing.

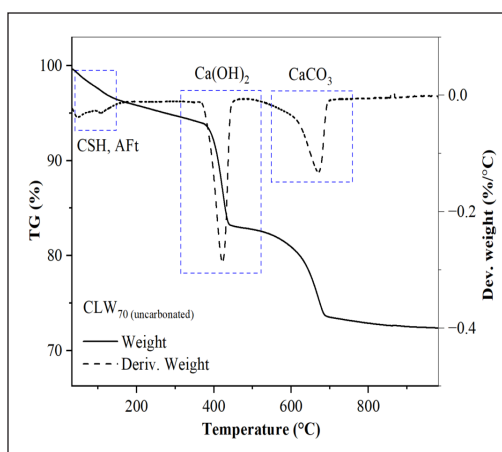
Figure 5 illustrates the mechanical properties of CLW₇₀ mortars subjected to various accelerated CO₂ curing durations and postconditioning treatments. Wet gunny (CLW_{PC70WG}) and air curing (CLW_{PC70AC}) improved compressive strength by 16.9%–21.5% and 21.5%–33.4%, respectively, after 1 and 3 days of accelerated CO₂ curing, compared to the control sample (CLW_{PC70}), as shown in Figure 5(a). In contrast, water curing had minimal impact on the later-age strength of CLW_{PC70} across all curing durations, likely due to the higher



(a)

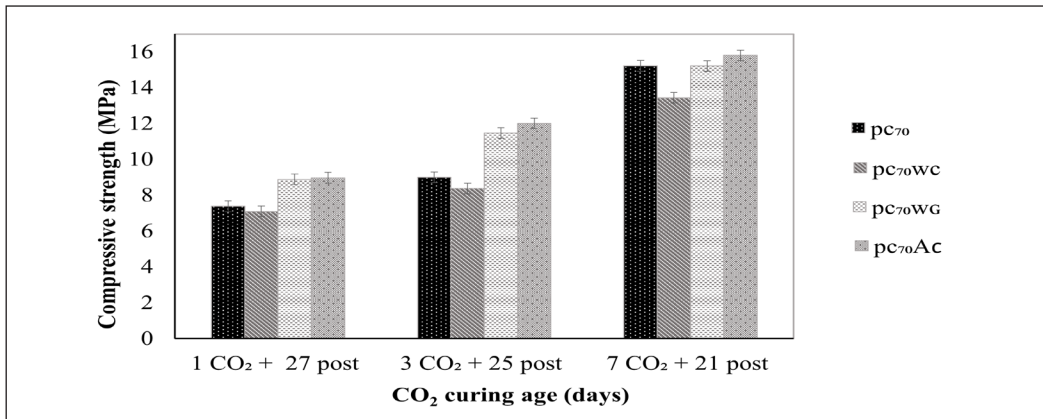


(b)

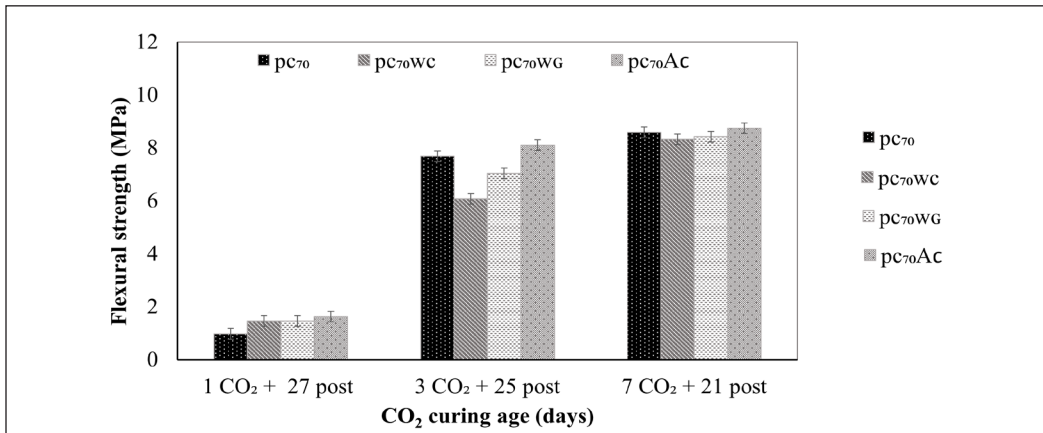


(c)

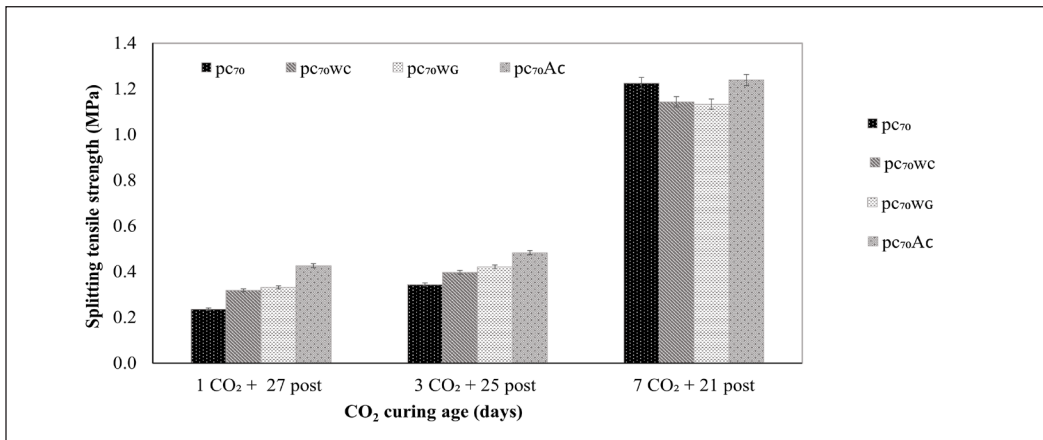
Figure 4. TGA of mortar paste samples: (a) CLW₆₀; (b) CLW₇₀; and (c) CLW₇₀ (uncarbonated)



(a)



(b)



(c)

Figure 5. Mechanical strength of optimum CLW mortars with different CO₂ curing and post-curing age: (a) Compressive; (b) Flexural; and (c) Splitting tensile

water absorption of CLW, which hinders hydration during postconditioning, as shown in Figure 6.

Since CLW primarily consists of Ca(OH)₂, it plays a crucial role in reacting with CO₂ during postconditioning. In semi-wet and dry conditions, such as wet gunny and air curing, any remaining unhydrated Ca(OH)₂ reacts with CO₂, contributing to the strength development. However, by day 7 of accelerated CO₂ curing, both methods reached a plateau, with no significant strength improvement compared to the control after 28 days of hydration. It is likely due to the complete transformation of Ca(OH)₂ into CaCO₃, which densifies the mortar and retains its strength. Similar strength trends were observed for flexural and splitting tensile strength tests, as shown in Figures 5(b) and 5(c). Air curing was sufficient to complete the hydration process, as all hydration products had been converted to CaCO₃.

Figure 6 shows the water absorption rates for CLW₇₀ mortars after 28 days. CLW₇₀ mortars had higher water absorption rates than those subjected to postconditioning. The rate decreased from 19% to 14% after CO₂ curing. Previous studies have shown that increasing the CS content to 80% in mortars increases water absorption (Luo et al., 2022). CLW, with its large surface area and porous structure, tends to absorb more water, leading to increased water consumption for standard consistency, reduced compressive strength, and higher water absorption of the mortar.

However, the water absorption rate decreased when high-volume CLW mortars (up to 70%) were subjected to accelerated CO₂ curing followed by postconditioning. This reduction is attributed to the carbonation process, which forms CaCO₃ and fills the pores of the mortar, reducing water uptake. The longer the CO₂ curing duration, the greater the strength improvement and reduction in water absorption. It is due to the structural densification of CLW mortars through CaCO₃ formation, which limits water absorption. The mechanical strength of the CLW mortars subjected to 7 days of CO₂ curing was higher than that of those cured for 1 and 3 days only.

The primary objective of this test was to evaluate the effect of accelerated CO₂ curing and postconditioning on water absorption. The results showed that both factors contributed to significant changes in water absorption capacity. The accelerated CO₂ curing duration played a critical role in transforming Ca(OH)₂ into CaCO₃ while postconditioning

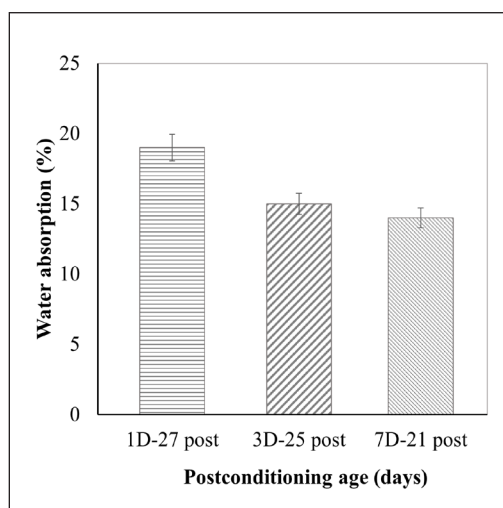


Figure 6. Water absorption of CLW₇₀

completed the hydration process. Therefore, longer curing durations resulted in lower water absorption, as CaCO_3 precipitated and filled the mortar's pores.

Figure 7 highlights the carbonation depth of CLW_{70} mortars after 7 days of accelerated CO_2 curing. Mortars subjected to postconditioning treatments (water curing, $\text{CLW}_{\text{PC70WC}}$; wet gunny curing, $\text{CLW}_{\text{PC70WG}}$; and air curing, $\text{CLW}_{\text{PC70AC}}$) were compared to control samples without postconditioning. In all cases, the cross-section of CLW_{70} mortars was fully carbonated, indicating that CLW is highly effective at capturing CO_2 . This evaluation confirms that all $\text{Ca}(\text{OH})_2$ had been converted into CaCO_3 , as the phenolphthalein indicator test showed the colourless region of the mortar surface. When the transformation is complete, CaCO_3 crystals fill the pores and densify the matrix by CaCO_3 precipitation that provides the protection layer of CLW mortar. The XRD test was further examined to confirm the significant calcite transformation at all the peaks.

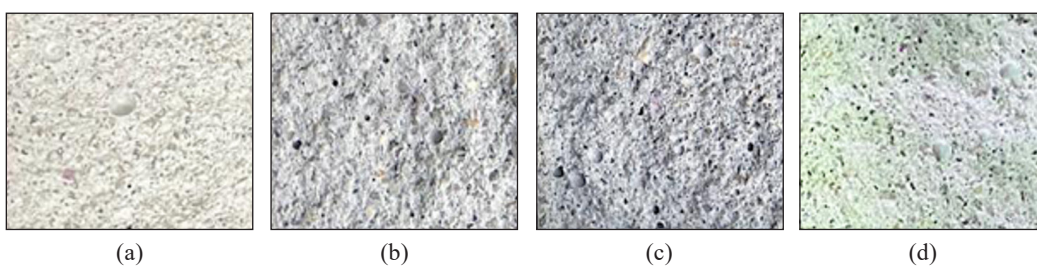


Figure 7. Accelerated CO_2 curing (CLW_{70}) under various postconditioning treatments: (a) CLW_{70} ; (b) $\text{CLW}_{\text{PC70WC}}$; (c) $\text{CLW}_{\text{PC70WG}}$; and $\text{CLW}_{\text{PC70AC}}$

XRD analysis of the postconditioning CLW_{PC70} mortars revealed the phase changes during further curing, as shown in Figure 8. Calcite (CaCO_3) was the dominant mineral, with its highest peak intensity at 29.36° , confirming the high amount of portlandite captured using TGA [Figure 3(a)] that had been converted to calcite. The highest intensity of calcite was observed in air-cured mortars, followed by wet gunny and water-cured mortars.

Water curing limited further carbonation by keeping the mortars moist, resisting CO_2 penetration into the material. It explains why water-cured samples had the lowest calcite peak intensity. XRD analysis confirmed the findings from TGA in Figures 4(a) and 4(b) that no further hydration products were produced during postconditioning. The densification of CaCO_3 in the mortar's outer layer inhibited water penetration, confirming that the strength gained by CLW mortars was primarily due to CaCO_3 precipitation. Besides, the water curing provides moisture that facilitates the hydration of cement, thereby facilitating the development of strength. However, CO_2 becomes limited, which is the main reactant in the formation of CaCO_3 , since the water occupies the pore spaces, preventing CO_2 from reacting with any unreacted $\text{Ca}(\text{OH})_2$ in the mortars. In addition, CO_2 has a low capability to dissolve in water. Hence, the carbonation reaction remains low. This carbonation

process efficiently converts Ca(OH)₂ into CaCO₃; hence, CLW mortar usually does not need water curing as a postconditioning treatment. It is sufficient to use air curing as a postconditioning treatment due to this self-sustaining strength and calcite enhancement. The mortar maintains adequate moisture for further carbonation under ambient environments; hence, the material reaches an appropriate strength range without further water treatment.

CONCLUSION

This study demonstrates the effectiveness of incorporating high-volume CLW as a cement replacement under accelerated CO₂ curing. The key findings include:

1. High-volume CLW mortars exhibited enhanced CaCO₃ precipitation with an increased accelerated CO₂ curing duration, which increased the CO₂ capturing capability and compressive strength.
2. CLW₇₀ achieved full carbonation 100% and 70% CaCO₃ precipitation within 7 days, with compressive strength increasing from 2.62 MPa on day 1 to 17.01 MPa by day 7.
3. Postconditioning treatments, particularly air curing, further enhanced the later-age strength of the optimum CLW₇₀ mortars, followed by wet gunny and water curing methods. XRD analysis confirmed that air-cured mortars exhibited the highest calcite content, contributing to superior mechanical performance.
4. Water absorption rates decreased with increased CO₂ curing age, reflecting the densification of CLW mortars due to CaCO₃ precipitation, which reduced water intake.

The findings underscore CLW's potential for CO₂ sequestration and mechanical performance enhancement in mortar applications. Future studies should investigate the durability of CLW mortars under various weathering and chemical exposure conditions to further validate their use in construction.

ACKNOWLEDGMENT

The authors are grateful for the financial support provided by Universiti Teknologi Malaysia under university's grant with registration numbers Q.J130000.3822.22H88 and

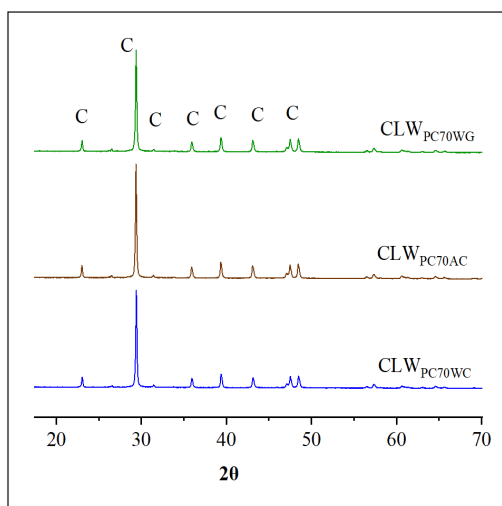


Figure 8. The characteristics of carbonation products are optimum CLW₇₀ mortar underwater, wet gunny and air curing condition

R.J130000.7622.4C806. Additionally, the authors extend their appreciation to the Mineral Research Centre, Minerals and Geoscience Department Malaysia, and the ASEAN-ROK Award for Excellence in Science, Technology and Innovation Korea for their invaluable encouragement and support throughout this research.

REFERENCES

- Adamu, M., Ibrahim, Y. E., Al-Atroush, M. E., & Alanazi, H. (2021). Mechanical properties and durability performance of concrete containing calcium carbide residue and nano silica. *Materials*, *14*(22), 1–28. <https://doi.org/10.3390/ma14226960>
- ASTM C109/C109M-02. (2012). Standard test method for compressive strength of hydraulic cement mortars. *Annual Book of ASTM Standards*, *04(C)*, 9. <https://doi.org/10.1520/C0109>
- ASTM C348-21. (2021). Standard test method for flexural strength of hydraulic-cement mortars. *Annual Book of ASTM Standards*, *04(1)*, 1–5. <https://doi.org/10.1520/C0348-08.2>
- Cizer, Ö., Rodriguez-Navarro, C., Ruiz-Agudo, E., Elsen, J., Van Gemert, D., & Van Balen, K. (2012). Phase and morphology evolution of calcium carbonate precipitated by carbonation of hydrated lime. *Journal of Materials Science*, *47*(16), 6151–6165. <https://doi.org/10.1007/s10853-012-6535-7>
- Gloria, A. C., Ogbonnaya, O. D., & Olujide, A. O. (2017). Flexural and split tensile strength properties of lime cement concrete. *Civil and Environmental Research*, *9*(3), 10–16–16.
- Li, L., & Wu, M. (2022). An overview of utilizing CO₂ for accelerated carbonation treatment in the concrete industry. *Journal of CO₂ Utilization*, *60*(3), Article 102000. <https://doi.org/10.1016/j.jcou.2022.102000>
- Li, X., & Ling, T. C. (2020). Instant CO₂ curing for dry-mix pressed cement pastes: Consideration of CO₂ concentrations coupled with further water curing. *Journal of CO₂ Utilization*, *38*, 348–354. <https://doi.org/10.1016/j.jcou.2020.02.012>
- Liu, P., Chen, Y., Yu, Z., & Zhang, R. (2019). Effect of temperature on concrete carbonation performance. *Advances in Materials Science and Engineering*, *2019*, 1–7. <https://doi.org/10.1155/2019/9204570>
- Liu, Z., & Meng, W. (2021). Fundamental understanding of carbonation curing and durability of carbonation-cured cement-based composites: A review. *Journal of CO₂ Utilization*, *44*, Article 101428. <https://doi.org/10.1016/j.jcou.2020.101428>
- Lorca, P., Calabuig, R., Benlloch, J., Soriano, L., & Payá, J. (2014). Microconcrete with partial replacement of Portland cement by fly ash and hydrated lime addition. *Materials and Design*, *64*, 535–541. <https://doi.org/10.1016/j.matdes.2014.08.022>
- Lu, B., Drissi, S., Liu, J., Hu, X., Song, B., & Shi, C. (2022). Cement and concrete research effect of temperature on CO₂ curing, compressive strength and microstructure of cement paste. *Cement and Concrete Research*, *157*, Article 106827. <https://doi.org/10.1016/j.cemconres.2022.106827>
- Luo, K., Cheng, X., Li, J., Lu, Z., Deng, X., Hou, L., & Jiang, J. (2022). Performance of hydraulic lime by using carbide slag. *Journal of Building Engineering*, *51*, Article 104208. <https://doi.org/10.1016/j.job.2022.104208>

- Ma, H. (2014). Mercury intrusion porosimetry in concrete technology: Tips in measurement, pore structure parameter acquisition and application. *Journal of Porous Materials*, 21(2), 207–215. <https://doi.org/10.1007/s10934-013-9765-4>
- Nwankwo, C. O., Bamigboye, G. O., Davies, I. E. E., & Michaels, T. A. (2020). High volume Portland cement replacement: A review. *Construction and Building Materials*, 260, Article 120445. <https://doi.org/10.1016/j.conbuildmat.2020.120445>
- Roy, S. K., Poh, K. B., & Northwood, D. O. (1999). Durability of concrete - Accelerated carbonation and weathering studies. *Building and Environment*, 34(5), 597–606. [https://doi.org/10.1016/S0360-1323\(98\)00042-0](https://doi.org/10.1016/S0360-1323(98)00042-0)
- Sharma, D., & Goyal, S. (2018). Accelerated carbonation curing of cement mortars containing cement kiln dust: An effective way of CO₂ sequestration and carbon footprint reduction. *Journal of Cleaner Production*, 192, 844–854. <https://doi.org/10.1016/j.jclepro.2018.05.027>
- Wu, H., Liang, C., Xiao, J., & Ma, Z. (2021). Properties and CO₂-curing enhancement of cement-based materials containing various sources of waste hardened cement paste powder. *Journal of Building Engineering*, 44, Article 102677. <https://doi.org/10.1016/j.jobe.2021.102677>
- Xu, Z., Zhang, Z., Huang, J., Yu, K., Zhong, G., Chen, F., Chen, X., Yang, W., & Wang, Y. (2022). Effects of temperature, humidity and CO₂ concentration on carbonation of cement-based materials: A review. *Construction and Building Materials*, 346, Article 128399. <https://doi.org/10.1016/j.conbuildmat.2022.128399>
- Zhang, D., Cai, X., & Shao, Y. (2016). Carbonation curing of precast fly ash concrete. *Journal of Materials in Civil Engineering*, 28(11), Article 04016127. [https://doi.org/10.1061/\(asce\)mt.1943-5533.0001649](https://doi.org/10.1061/(asce)mt.1943-5533.0001649)
- Zhang, G., Peng, G. F., Zuo, X. Y., Niu, X. J., & Ding, H. (2023). Adding hydrated lime for improving microstructure and mechanical properties of mortar for ultra-high performance concrete. *Cement and Concrete Research*, 167, Article 107130. <https://doi.org/10.1016/j.cemconres.2023.107130>

Review Article

An Overview of the 5G Patent Landscape

Mohammad Sadegh Naghipour* and Zulhasni Abdul Rahim

Malaysia-Japan International Institute of Technology, University of Technology Malaysia, Jalan Sultan Yahya Petra, 54100, Kuala Lumpur, Malaysia

ABSTRACT

The fifth generation of mobile networks (5G) is the most recent iteration in cellular technology. To develop and implement new technologies, remain competitive, and maintain their market position, 5G patents are essential for businesses in the telecommunications industry. Examining 5G patents offers important insights into the industry's overall environment and technological development. This study aims to comprehensively analyze the 5G patent landscape by simultaneously examining technological, scientific, and financial aspects. The analysis was conducted using Questel's Orbit Insight patent research software. The analysis of 5G patents reveals significant patterns in patent applications, notable industry participants, and consequences for technological standards and market competition. 5G patents will continue to drive innovation and have a significant impact on market dynamics, shaping future industrial competitiveness and technological standards. Businesses and legislators must carefully analyze their patent strategies to successfully traverse the rapidly changing 5G ecosystem. Subsequent investigations into 5G patent analysis could also explore the effects of emerging technologies and legislative advancements on patent portfolios while also monitoring the evolution of 5G patent trends and their influence on industry dynamics.

Keywords: 5G, patent analysis, research and development (R&D), strategy, technology landscape, telecommunications industry

ARTICLE INFO

Article history:

Received: 16 May 2024

Accepted: 18 November 2024

Published: 21 February 2025

DOI: <https://doi.org/10.47836/pjst.33.2.08>

E-mail addresses:

naghipour@graduate.utm.my (Mohammad Sadegh Naghipour)

zulhasni@utm.my (Zulhasni Abdul Rahim)

* Corresponding author

INTRODUCTION

5G is the most recent iteration in cellular technology. Compared to earlier wireless standards, 5G was designed to significantly boost wireless network speed and bandwidth while lowering latency (Gillis & Gerwig, 2024). While the primary goal of technological advancements in 2G, 3G, and 4G has been to improve user experience, 5G

and any further developments will profoundly revolutionize our daily lives and commercial operations (Ericsson, 2024).

This new generation of international wireless standards will affect a variety of devices that millions of people use daily. While mobile phone users were the main beneficiaries of 3G and 4G, 5G links additional devices within a network, including drones, electric cars, and virtual reality (VR) technologies. Producers of these products will be obliged to depend on 5G standards for connectivity, which are protected by standard essential patents (SEPs). Having SEPs in the field of 5G technology will make it more difficult to monetize and enforce a patent portfolio, underscoring for the business community the significance of putting an intellectual property strategy in place (Spohr, 2024).

The development and commercialization of 5G technology have resulted in a significant increase in patenting activities related to high-speed, low-latency communication systems that facilitate the interconnection of all things (Xu, 2022).

Patent analysis in the 5G domain is critical for assessing technological progress and innovation activities. It provides valuable insights into the competitive landscape, enabling companies and countries to evaluate their positions in various technological domains (Rita et al., 2023). For instance, patent statistics can be utilized to identify leading innovators, track technological trends, and inform strategic decision-making in research and development.

The significance of 5G patents extends beyond mere technological advancement. They play a crucial role in shaping industry dynamics, influencing market competition and driving economic growth. Patent analysis in this field can reveal innovation patterns, technologies' evolution, and potential areas for future development (Lee & Lee, 2013).

5G patents and their analyses are instrumental in comprehending the technological landscape, guiding innovation strategies, and fostering competitiveness in the rapidly advancing telecommunications sector. As 5G technology continues to mature and find widespread applications, the strategic utilization of patent intelligence will become increasingly crucial for businesses and policymakers alike (Wang, 2011).

Archibugi and Planta (1996) noted that the complexity and heterogeneity of technological change make it challenging to identify metrics that adequately capture the scope, intensity, pace, and direction of inventive activities. Ernst (2003) highlights the importance of patent information in influencing corporate decision-making processes and strategic technology management. Owing to its extensive coverage, variety of information, and database accessibility, patent information is essential for analytical tasks.

Thorough awareness of the entire patent landscape and the most pertinent patents is fundamentally necessary to facilitate the smooth implementation of 5G, maintain profitability, and safeguard the capacity to market new goods and services with sufficient access to the required third-party patent rights. Companies that intend to leverage 5G

technology to enhance their offerings and operational efficiency must consider the potential impact of constantly growing collections of pertinent patents on their operational viability (Deloitte, 2021).

Investigating 5G patents is essential owing to their profound technological advancements, economic implications, and strategic significance. This field offers insights into the latest innovations and future trends as companies invest heavily in 5G, spurring a competitive race for patent superiority. Patents are pivotal in standard-setting processes and influence global competition. This multidisciplinary research area encompasses electrical engineering, computer science, and telecommunications and provides valuable perspectives across technology, economics, law, and policy.

Analyzing 5G patents reveals broader innovation trends in hardware, software, and applications and informs legal and policy discussions on intellectual property rights, licensing, and the balance between innovation and competition. Identifying emerging core technologies through patent analysis offers foresight into future technological advancements, which are particularly pertinent for 5G, given the rapid development and integration of new technologies. Patent analysis helps pinpoint which innovations are likely to become foundational in the near future (Noh et al., 2016).

Examining 5G patents provides a comprehensive understanding of the technological, economic, legal, and geopolitical elements shaping the future of global communication. The uniqueness of studying 5G patents lies in grasping cross-country knowledge exchange and innovation trends and offering insights into the collaborative and competitive nature of modern technology development. It allows researchers and stakeholders to better navigate the complex and evolving 5G landscape. Analyzing patent data reveals how various countries contribute to and benefit from 5G innovations, aiding in the understanding of the global distribution of technological progress and the interaction between national innovation systems (Xuan et al., 2023).

Innovative approaches, such as the integrated bibliometric-textmetric approach, can be employed to study 5G patents. This method combines data and text analysis to identify emerging trends and core technologies more effectively, providing fresh insights into the evolution of 5G (Mendonça et al., 2022). This research adopts a method comparable to the integrated bibliometric-textmetric approach, providing a comprehensive and balanced insight into the influence and substance of patents. Additionally, this method is particularly effective for reviewing patent literature as it merges the quantitative evaluation of patent citations, trends, and collaborations with the qualitative examination of patent document text. It facilitates the identification of various patents and the comprehension of the technical content, innovations, and themes they entail.

This study attempts to comprehensively analyze the 5G patent landscape by simultaneously examining technological, scientific, and financial aspects. This analysis

can provide valuable insights for policymakers, industry stakeholders, and researchers to guide future developments and investment strategies in 5G technology. Furthermore, it may reveal emerging subfields within 5G technology and highlight areas of intense competition or collaboration among patent holders. Some key points regarding the novelty of this approach are as follows:

1. **Holistic perspective:** This study takes a more holistic and diversified approach by covering the technological, scientific, and financial aspects of 5G patents simultaneously rather than aiming at just one dimension.
2. **Use of advanced patent analysis software:** The analysis utilizes Questel's Orbit Insight patent research software, which allows for a thorough and multi-faceted examination of patent data.
3. **Comprehensive search query:** This study combined three search queries to achieve more relevant, accurate, and meaningful results in identifying 5G-related patents.
4. **Multi-dimensional analysis:** Beyond patent counts, this study examines various aspects, such as technological concepts, application areas, investment dynamics, innovation cycles, collaboration networks, and geographic distribution of patents.
5. **Integration of scientific literature:** The analysis incorporates scientific publications related to 5G, providing insights into research trends, academic contributions, and patent data.
6. **Global perspective:** This study adopts a worldwide view of 5G patents, avoiding concentrating on any single country or region.
7. **Inclusion of startups:** This analysis considers the role of startups in the 5G ecosystem, not just established companies.
8. **Forward-looking insights:** This study aims to provide insights that can help stakeholders navigate the rapidly evolving 5G landscape and inform future research directions.

By combining these elements, this study seeks to provide a unique and comprehensive overview of the 5G patent landscape that goes beyond traditional patent analysis approaches.

This investigation specifically aims to examine 5G patent ownership and distribution among prominent international establishments and its implications for market competition and technological advancement. Moreover, this holistic analysis can help identify emerging trends, potential collaborations, and areas of untapped opportunities within the 5G ecosystem.

The examination of 5G patents offers important insights into the overall environment and technological developments in the telecom industry. Furthermore, the analysis of 5G patents can provide valuable insights into licensing and litigation strategies, which in turn can shape the future of 5G patents and their ability to spur innovation in the relevant sectors.

This study seeks to divulge its own patent analysis by taking a more holistic and diversified approach to analyzing the 5G patent landscape, covering technological, scientific, and financial aspects. Zhang et al. (2021) emphasize that such studies should optimize patent search terms, gather patents from major worldwide patent databases, eliminate duplicate patents, and locate trustworthy patent data to improve the research's enterprise and academic values.

Based on this foundation, the subsequent analysis delves into the intricate landscape of 5G patents, offering a comprehensive examination of their technological, economic, and strategic implications. This exploration is crucial for understanding the current state and future trajectory of 5G innovation. By scrutinizing patent data, we gain valuable insights into the key players, emerging trends, and potential challenges in the 5G ecosystem. The analysis will furnish observations of how patent portfolios shape competitive dynamics, influence standardization processes, and drive technological advancements. Furthermore, it will provide a nuanced perspective on the global distribution of 5G innovation, highlighting the interplay between different countries and organizations. This in-depth examination of 5G patents contributes to academic discourse and offers practical implications for policymakers, industry leaders, and researchers navigating the complex and rapidly evolving 5G landscape. To fully appreciate the significance of this patent analysis, it is important to first understand the fundamental concepts and rapid development of 5G technology.

BACKGROUND

An Outline of 5G

The rapid progress in cellular technology has resulted in a considerable rise in the global adoption of 5G networks. This pattern reflects the growing need for faster and more dependable mobile connectivity. By the end of 2023, there were 1.5 billion 5G smartphone subscriptions globally; by the conclusion of this year, the subscriptions will soar to over two billion (Richter, 2024). The impressive surge in 5G adoption is due to swift advancements in telecommunications technology, the broader availability of 5G infrastructure, and the rising demand for fast and reliable mobile internet services. As additional countries and regions expand their 5G networks, the number of subscriptions is expected to grow exponentially. This number is expected to surpass five billion by 2029, signifying a global and nearly omnipresent adoption of 5G technology. This proliferation of 5G will transform personal and business communications and pave the way for innovations in various sectors. Thenceforward, the beginning of the 6G era is anticipated, and the next generation of cellular networks will gradually supersede 5G. Figure 1 depicts the 3G, 4G, and 5G adoption trends from 2012 until 2029. It particularly shows the rapid growth and adoption of 5G, depicting its growing prominence in mobile communication technology over time. It offers a distinct projection of 5G's expected widespread availability and near-ubiquitous

presence by the end of the decade. As 5G networks continue to expand globally, they are expected to revolutionize industries, drive innovation, and significantly impact the technological landscape.

5G technology is set to revolutionize the way we interact with the digital world. Despite its benefits, the journey toward widespread 5G adoption has been smooth. Although 5G is the preferred option for connecting mobile phones and other devices worldwide, it is still met with skepticism in business. There have been some hiccups in the rollout of 5G, and businesses have not taken off this technology. Infrastructure challenges, high deployment costs, and security concerns have contributed to many enterprises' cautious approach. Nevertheless, industry participants predict that this year's commercial rollouts of 5G or 5G-Advanced networks will change this situation (Yu, 2024). As the initial release of 5.5G standards (3GPP Release 18) has frozen in the first half of 2024 and related technologies have been thoroughly established, the 5.5G industry is anticipated to expand rapidly (The Star, 2023). This anticipated growth is expected to address many of the existing concerns, provide more reliable and efficient solutions for businesses, and pave the way for a new era of digital transformation.

While 5G technology has faced some obstacles in its initial rollout, including infrastructure challenges, high costs, and security concerns, the landscape is poised for significant changes. The cautious approach adopted by businesses thus far may soon give way to increased adoption and implementation. The evolving 5G ecosystem is expected to address current limitations and unlock new possibilities for digital transformation across various industries.

As industries and consumers worldwide anticipate full-scale deployment of 5G networks, it is essential to understand the foundational principles that underpin this transformative technology. The classification of 5G applications is indicated by the 3rd Generation Partnership Project (3GPP)-approved 5G triangle. Figure 2 shows the three primary benefits of 5G deployment, namely Ultra Reliable Low Latency Communication (uRLLC), Massive Machine Type Communication (mMTC), and Enhanced Mobile Broadband (eMBB). This structure catalyzes 5G's novel applications, yielding multiple advantages of 5G over its predecessor generations.

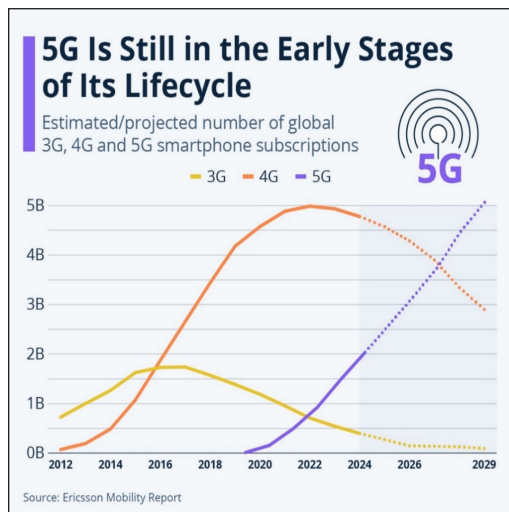


Figure 1. Forecast of 5G subscriptions worldwide (Richter, 2024)

According to Miller and Cavazos (2022), Enhanced Mobile Broadband (eMBB) refers to improved peak and average data speeds, capacity, and coverage of 5G compared to traditional mobile broadband. eMBB is a 5G specification that allows for a maximum download speed of 20 gigabits per second (Gbps) and a maximum upload speed of 10 Gbps. Massive Machine Type Communication (mMTC) refers to the capability of 5G networks to enable the Internet of Things (IoT) to use cases involving many linked devices and sensors, numbering in billions.

This case encompasses devices with low data rates and bandwidth transmitting only sporadically. These devices also require a long battery life. In addition, it includes devices that have very high bandwidths and data rates. Ultra-Reliable Low Latency Communication (uRLLC) refers to a type of extremely dependable communication with minimal delays. uRLLC is specifically designed for applications that require highly reliable real-time communications. Autonomous vehicles, smart grids, industrial Internet, infrastructure security, and intelligent transportation systems are a few examples. By introducing these concepts, the stage is set for a precis of how these technologies shape the future of connectivity and enable a wide range of innovative applications across various industries.

5G technology differs from its predecessors in a number of important features and advantages, as shown in Figure 3. The 11 features highlighted in Figure 3 are the translation of the 5G triangle into its corresponding applicable domains. By understanding these practical applications, we can better appreciate the transformative potential of 5G technology and its role in influencing the course of connectivity, innovation, and economic development. All these characteristics culminate in a digital ecosystem that is more sophisticated, efficient, and interconnected. Although 5G technology is still in its infancy, it has the potential to revolutionize both our personal and professional lives by opening a world of inventive applications that were previously unattainable with earlier iterations of mobile networks. Building upon these key features and applications, the impact of 5G technology extends far beyond faster internet speeds for mobile devices. As 5G networks continue to evolve and mature, they are likely to unlock new possibilities for innovation and economic growth, paving the way for a more interconnected, technologically advanced era.

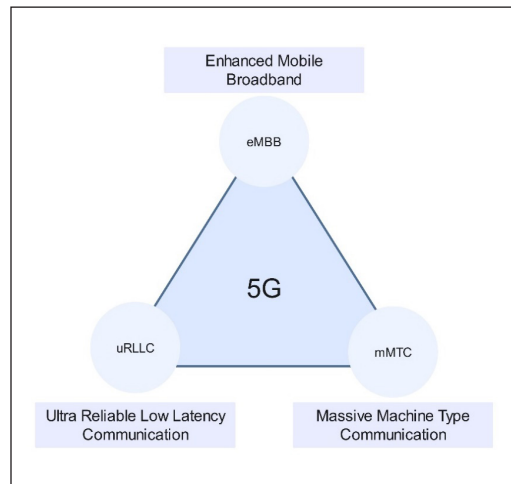


Figure 2. The trilateral classification of 5G applications. Own work

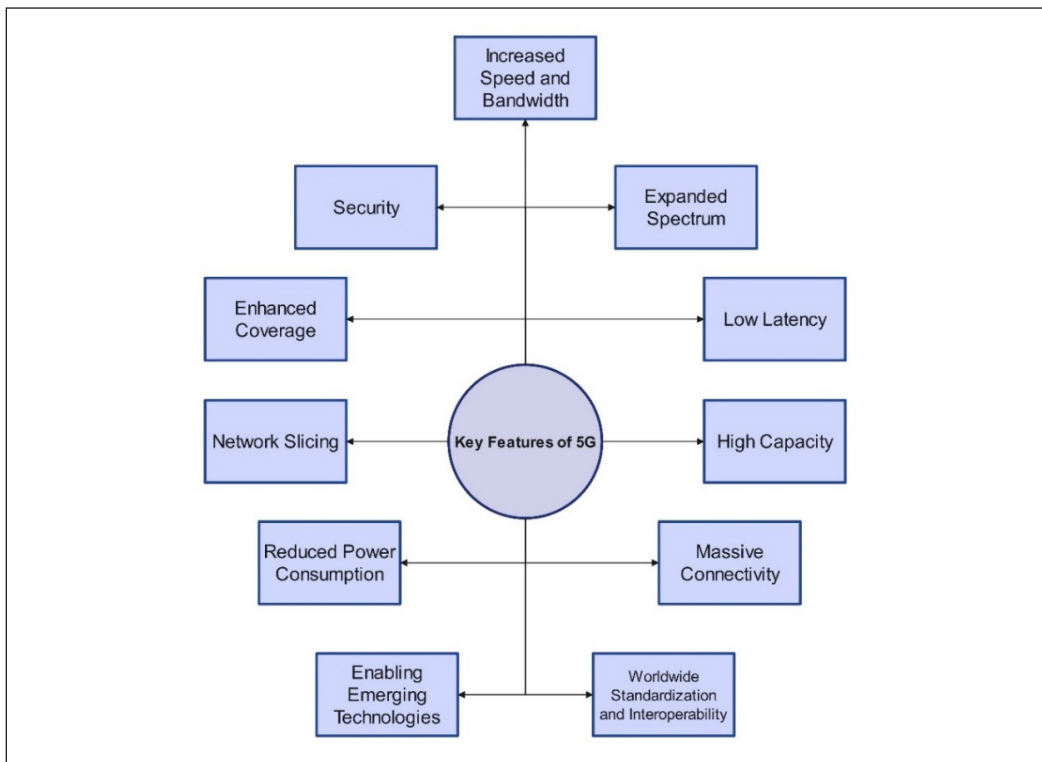


Figure 3. Key features of 5G technology. Own work

An Outline of 5G Patents

The rapid evolution of 5G technology has revolutionized the telecommunications industry, ushering in a new era of connectivity and innovation. As companies strive to establish their dominance in this competitive landscape, the strategic importance of 5G patents has become increasingly apparent. To develop and implement new technologies, remain competitive, and maintain their market position, 5G patents are essential for businesses in the telecommunications industry. In addition to safeguarding intellectual property, these patents encourage innovation and open doors for industrial partnerships and collaborations. Through an analysis of the impact of 5G patents on telecommunications, this study attempts to shed light on the strategic significance of patents in this context. A crucial aspect of understanding the landscape of 5G patents is the concept of a patent family. A patent family refers to a compilation of published patent documents pertaining to the same invention or multiple inventions that share a common characteristic and were issued at different points within the same nation or in different nations or regions (<https://iamip.com/wiki/patent-family/>). Based on extant research on 5G patents, as of September 2021, the Chinese company Huawei holds the highest number of 5G technology patent families globally,

with ownership of more than 5600 patent families. Among the remaining owners of 5G patents, Qualcomm Incorporated, an American company, held the second-highest number of patent families, with a total of 4133 (Taylor, 2023). Table 1 is a list of global patent ownership acquired through the existing literature dating to 2021. The table, which lists the top 30 worldwide holders of 5G patents, reveals diverse international distribution. Chinese companies dominate, with nine entries, followed by six from the United States. Five companies represent Japan, whereas South Korea has four. Taiwan contributed three companies to this list. The remaining entries were one company each from Finland, Sweden, and Canada.

Understanding the intricate dynamics of patent families is essential for understanding the landscape of technological innovation, especially in rapidly evolving fields such as telecommunications. A patent family comprises an assembly of patent applications that pertain to technical content that is identical or comparable. Priority claims establish a connection between applications within the same family, signifying a common groundwork for inventive ideas and innovations (<https://www.epo.org/en/searching-for-patents/helpful-resources/first-time-here/patent-families>). The foundational understanding of patent families is crucial when considering the global distribution of 5G patents. Statista

(2023) indicates that as of February 2021, Huawei possessed the largest proportion of 5G patent families globally, with 15.39% of all 5G patent families. Qualcomm secured the second position with ownership of 11.24% of all patent families related to 5G, as

Table 1
5G patents held by leading companies worldwide as of 2021 (Taylor, 2023)

Ownership of 5G patents worldwide		
Ranking	Company	Country
1	Huawei	China
2	Qualcomm	United States
3	Samsung Electronics	South Korea
4	ZTE	China
5	LG Electronics	South Korea
6	Nokia	Finland
7	CATT Datang Mobile	China
8	Ericsson	Sweden
9	Oppo	China
10	Sharp	Japan
11	Vivo	China
12	NTT Docomo	Japan
13	Xiaomi	China
14	Apple	United States
15	Intel	United States
16	InterDigital	United States
17	Lenovo	China
18	FG Innovation	China
19	MediaTek	Taiwan
20	NEC	Japan
21	ETRI	South Korea
22	Shanghai Langbo	China
23	Motorola Mobility	United States
24	Panasonic	Japan
25	BlackBerry (BlackBerry Limited)	Canada
26	Fujitsu	Japan
27	ASUSTeK	Taiwan
28	KT	South Korea
29	Google (Alphabet Inc.)	United States
30	HTC	Taiwan

Note. Data as of 2021

shown in Figure 4. This figure represents the distribution of patent family ownership among the 21 companies, shown as a percentage of their respective ownership types. Huawei dominates the 5G patent landscape, accounting for 15.39% of all patent families and demonstrating significant investment in research and development. This portfolio provides Huawei with a strategic advantage in licensing and cross-licensing agreements. Qualcomm, holding 11.24%, follows closely behind, indicating a competitive innovation ecosystem. The distribution of patents among companies can influence the development, implementation, and standardization of 5G networks worldwide, potentially impacting consumer devices, industrial applications, and smart city infrastructure. The implications of this patent ownership structure make it crucial to consider how it affects intellectual property schemes, market competition, global standardization efforts, and the potential for collaborative innovation.

In the field of advanced telecommunications, analyzing the financial investments of major corporations offers crucial insights into the industry’s technological capabilities and market preparedness. Technological strength and market maturity can be effectively assessed by examining the expenditure levels of the primary players in the industry.

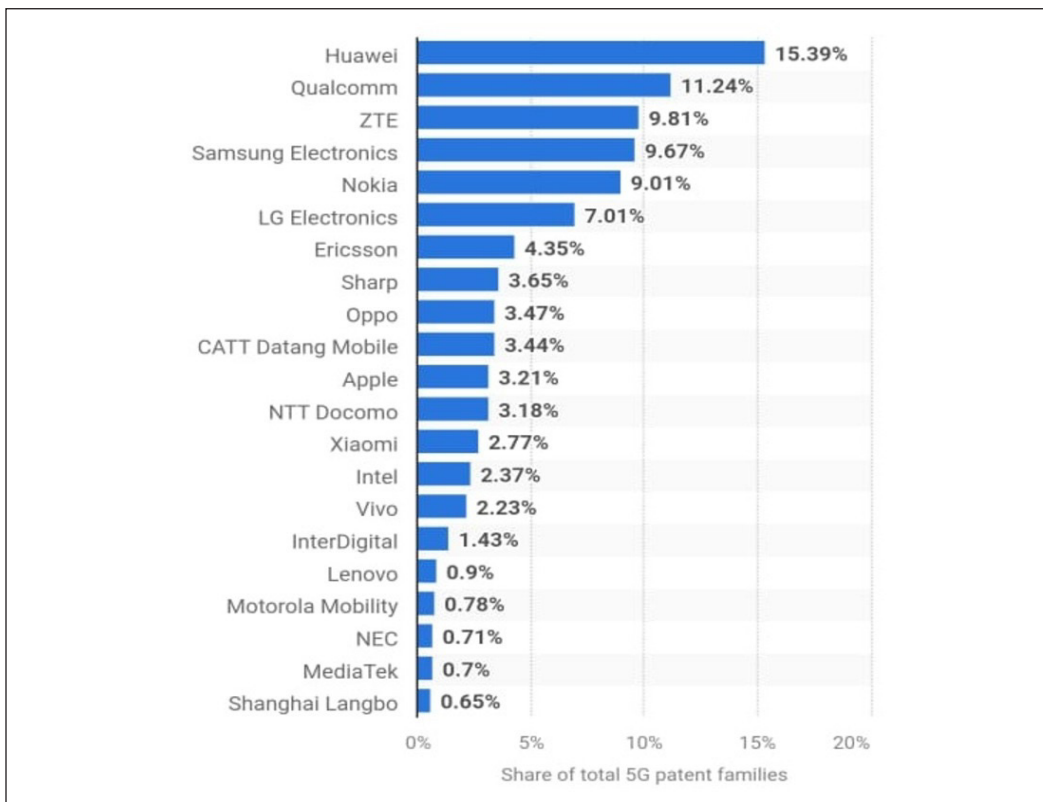


Figure 4. Percentage of 5G patent family ownership by leading companies in 2021 (Statista, 2023)

Generally, a higher volume of spending indicates greater market demand. The 5G IP market is a substantial market, with an estimated value of approximately \$3 billion. As shown in Figure 5, this significant market size underscores its substantial impact and potential within the industry. This market attracts established and emerging companies owing to its significant economic impact and potential for further growth. Significant investments reflect the growing demand for innovative solutions, indicating a market's readiness for technological development.

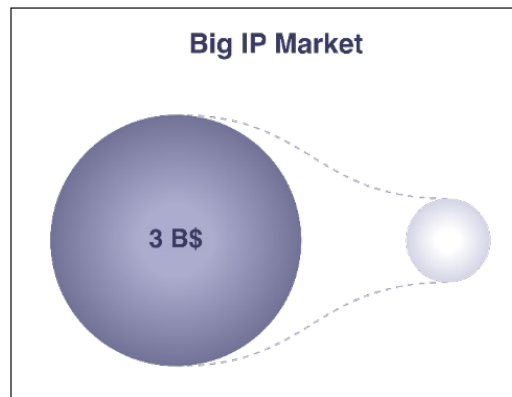


Figure 5. 5G Intellectual Property market value
 Note. The figure is retrieved from Orbit Insight

The substantial market size of the 5G IP industry implies several key points:

1. Significant industry growth potential: The large market value suggests considerable room for expansion and innovation in 5G technology.
2. High level of competition: A market of this size is likely to attract numerous players, leading to increased competition and potentially faster technological advancement.
3. Substantial investment opportunities: A sizeable market indicates attractive prospects for investors and venture capitalists interested in the 5G sector.
4. Increased research and development efforts: Companies will likely allocate significant resources to R&D to maintain their competitive edge in this lucrative market.
5. Potential economic impact: The large market size suggests that 5G technology could have far-reaching effects on various sectors of the economy, potentially driving job creation and economic growth.
6. Consumer benefits: As the market matures and competition intensifies, consumers may benefit from improved 5G services and lower costs over time.
7. Geopolitical effects: Given the strategic importance of 5G technology, a substantial market size may lead to increased international competition and potential government policy interventions.

Considering the strategic importance and sizable economic value of 5G technology, a methodical approach to examining patents is crucial for understanding the present landscape of 5G patents.

PATENT ANALYSIS STRATEGY

Patent analysis involves multiple stages, including gathering data, analyzing it to identify trends, and presenting findings (<https://www.wipo.int/web/patent-analytics>). This study performed a thorough data analysis by utilizing patent research software called Orbit

Insight by Questel (<https://insight.orbit.com/>). The Software Suite is a streamlined collection of specialized solutions that can address the specific stages of the innovation process from start to finish. The Insight portfolio connects the entire innovation ecosystem. It continuously monitors and analyzes over 500 data sources, totaling over 125 million pieces of information. Insight’s AI engine requires only a search term or a list of relevant industry organizations to generate a comprehensive overview of the technology field. Patent activity, academic research, mergers and acquisitions (M&A) activity, and a variety of other indicators are used to assess maturity, the stage of the innovation cycle, the most active players, and opinion leaders. This solution is completely automated and constantly updated. A screenshot of Orbit Insight’s homepage is shown in Figure 6, which displays where the search for patents begins and what functionalities are available. AI-driven analysis extends beyond raw data collection, offering valuable insights into emerging trends and potential disruptors within the industry. It also allows organizations to make informed decisions about their innovative strategies and resource allocation. The automated nature of the platform ensures that users have access to the most up-to-date information, enabling them to make informed decisions and stay ahead of the competition.

The patent search query for this study consisted of a combination of three different sets of queries to achieve the most relevant, accurate, and meaningful results. The queries were as follows:

- 5G
- 5G Network **OR** 5G Communication, 5G Cellular Network, 5G Mobile Network, Radio Access Network, 3GPP, Mobile Broadband

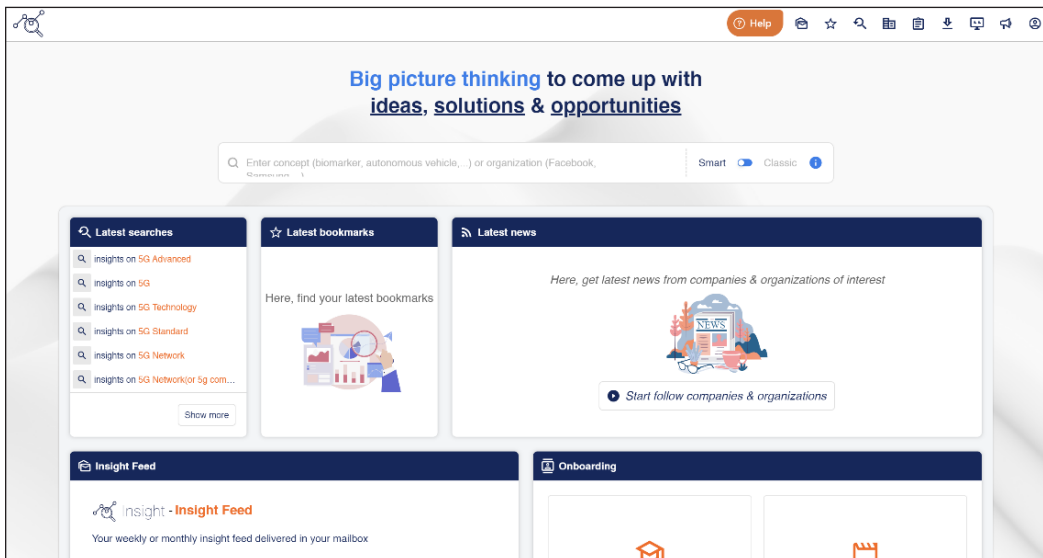


Figure 6. Orbit Insight homepage (<https://insight.orbit.com/>)

- **5G AND 5G Network OR 5G Communication, 5G Cellular Network, 5G Mobile Network, Radio Access Network, 3GPP, Mobile Broadband**

The data range was from the last 10 years, and the location of the data source was worldwide. The aggregation of all three of the above queries served as the basis for performing this study. The selected search terms were formulated to cover a wide range of 5G-related advancements, spanning from technological to financial aspects. However, this broad approach might incorporate patents that are nonessential to the core 5G concepts. To address this potential limitation, we sought to mitigate this impact by meticulously examining and classifying the retrieved patents.

Having established the patent analysis procedure, including the comprehensive search query and data parameters, the attention of this study turns to the patent landscaping phase. This crucial step will provide a visual representation of the 5G technology landscape, offering insights into key players, technological trends, and areas of innovation concentration. Analyzing the patents identified through carefully constructed queries aims to uncover patterns and relationships that will inform strategic decision-making in the rapidly evolving 5G domain. The following patent landscaping analysis will leverage the data collected to present a clear and actionable overview of the current state and future directions of 5G technology development.

PATENT LANDSCAPING

Technology Landscape

While standing on the cusp of a new technological frontier, it is imperative to examine the key indicators shaping this potent field’s landscape. This analysis provides insights into the current state of wireless technology and offers a glimpse into its future trajectory. Patents serve as a window into cutting-edge developments and widely adopted technologies driving the industry forward. They are critical indicators of prevailing trends and widely adopted technologies in technological innovation. By examining the key terms frequently found in patents within the studied field, it is possible to identify the most widely adopted technologies. This study’s analysis of 5G patents reveals that the predominant concentration is on wireless communication, base stations, and user equipment, as shown in Figure 7. This figure shows the most significant 5G technical concepts through a word cloud consisting of 10 concentration areas. This suggests that these areas are at the forefront of innovation in

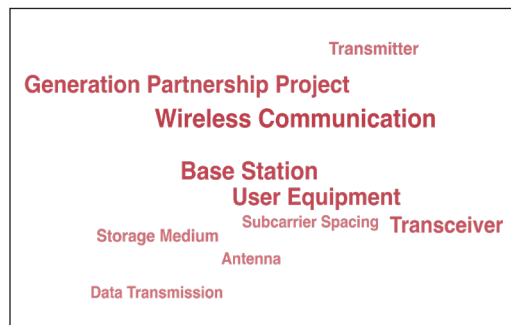


Figure 7. 5G technical concepts
 Note. The figure is retrieved from Orbit Insight

the telecommunications sector. The emphasis on these specific components indicates that industry efforts are largely directed toward improving the network infrastructure and enhancing the capabilities of end-user devices. Such findings can be instrumental for industry stakeholders, including researchers, investors, and policymakers, as they make decisions about resource allocation, research priorities, and strategic planning in the rapidly evolving landscape of wireless technology.

In the rapidly evolving world of technology, understanding primary technological areas is crucial for steering innovation and identifying potential applications for new inventions. Principal technological areas serve as excellent resources for identifying potential applications for new inventions. By inspecting the domains in which other patents within the same field are classified, it becomes possible to gain valuable insights into the intended applications and purposes envisioned by both examiners and applicants. The primary utilization areas for 5G technology are telecommunications, digital communication, and computer technology, as illustrated in Figure 8. All six leading utilization areas in this figure reflect the transformative nature of 5G. These areas highlight the broad implications of 5G, extending beyond traditional mobile communications to encompass a wide range of applications in various sectors. For instance, integrating 5G with computer technology suggests its potential to revolutionize edge computing, Internet of Things (IoT) devices, and artificial intelligence applications. Similarly, digital communication points to 5G’s role in enabling more sophisticated

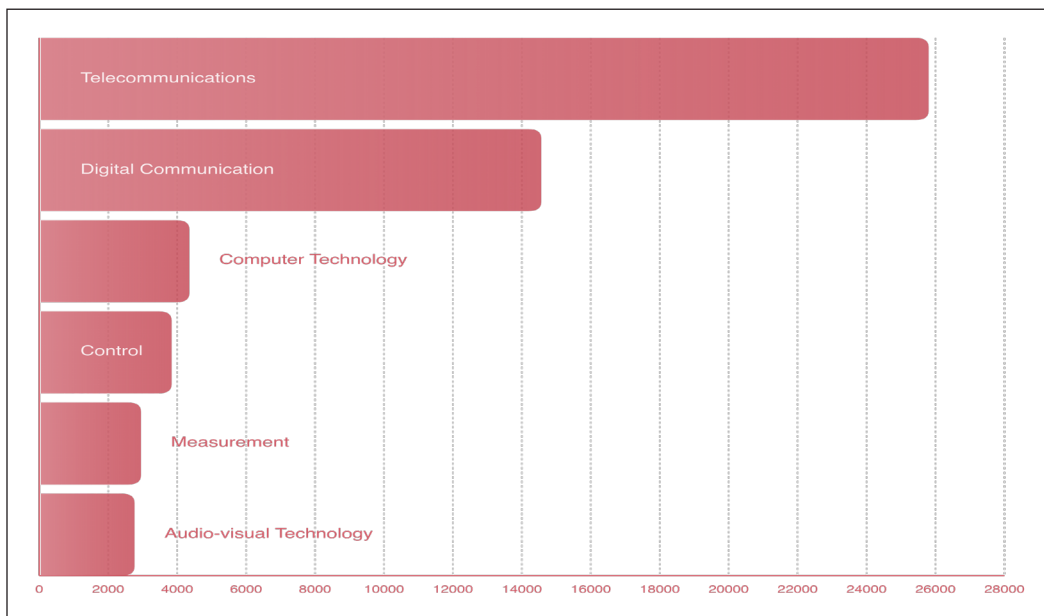


Figure 8. 5G main applications

Note. The figure is retrieved from Orbit Insight

and efficient data transfer methods, which could have far-reaching effects on industries ranging from healthcare to smart cities and autonomous vehicles.

When industries rapidly evolve, and new technologies emerge, companies and researchers constantly seek ways to establish their presence and secure their position in the market. It leads to an increased accent on intellectual property rights and the strategic use of various tools to protect and leverage them. Strategic publishing, patents, and standard contributions are critical for technological development because they provide fresh scientific knowledge, foster the growth of ideas, and offer companies a competitive edge (Buggenhagen & Blind, 2022). 5G patents expose significant patterns in patent applications, noteworthy industry participants, and implications for technology standards and market competition. Understanding the 5G patent landscape is essential for businesses to formulate successful strategies in this rapidly evolving environment.

The temporal distribution of patent filings and institutional investments provides a foundation for understanding the strategic positioning of key players in the 5G ecosystem. It will highlight the significant growth in patent investments and institutional funding, offering a quantitative perspective on the industry’s expansion and prospects.

There has been an increase in 5G patent and institutional investments since the rollout of technology at the start of the decade. Patent investments peaked during the years 2020 and 2021, while institutional investments reached their apex in 2022. Both types of investments are experiencing an upward trend and are likely to continue until the latter stages of this decade. The potential of the industry is further illustrated in Figure 9. This figure displays a 12-year period of 5G patent investment, with a notable increase of 41.42% happening from

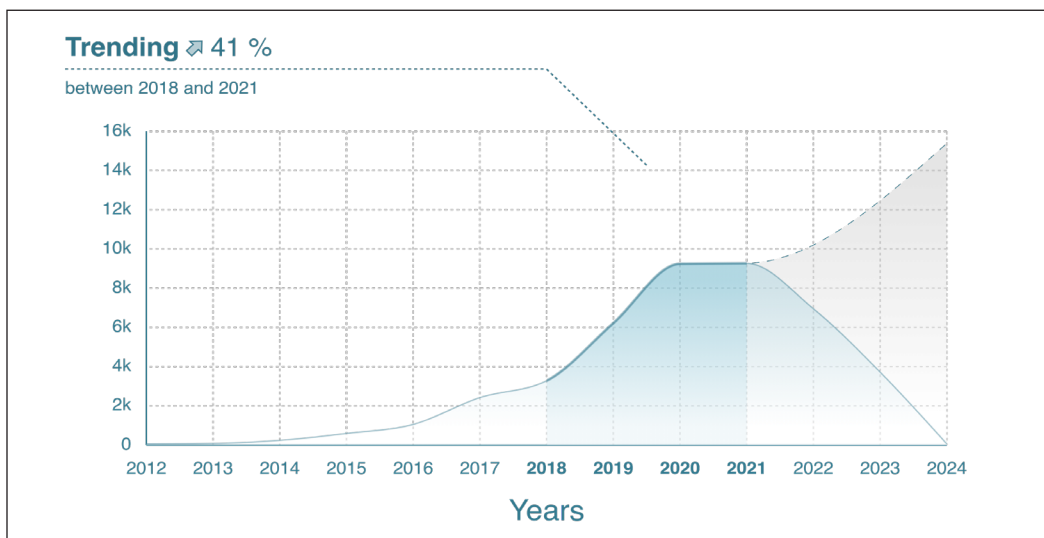


Figure 9. 5G patent investment dynamics

Note. The figure is retrieved from Orbit Insight

2018 to 2021. This substantial growth in patent filings reflects the competitive landscape of 5G development and hints at the diverse range of technologies and solutions being explored to fully leverage the capabilities of 5G networks.

In an era where technological advancements drive global progress, assessing whether technology is at the forefront of government or public institutional investment can be done by examining the funding of institutional projects. Some technologies are deemed significant at a national or international level due to their potential impacts on economic growth, national security, or societal advancement. In the case of 5G, a comparison of institutional investments in this technology between 2019 and 2022 shows that it received moderate funding of \$33.95 million, with an investment growth rate of 167.91% during this five-year interval, as shown in Figure 10. While countries and organizations continue to recognize the transformative power of 5G, it is likely that investments will continue to grow, centering on infrastructure development, security enhancements, and the exploration of new applications that can leverage this advanced communication technology.

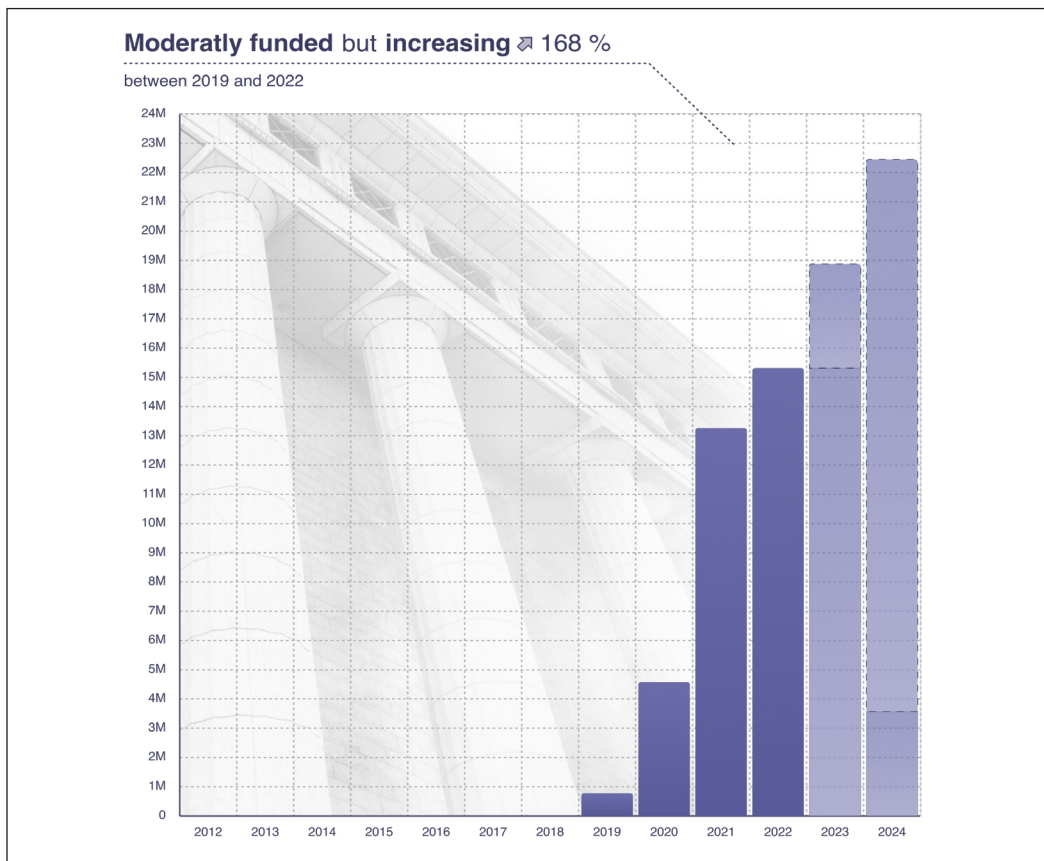


Figure 10. 5G institutional investments
 Note. The figure is retrieved from Orbit Insight

Understanding the nuances of the innovation process is crucial for identifying challenges, efficiently allocating resources, and fostering a culture of continuous improvement. It helps individuals and organizations navigate obstacles, find creative solutions, and stay ahead of competition in a rapidly changing world. Excelling the complexities of the innovation process can lead to more successful outcomes, driving growth and progress in various fields. The innovation process for this technology is primarily gradual, with an originality rate of 70.7%. When assessing the distribution of portfolios, it becomes evident that the pace of the 5G innovation cycle is decelerating. This slowdown can be attributed to various factors, including market saturation, the complexity of further advancements, and potential regulatory hurdles. Figure 11 displays the current state of 5G technology, suggesting that while innovation continues, it is occurring at a more measured rate compared to prior periods of rapid development. This shift suggests that technology may enter a phase of refinement and optimization rather than radical transformation. As the industry navigates this evolving landscape, emphasis may shift towards enhancing efficiency, addressing specific use cases, and overcoming implementation challenges rather than pursuing dramatic leaps in capability. This measured approach could lead to more stable and reliable 5G solutions, albeit at the cost of rapid progress observed in technology’s infancy.

Examining the intellectual property players in the 5G landscape is crucial based on this understanding of the innovation process. Maintaining a competitive edge in the fast-paced world of modern technology necessitates a thorough understanding of major players and their strategic actions. Analyzing the key participants in the field provides valuable insights into the innovation capabilities of the most active competitors and their efforts to protect their legal rights. Even if these competitors do not currently sell products in the relevant market, they may still pose a significant potential challenge. Their innovative prowess and proactive legal strategies suggest that they are preparing to enter new markets or disrupt existing ones. With a portfolio of 6136 inventions, Samsung Electronics is the dominant player in this field. This substantial number of inventions demonstrates Samsung’s R&D capability and positions the company as a leader in shaping industry trends and standards. The sheer volume of inventions suggests diverse technological applications spanning various

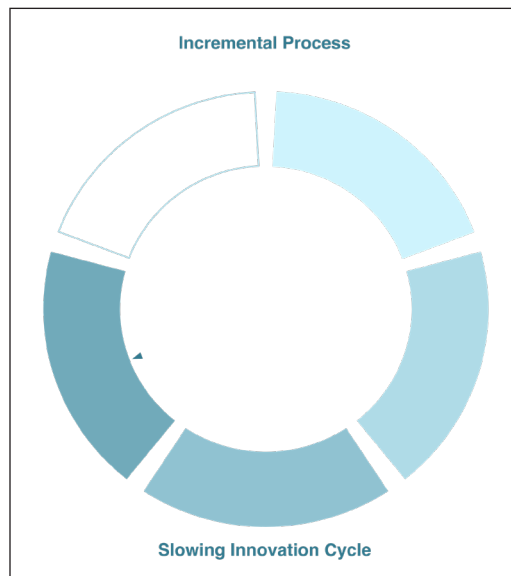


Figure 11. 5G innovation cycle
 Note. The figure is retrieved from Orbit Insight

electronics industry sectors. In conjunction with each other, four key companies, Huawei, LG Electronics, Qualcomm, and Ericsson, along with Samsung, comprise 27.16% of the Top 100 5G IP players, as shown in Figure 12. This concentration of innovative power among a relatively small group of companies highlights the industry’s competitive nature and the importance of maintaining a strong patent portfolio. It also suggests that these key players are likely to have a considerable influence on future technological development and market dynamics within their respective sectors.

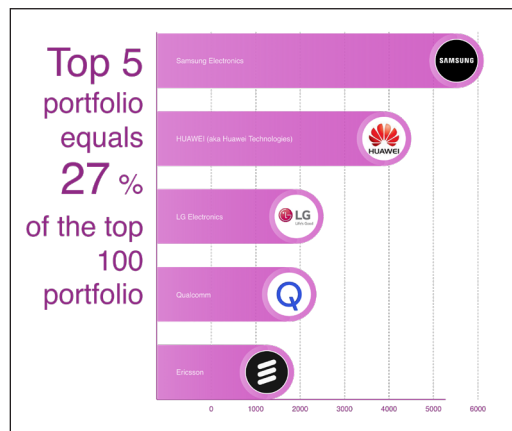


Figure 12. 5G IP players

Note. The figure is retrieved from Orbit Insight

While individual companies play significant roles, the 5G ecosystem thrives on collaboration. The importance of collaboration cannot be overstated in an increasingly interconnected world of R&D. Synergy between various entities, ranging from academic institutions to private companies and research labs, drives innovation and progress. The worldwide 5G collaboration network is heavily mutualized between academics (222) and companies (228), resulting in a total of 450 linkages. This collaboration extends beyond just academics and companies, with additional clusters (4), networks (23), and institutions and R&D labs (23), all of which play a vital part in the global network. There are 50 connections among these entities, demonstrating the deep and diversified level of collaboration within the global collaborative landscape, as shown in Figure 13. This figure reveals a multi-faceted collaborative landscape in which astuteness flows through various channels. This intricate web of relationships fosters innovation and ensures that advancements in 5G technology are approached from multiple perspectives, potentially leading to more comprehensive and widely applicable solutions. The global nature of this collaboration network also suggests that 5G development is an international effort, with expertise and resources being shared across borders to accelerate progress in this critical technological domain.

After examining the collaboration network, it is important to identify specific entities driving 5G innovation within this network. By scrutinizing this network and different interactions within the 5G ecosystem, companies, researchers, and startups that proactively contribute to 5G initiatives can be identified. This comprehensive analysis helps pinpoint the key players who are making progress in this cutting-edge field.

One group of major players are organizations that play a critical role in fostering innovation, advancing the development and uptake of new technologies, and revolutionizing markets and society. They interact with other organizations to share knowledge, coordinate

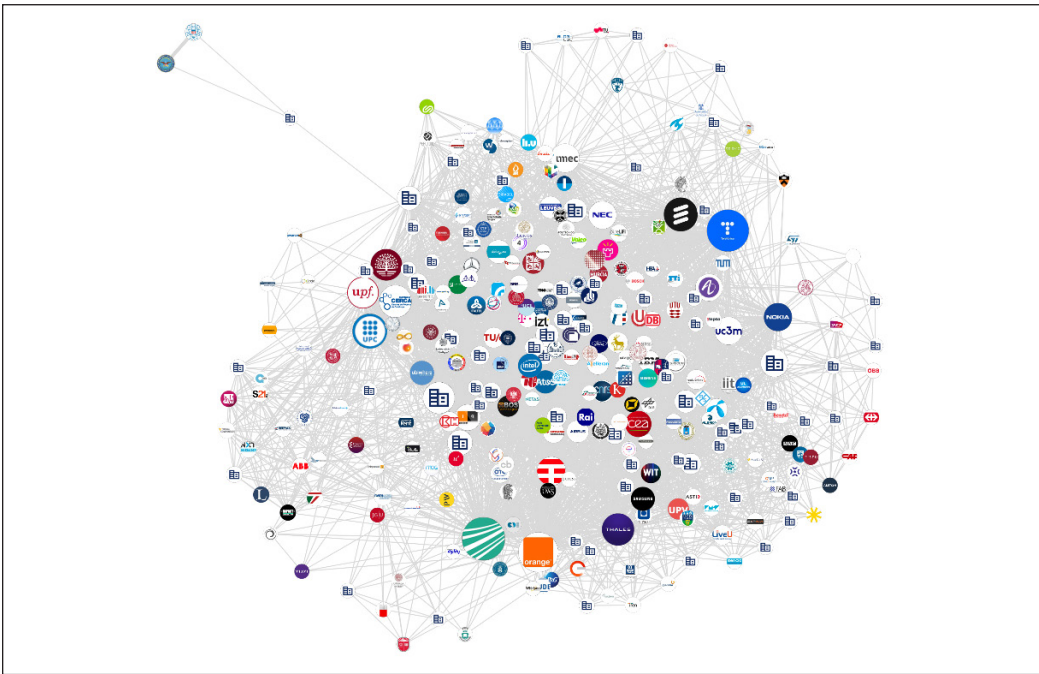


Figure 13. The 5G collaboration network

Note. The figure is retrieved from Orbit Insight

activities and offer the infrastructure, resources, and expertise needed to develop and test innovative technologies. Organizations also set best practices and standards, offering advice on matters such as data privacy, cybersecurity, and environmental impact to guarantee the ethical, sustainable, and safe use of emerging technology. Figure 14 displays the names, types, and countries of 18 upper-echelon organizations involved in publishing, patenting, and standardizing 5G, which suggests that patent-heavy businesses maximize their influence on 5G technology development. Organizations that invest in 5G research and development are crucial for economic growth and competitiveness in the global technology landscape. Their investments create high-skilled job opportunities, stimulate technological entrepreneurship, and attract foreign investments. The innovations they generate can revolutionize manufacturing, healthcare, transportation, and entertainment sectors, unlocking new business models and revenue streams. They also shape the public policy and regulatory frameworks around 5G technology, advocating policies that support innovation while addressing societal concerns. This proactive approach creates a balanced regulatory environment that fosters technological progress while safeguarding the public interest. As the 5G landscape evolves, these organizations will continue to drive innovation, set standards, and shape the future of telecommunications, paving the way for the next generation of wireless communication systems.





































Organizations			View all: 2473 organizations	
<input type="checkbox"/>	NAME	CLASSIFICATION	TYPE	COUNTRY
<input type="checkbox"/>	 Samsung Electronics		Company	 South K..
<input type="checkbox"/>	 Ericsson		Company	 Sweden
<input type="checkbox"/>	 U.S. Department of Defense		National/Govern...	 United S..
<input type="checkbox"/>	 Qualcomm		Company	 United S..
<input type="checkbox"/>	 Intel		Company	 United S..
<input type="checkbox"/>	 Deutsche Telekom AG		Company	 Germany
<input type="checkbox"/>	 Fraunhofer-Gesellschaft		National/Govern...	 Germany
<input type="checkbox"/>	 Telefonica		Company	 Spain
<input type="checkbox"/>	 Orange SA		Company	 France
<input type="checkbox"/>	 U.S. Department of Health & Human...		National/Govern...	 United S..
<input type="checkbox"/>	 Polytechnic University of Catalonia		University	 Spain
<input type="checkbox"/>	 United States Coast Guard		Government	 United S..
<input type="checkbox"/>	 National Science Foundation		Government	 United S..
<input type="checkbox"/>	 Huawei Investment & Holding Co., Ltd		Company	 China
<input type="checkbox"/>	 Thales Group		Company	 France
<input type="checkbox"/>	 NEC Corporation		Company	 Japan
<input type="checkbox"/>	 imec		Research Institute	 Belgium
<input type="checkbox"/>	 Apple		Company	 United S..

Figure 14. Organizations participating in the 5G locale

Note. The figure is retrieved from Orbit Insight

Smaller and more agile companies play a crucial role in this landscape. They often bring innovation, flexibility, and niche expertise that larger corporations may struggle to provide. Startups are another significant entity, critical to the development of breakthrough technologies, and typically established by enterprising individuals who recognize market deficiencies and are motivated by a determination to address challenges or introduce new solutions. Startups are integral to the technological ecosystem, as they stimulate innovation, challenge limits, and contribute to the progress of technology, ultimately enhancing people’s lives in various ways. On the one hand, 5G technology allows companies to deliver faster and more dependable services to their clients, leading to enhanced customer happiness and greater brand loyalty. On the other hand, it also presents fresh prospects for companies to create inventive, previously unattainable products and services. The startups shown in Figure 15 are creating inventive and cost-effective 5G solutions that have the potential to enhance accessibility to 5G for users across various countries. This increased accessibility has the potential to bridge the digital divide and foster economic growth in

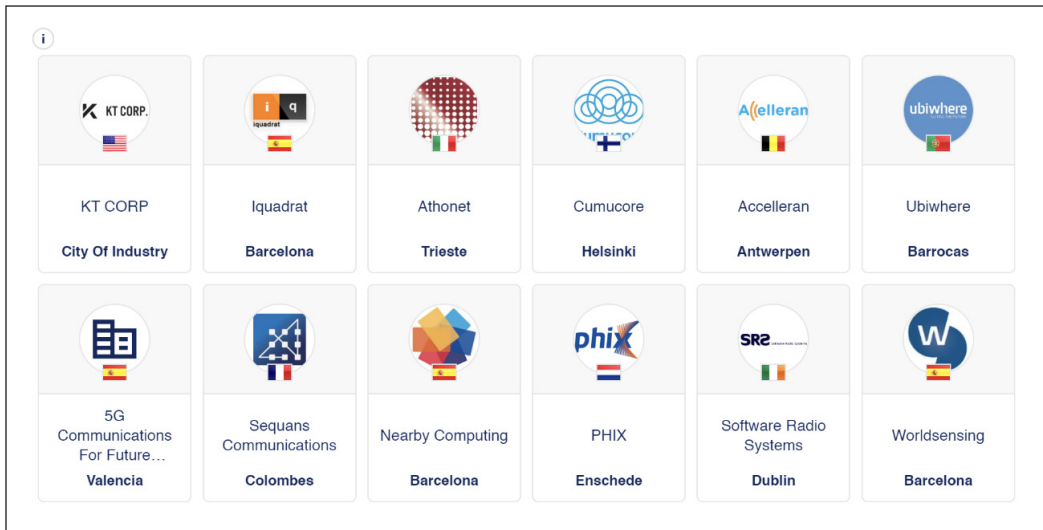


Figure 15. Startups participating in the 5G locale
 Note. The figure is retrieved from Orbit Insight

previously underserved regions. Moreover, competition and innovation driven by these startups contribute to the overall maturation of the 5G ecosystem, encouraging established players to adapt and improve their offerings. As a result, the entire technological landscape benefits from the fresh perspectives and disruptive ideas that startups bring to the table, ultimately accelerating the widespread adoption and utilization of 5G technology. Figure 15 lists the 12 startups in the foreground of 5G innovations.

Inventions

The activities of these key players and startups culminate in a rich landscape of intellectual property. The landscape of intellectual property in the realm of 5G technology is dynamic and evolving. Understanding the status of inventions is crucial to gauging the progress and competitiveness of various establishments in this domain. The following provides a comprehensive overview of the current state of 5G inventions, highlighting the legal status of these innovations: Running a search on the patent database yielded 105100 inventions. Out of all the inventions, 84.76% are still active, while just 463 have reached their expiration. The countries with the highest level of protection are China, the United States, and South Korea. The first-filing countries are China, the United States, and South Korea. As for the writing of this research paper, there have been 49,900 awarded innovations, 39,215 pending inventions, 11,937 lapsed inventions, and 3,585 revoked inventions. These numbers represent a broad ratio of 5G patents' legal status, indicating that the majority of 5G patents are either granted or pending, with less than 15% of the filings being lapsed or revoked. The statuses divided into granted, pending, lapsed, revoked, and expired are

visually represented in Figure 16. This overall distribution paints a picture of a thriving and competitive technological landscape where most of the statuses are being granted, and many are pending approval for upcoming purposes.

Geographic Protection

While the legal status of inventions provides one perspective, examining their geographic distribution offers another extent of insight. By examining the countries in which patent families are protected, as shown in Figure 17, it is possible to identify the main markets utilizing this technology. This figure includes the number of inventions split into protected patents and first filings by country and countries that have had the best acceleration in 5G patent filings. This analysis reveals regions where technology is thriving, absent, or declining. Unexploited regions will also become evident through this process. Most companies file their initial patent applications in the countries where they conduct their research and development. Studying these initial filings makes it easy to spot key countries. Therefore, ensuring robust patent protection in these critical regions is essential. By doing so, companies can safeguard their intellectual property, maintain a competitive edge, and capitalize on licensing opportunities in emerging markets. Additionally, these data can help identify potential gaps in the global 5G landscape, which may present new opportunities for market expansion.

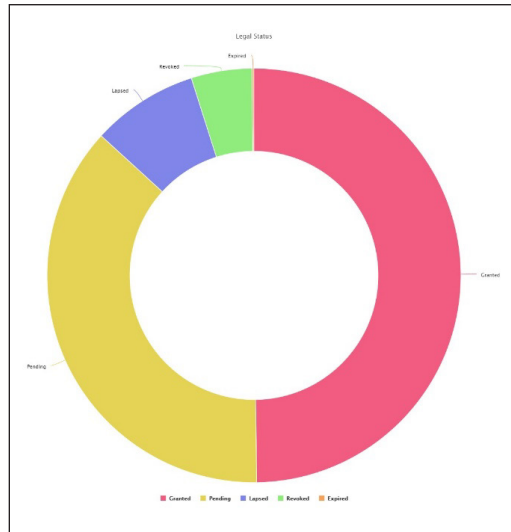


Figure 16. 5G inventions legal status
 Note. The figure is produced by inputting data into RapidMiner Studio

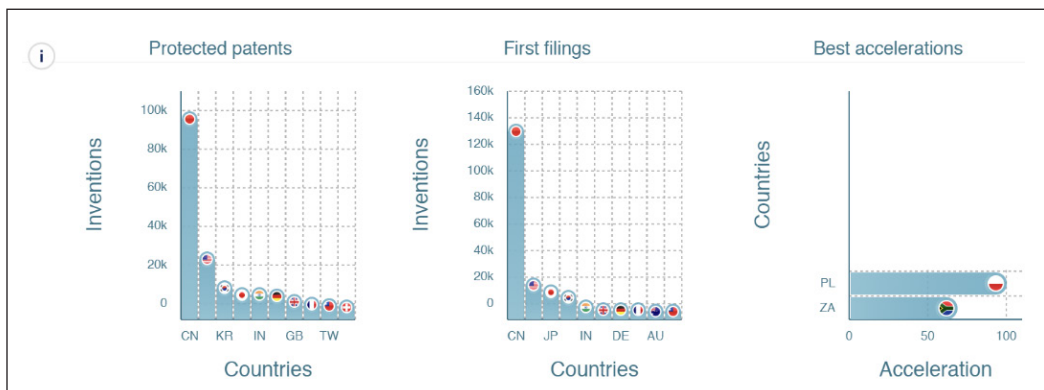


Figure 17. Geographic distribution of 5G patents filings
 Note. The figure is retrieved from Orbit Insight

SCIENTIFIC WORKS

Scientific research plays a vital role in advancing 5G technology, complementing the patent landscape. In view of scientific production (articles, theses, conferences), intellectual property (IP), networks, projects, clinical trials, and web exposure in conjunction with numerous involvements in the ecosystem, a total of 495 academics, 673 companies, and 500 startups were found to match the search. The non-patent literature (NPL) database search produced 32209 scientific activities that are related to 5G. Most of the scientific works are journal articles.

Figure 18 depicts the top countries in terms of scientific outputs pertaining to 5G, while Figure 19 illustrates the publication types of scientific works. Figure 20 delineates the number of scientific productions associated with 5G over time.

Figure 18 includes the volume of scientific work among 20 countries. It reveals the growing interest and accelerated research efforts in 5G technology over recent years, coinciding with its increasing importance in global telecommunications and digital infrastructure development. China, the United States, France, and India have led the pack, while the other countries have contributed a decent amount of scientific work.

Figure 19 presents the sum of scientific works based on publication type. Journal articles and conference proceedings articles have the greatest proportion of publication types, with book chapter abstracts separating themselves from the rest, followed by journal and conference proceedings articles. In addition, the X-axis is reversed in Figure 19, with the highest ranking toward the summit of the chart and the lowest ranking toward the bottom.

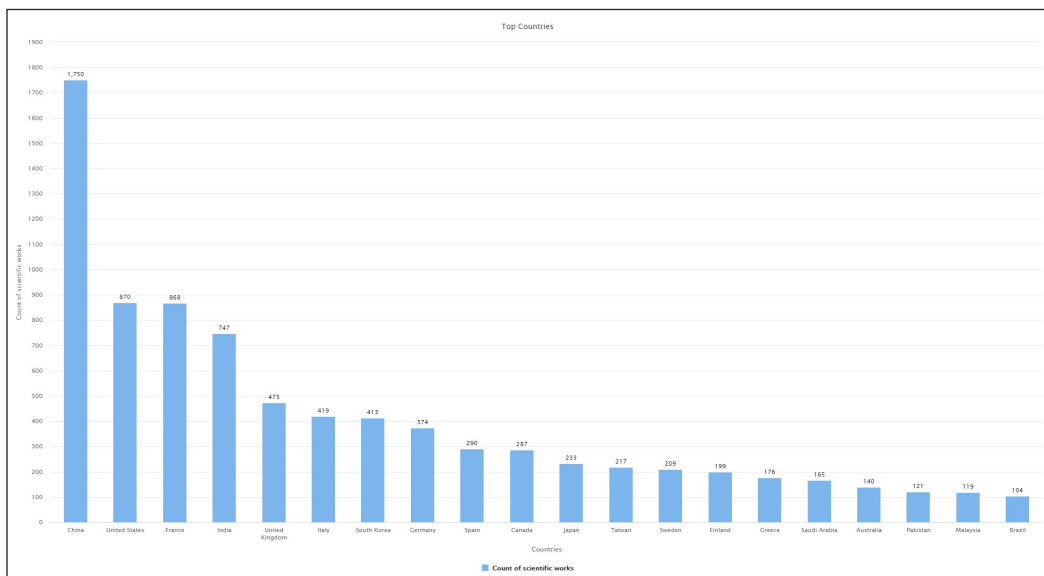


Figure 18. The top countries contributing to 5G in terms of scientific works

Note. The figure is produced by inputting data into RapidMiner Studio

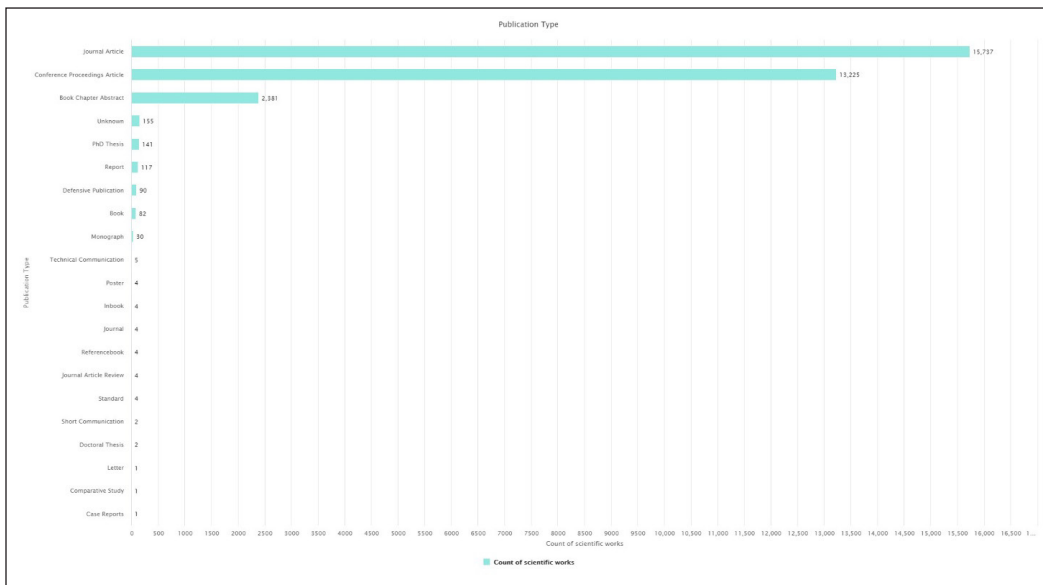


Figure 19. The count of 5G publication types

Note. The figure is produced by inputting data into RapidMiner Studio

Figure 20 displays scientific works related to 5G over a 20-year period, starting from 2004 to 2024. Since 2019, these scientific studies have witnessed a steep rise and remained at high levels until 2024, which will only be accurately measurable when they have been concluded. It is expected that 2024 will maintain a strong tally for 5G-related scientific works.

Examining the role of academia is essential to fully appreciate the scientific contribution to 5G. The intersection between academia and technology is a key driver of innovation and progress. Academic institutions serve as the foundation for technological advancement through their research initiatives and educational programs. Their collaboration with industry partners pushes the boundaries of current technology and prepares the next generation of professionals to tackle future challenges. This dynamic is particularly evident in the context of 5G. Strategic investments by universities and research centers can yield significant benefits in terms of attracting talent and securing research funding. Academic institutions, such as universities and research centers, play a pivotal role in technological progress through their research, formulation of new theories, and education of future professionals. By collaborating with industry partners, they contribute to advancing technology standards and preparing the workforce for upcoming challenges. The academic community has shown careful consideration in its approach to investing in 5G technology. Institutions that embrace this technology may gain an advantage in attracting students, instructors, and research funding. Figure 21 depicts a dozen prominent academics participating in 5G. Institutions in Spain, Finland, Sweden, the United Kingdom,

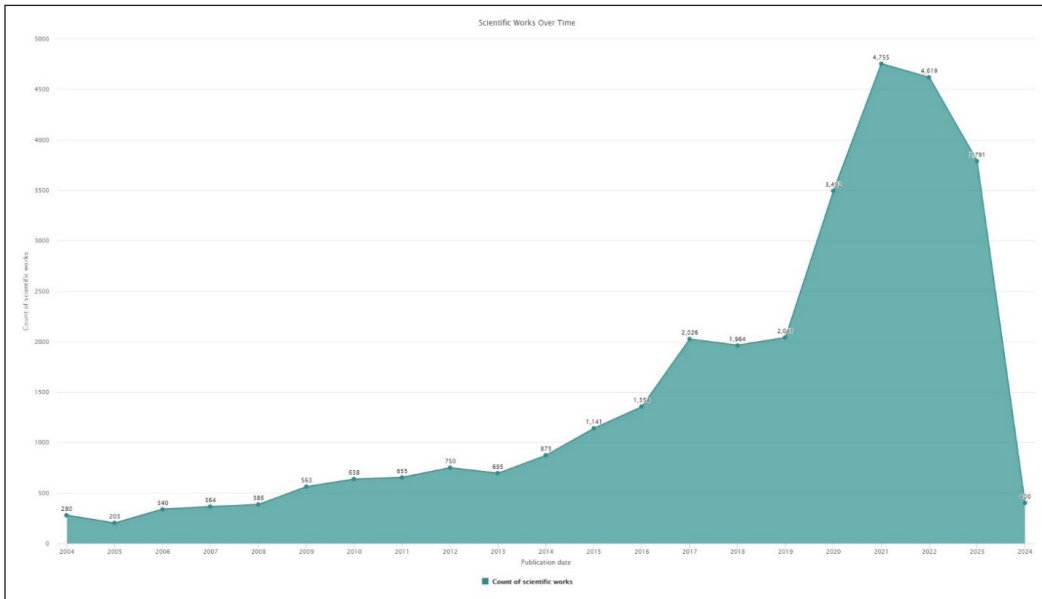


Figure 20. 5G-related scientific works overtime

Note. The figure is produced by inputting data into RapidMiner Studio

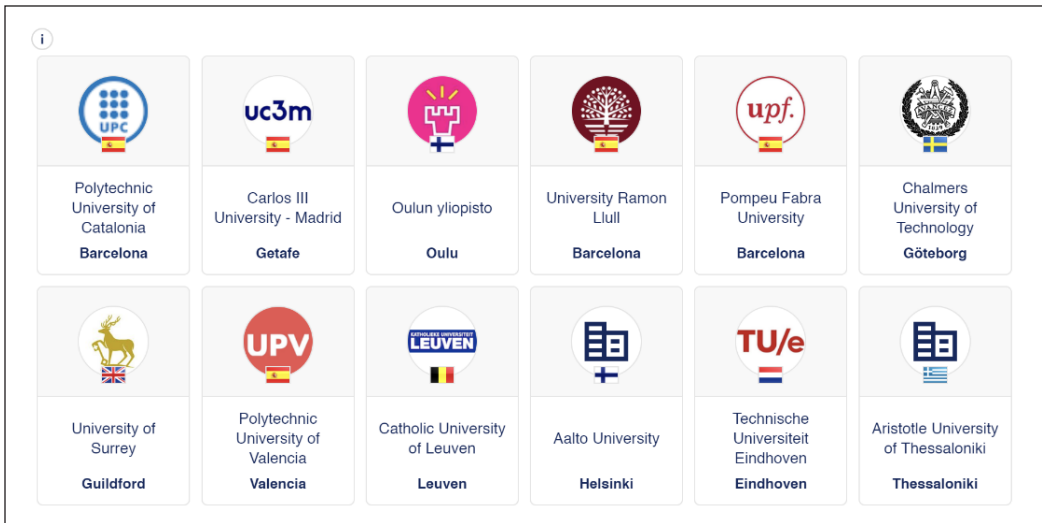


Figure 21. The academia participating in the 5G locale

Note. The figure is retrieved from Orbit Insight

Belgium, the Netherlands, and Greece formed these participants. By pooling resources, expertise, and perspectives, these institutions contribute to a more comprehensive and robust development of 5G technology, which is likely to have far-reaching implications for various sectors and industries worldwide.

As a result of this academic involvement, certain research themes have emerged as particularly significant. In this regard, the most prevalent ideas in scientific publications within a particular subject area can be identified by exploring the most commonly used keywords. This method allows a clearer understanding of the dominant themes and trends in research. When it comes to 5G research, examining scientific publications reveals that the core topics often revolve around cellular, mobile, and fifth-generation networks. By emphasizing these key areas, researchers can gain valuable insights into the current state of 5G technology and its future direction. Analyzing the frequency and context of specific keywords within these publications helps to highlight the mainstream ideas and research priorities. This approach uncovers the prevailing concepts and sheds light on emerging trends and potential areas for further investigation, as shown in Figure 22. This figure shows the most critical scientific activities related to 5G through a word cloud containing 10 principal topics. This representation highlights key scientific activities in 5G research by displaying prevalent expressions. It can reveal the relationships between different aspects of 5G technology, enabling researchers to identify gaps in current knowledge and potential avenues for innovation. It facilitates interdisciplinary understanding by providing a quick overview of the field to researchers from different disciplines. It serves as a powerful tool for synthesizing and presenting complex information on 5G technology research.

Although keywords provide a snapshot of research trends, understanding the fundamental scientific disciplines underpinning 5G offers a more overarching view. It is essential to delve into its core scientific disciplines to understand the scope and impact of 5G technology. By examining the primary areas of investigation within 5G, we can gain insights into the fundamental principles and innovations driving this technology forward. As graphically represented in Figure 23, the three main scientific fields that underpin 5G are networking and telecommunication, general computer science, and general astrophysics. By examining these primary scientific disciplines, researchers can comprehensively understand the multi-faceted nature of 5G technology and its applications. This holistic view helps identify the critical areas of research and development, thereby guiding future innovations and improvements in the field. As shown in Figure 23, all six of the prime 5G scientific domains indicate that 5G extends beyond traditional telecommunications and encompasses a diverse range of fields that contribute to its advanced capabilities. 5G technology relies on networking and telecommunications for robust infrastructure, efficient data

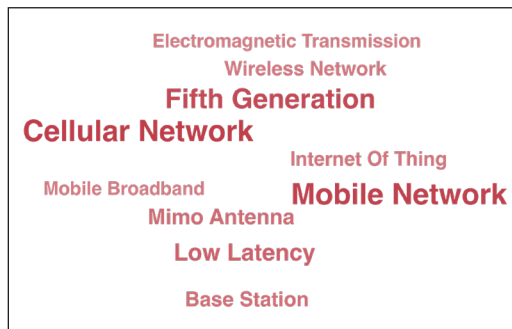


Figure 22. 5G scientific activity
 Note. The figure is retrieved from Orbit Insight

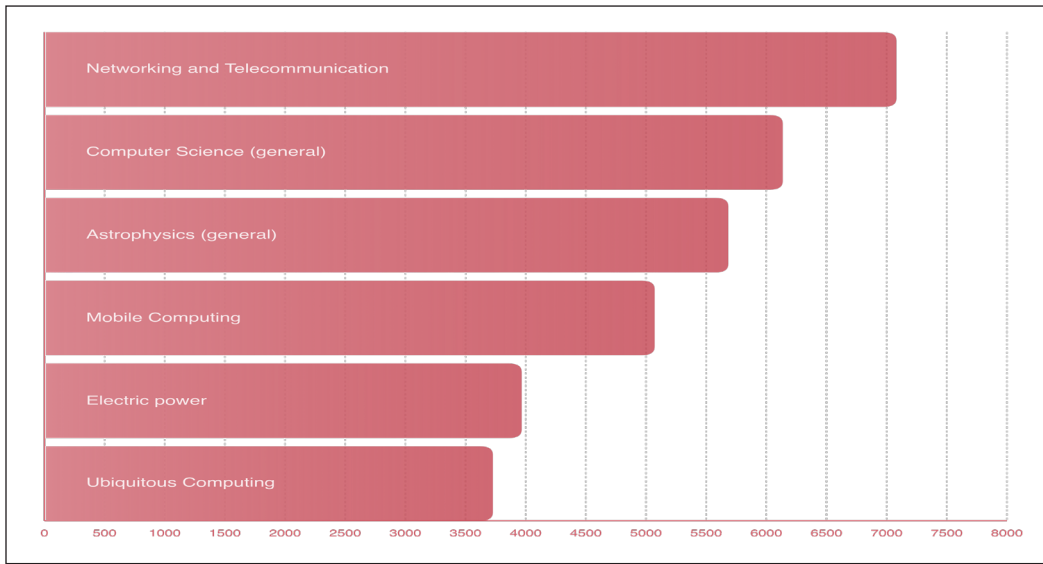


Figure 23. 5G scientific domains

Note. The figure is retrieved from Orbit Insight

transmission protocols, and advanced network architecture. General computer science provides computational foundations for data processing, machine-learning algorithms, and software-defined networking. General astrophysics plays a significant role in satellite communications and space-based network components, understanding signal propagation, and designing global-coverage satellite constellations. Integrating these three scientific fields— networking and telecommunications, general computer science, and general astrophysics—creates a synergistic approach to 5G development. This interdisciplinary collaboration enables the creation of a highly advanced, efficient, and versatile communication ecosystem that supports a wide range of applications.

DISCUSSION

The 5G technology patent landscape is marked by fierce competition, the critical role of SEPs, and their potential for groundbreaking societal applications. As industries continue to innovate and merge 5G with other technologies, continuous patent analysis is vital for discerning trends, steering strategic decisions, and maintaining equitable competition in the 5G sphere.

The 5G patent landscape represents a complex and evolving sector that sheds light on telecommunication technology’s current state and future direction. Major players, such as Samsung, Huawei, Qualcomm, Nokia, and Ericsson, dominate this arena, holding a substantial share of the total 5G patents. This concentration underscores the competitive nature of the telecommunications industry and the considerable investments

these companies make in research and development. The geographic distribution of 5G patents indicates that innovation hubs are primarily situated in the United States, China, Europe, and South Korea. This can be attributed to strong governmental backing, favorable regulatory conditions, and significant funding for technological innovation. However, it also raises concerns about global equity in technological advancement and the potential for the digital divide.

Patents' quality and impact are vital for innovation. Many of the patents filed are high quality, broadly applicable, and represent significant technological contributions. SEPs play a crucial role in the 5G ecosystem by ensuring interoperability and compatibility across devices and networks. Leading companies possess a high number of SEPs, highlighting their strategic position to influence global 5G standards.

A high concentration of 5G patents raises issues related to Intellectual Property Rights (IPR) and market dynamics. Companies with extensive patent portfolios can leverage their patents to establish licensing agreements, generate revenue and engage in litigation. While this can incentivize innovation, it may also create barriers to entry for smaller firms and new market entrants. Policymakers and industry stakeholders must navigate these challenges to balance the protection of IPR with the promotion of healthy competition and innovation.

As 5G technology progresses, the patent landscape is likely to shift in response to emerging technological advancements and market needs. Policymakers must consider the implications of 5G patents for national security, economic competitiveness, and technological sovereignty. Collaborative efforts among governments, industry leaders, and international organizations are essential for establishing fair and transparent patent practices, promoting cross-border cooperation, and addressing potential geopolitical tensions arising from the strategic importance of 5G.

CONCLUSION AND REMARKS

This study aims to aid stakeholders worldwide in comprehending the 5G patent landscape to enhance strategic planning and gain a competitive edge. This underscores the strategic importance of 5G patents in shaping market dynamics and future industry competitiveness, aligning with Pohlmann et al. (2020), who noted that patents declared to the 5G standard significantly impact various sectors, including automotive and telecommunications. Additionally, this study suggests that 5G patents will continue to drive innovation and influence technological standards, consistent with Mendonça et al. (2022), who highlight the disruptive effects of 5G technologies on economies and societies. This research also recommends that policymakers financially support the patenting process and reduce related costs to encourage participation in 5G development. This recommendation aligns with other researchers advocating governmental support and standardization efforts to boost national and global competitiveness in 5G technology (Kochetkov & Almagambetov, 2021). Finally,

the study calls for future research to examine the impact of emerging technologies and legislative changes on 5G patent portfolios, echoing Trappey et al. (2023), who emphasize the need for continuous monitoring of patent trends to understand the evolving landscape of 5G technologies.

In contrast, Wang et al. (2022) analyzed the technical effects of 5G communication patents, such as security improvement, cost reduction, and reliability improvement; however, the conclusions and recommendations are specifically aimed at China and lack a global and panoramic view of the 5G patent landscape. Conversely, this study intends to assist companies and contingents in obtaining valuable insights into 5G technology, the market, and competitors by conducting a detailed and balanced review of 5G patents. A comprehensive study of 5G patents can help firms identify critical areas for innovation and development to sustain a competitive advantage in the 5G market. This information can be utilized to ensure that businesses are developing appropriate products and services to satisfy market demands and to concentrate research and development efforts in the right direction. In conclusion, analyzing 5G patents is an indispensable resource for organizations seeking to prosper in a dynamic and ever-changing 5G landscape.

By looking ahead, 5G patents will continue to drive innovation and have a significant impact on market dynamics, which will shape future industry competitiveness and technological standards. In general, examining 5G patents sheds light on the state of intellectual property and its strategic significance in the telecom sector. Businesses and legislators must carefully analyze their patent strategies to successfully traverse the rapidly changing 5G ecosystem. Policymakers should provide financial assistance, reduce the cost of patenting, and partially cover the expenses associated with international standardization to encourage participation in developing and commercializing telecommunications. Assertions that a single corporation or country is winning the 5G race are questionable (USPTO, 2022). Maintaining an advantage in the patent race is essential in the fast-developing 5G setting as technology develops. The paper concludes by highlighting the importance of 5G patents in influencing a multitude of sectors. Subsequent investigations into 5G patent analysis may also delve into the consequences of emerging technologies and legislative advancements on patent portfolios while also concentrating on the evolution of 5G patent trends and their impact on industry dynamics. This study recommends that policymakers prioritize facilitating collaborative patenting strategies between various 5G entities to stimulate constant innovation. Further research is required to examine the influence of emerging 6G technologies on the current 5G patent landscape.

ACKNOWLEDGEMENTS

This research did not receive any dedicated funding from public, private, or non-profit entities.

REFERENCES

- Archibugi, D., & Planta, M. (1996). Measuring technological change through patents and innovation surveys. *Technovation*, 16(9), 451–519. [https://doi.org/10.1016/0166-4972\(96\)00031-4](https://doi.org/10.1016/0166-4972(96)00031-4)
- Buggenhagen, M., & Blind, K. (2022). Development of 5G – Identifying organizations active in publishing, patenting, and standardization. *Telecommunications Policy*, 46(4), Article 102326. <https://doi.org/10.1016/j.telpol.2022.102326>
- Deloitte. (2021). *Navigating the 5G Patent Landscape*. Deloitte.com. <https://www.deloitte.com/global/en/services/financial-advisory/perspectives/navigating5gpatents.html>
- Ericsson. (2024). *To 5G and Beyond - Landmark 5G Patent Application*. Ericsson.com. <https://www.ericsson.com/en/patents/articles/to-5g-and-beyond>
- Ernst, H. (2003). Patent information for strategic technology management. *World Patent Information*, 25(3), 233–242. [https://doi.org/10.1016/s0172-2190\(03\)00077-2](https://doi.org/10.1016/s0172-2190(03)00077-2)
- Gillis, A. S., & Gerwig, K. (2024). 5G. *Networking*. TechTarget. <https://www.techtarget.com/searchnetworking/definition/5G>
- Kochetkov, D., & Almaganbetov, M. (2021). Using patent landscapes for technology benchmarking: A case of 5G networks. *Advances in Systems Science and Applications*, 21(2), 20–28. <https://doi.org/10.25728/assa.2021.21.2.988>
- Lee, K., & Lee, S. (2013). Patterns of technological innovation and evolution in the energy sector: A patent-based approach. *Energy Policy*, 59, 415–432. <https://doi.org/10.1016/j.enpol.2013.03.054>
- Mendonça, S., Damásio, B., De Freitas, L. C., Oliveira, L., Cichy, M., & Nicita, A. (2022). The rise of 5G technologies and systems: A quantitative analysis of knowledge production. *Telecommunications Policy*, 46(4), Article 102327. <https://doi.org/10.1016/j.telpol.2022.102327>
- Miller, L., & Cavazos, J. (2022). *5G & Beyond for Dummies*. Keysight Technologies. <https://www.keysight.com/my/en/assets/7121-1150/ebooks/5G-and-Beyond-For-Dummies.pdf>
- Noh, H., Song, Y., & Lee, S. (2016). Identifying emerging core technologies for the future: Case study of patents published by leading telecommunication organizations. *Telecommunications Policy*, 40(10–11), 956–970. <https://doi.org/10.1016/j.telpol.2016.04.003>
- Pohlmann, T., Blind, K., & Hess, P. (2020). *Fact Finding Study on Patents Declared to the 5G Standard*. LexisNexis IPLytics. https://www.iplytics.com/wp-content/uploads/2020/02/5G-patent-study_TU-Berlin_IPlytics-2020.pdf
- Richter, F. (2024). *5G is Still in the Early Stages of its Lifecycle*. Statista Daily Data. <https://www.statista.com/chart/9604/5g-subscription-forecast/>
- Rita, L. P. S., Da Silva, L. S. C. V., Kaczam, F., Macêdo, M. J. F. G., De Macêdo, Á. F. P., Da Silva, W. V., & Da Veiga, C. P. (2023). Relationship between industry 4.0 and patents. *World Patent Information*, 74, Article 102221. <https://doi.org/10.1016/j.wpi.2023.102221>
- Spoehr, C. (2024). *5G patent Ownership Booms: Who is leading the pack?* LexisNexis Intellectual Property Solutions. <https://www.lexisnexisip.com/resources/5g-patent-ownership-booms-who-is-leading-the-pack/>

- Statista. (2023). *Share of 5G Patent Families by Leading Companies 2021*. Statista. <https://www.statista.com/statistics/1230594/share-of-5g-patent-families-ownership-by-company/>
- Taylor, P. (2023). *Leading Owners of 5G Patents Worldwide 2021*. Statista. <https://www.statista.com/statistics/1276457/leading-owners-of-5g-patents-worldwide/>
- The Star. (2023, June 29). 5G worldwide users at 1.2 billion, industry moving towards 5.5G, 6G. *The Star*. <https://www.thestar.com.my/business/business-news/2023/06/29/5g-worldwide-users-at-12-billion-industry-moving-towards-55g-6g>
- Trappey, A. J., Wei, A. Y., Chen, N. K., Li, K., Hung, L., & Trappey, C. V. (2023). Patent landscape and key technology interaction roadmap using graph convolutional network – Case of mobile communication technologies beyond 5G. *Journal of Informetrics*, 17(1), Article 101354. <https://doi.org/10.1016/j.joi.2022.101354>
- USPTO. (2022). *Patenting Activity among 5G Technology Developers*. United States Patent and Trademark Office. <https://www.uspto.gov/sites/default/files/documents/USPTO-5G-PatentActivityReport-Feb2022.pdf>
- Wang, X. (2011). Patent intelligence and business strategy. *African Journal of Business Management*, 5(10), 3935–3941. <https://doi.org/10.5897/ajbm10.1383>
- Wang, X., Yang, W., Zhao, J., & Yang, X. (2022). Patent measurement analysis of 5G technology. In *EEI 2022 4th International Conference on Electronic Engineering and Informatics* (pp. 1-5). VDE Publishing.
- Xu, K. (2022). Research on industry-university-research collaborative innovation network from the perspective of patent – A case study of Huawei telecom direction (H04) patent. In *AIP Conference Proceedings* (Vol. 2474, No. 1). AIP Publishing. <https://doi.org/10.1063/5.0079467>
- Xuan, Y., Zhang, S., Li, X., & Li, X. (2023). Identify cross-country knowledge flow and innovation trajectory: Insights from patent citation network analysis of 5G technology. *Technology Analysis & Strategic Management*, 36(10), 2997-3019. <https://doi.org/10.1080/09537325.2023.2190418>
- Yu, E. (2024). 5.5G Touted as the Network to bring Improved Enterprise Connectivity. ZDNET. <https://www.zdnet.com/article/5-5g-touted-as-the-network-to-bring-improved-enterprise-connectivity/>
- Zhang, H. E., Wong, K. H., & Chang, V. (2021). Patent analysis in the 5G network. *Journal of Global Information Management*, 29(6), 1–28. <https://doi.org/10.4018/jgim.20211101.0a28>

Effective Vibration-Based Anomaly Detection in Water Pump Operation Using Arduino Microcontroller

Azahar Mohd¹, Khairil Anas Md Rezali^{1*}, Sharafiz Abdul Rahim¹,
Mohammad Yazdi Harmin², Abdul Murad Zainal Abidin³ and
Mohamad Fikri Mohamad Yunus³

¹Department of Mechanical and Manufacturing Engineering, Faculty of Engineering, Universiti Putra Malaysia, 43400 UPM, Serdang, Selangor, Malaysia

²Department of Aerospace Engineering, Faculty of Engineering, Universiti Putra Malaysia, 43400 UPM, Serdang, Selangor, Malaysia

³Mechanical Research Laboratory, Centre of Excellence for Engineering and Technology (CREaTE), Public Works Department Malaysia, 78000 Alor Gajah, Melaka, Malaysia

ABSTRACT

Arduino microcontroller and ADXL accelerometer are commonly paired devices, often considered for creating inexpensive vibration analysers. Many researchers have proven that both pairing devices have good performance in vibration measurement and have the potential for commercialisation. This study evaluates the feasibility of vibration measurement and monitoring using an Arduino microcontroller with an inexpensive accelerometer in detecting anomalies during water pump operation. A dedicated Arduino Mega and an ADXL345 accelerometer were attached to a water pump motor to facilitate continuous monitoring of vibrations. The vibration measurement was set at a sampling rate of 530 Hz. Vibration data in RMS value was sent to the cloud storage for monitoring. Raw data captured during normal and abnormal conditions were collected at the

site when anomalies were detected for further analysis. The results showed that the abnormal conditions could be clearly differentiated from normal conditions using the Fast Fourier Transform method and spectrogram analysis. In summary, this study confirms that integrating the Arduino Microcontroller with the ADXL accelerometer effectively detects irregularities in the operating conditions of the water pump.

Keywords: ADXL accelerometer, Arduino microcontroller, vibration monitoring, water pump anomalies

ARTICLE INFO

Article history:

Received: 29 May 2024

Accepted: 04 November 2024

Published: 21 February 2025

DOI: <https://doi.org/10.47836/pjst.33.2.09>

E-mail addresses:

gs67345@student.upm.edu.my (Azahar Mohd)

khairilanas@upm.edu.my (Khairil Anas Md Rezali)

sharafiz@upm.edu.my (Sharafiz Abdul Rahim)

myazdi@upm.edu.my (Mohammad Yazdi Harmin)

abdmurad@jkr.gov.my (Abdul Murad Zainal Abidin)

mfikri@jkr.gov.my (Mohamad Fikri Mohamad Yunus)

* Corresponding author

INTRODUCTION

Arduino Microcontroller is a popular platform in the field of electronic development, providing a microcontroller system that is easy to program and interact with various electronic devices (Kondaveeti et al., 2021; Pan & Zhu, 2018). One of the frequently used models is the Arduino Mega 2560, which offers a wide range of capabilities to control external sensors and devices, making it the primary choice for measurement and monitoring in a variety of environments. The importance and suitability of the water pump system in daily life make it suitable for applying this technology. Together with Arduino microcontrollers, accelerometers are often used as sensors to measure acceleration and position changes in three axes. The ADXL345 accelerometer, used as a sensor in this study, is notable for its compact size, lightweight design, user-friendliness, and high precision (Adli & Rusmin, 2020). These sensors enable vibration measurement in a variety of applications, including machine health monitoring and structural damage detection. In the context of water pumps, the use of this combination enables accurate and rapid monitoring of the operating conditions of water pumps, helping to avoid unwanted damage and ensuring the smoothness of the water supply for daily needs (ALTobi et al., 2019).

The cold-water supply system in a building is a system of basic needs that is very important and must be provided especially to ensure the quality of life and the health of the population is guaranteed. As living standards rise, there is a growing demand for improved comfort, quality, and safety at affordable prices (Lourenço et al., 2022). Water supply systems in buildings must keep pace with this trend to meet the demand for clean drinking water (Van Der Schee, 2009). For high-rise buildings, water distribution often relies on pumping systems due to the structure's height or inadequate water pressure from the source (Midiani et al., 2023; Altherr et al., 2019). In such scenarios, ensuring the continuous upkeep of the pump system is imperative to avoid disruptions in the water supply for the building's occupants (Kiliç et al., 2017). The malfunction of a water pump system causes inconvenience for users and substantially impacts maintenance expenses (Zhou et al., 2021; Dutta et al., 2020). Therefore, it is crucial to regularly maintain the system to extend its longevity and preserve its effectiveness (Dutta et al., 2020). Nevertheless, routine maintenance is insufficient, as pump faults or anomalies during operation can arise unexpectedly without immediate detection.

Anomalies in the water pump system can be caused by several factors, such as wear and tear, ageing components, bearing failure, shaft misalignment, and excessive physical stress (Chen et al., 2022; Shibnauth & Surnam, 2015; Yehl et al., 2008). Although these factors can be identified through physical examination, certain issues, such as cavitation and water hammer phenomena, are difficult to detect due to their unique characteristics. Cavitation is one of the biggest threats to the effectiveness and structural integrity of water pumping systems, a process that arises from the creation and collapse of vapour bubbles in

liquid phases (Hajnayeb et al., 2017). Cavitation is caused by low water pressure, prompting the formation of foam that can damage the impeller in the long term. In contrast, a water hammer is a hydraulic phenomenon that will cause a sudden pressure surge triggered by the closing of a valve or a change in fluid flow. This occurrence poses a significant risk to the pump and the integrity of the system. This situation makes the implementation of safety monitoring procedures and regular maintenance practices very critical.

It is important to acknowledge that MEMS accelerometers have been employed in fault detection for rotating machinery for many years (Mones et al., 2016; Feng et al., 2015; Adli & Rusmin, 2020). This study introduces a novel aspect by integrating the Arduino Mega 2560 with the ADXL345 accelerometer specifically for real-time monitoring of water pumps. This combination not only offers a cost-effective and accessible solution but also targets the detection of critical anomalies, such as cavitation and water hammer, which are essential for preserving the operational integrity of water pump systems. Unlike previous studies, this research highlights the practical application of widely available technology in cost-sensitive environments, where affordability and ease of deployment are vital considerations.

It is critical to comprehend these exacerbating variables as anomalies or pump damage are not always the same. Insufficient analysis of these intricate problems can impede the creation of effective treatment plans and prevention actions (Tian et al., 2022). The need for continuous monitoring also opens opportunities to predict or identify water pump anomalies before they become serious (Adeodu et al., 2020). By implementing an effective monitoring system, the pump maintenance team can take the necessary preventive actions before unwanted damage occurs. It provides an added advantage in maintaining the optimal performance of the pump system and ensuring uninterrupted operation. By emphasising the importance of water pump anomaly monitoring, this study seeks to provide a solid scientific and practical basis for the implementation of monitoring strategies in the daily operation of water pumping systems.

The vibration data acquired from the water pump motor holds significant value for analysis in maintenance management, particularly for implementing preventive or condition-based maintenance strategies. Preventive maintenance entails regular scheduling and continuous monitoring of equipment to forestall unforeseen breakdowns. The primary aim of scheduled maintenance is to maintain equipment in its optimal condition, ensuring optimal functionality and extending its operational lifespan for an extended period (Arunraj & Maiti, 2007; Smith & Hawkins, 2004). In contrast, condition-based maintenance relies on data collected during monitoring periods to determine suitable maintenance recommendations (Jardine et al., 2006). Maintenance tasks are performed upon reaching predetermined thresholds, guided by specific indicators identified beforehand. Neglecting the current state of the machine within the context of preventive or condition-based

maintenance can elevate the risk of unexpected and inevitable machine failure, resulting in unnecessary expenditure (Zhou et al., 2005).

Several studies have explored vibration analysis methodologies for detecting anomalies in water pump maintenance, employing a range of methodologies and techniques. For instance, Sunal et al. (2022), Bai et al. (2019), and Sun et al. (2018) explored the use of vibration analysis coupled with machine learning algorithms to diagnose faults in centrifugal pumps. Guimarães and de Oliveira Filho (2021) also conducted a study focusing on detecting cavitation in water pumps using vibration analysis techniques. Their study successfully identified vibration components caused by cavitation in centrifugal pumps using the Power Spectrum and Continuous Wavelet Transform, improving hydraulic performance and pump life (Guimarães & de Oliveira Filho, 2021). Additionally, Lee and Le (2020) investigated the application of wavelet transform and envelope analysis for fault diagnosis in water pump bearings (Lee & Le, 2020).

Recently, a study by Al-Haddad et al. (2024) developed a sophisticated vibration-current data fusion approach combined with a gradient boosting classifier to enhance the diagnosis of stator faults in three-phase permanent magnet synchronous motors. Their work demonstrates the effectiveness of data fusion techniques in improving fault detection accuracy, which is crucial for maintaining the operational integrity of complex machinery. Similarly, Jaber and Bicker (2017) proposed a wireless fault detection system for industrial robots, leveraging statistical control charts to monitor and detect anomalies in real time. This approach highlights the growing trend toward integrating wireless technologies for more efficient and responsive fault detection. Additionally, Ogaili et al. (2023) focused on wind turbine blades, employing vibration dataset analysis to diagnose faults, further underscoring the importance of vibration analysis in predictive maintenance across different types of machinery. These studies collectively emphasise the critical role of advanced diagnostic techniques and real-time monitoring in ensuring the reliability and longevity of mechanical systems, providing a strong foundation for the present study's focus on vibration monitoring in water pumps. All the studies demonstrate the diverse approaches and methodologies employed to leverage vibration analysis for anomaly detection in water pump systems, highlighting the importance of this field in ensuring the reliability and efficiency of pump operations.

However, despite the insights gained from these studies, challenges persist with the widespread adoption of expensive vibration devices for Internet of Things (IoT) applications. These challenges, including security concerns and the feasibility of permanent installation at sites, underscore the need for alternative solutions. Given the limitations associated with costly vibration devices, there is a growing interest in exploring the feasibility of low-cost alternatives, such as Arduino microcontrollers, for vibration monitoring in water pump systems (Agnoletti et al., 2020). However, it is essential to acknowledge the limitations of such

devices, which may impact their suitability for comprehensive monitoring. Arduino-based solutions often face constraints in terms of limited computational power and memory capacity, security vulnerabilities (Sainz-Raso et al., 2023), sampling rate, data transmission to the cloud, simultaneous measurement capabilities, accuracy, and sensitivity. These limitations can hinder their effectiveness in capturing nuanced vibration patterns and identifying subtle anomalies in pump operations. Thus, while Arduino devices offer affordability and accessibility, further research is needed to address these challenges and optimise their performance for reliable and robust vibration monitoring in real-world applications.

Studies on existing methods to detect water pump anomalies show the need to find more sophisticated and effective approaches. An introduction to recent developments in vibration sensors and monitoring technology provides insight into the potential use of inexpensive vibration sensors in water pump anomalies analysis (Ejimuda, 2020). This study evaluates the feasibility of utilising Arduino-based data acquisition to monitor water pump conditions using vibration analysis to identify anomalies. In this study, the anomalies were associated with cavitation, as shown in the results. The research involved the development of a vibration measurement apparatus employing an Arduino Mega 2560 and ADXL345 accelerometer, which was installed on a water pump motor for monitoring purposes. Through Wi-Fi connectivity, the device facilitated online monitoring by transmitting vibration data in real time, enabling the detection of anomalies such as water hammer and cavitation problems.

METHODOLOGY

This study evaluates the feasibility of using Arduino for measurement by considering several important factors. One key aspect is the choice of the Administration Building of the Engineering Faculty at Universiti Putra Malaysia as the study site, which offers a practical and real-world environment for testing the Arduino-based monitoring system. The presence of two units of similar Vertical Multistage centrifugal-type water pumps (Figure 1) operating alternately in the building offers a suitable setting to assess the effectiveness and reliability of the Arduino system in monitoring pump performance over an extended period. The specifications of the water pumps, including their power ratings, operating speeds, and flow rates, serve as crucial parameters for

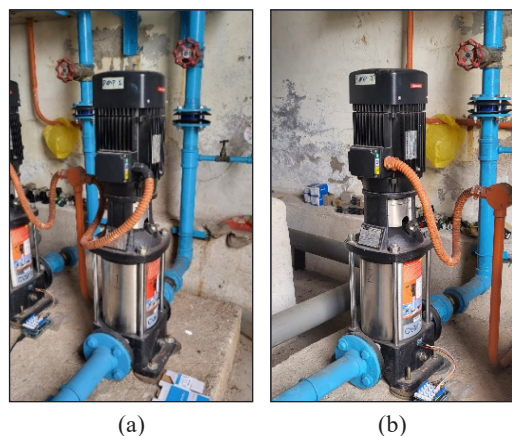


Figure 1. (a) Water pump No.1; and (b) Water pump No.2

evaluating the compatibility and capability of the Arduino platform for capturing relevant data accurately.

As previously mentioned, two units of similar Vertical Multistage centrifugal-type water pumps are utilised for the building, operating alternately. The specifications of these water pumps are detailed in Table 1.

The methodology of this project includes device design for data acquisition, device verification, the installation of the device, and the analysis of the data. The device is set using an Arduino Mega 2560 microcontroller and ADXL345 accelerometer called Arduino Data Acquisition system (ADAQ), divided into:

- Design and Development of ADAQ
- ADAQ Verification
- ADAQ Installation on Water Pumps Motor
- Data analysis

Table 1
Water pump specifications and electric motor specifications

Water Pump Specifications		Electric Motor Specifications	
Model	BUGATI CVM10-8	Model	YE2-90LA-2
H _{max}	84 m	Power	3.0 kW, 50Hz
H _N	62 m	Voltage	240/415V
QN	10m ³ /h	Ampere	9.8/5.7A
P2	3.0kW, 50Hz	Efficiency	84.6%
Rotation Speed	2900 r/min	Rotation Speed	2900 r/min

Design and Development of ADAQ

The design process began with defining the system requirements and selecting appropriate components to meet these requirements. Key considerations included ensuring compatibility between the Arduino Mega 2560 and the ADXL345 accelerometer, as well as integrating additional components for comprehensive functionality. Challenges faced during the design process included optimising data sampling rates and ensuring reliable data transmission. Careful accelerometer calibration was performed to address these challenges, and the software was programmed to handle data storage and transmission efficiently. ADAQ integrates an Arduino Mega 2560 microcontroller and an ADXL345 accelerometer, facilitating real-time data collection and analysis. Additional components include a microSD card adapter, a clock module, and an ESP8266 Wi-Fi module for internet connectivity. All components are shown in Figure 2, and their functions are listed in Table 2. The integration of these components required meticulous wiring and configuration to ensure proper communication and data flow. The ADAQ setup enables efficient monitoring of vibration levels in three axes (X, Y, Z) to assess pump performance.

Table 2
 Arduino data acquisition system components

Component	Function
Arduino MEGA: ESP8266WiFi Module microcontroller	Processing and sending data with internet connection capability
ADXL345 Accelerometer	Measure vibration in three axes
SD Card	Saving the raw data into micro-SD Card
Clock module	To link measurement with real-time
Base Shield v2	For easy connection between sensors and Arduino
LCD 16x2	To display selected output

The ADXL345 accelerometer could sample at a maximum rate of 530 points per second, which was limited by the components, instructions and ability of the microcontroller. The samples taken per measurement were set to 299 points per second to accommodate the dynamic memory’s limitations to optimise data collection. Additionally, challenges related to ensuring stable and accurate sampling were addressed through thorough testing and adjustment of the sampling parameters.

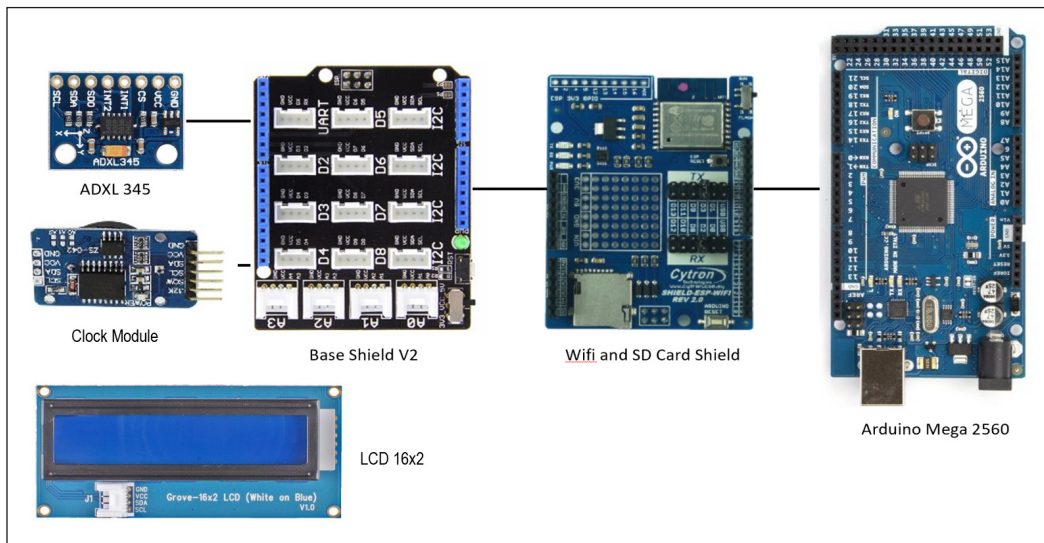


Figure 2. ADAQ component

ADAQ Verification

The verification of ADAQ’s performance and accuracy is based on a previous study that utilised the same ADAQ configuration and ADXL345 accelerometer. This study conducted random vibration measurements using the ADAQ and the National Instruments Data Acquisition System (NI DAQ), with vibration frequencies ranging from 10 to 150 Hz

(Rezali et al., 2022). Challenges encountered during verification included aligning the data from different systems and ensuring consistency across measurements. To overcome these issues, calibration procedures were implemented, and a comparative analysis was conducted to validate the accuracy of the ADAQ. The results indicated that the data obtained were reliable, showing differences of less than 10% (Rezali et al., 2022).

ADAQ Installation on Water Pump Motor

The installation of ADAQ on water pump motors involved mounting the ADXL345 accelerometer on each pump to measure vibration levels, as shown in Figure 3. It allowed for real-time monitoring of pump vibrations in the water pump room. During installation, challenges included ensuring the secure placement of the accelerometer and minimising potential interference from other equipment—solutions involved using appropriate mounting techniques and shielding to enhance measurement accuracy. Vibration measurements were converted to root-mean-square (RMS) acceleration values and transmitted to the cloud system for analysis. Additionally, raw vibration data was stored on the microSD card for further offline analysis.

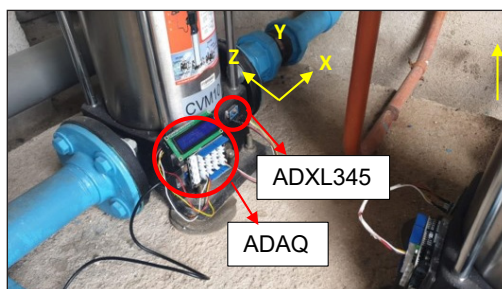


Figure 3. ADAQ installation at the water pump motor showing all axes' direction

Data Analysis

In the data analysis phase, vibration measurements obtained from ADAQ were subjected to time-domain and frequency-domain analyses to evaluate the vibration characteristics of the water pumps. Initially, the raw data were processed to calculate the Root Mean Square (RMS) values, which were then sent to the cloud for monitoring. The RMS value, a key indicator of vibration intensity, was computed using the following Equation 1:

$$RMS = \sqrt{\frac{1}{n} \sum_i x_i^2} \quad [1]$$

Where n is the number of data points, and x_i represents each individual vibration measurement point.

During data analysis, additional challenges included handling large data sets and ensuring accurate interpretation of vibration patterns. These challenges were addressed through the use of robust data processing techniques and validation against known benchmarks. Subsequently, the data underwent time-domain and frequency-domain

analyses. Time-domain analysis provided insights into vibration intensity and patterns over time, while frequency-domain analysis identified dominant frequencies, including the blade pass frequency (BPF). For frequency-domain analysis, the Welch method was employed using MATLAB, a widely used technique for signal processing power spectral density (PSD) estimation. This method provided a robust and accurate frequency-domain analysis, which, when combined with the time-domain analysis, offered a comprehensive understanding of the vibration characteristics of the water pumps.

The results of data analysis facilitated the identification of normal and abnormal operating conditions, aiding in the diagnosis of potential pump malfunctions or inefficiencies. In summary, the methodology outlined in this study ensures systematic data collection, verification, and analysis, enabling a comprehensive assessment of water pump performance and operational integrity.

RESULT AND DISCUSSION

Daily Vibration Measured at the Water Pump

Figures 4, 5, and 6 show vibration data measured at the water pump for 3 days before, during, and after the detected anomalies. The RMS value on 1st April 2023 did not fluctuate much and was stable throughout the day. The RMS values of all the axes were not significantly different, with the maximum amplitude value at 0.82 m/s².

On 3rd April 2023, the RMS vibration values in the x, y, and z axes surged to higher-than-normal levels compared to the previous operational period, beginning around 11:37 a.m., immediately after the pump restarted (Figure 5). This abnormal vibration continued on 4th April 2023, with the maximum RMS vibration value reaching up to 2.89 m/s², as

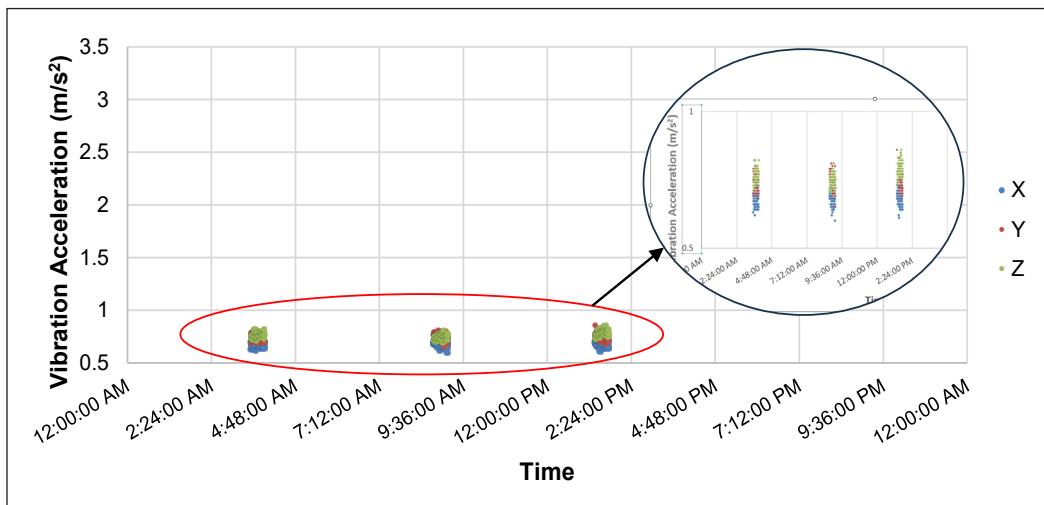


Figure 4. Vibration measured at the water pump on 1st April 2023

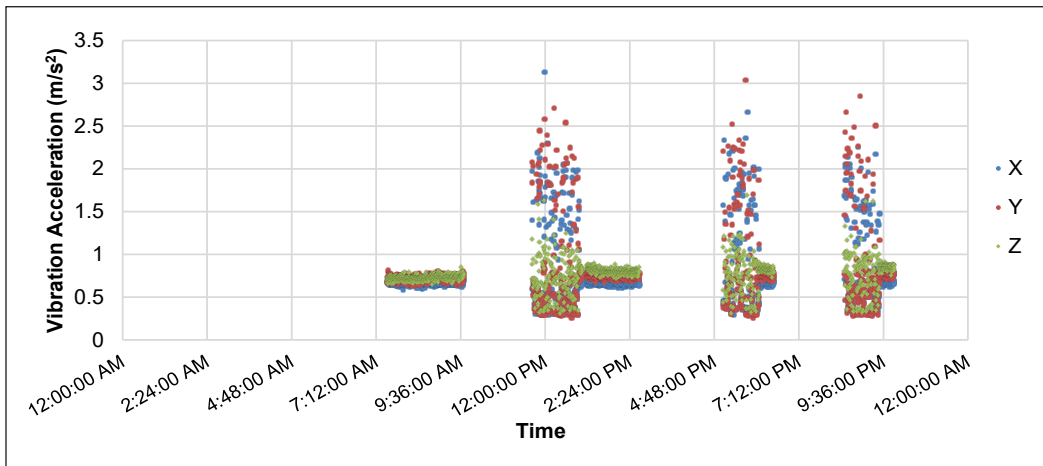


Figure 5. Vibration measured at the water pump on 3rd April 2023

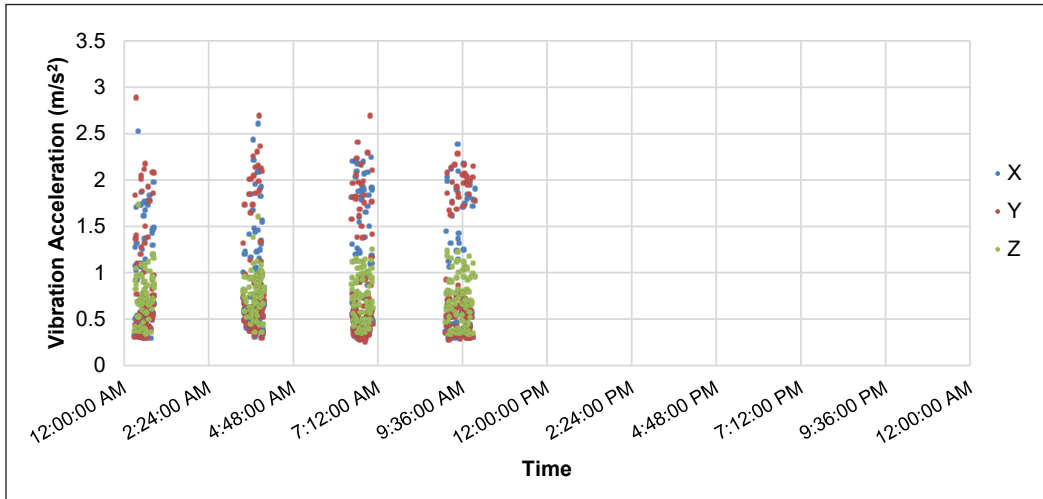


Figure 6. Vibration measured at the water pump on 4th April 2023

depicted in Figure 6. Subsequently, the pump was shut off and scheduled for maintenance and repair work.

Time Domain and Frequency Domain Vibration of the Water Pump

The summary of RMS values for the X, Y, and Z axes during normal (Figure 7) conditions and abnormal conditions (Figure 8) reveals distinct patterns. In normal conditions, the RMS values are relatively low: $X=0.3698 \text{ m/s}^2$, $Y=0.4064 \text{ m/s}^2$, and $Z=0.3804 \text{ m/s}^2$ indicating minimal vibration intensity along each axis. Conversely, notably higher RMS values are observed during abnormal conditions: $X=1.0365 \text{ m/s}^2$, $Y=1.1342 \text{ m/s}^2$, and $Z=0.5912 \text{ m/s}^2$.

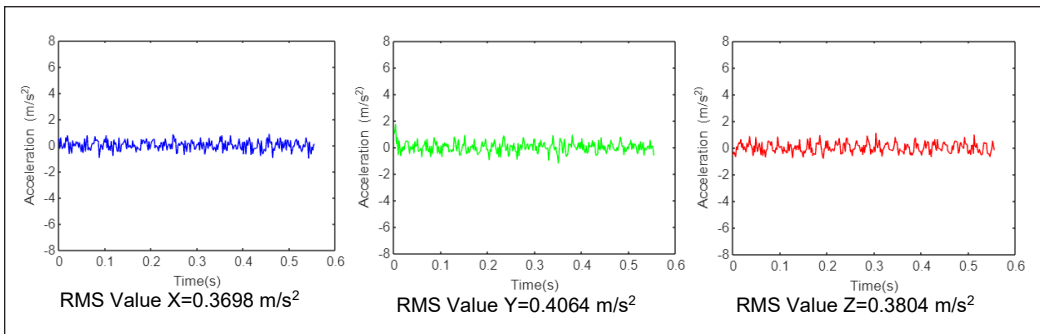


Figure 7. Vibration acceleration (time domain)—NORMAL CONDITION

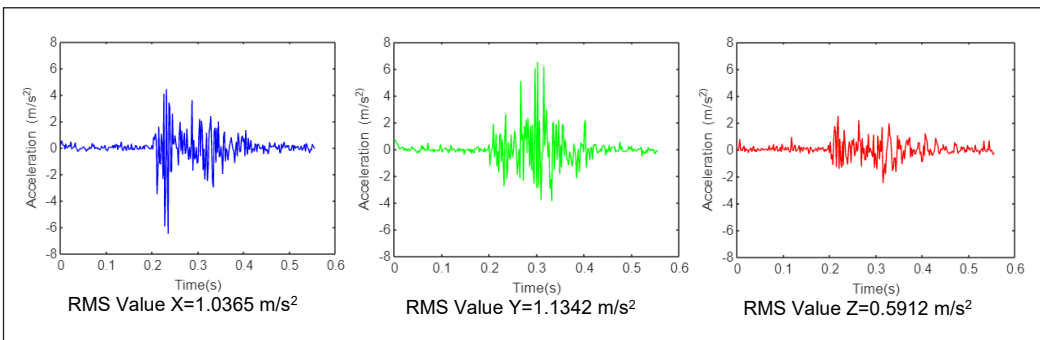


Figure 8. Vibration acceleration (time domain)—ABNORMAL CONDITION

This significant increase in RMS values suggests a substantial amplification of vibration intensity across all axes during abnormal conditions. Moreover, the time domain graphs corroborate these findings, showing a distinct pattern of sporadic spikes in vibration intensity during abnormal conditions, contrasting with the smoother, more uniform pattern observed during normal conditions. This discrepancy underscores the efficacy of RMS values as indicators of abnormal vibration behaviour, with higher RMS values corresponding to pronounced irregularities in vibration patterns. These results suggest that monitoring RMS values provides a reliable method for detecting and distinguishing between normal and abnormal conditions in vibration analysis, facilitating timely intervention to prevent potential equipment malfunction or failure.

The frequency domain analysis shows distinct differences between normal and abnormal conditions. During normal conditions, the graph prominently displays the blade pass frequency (BPF) or $1 \times$ frequency across all axes, with the occasional presence of higher harmonics up to $5 \times$ frequency on certain axes (Figure 9). This characteristic pattern is indicative of stable and consistent machinery operation. However, in the abnormal frequency domain graph, while BPF remains discernible, the graph exhibits irregularities above the BPF, manifesting as random frequencies (Figure 10). This deviation from the

expected pattern suggests the presence of anomalous vibration behaviour, potentially attributable to cavitation effects. Cavitation was induced by operating the pump under conditions of low NPSH (Net Positive Suction Head) and high flow rates, which promote cavitation (Sanchez et al., 2018). Verification of cavitation involved observing the characteristic changes in vibration frequency and amplitude patterns consistent with the symptoms of cavitation described in the literature (Hajnayeb et al., 2017; Abdulaziz & Kotb, 2017). Cavitation-induced irregularities in the frequency domain graph serve as a critical indicator of machinery malfunction or inefficiency, highlighting the importance of frequency domain analysis in detecting and diagnosing operational abnormalities in mechanical systems.

The analysis of vibration velocity in the time domain reveals notable differences between normal and abnormal conditions. During normal conditions, the RMS values for vibration velocity are relatively low: $X=0.8790$ m/s, $Y=1.3213$ m/s, and $Z=1.1997$ m/s, indicating moderate vibration intensity along each axis (Figure 11). Conversely, during abnormal conditions, significantly higher RMS values are observed: $X=2.2012$ m/s, $Y=2.2940$ m/s, and $Z=1.5368$ m/s, indicating a substantial amplification of vibration intensity across all axes (Figure 12). This consistent pattern persists even when converting from acceleration to velocity, underscoring the persistence of abnormal vibration behaviour across different domains. Such pronounced differences in vibration velocity between normal and abnormal

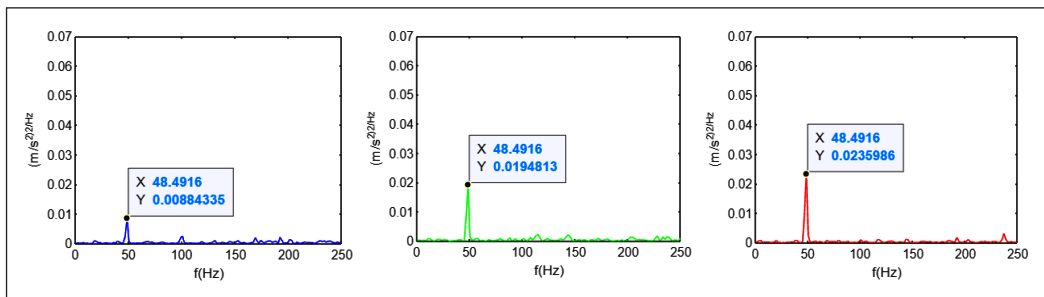


Figure 9. Vibration acceleration (frequency domain)—NORMAL CONDITION

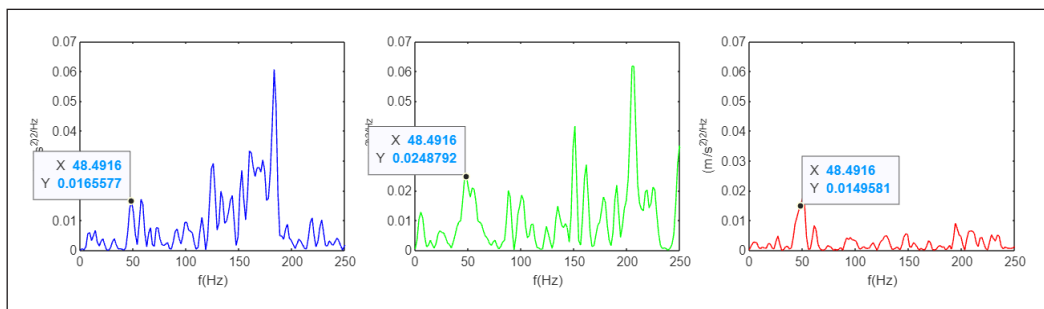


Figure 10. Vibration acceleration (frequency domain)—ABNORMAL CONDITION

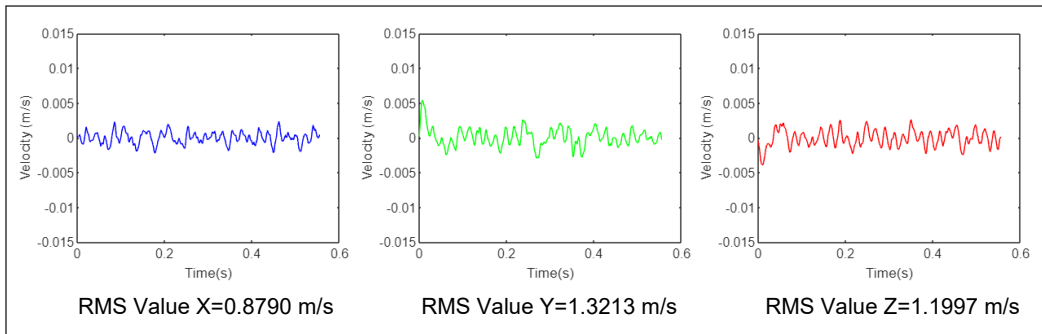


Figure 11. Vibration velocity (time domain)—NORMAL CONDITION

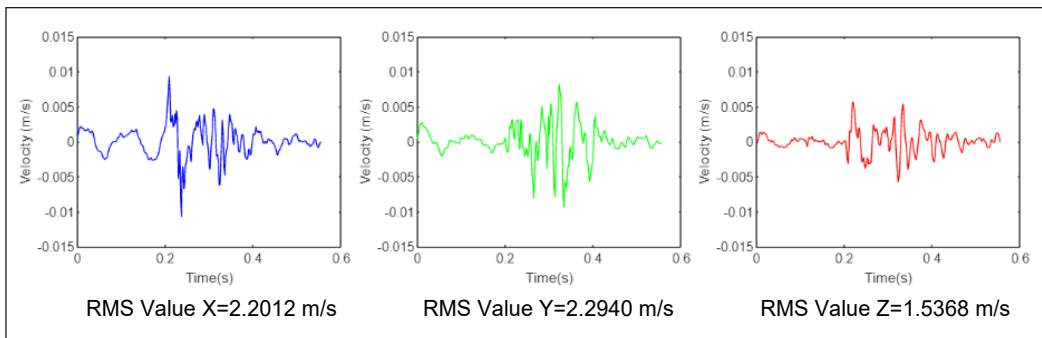


Figure 12. Vibration velocity (time domain)—ABNORMAL CONDITION

conditions highlight the potential severity of operational irregularities, necessitating prompt attention and intervention to mitigate potential equipment damage or failure.

In the frequency domain analysis of vibration velocity, distinct differences between normal and abnormal conditions emerge. During normal conditions, the blade pass frequency (BPF) remains clearly identifiable across all axes, indicating stable machinery operation (Figure 13). However, during abnormal conditions, while the BPF is still discernible in the X axis at 48.4916 Hz, significant alterations occur in the Y and Z axes, where the BPF shifts to 46.6957 Hz and 52.0836 Hz, respectively (Figure 14). This deviation in BPF frequencies across axes suggests irregularities in machinery operation, potentially indicative of underlying faults or inefficiencies. The changes in BPF frequencies align with known symptoms of cavitation, which typically affects the frequency spectrum and can shift the BPF due to changes in the pump (Kafeel et al., 2021). However, the absence of frequency peaks above the BPF complicates fault determination, as vibration velocities beyond the BPF fail to provide conclusive indications of pump system malfunctions. It underscores the limitations of using vibration velocity in the frequency domain for fault diagnosis in such monitoring scenarios, necessitating complementary diagnostic approaches for comprehensive system assessment.

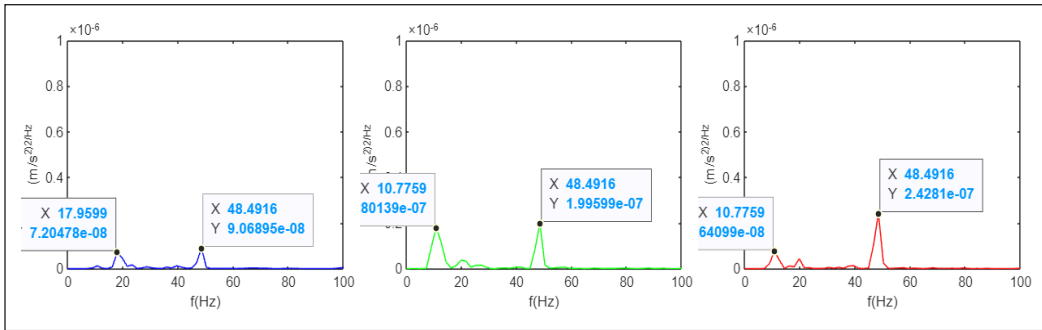


Figure 13. Vibration velocity (frequency domain)—NORMAL CONDITION

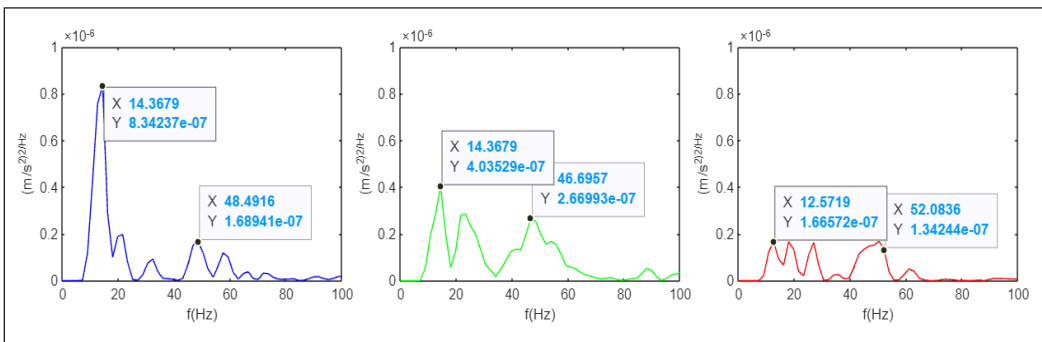


Figure 14. Vibration velocity (frequency domain)—ABNORMAL CONDITION

Vibration Spectrogram Graph

Based on the raw data, vibration spectrograms were generated for normal and abnormal conditions across all axes (Figure 15). During normal conditions, the spectrograms clearly indicate the blade pass frequency (BPF) in all axes, with additional harmonics observed up to $5 \times$ frequency on the X and Z axes. This consistent pattern suggests stable machinery operation and a well-defined frequency distribution. However, in abnormal spectrogram graphs, the smoothness of the graph is notably disrupted, indicating irregularities in vibration patterns. These disruptions are consistent with cavitation effects, which can cause fluctuating and erratic patterns in the spectrogram. These disruptions may signify the presence of anomalies or faults within the system, potentially leading to inefficiencies or malfunctions. Further analysis of the abnormal spectrogram graphs is warranted to pinpoint the specific nature and severity of these irregularities, facilitating timely intervention and maintenance to ensure optimal system performance and reliability.

The investigation into vibration patterns in both time and frequency domains, alongside spectrogram data analysis, reveals key findings consistent with prior research. Under normal operating conditions, stable machinery performance is indicated by consistent patterns

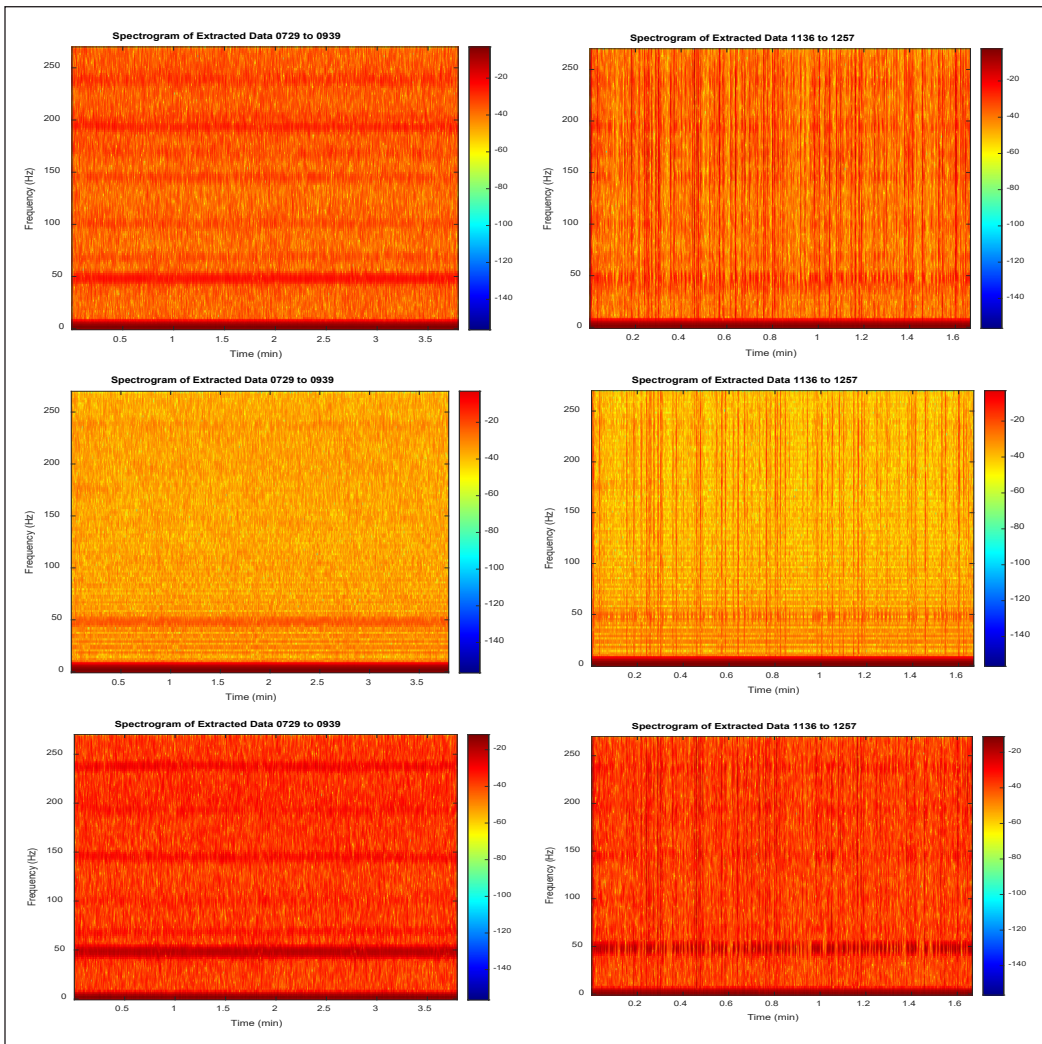


Figure 15. Vibration spectrogram graph during NORMAL conditions (left) and ABNORMAL conditions (right) for all axes, respectively

across various axes, including blade pass frequency (BPF) and harmonics (Bai et al., 2019). Conversely, abnormal conditions exhibit significant deviations from these established patterns, manifesting irregularities in vibration intensity and frequency distribution (Karagiovanidis et al., 2023). This discrepancy suggests the presence of anomalies or faults within the system, aligning with previous studies investigating factors such as cavitation or mechanical wear (Krishnachandran et al., 2020). Furthermore, the limitations of vibration velocity analysis in the frequency domain for fault diagnosis underscore the need for complementary diagnostic approaches. Overall, the comprehensive analysis of vibration data reveals valuable insights into the operational status of the pump system, highlighting

the importance of continuous monitoring and proactive maintenance to ensure optimal performance and reliability.

The outcomes of this study represent a significant advancement in the domain of water pump monitoring, particularly in the context of cavitation detection. The amalgamation of the ADXL345 accelerometer with Arduino Mega2560 has demonstrated its practicality and affordability in discerning irregularities within water pumps during operational phases (Hasibuzzaman et al., 2020). Specifically, the discernible rise in mean amplitude (RMS) during cavitation occurrences, compared to normal conditions, is a robust indicator of anomalous pump activity. This finding holds paramount importance as it furnishes a precise and quantifiable parameter for identifying cavitation, a phenomenon notorious for its detrimental effects on pump components.

However, it is important to note that while the Arduino Mega2560 coupled with the ADXL345 accelerometer shows promise, a direct comparison with other commercially available or research-grade vibration monitoring systems was not conducted in this study. Prior research, such as the work by Al-Haddad et al. (2024), has demonstrated the effectiveness of advanced vibration-current data fusion techniques and sophisticated classifiers like gradient boosting for enhanced fault detection in motors, suggesting that more complex systems may offer improved accuracy. Similarly, Jaber and Bicker (2017) highlight the potential of wireless fault detection systems that utilise statistical control charts to achieve real-time monitoring in industrial environments. Such comparisons would be valuable in assessing the relative performance, accuracy, and cost-effectiveness of the Arduino-based system. This gap presents an opportunity for future research to benchmark the system against established technologies, which could further validate its potential for broader industrial adoption.

The findings of this study not only validated the viability of Arduino Mega2560 coupled with the ADXL345 accelerometer for cavitation detection but also presented prospects for cost-effective and efficacious monitoring of water pump systems across various applications. However, while the affordability of the Arduino-based system is an important consideration, it is crucial to note that this study does not delve into a detailed cost-benefit analysis. The primary objective of this research is to evaluate the technical capability of the Arduino Mega2560 and MEMS accelerometer in capturing real-time faults within a water pump system. A comprehensive cost-benefit analysis, though valuable, falls outside the scope of this work and is suggested as an area for future research. The emphasis here remains on demonstrating the system's ability to detect faults reliably and efficiently, contributing to its potential application in various industrial contexts where real-time monitoring is essential. This research lays the groundwork for the integration of readily available technology into industrial contexts, fostering a proactive approach towards pump maintenance and system integrity.

CONCLUSION

This study demonstrated the effectiveness of the ADAQ in accurately monitoring the vibration conditions within water pump motors. By employing the Fast Fourier Transform (FFT) method and incorporating spectrogram analysis, valuable insights into pump performance and anomalies were obtained, laying the groundwork for proactive maintenance strategies. The integration of ADAQ offers a reliable approach for assessing water pump operational integrity and holds potential for predictive maintenance in industrial settings. However, while the current methodology has proven effective, there are opportunities for further refinement and enhancement.

Future research could explore the integration of advanced machine learning algorithms to further improve the accuracy and reliability of anomaly detection in vibration data. These algorithms could be trained to recognise subtle patterns that may precede mechanical failures, allowing for even earlier intervention. Additionally, expanding the ADAQ system to include real-time monitoring capabilities and wireless data transmission would increase its applicability in more complex industrial environments. Another potential area for improvement is the incorporation of multi-sensor fusion, which would allow for a more comprehensive assessment of pump health by combining data from multiple types of sensors, such as temperature, pressure, and flow rate, alongside vibration data.

Moreover, the current study primarily focused on detecting cavitation-related anomalies. Future studies could investigate the applicability of the ADAQ system to detect other common faults in water pumps, such as misalignment, imbalance, and bearing defects. This would further validate and expand the versatility of the ADAQ in various operational contexts.

In conclusion, while the ADAQ system has demonstrated significant potential in water pump monitoring, future research directions and improvements will contribute to developing even more robust and sophisticated vibration monitoring systems, ultimately leading to optimised maintenance practices and increased operational reliability in water pump operations.

ACKNOWLEDGMENTS

The first author sincerely thanks the Public Service Department of Malaysia for their scholarship support. The authors also express their gratitude to the Public Works Department Malaysia for the research funding provided for this project and to the University Putra Malaysia for its laboratory facilities and expertise.

REFERENCES

- Abdulaziz, A. M., & Kotb, A. (2017). Detection of pump cavitation by vibration signature. *Australian Journal of Mechanical Engineering*, 15(2), 103–110. <https://doi.org/10.1080/14484846.2015.1093261>

- Adeodu, A., Daniyan, I., Omitola, O., Ejimuda, C., Agbor, E., & Akinola, O. (2020). An adaptive industrial internet of things (IIoTs) based technology for prediction and control of cavitation in centrifugal pumps. *Procedia CIRP*, 91, 927–934. <https://doi.org/10.1016/j.procir.2020.03.125>
- Adli, B., & Rusmin, P. H. (2020). Vibration measuring tools for rotary pumping machine with accelerometer MEMS sensor. In *2020 FORTEI-International Conference on Electrical Engineering (FORTEI-ICEE)* (pp. 69-74). IEEE Publishing. <https://doi.org/10.1109/FORTEI-ICEE50915.2020.9249860>
- Agnoletti, L., Pedotti, S., Zago, R. M., Giesbrecht, M., & Fruett, F. (2020). Low-cost MEMS accelerometer network for rotating machine vibration diagnostics analyzing machine vibration. *IEEE Instrumentation & Measurement Magazine*, 23(7), 25-33. <https://doi.org/10.1109/MIM.2020.9234762>
- Al-Haddad, L. A., Jaber, A. A., Hamzah, M. N., & Fayad, M. A. (2024). Vibration-current data fusion and gradient boosting classifier for enhanced stator fault diagnosis in three-phase permanent magnet synchronous motors. *Electrical Engineering*, 106(3), 3253–3268. <https://doi.org/10.1007/s00202-023-02148-z>
- Altherr, L. C., Leise, P., Pfetsch, M. E., & Schmitt, A. (2019). Resilient layout, design and operation of energy-efficient water distribution networks for high-rise buildings using MINLP. *Optimization and Engineering*, 20(2), 605–645. <https://doi.org/10.1007/s11081-019-09423-8>
- ALTobi, M. A. S., Bevan, G., Wallace, P., Harrison, D., & Ramachandran, K. P. (2019). Centrifugal pump condition monitoring and diagnosis using frequency domain analysis. In *Applied Condition Monitoring* (Vol. 15, pp. 122–131). Springer. https://doi.org/10.1007/978-3-030-11220-2_13
- Arunraj, N. S., & Maiti, J. (2007). Risk-based maintenance-Techniques and applications. *Journal of Hazardous Materials*, 142(3), 653–661. <https://doi.org/10.1016/j.jhazmat.2006.06.069>
- Bai, L., Zhou, L., Jiang, X., Pang, Q., & Ye, D. (2019). Vibration in a multistage centrifugal pump under varied conditions. *Shock and Vibration*, 2019, 1–9. <https://doi.org/10.1155/2019/2057031>
- Chen, L., Wei, L., Wang, Y., Wang, J., & Li, W. (2022). Monitoring and predictive maintenance of centrifugal pumps based on smart sensors. *Sensors*, 22(6), Article 2106. <https://doi.org/10.3390/s22062106>
- Dutta, N., Kaliannan, P., & Subramaniam, U. (2020). Effect of motor vibration problems on power quality of water pumping at residency. *IOP Conference Series: Materials Science and Engineering*, 937(1), Article 012019. <https://doi.org/10.1088/1757-899X/937/1/012019>
- Ejimuda, C. (2020). Development and prediction of cavitation in centrifugal pumps using industrial internet of things technology. In *SPE Nigeria Annual International Conference and Exhibition* (p. D013S006R012). SPE Publishing. <https://doi.org/10.2118/203661-MS>
- Feng, G. J., Gu, J., Zhen, D., Aliwan, M., Gu, F. S., & Ball, A. D. (2015). Implementation of envelope analysis on a wireless condition monitoring system for bearing fault diagnosis. *International Journal of Automation and Computing*, 12(1), 14–24. <https://doi.org/10.1007/s11633-014-0862-x>
- Guimarães, T. A., & de Oliveira Filho, R. H. (2021). Analysis of vibration signals produced by the cavitation in centrifugal pumps using the Power Spectrum and Continuous Wavelet Transform. *Revista Brasileira de Ciência, Tecnologia e Inovação*, 5(1), 1-12. <https://doi.org/10.18554/rbcti.v5i1.3413>
- Hajnayeb, A., Azizi, R., Ghanbarzadeh, A., & Changizian, M. (2017). Vibration-based cavitation detection in centrifugal pumps. *Diagnostyka*, 18(3), 77–83.

- Hasibuzzaman, M., Shufian, A., Shefa, R. K., Raihan, R., Ghosh, J., & Sarker, A. (2020). Vibration measurement & analysis using arduino based accelerometer. In *2020 IEEE Region 10 Symposium (TENSYPMP)* (pp. 508-512). IEEE Publishing. <https://doi.org/10.1109/TENSYPMP50017.2020.9230668>
- Jaber, A. A., & Bicker, R. (2017). Wireless fault detection system for an industrial robot based on statistical control chart. *International Journal of Electrical and Computer Engineering*, *7*(6), 3421–3435. <https://doi.org/10.11591/ijece.v7i6.pp3421-3435>
- Jardine, A. K. S., Lin, D., & Banjevic, D. (2006). A review on machinery diagnostics and prognostics implementing condition-based maintenance. *Mechanical Systems and Signal Processing*, *20*(7), 1483–1510. <https://doi.org/10.1016/j.ymssp.2005.09.012>
- Kafeel, A., Aziz, S., Awais, M., Khan, M. A., Afaq, K., Idris, S. A., Alshazly, H., & Mostafa, S. M. (2021). An expert system for rotating machine fault detection using vibration signal analysis. *Sensors*, *21*(22), Article 7587. <https://doi.org/10.3390/s21227587>
- Karagiovanidis, M., Pantazi, X. E., Papamichail, D., & Fragos, V. (2023). Early detection of cavitation in centrifugal pumps using low-cost vibration and sound sensors. *Agriculture*, *13*(8), Article 1544. <https://doi.org/10.3390/agriculture13081544>
- Kiliç, R., Kozan, R., Karayel, D., & Özkan, S. S. (2017). Application of predictive maintenance system in drinking water pumping stations. *Acta Physica Polonica A*, *132*(3), 1016–1021. <https://doi.org/10.12693/APhysPolA.132.1016>
- Kondaveeti, H. K., Kumaravelu, N. K., Vanambathina, S. D., Mathe, S. E., & Vappangi, S. (2021). A systematic literature review on prototyping with arduino: Applications, challenges, advantages, and limitations. *Computer Science Review*, *40*, Article 100364. <https://doi.org/10.1016/j.cosrev.2021.100364>
- Krishnachandran, Samson, A., & Rajan, A. (2020). Condition monitoring of cavitation-induced centrifugal pump. In A. Suryan, D. H. Doh, M. Yaga & G. Zhang (Eds.), *Recent Asian Research on Thermal and Fluid Sciences* (pp. 393–408). Springer. https://doi.org/10.1007/978-981-15-1892-8_31
- Lee, C. Y., & Le, T. A. (2020). Intelligence bearing fault diagnosis model using multiple feature extraction and binary particle swarm optimization with extended memory. *IEEE Access*, *8*, 198343–198356. <https://doi.org/10.1109/ACCESS.2020.3035081>
- Lourenço, M., Silva-Afonso, A., & Pimentel-Rodrigues, C. (2022). Performance indicators for water supply in buildings. *WSEAS Transactions on Environment and Development*, *18*, 1115–1128. <https://doi.org/10.37394/232015.2022.18.106>
- Midiani, L. P. I., Irawan, I. M. D., Bangse, K., & Gunung, I. N. (2023). Design of clean water booster pump for high-rise buildings. *LOGIC: Jurnal Rancang Bangun Dan Teknologi*, *23*(3), 203–211. <https://doi.org/10.31940/logic.v23i3.203-211>
- Mones, Z., Feng, G., Ogbulaor, U. E., Wang, T., Gu, F., & Ball, A. D. (2016). Performance evaluation of wireless MEMS accelerometer for reciprocating compressor condition monitoring. In *Power Engineering: Proceedings of the International Conference on Power Transmissions 2016 (ICPT 2016)* (pp. 893-900). Taylor & Francis. <https://doi.org/10.1201/9781315386829-129>
- Ogaili, A. A. F., Jaber, A. A., & Hamzah, M. N. (2023). Wind turbine blades fault diagnosis based on vibration dataset analysis. *Data in Brief*, *49*, Article 109414. <https://doi.org/10.1016/j.dib.2023.109414>

- Pan, T., & Zhu, Y. (2018). Getting started with Arduino. In T. Pan & Y. Zhu (Eds.), *Designing Embedded Systems with Arduino* (pp. 3–16). Springer. https://doi.org/10.1007/978-981-10-4418-2_1
- Rezali, K. A. M., Rahim, S. A., Hassan, A. B. M., Abidin, A. M. Z., Khalid, S. N. A., & Mohd, A. B. (2022, July 24–28). *Development of an Arduino data acquisition system for condition-based monitoring* [Paper Presentation]. Proceedings of the International Congress on Sound and Vibration, 28th International Congress on Sound and Vibration, ICSV, Singapore.
- Smith, R., & Hawkins, B. (2004). *Lean maintenance: Reduce costs, improve quality, and increase market share*. Elsevier.
- Sainz-Raso, J., Martin, S., Diaz, G., & Castro, M. (2023). Security management on arduino-based electronic devices. *IEEE Consumer Electronics Magazine*, 12(3), 72–84. <https://doi.org/10.1109/MCE.2022.3184118>
- Sanchez, W., Carvajal, C., Poalacin, J., & Salazar, E. (2018). Detection of cavitation in centrifugal pump for vibration analysis. In *2018 4th International Conference on Control, Automation and Robotics (ICCAR)* (pp. 460–464). IEEE Publishing. <https://doi.org/10.1109/ICCAR.2018.8384720>
- Shibnauth, V. D., & Surnam, B. Y. R. (2015, April 20–21). *Issues affecting water distribution systems* [Paper Presentation]. International Conference on Computer Science, Data Mining & Mechanical Engineering (ICCDMMME), Bangkok, Thailand. <https://doi.org/10.15242/II.E.0415025>
- Sun, H., Yuan, S., & Luo, Y. (2018). Cyclic spectral analysis of vibration signals for centrifugal pump fault characterization. *IEEE Sensors Journal*, 18(7), 2925–2933. <https://doi.org/10.1109/JSEN.2018.2804908>
- Sunal, C. E., Dyo, V., & Velisavljevic, V. (2022). Review of machine learning based fault detection for centrifugal pump induction motors. *IEEE Access*, 10, 71344–71355. <https://doi.org/10.1109/ACCESS.2022.3187718>
- Tian, Q., Lin, C., Hu, R., Ya, C., & Xu, S. (2022). Numerical and experimental investigations on cavitation characteristics of inducer and impeller combination fuel pumps. In *CSAA/IET International Conference on Aircraft Utility Systems (AUS 2022)* (Vol. 2022, pp. 1369–1376). IET Publishing. <https://doi.org/https://doi.org/10.1049/icp.2022.1872>
- Van Der Schee, W. G. (2009, September 7–9). *Water systems in high rise residential buildings, guidelines for design and construction*. [Paper Presentation]. The 35th International Symposium CIB W062 on Water Supply and Drainage for Buildings, Düsseldorf, Germany.
- Yehl, C. C., Member, S., Sizovl, G. Y., Sayed-Ahmed, A., Povinellil, R. J., Member, S., Yazl, E. E., & Ionel, D. M. (2008). A reconfigurable motor for experimental emulation of stator winding inter-turn and broken bar faults in polyphase induction machines. *IEEE Transactions on Energy Conversion*, 23(2), 1005–1014. <https://doi.org/10.1109/TEC.2007.914201>
- Zhou, J., Li, X., Andernroomer, A. J., Zeng, H., Goh, K. M., Wong, Y. S., & Hong, G. S. (2005). Intelligent prediction monitoring system for predictive maintenance in manufacturing. In *31st Annual Conference of IEEE Industrial Electronics Society, 2005. IECON 2005* (pp. 6–pp). IEEE Publishing. <https://doi.org/10.1109/IECON.2005.1569264>
- Zhou, Y., Lee, E. W. M., Wong, L. T., & Mui, K. W. (2021). Environmental evaluation of pump replacement period in water supply systems of buildings. *Journal of Building Engineering*, 40, Article 102750. <https://doi.org/10.1016/j.jobe.2021.102750>

Temperature-corrected Performance Ratio of Grid-Connected Photovoltaic System: Tropical versus Continental Climate

Siti Nor Nadhirah Ibrahim¹, Hedzlin Zainuddin^{1,2*} and Shahril Irwan Sulaiman³

¹Faculty of Applied Sciences, Universiti Teknologi MARA, 40450 Shah Alam, Selangor, Malaysia

²Faculty of Applied Sciences, SPECTRA Research Interest Group, Universiti Teknologi MARA, 40450 Shah Alam, Selangor, Malaysia

³School of Electrical Engineering, College of Engineering, Universiti Teknologi MARA, 40450 Shah Alam, Selangor, Malaysia

ABSTRACT

Performance ratio (*PR*) is often used as a performance metric in commercial acceptance tests of an installed grid-connected photovoltaic (GCPV) system. Recently, *PR* has been claimed to significantly affect seasonal and weather variations, which would invite unnecessary risk to the commercial acceptance test. In the updated IEC 61724-1, the temperature-corrected performance ratio (*TCPR*) has been included as the performance metric to remove the seasonal and weather variations. However, not all climate regions experience these variations, which means that *TCPR* might not be necessary for certain climate regions. Due to that, this study aims to analyse the relevancy of determining *TCPR* in addition to the normal *PR* for GCPV systems for different climate regions. The analysis was conducted using PVsyst software by comparing the *PR* and *TCPR* of two similar GCPV systems: case A represents tropical climate and case B represents continental climate. The results evidently show that the *PR* and *TCPR* values are always very close for both climate regions if analysed annually. However, when analysed monthly, the normal *PR* varied significantly between 77.5% and 90.0%, indicating a 12.5% difference for continental climate, but for tropical climate, the difference is just 1.0%. Conversely, the monthly *TCPR* variation in the continental climate is insignificant, with the value ranging from 81.4% to 84.1%, indicating only a 2.7% difference. Thus,

the results of this study suggest that both *PR* and *TCPR* are relevant for continental climate. However, normal *PR* alone is already sufficient for tropical climate as the performance metric.

ARTICLE INFO

Article history:

Received: 29 May 2024

Accepted: 18 November 2024

Published: 21 February 2025

DOI: <https://doi.org/10.47836/pjst.33.2.10>

E-mail addresses:

sitinnadhirahibrahim251@gmail.com (Siti Nor Nadhirah Ibrahim)

hedz1506@uitm.edu.my (Hedzlin Zainuddin)

shahril@uitm.edu.my (Shahril Irwan Sulaiman)

* Corresponding author

Keywords: Continental, grid-connected photovoltaic, Koppen Geiger climate classification, performance ratio, PVsyst, temperature-corrected performance ratio, tropical

INTRODUCTION

The solar photovoltaic (PV) energy sector has long been hailed as one of the most promising sources of electricity (Comello et al., 2018). According to the International Energy Agency (IEA), by 2027, solar PV will have exceeded coal's installed power capacity, making it the largest electricity source in the world. The cumulative solar PV capacity is forecasted to nearly triple during the forecast period, increasing by almost 1500 GW, surpassing natural gas by 2026 and coal by 2027. This achievement is due to several factors. One is utility-scale solar PV, the least expensive option for new electricity generation in most countries worldwide despite rising commodity prices. Higher retail electricity prices and growing policy support to help consumers save money on their energy bills will also spur the growth of distributed solar PV, such as rooftop solar on buildings (International Energy Agency, 2022). Solar PV industry benefits extend beyond electricity generation.

As PV capacity increases worldwide, assessing the predicted performance of solar PV systems has become significantly important to determine whether they are suitable for a particular location. Many technical and climatic factors can influence PV system performance, such as irradiation, orientation, temperature, wind speed, humidity, PV module technology, dust, and degradation. There are a few parameters used to analyse the performance of GCPV systems, which include energy production, daily yield, annual yield, seasonal yield, reference yield (Y_r), final yield (P_f), array yield (Y_A), capacity factor (CF), system efficiencies, system losses and performance ratio (Anang et al., 2021; Ibrahim et al., 2023).

Performance ratio (PR) quantifies the overall effect of losses of a GCPV system. The seven main loss factors include temperature, mismatch, soiling, ageing, shading, inverter efficiency, and cable efficiency (SEDA, 2023). Temperature is often the highest contributor to GCPV system performance loss (Dey & Subudhi, 2020; Rout & Kulkarni, 2020; Abdullah et al., 2022; Vidur & Jagwani, 2022; Ibrahim et al., 2023; Rahim et al., 2024). A study conducted by Rahim et al. (2024) in Malaysia assessed the performance of a 10 kW_p GCPV system. The findings indicated that actual temperature loss could account for up to 8%, while soiling, cable, and mismatch each account for 3% losses. Mismatch accounted for an additional 2% in losses, and ageing was found to contribute the least, at 0.6%, based on simulation results. Another study was conducted in Malaysia to evaluate the performance of a 2.84 kW_p GCPV system and found that the temperature loss can reach a maximum value of 14%. At the same time, 3% each of soiling and cable losses, 2% each of mismatch and inverter losses, and 0.63% of ageing and shading are assumed to be none (Ibrahim et al., 2023).

Temperature is influenced by weather and seasonal variations. Season and weather notably affect PR through ambient temperature (T_{amb}) variations, consequently influencing the PV module temperature (T_{mod}). During high T_{amb} , T_{mod} increases, causing PR to decrease and vice versa. Due to the weather and seasonal variations, PR brings forth which

locations will yield the most productive GCPV system. *PR* is often used as a benchmark value in agreement among PV system installers and owners. Unfortunately, associated with this dependence on the weather and seasons is a bias error in the metric, which introduces unnecessary risk during testing and commissioning (T&C) (Dierauf et al., 2013).

T&C is a procedure that verifies the system's safe installation and faultless operation. The acceptable *PR* is a minimum of 0.75 to pass the Reliability Run Test under T&C. The T&C procedure requires measuring GCPV system output continuously, sampled at five-minute intervals for a minimum of seven consecutive days. The data measured is defined as expected output. Historical weather data is also required to be extracted via simulation software, such as Meteonorm, Solcast and Solargis, which are defined as predicted output (MS 2692, 2020). It is fair for the PV installer and owner to specify an annualised *PR* in the contract in the T&C, giving a rough idea of how much energy the PV owner will receive for one whole year. However, the variation in season and weather of the measurement affects the annual *PR*, leading to unnecessary risk for both parties. *PR* can swing entirely over a single day. *PR* is also expected to show a significant difference based on its monthly value. For example, during summer months, *PR* is expected to be lower than in winter months due to low T_{amb} indicating underprediction, which is a risk for PV installers, while high *PR* during winter months indicates overprediction, which is a risk for PV owners (Dierauf et al., 2013).

Globally, various regions are experiencing different climates. According to Köppen-Geiger climate classification, there are five major groups of climates, including tropical (A), arid (B), temperate (C), continental (D), and polar (E), which are then divided into 30 subgroups. The first letter of the subgroups represents the type of seasonal precipitation, while the second letter represents the T_{amb} levels (Triantafyllou & Tsonis, 1994; Kottek et al., 2006; Chen & Chen, 2013; Beck et al., 2018). This study will focus on two groups, tropical and continental climates since these groups exhibit characteristics that contrast each other in terms of variations of T_{amb} throughout the year. It is important to address their climate criteria, especially T_{amb} , since this will impact the *PR* of the GCPV system installed in these climate regions. Interestingly, no subgroup of T_{amb} is defined for the tropical climate, only the precipitation, since all subgroups of tropical climate experience the minimum T_{amb} of 18°C throughout the year. The tropical climate has a small range of the monthly average of T_{amb} , which is between 25°C and 28°C (Costa et al., 2023). However, Tropical climate could notably reach an average maximum of 35°C (U.S. Department of Commerce, 2023). Conversely, the continental climate generally has an average T_{amb} of the hottest month more than 10°C and an average T_{amb} of the coldest month less than or equal to 0°C.

Previous studies have shown that seasonal and weather variations affecting *PR* can be mitigated by referencing a 25°C T_{amb} under standard test conditions (STC) (Limmanee et

al., 2016; Prakhya & Kotha, 2018; Quansah & Adaramola, 2019; Karahüseyin & Abbasoğlu, 2022; Ogliari et al., 2023; Wassie & Ahlgren, 2023). This method usually results in a higher *PR* because modules more frequently operate at 45°C. While it essentially solves the problem of seasonal variations, it overestimated the actual performance, thus, incapacitated *PR* assessment based on the effect of local climate. For that reason, correction to 25°C is not an acceptable method for removing the seasonal variability in the *PR* metric because it would overestimate *PR*.

Therefore, the National Renewable Energy Laboratory (NREL) started to highlight and introduce temperature-corrected performance ratio (*TCPR*) as a new metric to assess the performance of a GCPV system, followed by the International Electrotechnical Commission (IEC). In the updated international standard of PV monitoring, *TCPR* was included to remove seasonal and weather variations without overestimating the actual annual *PR*. *TCPR* is able to estimate the annual *PR* regardless of the duration of the reporting period. It is expected to discard large seasonal and weather variations by incorporating the estimated annual average module temperature (Dierauf et al., 2013; IEC 61724, 2021). Therefore, *TCPR* is implemented by NREL and IEC61724-1:2021, introducing a power rating temperature adjustment factor ($C_{k,annual}$), which incorporates the annual average of module temperature ($T_{mod,annual-avg}$), which can be estimated by computing an irradiance-weighted average of the predicted module temperature (T_{mod}), and the value is chosen based on historical weather data for the specific site. It will reduce unnecessary risk from the effects of significantly high or significantly low T_{amb} on *PR* during the T&C since the $T_{mod,annual-avg}$ has been considered. It is particularly significant for climates with a wide range of annual T_{amb} , as in the continental climate. However, for the tropical climate, which experiences low annual T_{amb} variation throughout the year, the relevancy of *TCPR* is worth questioning and further studying.

A few studies have assessed the performance of GCPV systems using *TCPR*. A study was conducted using an installed PV system in Seville, Spain. This study has applied *TCPR* to account for the temperature effects on two different PV module technologies, thin film and monocrystalline silicon. The application of *TCPR* allows for a more standardised comparison between the two technologies (Sánchez-Lanuza et al., 2024). Next, a study analysed the impact of cell temperature on the performance ratio (*PR*) of photovoltaic (PV) systems through experimental and numerical methods. It found that higher cell temperatures lead to decreased *PR*, lowering system efficiency, especially in warmer climates like the Mediterranean, where managing temperature is key to maintaining performance (De Masi et al., 2024). A study evaluated the *PR* and *TCPR* of a utility-scale GCPV system under controlled spectral influences: airmass and precipitable water. The study took place in Northern Cape, South Africa, which is classified under an arid climate region. The results showed that *PR* is overestimated during winter and underestimated during summer. By comparing *PR* and

TCPR, *TCPR* showed more leveled results with low monthly fluctuations for the entire year. This indicated that *TCPR* is relevant in the arid climate region (Daniel-Durandt & Rix, 2022). Besides that, a study was conducted in Gozo, Malta, under a temperate climate region to analyse and compare 56 GCPV systems' output over one year. The systems involved ranged from residential to large-scale size. A comparison of *PR* and *TCPR* showed a close value of 61% and 62%, respectively. It indicated that *TCPR* is not relevant for performance assessment in the temperate climate region (Micallef & Staines, 2022).

Another study assessed a 3 kW_p GCPV system performance located in the tropical climate region at Sakon Nakhon, Thailand. By comparing *PR* and *TCPR*, the results show that monthly *PR* has larger variations compared to *TCPR*, with standard deviations of 2.39 and 5.07, respectively. This study suggested that *TCPR* is a relevant performance metric despite the tropical climate having low annual T_{amb} variations (Sathiracheewin et al., 2020). Conversely, research by Syahputra et al. (2018) showed that monthly *PR* values exhibit close variations compared to *TCPR* with standard deviations of 5.16 and 5.17, respectively. This study suggests that *TCPR* may not be essential for performance assessment in tropical climate regions. Additionally, a study by Gopi et al. (2021) assessed the performance of a 2 MW_p GCPV system conducted in Kerala, India, which under tropical climate showed similar results of small variations to those of Syahputra et al. (2018). *PR* reached a maximum value of 77.56% in January and went down to 74.07% in March. At the same time, *TCPR* varies from 77.61% to 74.88%. This result leads to the conclusion that *TCPR* is not relevant for performance assessment in the tropical climate region. Consequently, the necessity of evaluating *TCPR* in continental climate regions is also called into question, given the contrasting characteristics of these two climates. It is worth highlighting that the main differences between tropical and continental climates are the fluctuations of T_{amb} and four distinct seasonal variations. The tropical climate has consistent T_{amb} throughout the year with no four distinct seasons, while the opposite is true for the continental climate. Despite comparing the value of *PR* and *TCPR*, this study did not quantify the deviations between these two metrics. The relevance and necessity of applying *TCPR* remain ambiguous and inconclusive, and a quantitative comparison of the two metrics, especially monthly, is not provided. This study seeks to address the gap in the literature by comparing the monthly and annual *PR* and *TCPR* of GCPV systems in tropical and continental regions. The analysis will be conducted using PV design and simulation software PVsyst.

METHODS

The framework of this study consists of two main parts: proving the role of $C_{k,annual}$ on the *TCPR* mathematical model to remove seasonal and weather variations and comparing the *PR* and *TCPR* for two case studies, as illustrated in Figure 1. The cases were the GCPV

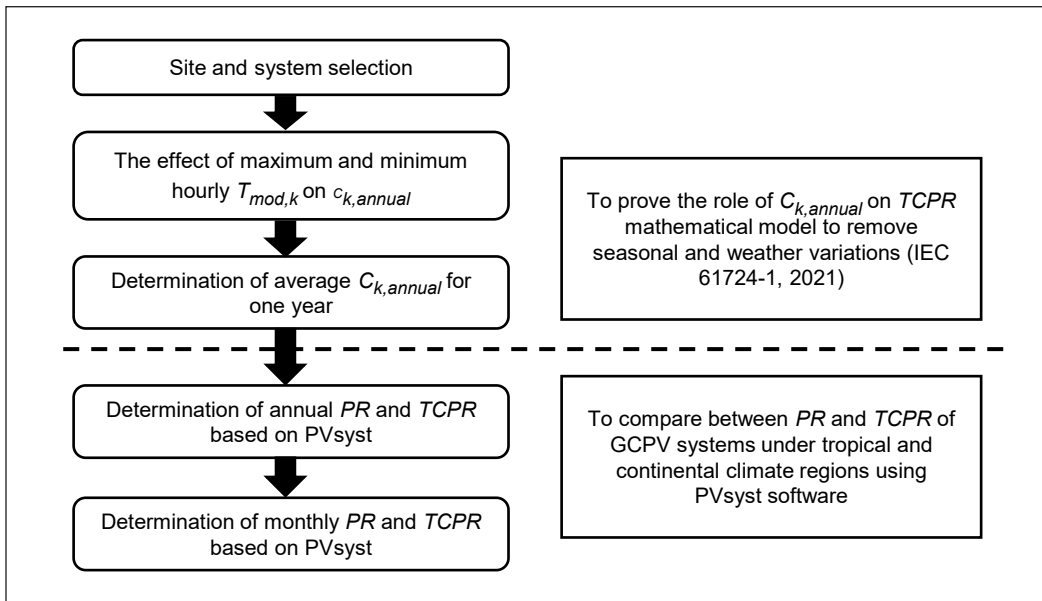


Figure 1. The study framework corresponding to the objectives

system located at Negeri Sembilan, Malaysia, under a tropical climate (referred to as Case A), and the GCPV system located at Almaty, Kazakhstan, under a continental climate (referred to as Case B).

Site and System Selection

The sites representing the two cases of tropical and continental climates were selected based on the Köppen-Geiger climate classification. Negeri Sembilan, Malaysia, has been selected to represent A_f , known as the tropical rainforest climate, while Almaty, Kazakhstan, represents D_{fa} , the hot summer continental climate with wet winters. The A_f climate is characterised by consistently high T_{amb} all year round, with the average monthly T_{amb} remaining above 18°C . There are no distinct seasonal variations, and this climate experiences substantial rainfall throughout the year without a dry season. On the other hand, the D_{fa} climate experiences a relatively hot summer, with T_{amb} frequently exceeding 30°C . Winters are cold, with T_{amb} falling below -3°C , often resulting in snowfall and frost. This climate sees more precipitation during the summer, while winters tend to be drier. Table 1 presents the selected sites with their corresponding coordinates. The two selected GCPV systems have been designed using identical technical specifications: the sizing ratio, the PV module specifications and the inverter specifications, as tabulated in Tables 2 and 3. The systems have a 10 kW_p PV array capacity and a 9 kW AC inverter. The PV modules were in $2 \text{ parallel} \times 20 \text{ series}$ configurations and ground-mounted.

Table 1
Sites for different climates and their coordinates

Case	Site	Climate	Coordinates	
			Latitude	Longitude
A	Negeri Sembilan, Malaysia	A _f	2.7297 °N	101.9381 °E
B	Almaty, Kazakhstan	D _{fa}	43.2500 °N	76.9167 °E

Table 2
PV module specifications

Specifications	Unit	
Technology	-	Polycrystalline
Maximum power at STC	W _p	250
Open circuit voltage	V	37.47
Short circuit current	A	8.76
Maximum power voltage	V	30.34
Maximum power current	A	8.24
Temperature coefficient of voltage	%°C ⁻¹	-0.34
Temperature coefficient of current	%°C ⁻¹	0.04
Temperature coefficient of power	%°C ⁻¹	-0.44

Technical Performance Evaluation Based on IEC 61724-1 (2021)

There are a few parameters under technical performance evaluation based on IEC 61724-1 (2021), which include DC energy (E_A), AC energy (E_{out}), PV array energy yield (Y_A), reference yield (Y_r), final yield (Y_f), PR , and the most recent parameter, is the $TCPR$. PR can be expressed as Equation 1:

$$PR = \left(\frac{E_{out}}{P_0}\right) / \left(\frac{H_{poa}}{G_{poa,ref}}\right) \tag{1}$$

where E_{out} is the AC output energy of the PV array in the unit (kWh), P_0 is the array power rating on the DC side in the unit (kW), H_{poa} is in-plane irradiation in the unit (kWh/m²), and $G_{poa,ref}$ is the irradiance at STC which is 1 kW/ m². However, PR can also be expressed as Equation 4 by expanding E_{out} as Equation 2 and H_{poa} as Equation 3 and moving P_0 to the denominator:

$$E_{out} = \sum_k P_{out,k} \times \tau_k \tag{2}$$

Table 3
Inverter specifications

Specifications	Unit	
Nominal power	kW	9.0
Maximum voltage	V	950
MPPT voltage	V	420..800
Maximum AC current	A	42
No. of MPPT	-	2
No. of inverter	-	1
Inverter efficiency	%	97.0

$$H_{poa} = \sum_k G_{poa,k} \times \tau_k \tag{3}$$

$$PR = \left(\sum_k P_{out,k} \times \tau_k \right) / \left(\sum_k \left(\frac{P_0 \times G_{poa,k} \times \tau_k}{G_{poa,ref}} \right) \right) \tag{4}$$

where P_{out} is the power output at the AC side, G_{poa} is in-plane irradiance in unit (kW/ m²), and τ is the time interval at the k^{th} recording interval within a reporting period in unit (h). On the other hand, $TCPR$ can be expressed as Equation 5:

$$TCPR = \left(\sum_k P_{out,k} \times \tau_k \right) / \left(\sum_k \left(\frac{(C_{k,annual} \times P_0) \times G_{poa,k} \times \tau_k}{G_{poa,ref}} \right) \right) \tag{5}$$

where $C_{k,annual}$ is the power rating temperature adjustment factor. It is the unique and distinctive parameter added to the previous PR equation and becomes the $TCPR$ parameter. This parameter serves to account for monthly temperature variations in a GCPV system by normalising or evening out the monthly PR throughout the year. It achieves this by compensating for the impact of temperature changes across different seasons and weather conditions using the annual average module temperature $T_{mod,annual-avg}$. Since $TCPR$ is designed to estimate the annual PR regardless of the reporting period’s length, all $T_{mod,k}$ values in the $TCPR$ calculations are balanced or neutralised by the $T_{mod,annual-avg}$, ensuring consistency in each interval calculation. The side-by-side comparison between PR and $TCPR$ is tabulated in Table 4.

Table 4
Comparison between PR and $TCPR$ mathematical model

PR	TCPR
$PR = \frac{(\sum_k P_{out,k} \times \tau_k)}{P_0} / \frac{\sum_k G_{poa,k} \times \tau_k}{G_{poa,ref}}$	$TCPR = \frac{(\sum_k P_{out,k} \times \tau_k)}{P_0} / \frac{\sum_k (C_{k,annual} \times G_{poa,k}) \times \tau_k}{G_{poa,ref}}$ $C_k = 1 + \gamma \times (T_{mod,k} - T_{mod,annual-avg})$ $T_{mod,annual-avg} = \frac{\sum_k (G_{poa,k} \times T_{mod,k})}{\sum_k (G_{poa,k})}$

$C_{k,annual}$ Determination

$C_{k,annual}$ is expected to play a role in removing seasonal and weather variations since it is the power rating temperature adjustment factor. To ensure the $TCPR$ concept is applied correctly, the value of the annual $TCPR$ should be close to the value of the annual PR . Despite the fact that $TCPR$ is expected to correct the monthly PR seasonal and weather variations, $TCPR$ will not overestimate or underestimate the annual PR . Since $C_{k,annual}$ is the only parameter distinguishing between $TCPR$ and PR , mathematically $C_{k,annual}$ should

be approximately one. $C_{k,annual}$ can be expressed as Equation 6:

$$C_{k,annual} = 1 + \gamma \times (T_{mod,k} - T_{mod,annual-avg}) \tag{6}$$

where γ is the relative maximum-power temperature coefficient in unit $^{\circ}\text{C}^{-1}$, $T_{mod,annual-avg}$ is the annual average PV module temperature in unit $^{\circ}\text{C}$ chosen based on historical weather data for the site. It should be calculated by computing an irradiance-weighted average of the predicted module temperature (T_{mod}) in unit $^{\circ}\text{C}$ which can be expressed as Equation 7:

$$T_{mod,annual-avg} = \frac{\sum (G_{poa,k} \times T_{mod,k})}{\sum (G_{poa,k})} \tag{7}$$

$T_{mod,annual-avg}$ is kept constant throughout the monthly calculation of $TCPR$.

In the interest of proving the $TCPR$ concept, the effect of maximum and minimum hourly $T_{mod,k}$ on $C_{k,annual}$ is calculated. Firstly, the hourly raw data was obtained from Solcast for one year (<https://toolkit.solcast.com.au/>). Table 5 presents the sample of raw data obtained from Solcast between 8 a.m. and 7 p.m. for every hour on the 5th of February 2023 for Case A. Next, the raw data took into account daytime data based on the filtration of $G_{poa} \geq 40 \text{ W/m}^2$ due to T_{amb} and T_{mod} reaching an equilibrium state when the G_{poa} reached 40 W/m^2 (Zainuddin, 2014). Then, the T_{mod} was calculated for every hour for one year. For Case A, this study has applied Zainuddin’s (2014) mathematical model, which can be expressed as Equation 8, to calculate T_{mod} , while for Case B, the Tamizhmani et al. (2003) mathematical model was applied, which can be expressed as Equation 9.

$$T_{mod} = -8.58 + 0.02 G_{poa} + 1.53 T_{amb} - 0.58 WS - 0.05 RH \tag{8}$$

Table 5
Environment data sample extracted from Solcast

Date	Period	Time	T_{amb} ($^{\circ}\text{C}$)	G_{poa} (W/m^2)	RH (%)	WS (ms^{-1})
5/2/2023	60min	8:00:00 AM	25	47	95.6	1.8
5/2/2023	60min	9:00:00 AM	26	237	89.9	1.8
5/2/2023	60min	10:00:00 AM	29	460	79.1	1.6
5/2/2023	60min	11:00:00 AM	31	658	70.9	1.8
5/2/2023	60min	12:00:00 PM	32	805	66	1.9
5/2/2023	60min	1:00:00 PM	33	876	61.4	1.8
5/2/2023	60min	2:00:00 PM	34	883	58.5	1.8
5/2/2023	60min	3:00:00 PM	33	647	62.3	1.8
5/2/2023	60min	4:00:00 PM	32	533	66.1	1.7
5/2/2023	60min	5:00:00 PM	32	198	66.2	1.3
5/2/2023	60min	6:00:00 PM	30	101	71.9	1.2
5/2/2023	60min	7:00:00 PM	28	44	80.7	1.2

$$T_{mod} = 4.3 + 0.028 G_{poa} + 0.943 T_{amb} - 1.528 WS \quad [9]$$

WS is the wind speed in the unit (ms^{-1}), and RH is the relative humidity in the unit (%). Afterwards, $T_{mod,annual-avg}$ can be calculated using Equation 7. Lastly, $C_{k,annual}$ was calculated for every hour for one year using Equation 6. The maximum and minimum hourly $T_{mod,k}$, with the respective $C_{k,annual}$, were identified from the one-year data.

Next, the average $C_{k,annual}$ for one year was determined using the same hourly $C_{k,annual}$ data obtained from Solcast. However, instead of assessing the extreme value of $T_{mod,k}$, the yearly average $C_{k,annual}$ has been calculated by averaging the hourly $C_{k,annual}$ for one year. It is to observe the result of $C_{k,annual}$ on a yearly basis.

Comparison Between *PR* and *TCPR* Using PVsyst Simulation

The comparison between *PR* and *TCPR* using PVsyst software involved GCPV systems simulation for cases of tropical and continental climates. The comparison was divided into two main sections: the determination on an annual basis and the determination on every month. The PVsyst simulation has been done by incorporating the mentioned sites and systems selection. The simulation design parameters were kept constant except for meteorological data selection that will represent each climate respectively. PVsyst offers a few meteorological databases, including Meteonorm 8.1, NASA-SSE, PVGIS TMY, NREL, Solcast TMY and SolarAnywhere. Users are allowed to upload their raw data if it matches the PVsyst format. This study selected Meteonorm 8.1 due to its accuracy in in-plane solar irradiation (H_{poa}) data compared to others (Rahim et al., 2024). PVsyst is able to simulate technical, economic, and environmental performance. However, this study is limited to the boundary of technical performance only. Running PVsyst simulation requires the user to incorporate various losses that are expected to affect the GCPV system. These losses were also determined carefully and kept constant for both climates to ensure a fair comparison. Table 6 presents the losses applied in the PVsyst simulation (PVsyst SA, 2024).

The PV array orientations have been selected thoughtfully for both sites since this is a fixed tilt system to avoid losses and ensure a fair comparison between the two climate regions. The tilt angle of a PV array is one of the crucial aspects of harvesting maximum irradiance (Tahsin, 2021). The tilt angle of the PV array was determined by following the rule of thumb, which is based on the latitude of the sites selected (Chen et al., 2018; Chinchilla et al., 2021). For case A, supposedly, the tilt angle is 3° . However, for sites with a latitude of less than 10° , the optimal tilt angle would be 10° to allow rain to naturally wash the PV modules (Jacobson & Jadhav, 2018). For case B, supposedly, the tilt angle is 43° ; even so, considering this study used PVsyst as a simulation tool to assess the performance of the GCPV system, the loss with respect to the optimum features in PVsyst

was considered. Therefore, the tilt angle was adjusted to reach 0% loss. Hence, the tilt angle is 40°. The azimuth angle simply depends on which hemisphere the sites are located in: southern hemisphere: 0° facing north and northern hemisphere: 0° facing south. Table 7 summarises the tilt angle and azimuth angle for both cases.

Table 6
GCPV system losses in PVsyst

No.	Losses	Values	Description/Assumption
1	Field thermal loss factor	29.0 W/m ² K	PVsyst default value (Assuming that the PV array mounting is open rack)
2	Ohmic loss	1.5%	PVsyst default value
3	Module quality	-0.5%	PVsyst default value
4	Light-induced degradation	2.0%	PVsyst default value
5	Module mismatch loss	2.0%	PVsyst default value
6	Strings voltage mismatch	0.15%	PVsyst default value
7	Yearly soiling loss factor	3.0%	PVsyst default value
8	Incidence angle modifier	1.8%	Based on the PV module datasheet
9	Ageing	0%	The system is new (assuming for new installation)
10	Shading loss	0%	Assuming the system is free from shading.

Table 7
GCPV system orientation

Case	Sites	Climate	Tilt angle	Azimuth angle
A	Negeri Sembilan, Malaysia	A _f	10°	0° facing south
B	Almaty, Kazakhstan	D _{fa}	40°	0° facing south

RESULTS AND DISCUSSION

The results are divided into two parts to satisfy the research objectives. The first objective is to prove the role of $C_{k,annual}$ in the $TCPR$ mathematical model to remove seasonal and weather variations (IEC 61724-1, 2021). The second objective is to compare the PR and $TCPR$ of GCPV systems under tropical and continental climate regions using PVsyst software.

The Effect of Maximum and Minimum Hourly T_{mod} on $C_{k,annual}$

$C_{k,annual}$ was calculated by incorporating the maximum and minimum hourly $T_{mod,k}$ into the calculation. The effect of extreme hourly PV module temperatures was analysed to prove the $TCPR$ concept of removing seasonal and weather variations. Based on the PR and $TCPR$ equations, the difference is just adding the $C_{k,annual}$ parameter into the normal PR equation and is later addressed as $TCPR$ (Dierauf et al., 2013; IEC 61724, 2021). This

means $C_{k,annual}$'s value should be approximately one ($C_{k,annual} \approx 1$), so PR and $TCPR$ are close. $C_{k,annual}$ has been calculated to verify that the $TCPR$ concept was applied correctly using raw data extracted from Solcast for tropical and continental climate regions. Table 8 presents the environmental data pertaining to the highest and the lowest T_{mod} of the year based on average hourly data with $C_{k,annual}$ for Case A, while Table 9 for Case B.

Table 8
Extreme T_{mod} (°C) and the $C_{k,annual}$ for Case A

Date	Time	T_{amb} (°C)	G_{poa} (W/m ²)	$T_{mod,k}$ (°C)	$T_{mod,annual-avg}$ (°C)	$C_{k,annual}$
2023-05-02	2:00:00 PM	34	883	57.13	43.50	0.94
2023-02-06	9:00:00 AM	23	53	21.64		1.10

Table 9
Extreme T_{mod} (°C) and the $C_{k,annual}$ for Case B

Date	Time	T_{amb} (°C)	G_{poa} (W/m ²)	$T_{mod,k}$ (°C)	$T_{mod,annual-avg}$ (°C)	$C_{k,annual}$
2023-07-26	1:00:00 PM	31	972	57.08	31.92	0.89
2023-01-13	8:00:00 AM	-25	42	-21.31		1.23

For Case A, the highest T_{mod} was 57.13°C, resulting in $C_{k,annual}$ being 0.94, while the lowest T_{mod} was 21.64°C, resulting in $C_{k,annual}$ being 1.10. On the other hand, for Case B, the highest T_{mod} was 57.08°C, resulting in $C_{k,annual}$ being 0.89, while the lowest T_{mod} was -21.31°C, resulting in $C_{k,annual}$ being 1.23. When T_{mod} is more than $T_{mod,annual-avg}$, $C_{k,annual}$ will be less than 1 and vice versa. During cases where $C_{k,annual}$ is equal to one, there is no temperature adjustment or removal of seasonal variations on PR . These results portray the role or contribution of $C_{k,annual}$ in the $TCPR$ equation mathematically to remove seasonal and weather variation encountered previously in normal PR . Thus, $TCPR$ is anticipated to treat seasonal and temperature variations monthly and yearly.

Determination of Average $C_{k,annual}$ for One Year

The average $C_{k,annual}$ for one year has been calculated and presented in Table 10. Compared to extreme T_{mod} , on a yearly basis, both cases show that $C_{k,annual}$ is closer to one. During extreme T_{mod} , the power rating has been adjusted to compensate for the differences between the maximum or minimum T_{mod} and the $T_{mod,annual-avg}$. For the annual average, there is no adjustment since there is no difference between the T_{mod} (yearly) and $T_{mod,annual-avg}$. This means that while $C_{k,annual}$ reduces seasonal and weather variations on monthly $TCPR$, it does not affect yearly. Thus, the $TCPR$ concept of removing seasonal and weather variations without overestimating the annual PR has been done in accordance with IEC 61724-1 (2021).

Table 10
Yearly average $C_{k,annual}$

Case	Site	Climate	$T_{mod,annual-avg}$ (°C)	$C_{k,annual}$
A	Negeri Sembilan, Malaysia	A _f	43.50	1.02
B	Almaty, Kazakhstan	D _{fa}	31.92	1.03

Determination of Annual PR and TCPR Based on PVsyst

Next, the annual PR and TCPR were extracted from PVsyst, and the mean bias error (MBE) for both parameters was calculated. PVsyst calculates PR and TCPR based on IEC 61724-1 (2021), as stated in the PVsyst help content. Figure 2 illustrates the graph of PR and TCPR against climate with their MBE to compare annual PR and annual TCPR for tropical and continental climate regions.

The values of the annual PR and annual TCPR are close to each other for both climates. The positive MBE indicates TCPR is higher than PR, while the negative MBE is vice versa. This indicates that the TCPR concept of removing seasonal and weather variations without overestimating the actual PR is proven.

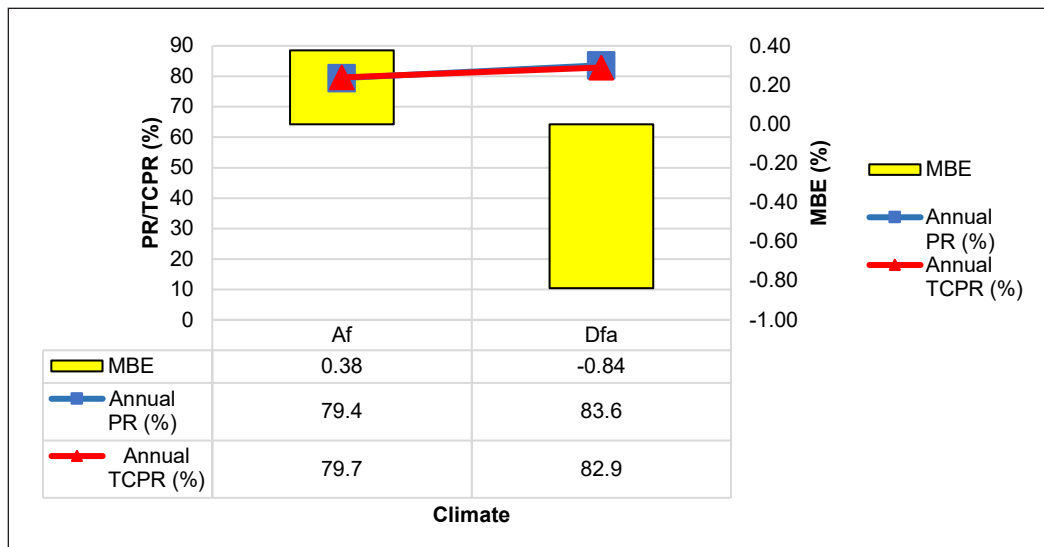


Figure 2. Annual comparison between PR and TCPR for Case A and Case B

Determination of Monthly PR and TCPR Based on PVsyst

Analysis of monthly PR and monthly TCPR extracted from PVsyst has been conducted to observe the effect of seasonal and weather variations on PR, focusing especially on monthly T_{amb} . Table 11 tabulates the monthly data for Case A, including the H_{poa} , T_{amb} , E_{outs} , PR and TCPR, while Figure 3 illustrates the result in a graph.

Table 11
Monthly data for Case A

Month	H_{pou} (kWh/m ²)	T_{amb} (°C)	E_{out} (kWh)	PR (%)	TCPR (%)
Jan	159.7	27.03	1272	79.7	80
Feb	164.3	27.67	1305	79.4	80.4
Mar	170.2	27.99	1348	79.2	80.1
Apr	158.8	27.68	1257	79.1	79.8
May	146.9	28.41	1159	78.9	79.3
Jun	125.1	27.92	993	79.4	79
Jul	133.5	27.91	1059	79.4	79.1
Aug	141.4	27.78	1125	79.5	79.5
Sep	141.3	27.2	1121	79.4	79.5
Oct	147.8	27.58	1175	79.5	79.8
Nov	136.9	26.68	1093	79.8	79.9
Dec	137.5	26.99	1094	79.6	79.8
Year	1763.4	27.57	14001	79.4	79.7

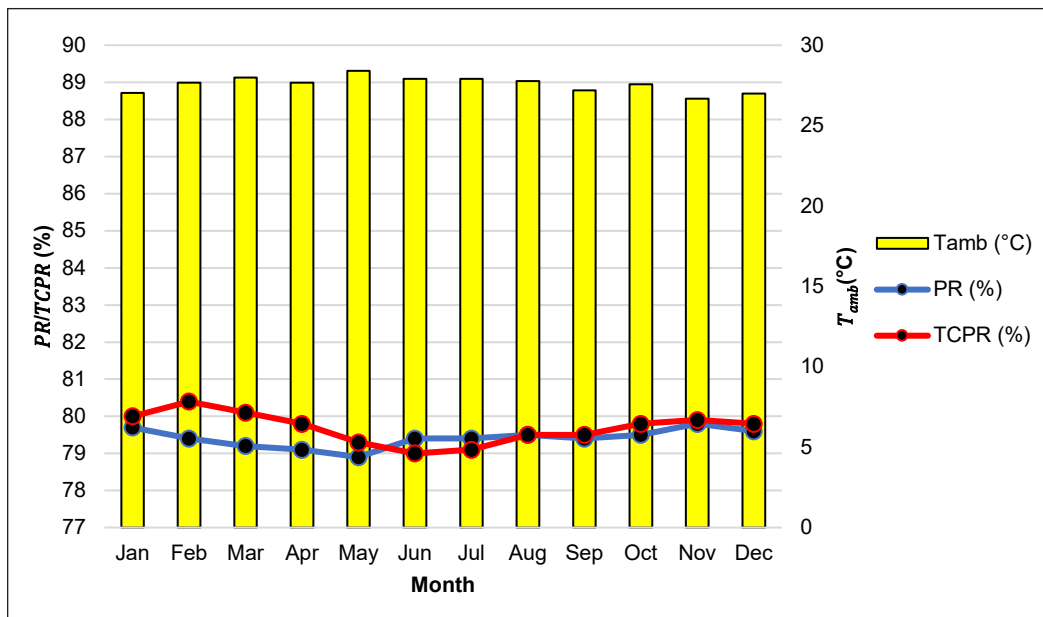


Figure 3. Monthly comparison of PR and TCPR for Case A

Based on Figure 3, the TCPR line trend is in good agreement with the PR line throughout the year, with minor deviations. The minimum PR recorded was in May, with 78.9% during the highest T_{amb} of 28.41°C. The corresponding TCPR was 79.3%. TCPR has adjusted the seasonal and weather variations by increasing the value; thus, the value is leveled with other months. The maximum PR recorded was in August, with 79.8% during

the lowest T_{amb} of 26.68°C. $TCPR$ has adjusted for the seasonal and weather variations by decreasing the value; thus, the value is leveled with other months. However, the difference between PR and $TCPR$ is found to be insignificant. This indicates that $TCPR$ is not relevant in tropical climate regions.

On the other hand, Table 12 presents the monthly data for Case B, including the H_{poa} , T_{amb} , E_{out} , PR and $TCPR$, while Figure 4 illustrates the results in a graph.

Table 12
Monthly data for Case B

Month	H_{poa} (kWh/m ²)	T_{amb} (°C)	E_{out} (kWh)	PR (%)	$TCPR$ (%)
Jan	91.3	-6.36	822	90	83.9
Feb	108.7	-3.92	968	89	84.1
Mar	146.2	5.23	1258	86	83.8
Apr	141.6	11.73	1176	83	82.5
May	172.6	17.74	1383	80.1	82.2
Jun	161.4	22.4	1265	78.4	81.4
Jul	180.7	25.21	1401	77.5	82
Aug	176.8	23.85	1381	78.1	82.4
Sep	163.3	17.58	1325	81.1	83.2
Oct	132.1	9.94	1111	84.1	83.9
Nov	81.7	2.16	714	87.4	83.2
Dec	64.7	-4.3	575	88.9	82.5
Year	1621.1	10.11	13379	83.6	82.9

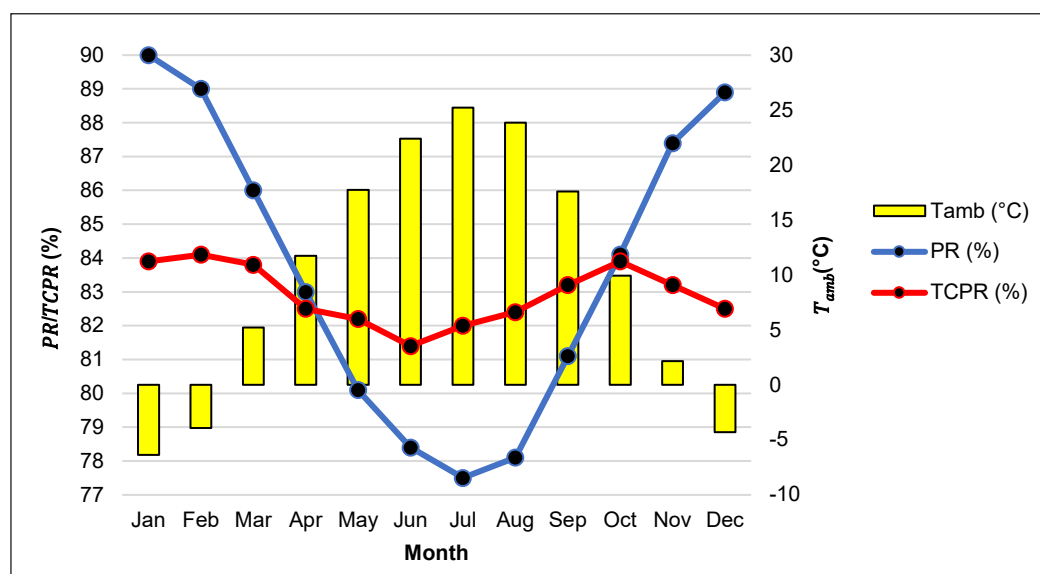


Figure 4. Monthly comparison of PR and $TCPR$ for Case B

Based on Figure 4, the PR line is interestingly curved like a U-shape, indicating that the monthly values are in a larger range throughout the year. There is a distinct difference between maximum and minimum monthly values. Inversely, the $TCPR$ line is more balanced, indicating a small difference between maximum and minimum monthly values. Thus, $TCPR$ is leveled for every month. The minimum PR recorded was in July, with 77.5% during the highest T_{amb} of 25.21°C. The corresponding $TCPR$ was 82%. $TCPR$ has adjusted the seasonal and weather variations by increasing the value by 4.5%; thus, the value level is revised with other months. The maximum PR recorded was in August, at 90.0%, during the lowest T_{amb} at -6.36°C. The corresponding $TCPR$ was 83.9%. $TCPR$ has adjusted the seasonal and weather variations by decreasing the value by 6.1%; thus, the value leveled with other months. It is apparent that the difference between PR and $TCPR$ is significant. It is worth highlighting that $TCPR$ is relevant in the continental climate region.

The minimum PR (PR_{min}), maximum PR (PR_{max}), minimum $TCPR$ ($TCPR_{min}$), and maximum $TCPR$ ($TCPR_{max}$) are summarised in Table 13 for both cases. The PR_{diff} and $TCPR_{diff}$ were also calculated by subtracting the maximum and minimum of the respective parameters. The purpose of obtaining the PR_{diff} and $TCPR_{diff}$ was to observe the range or variations of the monthly values, which was highly expected due to season or weather. Large PR_{diff} or $TCPR_{diff}$ indicates large variations and the other way around for small values. PR_{diff} and $TCPR_{diff}$ should be compared to see the effectiveness of applying $TCPR$.

For Case A, the range of monthly PR is between 78.9% and 79.8%, indicating a 1% PR_{diff} . The range of monthly $TCPR$ is between 79.0% and 80.4%, indicating a 1.3% $TCPR_{diff}$. Since the difference between PR_{diff} and $TCPR_{diff}$ is small, there is minimal risk of seasonal and weather variations. Thus, this case study has highlighted that PR assessment is sufficient without the $TCPR$ assessment for the tropical climate region.

For Case B, the range of monthly PR is between 77.5% and 90.0%, indicating a 12.5% PR_{diff} . The range of monthly $TCPR$ is between 81.4% and 84.1%, indicating a 2.7% $TCPR_{diff}$. Since PR_{diff} is large, seasonal and weather variations are significantly risky. The range of $TCPR_{diff}$ significantly reduced compared to PR_{diff} . Thus, this case study has proven that the implementation of $TCPR$, as recommended by IEC 61724-1 (2021), is relevant for the continental climate region due to the wide range of annual T_{amb} .

Table 13
Analysis of monthly PR and $TCPR$

Case	PR_{min} (%)	PR_{max} (%)	PR_{diff} (%)	$TCPR_{min}$ (%)	$TCPR_{max}$ (%)	$TCPR_{diff}$ (%)	$TCPR_{diff} - PR_{diff}$ (%)
A	78.9	79.9	1	79	80.4	1.3	-0.3
B	77.5	90	12.5	81.4	84.1	2.7	9.8

CONCLUSION

$C_{k,annual}$ is determined by incorporating $T_{mod,annual-avg}$, which is actually the irradiance-weighted PV module temperature. For the tropical climate, the hourly highest and lowest T_{mod} analysis resulted in $C_{k,annual}$ of 0.94 and 1.10, respectively. On the other hand, for the continental climate, the analysis of hourly highest and lowest T_{mod} resulted in $C_{k,annual}$ of 0.89 and 1.23, respectively. These results indicate that $C_{k,annual}$ varies significantly with hourly extreme T_{mod} . However, when analysed annually, the $C_{k,annual}$ for both climates are 1.02 and 1.03. It has been proven that $C_{k,annual}$ role in removing seasonal and weather variations in the *TCPR* mathematical model is successful for both climates.

The annual *PR* and *TCPR* have no notable difference for tropical and continental climates. Nevertheless, the monthly *PRs* have shown obvious variations ranging from 77.5% to 90% for the continental climate. However, when *TCPR* is applied, the variation is in the range of 81.4% to 84.1%, which is considered small. It is due to the $C_{k,annual}$ role in removing seasonal and weather variations in the *TCPR* mathematical model. For tropical climate, it is interesting to highlight that the monthly *PRs* have no obvious variations ranging from 78.9% to 79.8%. The same results appear for monthly *TCPR*, which ranges from 79% to 80.4%. Thus, the results of this study acknowledge that both *PR* and *TCPR* are relevant for the continental climate. However, normal *PR* alone is already sufficient for tropical climate as the performance metric.

ACKNOWLEDGEMENT

The authors express gratitude to the Solar Photovoltaic Energy Conversion Technology and Research Application (SPECTRA) group for the valuable inputs and the Journal Support Fund, UiTM, for funding this research.

REFERENCES

- Abdullah, A. Z., Amlus, M. H., Azizan, N., Sali, I. M., & Rahim, M. H. (2022). Performance analysis of different type PV module for 3kW residential roof top PV system using PVSyst simulation tool. *Journal of Physics: Conference Series*, 2312(1), Article 012042. <https://doi.org/10.1088/1742-6596/2312/1/012042>
- Anang, N., Azman, S. N. A. S. N., Muda, W. M. W., Dagang, A. N., & Daud, M. Z. (2021). Performance analysis of a grid-connected rooftop solar PV system in Kuala Terengganu, Malaysia. *Energy and Buildings*, 248, Article 111182. <https://doi.org/10.1016/j.enbuild.2021.111182>
- Beck, H. E., Zimmermann, N. E., McVicar, T. R., Vergopolan, N., Berg, A., & Wood, E. F. (2018). Present and future köppen-geiger climate classification maps at 1-km resolution. *Scientific Data*, 5(1), 1-12. <https://doi.org/10.1038/sdata.2018.214>
- Chen, D., & Chen, H. W. (2013). Using the Köppen classification to quantify climate variation and change: An example for 1901-2010. *Environmental Development*, 6(1), 69–79. <https://doi.org/10.1016/j.envdev.2013.03.007>

- Chen, X. M., Li, Y., Zhao, Z. G., Ma, T., & Wang, R. Z. (2018). General method to obtain recommended tilt and azimuth angles for photovoltaic systems worldwide. *Solar Energy*, *172*, 46–57. <https://doi.org/10.1016/j.solener.2018.06.045>
- Chinchilla, M., Santos-Martín, D., Carpintero-Rentería, M., & Lemon, S. (2021). Worldwide annual optimum tilt angle model for solar collectors and photovoltaic systems in the absence of site meteorological data. *Applied Energy*, *281*, Article 116056. <https://doi.org/10.1016/j.apenergy.2020.116056>
- Comello, S., Reichelstein, S., & Sahoo, A. (2018). The road ahead for solar PV power. In *Renewable and Sustainable Energy Reviews* (Vol. 92, pp. 744–756). Elsevier Ltd. <https://doi.org/10.1016/j.rser.2018.04.098>
- Costa, H., Sprout, E., Teng, S., McDaniel, M., Hunt, J., Boudrea, D., Ramroop, T., Rutledge, K., & Hall, H. (2023). Tropics. In J. Evers, K. West, & Emdash Editing (Eds.), *National Geographic*. National Geographic Society.
- Daniel-Durandt, F., & Rix, A. (2022). Spectral influences on performance: A South African PV plant after 4 years of operation. In *2022 International Conference on Electrical, Computer, Communications and Mechatronics Engineering (ICECCME)* (pp. 1-6). IEEE Publishing. <https://doi.org/10.1109/ICECCME55909.2022.9988688>
- De Masi, R. F., Gigante, A., Ruggiero, S., & Vanoli, G. P. (2024). Experimental and numerical approach for the evaluation of PV-system performance on energy and environmental behavior of nearly zero energy buildings: Case study in Mediterranean climate. *Renewable Energy*, *227*, Article 120609. <https://doi.org/10.1016/j.renene.2024.120609>
- Dey, D., & Subudhi, B. (2020). Design, simulation and economic evaluation of 90 kW grid connected Photovoltaic system. *Energy Reports*, *6*, 1778–1787. <https://doi.org/10.1016/j.egy.2020.04.027>
- Dierauf, T., Growitz, A., Kurtz, S., Becerra, J. L., Fichtner, C., Riley, E., & Hansen, C. (2013). *Weather-Corrected Performance Ratio*. U.S. Department of Energy. <http://www.osti.gov/bridge>
- Gopi, A., Sudhakar, K., Keng, N. W., & Krishnan, A. R. (2021). Comparison of normal and weather corrected performance ratio of photovoltaic solar plants in hot and cold climates. *Energy for Sustainable Development*, *65*, 53–62. <https://doi.org/10.1016/j.esd.2021.09.005>
- Ibrahim, S. N. N., Zainuddin, H., Rahim, Y. I. A. A., Mansor, N. A., Muhammad, N., & Khir, F. L. M. (2023). Simulation and prediction of residential grid-connected photovoltaic system performance. *International Journal of Power Electronics and Drive Systems*, *14*(1), 506-515. <https://doi.org/10.11591/ijpeds.v14.i1.pp506-515>
- IEC 61724. (2021). *International Standard*. International Electrotechnical Commission. www.iec.ch
- International Energy Agency. (2022). *Renewables 2022 Analysis and Forecast to 2027*. International Energy Agency. www.iea.org
- Jacobson, M. Z., & Jadhav, V. (2018). World estimates of PV optimal tilt angles and ratios of sunlight incident upon tilted and tracked PV panels relative to horizontal panels. *Solar Energy*, *169*, 55–66. <https://doi.org/10.1016/j.solener.2018.04.030>
- Karahüseyin, T., & Abbasoğlu, S. (2022). Performance loss rates of a 1 MWp PV plant with various tilt angle, orientation and installed environment in the capital of Cyprus. *Sustainability*, *14*(15), Article 9084. <https://doi.org/10.3390/su14159084>

- Kottek, M., Grieser, J., Beck, C., Rudolf, B., & Rubel, F. (2006). World map of the Köppen-Geiger climate classification updated. *Meteorologische Zeitschrift*, *15*(3), 259–263. <https://doi.org/10.1127/0941-2948/2006/0130>
- Limmanee, A., Udomdachanut, N., Songtraï, S., Kaewniyompanit, S., Sato, Y., Nakaishi, M., Kittisontirak, S., Sriprapha, K., & Sakamoto, Y. (2016). Field performance and degradation rates of different types of photovoltaic modules: A case study in Thailand. *Renewable Energy*, *89*, 12–17. <https://doi.org/10.1016/j.renene.2015.11.088>
- Micallef, A., & Staines, C. S. (2022). Generation performance analysis for installed photovoltaic systems on the Maltese Islands. In *2022 Workshop on Blockchain for Renewables Integration (BLORIN)* (pp. 74–79). IEEE Publishing. <https://doi.org/10.1109/BLORIN54731.2022.10028183>
- MS 2692. (2020). *Testing and Commissioning of Grid-Connected Photovoltaic System*. Department of Standards Malaysia. <http://www.jsm.gov.my>
- Ogliari, E., Dolara, A., Mazzeo, D., Manzolini, G., & Leva, S. (2023). Bifacial and monofacial PV systems performance assessment based on IEC 61724-1 standard. *IEEE Journal of Photovoltaics*, *13*(5), 756–763. <https://doi.org/10.1109/JPHOTOV.2023.3295869>
- Prakhya, R. K., & Kotha, S. R. (2018). Temperature effect on the performance metrics of grid-tied SPV plant. *International Journal of Engineering Research and Technology*, *11*(6), 909–923. <http://www.irphouse.com>
- PVsyst SA. (2024). *PVsyst 7.4 - Photovoltaic System Study*. PVsyst SA. https://www.pvsyst.com/help/index.html?contents_table.htm
- Quansah, D. A., & Adaramola, M. S. (2019). Assessment of early degradation and performance loss in five co-located solar photovoltaic module technologies installed in Ghana using performance ratio time-series regression. *Renewable Energy*, *131*, 900–910. <https://doi.org/10.1016/j.renene.2018.07.117>
- Rahim, Y. I. A. A., Zainuddin, H., Setiawan, E. A., Madsuha, A. F., Hussin, M. Z., Sulaiman, S. I., & Ibrahim, S. N. N. (2024). Performance of grid-connected photovoltaic systems in Northern and Southern Hemispheres under equatorial climate. *International Journal of Power Electronics and Drive Systems*, *15*(2), 858–873. <https://doi.org/10.11591/ijpeds.v15.i2.pp858-873>
- Rout, K. C., & Kulkarni, P. S. (2020). Design and performance evaluation of proposed 2 kW solar PV rooftop on grid system in Odisha using PVsyst. In *2020 IEEE International Students' Conference on Electrical, Electronics and Computer Science (SCEECS)* (pp. 1–6). IEEE Publishing. <https://doi.org/10.1109/SCEECS48394.2020.124>
- Sánchez-Lanuza, M. B., Lillo-Bravo, I., Moreno-Tejera, S., Rodríguez, J. S., & Delgado-Sánchez, J. M. (2024). Experimental CIGS technology performance under low concentration photovoltaic conditions. *Journal of Cleaner Production*, *446*, Article 141384. <https://doi.org/10.1016/j.jclepro.2024.141384>
- Sathiracheewin, S., Sripadungtham, P., & Kamuang, S. (2020). Performance analysis of grid-connected PV Rooftop, at Sakon Nakhon Province, Thailand. *Advances in Science, Technology and Engineering Systems*, *5*(4), 816–823. <https://doi.org/10.25046/AJ050496>
- SEDA. (2023). *Design and Sizing of Grid-connected Photovoltaic Power System* (3rd ed.). SEDA Malaysia. www.seda.gov.my

- Syahputra, E., Fajarin, R. A., & Setiawan, E. A. (2018). Characteristic analysis of photovoltaic on-grid system in tropical region for weather-corrected performance ratio calculation method implementation. In *E3S Web of Conferences* (Vol. 67, p. 01025). EDP Sciences. <https://doi.org/10.1051/e3sconf/20186701025>
- Tahsin, A. (2021). *Tilt angle optimization of photovoltaic modules considering the effect of dust*. [Master dissertation]. Bangladesh University of Engineering and Technology, Bangladesh. <http://lib.buet.ac.bd:8080/xmlui/bitstream/handle/123456789/6062/Full%20Thesis.pdf?sequence=1&isAllowed=y>
- Tamizhmani, G., Ji, L., Tang, Y., Petacci, L., & Osterwald, C. (2003). Photovoltaic module thermal/wind performance: Long-term monitoring and model development for energy rating. In *NCPV and Solar Program Review Meeting Proceedings* (No. NREL/CP-520-35645). National Renewable Energy Laboratory.
- Triantafyllou, G. N., & Tsonis, A. A. (1994). Assessing the ability of the Koppen system to delineate the general world pattern of climates. *Geophysical Research Letters*, *21*(25), 2809–2812.
- U.S. Department of Commerce. (2023). *Tropical Weather Systems*. National Oceanic and Atmospheric Administration. <https://www.noaa.gov/jetstream/tropical>
- Vidur, P. R., & Jagwani, S. (2022). Design and simulation of a Rooftop solar PV system Using PV syst software. In *2022 4th International Conference on Smart Systems and Inventive Technology (ICSSIT)* (pp. 724-728). IEEE Publishing. <https://doi.org/10.1109/icssit53264.2022.9716348>
- Wassie, Y. T., & Ahlgren, E. O. (2023). Performance and reliability analysis of an off-grid PV mini-grid system in rural tropical Africa: A case study in southern Ethiopia. *Development Engineering*, *8*, Article 100106. <https://doi.org/10.1016/j.deveng.2022.100106>
- Zainuddin, H. (2014). *Module Temperature Modelling for Free-Standing Photovoltaic System in Equatorial Climate*. [Doctoral dissertation]. Universiti Teknologi MARA, Malaysia. <https://ir.uitm.edu.my/id/eprint/16413/>

Review Article

Machine Learning Applications in Multiplayer Online Battle Arena Esports—A Systematic Review

Ahmad Alif Kamal^{1,2}, Mohd. Asyraf Mansor^{1*}, Liyana Truna²,
Norhunaini Mohd. Shaipullah² and Nor Hafizie Habib Sultan³

¹*School of Distance Education, Universiti Sains Malaysia, 11800 USM, Pulau Pinang, Malaysia*

²*Centre for Pre-University Studies, Universiti Malaysia Sarawak, 94300 UNIMAS, Kota Samarahan, Sarawak, Malaysia*

³*Instalock Esports Enterprise, Universiti Malaysia Sarawak, 94300 UNIMAS, Kota Samarahan, Sarawak, Malaysia*

ABSTRACT

Machine learning (ML) is an emerging field, while multiplayer online battle arena (MOBA) esports has seen a rise as a research subject of interest. The applications of ML in MOBA are an interesting field of study as the esports genre is enriched by a plethora of data. Moreover, the MOBA esports industry is a budding economic sector with stakeholders looking for innovative scientific studies. This necessitates the need for a systematic review to provide insights for future studies. The databases (Scopus, Web of Science, PubMed, ScienceDirect and Google Scholar) were systematically searched to identify published peer-reviewed academic articles. The Preferred Reporting Items for Systematic Reviews and Meta-Analyses (PRISMA) method was used for the analysis. Papers were included if they contained ML applications for MOBA, excluding game design or non-esports-related studies. There are 35 studies included in this systematic review, with most studies on Defence of the Ancients 2 (DotA 2) and League of Legends (LoL). ML algorithms are used to make predictions for different purposes using game mechanics and player profiles as datasets, with random forests, decision trees, logistic regression, neural networks, and more. The performance of ML models was deemed impressive, given their simplicity and the datasets used. Key findings highlight the potential

future area of research in the empowerment of mobile phone-based MOBA, commercialisation opportunities using ML technology in authentic settings, and overcoming challenges in data access and regional differences.

ARTICLE INFO

Article history:

Received: 22 March 2024

Accepted: 24 December 2024

Published: 07 March 2025

DOI: <https://doi.org/10.47836/pjst.33.2.11>

E-mail addresses:

kaalif@student.usm.my (Ahmad Alif Kamal)

asyrafman@usm.my (Mohd. Asyraf Mansor)

tliyana@unimas.my (Liyana Truna)

msnorhunaini@unimas.my (Norhunaini Mohd. Shaipullah)

instalockesports@gmail.com (Nor Hafizie Habib Sultan)

* Corresponding author

Keywords: Esports, machine learning, MOBA, PRISMA, systematic review

INTRODUCTION

ML, a subfield of artificial intelligence (AI), is the field that focuses on the development of algorithms and models that can learn from and make predictions based on data, a so-called machine learning approach (Tan, 2022). ML involves the use of statistical and mathematical methods to enable computers to learn from data without being explicitly programmed to perform a specific task. ML is applied in a vast range of disciplines, from natural language processing and computer vision to finance and healthcare (Oyebode et al., 2023), leading to significant advances in our understanding and ability to solve authentic and complex problems (Sclavounos & Ma, 2018). ML helps researchers automate rigorous repetitive tasks, discover hidden patterns in data, and make predictions or decisions based on data (Truong et al., 2019; Zomlot et al., 2013). The impact of ML in research is constantly growing (Jordan & Mitchell, 2015) as more data is generated and new techniques are developed, making it a key area of study for researchers in various fields.

In recent years, esports, also known as electronic sports, has been a rapidly growing industry involving competitive video gaming (Reitman et al., 2020). It refers to organised, competitive multiplayer video gaming events that are played either online or in person and that often involve professional players and large prize pools, transforming hobbies into a rewarding career that may shake the economic sector (Railsback & Caporusso, 2019). Esports popularity in recent years attracted large audiences, both online and offline, and inspired the creation of numerous professional teams and leagues. For Malaysia, the recent national budget year 2024 showcased the importance of the growth of esports by allocating as much as RM30 million (Bernama, 2023). With the increasing interest in esports, it has also become a subject of academic research and exploration (Wan Jr et al., 2021; Meng-Lewis et al., 2022), with the goal of better understanding its potential for society and economy.

Currently, ML is having a significant impact on esports-related research in several ways. For instance, ML algorithms are used for performance analysis. With this, ML contributes to the analysis of game data and player performance, helping teams and players improve their strategies and decision-making processes (Kulkarni, 2012). Next, ML can also be used to train players by simulating game scenarios and providing personalised feedback. This can help players identify their strengths and weaknesses and improve their gameplay (Eisen, 2017). Other than that, ML algorithms are utilised to develop and enhance game features, such as recommendation systems, which can provide a better gaming experience for players (Fanca et al., 2020). Among others, ML is widely used to predict the outcome of esports matches and events, providing valuable insights for fans, players, and teams (Bailey, 2020). Overall, ML is having a positive impact on the esports industry by providing new tools and insights for players, teams, and fans to help drive innovation and growth in the industry. This study is intrigued to review the plethora of implementations of ML approaches for the benefits of esports with systematic tools.

One of the remarkably interesting esports genres that capitalised on ML approaches is MOBA esports, a competitive video game competition that focuses on real-time strategy gameplay (Yang et al., 2016). In MOBA esports, two teams of 5 players compete against each other, with each player controlling a single character (known as a “hero” or “champion”, depending on the game) with unique abilities and strengths. The goal of MOBA is for each team to destroy the opponent’s base, which is typically located at the opposite end of the game map. To do this, players must work together to defeat the opponent’s heroes and control key objectives on the map, such as towers, creeps or minions, and neutral monsters. MOBA esports have become increasingly popular in recent years, with games like DotA 2, LoL, and Heroes of the Storm attracting large audiences and offering substantial prize pools (Bankov, 2019). MOBA tournaments are often organised by game developers, esports organisations, or independent organisers and can be watched live or online by fans around the world. Thus, as avid fans of esports, we intend to fill the important gaps in the academic literature for MOBA esports towards embracing the future of AI through many facets of ML by asking the following research questions (RQ):

RQ1. What are the ML algorithms used in various MOBA esports research?

RQ2. How does the implementation of ML benefit MOBA esports?

RQ3. How well do the ML algorithms perform in the included studies?

RQ4. What is the potential risk of biases in the included studies?

RQ5. What are the various MOBA game features used as predictors?

RQ6. Which player skill levels and regions are being prominently researched in these fields?

RQ7. To what extent do humans need to intervene in applying ML for MOBA esports studies?

MATERIALS AND METHODS

Eligibility Criteria

Studies had to be peer-reviewed, published between 2010 and 2022, and written in English. All studies chosen were related to the application of ML for various purposes in MOBA esports. This included predicting wins from many forms of game mechanics and features to the development of AI to play MOBA games. Interestingly, an investigation into predicting toxic behaviour is also included. Similarly, a report on the application of ML for tournament live streaming, which is the media to display the gameplay between contestants, was also reviewed. Studies were excluded if they focused solely on game designs and structures without the aspect of esports. Other than that, reports on video game genres in esports other than MOBA, such as first-person shooter (FPS), fighting games, real-time strategy (RTS), battle royale (BR), and sports, are excluded from this review.

Information Sources

Online databases such as Scopus, Web of Science, PubMed, and ScienceDirect were systematically searched for relevant literature. However, the search was performed unsystematically for Google Scholar, and the results yielded more than a thousand returns. All the searches were performed and recorded in early January 2023, up until the end of November 2023.

Search Strategy

The search strings used in Scopus, Web of Science, PubMed, and ScienceDirect were shown in Table 1. However, the search string used for Google Scholar was altered to obtain a much more niche result (Table 1).

Table 1
The search string used in online databases and Google Scholar

Search strings in online databases	("electronic sports" OR esports OR e-sports OR "competitive video game" OR "multiplayer online games" OR moba OR "multiplayer online battle arena") AND "machine learning"
Search string in Google Scholar	("electronic sports" OR esports OR "multiplayer online games" OR moba OR "multiplayer online battle arena") AND "machine learning" -trial -review -book -sports

Selection Process

The first author independently searched for literature that met the inclusion criteria. The results from the search were exported in BibTeX format, enabling the second, third and fourth authors to upload them into a collaborative, online electronic programme. Next, the duplicated records were removed. Then, all authors screened the titles independently to ensure the reports were eligible for the full-text retrieval process. After that, we performed a screening by reading the abstracts and keywords to determine the finalised list for inclusion. During this process, the excluded papers were due to the fact that the reported esports games do not belong to the MOBA genre.

Data Collection Process

The electronic search results were uploaded into Mendeley Library, a reference management program for duplicate removal. The entire screening process was completed in the Mendeley workspace. Finally, the data extraction process was conducted manually in a Microsoft Excel sheet.

Data Items

All four authors were involved in the selection of our study outcomes by ensuring ML approaches were implemented and games from the MOBA genre. Table 2 shows the

items extracted from the included studies. However, for certain item(s) with missing or unclear information, all the authors agreed to report as unspecified. For ML-based studies, it is difficult to assume certain information, data, or steps are taken by the researchers involved in the reported experiment and investigation, as this assumption can alter the entire process and results of the studies. Hence, the authors believed this mutual consensus is a more reliable and valid way of performing this review.

Table 2
Items extracted from the included studies for RQ1 to RQ3

RQ	Items extracted
RQ1	<ul style="list-style-type: none"> • Game name(s) • Game mechanic(s) • ML algorithm(s) • ML algorithm class(es) • ML tool(s)/software
RQ2	<ul style="list-style-type: none"> • Findings (discussion) • Limitations, if specified • Future area, if specified
RQ3	<ul style="list-style-type: none"> • ML metrics • ML challenges

Study Risk of Bias Assessment

In this systematic review, the process of assessing the quality of ML-based studies and publications is challenging due to the diverse nature of research in the field (Le Glaz et al., 2021). To date, there is a lack of standardised guidelines for evaluation purposes (Marshall & Wallace, 2019). However, a tool called prediction model risk of bias assessment tool (PROBAST) can assess the risk of bias and the applicability of diagnostic and prognostic prediction models (Wolff et al., 2019). PROBAST assess the risk of biases in 4 domains: participants, predictors, outcome, and analysis (de Jong et al., 2021), governed by signalling questions (such as “*Are the participants representative of the target population?*” or “*Was the outcome measured appropriately?*”) to determine the level of risk of bias (low, moderate or high) for a study (Navarro et al., 2020). PROBAST is useful and practical in ML-related works (Collins et al., 2021; Jiu et al., 2024; Yang et al., 2023).

In the event of disagreements during the bias assessment, the reviewers discussed the conflicting assessments to understand the reason and rationale for each perspective. If consensus was not reached through discussion, the final decision was made based on the majority opinion through the re-assessment of the evidence process. This guarantees that all disagreements were transparently resolved to ensure consistency and minimised bias in the overall assessment.

Synthesis Methods

The study design of the included works in this systematic review was expected to be heterogeneous, where they could have different study designs and scopes. This resulted in the authors having difficulties synthesising the results of the studies and performing statistical meta-analysis, as different study designs can have different limitations and sources of bias. However, the authors agreed that meta-analysis will be done as much as possible

for equivalent criteria from multiple studies based on the data extracted. This includes distinguishable data distribution, individual frequency of occurrence, and collective mean with its distributions. Additionally, subgroup analyses are conducted to provide a more comprehensive analysis of ML applications in MOBA and yield richer insights.

RESULTS AND DISCUSSIONS

Study Selection

In Figure 1, the PRISMA flow diagram shows that 501 articles were identified in Scopus, Web of Science, PubMed ScienceDirect databases, and Google Scholar. After removing the duplicated articles ($n = 29$), the acquired articles underwent screening ($n = 472$). The titles and abstracts were screened, and some did not fit the inclusion criteria ($n = 345$). Therefore, the remaining studies were sought for retrieval ($n = 127$), but about half of them were not accessible ($n = 51$). Hence, the retrieved full-text articles were assessed for eligibility ($n = 76$). However, some studies have not been performed on games from the MOBA genre ($n = 25$) and have focused on non-game-related features and mechanics ($n = 16$). Finally, the eligible studies were included in this systematic review for the analysis ($n = 35$).

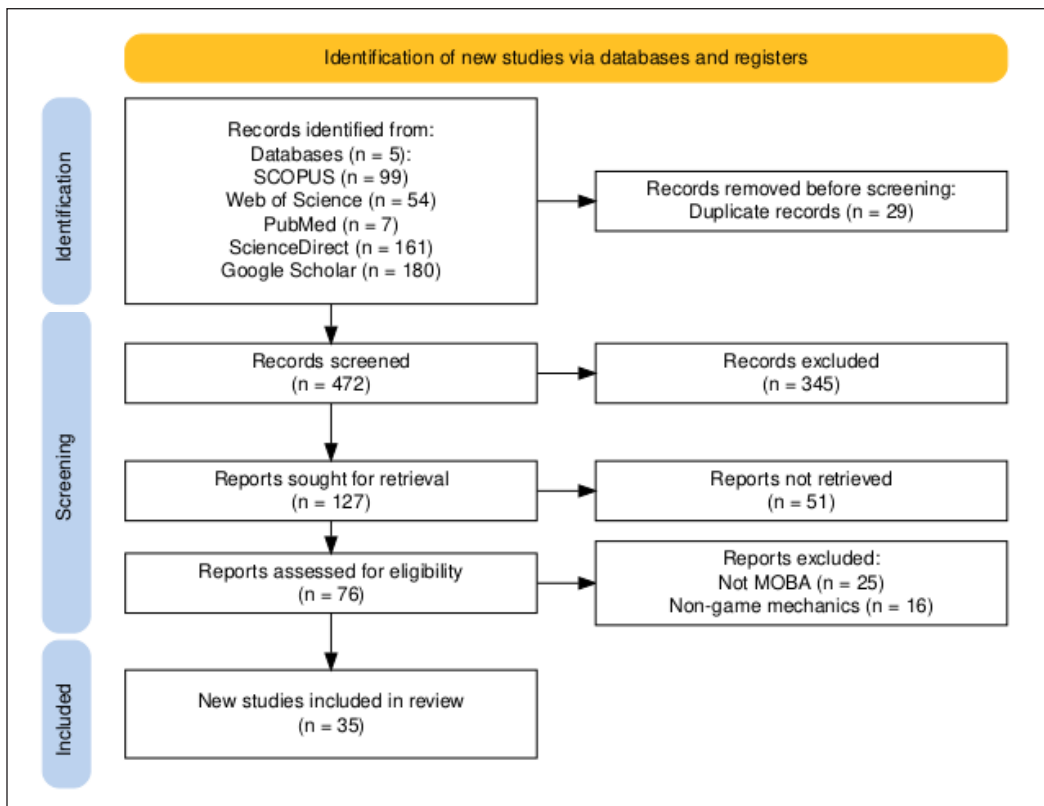


Figure 1. PRISMA flow diagram

Study Characteristics

Table 3 displays the study characteristics deployed by the authors of the 35 included studies. The description provided here is to answer RQ1. From the table, the most used games for ML-based studies are DotA 2, with 47.2%, followed by LoL, with 41.7% of the studies. Next is Honor of Kings (HoK) at 8.3% and For Honor at 2.8%. Figure 2 visually represents the game distributions for the 35 included studies.

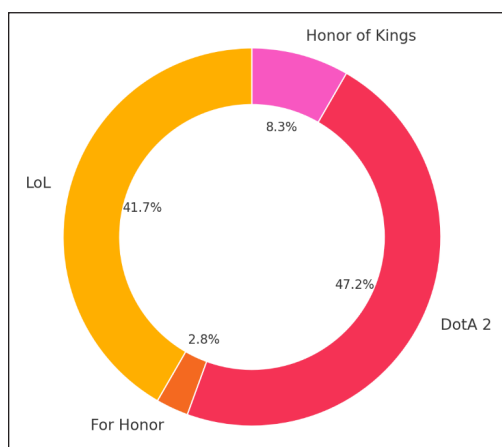


Figure 2. Game distributions from the included studies

Game mechanics include game and player datasets. Game datasets include data extracted before, during, and after the match. Pre-match data considers the state before the match, such as the hero or champion draft. In-match data is obtained during the match, like the first 10 minutes of match data. Some features include scores obtained by the players, such as gold earned, experience per minute (XPM), KDA ratio, vision point, and more. Post-match data is obtained after the match has ended, and statistics from the match include total camps stacked, gold per minute (GPM), total healing done, KDA of all players, and more. Player datasets were extracted from the players' profiles of the game, including winning rate, proficiency, and experience using certain heroes or champions, and match-making rating (MMR) was collected from their gameplay rating in the ranked game mode.

The ML algorithms deployed in the included studies are logistic regression (LR), support vector machines (SVM), k-nearest neighbours (k-NN), random forest (RF), Naïve Bayes (NB), decision tree (DT), support vector classification (SVC), gradient boosting (GBOOST), neural network (NN) (including deep NN), eXtreme Gradient Boosting Regressor (XGB), MultiLayer Perceptron (MLP), long short-term memory (LSTM) (one is modified as CBOW-LSTM), graph convolutional network (GCN), genetic algorithm, factorisation machines, XGBoost, and ExtraTree. Figure 3 shows the frequency of each algorithm reported in the included studies. The ML algorithms used in the studies include supervised, unsupervised, semi-supervised, reinforcement learning, and mixed. Most studies deployed supervised learning (73%), as can be seen in Figure 4.

The ML algorithm with the greatest number of applications for MOBA is RF. The earliest work related to ML is a DotA 2 hero selection recommendation system before the game using the LR model by Conley and Perry (2013), which amassed a high number of citations (42). A few more works with a similar approach include Kinkade and Lim (2015) and Song et al. (2015), which provide a better foundation for academic work on LR and DotA 2, specifically ML and MOBA.

Table 3
Study characteristics

Authors (year)	Game name(s)	Game mechanic(s)	ML algorithm(s)	ML algorithm class(es)	ML tool(s)/software
Bahrololloomi et al. (2023)	LoL	Player experience-points per minute (XPM)	XGBoost, CatBoost, RF	Supervised Learning	Python, Featurewiz
Bisberg & Ferrara (2022)	LoL	30 features about matches and players: Match history, player performance metrics, gold earned, experience gained, kills, vision control	GCN-cheby	Semi-supervised learning	Python, TensorFlow
Canossa et al. (2021)	For Honor	36 features related to player behaviour, including activity modes, match performance, and chat actions	RF, SVM	Supervised Learning	Python (custom implementation)
Costa et al. (2021)	LoL	51 features include banned and picked champions, player statistics (win rate, games played, KDA)	RF, LR, SVM	Supervised Learning	R, Python
Da Silva et al. (2017)	LoL	Keystroke and mouse dynamics, including movement speed, click frequency, latency, and key combinations	MLP, BN, RBF Network	Supervised Learning	WEKA
Do et al. (2020)	LoL	Champion Mastery Points (CMP), normalised play frequency, top 5 champion preferences	SVD	Not specified	Python, Surprise library
Do et al. (2021)	LoL	Champion mastery points, player-champion win rate, total games played, recent games played	DNN, SVC, RF, GBoost, kNN	Supervised Learning	Python, Keras, Scikit-learn
Edge (2013)	DotA 2	Player churn behaviour, KDA ratio, player empowerment, progress towards goals	k-NN, NB, DT	Supervised Learning	WEKA
Franco et al. (2019)	DotA 2	36 player performance attributes, including Kills, Deaths, Assists, Gold per Minute, Hero Healing, and Observer Wards Placed	k-means clustering, Genetic Algorithm	Unsupervised Learning	Python, OpenDota API
Guzmán & Medina (2021)	LoL, Dota 2	165 variables including gold, creeps, assists, deaths, KDA ratio, items, roles	RF, LR, NN	Supervised Learning, Unsupervised Learning	Python, R, WEKA
Hodge et al. (2021)	LoL	Player performance metrics, including metrics like KillsR-D and NetworthR-D	RF, LightGBM	Supervised Learning	Python, CfsSubsetEval
Hong & Lee (2022)	LoL	Detection of in-game events using screen analysis; events include kills, tower, and inhibitor destruction	ResNet	Supervised Learning	Python

Table 3 (continue)

Authors (year)	Game name(s)	Game mechanic(s)	ML algorithm(s)	ML algorithm class(es)	ML tool(s)/software
Jiang et al. (2020)	LoL	Contextual data such as champion type, match duration, player roles, and game versions	Neural Individualized Context-Aware Embeddings	Not specified	Python, Tensor Toolbox
Kim et al. (2020)	LoL	In-game data such as champion composition, gold, experience difference, and number of kills	MLP	Supervised Learning	Python, PyTorch
Kokkinakis et al. (2020)	DotA 2	Player performance, in-game events, match statistics	Various algorithms for data visualisation and storytelling	Unsupervised Learning	Weavr Companion App, custom analytics engine
Liang (2021)	LoL	38 features, including gold difference, experience difference, wards placed, kills, assists	SVM, DT	Supervised Learning	Python, Kaggle dataset
Luo et al. (2019)	DotA 2	In-game events like using Black King Bar, Roshan fight, tower destruction	ResNet152, Teacher-Student Model, Zero-Shot, Network Pruning	Supervised Learning	Python, PyTorch
Lyu et al. (2022)	DotA 2	152 behavioural features, including gold per minute, hero kills, experience per minute, ward placement, item usage	GPR, RF	Supervised Learning	WEKA, R
Marchenko & Sushevskiy (2018)	DotA 2	Player transfers, regions, Elo ratings, participation in The International, player roles, fantasy points	Exponential Random Graph Model (ERGM), Association Rules Mining	Mixed Methods	R, ERGM, Apriori algorithm
Martens et al. (2015)	DotA 2	Chat logs, player communication patterns, in-game events such as kills and match outcomes	NLP, SVM	Supervised Learning	Python, Scikit-learn
Mohammed et al. (2022)	DotA 2	Hero picks and bans during the drafting phase, focusing on team synergy and counter-picking strategies	CBOW, LSTM	Supervised Learning	Python, Gensim
Mora-Cantalops & Sicilia (2018)	LoL	Player networks, match history, structural network indicators like degree, betweenness, modularity	Affinity Propagation Clustering	Unsupervised Learning	Python, NetworkX, Gephi
do Nascimento Junior et al. (2017)	LoL	Player performance statistics such as gold earned, number of monsters killed, and total damage dealt	k-means clustering	Unsupervised Learning	Python

Table 3 (continue)

Authors (year)	Game name(s)	Game mechanic(s)	ML algorithm(s)	ML algorithm class(es)	ML tool(s)/software
Porokhnenko et al. (2019)	DotA 2	Hero picks, team compositions, match outcomes	Linear Regression, SVM, NN	Supervised Learning	Python, Scikit-learn, TensorFlow
Prakannoppakun & Sinthupinyo (2016)	DotA 2	Player roles, kills, deaths, assists, gold per minute, hero damage	NN, MLP	Supervised Learning	DotA 2 API, Custom Model
Semenov et al. (2017)	DotA 2	Hero drafts, team composition, player skill levels	NB, LR, GBoost, Factorization Machines	Supervised Learning	Python, FastFM, XGBoost
Shen (2022)	LoL	First 10 minutes data, including kills, wards placed, gold difference, experience difference	AdaBoost, GBoost, RF, ExtraTree, SVM, NB, kNN, LR, DT	Supervised Learning	Python
Stanly et al. (2022)	DotA 2	Hero and item choices, in-game stats, player behaviour, match data	DT, Random Tree, XGBoost	Supervised Learning	Python, XGBoost, Scikit-learn
Summerville et al. (2021)	DotA 2	Hero picks and bans during the drafting phase, player team roles, historical match outcomes	BN, LSTM	Supervised	Torch, Python
Vardal et al. (2022)	DotA 2	Hero picks and bans during the drafting phase	BN, LSTM, RNN	Supervised Learning	Torch, GeNIe & SMILE
Wang et al. (2018)	DotA 2	17 features including hero damage, tower damage, gold per minute, experience per minute, winning probability	LR, RF, SVM	Supervised Learning	Scikit-learn, Python
Wei et al. (2022)	Honor of Kings	Observation, Action, Reward, State, Skill, Opponent Hero, Target Hero	Proximal Policy Optimization (PPO), DQN	Reinforcement Learning	Python-based interface
Wong et al. (2022)	DotA 2	Hero selection, First Blood	NB, LR, k-NN, SVM, Kernel SVM, NN	Supervised Learning	Python
Ye et al. (2022)	Honor of Kings	Macro-strategy (where to go), Micromanagement (what to do)	CNN	Supervised Learning	Python
Zhang (2021)	Honor of Kings	Push-Turret, Combat, Lane-Farm, Jungle-Farm, Return, Navigation	Multimodal and Multitask NN	Supervised Learning	Python, NumPy, C++ (highly optimised code)

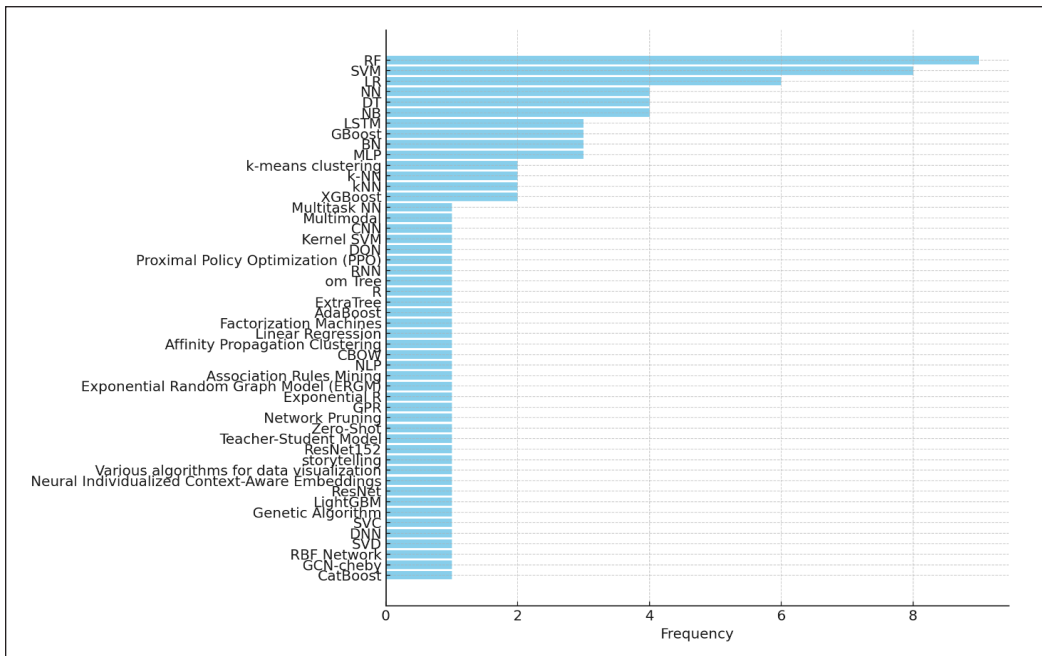


Figure 3. The frequency of each algorithm used in the 35 studies

Results of Individual Studies

Table 4 shows the results of individual studies included in this systematic review, including the findings, reported limitations, and future areas of work if the authors and researchers provide any. The data extracted in Table 4 is to answer RQ2. The studies included in this review mostly aimed to predict the winning team in MOBA games using various predictors. The challenge was to achieve the best prediction results using as few datasets as possible. MOBA games involve numerous players and massive amounts of data, including game environment factors, player actions, opponent actions, and decision-making processes. Developing effective predictors requires deep knowledge and experience of the game, as well as a hypothesis-driven approach. Some studies focused on testing and improving ML algorithms, while others investigated the effectiveness of certain predictors for accurate predictions. One

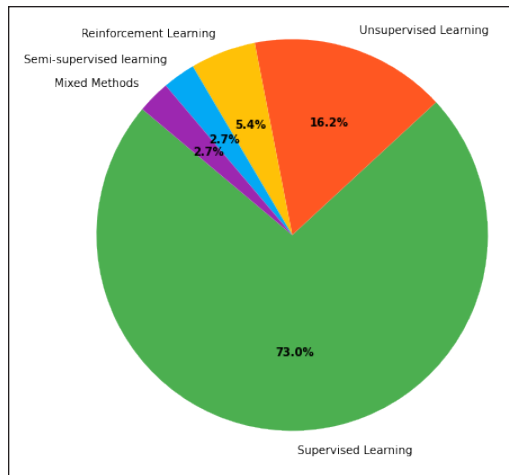


Figure 4. ML algorithm classes obtained from the included studies

Table 4
Results of individual studies (findings, limitations, and future area)

Authors (year)	Findings	Limitations	Future area
Bahrololloomi et al. (2023)	GradB model gave the best results in stability and accuracy	Not specified.	Not specified.
Bisberg & Ferrara (2022)	GCN models outperformed traditional ML models; GCN-cheby with delta features, a convolution layer, had the best accuracy	It only includes regular-season games and focuses on league structure, not individual team skill changes.	Use heterogeneous and directed GCN models; Apply models to other esports and sports with similar structures
Canossa et al. (2021)	Detected toxic behaviour patterns using selected game features	The dataset is proprietary and cannot be shared publicly	Explore other genres and apply methods to detect positive player behaviours
Costa et al. (2021)	The most important predictors were player statistics (win rate and KDA); banned champions were less impactful	The study only focuses on pre-game information and does not include in-game dynamics	Future work should explore real-time data and additional feature engineering
Da Silva et al. (2017)	The Multilayer Perceptron achieved the highest accuracy for user identification using gaming biometric data	The study was limited by the small sample size and lack of real-time data	Future work should explore early, mid, and late-game phases separately to account for role changes
Do et al. (2020)	Players preferred recommendations from the system over random selections; CMP effectively captured player preferences	Limited by the availability of public data from Riot Games; challenges with popularity bias	Tune SVD model parameters for improved accuracy; explore real-time and more diverse player data
Do et al. (2021)	Player-champion experience was a strong predictor of match outcomes, with DNN achieving the highest accuracy	Limited to data from the North American server and focused on ranks Iron to Diamond	Future work could explore other regional servers and investigate the impact of player role experience
Edge (2013)	The study successfully predicts player churn in DotA 2 using empowerment and performance metrics; players are more likely to leave when performing poorly relative to their team and opponents	The model only uses end-of-game statistics and lacks real-time data	Future work should include event logs and consider player habits to improve prediction accuracy.
Franco et al. (2019)	Proposed a new metric (GDM) that better differentiates player profiles compared to KDA	Focused on a dataset of professional players only; limited generalisability to casual players	Extend the GDM approach to other e-sports games; involve real players in evaluating the new metric
Guzmán & Medina (2021)	Identified key independent variables for training ML models in MOBA games, with NN being the most effective	Some variables are game-specific and may not generalise well across different games	Focus on optimising variable selection and account for game updates

Table 4 (continue)

Authors (year)	Findings	Limitations	Future area
Hodge et al. (2021)	RF accuracy increases until mid-game and then declines, key prediction features evolve over time	Long matches are less predictable, with accuracy dropping in late-game stages.	Improve real-time prediction accuracy and explore other feature selection methods
Hong & Lee (2022)	The system detects in-game events without game APIs, demonstrating robust performance in live-streaming scenarios	Limited to predefined events and game objects, it may not capture all possible in-game scenarios	Extend the detection system to other game genres like FPS and RTS; improve detection of additional event types
Jiang et al. (2020)	The NICE model significantly improves prediction accuracy by incorporating individualised contextual factors	The model was tested on data from a specific period, which may not generalise to other timeframes or game versions	Extend the model to other games and apply it to different types of contextual data
Kim et al. (2020)	The proposed method achieved the best calibration among compared methods, reducing errors	The method was only tested on a limited set of matches, and its performance may vary across different datasets	Expand to other game genres and explore the impact of varying input features on calibration accuracy
Kokkinakis et al. (2020)	The Weavr app enhanced viewer engagement by offering data-driven insights and real-time interactive content	The app was limited to specific in-game events and was tested only on Dota 2 tournaments	Expanding the system to other esports titles and integrating more comprehensive data feature
Liang (2021)	SVM with linear kernel achieved better game outcome prediction compared to DT	Limited by low dimensionality of data with only 38 features; performance may vary with more complex feature sets	Include more features like hero combinations, player skills, and real-time event data to improve prediction accuracy
Luo et al. (2019)	Teacher-student approach reduces training time while maintaining accuracy; Zero-shot approach compromises accuracy for speed; Network pruning cuts down memory usage without significant accuracy loss.	Limited to specific in-game events; computational improvements might not scale to other game genres with different visual aesthetics	Apply methods to more diverse game genres and explore alternative architectures for further optimisation.
Lyu et al. (2022)	GPR achieved the best prediction accuracy, indicating stable performance for predicting risk propensity	Limited to Dota 2; did not include linguistic features or other potential variables	Incorporate linguistic features, expand to other games, explore feature similarity across models
Marchenko & Sushevskiy (2018)	Found that regional affiliation, participation in major tournaments, and team organisation significantly influence player transfers	Limited to transfers between 2016-2017; did not differentiate between voluntary and forced transfers	Explore different types of mobility and develop qualitative methods such as player interviews to better understand transfer reasons

Table 4 (continue)

Authors (year)	Findings	Limitations	Future area
Martens et al. (2015)	Detected toxicity through chat analysis using NLP, showing that toxic behaviour is linked to lower chances of game success	Limited to textual data from chat logs, ignoring other forms of communication like voice chat	Expand to other MOBAs and include voice communication analysis for comprehensive toxicity detection
Mohammed et al. (2022)	The draft recommendation system suggests the best heroes for the last pick, enhancing the team to counter opponents	Limited to DotA 2 and only considers predefined scenarios; accuracy is affected by game updates and new patches	Extend to other MOBA games and refine models to adapt to frequent game updates and meta shifts
Mora-Cantallops & Sicilia (2018)	Identified four player types based on social interaction in games, ranging from solo to team players	Limited to structural network data, no demographic or personal player data included	Incorporate demographic data to enhance understanding of player behaviours and social dynamics
do Nascimento Junior et al. (2017)	Identified 7 distinct team profiles, revealing patterns of successful and unsuccessful teams based on performance metrics	Limited to static, end-of-game performance data; did not include dynamic in-game behaviour changes	Extend analysis to include time-dependent statistics and explore other MOBA games.
Porokhnenko et al. (2019)	A linear regression model was the fastest and most suitable for practical implementation; SVM and neural networks provided high accuracy.	Focused on hero picks without considering other in-game factors; results may vary with different datasets and hyperparameters	Explore other game-related factors and optimise hyperparameters to improve prediction accuracy
Prakannoppakun & Sinthupinyo (2016)	Neural Network-based skill rating method outperformed traditional Elo rating by better measuring individual contributions to match outcomes.	Limited by static data from completed games; only considered attributes of selected heroes, ignoring team dynamics and communication	Expand to include real-time analysis and other aspects like player behaviours, communication, and team dynamics.
Semenov et al. (2017)	Factorisation Machines provided the best results for predicting game outcomes, showing effectiveness in modelling hero interactions	The study focused only on hero drafts, excluding real-time in-game factors and other team dynamics	Incorporate real-time data and expand the model to other MOBA games to improve predictive power
Shen (2022)	A Voting Classifier combining the best-performing models achieved good prediction accuracy	Limited to early-game data; does not account for late-game dynamics or champion-specific details	Explore the use of real-time data from different game phases, expand to other MOBA game
Stanlly et al. (2022)	XGBoost achieved the best performance, indicating item and hero choices significantly impact match outcomes	Focused on static in-game data; dynamic player decisions during the match were not considered	Integrate real-time decision-making models and expand to other esports games.

Table 4 (continue)

Authors (year)	Findings	Limitations	Future area
Summerville et al. (2021)	LSTM performed best in predicting draft picks, with higher accuracy in the later stages of the draft compared to Bayes Nets	Limited to historical match data from professional games, which may not generalise to other contexts or amateur play	Incorporate amateur match data and adapt models for changing game patches and evolving strategies
Vardal et al. (2022)	LSTM models outperform Bayesian networks, predicting draft choices with good accuracy	Limited data due to professional match focus; only 1518 matches were analysed, which may not generalise across patches	Incorporate data from more patches and explore deeper history in drafting for more complex pattern recognition.
Wang et al. (2018)	A new feature extraction method improved prediction accuracy, showing that detailed hero features enhance outcome prediction	Limited to high-level matches; does not consider dynamic in-game interactions or player-specific strategies	Extend feature extraction to include more in-game variables and test across different MOBA games.
Wei et al. (2022)	RL methods face challenges in generalisation across different heroes and opponents	Existing RL methods struggle with transferability across tasks in competitive settings.	Future work involves enhancing RL model generalisation and transferability across different tasks.
Wong et al. (2022)	Prediction of first blood and match outcome; first blood is not a strong predictor of match outcome	First blood does not add significant predictive power for match outcome	Future work will include hyperparameter tuning, different data encoding, and exploring other classifiers like DT and RF
Ye et al. (2022)	JueWu-SL AI performs at the human level, achieving a high win rate against top human players	AI struggles with Jungle invasion strategy and fast adaptation to opponent's tactics	Future work involves combining Supervised Learning with Reinforcement Learning to improve adaptability
Zhang (2021)	AI achieves human-level performance, handling complex macro-strategy and micromanagement tasks	The AI struggles with the Jungle invasion strategy and fast adaptation	Future work includes enhancing adaptability using Reinforcement Learning

study even developed an AI system to play the game and tested it against real matches and professional players.

Despite their achievements, the studies reported several limitations, such as the need for greater resources for more accurate predictions, algorithm complexity, and multi-step approaches. Some studies used restricted data sources due to gameplay differences among players from different regions. Other studies faced challenges in accessing certain types of data due to game developers' policies and terms and conditions. The studies later identified potential areas for further investigation by future researchers. Those experimenting with predictors suggested adding more predictors, applying more models, and designing a recommendation system for professional teams and organisations. Those working on improving ML algorithms suggested exploring different approaches to the improved method and using more data in future models. These findings can help guide future research in MOBA esports prediction and can benefit the esports community.

Table 5 presents the metrics of ML performance proposed in the included studies, which provide insights for answering RQ3. The proposed ML approaches were assessed using accuracy, precision-recall, cross-validation, and AUC-ROC. The reported performance percentages ranged from 10% to 80% and were deemed impressive, given the simplicity of the datasets used. Such predictions are highly valuable for organisations seeking to simulate or analyse future improvements. Most studies that aimed to enhance ML algorithms reported significant improvements and more than satisfactory results despite an increase in computing resources required and hold promise for future research.

Table 5
Results of individual studies (metrics of ML performance)

Authors (year)	ML metrics
Bahrololloomi et al. (2023)	Accuracy: 92.78%, R ² : 0.8327
Bisberg & Ferrara (2022)	GCN-cheby (1 layer) accuracy: 61.9%; RF accuracy: 57.8%; SCOPE accuracy: 59.7%
Canossa et al. (2021)	Accuracy: High precision with RF and SVM
Costa et al. (2021)	AUC of 0.97 for RF and LR
Da Silva et al. (2017)	MLP accuracy: 86.27% (5 min interval); Bayesian Network accuracy: 75.55% (3 min interval); RBF Network accuracy: 76.1% (3 min interval)
Do et al. (2020)	System recommendations rated higher than random: mean score 6.46 vs. 5.18, p = 0.01257
Do et al. (2021)	DNN accuracy: 75.1%; GBOOST accuracy: 75.4%; RF accuracy: 74.7%; SVC accuracy: 74.3%; kNN accuracy: 72.7%
Edge (2013)	NB: sensitivity 70.5%, specificity 67.8%
Franco et al. (2019)	GDM better discriminate player profiles than KDA, with clusters validated by silhouette scores
Guzmán & Medina (2021)	Emphasis was on identifying relevant variables rather than specific accuracy metrics.

Table 5 (continue)

Authors (year)	ML metrics
Hodge et al. (2021)	RF accuracy varies, peaking mid-game and declining afterwards
Hong & Lee (2022)	Achieved event detection accuracy with minimal missed events at optimal parameter settings
Jiang et al. (2020)	The NICE model outperformed baseline models with an AUC of 0.953 for predicting match outcomes
Kim et al. (2020)	Achieved accuracy: 73.81%; ECE: 0.57%; MCE: 1.26%
Kokkinakis et al. (2020)	High user engagement during live matches
Liang (2021)	SVM (linear) accuracy: 73%; SVM accuracy: 72.8%; DT accuracy: 68.6%
Luo et al. (2019)	The teacher-student-student approach achieved 99.8% test the curacy; the standard ResNet152 model achieved 94.6% a, with curacy; significant reduction in training and execution time with optimised approaches.
Lyu et al. (2022)	GPR: RMSE = 1.10, $R^2 = 0.17$; RF: RMSE = 1.20, $R^2 = 0.01$.
Marchenko & Suschevskiy (2018)	ERGM results showed a significant influence of region and major tournament participation on transfers; association rules highlighted differences between captains and non-captains
Martens et al. (2015)	SVM classification accuracy varied based on the features used; specific numerical metrics were not provided
Mohammed et al. (2022)	Achieved high accuracy in recommending heroes that align with team strategies; specific numerical metrics not provided
Mora-Cantalops & Sicilia (2018)	No specific metrics for ML performance; it focuses on clustering based on network structure.
do Nascimento Junior et al. (2017)	Clustering achieved a significant reduction in data variability, with certain profiles showing high win rates
Porokhnenko et al. (2019)	Linear Regression and SVM achieved an AUC of 0.7739; neural networks showed similar performance with optimised hyperparameters.
Prakannoppakun & Sinthupinyo (2016)	Improved accuracy in predicting match outcomes compared to Elo Rating; specific numerical metrics not provided
Semenov et al. (2017)	Factorization Machines achieved the highest AUC: 0.706 for normal skill level, 0.670 for high skill level, and 0.660 for very high skill level.
Shen (2022)	Voting Classifier accuracy: 72.68%; individual model performances varied but were generally lower
Stanly et al. (2022)	XGBoost accuracy: 93%; DT accuracy: 82%; RF accuracy: 91%
Summerville et al. (2021)	LSTM achieved 11.94% accuracy in hero prediction, outperforming Bayes Nets and human analysts in strict predictions
Vardal et al. (2022)	LSTM accuracy: 11.94%; Bayes Nets accuracy: up to 11.48%
Wang et al. (2018)	LR: Accuracy improved to 63.8%, SVM: Accuracy improved to 64.3%
Wei et al. (2022)	Win rate: 90% for Diaochan vs. Diaochan, drops when the opponent or target changes; Reward and Elo score provided in specific cases
Wong et al. (2022)	Accuracy: 57%–59%, precision, recall, F1-score
Ye et al. (2022)	Win rate: 86%–100% against various baselines, matches against top human players: AI won 7 out of 10 matches
Zhang (2021)	Win rate: 86%–100%, AI won 7 out of 10 matches against human

Figure 5 displays the percentage distribution of different ML algorithm challenges reported by the studies. The key challenges revolve around the following issues. Overfitting and underfitting hinder model reliability, especially in high-dimensional or imbalanced datasets, affecting predictive power. Generalizability is impacted by constraints in data representativeness, timeframes, and specific game contexts, making it difficult for models to adapt to varied environments. Data is often limited due to privacy concerns or limited feature availability, while high computational demands and model complexity present resource-related constraints. Interpretability challenges arise in unsupervised models and high-dimensional data, limiting insight into model outputs. Scalability issues restrict model application across broader datasets or different games while maintaining predictive accuracy, which is challenging in prolonged, dynamic gaming environments. These challenges underscore the need for tailored ML approaches that address these constraints in data-driven research for gaming and esports applications.

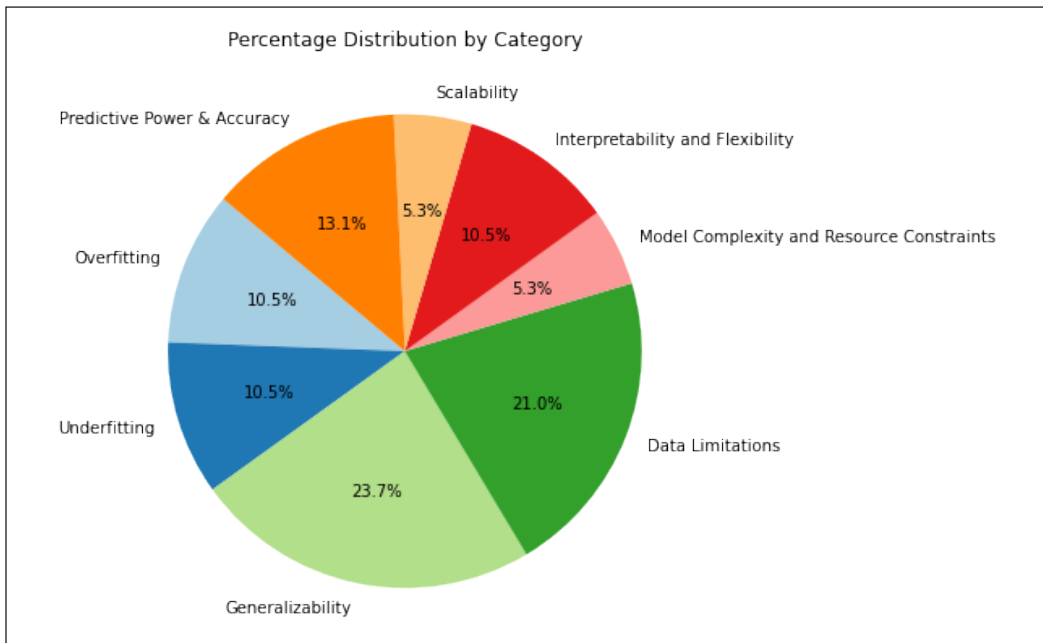


Figure 5. Challenges for ML algorithms deployed in the included studies

Risk of Bias Assessment

Figure 6 shows the risk of bias assessment results for the 35 included studies using PROBAST. All the included studies were assessed to have “low risk” across all domains, indicating reliability and robust methodologies. The participant selection, predictor measurement, outcome assessment, and analytical methods are appropriate and free from significant bias. Their findings can be considered reliable and valuable contributions to

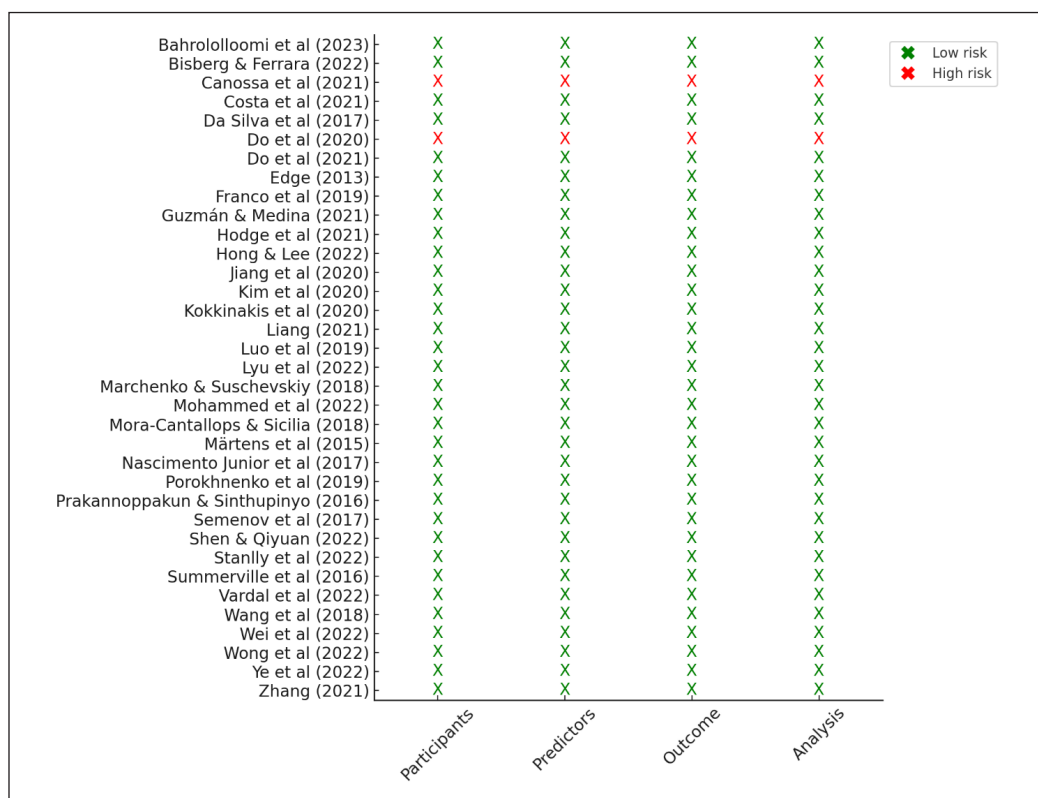


Figure 6. Risk of bias assessment results for the 35 included studies

respective fields. This reliability is crucial for advancing knowledge in the areas of MOBA game analytics and esports research, mostly focusing on Dota 2 and LoL using advanced ML techniques for predictive analysis. The methodologies and ML models used are sound, showing the value of the studies as resources for further research and practical applications in esports. Since these studies show a high standard of research quality, future studies can build upon these findings with confidence, with similar methodologies that could be applied or adapted for future research to continue producing high-quality results.

Results of Syntheses

Figure 7 shows the mean accuracy of different ML algorithms from the studies which reported the accuracy of models' performance. Figure 8 shows the distribution of the accuracy values from the ML algorithms. Among the algorithms with available accuracy data, XGBoost showed high performance with an accuracy of 92.78% in Bahrololloomi et al. (2023) and 93% in Stanlly et al. (2022), indicating its effectiveness in scenarios involving structured data with complex interactions. RF is frequently used and has shown strong performance with accuracies of around 97% (Costa et al., 2021), suggesting that

RF is a reliable choice for handling datasets with numerous predictors. Deep NN also showed high performance, with an accuracy of 75.1%, as reported by Do et al. (2021). This performance reflects the capability of DNNs to capture complex patterns and interactions in player behaviours and game dynamics. SVM models displayed moderate performance, with accuracies of around 73% (Liang, 2021). SVMs are effective for binary classification tasks and are suitable for smaller datasets where feature space dimensionality is manageable. Both k-NN and NB had relatively lower performance in comparison to others, with accuracies

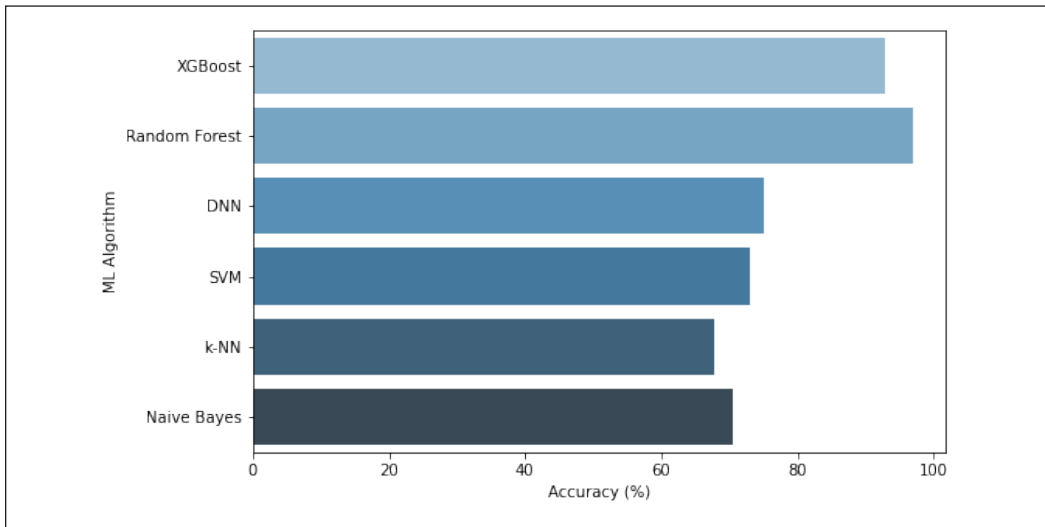


Figure 7. The mean accuracy of different ML algorithms reported in the included studies

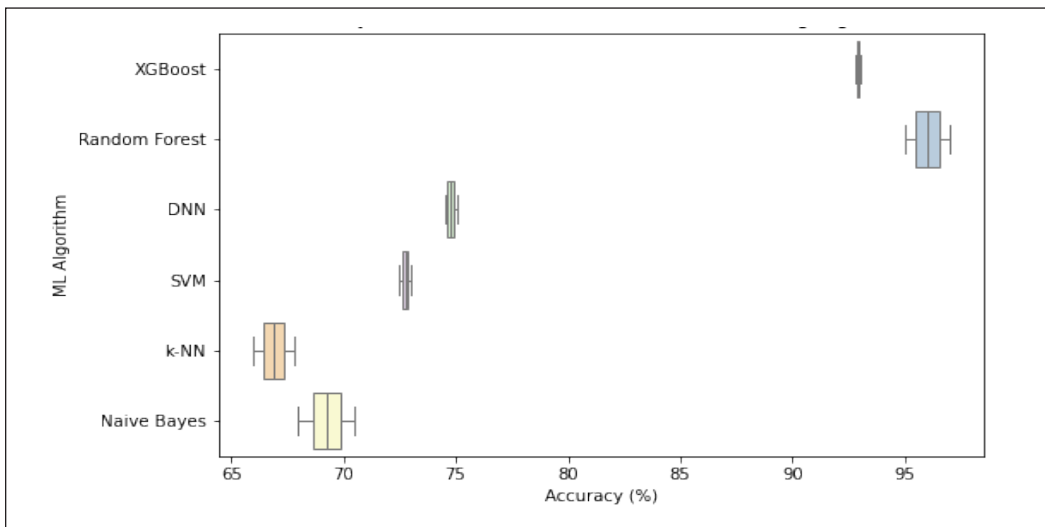


Figure 8. Accuracy distribution of different ML algorithms from the included studies

around 67.8% (Edge, 2013), as they are considered simple models and may not capture complex patterns as effectively as ensemble methods or NN.

Various features encircling MOBA games and esports have been used as predictors in ML modelling. From the 35 included studies, there are four main categories, including player performance and statistics ($n = 11$), in-game events and match statistics ($n = 7$), game mechanics and interaction ($n = 7$), and player behaviour and communication ($n = 3$), with only a study did not have any dataset in their work ($n = 1$), as shown in Figure 9. The highest category shows that a significant focus of the studies is on player-related metrics such as experience points, kill/death ratios (KDA), player statistics, and overall game performance, as the understanding of individual player contributions and behaviours is a crucial aspect in ML modelling given that player performance directly affects game outcomes. In-game events form the second most emphasised category, such as hero kills, tower destruction, and match outcomes, with features that provide insights into how specific in-game events affect the outcome of a match. This highlights the dynamic nature of MOBA, where real-time events play a significant role in match progression. Incorporating these features allows ML models to account for the ever-changing nature of gameplay. The third category (game

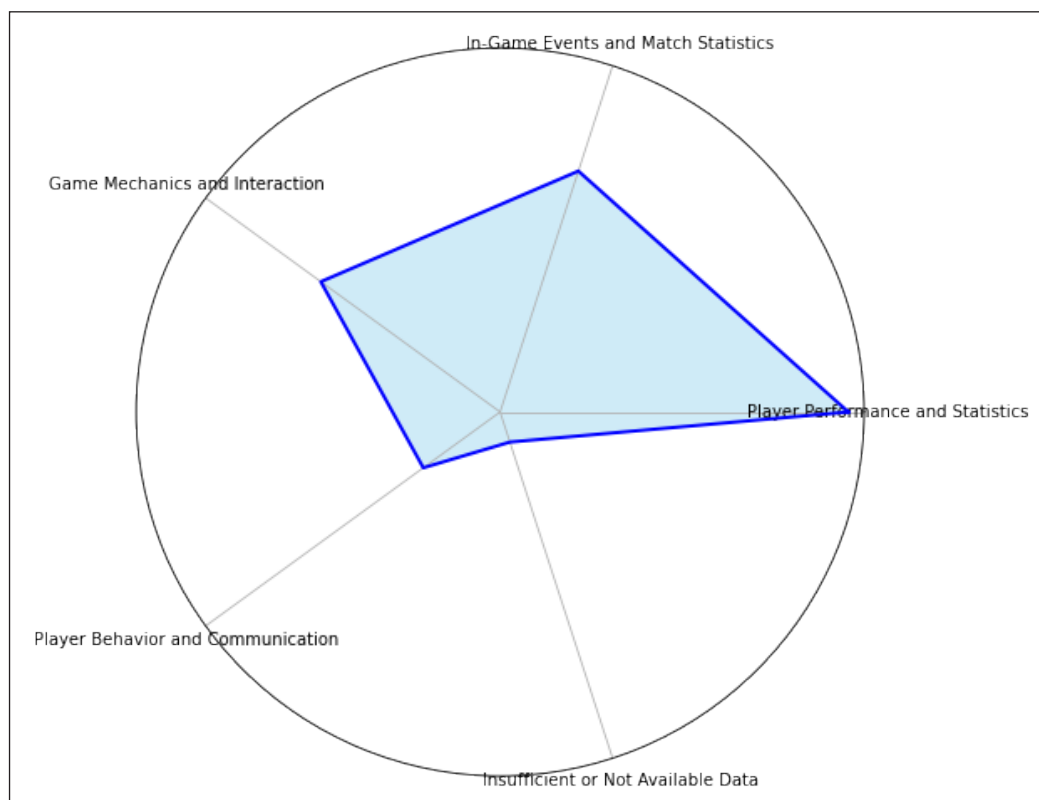


Figure 9. Distribution of predictors' categories used in the included studies

mechanics and interaction) encompasses features like keystrokes, character picks and bans, and team strategies. This reflects the studies’ interest in understanding how the mechanics of the game itself affect overall performance. As the interactions between players and game mechanics directly are important, this category is vital for models aiming to simulate match dynamics. This emphasises how player decisions and interactions with game mechanics contribute to the complexity of MOBA games. The least represented category focuses on player behaviour patterns and communication (chat logs), which is less emphasised in current predictive modelling, potentially due to the challenges in quantifying these aspects or their less direct impact on match outcomes.

The distribution of player skill levels used as data in the ML studies is shown in Figure 10. A considerable number of studies in MOBA esports focus on high-level and professional players. This trend suggests that researchers prioritise understanding patterns of elite players, who are often seen as benchmarks for game mastery, as professional players represent the highest skill level and typically have access to more advanced strategies and gameplay. Analysing their data provides valuable information in optimising ML models and AI agents to mimic or counter against top-tier playstyles. The mixed or varying skill levels reflect the recognition that player performance differs widely across skill levels, from beginner to advanced. Including players of varying skill levels allows researchers to develop more generalisable models. This indicates a desire to build models that adapt to different gameplay styles, making the findings more applicable to the average player. While smaller, the advanced/human skill level highlights an interest in comparing ML or AI performance against human capabilities. As AI systems continue to evolve, the

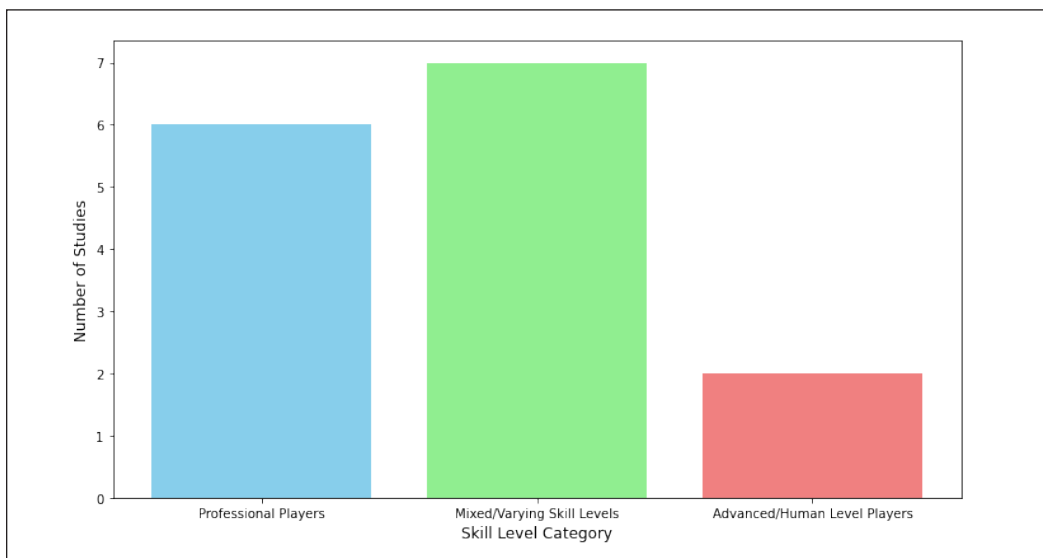


Figure 10. Distribution of the target player skills levels in the included studies

comparison with human-level skills serves as a benchmark for how AI can surpass human capabilities in certain areas.

Figure 11 shows the distribution of included studies based on the dataset regions. The analysis shows that most of the studies focus on data from CN (17.65%) and NA (11.76%). This indicates that the research in MOBA esports is primarily centred around regions with a significant presence in esports. These findings may not fully represent player behaviours or dynamics in other less-studied regions. A considerable number of studies (20.59%) did not specify their dataset region, reducing the transparency of the findings. This scarcity makes it difficult to assess regional diversity and limits the ability to understand regional influence. Several studies (11.76%) have global or international focus, indicating efforts to analyse MOBA esports from a broader perspective. These studies likely offer insights that are more generalised but may still have minute-overlooked differences in a global analysis. Asia (South Korea, Thailand, Indonesia), the EU (United Kingdom), and SA (Brazil) have very few studies (around 2.94% each). Despite South Korea being a major esports hub, it appears to be underrepresented in the dataset. More comprehensive research in diverse regions is needed.

Figure 12 shows the frequency of included studies based on their automation level. High automation is characterised by its ability to handle complex data structures and advanced algorithms with minimal human intervention after the initial setup. These systems excel in efficiency, accuracy, and scalability, making them ideal for real-time data processing and large-scale analytics in dynamic environments like MOBA esports. Lower automation involves a significant increase in human involvement in tasks such as data preparation, model training, and evaluation, often employing simpler techniques (collaborative filtering

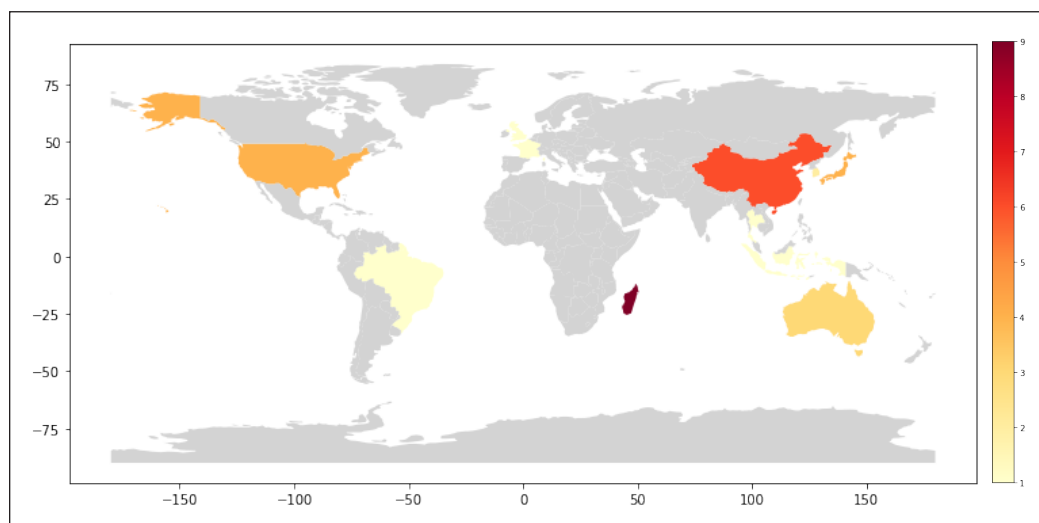


Figure 11. The distribution of the included studies based on dataset regions

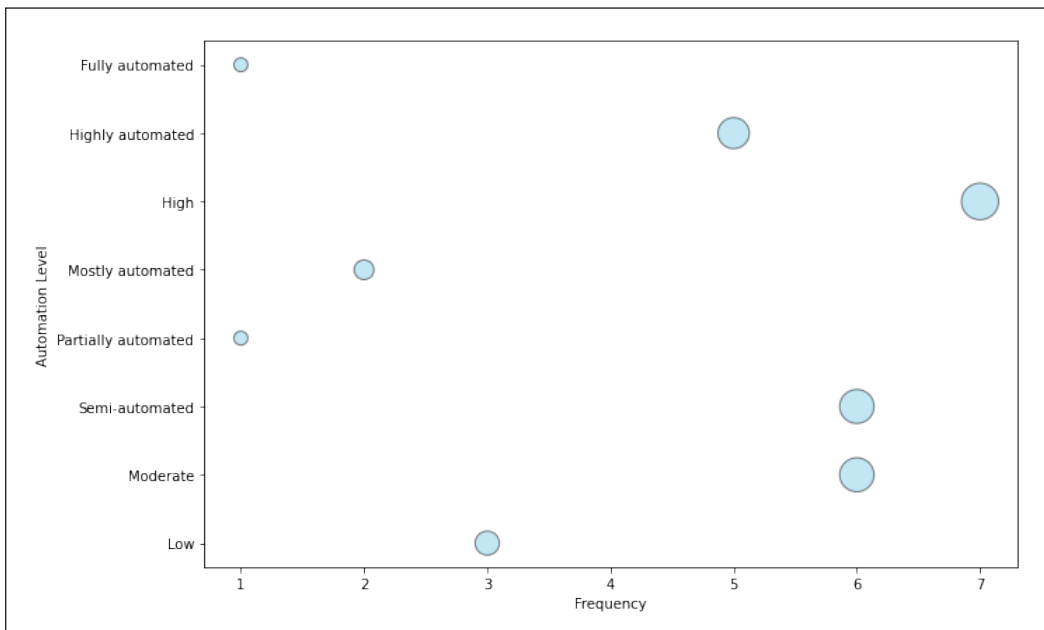


Figure 12. The frequency of studies by automation level

and basic reinforcement learning). Low automation offers flexibility and allows for domain-specific adjustments, but it is more time-consuming, less adaptable to changing data patterns, and limited in scalability.

General Interpretation of Results

This systematic review represents the first attempt to comprehensively explore the use of ML approaches in esports, with a focus on the MOBA genre. Following a rigorous screening process, 35 studies were deemed eligible for inclusion in the subsequent data extraction phase.

Why DotA 2 and LoL?

Both these games are popular in ML research because they provide a rich and complex environment for studying artificial intelligence and decision-making (Guzmán & Medina, 2021; Summerville et al., 2021). Both games involve real-time strategy, and players need to make decisions quickly and adapt to changing circumstances to win. DotA 2 and LoL have been used as testbeds for studying multi-agent systems and reinforcement learning (Du et al., 2021). Each player controls a character (or “hero”) in these games and must work with their team to defeat the opposing team. This creates a complex environment with many interacting agents, making it an ideal setting for studying multi-agent coordination and cooperation. Moreover, both games provide large and publicly available gameplay

datasets, allowing researchers to train and evaluate ML algorithms on authentic data. This has led to the development of advanced AI systems for playing DotA 2 and LoL, which can compete at a prominent level against human players (Berner et al., 2019). Overall, DotA 2 and LoL are popular in ML research because they provide a challenging and realistic environment for studying AI and decision-making, as well as rich datasets for training and evaluating ML approaches.

PC and Mobile Phone MOBA

DotA 2 and LoL are some examples of computer-based MOBA. Other than PC, mobile phone MOBA has grown in popularity in recent years, with games such as Arena of Valor (AoV), Mobile Legends: Bang Bang (MLBB), and HoK leading the way (Yang et al., 2022). These games are especially popular in the Southeast Asia region, with a massive player base and even professional esports leagues (Ong et al., 2023). According to a report by market research firm Newzoo, mobile MOBA generated \$15.3 billion in revenue in 2020, the most profitable genre in mobile gaming. The report also stated that mobile MOBA has over 628 million players worldwide, with most coming from China and Southeast Asia. Surprisingly, despite its popularity, research in this part is still very scarce.

Recommendation Systems

ML can be utilised to develop recommendation systems for MOBA esports, helping players make informed decisions about their gameplay strategies. The studies have shown that ML algorithms can analyse a player's gameplay data (Maymin, 2021), such as their win-loss record (Porokhnenko et al., 2019), character selection (Chan et al., 2020), and in-game performance (Hodge et al., 2021), to predict favourable outcomes. However, studies have also identified challenges in implementing this approach for end-users. Despite the challenges, the benefits of ML for recommendation systems in MOBA are significant. For example, ML can provide improved personalisation and real-time recommendations during matches, enhancing player engagement and retention. Additionally, ML can help game developers identify balance issues and make data-driven changes to improve the overall gaming experience (Kokkinakis et al., 2020). Overall, ML-based recommendation systems offer numerous benefits to MOBA esports.

Real-time Decision-making

An emerging area with significant potential is the use of ML models for real-time decision-making during live esports matches. In fast-paced games like MOBA esports, ML models have the potential to offer actionable insights that can be used by players and coaches, such as optimal hero selections or item builds based on the current state of the game. ML algorithms could dynamically analyse player and team performance, map

control, and resource management to generate recommendations in real-time. Another promising application is an AI-powered coach that can provide players with feedback on their performance during games by identifying patterns in their gameplay and suggesting real-time improvements to help players adjust their tactics, making them more adaptable. However, integrating ML into live esports matches may pose unique challenges. Real-time models need to process large volumes of data with minimal latency to ensure that decisions are made quickly enough to be useful. Furthermore, the deployment of ML-driven decisions in real-time raises ethical and fairness considerations, particularly if certain teams or players have access to superior analytical tools that could create an imbalance in competitive play.

Data Access Challenges

One of the primary challenges faced by researchers in this field is access to comprehensive and high-quality game data. Game developers often restrict access to data to protect proprietary information, maintain player privacy, and adhere to regional regulations. These restrictions limit the scope of data, introducing biases that affect the generalisability of findings caused by sampling biases, where certain demographics are underrepresented. Additionally, data from publicly available sources or community-collected datasets may not cover all aspects of the game, leading to gaps in understanding player behaviours and game dynamics. Fostering collaborations between researchers and game developers could provide a pathway to better data access. These partnerships could facilitate access to anonymised or aggregated data, balancing the need for privacy with the research community's need for comprehensive datasets. Advocating for open data initiatives within the gaming industry could promote the sharing of data in a controlled and secure environment.

Regional Differences

The gameplay strategies, player behaviours, and game meta can vary significantly across different regions due to cultural influences, regional preferences, and local competitive environments. Players in one region may prefer aggressive strategies (SEA and CIS) and hero selections, while others favour defensive playstyles (EU and CN). These lead to inconsistencies in ML model performance that lack generalizability. This poses a challenge in synthesising results and drawing broad conclusions applicable to the global scene. Future research should aim to include cross-regional studies that compare gameplay and data in a worldwide setting so that researchers can better understand universal versus region-specific insights. Additionally, current research is skewed towards a few prominent regions, CN and NA, with other regions remaining underrepresented or unspecified. Future research should strive for greater inclusivity and transparency in regional data to provide holistic understanding and enhance the applicability of ML across diverse populations.

CONCLUSION

Implication for Future Research

Other than PC esports, there is a need to empower research on mobile phone-based MOBA. The popularity of mobile MOBA can be attributed to their accessibility, as they can be played on a wide range of mobile devices and social aspects, with players being able to team up with friends and participate in global tournaments. Additionally, the fast-paced gameplay and constant updates and events keep players engaged. Mobile phone MOBA often has more diverse player bases and unique game mechanics compared to traditional PC-based MOBA, making them an attractive field of study for researchers. This would have immense potential to gain access to a much bigger data mine for a great prospect on ML-based studies. Researchers might be intrigued by *“How to develop mobile phone-based MOBA ML models for prediction”* or *“What specific challenges and opportunities in using mobile phone-based MOBA data for ML research compared to traditional PC-based MOBA.”*

The syntheses of subgroups reflect the complexity of MOBA esports. The insights from most predictors used suggest that researchers prioritise quantifiable and directly impactful features when constructing ML models. There is potential for growth in examining less-explored aspects, such as player communication, teamwork, and leadership, which could enrich predictive analytics. Based on players' skill levels, there is a need to analyse a wider spectrum of skill levels to better understand learning curves, mistakes, and strategies unique to less experienced players. Given the varying skill levels, ML models should be designed to be more adaptive to the provided datasets. In terms of human intervention, high automation could streamline predictive analytics and provide rapid insights, while low automation could enhance understanding in scenarios requiring human analysis. Future research may aim to integrate both approaches for maximum efficiency, leveraging their strengths.

Another broad aspect of implications is to push for the commercialisation potential for ML-based applications that non-researchers like MOBA esports teams and managements can deploy. Players and teams can train effectively by using quantitative and scientific methods to perform analysis and develop decision-support systems. However, providers must take secure measures should commercial products with ML technologies use professional data. ML with the ability to analyse large volumes of game data may commercialise:

1. **Performance analysis application:** An app that highlights strengths, weaknesses, and areas for improvement for individual players and teams, providing detailed feedback on gameplay mechanics (positioning, skill usage, and team coordination) to help players refine their strategies and optimise their in-game decisions based on match reports.
2. **Strategic decision-support system:** A third-party software for commercial use that can act like a virtual coach that provides real-time recommendations during practices, helping teams learn to adapt to changing conditions. This system might

also analyse opponent behaviours, predict future moves, and suggest optimal responses after matches.

3. **Customised training program:** An enhanced match reporting API or web-based system that facilitates personalised training programs by analysing a player's historical performance data and tailoring training routines to address specific weaknesses with automated coaching systems to accelerate target growth area.
4. **Fan engagement and content creation:** Plugins or tooltips in live or video streaming services provide deep insight into professional players' thoughts and actions before, during and after matches for general audiences and players.
5. **Real-time decision-making tool:** Advanced AI systems that support non-players and teams during gameplay enhance competitive performance and viewer engagement. This approach could also open new avenues for the commercialisation of AI tools in esports, making ML-driven decision-making an integral part of competition viewership.

Deploying ML in esports faces several challenges, including data privacy concerns, scalability, and integration with existing infrastructure. However, the success story of DotA 2 OpenAI displayed how AI and ML can benefit the esports industry as a whole (Berner et al., 2019). From a simple project of creating a mode where a team of five humans fight against 5 AI opponents, the DotA 2 community and players (casual and serious) enjoyed the mode and successfully improved their gameplay as AI opponents have very high skill levels. Content creators and professional teams alike produce huge numbers of content and engagement through this mode, showing the significance of AI advancement.

Further, developing robust methodologies for data access restrictions and regional variations is important. Future research should prioritise transparency in data collection methods, clearly outlining any limitations and biases. The development of standardised protocols for data sharing can help mitigate the impact of these challenges for more reliable and generalisable findings. Normalisation techniques might be helpful in standardising data from various regions, making it more comparable and reducing regional biases. Transfer learning could also be employed to improve model applicability for multi-region studies. By addressing these issues, the field of ML applications in MOBA esports can advance, providing insights that are both scientifically rigorous and practically relevant to the global gaming community.

Limitations

Conducting a systematic review for ML in MOBA is challenging due to the small number of studies available, which can limit the scope and generalizability of the findings. This can be because ML is a new field in esports research (Reitman et al., 2020), and MOBA

is just one genre of many in esports. There is also a potential for bias or inconsistencies in the methodology or reporting of the studies included in this review, which can affect the accuracy and reliability of the results. The rapid evolution of both the field of ML and the esports industry, too, in general, can mean that the studies included in the review may become outdated quickly. Another limitation of this systematic review is the possibility of missing relevant studies. The search strategy used may not be comprehensive enough to capture all relevant studies, or some studies may be published in non-English language journals and may not be included in the earlier search and screening process. In addition, the studies included in the review may have used different datasets, variables, and ML algorithms, which can make direct comparisons difficult.

ACKNOWLEDGEMENTS

The authors would like to express their sincerest gratitude to USM and UNIMAS for their invaluable support, which significantly contributed to the completion of this systematic review. They would also like to thank Instalock Esports Ent. for their significant academic contribution to this study.

REFERENCES

- Bahrololloomi, F., Klonowski, F., Sauer, S., Horst, R., & Dörner, R. (2023). E-sports player performance metrics for predicting the outcome of league of legends matches considering player roles. *SN Computer Science*, 4(3), Article 238. <https://doi.org/10.1007/s42979-022-01660-6>
- Bailey, K. (2020). *Statistical Learning for Esports Match Prediction*. (Master's dissertation). California State Polytechnic University, California. <https://scholarworks.calstate.edu/downloads/kw52jb221>
- Bankov, B. (2019). The impact of social media on video game communities and the gaming industry. *Conferences of the Department Informatics*, 1, 198–208.
- Bernama. (2023, October 14). Belanjawan 2024: Sasar jadikan Malaysia hub e-sukan [Budget 2024: Aim to Make Malaysia an E-sports Hub]. *Berita Harian Online*. <https://www.bharian.com.my/bisnes/lain-lain/2023/10/1165080/belanjawan-2024-sasar-jadikan-malaysia-hub-e-sukan>
- Berner, C., Brockman, G., Chan, B., Cheung, V., Dębiak, P., Dennison, C., Farhi, D., Fischer, Q., Hashme, S., Hesse, C., Józefowicz, R., Gray, S., Olsson, C., Pachocki, J., Petrov, M., Pinto, H. P. d. O., Raiman, J., Salimans, T., Schlatter, J., & ... Zhang, S. (2019). *Dota 2 with large scale deep reinforcement learning*. ArXiv Preprint. <https://doi.org/10.48550/arxiv.1912.06680>
- Bisberg, A. J., & Ferrara, E. (2022). GCN-WP - Semi-supervised graph convolutional networks for win prediction in esports. In *2022 IEEE Conference on Games (CoG)* (pp. 449-456). IEEE Publishing. <https://doi.org/10.1109/CoG51982.2022.9893671>
- Canossa, A., Salimov, D., Azadvar, A., Harteveld, C., & Yannakakis, G. (2021). For honor, for toxicity. *Proceedings of the ACM on Human-Computer Interaction*, 5, 1–29. <https://doi.org/10.1145/3474680>

- Chan, A. S., Fachrizal, F., & Lubis, A. R. (2020). Outcome prediction using Naïve Bayes algorithm in the selection of role hero mobile legend. *Journal of Physics: Conference Series*, 1566(1), Article 012041. <https://doi.org/10.1088/1742-6596/1566/1/012041>
- Collins, G. S., Dhiman, P., Navarro, C. L. A., Ma, J., Hooft, L., Reitsma, J. B., Logullo, P., Beam, A. L., Peng, L., Van Calster, B., van Smeden, M., Riley, R. D., & Moons, K. G. (2021). Protocol for development of a reporting guideline (TRIPOD-AI) and risk of bias tool (PROBAST-AI) for diagnostic and prognostic prediction model studies based on artificial intelligence. *BMJ Open*, 11(7), Article e048008. <https://doi.org/10.1136/bmjopen-2020-048008>
- Conley, K., & Perry, D. (2013). *How Does He Saw Me? A Recommendation Engine for Picking Heroes in Dota 2*. CS229 Previous Projects. <https://cs229.stanford.edu/proj2013/PerryConley-HowDoesHeSawMeARecommendationEngineForPickingHeroesInDota2.pdf>
- Costa, L. M., Mantovani, R. G., Souza, F. C. M., & Xexeo, G. (2021). Feature analysis to league of legends victory prediction on the picks and bans phase. In *2021 IEEE Conference on Games (CoG)* (pp. 01-05). IEEE Publishing. <https://doi.org/10.1109/CoG52621.2021.9619019>
- Da Silva, C. A., da Silva, V. R., & Da Costa-Abreu, M. (2017). An empirical biometric-based study for user identification from different roles in the online game League of Legends. In *Proceedings of the III Potiguar Games, Entertainment and Education Meeting* (Vol. 2117, pp. 1-10). CEUR Workshop Proceedings.
- de Jong, Y., Ramspek, C. L., Zoccali, C., Jager, K. J., Dekker, F. W., & van Diepen, M. (2021). Appraising prediction research: a guide and meta-review on bias and applicability assessment using the prediction model risk of bias assessment tool (PROBAST). *Nephrology*, 26(12), 939–947. <https://doi.org/10.1111/nep.13913>
- do Nascimento Junior, F. F., da Melo, A. S. C., da Costa, I. B., & Marinho, L. B. (2017). Profiling Successful Team Behaviors in League of Legends. In *Proceedings of the 23rd Brazillian Symposium on Multimedia and the Web* (pp. 261-268). <https://doi.org/10.1145/3126858.3126886>
- Do, T. D., Wang, S. I., Yu, D. S., McMillian, M. G., & McMahan, R. P. (2021). Using machine learning to predict game outcomes based on player-champion experience in league of legends. In *Proceedings of the 16th International Conference on the Foundations of Digital Games* (pp. 1-5). <https://doi.org/10.1145/3472538.3472579>
- Do, T. D., Yu, D. S., Anwer, S., & Wang, S. I. (2020). Using collaborative filtering to recommend champions in league of legends. In *2020 IEEE Conference on Games (CoG)* (pp. 650-653). IEEE Publishing. <https://doi.org/10.1109/CoG47356.2020.9231735>
- Du, X., Fuqian, X., Hu, J., Wang, Z., & Yang, D. (2021). Uprising E-sports Industry: machine learning/AI improve in-game performance using deep reinforcement learning. In *2021 International Conference on Machine Learning and Intelligent Systems Engineering (MLISE)* (pp. 547-552). IEEE Publishing. <https://doi.org/10.1109/MLISE54096.2021.00112>
- Edge, R. (2013). *Predicting Player Churn in Multiplayer Games using Goal-Weighted Empowerment* [Technical Report; 13-024]. University Digital Conservancy. <https://hdl.handle.net/11299/215927>
- Eisen, P. (2017). *Simulating human game play for level difficulty estimation with convolutional neural networks*. (Master dissertation). KTH Royal Institute of Technology, Sweden. <https://urn.kb.se/resolve?urn=urn:nbn:se:kth:diva-215699>

- Fanca, A., Puscasiu, A., Gota, D. I., & Valean, H. (2020). Recommendation systems with machine learning. In *2020 21th International Carpathian Control Conference (ICCC)* (pp. 1-6). IEEE Publishing. <https://doi.org/10.1109/ICCC49264.2020.9257290>
- Franco, G., Ribeiro, M. H. F., & Comarela, G. (2019). Towards an interpretable metric for DOTA 2 players: An unsupervised learning approach. In *2019 8th Brazilian Conference on Intelligent Systems (BRACIS)* (pp. 341-346). IEEE Publishing. <https://doi.org/10.1109/BRACIS.2019.00067>
- Guzmán, J. G. L., & Medina, C. J. B. (2021). Relevant independent variables on MOBA video games to train machine learning algorithms. *Computer Science Research Notes*, *3101*, 171–180. <https://doi.org/10.24132/CSRN.2021.3101.19>
- Hodge, V. J., Devlin, S., Sephton, N., Block, F., Cowling, P. I., & Drachen, A. (2021). Win prediction in multiplayer esports: Live professional match prediction. *IEEE Transactions on Games*, *13*(4), 368–379. <https://doi.org/10.1109/TG.2019.2948469>
- Hong, S. J., & Lee, S. K. (2022). Detecting in-game play event in live esports stream. In *2022 13th International Conference on Information and Communication Technology Convergence (ICTC)* (pp. 1929-1931). IEEE Publishing. <https://doi.org/10.1109/ICTC55196.2022.9952770>
- Jiang, J., Lerman, K., & Ferrara, E. (2020). Individualized context-aware tensor factorization for online games predictions. In *2020 International Conference on Data Mining Workshops (ICDMW)* (pp. 292-299). IEEE Publishing. <https://doi.org/10.1109/ICDMW51313.2020.00048>
- Jiu, L., Wang, J., Somolinos-Simón, F. J., Tapia-Galisteo, J., García-Sáez, G., Hernando, M., Li, X., Vreman, R. A., Mantel-Teeuwisse, A. K., & Goettsch, W. G. (2024). A literature review of quality assessment and applicability to HTA of risk prediction models of coronary heart disease in patients with diabetes. *Diabetes Research and Clinical Practice*, *209*, Article 111574. <https://doi.org/10.1016/j.diabres.2024.111574>
- Jordan, M. I., & Mitchell, T. M. (2015). Machine learning: Trends, perspectives, and prospects. *Science*, *349*(6245), 255–260. <https://doi.org/10.1126/SCIENCE.AAA8415>
- Kim, D. H., Lee, C., & Chung, K. S. (2020). A confidence-calibrated MOBA game winner predictor. In *2020 IEEE Conference on Games (CoG)* (pp. 622-625). IEEE Publishing. <https://doi.org/10.1109/CoG47356.2020.9231878>
- Kinkade, N., & Lim, K. Y. K. (2015). *DOTA 2 win prediction*. *University of California*, *1*, 1-13.
- Kokkinakis, A. V., Demediuk, S., Nölle, I., Olarewaju, O., Patra, S., Robertson, J., York, P., Chitayat, A. P. P., Coates, A., Slawson, D., Hughes, P., Hardie, N., Kirman, B., Hook, J., Drachen, A., Ursu, M. F., & Block, F. (2020). DAX: Data-driven audience experiences in esports. In *Proceedings of the 2020 ACM International Conference on Interactive Media Experiences* (pp. 94-105). ACM Publishing. <https://doi.org/10.1145/3391614.3393659>
- Kulkarni, P. (2012). *Reinforcement and Systemic Machine Learning for Decision Making*. John Wiley & Sons.
- Le Glaz, A., Haralambous, Y., Kim-Dufor, D. H., Lenca, P., Billot, R., Ryan, T. C., Marsh, J., DeVylder, J., Walter, M., Berrouguet, S., & Lemey, C. (2021). Machine learning and natural language processing in mental health: Systematic review. *Journal of Medical Internet Research*, *23*(5), Article e15708. <https://doi.org/10.2196/15708>

- Liang, M. (2021). Research on prediction of the game winner based on artificial intelligence methods. In *Proceedings of the 5th International Conference on Advances in Image Processing* (pp. 97-102). ACM Publishing. <https://doi.org/10.1145/3502827.3502843>
- Luo, Z., Guzdial, M., & Riedl, M. (2019). Making CNNs for video parsing accessible: Event extraction from DOTA2 gameplay video using transfer, zero-shot, and network pruning. In *Proceedings of the 14th International Conference on the Foundations of Digital Games* (pp. 1-10). ACM Publishing. <https://doi.org/10.1145/3337722.3337755>
- Lyu, S., Zhao, N., Zhang, Y., Chen, W., Zhou, H., & Zhu, T. (2022). Predicting risk propensity through player behavior in DOTA 2: A cross-sectional study. *Frontiers in Psychology, 13*, Article 827008. <https://doi.org/10.3389/fpsyg.2022.827008>
- Marchenko, E., & Suschevskiy, V. (2018). Analysis of players transfers in esports. The case of Dota 2. In *Proceedings of the 22nd International Academic Mindtrek Conference* (pp. 255-257). ACM Publishing. <https://doi.org/10.1145/3275116.3275151>
- Marshall, I. J., & Wallace, B. C. (2019). Toward systematic review automation: A practical guide to using machine learning tools in research synthesis. *Systematic Reviews, 8*(1), Article 163. <https://doi.org/10.1186/s13643-019-1074-9>
- Martens, M., Shen, S., Iosup, A., & Kuipers, F. (2015). Toxicity detection in multiplayer online games. In *2015 International Workshop on Network and Systems Support for Games (NetGames)* (pp. 1-6). IEEE Publishing. <https://doi.org/10.1109/NetGames.2015.7382991>
- Maymin, P. Z. (2021). Smart kills and worthless deaths: ESports analytics for League of Legends. *Journal of Quantitative Analysis in Sports, 17*(1), 11–27. <https://doi.org/10.1515/jqas-2019-0096>
- Meng-Lewis, Y., Lewis, G., Lin, Z., & Zhao, Y. (2022). Examination of esports fans' live streaming experiences using an extended expectation-confirmation model: A case study of the King Pro League. *International Journal of Human-Computer Interaction, 40*(5), 1282-1297. <https://doi.org/10.1080/10447318.2022.2141008>
- Mohammed, Y., Srinivasan, S., Iyer, S., & Nagarajan, A. (2022). Defense of the ancients (DOTA 2)-draft recommendation system. In *2022 6th International Conference on Trends in Electronics and Informatics (ICOEI)* (pp. 13-17). IEEE. <https://doi.org/10.1109/ICOEI53556.2022.9776822>
- Mora-Cantallops, M., & Sicilia, M. Á. (2018). Player-centric networks in League of Legends. *Social Networks, 55*, 149–159. <https://doi.org/10.1016/j.socnet.2018.06.002>
- Navarro, C. L. A., Damen, J. A. A. G., Takada, T., Nijman, S. W. J., Dhiman, P., Ma, J., Collins, G. S., Bajpai, R., Riley, R. D., Moons, K. G., & Hooft, L. (2020). Protocol for a systematic review on the methodological and reporting quality of prediction model studies using machine learning techniques. *BMJ Open, 10*(11), Article e038832. <https://doi.org/10.1136/bmjopen-2020-038832>
- Ong, A. K. S., Prasetyo, Y. T., Robas, K. P. E., Persada, S. F., Nadlifatin, R., Matillano, J. S. A., Macababba, D. C. B., Pabustan, J. R., & Taningco, K. A. C. (2023). Determination of factors influencing the behavioral intention to play “Mobile Legends: Bang-Bang” during the COVID-19 pandemic: Integrating UTAUT2 and system usability scale for a sustainable E-sport business. *Sustainability, 15*(4), Article 3170. <https://doi.org/10.3390/SU15043170>

- Oyebode, O., Fowles, J., Steeves, D., & Orji, R. (2023). Machine learning techniques in adaptive and personalized systems for health and wellness. *International Journal of Human-Computer Interaction*, 39(9), 1938–1962. <https://doi.org/10.1080/10447318.2022.2089085>
- Porokhnenko, I., Polezhaev, P., & Shukhman, A. (2019). Machine learning approaches to choose heroes in Dota 2. In *2019 24th Conference of Open Innovations Association (FRUCT)* (pp. 345-350). IEEE Publishing. <https://doi.org/10.23919/FRUCT.2019.8711985>
- Prakannoppakun, N., & Sinthupinyo, S. (2016). Skill rating method in multiplayer online battle arena. In *2016 8th International Conference on Electronics, Computers and Artificial Intelligence (ECAI)* (pp. 1-6). IEEE. Publishing. <https://doi.org/10.1109/ECAI.2016.7861165>
- Railsback, D., & Caporusso, N. (2019). Investigating the human factors in esports performance. In *Advances in Human Factors in Wearable Technologies and Game Design: Proceedings of the AHFE 2018 International Conferences on Human Factors and Wearable Technologies, and Human Factors in Game Design and Virtual Environments* (Vol. 795, pp. 325–334). Springer. https://doi.org/10.1007/978-3-319-94619-1_32
- Reitman, J. G., Anderson-Coto, M. J., Wu, M., Lee, J. S., & Steinkuehler, C. (2020). Esports research: A literature review. *Games and Culture*, 15(1), 32–50. <https://doi.org/10.1177/1555412019840892>
- Sclavounos, P. D., & Ma, Y. (2018). Artificial intelligence machine learning in marine hydrodynamics. In *International Conference on Offshore Mechanics and Arctic Engineering* (Vol. 51302, p. V009T13A028). American Society of Mechanical Engineers. <https://doi.org/10.1115/OMAE2018-77599>
- Semenov, A., Romov, P., Korolev, S., Yashkov, D., & Neklyudov, K. (2017). Performance of machine learning algorithms in predicting game outcome from drafts in Dota 2. In *International Conference on Analysis of Images, Social Networks and Texts* (pp. 26-37). Springer International Publishing. https://doi.org/10.1007/978-3-319-52920-2_3
- Shen, Q. (2022). A machine learning approach to predict the result of League of Legends. In *2022 International Conference on Machine Learning and Knowledge Engineering (MLKE)* (pp. 38-45). IEEE Publishing. <https://doi.org/10.1109/MLKE55170.2022.00013>
- Song, K., Zhang, T., & Ma, C. (2015). *Predicting the winning side of DotA2*. https://cs229.stanford.edu/proj2015/249_report.pdf
- Stanlly, Putra, F. A., & Qomariyah, N. N. (2022). DOTA 2 Win Loss Prediction from Item and Hero Data with Machine Learning. In *2022 IEEE International Conference on Industry 4.0, Artificial Intelligence, and Communications Technology (IAICT)* (pp. 204-209). IEEE Publishing. <https://doi.org/10.1109/IAICT55358.2022.9887525>
- Summerville, A., Cook, M., & Steenhuisen, B. (2021). Draft-analysis of the ancients: Predicting draft picks in DotA 2 using machine learning. *Proceedings of the AAAI Conference on Artificial Intelligence and Interactive Digital Entertainment*, 12(2), 100–106. <https://doi.org/10.1609/aiide.v12i2.12899>
- Tan, K. H. (2022). *A short review on machine learning*. Authorea Preprints. <https://doi.org/10.22541/au.166490976.66390273/v1>
- Truong, A., Walters, A., Goodsitt, J., Hines, K., Bruss, C. B., & Farivar, R. (2019). Towards automated machine learning: Evaluation and comparison of AutoML approaches and tools. In *2019 IEEE 31st international*

- conference on tools with artificial intelligence (ICTAI)* (pp. 1471-1479). IEEE Publishing. <https://doi.org/10.1109/ICTAI.2019.00209>
- Vardal, O., Bonometti, V., Drachen, A., Wade, A., & Stafford, T. (2022). Mind the gap: Distributed practice enhances performance in a MOBA game. *PLoS ONE*, *17*, 1–23. <https://doi.org/10.1371/journal.pone.0275843>
- Wan Jr, J. A., Kamal, A. A., & Rahman, S. A. (2021). Weighting the position & skillset of players in league of legends using analytic hierarchy process. *Journal of IT in Asia*, *9*(1), 49–64. <https://doi.org/10.33736/JITA.2846.2021>
- Wang, N., Li, L., Xiao, L., Yang, G., & Zhou, Y. (2018). Outcome prediction of DOTA2 using machine learning methods. In *Proceedings of 2018 International Conference on Mathematics and Artificial Intelligence* (pp. 61-67). <https://doi.org/10.1145/3208788.3208800>
- Wei, H., Chen, J., Ji, X., Qin, H., Deng, M., Li, S., Wang, L., Zhang, W., Yu, Y., Liu, L., Huang, L., Ye, D., Fu, Q., & Yang, W. (2022). *Honor of Kings Arena: An Environment for Generalization in Competitive Reinforcement Learning*. ArXiv Preprint. <http://arxiv.org/abs/2209.08483>
- Wolff, R. F., Moons, K. G. M., Riley, R. D., Whiting, P. F., Westwood, M., Collins, G. S., Reitsma, J. B., Kleijnen, J., & Mallett, S. (2019). PROBAST: A tool to assess the risk of bias and applicability of prediction model studies. *Annals of Internal Medicine*, *170*(1), Article 51. <https://doi.org/10.7326/M18-1376>
- Wong, N. H. L., Kwok, S., & Tan, J. L. (2022). Predictive analytics of first blood and match outcome in Dota 2. In *TENCON 2022-2022 IEEE Region 10 Conference (TENCON)* (pp. 1-6). IEEE Publishing. <https://doi.org/10.1109/TENCON55691.2022.9977786>
- Yang, Q., Fan, X., Cao, X., Hao, W., Lu, J., Wei, J., Tian, J., Yin, M., & Ge, L. (2023). Reporting and risk of bias of prediction models based on machine learning methods in preterm birth: A systematic review. *Acta Obstetrica et Gynecologica Scandinavica*, *102*(1), 7–14. <https://doi.org/10.1111/aogs.14475>
- Yang, Y., Qin, T., & Lei, Y. H. (2016). *Real-time eSports Match Result Prediction*. <http://www.forbes.com/sites/leighsteinberg/2015/08/18/changing-the-game-the-rise-of-sports-analytics/>
- Yang, Z., Pan, Z., Wang, Y., Cai, D., Shi, S., Huang, S.-L., Bi, W., & Liu, X. (2022). Interpretable real-time win prediction for Honor of Kings - A popular mobile MOBA esport. *IEEE Transactions on Games*, *14*(4), 589–597. <https://doi.org/10.1109/TG.2022.3149044>
- Ye, D., Chen, G., Zhao, P., Qiu, F., Yuan, B., Zhang, W., Chen, S., Sun, M., Li, X., Li, S., Liang, J., Lian, Z., Shi, B., Wang, L., Shi, T., Fu, Q., Yang, W., & Huang, L. (2022). Supervised learning achieves human-level performance in MOBA games: A case study of Honor of Kings. *IEEE Transactions on Neural Networks and Learning Systems*, *33*(3), 908–918. <https://doi.org/10.1109/TNNLS.2020.3029475>
- Zhang, Y. (2021). Prediction of esports game results using early game datasets. In *ICMLCA 2021; 2nd International Conference on Machine Learning and Computer Application* (pp. 1-6). VDE Publishing.
- Zomlot, L., Chandran, S., Caragea, D., & Ou, X. (2013). Aiding intrusion analysis using machine learning. In *2013 12th International Conference on Machine Learning and Applications* (Vol. 2, pp. 40-47). IEEE Publishing. <https://doi.org/10.1109/ICMLA.2013.103>

Estimation of Mangrove Gross Primary Productivity Using Sentinel-2 Imagery Data: A Case Study in Ujung Pangkah East Java, Indonesia

Zainul Hidayah^{1*}, Abd Rahman As-Syakur^{2,3}, Herlambang Aulia Rachman¹, Linda Sri Rahayu Romadhoni¹ and Martiwi Diah Setiawati⁴

¹Department of Marine Science and Fisheries, Faculty of Agriculture Trunojoyo University of Madura, Raya Telang 02 Madura East Java, 69162 Indonesia

²Department of Marine Science, Faculty of Marine and Fisheries, Udayana University Bukit Jimbaran Campus Bali, 80361 Indonesia

³Centre for Remote Sensing and Ocean Science (CReSOS) Udayana University Bali, 80361 Indonesia

⁴Institute for the Advanced Study of Sustainability (UNU-IAS), United Nations University, Tokyo, 150-8925 Japan

ABSTRACT

Mangrove forests are the main carbon absorption and sequestration source, serving as a typical ecosystem in coastal areas. Despite numerous studies on temporal changes in carbon storage, there is limited information on the examination of gross primary productivity (GPP) in mangrove forests. GPP is the overall quantity of organic matter produced in the vegetation through photosynthesis, including the portion used for respiration. In the context of global warming and climate change, GPP is frequently used as an indicator of the total amount of carbon dioxide (CO₂) assimilated by the ecosystem, particularly vegetation. The advancement of geographic information systems (GIS)

and remote sensing methods has enabled the estimation of GPP rates on a spatial-temporal basis. Therefore, this study aimed to estimate and explore the relationship between GPP and vegetation density in the mangrove forest of Ujung Pangkah, Indonesia. Multi-temporal Sentinel-2 image data from 2018 to 2022 were used for analysis, while the Vegetation Production Model (VPM) was applied to calculate GPP. The results showed a steady increase in average GPP from 1997.91 grC m⁻² yr⁻¹ in 2018 to 2290.09 grC m⁻² yr⁻¹ in 2022. The increase showed significant improvement in the condition of the Ujung Pangkah mangrove forest.

ARTICLE INFO

Article history:

Received: 16 April 2024

Accepted: 24 December 2024

Published: 07 March 2025

DOI: <https://doi.org/10.47836/pjst.33.2.12>

E-mail addresses:

zainulhidayah@trunojoyo.ac.id (Zainul Hidayah)

ar.assyakur@pplh.unud.ac.id (Abd Rahman As-syakur)

herlambang.rachman@trunojoyo.ac.id (Herlambang Aulia Rachman)

linda.rahayu@trunojoyo.ac.id (Linda Sri Rahayu Romadhoni)

martiwidiah@unuias.ac.id (Martiwi Diah Setiawati)

* Corresponding author

This was further confirmed by the strong relationship between GPP and the Normalized Difference Vegetation Index (NDVI), which was used to determine vegetation density ($R^2 > 0.9$, $p < 0.05$).

Keywords: Gross primary productivity, mangrove, photosynthesis, Sentinel-2, Ujung Pangkah

INTRODUCTION

Global warming is the catalyst for climate change, negatively affecting land and marine environments. This phenomenon causes high sea surface temperatures, changes in rainfall patterns, extreme weather conditions, and cyclonic storms. The most concerning increase in emissions is carbon dioxide (CO₂) due to higher concentration and long lifetime in the atmosphere. According to a recent World Meteorological Organization (WMO) report, the global atmospheric CO₂ concentration has reached a new high record of 415.7 ± 0.2 ppm in 2021 (Tang et al., 2023). On average, the increase in global CO₂ concentration in the last 2 decades is approximately 2.25 ppm/year (Friedlingstein et al., 2022). This continuous increase is significantly attributed to uncontrolled consumption of fossil fuels and massive land cover changes (Ayompe et al., 2020; Basu et al., 2020; Goldstein et al., 2020; Yoro & Daramola, 2020). The mangrove ecosystem has been proven effective due to its high carbon storage capacity.

The mangrove ecosystem is estimated to have five times the carbon storage capacity of terrestrial rainforest per hectare (Donato et al., 2011), with an optimal carbon sequestration function of approximately 77.9% (Chatting et al., 2022). Furthermore, high productivity combined with slow soil decay rates improves the ability to capture and preserve organic carbon (Alongi, 2012; Kauffman & Bhomia, 2017; Bacar et al., 2023; Hidayah et al., 2022). Indonesia has approximately 2.95 million ha of mangrove forest, accounting for 20.09% of the world's mangrove area (Bunting et al., 2022).

Although mangrove forests play significant ecological roles in coastal environments, this ecosystem is under threat from illegal logging, deforestation, and changes in land use. According to the United Nations Statistics geographic regions, the estimated extent of mangroves worldwide in 1996 was 15.26 million ha. In 2020, deforestation decreased to 14.73 million ha, with a rate of mangrove loss of 37,464 ha/year. During this period, the area of mangroves in Indonesia decreased by over 174,000 ha, from 3.12 million ha in 1996 to 2.95 million ha in 2020 (Bunting et al., 2022). Further studies showed that 70% of mangroves capable of producing organic compounds were deforested, and 30% were degraded (Hidayah et al., 2022; Bunting et al., 2022).

In this context, primary productivity is essential for the formation of energy-rich organic compounds from inorganic compounds. Gross and net primary productivity are both components of primary productivity. Net Primary Productivity (NPP) is the amount of primary productivity that remains after being used by organisms for respiration. Meanwhile, Gross Primary Productivity (GPP) is the total amount of organic compounds

formed in organism tissues during photosynthesis (Chapin et al., 2006; Wang et al., 2012). GPP is considered the total value of carbon fixation in terrestrial ecosystems through photosynthesis in a specific period, which is used to quantify the amount of CO₂ assimilated by vegetation (Nuarsa et al., 2018), particularly in mangrove ecosystems (Wang et al., 2012).

Several studies have been carried out on temporal changes and carbon stocks in mangrove biomass and sediment in Indonesia (Cameron et al., 2019; Harefa et al., 2022; Lukman et al., 2022; Pricillia et al., 2021; Trissanti et al., 2022). Allometric equations are commonly used to calculate carbon stocks in mangrove biomass (Hidayah et al., 2022; Indrayani et al., 2021; Suardana et al., 2023), with the regular procedure dependent on biophysical measurements. These include tree diameter at breast height, tree height, or wood density of various plant species, thereby limiting extrapolation to regional scales. This study used a combination of GIS and remote sensing methods to estimate GPP over time through the relationship with the fraction of absorbed photosynthetically active radiation (f-APAR) driven by vegetation indexes (Nuarsa et al., 2018). According to previous studies, the Moderate-resolution Imaging Spectroradiometer (MODIS) data were used to calculate GPP on vast terrestrial and coastal forest ecosystems (Kanniah et al., 2021; Turner et al., 2003). Landsat data were more frequently used for the estimation of other land cover types (Celis et al., 2023; Nuarsa et al., 2018; Raj et al., 2020; Shirkey et al., 2022). Therefore, this study aimed to estimate the GPP of Ujung Pangkah in East Java, Indonesia, using Sentinel-2 satellite data from 2018 to 2022. The analysis focused on three main objectives: to measure the change in the mangrove area. Second, analysis was conducted to estimate Ujung Pangkah's annual GPP using VPM, and third, to investigate the relationship between GPP and vegetation density.

MATERIAL AND METHODS

Study Location

Ujung Pangkah mangrove forest is located at the estuary of Bengawan Solo River, one of the longest and largest rivers in Indonesia. Geographically, this study area is located on Java Island's north coast, in the administrative area of Gresik Regency, East Java Province, as shown in Figure 1. Since 2021, Indonesia's Ministry of Environment and Forestry has designated this location as an Essential Ecosystem Area. The initiative is part of the Indonesian government's efforts to preserve wetland areas as defined by the Ramsar Convention, a UN-initiated intergovernmental convention for wetland conservation. Ujung Pangkah is located close to Gresik City, which is one of the largest industrial areas in Eastern Indonesia. This shows that factory operations in the area may emit excessive CO₂ into the atmosphere daily. Therefore, there is a need for more carbon-absorbing areas to balance the atmospheric carbon cycle.

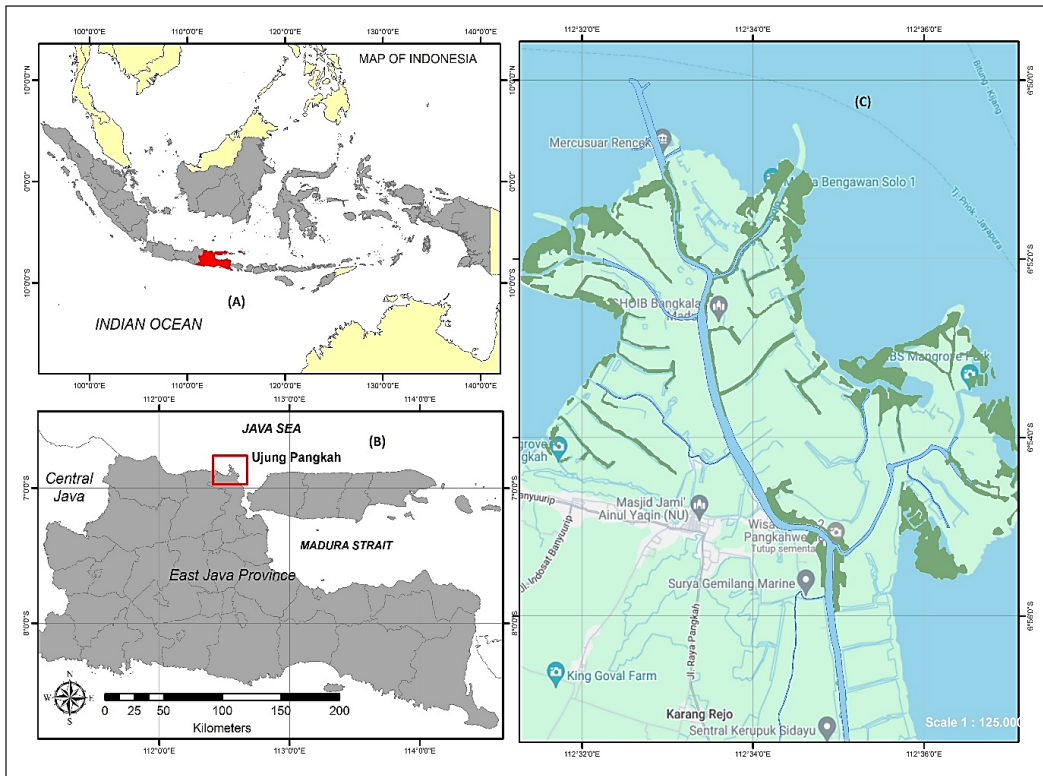


Figure 1. Study site: (A) East Java Province of Indonesia, (B) The location of Ujung Pangkah in East Java Province, (C) Coastal study sites in Ujung Pangkah with mangrove forests extracted from Sentinel-2 image

Data Description

The primary data used in this study was a set of multi-spectral Sentinel-2 Level 1C satellite images acquired from 2018 to 2022. These images were collected using the Google Earth Engine (GEE) platform <https://developers.google.com/earth-engine/datasets/catalog/sentinel>. European Space Agency (ESA) administered this satellite under the Copernicus Land Monitoring project. Sentinel-2 comprised two satellites with similar characteristics (Sentinel 2A and 2B), each equipped with a 13-band MSI (Multi-Spectral Instrument) optical sensor that covers the visible light to infrared spectrum. Every Sentinel-2 image covered a 290-kilometer strip, combined with its spatial resolution of 10 to 60 meters per pixel and 15 days of temporal resolution (Table 1).

Image processing was performed using the cloud computing platform GEE, accessible at <https://earthengine.google.com>. The investigation used a Sentinel-2 harmonized dataset, which included Surface Reflectance (SR) values. Annually, the analysis used composites obtained from data gathered from June to October, which was consistent with the dry season characterized by low cloud cover. Initially, only images that had a cloud cover of less than 30% were selected. Median composites were created by averaging the values of

Table 1
Spectral and spatial characteristics of Sentinel-2 imagery data

Bands	Wavelength (μm)	Spatial Resolution (m)
Band-1 Coastal Aerosol	0.433–0.453	60
Band 2: Blue	0.458–0.523	10
Band 3: Green	0.543–0.578	10
Band 4: Red	0.650–0.680	10
Band 5: Vegetation Red Edge	0.698–0.713	20
Band 6: Vegetation Red Edge	0.733–0.748	20
Band 7: Vegetation Red Edge	0.765–0.785	20
Band 8: NIR	0.758–0.900	10
Band 8A: Vegetation Red Edge	0.855–0.875	20
Band 9: Water Vapour	0.930–0.950	60
Band 10: SWIR Cirrus	1.365–1.385	60
Band 11: SWIR	1.565–1.655	20
Band 12: SWIR	2.100–2.280	20

Source: Sentinel-2 User's Guide (<https://sentinels.copernicus.eu/web/sentinel/user-guides/sentinel-2-msi/overview>)

each band over the complete dataset during this period. The method was used to mitigate the influence of cloud cover before categorization and subsequent analysis. Furthermore, this study used local monthly average temperature data from the meteorological station BMKG (Meteorological, Climatological, and Geophysical Agency) Sangkapura, available at https://dataonline.bmkg.go.id/data_iklim. Monthly sun radiation statistics data were also acquired from the European Centre for Medium-Range Weather Forecasts (ECMWF), accessible at <https://developers.google.com/earth-engine/datasets/catalog>.

Gross Primary Productivity (GPP) Calculation

Empirical models, such as the Satellite-based Light-Use Efficiency (LUE), are used to estimate GPP due to the challenges associated with direct measurement. According to the LUE model, carbon exchange can be determined through the quantity of light energy absorbed by vegetation and the effectiveness of converting carbon (Xiao et al., 2005). Vegetation Production Model (VPM) is one of the LUE models commonly used to estimate GPP based on remote sensing image data as well as the effects of temperature, water stress, and phenology. In VPM, three sets of parameters, namely light temperature parameters (T-scalar), water parameters (W-scalar), and leaf phenology (P-scalar), are used to estimate GPP (Xiao et al., 2005). Previous studies have confirmed the accuracy of GPP calculations derived from satellite image data using VPM estimation. The results show a strong correlation with CO₂ eddy flux towers, a widely used micro-meteorological method that measures the vertical concentration gradients of Green House Gases (GHGs) continuously (Huang et al., 2022; Kumar et al., 2017; Peddinti et al., 2020). Details of

Sentinel-2 image processing using GEE to calculate mangrove area and estimate annual GPP are systematically presented in Figure 2.

Sentinel-2 Image Processing

This study analyzed satellite images to acquire the remote sensing indexes required for calculating GPP. Initially, the pre-processing stage included using the GEE platform to mask clouds and perform rectification. This was followed by the computation of the Normalized Difference Vegetation Index (NDVI), Enhanced Vegetation Index (EVI), and Land Surface Water Index (LSWI). NDVI was used to differentiate mangrove vegetation from other forms of land cover. This vegetation index was computed using the proportion of near-infrared (NIR) of band eight and the red spectrum of band four from the Sentinel-2 image. The following Equation 1 was used to compute NDVI from image data.

$$NDVI = \frac{Nir - Red}{Nir + Red} \quad [1]$$

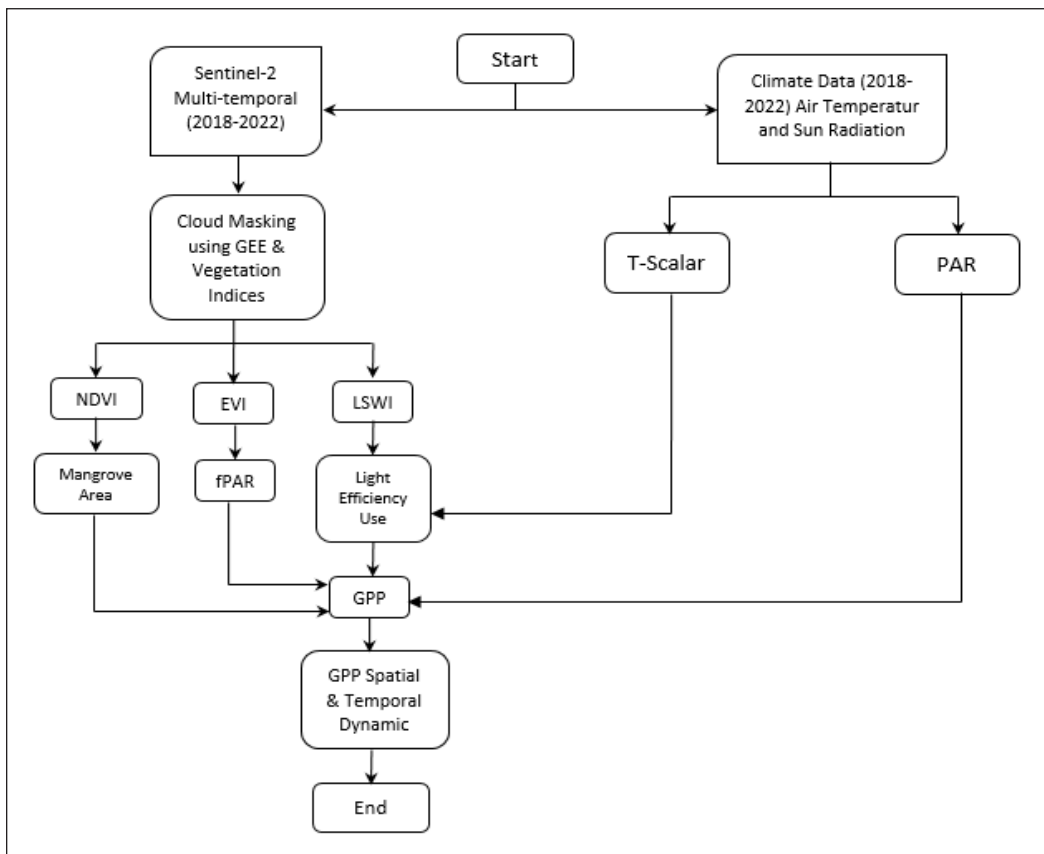


Figure 2. Flow chart of GPP data analysis using Vegetation Photosynthesis Model (VPM)

EVI was used due to the linear relationship with the leaf green index derived from multi-spectral data and the ability to determine changes in the cover of plants (Xiao et al., 2004). This index used a blue band to fix the atmosphere as well as blue, red, and NIR bands to observe the changing reflectance of soil and the canopy background (Nuarsa et al., 2018). Subsequently, EVI was calculated using three specific bands from Sentinel-2, including NIR (band 8), red (band 4), and blue (band 2). The values of EVI varied from -1 to +1, which was calculated using Equation 2 provided by Huete et al. (1997).

$$EVI = 2.5 \times \frac{\rho_{nir} - \rho_{red}}{\rho_{nir} + (6 \times \rho_{red} - 7.5 \times \rho_{blue}) + 1} \quad [2]$$

An additional index required for VPM, LSWI, was calculated using NIR (band 8) and SWIR (band 11) of the Sentinel-2 image. Increasing the amount of water in the leaf or the moisture in the soil led to greater absorption of shortwave infrared (SWIR) light and reduced reflection of NIR light. The value of LSWI ranged from -1 to +1, calculated using Equation 3 provided by Xiao et al. (2005).

$$LSWI = \frac{\rho_{nir} - \rho_{swir}}{\rho_{nir} + \rho_{swir}} \quad [3]$$

Vegetation Production Model (VPM)

In VPM, the T-scalar parameter was used to determine photosynthesis temperature using the Terrestrial Ecosystem Model (Equation 4) (Raich, 1991):

$$T - scalar = \frac{(T - T_{min}) \times (T - T_{maks})}{[(T - T_{min}) \times (T - T_{max})] - (T - T_{opt})^2} \quad [4]$$

The terrestrial ecosystem model measured the temperature for photosynthesis, often known as Tscalar, in degrees Celsius (°C). At this point, T represents the mean monthly temperature obtained from the meteorological station BMKG Sangkapura. This study used the following settings for Tmin, Tmax, and Topt at 0°C, 48°C, and 28°C, respectively (Nuarsa et al., 2018). Additionally, the W-scalar parameter was applied to quantify the impact of water on vegetation photosynthesis, as stated by Nuarsa et al. (2018). The calculation of this parameter was derived from LSWI obtained from the analysis of the Sentinel-2 image, as shown in Equation 5.

$$W - scalar = \frac{1 + LSWI}{1 + LSWI_{max}} \quad [5]$$

The final parameter in VPM was P-scalar, a leaf phenology value used to evaluate the influence of leaf age on photosynthesis at the canopy level. The duration of the leaf

lifespan determined the P-scalar value. For a canopy dominated by leaves with a one-year life expectancy, P-scalar was calculated as a linear function of two distinct phases using Equation 6 provided by Xiao et al. (2005).

$$P - \text{scalar} = \frac{1 + LSWI}{2} \quad [6]$$

The next calculation was performed to determine light use efficiency (ϵg), which was the function of temperature (T_{scalar}), water effect on photosynthesis (W_{scalar}), and leaf phenology (P_{scalar}), as expressed in Equation 7 (Xiao et al., 2005). In Equation 7, $\epsilon 0$ is the maximum light use efficiency and is equal to 0.40 gC mol^{-1}

$$\epsilon g = \epsilon 0 \times T_{\text{scalar}} \times W_{\text{scalar}} \times P_{\text{scalar}} \quad [7]$$

Equation 8 uses incoming solar radiation (R) data to calculate the photosynthetic active radiation (PAR) in $\mu\text{mol}/\text{m}^2\text{sec}$. Equation 8 estimates that approximately 45% of solar radiation (W m^{-2}) is transformed into PAR. Moreover, the final factor in determining GPP is F-PARchl, which represents the fraction of photosynthetic active radiation absorbed by chlorophyll. The VPM model assumes that F-PARchl in photosynthesis is a linear function of EVI, with a coefficient A set to 1 (Equations 8 and 9).

$$PAR = 0.45 \times R \quad [8]$$

$$fPARchl = EVI \times A \quad [9]$$

The VPM model developed to estimate GPP according to PAV (photosynthetically active vegetation) and NPV (non-photosynthetic vegetation) is determined using Equation 10 (Xiao et al., 2005).

$$GPP = \epsilon g \times fPARchl \times PAR \quad [10]$$

RESULTS AND DISCUSSION

Temporal Change of Mangrove Area

The use of multitemporal satellite images in this study is exceptionally beneficial to understanding the dynamics of change in the mangrove forest of Ujung Pangkah. As a coastal ecosystem, mangrove vegetation grows in response to temperature, humidity, rainfall, and sunlight intensity. This ecosystem can be influenced by coastal erosion, which naturally reduces the area of mangrove forests, while accretion or sedimentation contributes to increasing capacity.

This study used NDVI to identify mangrove land covers due to the ability to differentiate between vegetation and other types of land cover. The value ranged from -1

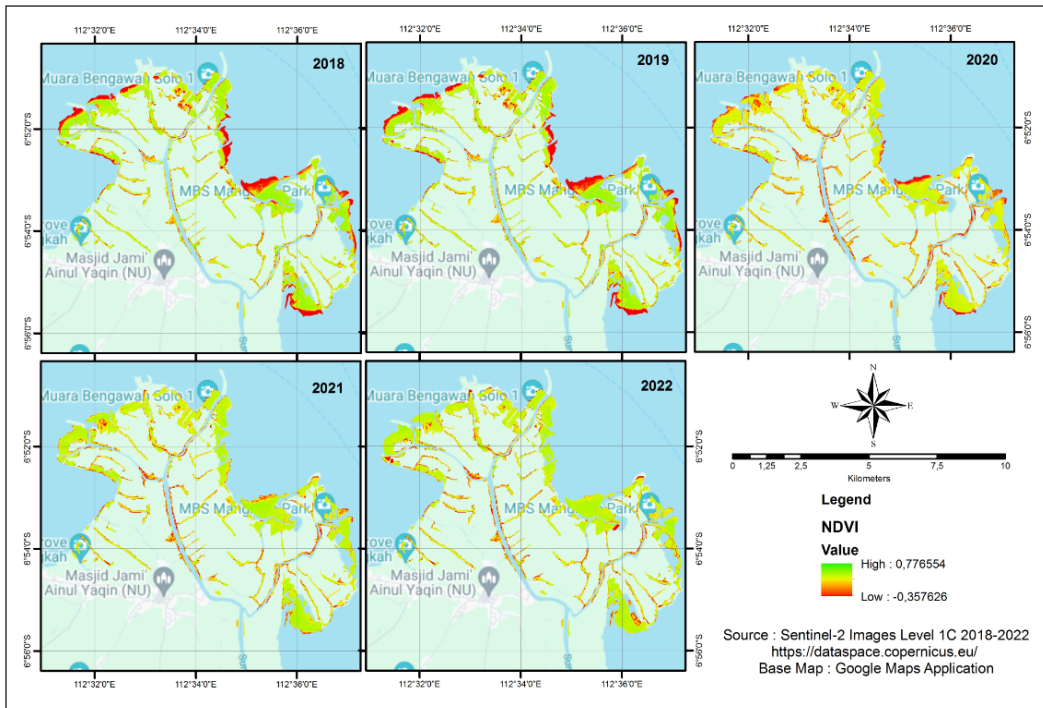


Figure 3. Distribution Map of Mangrove Forest of Ujung Pangkah East Java from 2018–2022

Table 2
Statistical parameters of NDVI and area of mangrove forest in Ujung Pangkah

Observation Year	NDVI Statistics				Total Area (Ha)
	Min	Max	Mean	Stdev	
2018	-0.32	0.61	0.48	0.25	1187.63
2019	-0.31	0.65	0.52	0.19	1217.21
2020	-0.25	0.70	0.48	0.17	1229.69
2021	-0.35	0.75	0.57	0.17	1239.24
2022	-0.35	0.77	0.56	0.17	1262.25

to 1, where vegetation was identified with $NDVI > 0$. Furthermore, using a supervised classification method, it was possible to identify mangrove vegetation based on unique growth patterns surrounding river estuaries. Figure 3 shows the map illustrating the distribution of mangroves in Ujung Pangkah.

According to the results of NDVI analysis in Table 2, the condition of the mangrove forest in Ujung Pangkah showed signs of enhancement during the past 5 years. This was supported by at least two indicators, including the expansion of mangrove coverage and the corresponding rise in average and maximum NDVI values. The area was 1187.63

Ha in 2018 and gradually increased to 1262.25 Ha by 2022, with the expansion strongly correlated to a high canopy density. Despite fluctuations in the average NDVI value, the maximum NDVI value gradually increased from 0.61 in 2018 to 0.77 in 2022.

The trend towards improving the condition of the mangrove forest ecosystem in Ujung Pangkah was supported by the position at Bengawan Solo estuary. The high rate of sedimentation in the year produced mud deposits rich in organic material, which served as a medium for vegetation growth. Suitable environmental conditions, as well as the absence of illegal logging or land conversion by local residents, played an important role in improving the condition of the mangrove ecosystem (Hagger et al., 2022). In recent years, the trend of expanding mangrove forest areas observed by medium-resolution satellite images was detected in several locations. These included Surabaya east coast and Teluk Pangpang of East Java, Indonesia; Thane Creek of Mumbai, India; than Hoa Estuary of Vietnam and Jiulong river estuary of China (Hidayah et al., 2022; Hidayah et al., 2024; Nguyen et al., 2020; Azeez et al., 2022; Wang et al., 2018).

Fluctuations in Yearly Temperature

Data on weather and environmental conditions at the research site were required to determine GPP using VPM. The annual temperature parameters obtained from Sangkapura weather station showed that from 2018 to 2022, the average annual air temperature in Ujung Pangkah mangrove forest ranged from 28.23°C to 28.53°C, with a small standard deviation of 0.46°C to 0.83°C. However, the average annual temperatures measured in the Ujung Pangkah mangrove forest area showed no significant difference (One Way ANOVA, $p > 0.05$, $df = 4$).

Figure 4 shows that the average annual temperature fluctuates over a 5-year period. The average annual temperature in 2018 was 28.50°C, which increased to 28.53°C in 2021 before decreasing to 28.36°C in 2022. Based on the results, 2018 had the smallest monthly temperature fluctuations ($\sigma = 0.46$), while the highest value occurred in 2020 ($\sigma = 0.83$). According to the Indonesian climate, the air temperature is often higher during the peak of the dry season, which occurs between July and September, compared to the rainy season (February). These parameters, particularly air temperature, often influence the growth and formation of mangrove vegetation (Duke et al., 1998; Hutchison et al., 2014). Temperature is essential in physiological processes such as photosynthesis and respiration (Bernacchi et al., 2001). Therefore, optimum mangrove growth requires an average temperature of over 20°C and seasonal differences of no more than 5°C (Quisthoudt et al., 2012).

Estimation of Annual GPP

During the 5 years of observation, GPP calculations estimated using VPM produced distinctive results. At the start of observations in 2018, GPP in Ujung Pangkah mangrove

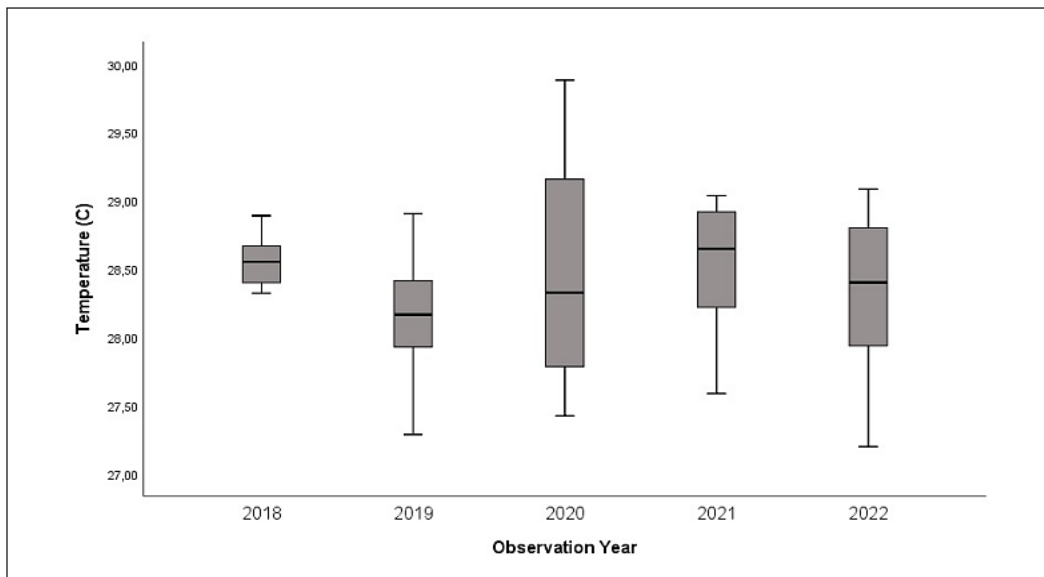


Figure 4. Monthly temperature fluctuations in the Ujung Pangkah mangrove forest area

forest ranged from $0.50 \text{ grC m}^{-2} \text{ yr}^{-1}$ to $4059.93 \text{ grC m}^{-2} \text{ yr}^{-1}$, with an average of $1997.90 \text{ grC m}^{-2} \text{ yr}^{-1}$. Meanwhile, in 2022, the final year of measurements, it ranged from $0.58 \text{ grC m}^{-2} \text{ yr}^{-1}$ to $4056 \text{ grC m}^{-2} \text{ yr}^{-1}$, with the average increase to $2290.09 \text{ grC m}^{-2} \text{ yr}^{-1}$.

The results showed that the expansion of the mangrove forest area directly impacted the rise in total (tC yr^{-1}). Table 3 shows the dynamics of changes in the GPP of the Ujung Pangkah mangrove forest, while spatial distribution based on Sentinel-2 image from 2018–2022 is presented in Figure 5. The increase in GPP can be attributed to the area’s improving mangrove ecosystem, which significantly contributes to high vegetation productivity, followed by canopy size and tree density growth. This phenomenon leads to improved Fraction of Absorbed Photosynthetically Active Radiation (fAPAR) and higher LUE, contributing to an increase in GPP (Zheng & Takeuchi, 2021).

During 5 years of observations using Sentinel-2 image, the Ujung Pangkah mangrove forest was dominated by areas with GPP in the range of $2401\text{--}3200 \text{ grC m}^{-2} \text{ yr}^{-1}$, covering 394.8 ha to 661.80 ha , or approximately $33.34\%\text{--}53.38\%$ of the total mangrove area each year. Meanwhile, areas with GPP in the range $3201\text{--}4010 \text{ grC m}^{-2} \text{ yr}^{-1}$ had the lowest percentage over the same period, ranging from 29.85% to 46.53% (Table 3). Based on Figure 5, changes in GPP occurred along the edges of the Ujung Pangkah mangrove forest, particularly to the east and north, which was predominantly dominated by GPP from 0.5 to $800 \text{ gr m}^{-2} \text{ yr}^{-1}$. 2018, the mangrove area with GPP 0.5 to $800 \text{ grC m}^{-2} \text{ yr}^{-1}$ was approximately 307.53 ha . In subsequent years, the area of mangroves with low GPP decreased, reaching 93.38 ha in 2022 (Table 4). Although not excessively large, the area

Table 3
Annual GPP of Ujung Pangkah mangrove forest from Sentinel-2 Images 2018–2022

Year	GPP (grC m ⁻² yr ⁻¹)				Total GPP (tC yr ⁻¹)
	Min	Max	Mean	Stdev	
2018	0.497	4053.97	1997.91	844.87	23.728
2019	0.655	3645.43	1909.96	796.96	23.248
2020	0.632	3547.94	2022.25	773.58	24.867
2021	0.978	3893.96	2137.87	746.15	26.493
2022	0.508	4056.06	2290.09	689.33	28.907

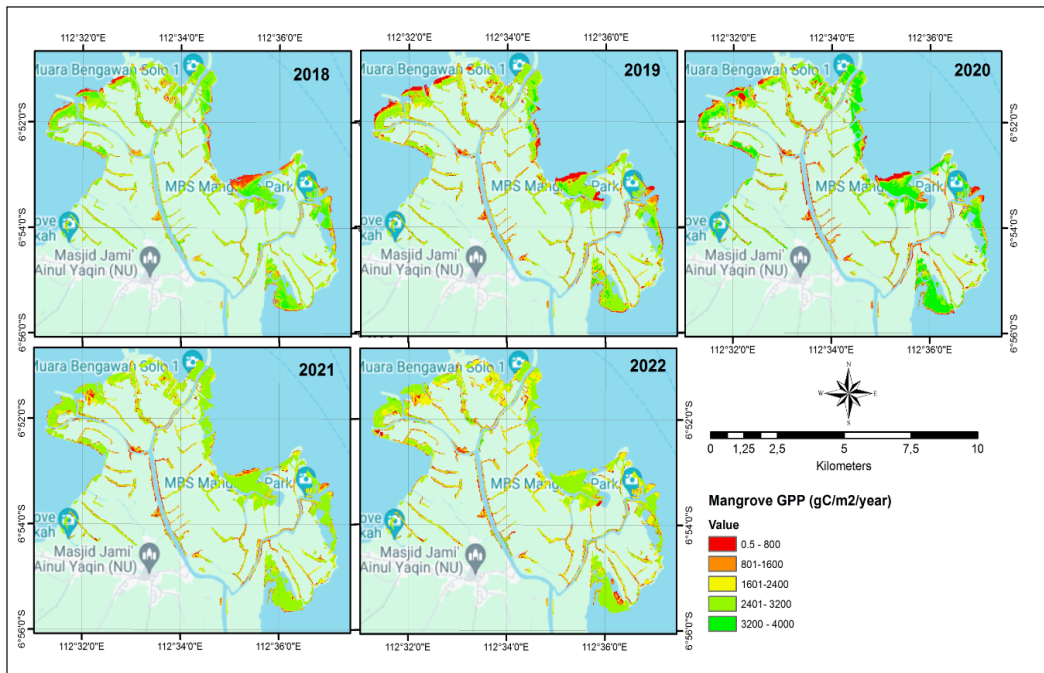


Figure 5. Annual GPP change in Ujung Pangkah mangrove forest East Java 2018–2022

Table 4
Total mangrove area covered based on GPP range

GPP Range (grC m ⁻² yr ⁻¹)	Mangrove Area (Ha)				
	2018	2019	2020	2021	2022
0.5–800	307.53	150.19	148.24	79.48	93.38
801–1600	158.86	173.46	183.43	143.86	149.58
1601–2400	291.4	305.27	353.51	308.94	438.46
2401–3200	394.8	552.96	501.31	661.8	536.08
3201–4010	29.85	35.92	42.93	45.62	46.53
Total	1185.44	1217.8	1229.42	1239.7	1264.83

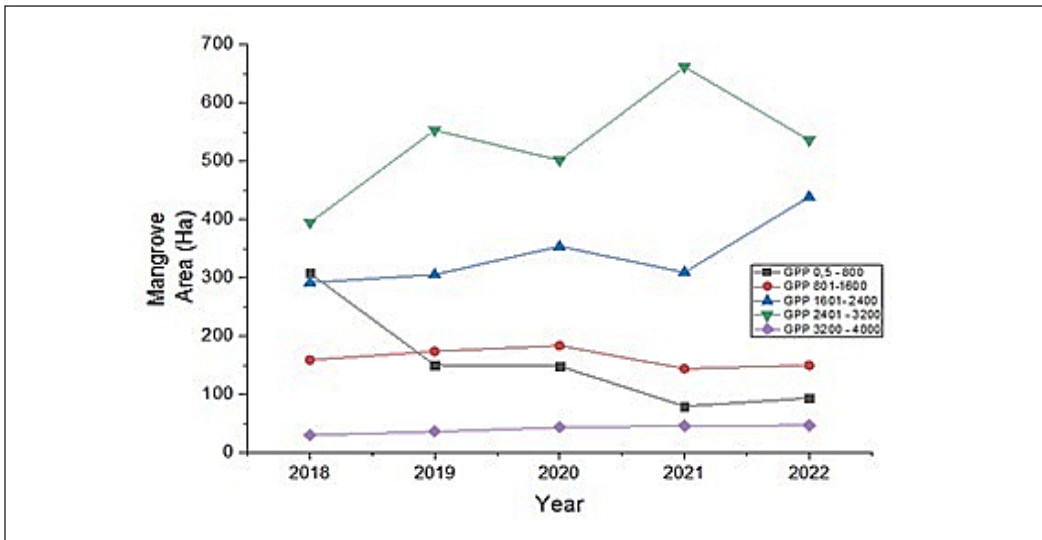


Figure 6. The dynamic of mangrove area based on GPP of Ujung Pangkah mangrove forest

of mangrove forest with the highest GPP interval in this study (3201–4010 grC m⁻² yr⁻¹) increased from 29.85 ha (2.58% of the total area) in 2018 to approximately 46.53 ha (3.68%) in 2022. The estimation of GPP provided information about mangrove health in terms of photosynthetic efficiency and carbon sequestering (Kumar & Das, 2023). Further investigation confirmed a clear indication of improvements in the mangrove health of Ujung Pangkah. The phenomenon was observed by a consistent decrease in mangrove area with GPP in low intervals, namely 0.5–800 grC m⁻² yr⁻¹ and 801–1600 grC m⁻² yr⁻¹. This was followed by an increase in GPP at higher intervals, namely 1601–2400 grC m⁻² yr⁻¹ and 3201–4010 grC m⁻² yr⁻¹, respectively (Figure 6).

Several studies have emphasized GPP as an essential parameter in the assessment of the global carbon budget of mangrove ecosystems (Beer et al., 2010; Alongi, 2014; Zheng & Takeuchi, 2022). Presently, the primary methods for determining forest GPP include direct observations, flux tower methods, and remote sensing models. The direct measuring method assesses leaf photosynthesis within a controlled laboratory setting. However, it is impractical to quantify the gross primary productivity (GPP) of forests across extensive areas (Zhao et al., 2023). The flux tower approach quantifies the exchange of carbon dioxide (CO₂) between ecosystems and the atmosphere by employing eddy correlation (EC) techniques. This method requires the collection of continuous observation data. Nonetheless, the number of operational flux tower sites is currently limited, and they have limited availability over the globe (Wang et al., 2019; Gnanamoorthy et al., 2020). The estimation of GPP using remote sensing data depends on the light-use efficiency (LUE) under various environmental circumstances and ecosystem structures (Z. Zhang et al., 2023). Additionally, global or regional GPP estimations can be derived from site-level

GPP observations through spatial extrapolation using remote sensing models (Huang et al., 2019; Markiet & Mottus, 2020; Y. Zhang et al., 2023).

Utilizing remote sensing techniques to implement modeled GPP has the potential to enhance and expand the investigation of carbon processes in mangroves on a larger scope. A comparison of the modeled GPP with in-situ flux tower data is required to assess its validity. Due to the absence of flux tower data near the location of this study, the comparison cannot be done. However, the GPP estimation of this study in the Ujung Pangkah mangrove forest was not significantly different and remained within the confidence interval of measurement results obtained from flux-tower measurements in multiple locations; for example, GPP measurements in Zhangjiang, China, reported an average result of 1729 grC m⁻² yr⁻¹ to 1924 grC m⁻² yr⁻¹ (Li et al., 2015). Meanwhile, GPP measurements in India's Picharam mangrove forest revealed slightly higher results, around 2305 grC m⁻² yr⁻¹ (Gnanamoorthy et al., 2020). However, measurements in the Sunderbans obtained lower results of 1271 grC m⁻² yr⁻¹ (Rodda et al., 2016).

Variations in GPP estimates across sites could be attributed to differences in climate-hydrological conditions, mangrove species, and age (Li et al., 2015). Meanwhile, several factors influenced these variations at the same site, including forest vegetation structure and stand parameters such as stem size, canopy cover, basal area, leaf area index, and vegetation density (Kanniah et al., 2021). Several studies also reported that specific environmental variables such as high salinity and extremely low temperatures could limit GPP (Inoue et al., 2022; Krauss et al., 2008; Reef & Lovelock, 2015).

Relationship Between NDVI and GPP

Further analysis was conducted to determine the relationship between mangrove NDVI and GPP. Moreover, NDVI was selected over other vegetation indexes because of its wide application to estimate mangrove forest density based on canopy cover (Razali et al., 2020; Zaitunah et al., 2021; Zhao & Qin, 2020). Despite accuracy issues caused by weather disturbances, satellite movement, and zonal peak angle, which interfered with the vegetation canopy reflectance response signal (Rafique et al., 2016), NDVI was extensively used to understand the spatiotemporal pattern of vegetation cover change (Kaufmann et al., 2003; Wang et al., 2021). This study modeled the relationship between NDVI and GPP using linear regression (Figure 7).

Based on the regression model, NDVI had a significant influence on GPP. This was explained by the consistency of linear regression results across observation years, with a coefficient of determination (R^2) greater than 0.90, indicating that NDVI showed an adequate indicator for estimating GPP. Vegetation indexes, such as NDVI, were used in multi-channel image processing to show aspects of vegetation density or other density-related characteristics, such as biomass and chlorophyll concentration. A high vegetation

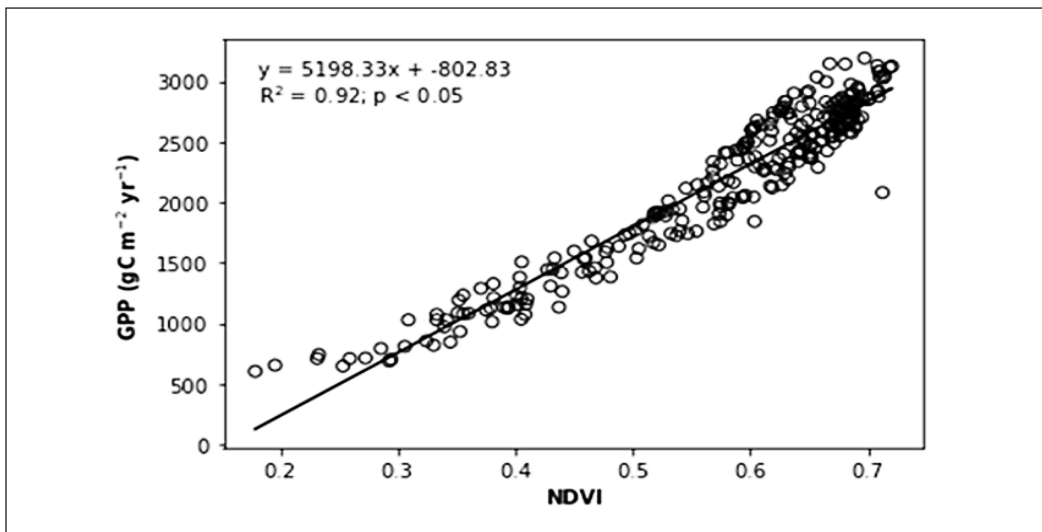


Figure 7. Linear regression models NDVI and GPP of Ujung Pangkah mangrove forest

index value showed that the area under observation had elevated levels of greenness, such as dense forest areas. Meanwhile, a low vegetation index value showed a decrease in vegetation greenness and cover.

It is noteworthy that GPP has more direct relations to the photosynthesis rate, leaves, and biomass growth. In relation to GPP, NDVI primarily indicates vegetation coverage and chlorophyll content without a direct relationship to vegetation photosynthesis as the primary parameter in the LUE model used to calculate GPP in this study. Many studies have discovered that biophysical conditions have a significant impact on NDVI in mangrove ecosystems (Alongi, 2022; Hidayah et al., 2022; Lukman et al., 2022; Hidayah et al., 2024). Furthermore, NDVI in mangroves provides a comprehensive view of ecosystem conditions. Accordingly, NDVI trends fluctuate in response to meteorological factors, such as temperature and precipitation (Ichii et al., 2022). Given the positive results of this study in modeling the relationship between NDVI and GPP, it can be argued that spatial and temporal changes in NDVI can be used as an observational proxy for studying global, regional, and temporal changes in GPP.

Previous studies discovered that biophysical conditions had a significant impact on NDVI in mangrove ecosystems (Alongi, 2022; Hidayah et al., 2022; Lukman et al., 2022; Hidayah et al., 2024). Moreover, NDVI trends fluctuate in response to meteorological factors, such as temperature and precipitation (Ichii et al., 2022). Based on the positive results, it was discovered that spatial and temporal changes in NDVI could be used as an observational proxy for exploring global, regional, and temporal changes in GPP.

The gross amount of organic matter produced by mangroves indicated the ability to absorb atmospheric CO₂ and convert it to biomass through photosynthesis. Discovering the

spatial and temporal variations of GPP in mangroves is crucial for accurately estimating the capacity of coastal ecosystems to store carbon. Climate conditions, vegetation types, and their spatial distribution, as well as factors that influence mangrove distribution, such as land-use practices and land cover conversion, primarily control spatial variations of GPP. Similarly, the seasonal phenology of vegetation and climate conditions influence the temporal variations of GPP (Cao et al., 2004; Nemani et al., 2003).

The Importance of Mangrove GPP in Global Carbon Studies

The significance of studying the contribution of mangrove forests to carbon sequestration is heightened when considering the implications of global warming and climate change. Industrialized countries with high carbon emissions are strongly believed to be a major cause of global warming, which poses a significant threat to environmental sustainability and human well-being (Alongi, 2020). In order to proactively address the issue of global warming, numerous governments have implemented carbon-neutral policies that are centered around the concept of carbon reduction (Huang & Zhai, 2021; Chen et al., 2022). China has declared its climate objectives, which include reaching the peak of carbon emissions by 2030 and achieving carbon neutrality by 2060 (Zeng et al., 2022), whereas the European Union has set its goal of carbon neutrality by 2050 (Perissi & Jones, 2022).

Blue carbon ecosystems (BCEs), which encompass mangrove forests, seagrass meadows, and tidal marshes, serve as carbon sinks and offer additional advantages, including protecting the coastline and improving fisheries. BCE sequestration is proposed as a natural system to address climate change and prevent the further impact of global warming (Hilmi et al., 2021; Mengis et al., 2023). On a global scale, BCEs have an estimated carbon storage capacity of around 30,000 Tg C and conserving these ecosystems prevents annual emissions of 141-466 Tg CO₂ equivalent (CO₂e) (Macreadie et al., 2021). It is imperative that mangrove forests provide an essential function in the global carbon cycle; therefore, accurately estimating carbon stock and release to comprehend the carbon budget in BCEs is vital (Zhao et al., 2023).

In this regard, mangrove GPP studies, which can reflect the capacity of carbon capture and sequestration potential by coastal vegetation, play an important role. Properly estimating GPP in mangrove forests is vital for monitoring and evaluating the growth of vegetation, carbon balance, and carbon conversion (Zhu et al., 2021; Paramanik et al., 2022). In addition, GPP studies offer extensive significance in surveilling the terrestrial carbon cycle and determining the magnitude of carbon sources and sinks in the Earth system (Bertram et al., 2021; Zhu et al., 2021). Hence, by monitoring the spatial and temporal patterns of GPP, changes in the carbon budget at a regional level can be determined. This information can then be used as a scientific foundation for creating policies that aim to address climate adaptation and achieve carbon neutrality objectives.

CONCLUSION

In conclusion, this study showed the use of Sentinel-2 image to estimate GPP in the mangrove forest of Ujung Pangkah, East Java, Indonesia. The results showed a significant increase in mangrove area, from 1187.63 ha in 2018 to approximately 1262.25 ha in 2022. This improvement has had a positive impact on mangroves' ability to absorb carbon, as shown by an increase in average GPP from 1997.91 grC m⁻² yr⁻¹ to 2290.09 grC m⁻² yr⁻¹. Mangrove forest GPP fluctuations over time were determined by vegetation density. This was confirmed by the positive relationship between GPP and NDVI, which measured mangrove vegetation density through satellite image processing ($R^2 > 0.9$, $p < 0.05$). This study also emphasized that the application of remote sensing and GIS has the potential to improve and broaden the study of carbon dynamics, particularly GPP in mangrove forests, on a larger scale.

ACKNOWLEDGEMENT

This work was supported by funding from the Institute of Research and Community Development (LPPM) National Collaboration Scheme (University of Trunojoyo Madura and Udayana University) 2024.

REFERENCES

- Alongi, D. M. (2012). Carbon sequestration in mangrove forests. *Carbon Management*, 3(3), 313-322.
- Alongi, D. M. (2014). Carbon cycling and storage in mangrove forests. *Annual Review of Marine Science*, 6, 195-219.
- Alongi, D. M. (2020). Carbon balance in salt marsh and mangrove ecosystems: A global synthesis. *Journal of Marine Science and Engineering*, 8(10), Article 767. <https://doi.org/10.3390/jmse8100767>
- Alongi, D. M. (2022). Impacts of climate change on blue carbon stocks and fluxes in mangrove forests. *Forests*, 13(2), Article 149. <https://doi.org/10.3390/f13020149>
- Ayompe, L. M., Davis, S. J., & Egoh, B. N. (2020). Trends and drivers of African fossil fuel CO₂ emissions 1990-2017. *Environmental Research Letters*, 15(12), Article 124039. <https://doi.org/10.1088/1748-9326/abc64f>
- Azeez, A., Gnanappazham, L., Muraleedharan, K. R., Revichandran, C., John, S., Seena, G., & Thomas, J. (2022). Multi-decadal changes of mangrove forest and its response to the tidal dynamics of thane creek, Mumbai. *Journal of Sea Research*, 180, Article 102162.
- Bacar, F. F., Lisboa, S. N., & Siteo, A. (2023). The mangrove forest of Quirimbas National Park reveals high carbon stock than previously estimated in Southern Africa. *Wetlands*, 43(6), 1–15. <https://doi.org/10.1007/s13157-023-01707-1>
- Basu, S., Lehman, S. J., Miller, J. B., Andrews, A. E., Sweeney, C., Gurney, K. R., Xu, X., Southon, J., & Tans, P. P. (2020). Estimating US fossil fuel CO₂ emissions from measurements of 14C in atmospheric CO₂. *Proceedings of the National Academy of Sciences of the United States of America*, 117(24), 13300–13307. <https://doi.org/10.1073/pnas.1919032117>

- Beer, C., Reichstein, M., Tomelleri, E., Ciais, P., Jung, M., Carvalhais, N., Rödenbeck, C., Arain, M. A., Baldocchi, D., Bonan, G. B., Bondeau, A., Cescatti, A., Lasslop, G., Lindroth, A., Lomas, M., Luysaert, S., Margolis, H., Oleson, K. W., Rouspard, O., ... & Papale, D. (2010). Terrestrial gross carbon dioxide uptake: Global distribution and covariation with climate. *Science*, 329(5993), 834-838. <https://doi.org/10.1126/science.1184984>
- Bernacchi, C. J., Singaas, E. L., Pimentel, C., Portis, A. R., & Long, S. P. (2001). Improved temperature response functions for models of Rubisco-limited photosynthesis. *Plant, Cell & Environment*, 24(2), 253-259.
- Bertram, C., Quaas, M., Reusch, T. B., Vafeidis, A. T., Wolff, C., & Rickels, W. (2021). The blue carbon wealth of nations. *Nature Climate Change*, 11(8), 704-709. <https://doi.org/10.1038/s41558-021-01089-4>
- Bunting, P., Rosenqvist, A., Hilarides, L., Lucas, R. M., Thomas, N., Tadono, T., Worthington, T. A., Spalding, M., Murray, N. J., & Rebelo, L. M. (2022). Global mangrove extent change 1996–2020: Global mangrove watch version 3.0. *Remote Sensing*, 14(15), Article 3657. <https://doi.org/10.3390/rs14153657>
- Cameron, C., Hutley, L. B., Friess, D. A., & Brown, B. (2019). Community structure dynamics and carbon stock change of rehabilitated mangrove forests in Sulawesi, Indonesia. *Ecological Applications*, 29(1), Article e01810. <https://doi.org/10.1002/eap.1810>
- Cao, M., Prince, S. D., Small, J., & Goetz, S. J. (2004). Remotely sensed interannual variations and trends in terrestrial net primary productivity 1981–2000. *Ecosystems*, 7, 233–242. <https://doi.org/10.1007/s10021-003-0189-x>
- Celis, J., Xiao, X., White, P. M., Cabral, O. M. R., & Freitas, H. C. (2023). Improved modeling of gross primary production and transpiration of sugarcane plantations with time-series Landsat and Sentinel-2 images. *Remote Sensing*, 16(1), Article 46. <https://doi.org/10.3390/rs16010046>
- Chapin, F. S., Woodwell, G. M., Randerson, J. T., Rastetter, E. B., Lovett, G. M., Baldocchi, D. D., Clark, D. A., Harmon, M. E., Schimel, D. S., Valentini, R., Wirth, C., Aber, J. D., Cole, J. J., Goulden, M. L., Harden, J. W., Heimann, M., Howarth, R. W., Matson, P. A., McGuire, A. D., ... & Schulze, E. D. (2006). Reconciling carbon-cycle concepts, terminology, and methods. *Ecosystems*, 9(7), 1041–1050. <https://doi.org/10.1007/s10021-005-0105-7>
- Chatting, M., Al-Maslamani, I., Walton, M., Skov, M. W., Kennedy, H., Husrevoglu, Y. S., & Le Vay, L. (2022). Future mangrove carbon storage under climate change and deforestation. *Frontiers in Marine Science*, 9, 1–14. <https://doi.org/10.3389/fmars.2022.781876>
- Chen, L., Msigwa, G., Yang, M., Osman, A. I., Fawzy, S., Rooney, D. W., & Yap, P. S. (2022). Strategies to achieve a carbon neutral society: A review. *Environmental Chemistry Letters*, 20(4), 2277-2310. <https://doi.org/10.1007/s10311-022-01435-8>
- Donato, D. C., Kauffman, J. B., Murdiyarso, D., Kurnianto, S., Stidham, M., & Kanninen, M. (2011). Mangroves among the most carbon-rich forests in the tropics. *Natural Geoscience*, 4, 293–297.
- Duke, N. C., Ball, M. C., & Ellison, J. C. (1998) Factors influencing biodiversity and distributional gradients in mangroves. *Global Ecology Biogeography Letter*, 7(1),27–47. <https://doi.org/10.2307/299769>
- Friedlingstein, P., Jones, M. W., O’Sullivan, M., Andrew, R. M., Bakker, D. C. E., Hauck, J., Le Quééré, C., Peters, G. P., Peters, W., Pongratz, J., Sitch, S., Canadell, J. G., Ciais, P., Jackson, R. B., Alin, S. R.,

- Anthoni, P., Bates, N. R., Becker, M., Bellouin, N., ... & Zeng, J. (2022). Global Carbon Budget 2021. *Earth System Science Data*, 14(4), 1917–2005. <https://doi.org/10.5194/essd-14-1917-2022>
- Gnanamoorthy, P., Selvam, V., Burman, P. K. D., Chakraborty, S., Karipot, A., Nagarajan, R., & Grace, J. (2020). Seasonal variations of net ecosystem (CO₂) exchange in the Indian tropical mangrove forest of Pichavaram. *Estuarine, Coastal and Shelf Science*, 243, Article 106828. <https://doi.org/10.1016/j.ecss.2020.106828>
- Goldstein, A., Turner, W. R., Spawn, S. A., Anderson-teixeira, K. J., Cook-patton, S., Fargione, J., Gibbs, H. K., Griscom, B., Hewson, J. H., Howard, J. F., Ledezma, J. C., Page, S., Koh, L. P., Rockström, J., Sanderman, J., & Hole, D. G. (2020). Protecting irrecoverable carbon in Earth's ecosystems. *Nature Climate*, 10(4), 287–295. <https://doi.org/10.1038/s41558-020-0738-8>
- Hagger, V., Worthington, T. A., Lovelock, C. E., Adame, M. F., Amano, T., Brown, B. M., Friess, D. A., Landis, E., Mumby, P. J., Morrison, T. H., O'Brien, K. R., Wilson, K. A., Zganjar, C., & Saunders, M. I. (2022). Drivers of global mangrove loss and gain in social-ecological systems. *Nature Communications*, 13(1), 1–16. <https://doi.org/10.1038/s41467-022-33962-x>
- Harefa, M. S., Nasution, Z., Mulya, M. B., & Maksun, A. (2022). Mangrove species diversity and carbon stock in silvofishery ponds in Deli Serdang District, North Sumatra, Indonesia. *Biodiversitas*, 23(2), 655–662. <https://doi.org/10.13057/biodiv/d230206>
- Hidayah, Z., Rachman, H. A., & As-Syakur, A. R. (2022). Mapping of mangrove forest and carbon stock estimation of east coast Surabaya, Indonesia. *Biodiversitas*, 23(9), 4826–4837. <https://doi.org/10.13057/biodiv/d230951>
- Hidayah, Z., Utama, R. Y. S., As-Syakur, A. R., Rachman, H. A., & Wiyanto, D. B. (2024). Mapping mangrove above ground carbon stock of benoa bay bali using sentinel-1 satellite imagery. In *IOP Conference Series: Earth and Environmental Science* (Vol. 1298, No. 1, p. 012013). IOP Publishing. <https://doi.org/10.1088/1755-1315/1298/1/012013>
- Hidayah, Z., Rachman, H. A., & Wiyanto, D. B. (2024). Assessment of spatio-temporal dynamics of mangrove forest in Teluk Pangpang, Banyuwangi, East Java, Indonesia. *Biodiversitas: Journal of Biological Diversity*, 25(7), 3138-3150. <https://doi.org/10.13057/Biodiv/D250736>
- Hilmi, N., Chami, R., Sutherland, M. D., Hall-Spencer, J. M., Lebleu, L., Benitez, M. B., & Levin, L. A. (2021). The role of blue carbon in climate change mitigation and carbon stock conservation. *Frontiers in climate*, 3, Article 710546. <https://doi.org/10.3389/fclim.2021.710546>
- Huang, Q., Qiu, F., Fan, W., Liu, Y., & Zhang, Q. (2019). Evaluation of different methods for estimating the fraction of sunlit leaves and its contribution for photochemical reflectance index utilization in a coniferous forest. *Remote Sensing*, 11(14), Article 1643. <https://doi.org/10.3390/rs11141643>
- Huang, M. T., & Zhai, P. M. (2021). Achieving Paris Agreement temperature goals requires carbon neutrality by middle century with far-reaching transitions in the whole society. *Advances in Climate Change Research*, 12(2), 281-286. <https://doi.org/10.1016/j.accre.2021.03.004>
- Huang, X., Lin, S., Li, X., Ma, M., Wu, C., & Yuan, W. (2022). How well can matching high spatial resolution landsat data with flux tower footprints improve estimates of vegetation gross primary production. *Remote Sensing*, 14(23), Article 6062. <https://doi.org/10.3390/rs14236062>
- Huete, A. R., Liu, H. Q., Batchily, K. V., & Van Leeuwen, W. J. D. A. (1997). A comparison of vegetation indices over a global set of TM images for EOS-MODIS. *Remote Sensing of Environment*, 59(3), 440-451.

- Hutchison, J., Manica, A., Swetnam, R., Balmford, A., & Spalding, M. (2014). Predicting global patterns in mangrove forest biomass. *Conservation Letter*, 7(3), 233–240. <https://doi.org/10.1111/conl.12060>
- Ichii, K., Kawabata, A., & Yamaguchi, Y. (2002). Global correlation analysis for NDVI and climatic variables and NDVI trends: 1982-1990. *International Journal of Remote Sensing*, 23(18), 3873-3878. <https://doi.org/10.1080/01431160110119416>
- Indrayani, E., Kalor, J. D., Warpur, M., & Hamuna, B. (2021). Using allometric equations to estimate mangrove biomass and carbon stock in Demta Bay, Papua Province, Indonesia. *Journal of Ecological Engineering*, 22(5), 263–271. <https://doi.org/10.12911/22998993/135945>
- Inoue, T., Akaji, Y., & Noguchi, K. (2022). Distinct responses of growth and respiration to growth temperatures in two mangrove species. *Annals of Botany*, 129(1), 15–28. <https://doi.org/10.1093/aob/mcab117>
- Kanniah, K. D., Kang, C. S., Sharma, S., & Amir, A. A. (2021). Remote sensing to study mangrove fragmentation and its impacts on leaf area index and gross primary productivity in the south of peninsular malaysia. *Remote Sensing*, 13(8), Article 1427. <https://doi.org/10.3390/rs13081427>
- Krauss, K. W., Lovelock, C. E., McKee, K. L., López-Hoffman, L., Ewe, S. M. L., & Sousa, W. P. (2008). Environmental drivers in mangrove establishment and early development: A review. *Aquatic Botany*, 89(2), 105–127. <https://doi.org/10.1016/j.aquabot.2007.12.014>
- Kaufmann, R. K., Zhou, L., Myneni, R. B., Tucker, C. J., Slayback, D., Shabanov, N. V., & Pinzon, J. (2003). The effect of vegetation on surface temperature: A statistical analysis of NDVI and climate data. *Geophysical research letters*, 30(22), Article 2147. <https://doi.org/10.1029/2003GL018251>
- Kauffman, J. B., & Bhomia, R. K. (2017). Ecosystem carbon stocks of mangroves across broad environmental gradients in West-Central Africa: global and regional comparisons. *PLoS One*, 12, Article e0187749. <https://doi.org/10.1371/journal.pone.0187749>
- Kumar, A., Bhatia, A., Fagodiya, R., Malyan, S., & Meena, B. (2017). Eddy covariance flux tower: A promising technique for greenhouse gases measurement. *Advances in Plants & Agriculture Research*, 7(4), 337–340. <https://doi.org/10.15406/apar.2017.07.00263>
- Kumar, T., & Das, P. K. (2023). Estimation of gross primary productivity of Indian Sundarbans mangrove forests using field measurements and Landsat 8 Operational Land Imager data. *Tropical Ecology*, 64(1), 167-179. <https://doi.org/10.1007/s42965-022-00256-8>
- Lukman, A. H., Hidayat, M. F., Sugara, A., & Arief, M. C. W. (2022). Mangroves composition, biomass, carbon stock and their role in the climate change mitigation in Bengkulu City, Indonesia. *AAEL Bioflux*, 15(4), 1975–1988.
- Li, L., Wu, X., & Liu, S. (2015). Characteristics of photosynthesis and photosynthetic carbon fixation capacity of five mangrove tree species in Zhanjiang City. *Guangxi Zhiwu/Guihaia*, 35(6), 825-832.
- Macreadie, P. I., Costa, M. D., Atwood, T. B., Friess, D. A., Kelleway, J. J., Kennedy, H., Lovelock, C. E., Serrano, O., & Duarte, C. M. (2021). Blue carbon as a natural climate solution. *Nature Reviews Earth & Environment*, 2(12), 826-839. <https://doi.org/10.1038/s43017-021-00224-1>
- Markiet, V., & Möttus, M. (2020). Estimation of boreal forest floor reflectance from airborne hyperspectral data of coniferous forests. *Remote Sensing of Environment*, 249, Article 112018. <https://doi.org/10.1016/j.rse.2020.112018>

- Mengis, N., Paul, A., & Fernández-Méndez, M. (2023). Counting (on) blue carbon - Challenges and ways forward for carbon accounting of ecosystem-based carbon removal in marine environments. *PLOS Climate*, 2(8), Article e0000148. <https://doi.org/10.1371/journal.pclm.0000148>
- Nemani, R. R., Keeling, C. D., Hashimoto, H., Jolly, W. M., Piper, S. C., Tucker, C. J., Myneni, R. B., & Running, S. W. (2003). Climate-driven increases in global terrestrial net primary production from 1982 to 1999. *Science*, 300(5625), 1560-1563. <https://doi.org/10.1126/science.1082750>
- Nguyen, H. H., Nghia, N. H., Nguyen, H. T. T., Le, A. T., Tran, L. T. N., Duong, L. V. K., Bohm, S., & Furniss, M. J. (2020). Classification methods for mapping mangrove extents and drivers of change in Thanh Hoa province, Vietnam during 2005-2018. *Forest and Society*, 4(1), 225–242. <https://doi.org/10.24259/fs.v4i1.9295>
- Nuarsa, W., As-Syakur, A. R., Gunadi, I. G. A., & Sukewijaya, I. M. (2018). Changes in gross primary production (GPP) over the past two decades due to land use conversion in a tourism city. *ISPRS International Journal of Geo-Information*, 7(2), Article 57. <https://doi.org/10.3390/ijgi7020057>
- Paramanik, S., Varghese, R., Behera, M. D., Barnwal, S., Behera, S. K., & Bhattyacharya, B. K. (2022). Photosynthetic variables estimation in a mangrove forest. In P. C. Pandey & P. Arellano (Eds.), *Advances in Remote Sensing for Forest Monitoring* (pp. 126-149). John Wiley & Sons Ltd. <https://doi.org/10.1002/9781119788157.ch6>
- Peddinti, S. R., Kambhammettu, B. V. N. P., Rodda, S. R., Thumaty, K. C., & Suradhaniwar, S. (2020). Dynamics of ecosystem water use efficiency in citrus orchards of Central India using eddy covariance and landsat measurements. *Ecosystems*, 23(3), 511–528. <https://doi.org/10.1007/s10021-019-00416-3>
- Perissi, I., & Jones, A. (2022). Investigating European Union decarbonization strategies: Evaluating the pathway to carbon neutrality by 2050. *Sustainability*, 14(8), Article 4728. <https://doi.org/10.3390/su14084728>
- Pricillia, C. C., Patria, M. P., & Herdiansyah, H. (2021). Environmental conditions to support blue carbon storage in mangrove forest: A case study in the mangrove forest, nusa lembongan, bali, indonesia. *Biodiversitas*, 22(6), 3304–3314. <https://doi.org/10.13057/biodiv/d220636>
- Quisthoudt, K., Schmitz, N., Randin, C. F., Dahdouh-Guebas, F., Robert, E. M., & Koedam, N. (2012). Temperature variation among mangrove latitudinal range limits worldwide. *Trees*, 26, 1919-1931. <https://doi.org/10.1007/s00468-012-0760-1>
- Rafique, R., Zhao, F., De Jong, R., Zeng, N., & Asrar, G. R. (2016). Global and regional variability and change in terrestrial ecosystems net primary production and NDVI: A model-data comparison. *Remote Sensing*, 8(3), Article 177. <https://doi.org/10.3390/rs8030177>
- Raich, J. W. (1991). Potential net primary productivity in South America: Application of a global model. *Ecological Applications*, 1(4), 399–429. <https://doi.org/10.2307/1941899>
- Raj, R., Bayat, B., Lukeš, P., Šigut, L., & Homolová, L. (2020). Analyzing daily estimation of forest gross primary production based on harmonized landsat-8 and sentinel-2 product using scope process-based model. *Remote Sensing*, 12(22), 1–23. <https://doi.org/10.3390/rs12223773>
- Razali, S. M., Nuruddin, A. A., & Kamarudin, N. (2020). Mapping mangrove density for conservation of the RAMSAR site in Peninsular Malaysia. *International Journal of Conservation Science*, 11(1), 153-164.

- Reef, R., & Lovelock, C. E. (2015). Regulation of water balance in mangroves. *Annals of Botany*, *115*(3), 385–395. <https://doi.org/10.1093/aob/mcu174>
- Rodda, S. R., Thumaty, K. C., Jha, C. S., & Dadhwal, V. K. (2016). Seasonal variations of carbon dioxide, water vapor and energy fluxes in tropical Indian mangroves. *Forests*, *7*(2), Article 35. <https://doi.org/10.3390/f7020035>
- Shirkey, G., John, R., Chen, J., Dahlin, K., Abraha, M., Sciusco, P., Lei, C., & Reed, D. E. (2022). Fine resolution remote sensing spectra improves estimates of gross primary production of croplands. *Agricultural and Forest Meteorology*, *326*, Article 109175. <https://doi.org/10.1016/j.agrformet.2022.109175>
- Suardana, A. A. M. A. P., Anggraini, N., Nandika, M. R., Aziz, K., As-Syakur, A. R., Ulfa, A., Wijaya, A. D., Prasetyo, W., Winarso, G., & Dimiyati, R. D. (2023). Estimation and mapping above-ground mangrove carbon stock using Sentinel-2 data derived vegetation indices in Benoa Bay of Bali Province, Indonesia. *Forest and Society*, *7*(1), 116–134. <https://doi.org/10.24259/fs.v7i1.22062>
- Tang, Y., Li, T., Yang, X. Q., Chao, Q., Wang, C., Lai, D. Y. F., Liu, J., Zhu, X., Zhao, X., Fan, X., Zhang, Y., Hu, Q., & Qin, Z. (2023). Mango-GPP: A process-based model for simulating gross primary productivity of mangrove ecosystems. *Journal of Advances in Modeling Earth Systems*, *15*(12), Article e2023MS003714. <https://doi.org/10.1029/2023MS003714>
- Trissanti, V. N., Amalo, L. F., Handayani, L. D. W., Nugroho, D., Yuliani, A. R., & Mulyana, D. (2022). The estimation of biomass and carbon stocks in mangrove forest ecosystem of Karawang Regency, West Java. In *IOP Conference Series: Earth and Environmental Science* (Vol. 1109, No. 1, p. 012099). IOP Publishing. <https://doi.org/10.1088/1755-1315/1109/1/012099>
- Turner, D., Ritts, W. D., Cohen, W. B., Gower, S. H., Zhao, M., Running, S. W., Wofsky, S., Urbansky, S., Dunn, A. D., & Munger, J. (2003). Scaling Gross Primary Production (GPP) over boreal and deciduous forest landscapes in support of MODIS GPP product validation. *Remote Sensing of Environment*, *88*(1), 256–270. <https://doi.org/10.1016/j.rse.2003.06.005>
- Wang, X., Ma, M., Huang, G., Veroustraete, F., Zhang, Z., Song, Y., & Tan, J. (2012). Vegetation primary production estimation at maize and alpine meadow over the Heihe River Basin, China. *International Journal of Applied Earth Observation and Geoinformation*, *17*(1), 94–101. <https://doi.org/10.1016/j.jag.2011.09.009>
- Wang, M., Cao, W., Guan, Q., Wu, G., & Wang, F. (2018). Assessing changes of mangrove forest in a coastal region of southeast China using multi-temporal satellite images. *Estuarine, Coastal and Shelf Science*, *207*, 283–292. <https://doi.org/10.1016/j.ecss.2018.04.021>
- Wang, L., Jia, M., Yin, D., & Tian, J. (2019). A review of remote sensing for mangrove forests: 1956–2018. *Remote Sensing of Environment*, *231*, Article 111223. <https://doi.org/10.1016/j.rse.2019.111223>
- Wang, H., Li, Z., Cao, L., Feng, R., & Pan, Y. (2021). Response of NDVI of natural vegetation to climate changes and drought in China. *Land*, *10*(9), Article 966. <https://doi.org/10.3390/land10090966>
- Xiao, X., Zhang, Q., Saleska, S., Hutyyra, L., De Camargo, P., Wofsy, S., Frohling, S., Boles, S., Keller, M., & Moore, B. (2005). Satellite-based modeling of gross primary production in a seasonally moist tropical evergreen forest. *Remote Sensing of Environment*, *94*(1), 105–122. <https://doi.org/10.1016/j.rse.2004.08.015>

- Xiao, X., Hollinger, D., Aber, J., Goltz, M., Davidson, E. A., Zhang, Q., & Moore III, B. (2004). Satellite-based modeling of gross primary production in an evergreen needleleaf forest. *Remote Sensing of Environment*, 89(4), 519-534. <https://doi.org/10.1016/j.rse.2003.11.008>
- Yoro, K. O., & Daramola, M. O. (2020). CO₂ emission sources, greenhouse gases, and the global warming effect. In M. R. Rahimpour, M. Farsi & M. A. Makarem (Eds.), *Advances in Carbon Capture* (pp. 3-28). Woodhead Publishing. <https://doi.org/10.1016/B978-0-12-819657-1.00001-3>
- Zaitunah, A., Meliani, S., Syahputra, O. K., Budiharta, S., Susilowati, A., Rambe, R & Azhar, I. (2021). Mapping of mangrove forest tree density using Sentinel 2A satellite image in remained natural mangrove forest of Sumatra eastern coastal. In *IOP Conference Series: Earth and Environmental Science* (Vol. 912, No. 1, p. 012001). IOP Publishing. <https://doi.org/10.1088/1755-1315/912/1/012001>
- Zeng, N., Jiang, K., Han, P., Hausfather, Z., Cao, J., Kirk-Davidoff, D., Ali, S., Zhou, S. (2022). The Chinese carbon-neutral goal: Challenges and prospects. *Advances in Atmospheric Sciences*, 39(8), 1229-1238. <https://doi.org/10.1007/s00376-021-1313-6>
- Zhang, Y., Hu, Z., Wang, J., Gao, X., Yang, C., Yang, F., & Wu, G. (2023). Temporal upscaling of MODIS instantaneous FAPAR improves forest gross primary productivity (GPP) simulation. *International Journal of Applied Earth Observation and Geoinformation*, 121, Article 103360. <https://doi.org/10.1016/j.jag.2023.103360>
- Zhang, Z., Guo, J., Jin, S., & Han, S. (2023). Improving the ability of PRI in light use efficiency estimation by distinguishing sunlit and shaded leaves in rice canopy. *International Journal of Remote Sensing*, 44(18), 5755-5767. <https://doi.org/10.1080/01431161.2023.2252165>
- Zhao, C., & Qin, C. Z. (2020). 10-m-resolution mangrove maps of China derived from multi-source and multi-temporal satellite observations. *ISPRS Journal of Photogrammetry and Remote Sensing*, 169, 389-405. <https://doi.org/10.1016/j.isprsjprs.2020.10.001>
- Zhao, D., Zhang, Y., Wang, J., Zhen, J., Shen, Z., Xiang, K & Wu, G. (2023). Spatiotemporal dynamics and geo-environmental factors influencing mangrove gross primary productivity during 2000–2020 in Gaoqiao Mangrove Reserve, China. *Forest Ecosystems*, 10, Article 100137. <https://doi.org/10.1016/j.fecs.2023.100137>
- Zheng, Y., & Takeuchi, W. (2021). *Improving Remote Sensing-Based Estimation of Mangrove Forest Gross Primary Production by Quantifying Environmental Stressors: Sea Surface Temperature, Salinity, and Photosynthetic Active Radiation*. Research Square.
- Zheng, Y., & Takeuchi, W. (2022). Estimating mangrove forest gross primary production by quantifying environmental stressors in the coastal area. *Scientific Reports*, 12(1), Article 2238.
- Zhu, X., Hou, Y., Zhang, Y., Lu, X., Liu, Z., & Weng, Q. (2021). Potential of sun-induced chlorophyll fluorescence for indicating mangrove canopy photosynthesis. *Journal of Geophysical Research: Biogeosciences*, 126(4), Article e2020JG006159. <https://doi.org/10.1029/2020JG006159>

Stock Trend Prediction Using Multi-attention Network on Domain-specific and Domain-general Features in News Headline

Phaik Ching Soon*, Tien-Ping Tan, Huah Yong Chan and Keng Hoon Gan

School of Computer Sciences, Universiti Sains Malaysia, 11800 USM, Penang, Malaysia

ABSTRACT

In stock market prediction, using news headlines to anticipate stock trends has become increasingly important. Analyzing sentiment from these headlines makes it possible to predict the stock price trends of the targeted company and profit from the resulting trades. This study examines the impact of company-related news headlines on stock price trends. The objectives of this study are as follows: First, we propose a multi-attention network that incorporates the strength of long short-term memory (LSTM) and bidirectional encoder representations from transformers (BERT) to model domain-specific and domain-general features in news headlines to predict the stock price trend of companies. Second, the proposed model can model and evaluate the effect of news on the stock price trend of different companies. Third, we construct the Bursa Malaysia news headline dataset and automatically align headlines with target companies and their stock price trend. This study proposes that the LSTM WITH ATTENTION +BERT model should use domain-specific and domain-general features to predict stock price trends using news headlines. The proposed model is compared to several convention models and deep learning models. The LSTM WITH ATTENTION +BERT model achieved an accuracy of 50.68%, showing notable improvements over other approaches. It surpassed the Decision Tree by 11.2%, Naïve Bayes by 20.13%, and Support Vector Machine by 5.12%. Compared to the CNN, LSTM, and BERT models, the proposed model is 4.27%, 2.91% and 1.64% higher, respectively, in terms of accuracy. These results highlight the strength of the proposed model.

ARTICLE INFO

Article history:

Received: 07 May 2024

Accepted: 18 November 2024

Published: 07 March 2025

DOI: <https://doi.org/10.47836/pjst.33.2.13>

E-mail addresses:

phaikchingsoon@student.usm.my (Phaik Ching Soon)

tienping@usm.my (Tien-Ping Tan)

hychan@usm.my (Huah Yong Chan)

khgan@usm.my (Keng Hoon Gan)

* Corresponding author

Keywords: Domain-general features, domain-specific features, multi-attention network, news sentiment analysis, stock price trend

INTRODUCTION

Classification is a fundamental task in machine learning, and deep neural networks have demonstrated notable advancements in classification. In text classification,

pre-trained large language models such as bidirectional encoder representations from transformers (BERT) have been used for transfer learning in tasks like sentiment analysis (Kabbani & Duman, 2022) and translation (Prachyachuwong & Vateekul, 2021). The idea of pretrained transformers in natural language processing is then introduced in image recognition, where we see the Vision Transformer in object recognition (Dosovitskiy et al., 2021) and facial recognition (Vaswani et al., 2017). In addition, in speech processing, similar developments can be seen where models such as Wav2Vec and WavLM have achieved remarkable performance in speech processing tasks such as automatic speech recognition (Karpagavalli & Chandra, 2016) and speaker diarization (Vaswani et al., 2017). However, despite these successes, applying deep learning models in financial markets, such as stock trend prediction, remains challenging. Financial markets involve complex dynamics, non-linear patterns, and high-frequency data due to changing government policies, companies' earnings, raw prices, and external events, making accurate prediction and classification difficult.

Investing and Trading

In general, investing in the stock market involves purchasing high-quality, undervalued stocks and holding them for the long term, as opposed to short-term trading. The underlying principle of this approach is the belief that the market is not efficient. Thus, it has not accurately assessed the true worth of these investments, creating an opportunity for future capital appreciation. Furthermore, by conducting a rigorous analysis of a company's financial statements, earnings, assets, and competitive advantages, value investors endeavor to uncover opportunities where the intrinsic value of a stock has been overlooked by the market (Azhikodan et al., 2019)

On the other hand, trading involves more frequent buying and selling of stocks. The main idea in stock trading is to identify the trend of stock so that a trader can make maximum profit by buying it when the price is going to go up and selling it before the price of the stock goes down.

An example of trading using stock price analysis is candlestick patterns, which help to identify potential uptrends or downtrends in stock price (Figure 1). For instance, the hammer pattern indicates a possible uptrend, while the shooting star pattern indicates a possible downtrend. Besides, technical indicators such as simple moving average (SMA), Moving Average Convergence

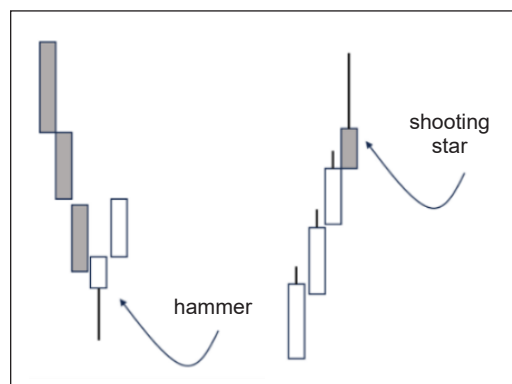


Figure 1. Example of candlestick chart patterns for stock trend prediction (Santur, 2022)

Divergence (MACD) and Relative Strength Index (RSI) are also used by traders to predict the stock price trend. Many machine learning studies in stock trend prediction also computed technical indicators as features for their models (Nguyen & Yoon, 2019)

News Headlines

News articles may influence the direction of stock prices (Hu et al., 2018; Akita et al., 2016; Liu & Carrio, 2018). In general, positive sentiment news will lead to an uptrend in the stock price and vice versa. There are many types of news. One of the types of news that have a major influence on stock price is company-related news. Here, we define company-related news as news that mentions one or more publicly listed companies. Before delving into stock trend prediction, it is essential to first understand the different types of company-related news. The company-related news can be categorized into three groups: quarterly reports, financial analyst reports, and events. Table 1 illustrates company news headlines and their corresponding stock price patterns on Bursa Malaysia.

Quarterly results refer to the financial performance of a company over three months, typically aligned with the company’s fiscal quarters. Consistent revenue growth may indicate a healthy business environment and potentially lead to a positive stock trend. For instance, the news headline, “Zhulian 3q profit jumps 138%,” indicates a substantial increase of 138% in profit compared to the corresponding period in the previous year. The term “profits” normally indicates a positive sentiment in the specified company. On the other hand, the news headline, “Zhulian falls 11.01% after 4q earnings decline 44%,” indicates a negative sentiment, which is reflected in the stock trend.

Table 1
Examples for all news types and stock trends

Type of Company-Related News	Examples of News Headlines	Company Involved	Stock Trend
Quarterly Result	Zhulian 3q profit jumps 138%	ZHULIAN	Up
	YTL Power 4q lifted by deferred tax credit recognition	YTLPOWR	Flat
	Zhulian falls 11.01% after 4q earnings decline 44%	ZHULIAN	Down
Financial Analyst Report	AppAsia may climb higher, says RHB Retail Research	APPASIA	Up
	AirAsia among airlines able to weather COVID-19 crisis, says Brand Finance	AIRASIA	Flat
	Zecon at higher high but ended weak, says AllianceDBS Research	ZECON	Down
Events	AirAsia increases the number of flights to meet holiday demand	AIRASIA	Up
	Yusri Md Yusof is the new Green Ocean MD as Tan See Meng quits post	GOCEAN	Flat
	Zelan falls 4.76% after unit faces RM16.12m arbitration claim	ZELAN	Down

In addition, financial analyst reports are documents prepared by financial analysts who study and analyze companies, industries, and financial markets. Analyst reports offer insights into the company's financial prospects, investment opportunities, and risks, helping investors and stakeholders make informed decisions about buying, selling, or holding a particular security. Table 1 shows the headline "AppAsia may climb higher, says RHB Retail Research." RHB Retail Research suggested that AppAsia may climb higher, indicating an uptrend in the stock price. This could be based on their analysis of the company's financials, market conditions, or other relevant factors that lead them to believe the stock is likely to rise. A financial analyst may also give an underweight rating on a stock, with a headline such as, "Zecon at higher high but ended weak, says AllianceDBS Research ." Financial analyst reports may give a rating on a particular stock based on the performance of the company and the stock prices. These recommendations can influence investor sentiment and impact the company's stock price trend.

A company event is a significant occurrence or development reported in the media and may potentially impact the specified companies and industries. These news events can include corporate mergers or acquisitions, product launches, legal disputes and natural disasters. Positive news, such as successful product launches, can drive stock prices higher and vice versa. For example, in Table 1, "AirAsia increases the number of flights to meet holiday demand," the news snippet indirectly suggested that increasing flights may positively impact the company's revenue and reflect the stock price. On the other hand, the news headline, "Zelan falls 4.76% after unit faces RM16.12m arbitration claim," gave investors a negative sentiment toward Zelan due to possible loss in revenue due to the lawsuit. Nevertheless, not all company news has an impact on the stock price. As shown in Table 1, "Yusri Md Yusof is the new Green Ocean MD as Tan See Meng quits post." "The market might not see the leadership change as a substantial factor influencing the company's financial prospects or overall direction. In such cases, the stock may experience a flat or neutral trend.

Research Questions and Contributions

Company-related news headlines have a significant impact on stock price trends, with positive news leading to an increase in stock prices and negative news leading to a decrease in stock prices. The sentiment and timing of the news publication influence the magnitude and direction of the stock price movement. This hypothesis sets the foundation for exploring the relationship between news sentiment and stock price fluctuations.

The research questions of this study are as follows:

- How do we model and predict stock price trends given a news headline?
- How do we model and predict stock price trends of different listed companies given a news headline?

- How does company-related news affect the stock price trend of listed companies in Bursa Malaysia?

The main contributions of this study are summarized as follows:

- We propose a multi-attention network that incorporates the strength of LSTM and BERT to model domain-specific and domain-general features in news headlines to predict the stock price trend of a company.
- The proposed model can model and evaluate the effect of news on the stock price trend of different companies. For example, in “Samsung sues Apple,” the effect of this news headline will be different for Samsung and Apple.
- We construct the Bursa Malaysia news headline dataset by collecting news headlines using a web crawler and automatically aligning headlines with target companies and their stock price trends from Bursa Malaysia. The dataset will be released to GitHub.

News Sentiment Analysis

Sentiment analysis, also known as opinion mining, is a natural language processing (NLP) technique used to evaluate the sentiment or emotional tone expressed in a text. Before conducting sentiment analysis, it is crucial to perform feature extraction on news data. Feature extraction can be broadly classified into frequency-based and vector-based approaches, each offering distinct advantages for capturing the context within news content.

Frequency-based feature extraction is well-suited for traditional machine learning models like Decision Trees, Support Vector Machines (SVM), and Naïve Bayes. This approach relies on normalized word counts and statistical measures such as frequency, probability, and term frequency-inverse document frequency (TF-IDF) as feature representations. For example, news articles or headlines are often transformed into a bag-of-words model, from which feature vectors are derived. These vectors are then used in machine learning algorithms for tasks like sentiment analysis or stock trend prediction. Agarwal et al. (2020) extracted word n-grams as features from the news; Tipirisetty (2018) implemented VADER to extract news features for model training. Similarly, Jariwala et al. (2020) utilized TF-IDF for news feature extraction.

Vector-based feature extraction, on the other hand, typically involves the use of word embeddings, which are often combined with neural network models. Word embeddings represent words as high-dimensional vectors that capture contextual meaning. These embeddings are generated using methods like autoencoders, which predict neighboring words (e.g., skip-gram) or target words (e.g., Continuous Bag of Words, CBOW). Compared to frequency-based methods, word embeddings are more effective at capturing semantic relationships between words. For example, Kaur (2017) implemented a neural network with pre-trained Word2Vec embeddings for sentiment analysis of news related

to a specific company. Hu et al. (2018) used CBOW embeddings to extract context from news articles.

Akita et al. (2016) implemented a combination of Paragraph Vectors for distributed representations of news articles and Long Short-Term Memory (LSTM) to model temporal effects on stock price. The Paragraph Vector model was utilized to generate continuous distributed representations for each news article and map variable-length text to fixed-length vectors using the Distributed Memory Model (PV-DM) and the Distributed Bag of Words model (PV-DBOW) simultaneously. Articles about 10 companies were represented as vectors and concatenated into a group article vector, with fixed positions assigned to each company; if no article is available for a company at a given timestep, a zero vector is inserted, and multiple articles for the same company are averaged. This approach assumes one article per company per timestep, which is addressed by inserting zero vectors or averaging multiple articles. Experiments conducted on data from fifty companies on the Tokyo Stock Exchange demonstrated that this method outperforms numerical-only and Bag-of-Words-based approaches. LSTM effectively captures time series influences, and considering industry-wide correlations improves stock price prediction.

Although CNN is commonly used on spatial data, such as image categorization and image segmentation, Liu and Carrio (2018) applied it to stock trend prediction. The researchers proposed a joint model combining the TransE model (knowledge graph into a continuous vector space) for representation learning and a CNN for feature extraction from financial news to improve stock price prediction. It also integrated daily trading data and technical indicators. Evaluated with SVM and LSTM, the model achieved 97.66% accuracy in news sentiment classification and 55.44% accuracy in predicting Apple's stock movement using the S&P 500 index. The joint learning approach outperformed traditional methods, providing better decision support for investors.

Similarly, Hu et al. (2018) utilized Hybrid Attention Networks (HAN) with a self-paced learning mechanism. HAN integrated several components to address the challenges posed by the volatile nature of the stock market and the variability in online news quality. It started with news embedding, where news articles were transformed into vectors using pre-trained Word2Vec embeddings. The news-level attention mechanism assigned importance weights to each news item based on its relevance, using a one-layer network and softmax function. For sequential modeling, Gated Recurrent Units (GRU) encoded the temporal sequences of news vectors, capturing both past and future contexts through bi-directional outputs. The temporal attention mechanism further refined this by weighing news over time to enhance classification. To tackle the difficulty of varying news quality, the framework employs Self-Paced Learning (SPL), which gradually incorporates challenging and noisy samples into the training process using a linear regularizer. The model's performance had an accuracy of 48%. However, it focused only on specific companies.

However, traditional word embeddings have a limitation: each word is represented by a single static vector, which does not account for varying contexts. Contextualized word embeddings have been developed to address this. Examples include Embeddings from Language Models (ELMo) and Bidirectional Encoder Representations from Transformers (BERT), which generate dynamic word embeddings based on the context in which a word appears, offering improved performance in sentiment analysis. Transformers leverage attention mechanisms to capture relationships within a sequence, enabling more effective handling of context and dependencies in text. Transformer-based models, such as Bidirectional Encoder Representations from Transformers (BERT), have recently emerged as a powerful financial news sentiment analysis tool.

Kabbani and Duman (2022) implemented a fine-tuned BERT model (FinBERT) for news sentiment analysis into trading strategies by calculating sentiment scores to enhance trading decisions. The process involved using a rule-based method to identify relevant headlines for an asset, applying the FinBERT model to determine the sentiment (positive, negative, or neutral) of each headline, and then averaging the sentiment scores for each asset daily. If the positive sentiment outweighed the negative, a score of +1 is assigned; otherwise, -1 is given. Neutral sentiments were disregarded under the assumption that any news mentioning an asset affects its price.

On the other hand, Prachyachuwong and Vateekul (2021) processed each headline using the BERT model with Multilingual Cased pre-training weights to adapt it to a specific headline corpus. The researchers used the first token from the BERT-Base output, typically employed for classification tasks, to represent the headlines. The model was trained until the convergence of the loss function, adhering to the BERT architecture workflow. Lastly, the optimal embedding values are retained and consolidated for each sector to represent the most relevant headlines of the day. Although BERT captures rich, context-dependent word meanings and performs well in classifying sentiments, it lacks domain-specific features.

Referring to Table 2, the limitations of those models are that they are trained on specific datasets without focusing on company names during feature extraction on news headlines, and the limitations of BERT are that they are trained on more generalized data. Liu and Carrio (2018) used a CNN + LSTM model focused on domain-specific tasks, excelling in spatial feature extraction and integrating news and stock price features during model training, though it was limited to sequence modeling and single-company predictions. Similarly, Akita et al. (2016) employed a Paragraph Vector + LSTM model to handle company-specific news, effectively combining news and stock price features, but encountered challenges when training data lacked news for certain companies. On the domain-general feature extraction, Hu et al. (2018) introduced HAN, benefiting from self-paced learning to enhance generalization but faced difficulties with non-financial news introducing noise. Kabbani and Duman (2022) leveraged BERT to capture nuanced

Table 2
Strengths and weaknesses of reviewed models

Author	Model	Domain	Strengths	Weaknesses
Liu and Carrio (2018)	CNN + LSTM	Domain-specific	Spatial feature extraction. Extract news features and stock price features on model training	Limited sequence modelling. Stock prediction on a single company
Akita et al. (2016)	Paragraph Vector + LSTM	Domain-specific	Handles news paragraph for selected company Extract news features and stock price features on model training	There is no news for a few companies on model training.
Hu et al. (2018)	HAN	Domain-general	Self-paced learning improves generalization.	Non-financial news causes noise.
Kabbani and Duman (2022)	BERT	Domain-general	Captures nuanced word meanings. Pretrained model with a large set of data.	Lack of local news context (such as company names)
Prachyachuwong and Vateekul (2021)	BERT	Domain-general	Multilingual pre-trained data	Specific for Thai news feature extraction

word meanings and took advantage of pre-trained models on large datasets, though it lacked sufficient local news context, particularly in company names. Prachyachuwong and Vateekul (2021) also utilized BERT with a multilingual dataset, focusing specifically on Thai news feature extraction.

Overall, vector-based approaches extract more context in vector form compared to frequency-based context extraction, but they still encounter challenges in addressing deeper contextual relationships within financial news regarding company names. However, without an attention mechanism for company names, the model cannot focus on the most critical information about company names appearing on the news headlines for stock trend prediction.

In addition, most researchers primarily concentrate on predicting stock trends for a limited number of specific companies. However, Akita's study is an exception, as it forecasts stock trends for all companies listed on the Tokyo Stock Exchange using data from the Nikkei Newspaper. We will employ a direction similar to that of Akita to forecast stock trends for all companies listed on Bursa Malaysia, utilizing news data from The Edge Newspaper.

MATERIALS AND METHODS

This study is conducted on companies listed in Bursa Malaysia to model the relationship between news headlines and stock price trends. We only focus on company news in this study. The reasons are threefold: firstly, company news often affects the stock price of the target companies. Thus, it is easier to analyze the causal and effect. Secondly, the target companies that are related to a news headline are often mentioned, and it is easier to find

out the target companies. Thirdly, the number of listed companies in Bursa Malaysia is more than eight hundred, and the amount of news data is not a lot. Thus, the amount of data may not be enough to robustly model the many-to-many relationship between a company and some news and between news and the stock price trend. Nevertheless, the approach proposed can also be applied to another type of news, given that sufficient data is available.

News Data

We crawl the financial news from The Edge Markets (which has been renamed The Edge Malaysia) since it is the leading financial news publisher in Malaysia, and the latest events are published very quickly online compared to other media. After a news article is crawled, we extract the news headlines and publication date and time from it. The target companies mentioned in the news headline are extracted using regular expressions. The news headlines are crawled and downloaded from The Edge Markets, September 2018 until September 2021. The news articles are first downloaded, and then the news headlines are extracted. The news headline must contain at least one company to retrieve the news headline into our data. Overall, 24388 news headlines with company names are extracted for stock trend prediction.

Stock Trend Annotation

The end-of-day (EOD) stock prices of listed companies in Bursa Malaysia, which consists of 883 companies, are retrieved from Yahoo Finance from March 2016 until March 2021.

Table 3 delineates distinct conditions used to label the stock price trend based on the news publication date and time. The general intuition of labeling a stock price trend (as uptrend, downtrend, or flat) is to get the publication time of news and then get the stock price before and after publication. If the relative change is +1% or more, then it is labeled as an uptrend; if the change is -1% or less, it is labeled as a downtrend. Otherwise, it is flat.

In the first scenario, if the news is reported during weekdays (D_i) between 9 am and 5 pm (that is Bursa Malaysia operating hours), the stock prices of the target companies, consisting of the Open price (D_i Open) and Close price (D_i Close) of the day, are retrieved and set as Price Before and Price After, respectively.

Table 3
Published time conditions to retrieve stock price

Published Day	Conditions	Price Before	Price After
D_i , 9 am–5 pm	D_i : Weekday	D_i Open	D_i Close
D_i , 5 pm– D_{i+1} , 9 am	Both days: Weekday (except Friday and holiday)	D_i Close	D_{i+1} Close
D_i – D_j , 9 am	D_i : Holiday, D_j : Weekday	D_{i-n} Close	D_j Close
D_i , 5 pm– D_j , 9 am	D_i : Friday, D_j : Monday	D_i Close	D_j Close

* Day: D, Open: Open Price, C: Close Price

In the second scenario, if the news is reported outside Bursa Malaysia's operating hours, which are between 5 pm and 9 am on the subsequent day (D_{i+1}), during weekdays but not Fridays and holidays, the stock prices of the target companies consist of the Close price of D_i (D_i Close) and the Close price of D_{i+1} (D_{i+1} Close) are retrieved and used as the stock Price Before and Price After, respectively, for calculating the stock price trend.

In the third scenario, if the news is reported between a holiday (D_i) and the subsequent weekday (D_j), the stock prices of the target companies, consisting of the Close price on the holiday (D_{i-n} Close) and the Close price on the subsequent weekday (D_j Close), are retrieved and set as the Price Before and Price After.

In the fourth scenario, if the news is reported from 5 pm on Friday (D_i) until 9 am on Monday of a new week (D_j), the stock prices of the target companies, consisting of the Close price on Friday (D_i Close) and the Close price on Monday (D_j Close), are retrieved and set as the Price Before and Price After.

With the Price Before and Price After, the relative Change formula in Equation 1 calculates the percentage change in a stock price before and after the publication of a news article. The following criteria are employed to classify news headlines according to stock trends: a relative change greater than 0.01 is designated as an uptrend, while a relative change less than -0.01 is categorized as a downtrend. A relative change falling between -0.01 and 0.01 is considered a flat trend.

$$\text{Relative Change} = \frac{\text{Price After} - \text{Price Before}}{\text{Price Before}} \quad [1]$$

To illustrate, the quarterly report "Zhulian 3q profit jumps 138%" was published on 2017-10-11 at 8:08 pm. The second scenario applies to the time the news was published. The Price Before the closing price of the stock on 2017-10-11 at 5 pm was RM 1.64, and the Price After was the closing price on the following day, 2017-10-12, which was RM 1.79. Applying the relative change equation, we got $\text{Relative Change} = (1.79 - 1.64) / 1.64 = 0.01$; a relative change of 0.01 is classified as an uptrend. This example demonstrates how the specified conditions in Table 3 and Equation 1 are utilized to calculate and interpret stock price movements.

News Trend Analysis

After annotating the stock price trend for the news headlines, we do a preliminary analysis by dividing the company news into the following groups: quarterly results, financial analyst reports, and news events.

The 24388 data samples have 2954 annual reports, 1707 financial analyst reports, and 19727 events. In news headlines, the company names are extracted by pattern matching the name in the company name list extracted from Bursa Malaysia 2021. If there is more

than one name listed in the news headlines, each of the companies in the news headlines is analyzed as a sample. For example, On December 21, 2020, the news “Kejuruteraan Asastera (KAB) wins three contracts worth RM57 m from Mah Sing” involved more than one company: KAB and Mah Sing. From this news headline, a total of 2 samples are created for the headline with different target company names. KAB has secured three contracts from Mah Sing Group, totaling RM57 million. This suggested positive developments for KAB as it had successfully won new business. The stock trend was calculated from stock price by referencing the company ticker, date, and time of the news. This news positively affected KAB company, as it was an uptrend for KAB with a relative change of 0.01942, but Mah Sing showed a downtrend.

Table 4 shows the analysis of various types of company news headlines and their minimum and maximum magnitude changes. The Absolute Relative Change is calculated using Equation 2 to quantify the changes in stock price due to news.

$$\text{Absolute Relative Change} = \text{Abs}\left[\frac{(\text{Price After} - \text{Price Before})}{\text{Price Before}}\right] \quad [2]$$

From our analysis, news related to annual reports makes a maximum of 0.5111 magnitude change. This shows that the most influential financial disclosures can result in a more than 50% change in stock prices, underscoring their significance in shaping investor perceptions. The lowest magnitude of 0.000 indicates that certain annual reports have no apparent impact on stock prices. On average, annual reports led to a relatively modest 2.34% change, highlighting the variability in market reactions.

Financial analysis reports, with the highest magnitude of 0.2964, point to a 29.64% potential change in stock prices following the most impactful analyses, showcasing the substantial influence of expert financial assessments. Instances where financial analysis reports have no impact are denoted by the lowest magnitude of 0.000, revealing the diverse responses to such analyses. The average magnitude of 0.0191 implies a comparatively smaller change on average.

Events exhibited the biggest potential magnitude change of 2.600, indicating more than two increases/decreases in stock prices following the most impactful event occurrences. The average magnitude of 0.0275 suggests that an event causes more than 2% of changes in the stock price of the target company. This analysis gives an insight into the potential

Table 4
Data analysis on different types of company news headlines

Type of News Headlines	Highest Magnitude	Lowest Magnitude	Average Magnitude
Annual Reports	0.5111	0.000	0.0234
Financial Analysis Report	0.2964	0.000	0.0191
Events	2.600	0.000	0.0275

rewards and risks associated with different types of news. It also shows the importance of stock trend prediction using news.

Proposed Multi-attention Network

This study proposed a multi-attention network with domain-specific and domain-general features to predict stock price trends given a news headline and the target company. The model learns the effect of the news on the target companies' stock price trend, recognizing that the effect of a headline like 'Samsung sues Apple' varies for Samsung and Apple.

The steps to predict the stock price trend given a news headline and a company name are as follows. First, a simple name matching using regular expressions matches the names of Bursa-listed companies with the news headline. If one or more companies are found in the headline, both the news headline and company names are input to the proposed multi-attention network consisting of an LSTM with an attention model and a BERT-based model to learn the relation between the stock price trend of the target company. LSTM with attention is implemented to model domain-specific features, where financial domain word embedding is trained using the financial text. On the other hand, the BERT is a pretrained large language model where we leverage the general-domain contextualized word embedding features to learn the relation between the stock price trend of the target company and the news headline associated across multiple positions through the mechanism of attention heads and layers. This complex problem is well-suited for Transformers that capture long-range dependencies and global patterns effectively. The predictions from the LSTM-based model and BERT-based model are normalized and combined to produce the outcome. The following paragraphs explain the proposed model in detail, referring to Figure 2.

The news headline and company name are converted to domain-specific word embedding vectors and input into LSTM encoders. Refer to the left neural network in Figure 2, 2a. A domain-specific word embedding model is first pretrained with texts from the financial domain using a word embedding to train the embedding vectors v_h and v_c from the text corpus. In LSTM_h, it inputs the v_h and outputs the hidden states h . In LSTM_c, it receives the v_c as input and outputs the hidden states c . The company attention distributions are calculated with the hidden states from the news headlines encoder and target company encoder using a dot product that produced an attention matrix with a size of $N \times M$, where N is the length of news headlines vectors, and M is the length of the company name vector. This shows the importance of the words/tokens in the news headline. The attention weights are then normalized using the SoftMax function and then concatenated to the hidden states output from the LSTM news headline encoder. It weighs the importance of company names on news headlines.

From the LSTM encoder, the output vectors go through a dense layer followed by a convolutional neural network (CNN) consisting of a 1D convolutional layer and a max pooling layer. The dense layer processes the flattened tensor by connecting each

element to every neuron, enabling the model to learn complex relationships and patterns across the input. The output of the dense layer is then input into the Softmax layer for label classification, transforming logits into a probability distribution over three classes (downtrend, flat, and uptrend), followed by normalization.

At the same time, the news headline and company name are used to fine-tune Bidirectional Encoder Representations from Transformers (BERT) to predict stock price trends. BERT is a powerful pre-trained transformer-based language model that captures contextual information and relationships within text. To model the target company name and news headline, we concatenate the company name with a delimiter (e.g., '|') and then append it to the news headline. Refer to Figure 2, 2b; following this concatenation, the resulting combined representation undergoes processing through a series of standard transformer blocks. These blocks consist of self-attention and feedforward layers, normalization layers, and residual connections (Jurafsky & Martin, 2022). Subsequently, the output vector passes through a dense layer, applying Softmax and normalization.

The final output of the network is derived through a two-step process. First, the normalized Softmax output from both the LSTM-based model and the BERT-based model are combined using an element-wise addition. This operation results in a fused probability distribution across the classes, referring to Equation 3. λ is the normalization weight, where

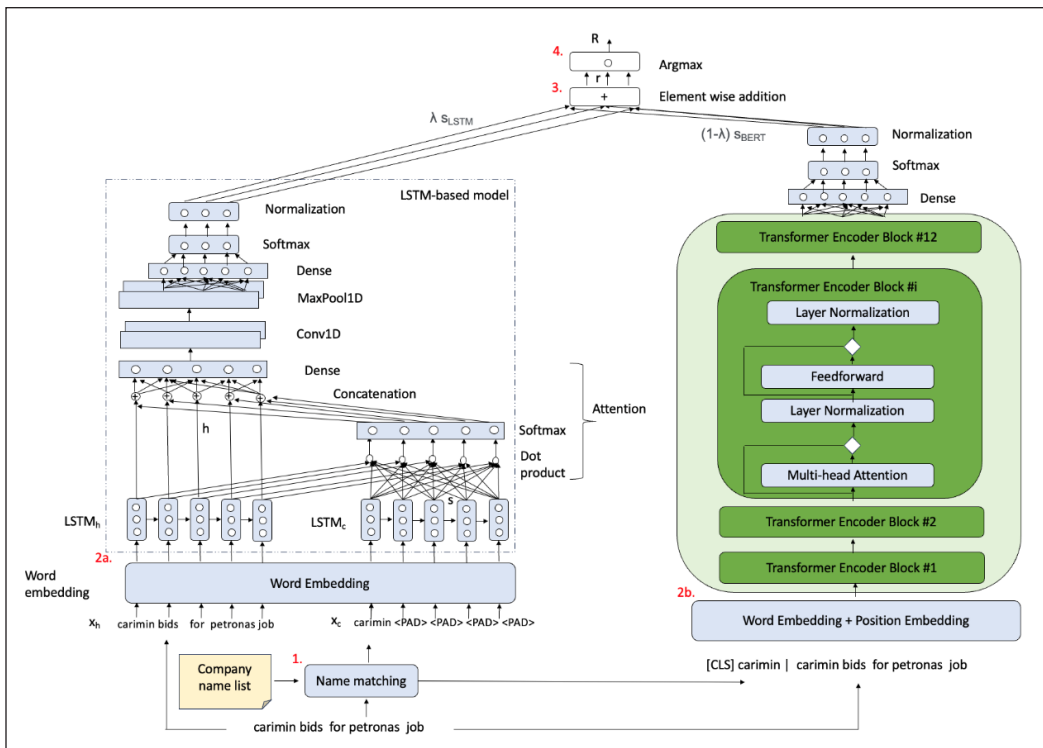


Figure 2. Proposed multi-attention network (LSTM + BERT) with domain-specific and domain-general features

$0 \leq \lambda \leq 1$, which can be determined experimentally from the validation data. λs_{LSTM} and $(1-\lambda)s_{\text{BERT}}$ are the probability distributions of the classes predicted from the LSTM-based and BERT models, respectively. Subsequently, the argmax function is applied to determine the joint prediction, referring to Equation 4. The class with the highest probability is selected as the final output (R). The proposed model allows the integration of predictions from both models, providing a comprehensive and combined assessment of the domain-specific features of the LSTM-based model and the domain-general features of the BERT-based model in determining the most likely class for the given input data.

$$r = \lambda s_{\text{LSTM}} + (1 - \lambda) s_{\text{BERT}} \quad [3]$$

$$R = \text{argmax}(r) \quad [4]$$

RESULTS AND DISCUSSION

A total of 24,388 samples were extracted, each corresponding to a specific company mentioned in the news headlines. For instance, the headline “Zhulian 3Q profit jumps 138%” was associated with Zhulian. The data extraction would produce two samples if a headline contained two different companies. The two samples consisted of the same headline with different target companies. Based on these news headlines, the model was trained to predict stock price trends for multiple companies. In 24388 data, it was split according to the date and time into a training set (17072), test set (5739), and validation set (4877), as shown in Table 5. The distributions of the data were as follows. The train set consisted of 4723 downtrends (0.2767), 6146 flat trends (0.3600), and 6203 uptrends (0.3633). On the other hand, the test set consisted of 645 downtrends (0.2644), 4438 flat trends (0.4666), and 656 uptrends (0.2690). The validation set consisted of 1434 downtrends (0.2940), 1984 flat trends (0.4068), and 1459 uptrends (0.2992).

Table 5
Count and distribution of news headlines dataset according to stock price trend

Trend	Train	Test	Validation	Total
Downtrend	4723 (0.2767)	645 (0.2644)	1434 (0.2940)	6802
Flat	6146 (0.3600)	1138 (0.4666)	1984 (0.4068)	9268
Uptrend	6203 (0.3633)	656 (0.2690)	1459 (0.2992)	8318
Total	17072	5739	4877	24388

Baseline Machine Learning Models

Table 6 presents the results of stock trend predictions using conventional machine learning algorithms, including Decision Trees, Naïve Bayes, and Support Vector Machine. The metrics used to evaluate the models were accuracy, precision, recall, and F1. Notably, the

Support Vector Machine model outshone its counterparts, boasting the highest accuracy at 0.4596 and F1 score of 0.4171. In contrast, the Naïve Bayes model exhibited the lowest accuracy and F1 score, standing at 0.3055 and 0.3621, respectively. Although Naïve Bayes could be computationally efficient and straightforward to implement, its performance was hampered by the assumption of feature independence and its inability to capture more intricate relationships within the data. The Decision Tree model, with an accuracy of 0.3916, demonstrated a balance between precision (0.3682) and recall (0.3688), yielding an F1 score of 0.3675. Decision Trees could be prone to overfitting, particularly in the context of complex and variable data such as text data from news headlines, which might result in a lower overall predictive accuracy. Overall, the Support Vector Machine emerged as the most effective conventional machine learning algorithm for stock trend prediction, offering a well-balanced performance across multiple evaluation criteria, as it could handle high-dimensional data, and its robustness to outliers contributed to its superior performance.

Table 6
Results of conventional machine learning models on stock trend prediction

Models	Accuracy	Precision	Recall	F1
Decision Tree	0.3916	0.3682	0.3688	0.3685
Naïve Bayes	0.3055	0.3729	0.3519	0.3621
Support Vector Machine	0.4596	0.4265	0.4082	0.4171

Deep Neural Networks

Next, we evaluated three deep neural networks: the CNN-based model, the LSTM-based model with attention, and the BERT-based model for stock trend prediction using news headlines and the target company as the input. Both the CNN-based model and LSTM-based model with attention use word embedding vectors trained using GloVe (Souma et al., 2019). We trained the domain-specific GloVe word embedding vectors using the news articles from The Edge Markets. About 16 MB of text data was used, and the vocabulary size was about 40 thousand.

The CNN-based model consisted of two CNN encoders that receive word embedding vectors as input, one from the news headline and another from the target company. The output from the encoders was joined using a dot product to form an attention matrix; then, the attention matrix was concatenated. The attention matrix is concatenated and passed through a dense layer, followed by a convolutional neural network (CNN). Each CNN comprised a convolutional layer with a filter size of 32 and a kernel size of 3, followed by max pooling with a pool size of 2. The flattened layer reshaped the tensor into a 1D vector, removing spatial structure while retaining sequential information. A dense layer processed the flattened tensor to capture complex relationships and patterns, and the output was fed

into a Softmax layer for stock trend label classification. The model used a learning rate 0.0001 and trained for 8 epochs with early stopping to prevent overfitting.

The LSTM-based model consisted of the left branch of the proposed model in Figure 2, 2a. Two LSTM models, LSTM_h and LSTM_c, were utilized to process news headlines vectors (v_h) and targeted company names (V_c). LSTM_h took v_h as input, while LSTM_c received v_c as input. This operation involved combining the encoder outputs and decoder outputs to create joined outputs using dot products to form an attention matrix. The attention matrix was concatenated and passed through a dense layer, followed by a convolutional neural network (CNN). Each CNN comprised a convolutional layer with a filter size of 32 and a kernel size of 3, followed by max pooling with a pool size of 2. The flattened layer reshaped the tensor into a 1D vector, removing spatial structure while retaining sequential information. A dense layer processed the flattened tensor to capture complex relationships and patterns, and the output was fed into a Softmax layer for label classification (downtrend, flat, uptrend). The model used a learning rate 0.0001 and trained for 8 epochs with early stopping to prevent overfitting.

While the BERT-based model consisted of the right branch of the proposed model in Figure 2, 2b, the encoded data, which consists of the company name and headline, are transformed into tensors, encompassing input IDs, attention masks, and corresponding labels for classification. Leveraging the Hugging Face Transformers library, the “bert-base-uncased” variant was chosen for its versatility in handling various NLP tasks. The chosen model architecture for this study was BertForSequenceClassification, a variant of BERT specifically designed for sequence classification tasks. It pre-trained on large language corpora, allowing it to capture intricate patterns and relationships within text. For efficient model training, the dataset tensors were organized into DataLoader objects with a batch size 8. The AdamW optimizer, specifically designed for transformer models, was employed with a learning rate of 0.00001. The training process was executed for a single epoch, considering the specific requirements of the task and computational constraints. The output was classified into three classes: downtrend, flat trend, and uptrend.

Table 7 presents the experiment results of deep neural networks for stock trend prediction using news headlines. All the deep neural networks performed better than conventional machine learning models in terms of accuracy and F1 score. The BERT-based model achieved the highest accuracy at 0.4903, surpassing the accuracy of the LSTM-based model with attention and the CNN-based model at 0.4777 and 0.4641, respectively. Nevertheless, the LSTM-based model with attention produced a higher F1 score at 0.4472 compared to the BERT-based model at 0.4396 and the CNN-based model at 0.4290.

The CNN-based model demonstrated the lowest performance in terms of both accuracy and F1 score compared to other models. In contrast, the LSTM-based model with attention achieved the highest F1 score of 0.4472, while the BERT-based model attained the highest accuracy at 0.4904. CNN models were well-suited for capturing spatial and local patterns

Table 7

Results of deep neural networks on stock trend prediction using news headlines

Deep Neural Network	Accuracy	Precision	Recall	F1
CNN-based model	0.4641	0.4667	0.3970	0.4290
LSTM-based model with attention	0.4777	0.4453	0.4492	0.4472
BERT-based model	0.4904	0.4545	0.4256	0.4396

in data, such as images or short text sequences. However, their ability to capture semantics in long sequential data, like news headlines, was limited compared to LSTM and BERT models. This likely explained CNN's weaker performance in this task. Both the LSTM-based attention and CNN-based models were trained using word embeddings from a small set of domain-specific data. The LSTM model's strength also stems from the use of pre-trained GloVe domain-specific word embeddings, which effectively capture the semantics within the domain. Also, the attention to company names on the news headlines contributed to better performance due to the deeper context and relation between company names and news headlines being captured. This might account for the LSTM-based attention model's higher F1 score compared to the BERT-based model. On the other hand, the BERT-based model, pre-trained on more than 3 billion words from diverse domains, demonstrated better generalization ability, which results in higher accuracy compared to the LSTM-based model.

Proposed Multi-attention Network

Finally, we evaluated our proposed multi-attention network. We applied identical hyperparameter settings, consistent with those previously detailed for both the LSTM-based model with attention and the BERT-based model in our proposed multi-attention network. During the experiment, we varied the normalization weight, denoted as λ , on the validation set to determine the optimal configuration for achieving the highest accuracy.

Table 8 shows the accuracy of the validation set when different λ was applied. During the experiment, we assessed a range of λ from 1 to 0, with intervals of 0.1. This enabled us to identify the most appropriate weightage that yielded the highest accuracy. The most optimum λ was 0.2, as it performed with the highest accuracy, 0.4693.

Table 8

The accuracies of the validation set with different λ

λ	Validation Set Accuracy
1	0.4380
0.9	0.4468
0.8	0.4521
0.7	0.4593
0.6	0.4618
0.5	0.4630
0.4	0.4650
0.3	0.4673
0.2	0.4693
0.1	0.4622
0	0.4581

In the experiment, we analyzed that the normalization weight λ of the multi-attention network was 0.2 on the test set and obtained an accuracy of 0.5068, precision of 0.4373, recall of 0.4657, and F1 of 0.4510. The result showed a higher accuracy and F1 score compared to the LSTM-based model with attention and the BERT-based model. The study showed that the proposed multi-attention network was able to take advantage of both domain-general features of the BERT-based model and the domain-specific features of the LSTM-based model with attention to perform better.

Bias and Limitations

We identified several limitations in this study. The first was the use of end-of-day (EOD) stock price data to calculate stock trends, particularly when a news event occurs during stock market trading hours. Real-time stock price data would be more accurate in this context, as it would allow for the tracking of stock prices immediately before a news event is published. However, due to the unavailability of real-time Bursa Malaysia stock data, we used the opening price from the EOD stock data as a substitute.

The second limitation was the assumption that only company-specific news affects stock trends. This study exclusively examined the impact of company-related news on stock prices, though macroeconomic factors and government policy announcements can also significantly influence stock movements. Additionally, only one news event per instance was modeled to predict stock trends, primarily due to the limited availability of data. Analyzing the contribution of multiple news items on stock price movements would require a much larger dataset. However, the study's approach could easily be extended in future research to incorporate various types of news and the simultaneous influence of multiple news events when sufficient data is available.

The third limitation was the reliance on news headlines for modeling and prediction. It was assumed that the headline accurately captures the key points and essence of the news article. While this assumption held in most cases, there were instances where the headline did not fully convey the content of the article.

Lastly, the study focused solely on news headlines to predict stock trends. As discussed earlier, stock trends could also be influenced by stock prices, technical indicators, chart patterns, and other latent variables. While the experimental results are promising, they also suggest that there is significant room for improvement in stock price trend prediction by incorporating a wider range of data.

CONCLUSION

In this study, we collected a news headline dataset and the stock price trend for Bursa Malaysia. We proposed an approach to automatically annotate the stock price trend based on the publication time of news and show that news can make changes in the stock price

of the target companies. Furthermore, the multi-attention network models domain-specific and domain-general features from news headlines and stock price trends of the targeted companies. The experiment showed that the proposed model performed the highest accuracy at 0.5068 and F1 score at 0.4510 compared to baseline deep learning approaches and conventional machine learning approaches. The performance of the LSTM WITH ATTENTION +BERT model was evaluated against several traditional methods. The LSTM WITH ATTENTION +BERT model achieved an accuracy of 50.68%, demonstrating a significant improvement over another model. Specifically, it outperformed the Decision Tree by 11.26%, the Naïve Bayes model by 20.1%, and the Support Vector Machine by 5.12%. Compared to the CNN, LSTM and BERT models, the proposed model is 4.27%, 2.91% and 1.64% higher, respectively, in terms of accuracy. These results highlight the advantages of integrating BERT's domain-general features with LSTM's sequential modeling capabilities.

Future studies could address some of the limitations identified in this research to further enhance stock trend prediction. First, researchers could explore news summarization techniques, which may provide a more comprehensive representation of a news article's content rather than relying solely on headlines. Summarizations could capture nuanced details that are often missed in short headlines, potentially leading to more accurate stock trend predictions. Second, it would be valuable to investigate the influence of other types of news, such as macroeconomic announcements, global political developments, and sector-specific events, on stock price movements. Understanding how these broader factors affect market trends could provide a more holistic approach to stock prediction. Third, future studies could focus on incorporating multiple news items within a specific timeframe to predict stock trends rather than analyzing isolated news events. This would better reflect real-world scenarios where multiple news stories can impact investor sentiment and market behavior simultaneously. Fourth, improving stock trend prediction models could involve integrating additional data such as real-time stock prices, technical indicators, financial reports, and market sentiment from social media or other sources. A more multi-faceted approach would allow models to capture a broader range of factors that influence stock movements, potentially improving predictive accuracy.

ACKNOWLEDGEMENT

This research is supported by the Fundamental Research Grant Scheme (FRGS/1/2021/ICT02/USM/02/4) of the Ministry of Higher Education, Malaysia.

REFERENCES

Agarwal, H., Jariwala, G., & Shah, A. (2020). Analysis and prediction of stock market trends using deep learning. In *Proceedings of First International Conference on Computing, Communications, and Cyber-Security (IC4S 2019)* (pp. 521-531). Springer. https://doi.org/10.1007/978-981-15-3369-3_39

- Akita, R., Toshihara, A., Matsubara, T., & Ushara, K. (2016). Deep learning for stock prediction using numerical and textual information. In *2016 IEEE/ACIS 15th International Conference on Computer and Information Science (ICIS)* (pp. 1-6). IEEE Publishing. [https://doi.org/ 10.1109/ICIS.2016.7550882](https://doi.org/10.1109/ICIS.2016.7550882)
- Azhikodan, A. R., Jadhav, M., & Bhat, A. (2019). Stock trading bot using deep reinforcement learning. In *Innovations in Computer Science and Engineering: Proceedings of the Fifth ICICSE 2017* (pp. 41-49). Springer. https://doi.org/10.1007/978-981-10-8201-6_5
- Dosovitskiy, A., Beyler, L., Kolesnikov, A., Weissenborn, D., Zhai, X., Unterthiner, T., Dehghani, M., Minderer, M., Heigold, G., Gelly, S., Uszkoreit, J., & Houlsby, N. (2021). *An Image is Worth 16x16 Words: Transformers for Image Recognition at Scale*. arXiv Preprint. <https://doi.org/10.48550/arXiv.2010.11929>
- Hu, Z., Hu, W., Bian, J., Liu, X., & Liu, T. Y. (2018). Listening to chaotic whispers: A deep learning framework for news-oriented stock trend prediction. In *Proceedings of the eleventh ACM International Conference on Web Search and Data Mining* (pp. 261-269). ACM Publishing. <https://doi.org/10.1145/3159652.3159690>
- Jariwala, G., Agarwal, H., & Jadhav, V. (2020). Sentimental analysis of news headlines for the stock market. In *2020 IEEE International Conference for Innovation in Technology (INOCON)* (pp. 1-5). IEEE Publishing. <https://doi.org/10.1109/INOCON50539.2020.9298333>
- Jurafsky, D., & Martin, J. H. (2022). *Speech and Language Processing: An introduction to natural language processing, computational linguistics, and speech recognition* (3rd ed.). ResearchGate.
- Kabbani, T., & Duman, E. (2022). Deep reinforcement learning approach for trading automation in the stock market. *IEEE Access*, *10*, 93564-93574. [https://doi.org/ 10.1109/ACCESS.2022.3203697](https://doi.org/10.1109/ACCESS.2022.3203697)
- Karpagavalli, S., & Chandra, E. (2016). A review of automatic speech recognition architecture and approaches. *International Journal of Signal Processing, Image Processing and Pattern Recognition*, *9*(4), 393-404. <https://doi.org/10.14257/ijsp.2016.9.4.34>
- Kaur, S. (2017). *Algorithmic Trading using Sentiment Analysis and Reinforcement Learning*. Stanford University. <https://api.semanticscholar.org/CorpusID:28323724>
- Liu, Y., & Carrio, A. (2018). Stock price movement from financial news with deep learning and knowledge graph embedding. In *Knowledge Management and Acquisition for Intelligent Systems: 15th Pacific Rim Knowledge Acquisition Workshop, PKAW 2018* (pp. 102-113). Springer International Publishing. https://doi.org/10.1007/978-3-319-97289-3_8
- Nguyen, T., & Yoon, S. (2019). A novel approach to short-term stock price movement prediction using transfer learning. *Applied Sciences*, *9*(22), Article 4745. [https://doi.org/ 10.3390/app9224745](https://doi.org/10.3390/app9224745)
- Prachyachuwong, K., & Vateekul, P. (2021). Stock trend prediction using deep learning approach on technical indicator and industrial specific information. *Information*, *12*(6), Article 250. <https://doi.org/10.3390/info12060250>
- Santur, Y. (2022). Candlestick chart based trading system using ensemble learning for financial assets. *Sigma Journal of Engineering and Natural Sciences*, *40*(2), 370-379. <https://doi.org/10.14744/sigma.2022.00039>
- Souma, W., Vodenska, I., & Aoyama, H. (2019). Enhanced news sentiment analysis using deep learning methods. *Journal of Computational Social Science*, *2*(1), 33-46. [https://doi.org/ 10.1007/s42001-019-00035-x](https://doi.org/10.1007/s42001-019-00035-x)

- Tipirisetty, A. (2018). *Stock Price Prediction using Deep Learning*. [Master Project]. San Jose State University, USA. <https://doi.org/10.31979/etd.bzmm-36m7>
- Vaswani, A., Shazeer, N., Parmar, N., Uszkoreit, J., Jones, L., Gomez, A. N., & Polosukhin, I. (2017). Attention is all you need. In *Advances in Neural Information Processing Systems 30 (NIPS 2017)* (pp. 6000–6010). NeurIPS Proceedings. <https://dl.acm.org/doi/10.5555/3295222.3295349>

Review Article

Recent Advances in Nickel Catalysts for Deoxygenation of Triglycerides and Fatty Acids: A Review

Syazwani Mahmad Puzi¹, Khairuddin Md Isa^{1,2*}, Farizul Hafiz Kasim^{1,2}, Tuan Amran Tuan Abdullah³, Mohd. Aizudin Abd. Aziz⁴ and Nur Amira Fatihah Bashari⁴

¹Faculty of Chemical Engineering and Technology, Universiti Malaysia Perlis, Arau, 02600, Perlis, Malaysia

²Centre of Excellence for Biomass Utilization (COEBU), Universiti Malaysia Perlis, Arau, 02600, Perlis, Malaysia

³Faculty of Chemical and Energy Engineering, Universiti Teknologi Malaysia, Skudai, 81310, Johor, Malaysia

⁴Faculty of Chemical Engineering and Process, Universiti Malaysia Pahang Al-Sultan Abdullah Lebu, Persiaran Tun Khalil Yaakob, Kuantan 26300, Pahang, Malaysia

ABSTRACT

The increasing global demand for fossil fuels and their negative environmental impact have spurred considerable interest in developing renewable fuel sources. Biodiesel, derived from vegetable oils and animal fats, shows great promise as an alternative fuel due to its similar combustion characteristics to fossil fuels. However, the high oxygen content of biodiesel leads to technical challenges in engines. To address this, catalytic deoxygenation has been developed to convert the fatty acids in vegetable oils into second-generation liquid hydrocarbons. This process offers a viable method for the transportation industry to produce biofuels from renewable feedstocks. Palladium (Pd) and platinum (Pt) are commonly used deoxygenation catalysts, known for their excellent performance, but their high cost limits their use in large-scale industrial applications. Nickel (Ni), a non-noble metal, has emerged as a more cost-effective alternative, demonstrating significant catalytic activity for deoxygenation. This review explores the latest advances in the use of Ni catalysts for the deoxygenation of triglycerides and fatty acids. Key focus areas include the deoxygenation process, the role of Ni catalysts, and recent innovations in combining Ni with auxiliary materials to enhance performance. Additionally, the

review examines how catalyst loading impacts the deoxygenation efficiency of triglycerides and fatty acids. This study provides crucial insights into the performance of Ni catalysts with different supports, offering a solid foundation for future research into biofuel production using Ni-based catalytic systems.

Keywords: Active metal, catalyst loading, catalyst, deoxygenation, mesoporous materials, metal oxides

ARTICLE INFO

Article history:

Received: 28 May 2024

Accepted: 04 November 2024

Published: 07 March 2025

DOI: <https://doi.org/10.47836/pjst.33.2.14>

E-mail addresses:

syazwanimahmad@unimap.edu.my (Syazwani Mahmad Puzi)

khairudin@unimap.edu.my (Khairuddin Md Isa)

maizudin@ump.edu.my (Mohd. Aizudin Abd. Aziz)

farizul@unimap.edu.my (Farizul Hafiz Kasim)

tamran@cheme.utm.my (Tuan Amran Tuan Abdullah)

amirabashari97@gmail.com (Nur Amira Fatihah Bashari)

* Corresponding author

INTRODUCTION

The twenty-first century is marked by a heavy reliance on fossil fuels to meet industrial and domestic energy demands. This includes the use of coal, oil, and natural gas, which are predominantly used to generate electricity and power transportation. Despite the advancements in renewable energy technologies, the demand for fossil fuels continues to grow due to their high energy density and cost-effectiveness. However, the use of these fuels raises concerns about environmental sustainability and the need to transition towards cleaner and more sustainable energy sources. It was reported that 44×10^{15} kg of atmospheric carbon was produced each year by fossil fuels consumption, which is 400 times the yearly carbon standard set by the primary productivity of the present world biota (Jeng et al., 2021). The continued dependence and usage of fossil fuels has caused a severe impact on the environment, leading to increased awareness and high demand for sustainable and renewable energy to replace fossil fuels (Jeng et al., 2021). This environmental issue is very worrying and has received the world's attention through international agreements like the Paris Climate Agreement, which 190 parties signed in January 2021.

Biofuels offer significant benefits in the energy sector, playing a key role in the global transition to sustainable and renewable energy. One of their main advantages is reducing greenhouse gas emissions. Unlike fossil fuels, which release carbon stored for millions of years, biofuels are made from biomass that absorbs CO₂ during growth, creating a more balanced carbon cycle (Prasad & Ingle, 2019). The International Energy Agency (IEA) highlights biofuels as an important tool in lowering CO₂ emissions and combating climate change (Jeng et al., 2021).

Biofuels also enhance energy security by diversifying energy sources. They can be produced from various feedstocks, including agricultural and forest sources, as well as specific energy crops (Wang et al., 2023). This reduces dependence on imported fossil fuels, boosts rural economies by creating jobs, and increases national energy security. The U.S. Department of Energy emphasizes the potential of biofuel production to support rural development and energy independence (Schwab, 2016). The future of biofuels is promising due to technological advancements and strong policy support. Innovations in advanced biofuels, like cellulosic ethanol and algae-based fuels, address many limitations of first-generation biofuels. These advanced biofuels, derived from non-food biomass, offer higher energy yields and reduced environmental impact (Popp et al., 2016). They are expected to play a crucial role in helping the transportation sector reduce its carbon footprint and meet renewable energy targets (Darda et al., 2019).

Biofuels can be generated as an alternative to fossil fuels for energy production by means of deoxygenation (Osman et al., 2023). The process of deoxygenation in vegetable oil is often linked to the cracking of hydrocarbon chains, resulting in the breaking of the chains and the removal of oxygen in the form of carbon dioxide and carbon monoxide through

decarboxylation and decarbonylation processes. Previous studies have demonstrated that platinum (Pt) and palladium (Pd), which are noble metals, exhibit favorable performance in deoxygenation reactions (Janampelli & Darbha, 2018). The study by Raut et al. (2016) showed that the application of palladium supported on SBA-16 was highly effective in removing oxygen from fatty acids. Platinum and palladium catalysts have been found to possess excellent capacities in removing oxygen from the feed. Nevertheless, this application is unsuitable for industrial utilization because of the exorbitant expenses associated with its implementation (Wang et al., 2019). Figure 1 exhibits a timeline for the development of noble metal Ni catalysts in renewable energy alternative fuel production.

Remarkably, the Ni-supported catalyst was discovered to possess exceptional deoxygenation capabilities, resulting in a diesel selectivity of 80% (Hafriz et al., 2020). Ni-supported catalysts are preferred for hydrodeoxygenation (HDO) applications as they efficiently cleave C-O bonds and exhibit high activity and selectivity (Ambursa et al., 2021; Yang et al., 2019). These qualities make them an exceptional choice among 3d transition metals for the process of hydrodeoxygenation in biofuel production. Their extraordinary ability to cleave C-O bonds is a significant characteristic of Ni catalysts in HDO, which is vital for eliminating oxygen from molecules derived from biomass (Attia et al., 2020). Ni-supported catalysts exhibit exceptional performance in hydrogenation reactions. They also demonstrate high selectivity towards the desired deoxygenated products and minimize

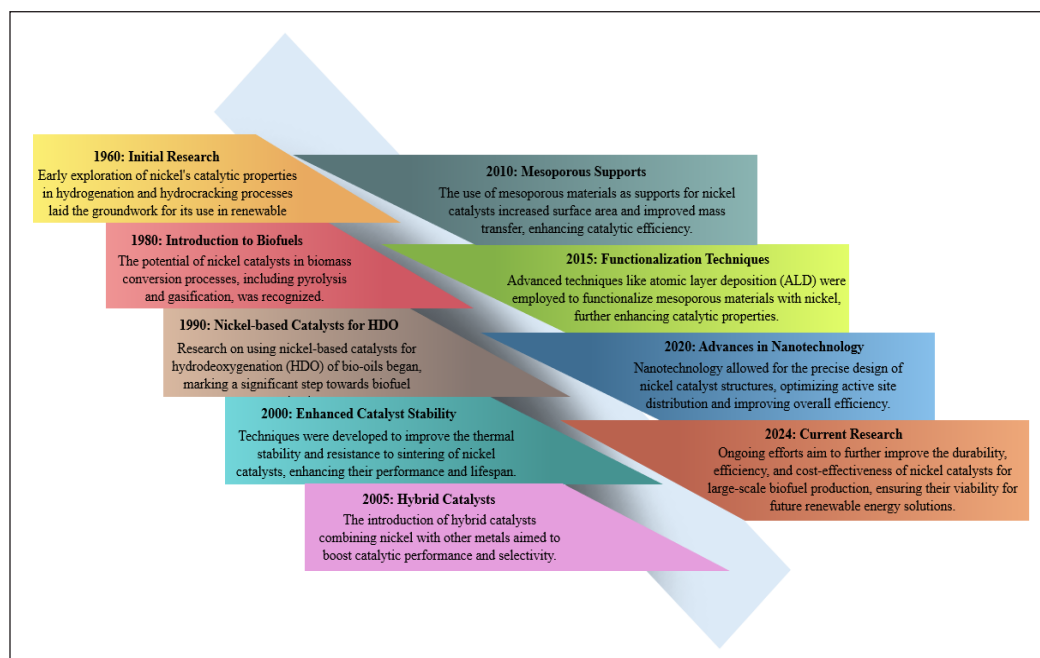


Figure 1. Timeline for the development of noble metal Ni catalysts in renewable energy alternative fuel production

undesired side reactions (Khalit et al., 2021). The ability to optimize activity and selectivity is crucial for efficiently utilizing different types of biomass feedstock. This makes Ni-supported catalysts highly flexible and versatile for various hydrodeoxygenation (HDO) applications (Yang et al., 2023).

Researchers have catalyzed palm fatty acid distillate deoxygenation using NiO/Al-SBA-15. Remarkably, NiO/Al-SBA-15 exhibited superior activity, producing 86% hydrocarbon with a notable preference for diesel fuel (Baharudin et al., 2019). This study strongly demonstrates that the presence of a Ni-supported catalyst significantly enhances the efficiency of oxygen removal. Therefore, the use of non-noble Ni catalysts to remove oxygen from triglycerides and fatty acids shows great potential as a cost-effective catalyst for producing biofuel.

Deoxygenation of Triglycerides and Fatty Acids

Deoxygenation is the simultaneous removal of oxygen by the processes of decarboxylation and decarbonylation of fatty acids, as depicted in Figure 2. This diagram demonstrates that direct decarboxylation removes the carboxyl group from the fatty acid by releasing carbon dioxide molecules, producing n-alkenes. Meanwhile, direct decarbonylation is a process that removes carboxyl groups by eliminating carbon monoxide and water molecules, resulting in the production of alkenes. Deoxygenation typically results in the formation of hydrocarbons with one less carbon atom than their initial fatty acids. Prior publications have extensively explored deoxygenation research involving acidic and basic catalysts applied to a range of fatty acids, triglycerides derived from different vegetable oils, and model oil molecules (Khalit et al., 2021). Most of the reaction conditions occurred within the temperature range of 230°C to 375°C in a hydrogen-rich atmosphere, with pressures ranging from 1 MPa to 11 MPa.

Although there has been a significant amount of research conducted in the past ten years on deoxygenation using environments with low levels of hydrogen and acid-catalyzed reactions, there are a few studies that specifically focus on the development of base and acid-base catalysts for selective deoxygenation in supercritical methanol solvent, which serves as a hydrogen source. This study primarily investigates the process of removing oxygen by using supercritical methanol as a hydrogen source, along with the assistance of base and acid-base catalysts.

Base-catalyzed deoxygenation has been proposed as a method to enhance the hydrolysis of triglycerides, causing them to break down into intermediate fatty acids (Romero et al., 2016). In a study by Tani et al. (2011), scientists used a MgO catalyst in a continuously stirred tank reactor to deoxygenate several bio-based feedstocks. The triglycerides underwent hydrolysis, catalyzed by the water in the feed, resulting in the initial breaking of the C-O bond and the formation of glycerol without fatty

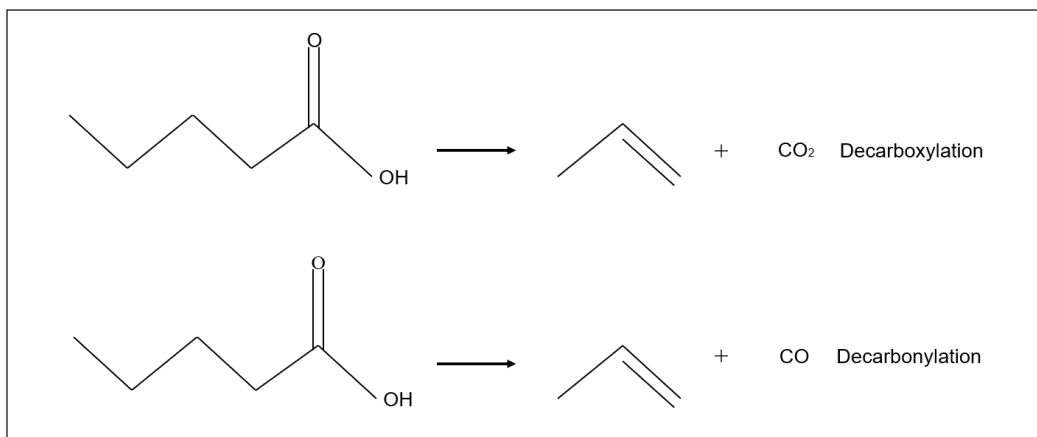


Figure 2. Deoxygenation routes (Bernas et al., 2010)

acids. Gaseous hydrocarbons such as propane are released as glycerol dehydrates, and water is continuously produced. Free fatty acids are generated during decarboxylation/decarbonylation. This is also in agreement with other researchers (Romero et al., 2016). The β -elimination mechanism is speculated to facilitate triglyceride cleavage during deoxygenation over an acidic or basic catalyst, as shown in Figure 3. This figure represents all four of the main reaction processes that have been suggested for the breakdown of triglycerides. There is a scarcity of reports regarding the processes of α -hydrogen transfer and direct deoxygenation reactions in typical deoxygenation reactions. Direct deoxygenation is a chemical process in which triglycerides decompose into intermediate compounds that are absorbed onto the surface of a catalyst without the formation of fatty acid intermediates. The α -hydrogen transfer mechanism shows potential for generating hydrocarbons with minimal hydrogen usage. However, it is expected to be a more significant reaction mechanism for hydrocracking processes than deoxygenation (Rogers & Zheng, 2016). Ester carbonyl carbons with unique characteristics were detected during the process of removing oxygen from soybean oil using Ni-Mg-Al Layered Double Hydroxides at a temperature of 300°C. It was suggested that it could facilitate these processes in specific conditions by acting as an acid-base neutralizer.

Fatty acids undergo decarboxylation or decarbonylation to produce alkanes or alkenes. Research shows that basic catalysts are more effective for decarboxylation compared to acidic catalysts (Tani et al., 2011). For instance, using Ca(OH)₂ and CaO, over 90% of n-C17 was produced from triolein oil deoxygenation CaO (Asikin-Mijan et al., 2016). Studies using MgO for palm oil deoxygenation without hydrogen also showed decarboxylation as the primary process, generating n-C15 and carbon dioxide (Tani et al., 2011). This aligns with research showing that deoxygenating triglycerides involves removing carboxyl groups and producing carbon dioxide and carbon monoxide (Morgan et al., 2012).

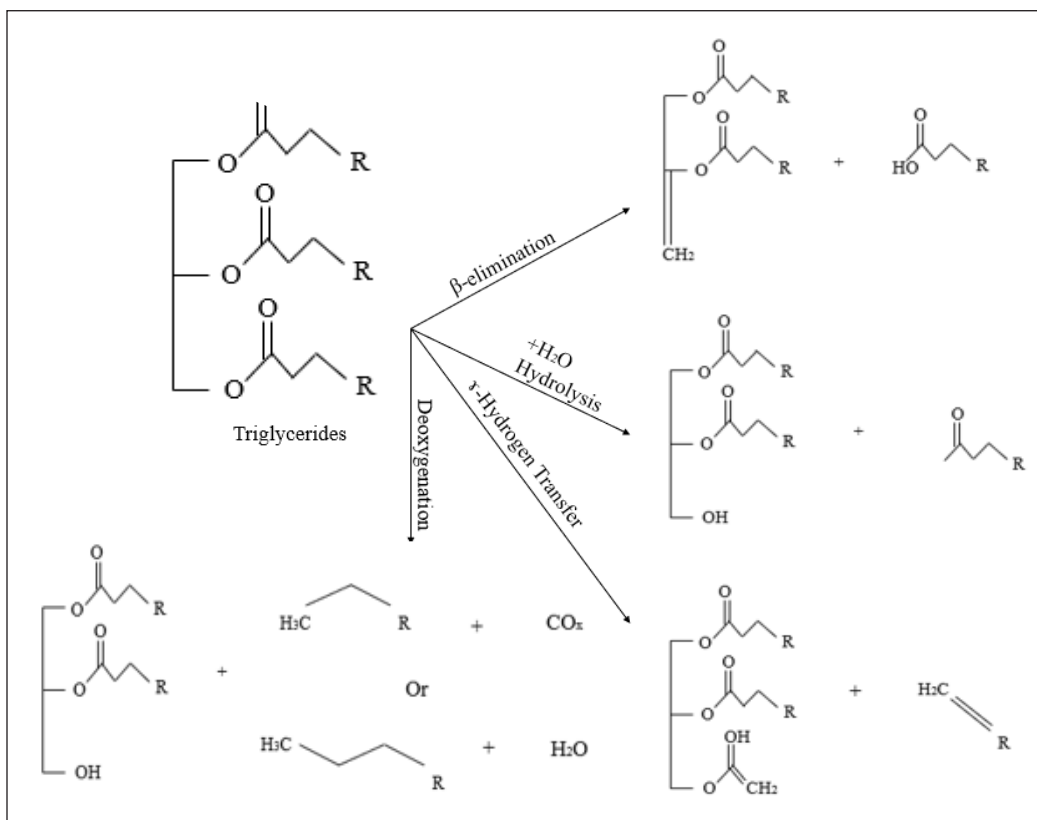


Figure 3. (a) β -elimination and (b) hydrolysis reactions (Rogers & Zheng, 2016)

However, acidic catalysts typically favor decarbonylation. For example, Co/SiO₂ and Co/H β catalysts promoted the decarbonylation of triglycerides, resulting in over 90% C₆/C₇ alkanes converting into heptanoic acid (Liu, Bie et al., 2014). In tristearin deoxygenation using acidic catalysts like Pt/C, Pd/C, and Ni/C, decarbonylated carbon monoxide was produced as a byproduct (Morgan et al., 2012).

Triglyceride deoxygenation catalysts fall into two main categories: noble and non-noble metals. Noble metals like platinum (Pt), palladium (Pd), and ruthenium (Ru) are highly effective and selective in deoxygenation processes but are too costly for large-scale use (Ouedraogo & Bhoi, 2020; Roldugina et al., 2018). Non-noble metals, such as nickel (Ni), cobalt (Co), and molybdenum (Mo), are more affordable and commonly used. Nickel, in particular, is known for its high catalytic performance and cost-effectiveness. It is often combined with other metals to improve stability and resistance to deactivation (Ambursa et al., 2021; Yang et al., 2019).

Metal hydrodeoxygenation (HDO) is favored for biofuel production due to its high selectivity in removing oxygen-containing groups while retaining the carbon in the

feedstock, resulting in high yields of fuel-grade products (Cheah et al., 2022). Ni-supported catalysts are especially versatile and suitable for various biomass feedstocks, which is crucial for industrial applications where feedstock variability is common (Cheah et al., 2022).

HDO is also more cost-effective for large-scale production because non-noble metals like Ni and Co are much cheaper than noble metals (Li et al., 2018). Coating Ni catalysts with alumina or combining them with molybdenum further enhances their stability and performance (Majewski et al., 2021). Continued research on metal HDO catalysts allows for ongoing improvements, making the process more efficient and scalable (Ruddy et al., 2014). In conclusion, metal HDO, especially with non-noble metals like nickel, is a highly viable method for producing biofuels due to its selectivity, versatility, cost-effectiveness, and stability.

HDO Using Supercritical Methanol

Hydrodeoxygenation (HDO) is a key reaction that removes oxygen from bio-oil, converting it into hydrocarbons (Oyedun et al., 2019). A novel approach uses supercritical methanol as both a solvent and a hydrogen source. When methanol reaches its supercritical state (above 240°C and 8.1 MPa), it exhibits lower viscosity and higher diffusivity, enhancing its ability to penetrate biomass and react with oxygenated compounds in bio-oil (Tomic et al., 2015). Supercritical methanol breaks down into hydrogen (H₂) and carbon monoxide (CO), or it directly donates hydrogen to help remove oxygen as water and methanol-derived byproducts, increasing the energy density and stability of bio-oil (Patil et al., 2011).

The use of catalysts, such as Ni, cobalt, and molybdenum, aids in breaking carbon-oxygen bonds during the HDO reaction. Supercritical methanol also serves as a hydrogen donor, reducing the need for external hydrogen sources (Park et al., 2021). This method operates at moderate conditions compared to conventional HDO, which requires higher temperatures and pressures (Ahamed et al., 2021). However, challenges include catalyst deactivation due to coke formation and metal sintering, as well as the need for precise control to prevent unwanted byproducts (Ahamed et al., 2021).

In conventional HDO, external hydrogen is supplied, typically requiring high temperatures (300–400°C) and pressures (up to 10 MPa) (Valle et al., 2019). In contrast, supercritical methanol generates hydrogen in situ, reducing the reliance on external sources and potentially lowering costs and simplifying the process (Shafaghat et al., 2019).

Deoxygenation Catalysts

Catalysts play a crucial part in deoxygenation. Different catalysts produce varying feedstock conversions and product selectivity (Rjeily et al., 2021). Catalysts utilized in deoxygenation can be categorized as homogeneous and heterogeneous, depending on their

physical properties, as shown in Figure 4. As depicted in this picture, a homogeneous catalyst is characterized by mixing substrates and catalytic components in the liquid phase throughout a reaction. While homogeneous catalysts enhance the deoxygenation process, they exhibit inferior activity in comparison to heterogeneous catalysts. This is because homogeneous catalysts frequently encounter issues, including poor thermal stability as well as difficulty in recovering and reusing (Britovsek, 2012; Sudarsanam et al., 2018). On the other hand, heterogeneous catalysts, such as Ni-supported catalysts, provide enhanced stability, increased resistance to deactivation, and simplified separation from reaction mixtures, so offering them efficiency for industrial-scale processes (Navalikhina & Krylov, 1998; Ren et al., 2020). The conversion of stearic acid in supercritical water at a temperature of 400°C was found to be only 2 mol percent after a duration of 30 minutes. However, when Sodium hydroxide (NaOH) and Potassium hydroxide (KOH) were used as catalysts, the conversion increased to 13 mol percent and 32 mol percent, respectively (Watanabe et al., 2006). A study was carried out on several homogeneous catalysts, namely Manganese chloride (MnCl₂), Zinc Chloride (ZnCl₂), Cobalt chloride (CoCl₂), Copper sulfate (CuSO₄), Magnesium sulfate (MgSO₄), Sodium hydroxide (NaOH), and Potassium hydroxide (KOH). The investigation revealed that all of these catalysts enhanced the process of palmitic acid deoxygenation (Fu et al., 2011). After 18 hours at 370°C, sodium hydroxide had the highest deoxygenation activity in the group, producing 7.1 mol percent pentadecane. Their deoxygenation activity, however, remains significantly lower than that of other typical heterogeneous catalysts like Pt/C and Pd/C. Furthermore, homogeneous

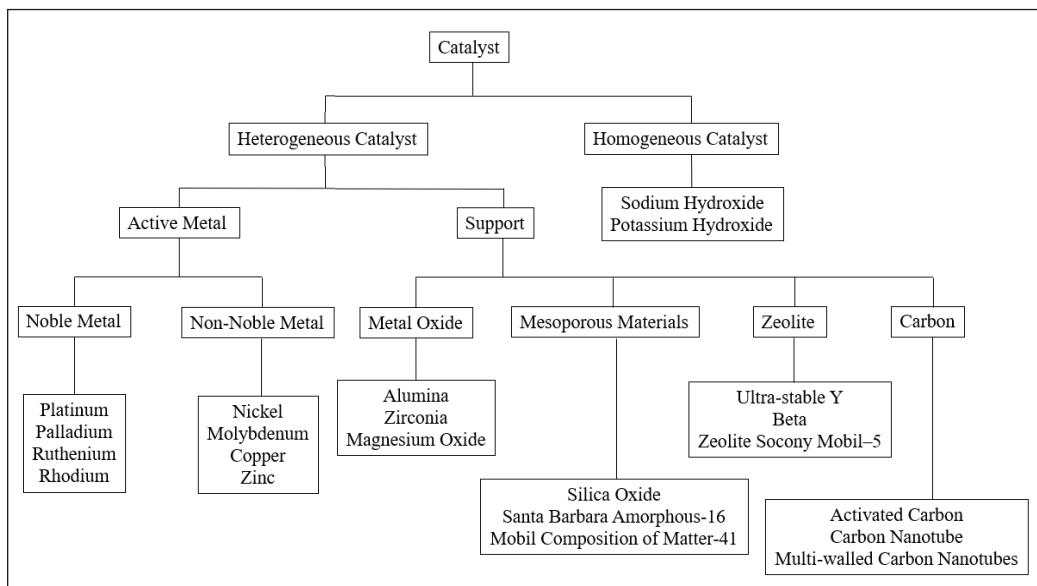


Figure 4. Classification of deoxygenation catalysts

catalysts are difficult to recover from feeds, so their reusability is limited. Heterogeneous catalysts, including metal-based catalysts consisting of support and doped active metals or metallic oxides, are widely developed and used in deoxygenation because of their exceptional performance. The supports used for dispersing and securing active metals or metallic oxides often possess a substantial surface area, and a significant number of them additionally exhibit deoxygenation activity (Ooi et al., 2019). The doped active metals can be categorized as noble and non-noble metals based on their scarcity and value.

Active Metals

The choice of active metal for deoxygenation is crucial as it has a substantial influence on both the quantity and the quality of the final product. Despite the extensive research conducted on deoxygenation, it has been constrained to catalysts. The predominant catalysts in this category are monometallic noble metals, including palladium (Pd), platinum (Pt), rhodium (Rh), and ruthenium (Ru). Figure 5 illustrates the transition metals, specifically iron (Fe), cobalt (Co), Ni, palladium (Pd), and platinum (Pt), which are classified in Groups 8–10 of the periodic chart, are recognized for exhibiting a high activity in hydrodeoxygenation (HDO) processes (Alkhoori et al., 2023; Jin et al., 2019). These transition metals exhibit excellent performance in cleaving the C-O bonds present in oxygenated compounds, which is crucial in the conversion of bio-oil into hydrocarbon fuels. Ni, a metal belonging to Group 10, has been extensively studied due to its cost-effectiveness and high catalytic activity in hydrodeoxygenation (HDO) reactions. Studies have demonstrated that Ni-supported catalysts successfully eliminate oxygen from various feedstocks produced from biomass, resulting in high-quality biofuels (Azman et al., 2021). The metal-support contact, which serves as the surface reaction mechanism, can strengthen the interaction between the support and the metal. The active metal nanoparticles are placed onto a support material to immobilize them. Table 1 displays the benefits and drawbacks of the active metals often employed for removing oxygen from triglycerides and fatty acids. From Table 1, platinum (Pt) and palladium (Pd) are very costly but show high activity and efficacy in hydrogen activation, favor carbon-carbon bond cleavage and are highly reactive in decarboxylation and decarbonylation reactions. Iridium (Ir) and rhodium (Rh) are also costly but give high selectivity in producing symmetrical ketones with poor selectivity toward deoxygenation and favor decarbonylation, respectively. Meanwhile, ruthenium (Ru) favors hydrodeoxygenation and possesses high selectivity in producing symmetrical ketones but has poor Ru/SiO₂ performance in producing deoxygenation products.

Remarkably, the deoxygenation activity was highest when Ni was used as a promoter, resulting in diesel selectivity of 80% (Hafriz et al., 2020). Ni catalysts possess numerous advantages over other non-precious metals employed in the production of biofuels, as shown in Figure 6. Ni catalysts' high activity and selectivity in cleaving carbon-oxygen

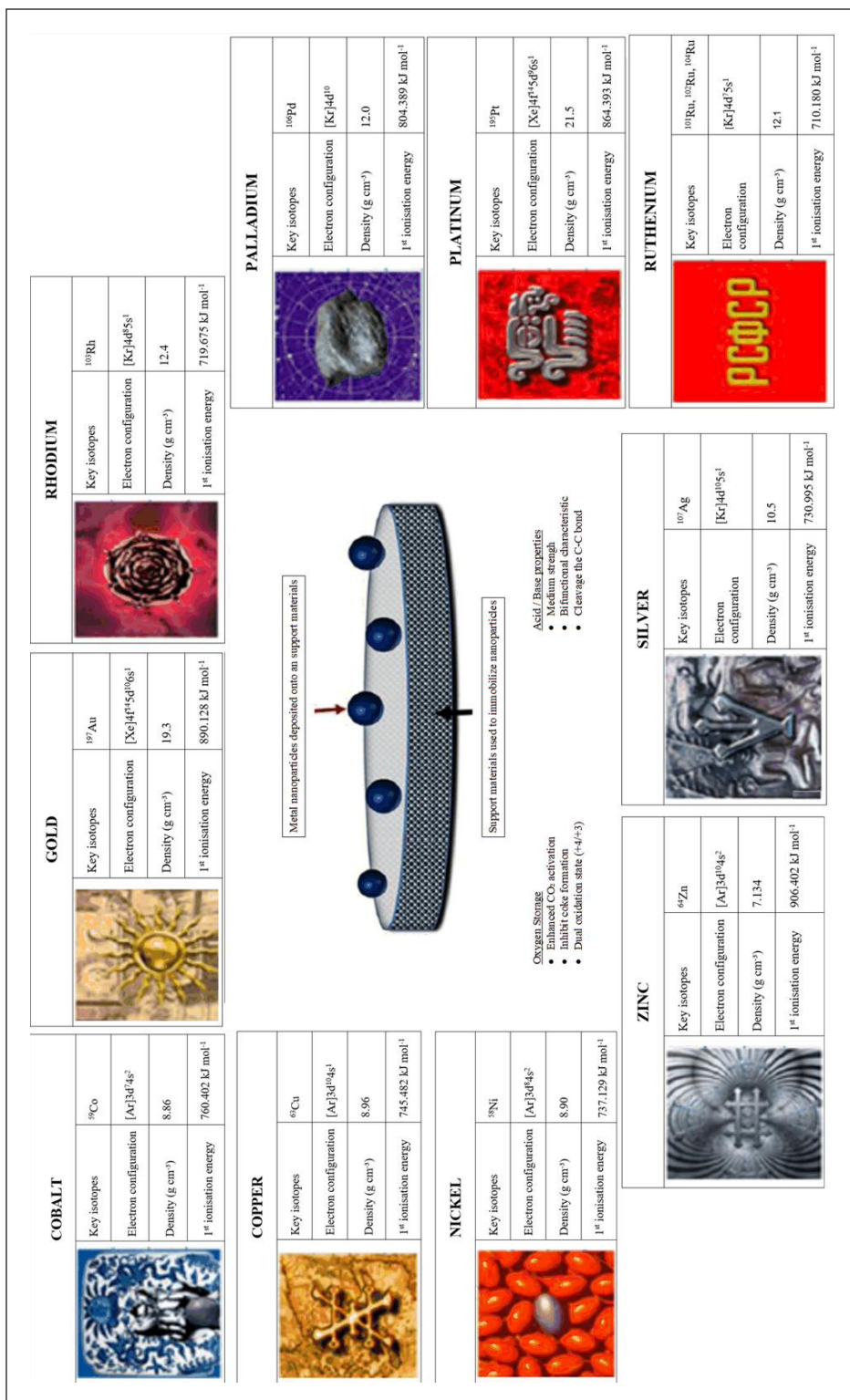


Figure 5. Active metals for fatty acid and triglyceride deoxygenation (Cheah et al., 2022)

Table 1

Main roles and limitations of reactive metals employed in deoxygenation studies (Cheah et al., 2022)

Elements	Main roles	Limitations	References
Platinum (Pt)	<input type="checkbox"/> High activity and efficacy in hydrogen activation <input type="checkbox"/> Favors carbon-carbon bond cleavage <input type="checkbox"/> Highly reactive in decarboxylation and decarbonylation	<input type="checkbox"/> Costly <input type="checkbox"/> Gradually poisoned by carbon monoxide and sulfur-based functional groups and carbon laydown	Fu et al., 2011
Palladium (Pd)	<input type="checkbox"/> High activity and efficacy in hydrogen activation <input type="checkbox"/> Favors carbon-carbon bond cleavage <input type="checkbox"/> Highly reactive in decarboxylation and decarbonylation	<input type="checkbox"/> Costly <input type="checkbox"/> Gradually poisoned by carbon monoxide and sulfur-based functional groups and carbon laydown	Cheah et al., 2022
Iridium (Ir)	<input type="checkbox"/> High selectivity in producing symmetrical ketones	<input type="checkbox"/> Costly <input type="checkbox"/> Poor selectivity toward deoxygenation	Di et al., 2017
Rhodium (Rh)	<input type="checkbox"/> Favors decarbonylation	<input type="checkbox"/> Costly	Di et al., 2017
Ruthenium (Ru)	<input type="checkbox"/> Favors hydrodeoxygenation <input type="checkbox"/> High selectivity in producing symmetrical ketones	<input type="checkbox"/> Poor Ru/SiO ₂ performance in producing deoxygenation products	Di et al., 2017

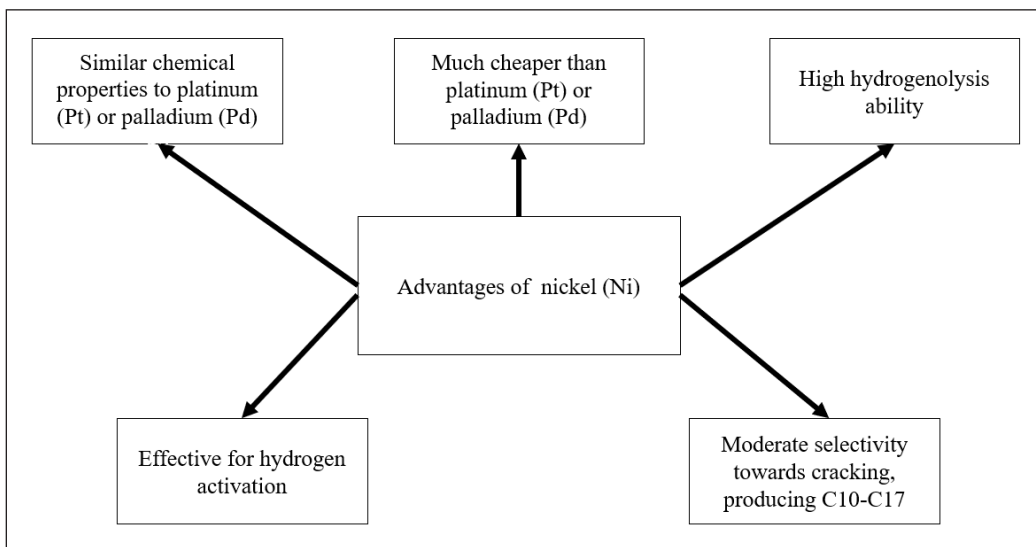


Figure 6. Advantages of non-noble Ni in biofuel production

(C-O) bonds in biomass-derived compounds is one of their most significant advantages. As a transition metal, Ni possesses exceptional catalytic characteristics for hydrogenation processes, which facilitate the effective elimination of oxygen and the conversion of bio-oil into valuable hydrocarbons (Ambursa et al., 2021; Yang et al., 2019). In addition, Ni catalysts are comparatively more cost-effective than noble metal catalysts like platinum

(Pt) and palladium (Pd), making them economically viable to produce biofuels on a wide scale.

Furthermore, Ni catalysts exhibit strong stability in the reaction conditions commonly used in HDO. They possess the ability to sustain their catalytic activity for extended durations and endure the elevated temperatures and pressures needed for optimal deoxygenation. This stability is important in continuous industrial operations, as catalyst lifespan has a direct impact on operational costs and efficiency (Shafaghat et al., 2019). In addition, Ni catalysts are versatile and can be used in various applications, such as supported Ni catalysts, Ni-supported alloys, and Ni on mesoporous materials (Khalit et al., 2021). This adaptability allows for the tailoring of catalytic characteristics to fulfill the specific requirements of a reaction and optimize performance. Moreover, Ni catalysts can perform in a variety of reaction environments, such as supercritical methanol. Ni catalysts are efficient in promoting the cleavage of methanol into hydrogen and carbon monoxide, which makes them valuable in operations where hydrogen is produced in situ. This enhances the overall efficiency of the HDO process as Ni catalysts can effectively promote hydrogenation reactions without the need for external hydrogen supplies (Shafaghat et al., 2019).

Progress in catalyst design has resulted in the development of bimetallic and multi-functional Ni catalysts that integrate the advantages of Ni with other metals or catalytic functions. For example, nickel-molybdenum (Ni-Mo) and nickel-cobalt (Ni-Co) catalysts have improved catalytic performance due to metal synergistic effects. These catalysts can enhance the efficiency of chemical reactions, the ability to selectively produce desired products, and the durability against deactivation caused by the creation of coke (Azman et al., 2021).

In conclusion, Ni catalysts offer numerous advantages in biofuel production. These include their exceptional catalytic activity, cost-effectiveness, ability to remain stable under reaction environments, versatility in form and function and compatibility with supercritical methanol environments. The presence of these qualities makes Ni catalysts a highly efficient and economically feasible choice for improving the efficiency and sustainability of the biofuel production process (Khalit et al., 2021).

Ni Loading

The presence of Ni has a substantial impact on both the speed of the reaction and the degree of selectivity or production of diesel-like hydrocarbons during deoxygenation (Hermida et al., 2015). Table 2 displays new research findings about the impact of Ni loading on the process of removing oxygen from vegetable oils and fatty acids. Liu, Zuo et al. (2014) conducted an experiment to investigate the deoxygenation of palm oil using a Ni/SAPO11 catalyst. The experiment involved adjusting the Ni loading from 2 wt.% to 9 wt.% and maintaining a temperature of 200°C and a hydrogen (H₂) pressure of 4 MPa.

The study's findings indicated that the Ni loading was augmenting from 2 wt.% to 7 wt.% led to an elevation in the production of liquid alkane and an enhancement in the selectivity of isomerization, with respective increases from 60% to 67.4% and from 46% to 61.5%. The absence of any significant impact on the production of liquid alkane was observed upon increasing Ni loading from 7% to 9 wt.%. Nevertheless, a notable enhancement in the selectivity of C1-C14 alkanes was observed. An isomerization selectivity of over 83% was achieved using 9 wt.% of Ni/SAPO-11.

Modifications in catalyst structures caused by metal loading can potentially impact catalytic activity. The influence of metal loading on deoxygenation processes is intimately related to various elements, including the preparation method, characteristics of support, and the metal's chemical state. The method of preparation has significant effects on the distribution and size of metal particles on the catalyst surface, which affects catalytic performance. Impregnation, co-precipitation, and sol-gel techniques can produce varied particle sizes and dispersion, which affects the accessibility of active sites for deoxygenation reaction (Li et al., 2015).

The stability of the catalyst and the dispersion of metal particles are significantly influenced by the characteristics of the support, including surface area, porosity, and the chemical composition of the support material (Liu, Bie et al., 2014). The catalytic activity is also influenced by the chemical state of the metal, which includes its oxidation state and the nature of its interaction with the support. The oxidation state can affect the metal's ability to activate and dissociate reactants, therefore influencing the efficiency of deoxygenation. The efficiency of metal-loaded catalysts in deoxygenation processes is determined by a combination of these parameters, emphasizing the significance of optimizing methods of preparation, carrier characteristics, and metal chemical states to attain desired catalytic performance (Wang et al., 2020).

According to the literature, Ni/HZSM-5 catalyst with a Ni loading of 7 wt.% demonstrated the best performance. The conversion rate for methyl hexadecanoate was 90%, and the selectivity for C5-C16 hydrocarbon was 83%. The observed phenomenon can be attributed to the synergistic interaction between the Ni metal and the HZSM-5 acid sites. Nevertheless, the concentration of NiO on the HZSM-5 surface was discovered to be significantly elevated and only became discernible for Ni loadings below 3 wt.%. In addition, the size of the NiO particles grew to 150 nm, and the catalyst surface experienced substantial agglomeration as the Ni loading reached 7 wt.% (Japar et al., 2020; Liu, Bie, et al., 2014). Hence, it is imperative to ascertain the ideal metal loading on the catalyst support to ensure that the catalyst's structure is conducive to catalyzing triglyceride deoxygenation.

Shi et al. (2023) studied the effect of the Ni loading amounts (2.5%–20%) on green diesel-like hydrocarbon production by H₂-free catalytic deoxygenation of oleic acid via Ni/MgO-Al₂O₃ catalysts. They revealed that Ni (10%)/MgO-Al₂O₃ catalysts exhibited

Table 2
Recent studies on the effects of Ni loading on the deoxygenation of fatty acids and vegetable oils

References	Type of reactor	Fatty acid/vegetable oil	Catalysts	Method of catalyst preparation	Reaction conditions	Conversion (%)	Hydrocarbon yield/selectivity (%)
Zhou et al. (2021)	Fixed bed	<i>Jatropha curcas</i> oil	2Ni/10W/AC 10Ni/10W/AC 20Ni/10W/AC	Carbothermal hydrogen reduction	T = 340°C P = 3 MPa RT = 5 h WHSV = 55.2 h ⁻¹ H ₂ /N ₂ = 1 FR = 200 mL/min	-	10Ni/10W/AC showed excellent performance with 94.5% of C15-C18
Maneechakr & Karnjanakom (2021)	Fixed bed	Waste palm kernel cake	5Ni/AC 10Ni/AC 15Ni/AC 20Ni/AC	Impregnation and pyrolysis	T = 550°C HR = 1000 °C/min Ultrasonic pretreatment time = 200 min	-	15Ni/AC demonstrated the best performance with 72% of hydrocarbon
Ameen et al. (2020)	Fixed bed	Rubber seed oil	3Ni/γ-Al ₂ O ₃ 12Ni/γ-Al ₂ O ₃ 15Ni/γ-Al ₂ O ₃	Impregnation	T = 350°C P = 3.5 MPa WHSV = 1 h ⁻¹ H ₂ :oil ratio = 1000 N (cm ³ /cm ³)	99.9	15Ni/γ-Al ₂ O ₃ produced the highest hydrocarbon selectivity of 55.1 wt. %
Chen et al. (2019)	Fixed bed	Methyl laurate	6Ni/γ-Al ₂ O ₃ 8Ni/γ-Al ₂ O ₃ 10Ni/γ-Al ₂ O ₃ 12Ni/γ-Al ₂ O ₃ 14Ni/γ-Al ₂ O ₃	Impregnation	T = 400°C P = 2 MPa FR = 50 mL/min	91.1	10Ni/γ-Al ₂ O ₃ showed the best performance with 68.6% of C11
Sánchez-Cárdenas et al. (2016)	Batch	Oleic acid	3Ni/γ-Al ₂ O ₃ 5Ni/γ-Al ₂ O ₃ 7Ni/γ-Al ₂ O ₃	Impregnation	T = 340°C P = 2.3 MPa H ₂ RT = 5 h	70.1 79.4 84.8	7Ni/γ-Al ₂ O ₃ gave the best performance with 69% of C17

*T=Temperature, P=Pressure, RT= Reaction Time, FR= Flow rate, HR=Heating rate, WHSV= Weight hourly space velocity, W= Tungsten, AC=Activated Carbon, Ni=Nickel

excellent catalytic performance with the highest HCs (95.12%), olefin content (57.37%) and green biodiesel content (75.90%) due to mild Brønsted-rich acidity sites, lower reduction temperature, higher active metallic Ni species content, suitable oxygen vacancy content and favorable texture properties via the decarbonylation reaction pathway. Yang et al. (2022) investigated a one-step synthesis of highly active and stable Ni-ZrO₂ catalysts for the conversion of methyl laurate to alkanes with varied Ni loading of 5.28 to 16.15%. They found that 10Ni-ZrO₂ exhibits the best catalytic performance for obtaining alkane products with nearly 100% yield (99.4%), and the selectivity to C11 is as high as 87.6%. Jeon et al. (2022) studied the effect of Ni loading amount (5 to 30%) over Ni/MgO–Al₂O₃ on deoxygenation of non-edible fatty acid for green diesel production. They found that the 20% Ni/MG70 catalyst showed excellent deoxygenation performance owing to its highest number of Ni active sites, easier reducibility, and appropriate acidity. Khalit et al. (2021) synthesized and characterized Ni-supported activated charcoal using different loading of Ni (5 to 20%) supported on commercial activated charcoal. They revealed that the highest conversion of hydrocarbon was achieved when the reaction undergoes using Ni20%AC as a catalyst. The presence of the higher-loading active metal showed a high deoxygenation reaction by decarboxylation and decarbonylation pathways with a high hydrocarbon yield of 83% and high selectivity of n-C15 and nC17.

Catalyst Supports

The selection of catalyst support is vital in developing a catalyst as it influences the type of reaction pathway used, product distribution, and overall deoxygenation performance. Prior studies have determined the effect of the structural characteristics of catalyst supports on the interaction bonding between the active site and the support and the degree of active site dispersion on the support surface. Figure 7 depicts the metal oxides and mesoporous materials that researchers frequently use as catalyst support for deoxygenation. These materials are known for their exceptional heat and chemical resistance, making them suitable for use in demanding working circumstances. This diagram illustrates that catalyst support has an impact on the choice of reaction pathway, the distribution of products, and the total deoxygenation activity. The metal oxide has a relatively high specific surface area ranging from 200 m²/g to 500 m²/g. It also has high physical strength and is resistant to thermal and chemical degradation. Additionally, it can activate oxygenated compounds and has excellent oxygen storage capacity with intrinsic redox properties. However, their lower surface area with lesser uniform pore structure could restrict the availability and accessibility of active sites (Mortensen et al., 2011).

On the other hand, mesoporous materials have a high specific surface area ranging from 600 m² to 1000 m². They have large pore diameters ranging from 2 to more than 10 nm and moderate acidity. Furthermore, they possess a broad distribution of weak protonic

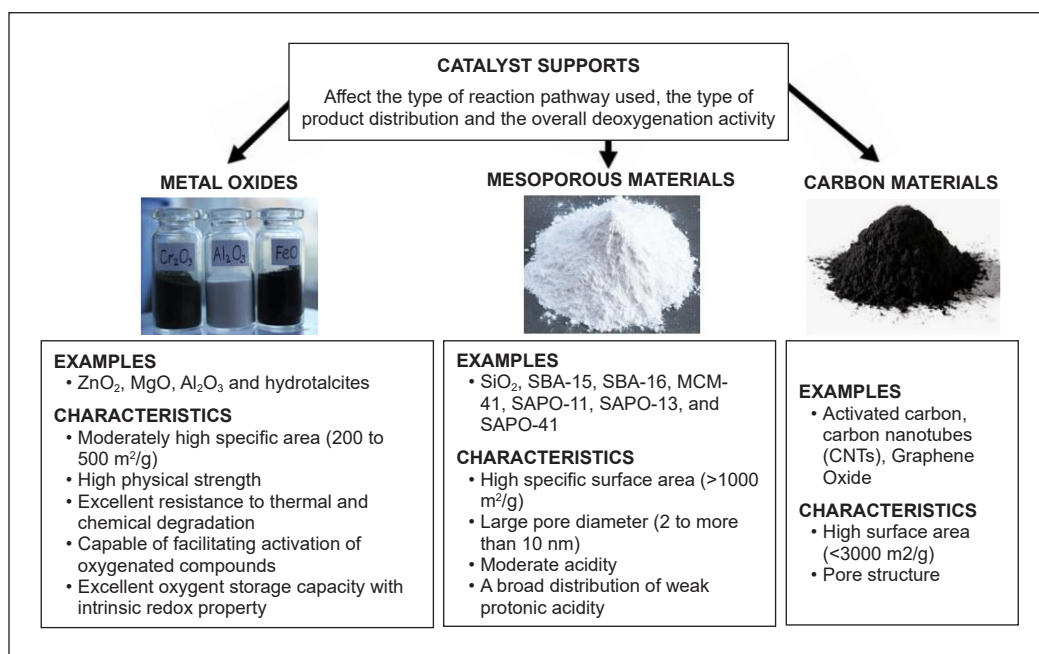


Figure 7. Catalyst supports that are frequently used in deoxygenation

acidity sites. These materials also have variable pore diameters and surface features that can be optimized for specific reactions (Corma, 2003). Nevertheless, mesoporous materials frequently have poorer thermal stability and mechanical strength than metal oxides, which can limit their use in harsh reaction conditions (Ren et al., 2012).

Studies on catalysts loaded with Ni on carbon support also have demonstrated excellent results in the production of biofuels, indicating their ability to improve catalytic performance and stability. Carbon catalysts impregnated with Ni are highly efficient in hydrodeoxygenation (HDO) processes, which are crucial for enhancing the quality of bio-oils to produce higher-quality biofuels. Carbon support possesses a large surface area and porous structure, assisting in the distribution of Ni particles and enhancing the accessibility of active sites. This structural advantage results in enhanced catalytic performance and greater conversion rates in biofuel production processes (Khalit et al., 2021). Despite that, carbon-supported catalysts face significant challenges, especially in terms of stability and durability, resulting in decreased catalytic activity (Zaman et al., 2022).

Future research on HDO catalyst development needs to focus on the utilization of hybrid supports that integrate the advantageous properties of the supports. For example, the integration of alumina and mesoporous silica in composite materials can take advantage of the heat resistance of metal oxides and the large surface area of mesoporous materials, leading to enhanced catalyst performance (Kankala et al., 2019) Furthermore, integrating mesoporous materials with metal oxides using methods such as atomic layer deposition

might result in synergistic effects that improve catalytic capabilities and resistance to deactivation (Kankala et al., 2019). Nanotechnology advancements also provide the opportunity to develop catalyst structures precisely, optimizing the distribution of active sites and enhancing mass transfer characteristics, resulting in more efficient and durable catalysts. Integrating these materials in unique ways makes it possible to produce highly efficient, stable, and cost-effective HDO catalysts for biofuel production.

Table 3 summarizes recent studies on the effect of catalyst supports on the oxygen removal process from vegetable oils and fatty acids. In one study, rapeseed oil was treated using various supports—Silica oxide (SiO₂), Titanium dioxide (TiO₂), and Alumina (Al₂O₃)—saturated with 3.3 wt.% Ni and 15 wt.% molybdenum (Mo) at 260–300°C and 3.5 MPa in a fixed-bed reactor (Kubička et al., 2014). The researchers found that the physical properties of the supports, such as size, dispersion, and reducibility of the active

Table 3
Recent studies on the effects of catalyst-support on the deoxygenation of fatty acids and vegetable oils

References	Reactor type	Fatty acid/vegetable oil	Catalyst	Reaction conditions	Findings
Khalit et al. (2021)	Semi-batch	Waste cooking oil	Ni/AC Ni/rGO Ni/Zeo	T = 350°C RT = 3 h	Ni/AC showed the best performance with 90% of hydrocarbon yield and 89% of n-(C15 + C17)
de Oliveira Camargo et al. (2020)	Batch	Oleic acid	Ni ₂ P/USY Ni ₂ P/H-ZSM-5 Ni ₂ P/Al-SBA-15	T = 300°C P = 5 MPa RT = 6 h	Ni ₂ P/Al-SBA-15 achieved the best performance with 42% of hydrocarbon (C10-C18)
Wang et al. (2020)	Reactor	Spirulina	NiO/SAPO-34 NiO/ZSM-5 NiO/USY NiO/γ-Al ₂ O ₃ NiO/SiO ₂	T = 270°C RT = 30 min	NiO/USY contributed to the best performance with 20.6% of hydrocarbon
Lee et al. (2020)	Semi-batch	Methyl palmitate	Ni/SiO ₂ Ni-Al/SBA-15 Ni-Al/SBA-16 Ni-Al/KIT-6	T = 280°C P = 2 MPa RT = 2 h	Ni/Al-SBA-15 showed the highest selectivity of 77.7% of hydrocarbon
Liu et al. (2019)	Batch	Palmitic acid	Co/SiO ₂ Co/γ-Al ₂ O ₃ Co/H-ZSM-22	T = 260°C P = 2 MPa H ₂ RT = 4 h	Co/HZP-22 gave the highest yield with 43.1% of n-C16
Raut et al. (2016)	Batch	Oleic acid, stearic acid, JCS oil	Pd/SBA-12 Pd/SBA-16	T = 300°C–325°C P = 0.5 MPa–3 MPa RT = 5 h	Pd/SBA-16 showed high catalytic performance

*T=Temperature, P=Pressure, RT= Reaction Time, Ni=Nickel, AC=Activated carbon, rGO= reduced graphene oxide, Zeo=zeolite, P, USY= ultrastable Y zeolite, SBA= Santa Barbara Amorphous, SAPO= Silicoaluminophosphate zeolite, ZSM-5= Zeolite Socony Mobil-5, SiO₂=silica oxide, KIT= Korea Advanced Institute of Science and Technology, JCS=*Jatropha curcas* seeds

sites, significantly impacted product selectivity. Similar findings were reported by Chen et al. (2015), showing that product selectivity depends on the texture of the support, the interaction between active sites and support, and the strength of metal-support bonding.

Metal Oxides

Metal oxides are affordable and commonly used as catalysts and support materials for deoxygenating triglycerides and fatty acids (Tani et al., 2011). Their surface contains oxygen vacancies, which help activate fatty acids and aid in removing the carboxyl group, enhancing the catalytic reduction of oxygenated compounds. Studies have highlighted the potential of solid base materials as supports for oleic acid deoxygenation (Li et al., 2015). A series of Ni/MO- Al_2O_3 catalysts (with M representing metals like Mg, Ca, Ni, Cu, and Zn) were tested, and Ni/ZnO- Al_2O_3 was found to be the most effective for converting mono-unsaturated fatty acids into n-alkanes, due to its moderate base strength (Li et al., 2015). The optimal Zn/Al ratio improved Ni particle distribution, maximizing alkane production at 95.8% by preventing particle clumping (Chen et al., 2017).

CeO_2 -based materials, known for their excellent oxygen storage capacity, were further enhanced by adding ZrO_2 , improving thermal stability and reducibility (Deng et al., 2019). A $\text{Ce}_{0.6}\text{Zr}_{0.4}\text{O}_2$ support achieved a 73.8% conversion rate and high decarbonylation selectivity in oleic acid deoxygenation (Shim et al., 2014). Basic supports perform poorly below 350°C (Arun et al., 2015), but Pt-WOx/ Al_2O_3 showed complete conversion of oleic acid, with C18 selectivity increasing from 67.1% to 80.8% through hydrodeoxygenation and C17 formation via decarboxylation (Janampelli & Darbha, 2018).

Mesoporous Materials

Mesoporous materials have attracted significant attention for their large pore size, high specific surface area (600–1000 m^2/g), and moderate acidity, which make them well-suited for use as high-performance deoxygenation catalysts. These materials exhibit a uniform pore size distribution (1.5–10 nm), which provides a greater number of active sites throughout the porous network. The wide range of pore sizes also facilitates access to these sites by larger organic molecules, making them more efficient for certain reactions (da Silva et al., 2019). SBA supports, particularly SBA-16, are favored for their stability and ability to accommodate large molecules due to their thicker walls and interconnected mesoporous structures, in contrast to the less stable MCM-41 (Arun et al., 2015). However, these materials often face challenges with structural instability under harsh hydrothermal conditions, leading to a steady reduction in surface area and the collapse of internal pore structures due to high temperatures and pressures, particularly when water is present.

SAPO molecular sieves, including SAPO-11, SAPO-31, and SAPO-41, are commonly used as selective catalysts for both isomerization and deoxygenation processes due to

their unique hierarchical mesoporous structures. SAPO materials are noted for their high isomerization-to-cracking ratios, thanks to their weak protonic acidity located at the boundary between silica and the SAPO phase (Rabaev et al., 2015). SAPO-11 features 10-membered elliptical rings, while SAPO-31 has circular channels, both of which contribute to their efficiency in producing multibranched alkanes. SAPO-41, with slightly larger elliptical pores, also shows promise in these reactions (Zhang et al., 2017). However, SAPO-11 has been found to have limited hydrothermal stability, degrading when exposed to high temperatures and pressures above 200°C and 1.7 MPa, making it unsuitable for extended hydrodeoxygenation reactions (Herskowitz et al., 2013).

The impact of acidic support on reactions such as cracking, isomerization, and cyclization has been extensively studied. Supports like Pt/SAPO-11 and platinum-chlorinated alumina enhance catalytic performance by increasing the number of active sites and surface area, but they are prone to issues like carbon deposition, which can reduce catalytic efficiency over time. Studies have shown that under acidic conditions, paraffin intermediates formed during decarboxylation can undergo cyclization and isomerization, producing cyclic, branched, and alkyl aromatic hydrocarbons (Ahmadi et al., 2014). Despite the benefits, SAPO materials face challenges with stability, particularly under hydrothermal conditions, limiting their use in prolonged catalytic processes (Lutz et al., 2010).

Further research into mesoporous materials as catalyst supports has explored their performance in the removal of oxygen from compounds like guaiacol, with experiments using Ni-Re/SiO₂, Ni-Re/TiO₂, and Ni-Re/ZrO₂ under varying conditions. Ni-Re/SiO₂ showed greater selectivity for cyclohexane, although its performance in deoxygenation was lower than that of other supports (Herskowitz et al., 2013). Similar studies using palm oil and catalysts such as Ni/Al₂O₃, Ni/ZrO₂, and Ni/SiO₂ found that SiO₂-supported catalysts were less selective towards C15-C18 products. These findings suggest that while mesoporous materials offer large surface areas and moderate acidity, their catalytic efficiency in deoxygenation processes can be limited compared to metal oxide supports, which offer higher acidity and better stability under reaction conditions (Herskowitz et al., 2013).

Carbon Material

Recent advancements in deoxygenation catalysts have seen significant progress using carbon materials. Various metal catalysts supported on carbon, TiO₂, SiO₂, ZrO₂, and Al₂O₃ have been developed to aid fatty acid deoxygenation. Noble metal catalysts, such as Pd, exhibit excellent performance due to their unique electron structures. For instance, Pd/C achieved a 96% yield of n-alkanes from stearic acid in just 30 minutes (Ford et al., 2012). The support material significantly influences performance, with Pd/C showing a much higher decarboxylation rate than Pd/SiO₂ or Pd/Al₂O₃, likely due to carbon's strong adsorption capacity for fatty acids (Giordano et al., 2016). Noble metals like Pt, Ru, and

Rh on carbon supports also performed well, with Pd and Pt favoring decarboxylation and decarbonylation, while Ru was more effective in hydrodeoxygenation (Giordano et al., 2016).

Nickel-loaded carbon catalysts have also proven effective in biofuel production. For example, 15% Ni-loaded activated carbon yielded 72% hydrocarbons from palm kernel cake pyrolysis (Chen et al., 2023), and Ni/bio-AC achieved high conversion rates in fatty acid pyrolysis to biodiesel (Chen et al., 2023). Ni-Cu/C catalysts also demonstrated impressive results, producing 91% 2-methylfuran from furfural and 80% 2,5-dimethylfuran from 5-hydroxymethylfurfural under similar conditions (Fu et al., 2017).

Effect of Catalyst Loading on Triglyceride Deoxygenation

Catalyst loading plays a crucial role in chemical reactions by enhancing reaction rates, catalytic performance, activity, and stability (Gousi et al., 2020). A moderate excess of catalyst is typically recommended to account for possible poisoning from contaminants and carbon deposition (Kwon et al., 2011). However, excessive catalyst loading can increase cracking, leading to the formation of undesirable short hydrocarbons (Jeon et al., 2022).

Experiments using catalyst loadings of 1% to 9% showed that loadings between 1% and 5% improved deoxygenation efficiency due to a larger active surface area (Kwon et al., 2011). A 5% catalyst loading resulted in the highest % green diesel yield of 80% (Asikin-Mijan et al., 2020). However, loadings beyond 5% reduced the yield due to potential polymerization reactions (Kwon et al., 2011).

Further studies confirmed that 5% catalyst loading was optimal for deoxygenation of JCO into diesel-grade biofuel, with yields between 78% and 95% (Asikin-Mijan et al., 2020). Higher loadings, however, did not improve performance and led to side reactions such as CC-cleavage and the production of short hydrocarbons (Asikin-Mijan et al., 2020). Overall, 3% to 5% catalyst loading is optimal for deoxygenating triglycerides and fatty acids, providing high deoxygenation activity without excessive byproduct formation. Catalyst loadings beyond 5% tend to cause undesirable polymerization (Asikin-Mijan et al., 2020).

CONCLUSION

This paper highlights the strong potential of Ni-supported catalysts for producing high-quality biofuel through deoxygenation, thanks to their excellent catalytic properties and cost-effectiveness. However, issues such as fouling, sintering, and poisoning, as shown in Figure 8, can lead to catalyst deactivation. Therefore, developing new, durable, and affordable bifunctional catalysts with superior deoxygenation performance is essential. In summary, deoxygenation technology offers a practical solution for global biofuel production, supporting sustainable development goals 7 and 13, which focus on clean energy access and addressing climate change.

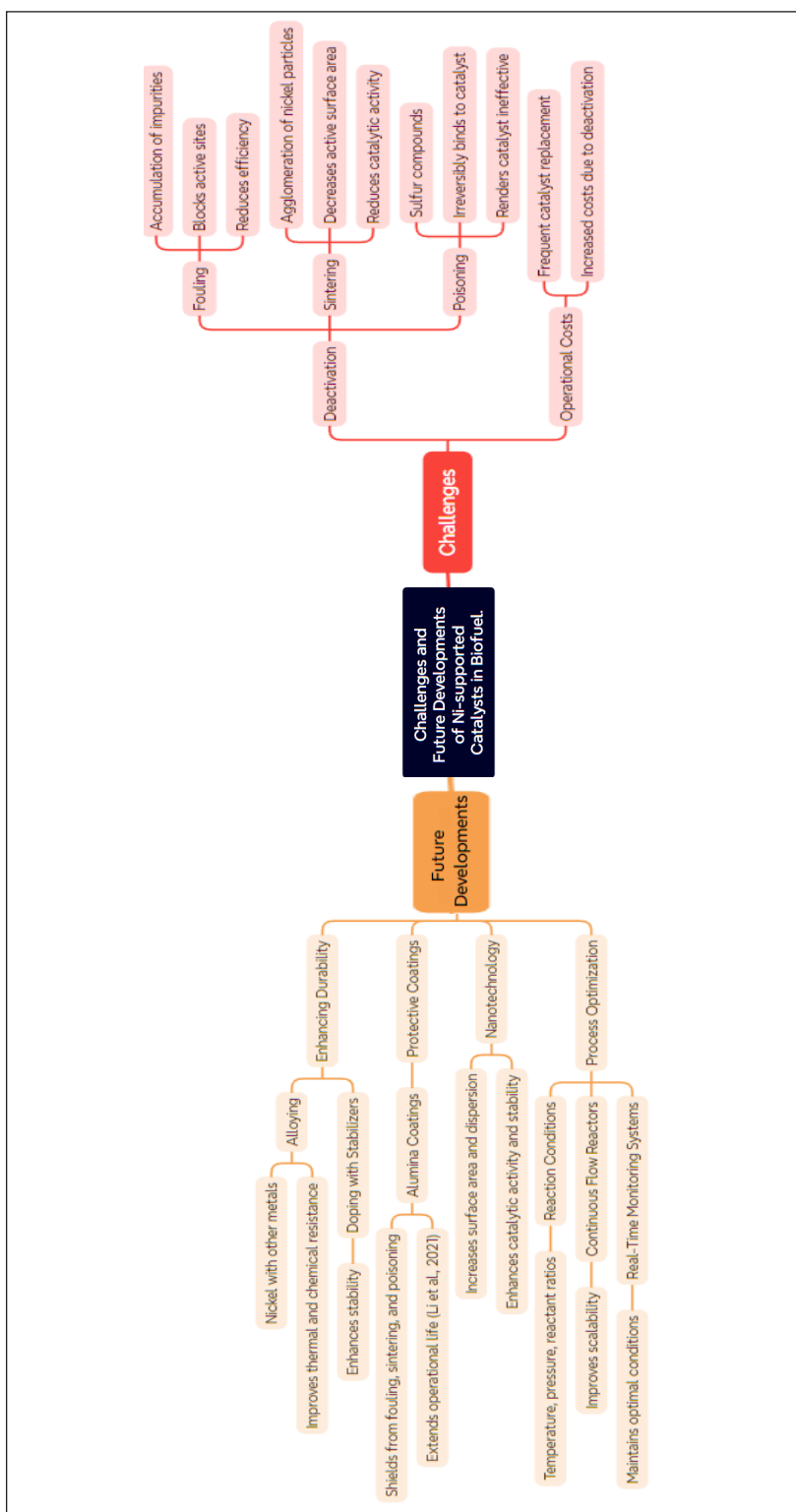


Figure 8. Challenges and future developments of Ni-supported catalysts in biofuel

ACKNOWLEDGEMENT

The authors acknowledged the support of the Fundamental Research Grant Scheme (FRGS) under the grant number FRGS/1/12019/STG05/UNIMAP/02/4 from the Ministry of Higher Education Malaysia.

REFERENCES

- Ahamed, T. S., Anto, S., Mathimani, T., Brindhadevi, K., & Pugazhendhi, A. (2021). Upgrading of bio-oil from thermochemical conversion of various biomass – Mechanism, challenges and opportunities. *Fuel*, 287, Article 119329. <https://doi.org/https://doi.org/10.1016/j.fuel.2020.119329>
- Ahmadi, M., Macias, E. E., Jasinski, J. B., Ratnasamy, P., & Carreon, M. A. (2014). Decarboxylation and further transformation of oleic acid over bifunctional, Pt/SAPO-11 catalyst and Pt/chloride Al_2O_3 catalysts. *Journal of Molecular Catalysis A: Chemical*, 386, 14-19. <https://doi.org/10.1016/j.molcata.2014.02.004>
- Alkhoori, S., Khaleel, M., Vega, L., & Polychronopoulou, K. (2023). Deoxygenation of vegetable oils and fatty acids: How can we steer the reaction selectivity towards diesel range hydrocarbons? *Journal of Industrial and Engineering Chemistry*, 127, 36-61. <https://doi.org/10.1016/j.jiec.2023.07.031>
- Ambursa, M. M., Juan, J. C., Yahaya, Y., Taufiq-Yap, Y. H., Lin, Y. C., & Lee, H. V. (2021). A review on catalytic hydrodeoxygenation of lignin to transportation fuels by using nickel-based catalysts. *Renewable and Sustainable Energy Reviews*, 138, Article 110667. <https://doi.org/https://doi.org/10.1016/j.rser.2020.110667>
- Ameen, M., Azizan, M. T., Ramli, A., Yusup, S., & Abdullah, B. (2020). The effect of metal loading over Ni/ γ - Al_2O_3 and Mo/ γ - Al_2O_3 catalysts on reaction routes of hydrodeoxygenation of rubber seed oil for green diesel production. *Catalysis Today*, 355, 51–64. <https://doi.org/10.1016/j.cattod.2019.03.028>
- Arun, N., Sharma, R. V., & Dalai, A. K. (2015). Green diesel synthesis by hydrodeoxygenation of bio-based feedstocks: Strategies for catalyst design and development. *Renewable and Sustainable Energy Reviews*, 48, 240-255. <https://doi.org/10.1016/j.rser.2015.03.074>
- Asikin-Mijan, N., Lee, H. V., Taufiq-Yap, Y. H., Juan, J. C., & Rahman, N. A. (2016). Pyrolytic–deoxygenation of triglyceride via natural waste shell derived $Ca(OH)_2$ nanocatalyst. *Journal of Analytical and Applied Pyrolysis*, 117, 46-55. <https://doi.org/10.1016/j.jaap.2015.12.017>
- Asikin-Mijan, N., Ooi, J. M., AbdulKareem-Alsultan, G., Lee, H. V., Mastuli, M. S., Mansir, N., Alharthi, F. A., Alghamdi, A. A., & Taufiq-Yap, Y. H. (2020). Free- H_2 deoxygenation of *Jatropha curcas* oil into cleaner diesel-grade biofuel over coconut residue-derived activated carbon catalyst. *Journal of Cleaner Production*, 249, Article 119381. <https://doi.org/10.1016/j.jclepro.2019.119381>
- Attia, M., Farag, S., & Chaouki, J. (2020). Upgrading of oils from biomass and waste: Catalytic hydrodeoxygenation. *Catalysts*, 10(12), Article 1381. <https://doi.org/10.3390/catal10121381>
- Azman, N. S., Marliza, T. S., Mijan, N. A., Hin, T. Y. Y., & Khairuddin, N. (2021). Production of biodiesel from waste cooking oil via deoxygenation using Ni-Mo/Ac catalyst. *Processes*, 9(5), Article 750. <https://doi.org/10.3390/pr9050750>

- Baharudin, K. B., Taufiq-Yap, Y. H., Hunns, J., Isaacs, M., Wilson, K., & Derawi, D. (2019). Mesoporous NiO/Al-SBA-15 catalysts for solvent-free deoxygenation of palm fatty acid distillate. *Microporous and Mesoporous Materials*, 276, 13-22. <https://doi.org/10.1016/j.micromeso.2018.09.014>
- Bernas, H., Eränen, K., Simakova, I., Leino, A.-R., Kordás, K., Myllyoja, J., Mäki-Arvela, P., Salmi, T., & Murzin, D. Y. (2010). Deoxygenation of dodecanoic acid under inert atmosphere. *Fuel*, 89(8), 2033-2039. <https://doi.org/10.1016/j.fuel.2009.11.006>
- Britovsek, G. (2012). *Homogeneous Catalysts. Activity—Stability—Deactivation*. By Piet W. N. M. van Leeuwen and John C. Chadwick. *Angewandte Chemie*, 51(7), 1518. <https://doi.org/10.1002/anie.201108293>
- de Oliveira Camargo, M., Pimenta, J. L. C. W., de Oliveira Camargo, M., & Arroyo, P. A. (2020). Green diesel production by solvent-free deoxygenation of oleic acid over nickel phosphide bifunctional catalysts: Effect of the support. *Fuel*, 281, Article 118719. <https://doi.org/10.1016/j.fuel.2020.118719>
- Cheah, K. W., Yusup, S., Loy, A. C. M., How, B. S., Skoulou, V., & Taylor, M. J. (2022). Recent advances in the catalytic deoxygenation of plant oils and prototypical fatty acid models compounds: Catalysis, process, and kinetics. *Molecular Catalysis*, 523, Article 111469. <https://doi.org/10.1016/j.mcat.2021.111469>
- Chen, B., Zhou, Z., Li, Y., Tan, K. B., Wang, Y., Rao, X., Huang, J., Zhang, X., Li, Q., & Zhan, G. (2023). Catalytic pyrolysis of fatty acids and oils into liquid biofuels and chemicals over supported Ni catalysts on biomass-derived carbon. *Applied Catalysis B: Environmental*, 338, Article 123067. <https://doi.org/10.1016/j.apcatb.2023.123067>
- Chen, H., Wang, Q., Zhang, X., & Wang, L. (2015). Effect of support on the NiMo phase and its catalytic hydrodeoxygenation of triglycerides. *Fuel*, 159, 430-435. <https://doi.org/10.1016/j.fuel.2015.07.010>
- Chen, L., Zhang, F., Li, G., & Li, X. (2017). Effect of Zn/Al ratio of Ni/ZnO-Al₂O₃ catalysts on the catalytic deoxygenation of oleic acid into alkane. *Applied Catalysis A: General*, 529, 175-184. <https://doi.org/10.1016/j.apcata.2016.11.012>
- Chen, W. T., Jin, K., & Wang, N. H. L. (2019). Use of supercritical water for the liquefaction of polypropylene into oil. *ACS Sustainable Chemistry & Engineering*, 7(4), 3749-3758. <https://doi.org/10.1021/acssuschemeng.8b03841>
- Corma, A. (2003). State of the art and future challenges of zeolites as catalysts. *Journal of Catalysis*, 216(1), 298-312. [https://doi.org/10.1016/S0021-9517\(02\)00132-X](https://doi.org/10.1016/S0021-9517(02)00132-X)
- Darda, S., Papalás, T., & Zabaniotou, A. (2019). Biofuels journey in Europe: Currently the way to low carbon economy sustainability is still a challenge. *Journal of Cleaner Production*, 208, 575-588. <https://doi.org/10.1016/j.jclepro.2018.10.147>
- Deng, J., Yuan, S., Xiong, L., Li, S., Wang, J., & Chen, Y. (2019). Synthesis and characterization of nanostructured CeO₂-ZrO₂ material with improved low-temperature reducibility. *Materials Characterization*, 155, Article 109808. <https://doi.org/10.1016/j.matchar.2019.109808>
- Di, L., Yao, S., Song, S., Wu, G., Dai, W., Guan, N., & Li, L. (2017). Robust ruthenium catalysts for the selective conversion of stearic acid to diesel-range alkanes. *Applied Catalysis B: Environmental*, 201, 137-149. <https://doi.org/10.1016/j.apcatb.2016.08.023>

- Ford, J. P., Immer, J. G., & Lamb, H. H. (2012). Palladium catalysts for fatty acid deoxygenation: Influence of the support and fatty acid chain length on decarboxylation kinetics. *Topics in Catalysis*, 55(3), 175-184. <https://doi.org/10.1007/s11244-012-9786-2>
- Fu, J., Lu, X., & Savage, P. E. (2011). Hydrothermal decarboxylation and hydrogenation of fatty acids over Pt/C. *ChemSusChem*, 4(4), 481-486. <https://doi.org/10.1002/cssc.201000370>
- Fu, Z., Wang, Z., Lin, W., & Song, W. (2017). Conversion of furan derivatives for preparation of biofuels over Ni-Cu/C catalyst. *Energy Sources, Part A: Recovery, Utilization, and Environmental Effects*, 39(11), 1176-1181. <https://doi.org/10.1080/15567036.2017.1310959>
- Giordano, N., Eaton, T., Bo, Z., Yacob, S., Yang, C. C., & Notestein, J. (2016). Silica support modifications to enhance Pd-catalyzed deoxygenation of stearic acid. *Applied Catalysis B: Environmental*, 192, 93-100. <https://doi.org/10.1016/j.apcatb.2016.03.041>
- Gousi, M., Kordouli, E., Bourikas, K., Symianakis, E., Ladas, S., Kordulis, C., & Lycourghiotis, A. (2020). Green diesel production over nickel-alumina nanostructured catalysts promoted by copper. *Energies*, 13(14), Article 3707. <https://doi.org/10.3390/en13143707>
- Hafriz, R. S. R. M., Shafizah, I. N., Salmiaton, A., Arifin, N. A., Yunus, R., Taufiq-Yap, Y. H., & Halim, S. A. (2020). Comparative study of transition metal-doped calcined Malaysian dolomite catalysts for WCO deoxygenation reaction. *Arabian Journal of Chemistry*, 13(11), 8146-8159. <https://doi.org/10.1016/j.arabjc.2020.09.046>
- Hermida, L., Abdullah, A. Z., & Mohamed, A. R. (2015). Deoxygenation of fatty acid to produce diesel-like hydrocarbons: A review of process conditions, reaction kinetics and mechanism. *Renewable and Sustainable Energy Reviews*, 42, 1223-1233. <https://doi.org/10.1016/j.rser.2014.10.099>
- Herskowitz, M., Landau, M. V., Reizner, Y., & Berger, D. (2013). A commercially-viable, one-step process for production of green diesel from soybean oil on Pt/SAPO-11. *Fuel*, 111, 157-164. <https://doi.org/10.1016/j.fuel.2013.04.044>
- Janampelli, S., & Darbha, S. (2018). Selective and reusable Pt-WO_x/Al₂O₃ catalyst for deoxygenation of fatty acids and their esters to diesel-range hydrocarbons. *Catalysis Today*, 309, 219-226. <https://doi.org/10.1016/j.cattod.2017.06.030>
- Japar, N. S. A., Aziz, M. A. A., & Rahman, N. W. A. (2020). Conversion of waste transformer oil into grease. In A. Z. Yaser (Ed.), *Advances in Waste Processing Technology* (pp. 23-35). Springer. https://doi.org/10.1007/978-981-15-4821-5_2
- Jeng, S., Lim, A., Yunus, J. J., Tan, W. T., Jusoh, M., & Zakaria, Y. (2021). Starch-derived solid acid catalyst for biodiesel production: A mini review. *Chemical Engineering Transactions*, 89, 487-492. <https://doi.org/10.3303/CET2189082>
- Jeon, K. W., Park, H. R., Lee, Y. L., Kim, J. E., Jang, W. J., Shim, J. O., & Roh, H. S. (2022). Deoxygenation of non-edible fatty acid for green diesel production: Effect of metal loading amount over Ni/MgO-Al₂O₃ on the catalytic performance and reaction pathway. *Fuel*, 311, Article 122488. <https://doi.org/10.1016/j.fuel.2021.122488>
- Jin, W., Pérez, L., Shen, D., Sepúlveda-Escribano, A., Gu, S., & Reina, T. R. (2019). Catalytic upgrading of biomass model compounds: Novel approaches and lessons learnt from traditional hydrodeoxygenation - A Review. *ChemCatChem*, 11(3), 894-1142. <https://doi.org/10.1002/cctc.201801722>

- Kankala, R. K., Zhang, H., Liu, C. G., Kanubaddi, K. R., Lee, C. H., Wang, S. B., Cui, W., Santos, H. A., Lin, K. L., & Chen, A. Z. (2019). Metal species–encapsulated mesoporous silica nanoparticles: Current advancements and latest breakthroughs. *Advanced Functional Materials*, 29(43), Article 1902652. <https://doi.org/10.1002/adfm.201902652>
- Khalit, W. N. A. W., Asikin-Mijan, N., Marliza, T. S., Gamal, M. S., Shamsuddin, M. R., Saiman, M. I., & Taufiq-Yap, Y. H. (2021). Catalytic deoxygenation of waste cooking oil utilizing nickel oxide catalysts over various supports to produce renewable diesel fuel. *Biomass Bioenergy*, 154(106248), 106248. <https://doi.org/10.1016/j.biombioe.2021.106248>
- Kubička, D., Horáček, J., Setnička, M., Bulánek, R., Zukal, A., & Kubičková, I. (2014). Effect of support-active phase interactions on the catalyst activity and selectivity in deoxygenation of triglycerides. *Applied Catalysis B: Environmental*, 145, 101-107. <https://doi.org/10.1016/j.apcatb.2013.01.012>
- Kwon, K. C., Mayfield, H., Marolla, T., Nichols, B., & Mashburn, M. (2011). Catalytic deoxygenation of liquid biomass for hydrocarbon fuels. *Renewable Energy*, 36(3), 907-915. <https://doi.org/10.1016/j.renene.2010.09.004>
- Lee, S. U., Kim, E. S., Kim, T. W., Kim, J. R., Jeong, K. E., Lee, S., & Kim, C. U. (2020). Effect of silica supports on deoxygenation of methyl palmitate over mesoporous silica-supported Ni/Al catalysts. *Journal of Industrial and Engineering Chemistry*, 83, 366–374. <https://doi.org/10.1016/j.jiec.2019.12.010>
- Li, G., Zhang, F., Chen, L., Zhang, C., Huang, H., & Li, X. (2015). Highly selective hydrodecarbonylation of oleic acid into heptadecane over a supported nickel/zinc oxide-alumina catalyst. *ChemCatChem*, 7(17), 2646-2653. <https://doi.org/10.1002/cctc.201500418>
- Li, X., Luo, X., Jin, Y., Li, J., Zhang, H., Zhang, A., & Xie, J. (2018). Heterogeneous sulfur-free hydrodeoxygenation catalysts for selectively upgrading the renewable bio-oils to second generation biofuels. *Renewable and Sustainable Energy Reviews*, 82, 3762-3797. <https://doi.org/https://doi.org/10.1016/j.rser.2017.10.091>
- Liu, M., Shi, Y., Wu, K., Liang, J., Wu, Y., Huang, S., & Yang, M. (2019). Upgrading of palmitic acid and hexadecanamide over Co-based catalysts: Effect of support (SiO₂, γ -Al₂O₃ and H-ZSM-22). *Catalysis Communications*, 129, Article 105726. <https://doi.org/10.1016/j.catcom.2019.105726>
- Liu, Q., Bie, Y., Qiu, S., Zhang, Q., Sainio, J., Wang, T., Ma, L., & Lehtonen, J. (2014). Hydrogenolysis of methyl heptanoate over Co based catalysts: Mediation of support property on activity and product distribution. *Applied Catalysis B: Environmental*, 147, 236-245. <https://doi.org/10.1016/j.apcatb.2013.08.045>
- Liu, Q., Zuo, H., Zhang, Q., Wang, T., & Ma, L. (2014). Hydrodeoxygenation of palm oil to hydrocarbon fuels over Ni/SAPO-11 catalysts. *Chinese Journal of Catalysis*, 35(5), 748-756. [https://doi.org/10.1016/s1872-2067\(12\)60710-4](https://doi.org/10.1016/s1872-2067(12)60710-4)
- Lutz, W., Kurzhals, R., Sauerbeck, S., Toufar, H., Buhl, J. C., Gesing, T., Altenburg, W., & Jäger, C. (2010). Hydrothermal stability of zeolite SAPO-11. *Microporous and Mesoporous Materials*, 132(1-2), 31-36. <https://doi.org/10.1016/j.micromeso.2009.08.003>
- Majewski, A. J., Singh, S. K., Labhasetwar, N. K., & Steinberger-Wilckens, R. (2021). Nickel–molybdenum catalysts for combined solid oxide fuel cell internal steam and dry reforming. *Chemical Engineering Science*, 232, Article 116341. <https://doi.org/10.1016/j.ces.2020.116341>

- Maneechakr, P., & Karnjanakom, S. (2021). Improving the bio-oil quality via effective pyrolysis/deoxygenation of palm kernel cake over a metal (Cu, Ni, or Fe)-doped carbon catalyst. *ACS Omega*, 6(30), 20006–20014. <https://doi.org/10.1021/acsomega.1c02999>
- Morgan, T., Santillan-Jimenez, E., Harman-Ware, A. E., Ji, Y., Grubb, D., & Crocker, M. (2012). Catalytic deoxygenation of triglycerides to hydrocarbons over supported nickel catalysts. *Chemical Engineering Journal*, 189-190, 346-355. <https://doi.org/10.1016/j.cej.2012.02.027>
- Mortensen, P. M., Grunwaldt, J. D., Jensen, P. A., Knudsen, K. G., & Jensen, A. D. (2011). A review of catalytic upgrading of bio-oil to engine fuels. *Applied Catalysis A: General*, 407(1-2), 1-19. <https://doi.org/10.1016/j.apcata.2011.08.046>
- Navalikhina, M. D., & V. Krylov, O. (1998). Heterogeneous catalysts of hydrogenation. *Russian Chemical Reviews*, 67(7), 587-616. <https://doi.org/10.1070/RC1998v067n07ABEH000413>
- Ooi, X. Y., Gao, W., Ong, H. C., Lee, H. V., Juan, J. C., Chen, W. H., & Lee, K. T. (2019). Overview on catalytic deoxygenation for biofuel synthesis using metal oxide supported catalysts. *Renewable and Sustainable Energy Reviews*, 112, 834-852. <https://doi.org/10.1016/j.rser.2019.06.031>
- Osman, A. I., Lai, Z. Y., Farghali, M., Yiin, C. L., Elgarahy, A. M., Hammad, A., Ihara, I., Al-Fatesh, A. S., Rooney, D. W., & Yap, P. S. (2023). Optimizing biomass pathways to bioenergy and biochar application in electricity generation, biodiesel production, and biohydrogen production. *Environmental Chemistry Letters*, 21(5), 2639-2705. <https://doi.org/10.1007/s10311-023-01613-2>
- Ouedraogo, A. S., & Bhoi, P. R. (2020). Recent progress of metals supported catalysts for hydrodeoxygenation of biomass derived pyrolysis oil. *Journal of Cleaner Production*, 253, Article 119957. <https://doi.org/10.1016/j.jclepro.2020.119957>
- Oyedun, A., Patel, M., Kumar, M., & Kumar, A. (2019). The upgrading of bio-oil via hydrodeoxygenation. In M. Crocker & E. Santillan-Jimenez (Eds.), *Chemical Catalysts for Biomass Upgrading* (pp. 35-60). Wiley. <https://doi.org/10.1002/9783527814794.ch2>
- Park, Y. K., Ha, J. M., Oh, S., & Lee, J. (2021). Bio-oil upgrading through hydrogen transfer reactions in supercritical solvents. *Chemical Engineering Journal*, 404, Article 126527. <https://doi.org/10.1016/j.cej.2020.126527>
- Patil, P. D., Gude, V. G., Mannarswamy, A., Deng, S., Cooke, P., Munson-McGee, S., Rhodes, I., Lammers, P., & Nirmalakhandan, N. (2011). Optimization of direct conversion of wet algae to biodiesel under supercritical methanol conditions. *Bioresource Technology*, 102(1), 118-122. <https://doi.org/10.1016/j.biortech.2010.06.031>
- Popp, J., Harangi-Rákos, M., Gabnai, Z., Balogh, P., Antal, G., & Bai, A. (2016). Correction: Popp, J., et al. Biofuels and their co-products as livestock feed: Global economic and environmental implications. *Molecules* 2016, 21, 285. *Molecules*, 21(4), Article 546.
- Prasad, S., & Ingle, A. P. (2019). Chapter 12 - Impacts of sustainable biofuels production from biomass. In M. Rai & A. P. Ingle (Eds.), *Sustainable Bioenergy* (pp. 327-346). Elsevier. <https://doi.org/10.1016/B978-0-12-817654-2.00012-5>
- Rabaev, M., Landau, M. V., Vidruk-Nehemya, R., Goldbourt, A., & Herskowitz, M. (2015). Improvement of hydrothermal stability of Pt/SAPO-11 catalyst in hydrodeoxygenation–isomerization–aromatization of vegetable oil. *Journal of Catalysis*, 332, 164–176. <https://doi.org/10.1016/j.jcat.2015.10.005>

- Raut, R., Banakar, V.V., & Darbha, S. (2016). Catalytic decarboxylation of non-edible oils over three-dimensional, mesoporous silica-supported Pd. *Journal of Molecular Catalysis A: Chemical*, *417*, 126–134. <https://doi.org/10.1016/j.molcata.2016.03.023>
- Ren, X. Y., Feng, X. B., Cao, J. P., Tang, W., Wang, Z. H., Yang, Z., Zhao, J. P., Zhang, L. Y., Wang, Y. J., & Zhao, X. Y. (2020). Catalytic conversion of coal and biomass volatiles: A review. *Energy & Fuels*, *34*(9), 10307-10363. <https://doi.org/10.1021/acs.energyfuels.0c01432>
- Ren, Y., Ma, Z., & Bruce, P. G. (2012). Ordered mesoporous metal oxides: Synthesis and applications. *Chemical Society Reviews*, *41*(14), 4909-4927. <https://doi.org/10.1039/C2CS35086F>
- Rjeily, M. A., Gennequin, C., Pron, H., Abi-Aad, E., & Randrianalisoa, J. H. (2021). Pyrolysis-catalytic upgrading of bio-oil and pyrolysis-catalytic steam reforming of biogas: A review. *Environmental Chemistry Letters*, *19*(4), 2825-2872. <https://doi.org/10.1007/s10311-021-01190-2>
- Rogers, K. A., & Zheng, Y. (2016). Selective deoxygenation of biomass-derived bio-oils within hydrogen-modest environments: A review and new insights. *ChemSusChem*, *9*(14), 1750–1772. <https://doi.org/10.1002/cssc.201600144>
- Roldugina, E. A., Naranov, E. R., Maximov, A. L., & Karakhanov, E. A. (2018). Hydrodeoxygenation of guaiacol as a model compound of bio-oil in methanol over mesoporous noble metal catalysts. *Applied Catalysis A: General*, *553*, 24-35. <https://doi.org/10.1016/j.apcata.2018.01.008>
- Romero, M. J. A., Pizzi, A., Toscano, G., Busca, G., Bosio, B., & Arato, E. (2016). Deoxygenation of waste cooking oil and non-edible oil for the production of liquid hydrocarbon biofuels. *Waste Management*, *47*, 62-68. <https://doi.org/10.1016/j.wasman.2015.03.033>
- Ruddy, D. A., Schaidle, J. A., Ferrell Iii, J. R., Wang, J., Moens, L., & Hensley, J. E. (2014). Recent advances in heterogeneous catalysts for bio-oil upgrading via “*ex situ* catalytic fast pyrolysis”: Catalyst development through the study of model compounds. *Green Chemistry*, *16*(2), 454-490. <https://doi.org/10.1039/C3GC41354C>
- Sánchez-Cárdenas, M., Medina-Valtierra, J., Kamaraj, S.-K., Medina Ramírez, R., & Sánchez-Olmos, L. (2016). Effect of size and distribution of Ni nanoparticles on γ -Al₂O₃ in oleic acid hydrodeoxygenation to produce n-alkanes. *Catalysts*, *6*(10), Article 156. <https://doi.org/10.3390/catal6100156>
- Schwab, A. (2016). *Bioenergy Technologies Office Multi-Year Program Plan. March 2016*. U.S. Department of Energy. <https://www.osti.gov/biblio/1245338>
- Shafaghat, H., Kim, J. M., Lee, I. G., Jae, J., Jung, S. C., & Park, Y. K. (2019). Catalytic hydrodeoxygenation of crude bio-oil in supercritical methanol using supported nickel catalysts. *Renewable Energy*, *144*, 159-166. <https://doi.org/10.1016/j.renene.2018.06.096>
- Shi, F., Wang, H., Chen, Y., Lu, Y., Hou, D., Liu, C., Lu, Y., Lin, X., Yang, X., Zheng, Z., & Zheng, Y. (2023). Green diesel-like hydrocarbon production by H₂-free catalytic deoxygenation of oleic acid via Ni/MgO-Al₂O₃ catalysts: Effect of the metal loading amount. *Journal of Environmental Chemical Engineering*, *11*(5), Article 110520. <https://doi.org/10.1016/j.jece.2023.110520>
- Shim, J. O., Jeong, D. W., Jang, W. J., Jeon, K. W., Jeon, B. H., Cho, S. Y., Roh, H. S., Na, J. G., Ko, C. H., Oh, Y. K., & Han, S. S. (2014). Deoxygenation of oleic acid over Ce(1-x)Zr(x)O₂ catalysts in hydrogen environment. *Renew. Energy*, *65*, 36-40. <https://doi.org/10.1016/j.renene.2013.07.008>

- da Silva, F. D. C., Costa, M. D. S., Da Silva, L. K. R., Batista, A. M., & da Luz Jr, G. E. (2019). Functionalization methods of SBA-15 mesoporous molecular sieve: A brief overview. *SN Applied Sciences*, 1(6), Article 654. <https://doi.org/10.1007/s42452-019-0677-z>
- Sudarsanam, P., Zhong, R., Van den Bosch, S., Coman, S. M., Parvulescu, V. I., & Sels, B. F. (2018). Functionalised heterogeneous catalysts for sustainable biomass valorisation. *Chemical Society Reviews*, 47(22), 8349-8402. <https://doi.org/10.1039/C8CS00410B>
- Tani, H., Hasegawa, T., Shimouchi, M., Asami, K., & Fujimoto, K. (2011). Selective catalytic decarboxy-cracking of triglyceride to middle-distillate hydrocarbon. *Catalysis Today*, 164(1), 410-414. <https://doi.org/10.1016/j.cattod.2010.10.059>
- Tomic, M., Micic, R., Kiss, F., Dedovic, N., & Simikic, M. (2015). Economic and environmental performance of oil transesterification in supercritical methanol at different reaction conditions: Experimental study with a batch reactor. *Energy Conversion and Management*, 99, 8-19. <https://doi.org/10.1016/j.enconman.2015.04.010>
- Valle, B., Remiro, A., García-Gómez, N., Gayubo, A. G., & Bilbao, J. (2019). Recent research progress on bio-oil conversion into bio-fuels and raw chemicals: A review. *Journal of Chemical Technology & Biotechnology*, 94(3), 670–689. <https://doi.org/10.1002/jctb.5758>
- Wang, H., Rogers, K., Zhang, H., Li, G., Pu, J., Zheng, H., Lin, H., Zheng, Y., & Ng, S. (2019). The effects of catalyst support and temperature on the hydrotreating of waste cooking oil (WCO) over CoMo sulfided catalysts. *Catalysts*, 9(8), Article 689. <https://doi.org/10.3390/catal9080689>
- Wang, H., Tian, W., Zeng, F., Du, H., Zhang, J., & Li, X. (2020). Catalytic hydrothermal liquefaction of Spirulina over bifunctional catalyst to produce high-quality biofuel. *Fuel*, 282, Article 118807. <https://doi.org/10.1016/j.fuel.2020.118807>
- Wang, H., Zhou, H., Yan, Q., Wu, X., & Zhang, H. (2023). Superparamagnetic nanospheres with efficient bifunctional acidic sites enable sustainable production of biodiesel from budget non-edible oils. *Energy Conversion and Management*, 297, Article 117758. <https://doi.org/10.1016/j.enconman.2023.117758>
- Watanabe, M., Iida, T., & Inomata, H. (2006). Decomposition of a long chain saturated fatty acid with some additives in hot compressed water. *Energy Conversion and Management*, 47(18–19), 3344–3350. <https://doi.org/10.1016/j.enconman.2006.01.009>
- Yang, H., Zeng, Y., Zhou, Y., Du, X., Li, D., & Hu, C. (2022). One-step synthesis of highly active and stable Ni-ZrO₂ catalysts for the conversion of methyl laurate to alkanes. *Journal of Catalysis*, 413, 297-310. <https://doi.org/10.1016/j.jcat.2022.06.035>
- Yang, Y., Qiao, L., Hao, J., Shi, H., & Lv, G. (2019). Hydrodeoxygenation upgrading of bio-oil on Ni-based catalysts with low Ni loading. *Chemical Engineering Science*, 208, Article 115154. <https://doi.org/10.1016/j.ces.2019.08.012>
- Yang, Y., Xu, X., He, H., Huo, D., Li, X., Dai, L., & Si, C. (2023). The catalytic hydrodeoxygenation of bio-oil for upgradation from lignocellulosic biomass. *International Journal of Biological Macromolecules*, 242, Article 124773. <https://doi.org/10.1016/j.ijbiomac.2023.124773>

- Zaman, S., Wang, M., Liu, H., Sun, F., Yu, Y., Shui, J., Chen, M., & Wang, H. (2022). Carbon-based catalyst supports for oxygen reduction in proton-exchange membrane fuel cells. *Trends in Chemistry*, 4(10), 886-906. <https://doi.org/10.1016/j.trechm.2022.07.007>
- Zhang, J., Wu, H., Zhao, A., Bai, X., Kikhtyanin, O. V., Wu, W., Xiao, L., Su, X., & Zhang, R. (2017). Synthesis of MgAPO-31 nanocrystals via different heating methods and their catalytic performance in the hydroisomerization of n-decane. *Journal of Porous Materials*, 24(2), 437-442. <https://doi.org/10.1007/s10934-016-0278-9>
- Zhou, K., Du, X., Zhou, L., Yang, H., Lei, X., Zeng, Y., Li, D., & Hu, C. (2021). The deoxygenation of jatropha oil to high quality fuel via the synergistic catalytic effect of Ni, W₂C and WC species. *Catalysts*, 11(4), Article 469. <https://doi.org/10.3390/catal11040469>

Better Network Optimization Through Batch Normalization in Left Ventricle Chamber Classification

Dayang Suhaida Awang Damit¹, Siti Noraini Sulaiman^{1,2,3*}, Muhammad Khusairi Osman¹, Noor Khairiah A Karim^{4,5} and Samsul Setumin¹

¹Electrical Engineering Studies, College of Engineering, Universiti Teknologi MARA Cawangan Pulau Pinang, Permatang Pauh Campus, 13500 Pulau Pinang, Malaysia

²Integrative Pharmacogenomics Institute (iPROMISE), UiTM Puncak Alam Campus, Bandar Puncak Alam, 42300 Puncak Alam, Selangor, Malaysia

³Advanced Rehabilitation Engineering in Diagnostic and Monitoring Research Group (AREDiM), Electrical Engineering Studies, College of Engineering, Universiti Teknologi MARA Cawangan Pulau Pinang, Permatang Pauh Campus, 13500 Pulau Pinang, Malaysia

⁴Department of Biomedical Imaging, Advanced Medical & Dental Institute, Universiti Sains Malaysia, Bertam, 13200 Kepala Batas, Pulau Pinang, Malaysia

⁵Heart Failure Research Initiative, Advanced Medical & Dental Institute, Universiti Sains Malaysia, Bertam, 13200 Kepala Batas, Pulau Pinang, Malaysia

ABSTRACT

Convolutional neural networks (CNNs) have emerged as a prominent deep learning technique for medical image classification. This study investigated the impact of batch normalization layer placement on the performance of the CNNs model in classifying the left ventricle segment in Delayed-enhancement cardiac magnetic resonance (De-CMR) image slices. Three batch normalization arrangements, including one without a batch normalization layer, were examined to assess their impact. Additionally, the influence of three learning rates (0.0001, 0.001, 0.01)

from two different types of optimizers, namely Adam and Sgdm, was explored to identify the optimal configuration for our proposed CNN model. A model without batch normalization was used as a baseline for comparison. The results show that placing batch normalization after the convolutional layers, combined with the Adam optimizer and a learning rate of 0.0001, yielded the best performance, improving classification accuracy from 83.1% to 88.4%. These results highlight the significance of batch normalization layers with optimal configuration in enhancing

ARTICLE INFO

Article history:

Received: 07 June 2024

Accepted: 18 November 2024

Published: 07 March 2025

DOI: <https://doi.org/10.47836/pjst.33.2.15>

E-mail addresses:

dayang671@uitm.edu.my (Dayang Suhaida Awang Damit)

sitioraini@uitm.edu.my (Siti Noraini Sulaiman)

khusairi@uitm.edu.my (Muhammad Khusairi Osman)

drkhairiah@usm.my (Noor Khairiah A Karim)

samsuls@uitm.edu.my (Samsul Setumin)

* Corresponding author

the performance in the classification of the left ventricle and non-LV chambers in De-CMR images, thereby facilitating improvements in the streamlined workflow for automated myocardial infarction diagnosis.

Keywords: Batch normalization, classification, convolution neural network, delayed-enhancement cardiac magnetic resonance, learning rate

INTRODUCTION

Ischemic heart disease stands as the top cause of death globally (World Health Organization, 2021). It is caused by clogged cardiac arteries, predominantly affecting the left ventricular (LV) region, leading to heart tissue death. This condition leads to heart attacks, or is also known as myocardial infarction. The exponential growth in the number of MRI scans performed can be attributed to recent research addressing a variety of cardiovascular involvements, including infarcted muscle in patients with post-COVID-19 (Huang et al., 2020; Li et al., 2023; Toro et al., 2021). This surge in demand has placed an overwhelming workload on radiologists, making it challenging to efficiently analyze each image and provide timely and accurate diagnoses. Delayed-enhancement Cardiac Magnetic Resonance (De-CMR) is a well-known method for characterizing cardiac tissue, especially for assessing regional scar formation and myocardial fibrosis by enhancing abnormal cardiac tissue. De-CMR acquires a stack of short-axis CMR image slices that cover the entire cardiac region, including the outermost slices (Im et al., 2019), as presented in Figure 1. However, not every image contains clinically relevant segments, as only slices that include left ventricular structures are essential for the early diagnosis of myocardial infarction. The uppermost basal and lowermost apical images do not contain the LV chamber. These images are highlighted in the yellow box in Figure 1 and are classified as non-LV chamber regions, while the intermediate slices contain the LV chamber. The standard diagnostic process used by radiologists involves manually reviewing multiple short-axis slices to identify infarcted tissue, with a primary focus on the LV chamber, where infarctions are most likely to occur (Karim et al., 2016). This process is time-consuming because each patient generates a stack of 15-45 image slices, depending on the image thickness and size of the heart. Each slice must be carefully examined to assess the condition of the myocardium, which can be labor-intensive, especially in high-demand clinical environments. This manual process can be further complicated by factors such as image quality variability due to patient movement or noise artifacts, anatomical variations, and overlapping structures. For instance, the basal and apical regions of the LV chamber are often difficult to distinguish from surrounding tissues, adding to the diagnostic challenge.

With the advancement of computer vision and image processing techniques, many studies focus on the segmentation of LV chambers but rely on manual image selection as a starting point (Chen et al., 2020; Leong et al., 2019; Shaaf et al., 2022). Surprisingly, the

initial step of identifying relevant image slices has been overlooked. Figure 2 illustrates our proposed automated LV chamber classification as a key component of the overall workflow for fully automated myocardial infarction diagnosis. This step eliminates the need for manual selection, ensuring that only the necessary images proceed to the segmentation phase. By developing an automated classification method that identifies the LV chamber before segmentation, this research enables a fully automated and streamlined process for diagnosing myocardial infarction, addressing a key limitation in existing methods.

Image classification, a fundamental task in computer vision, has gained significant traction in the field of medical imaging (Zorkafli et al., 2019; Abdullah et al., 2020). In recent years, Convolutional Neural Networks (CNNs) have emerged as a powerful tool for analyzing medical images due to their ability to automatically learn discriminative

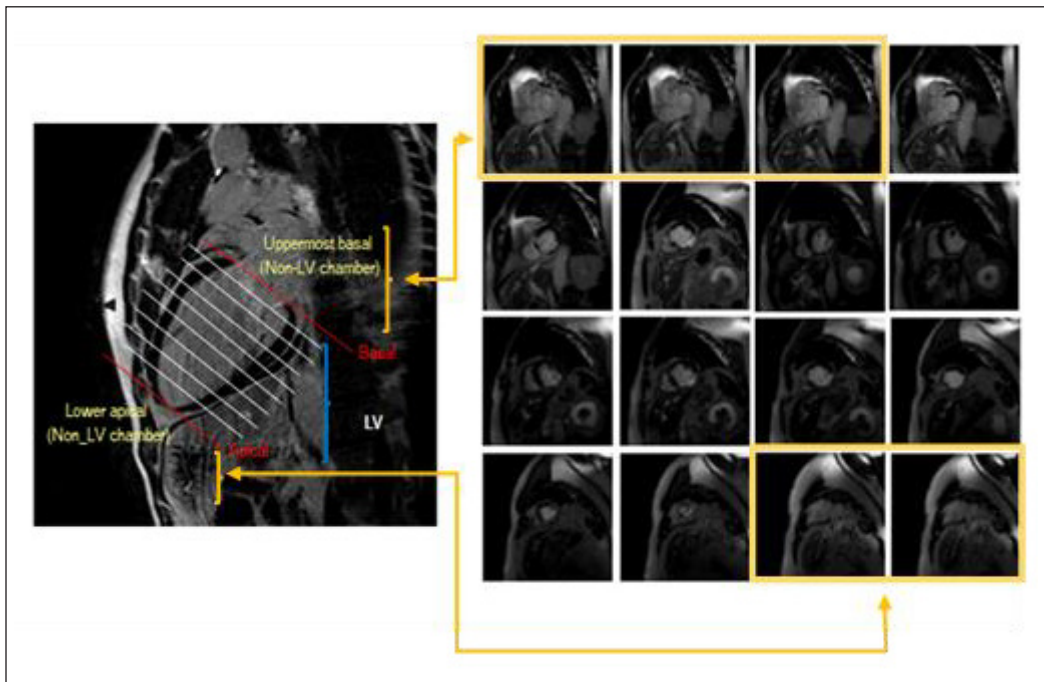


Figure 1. Example of De-CMR image sequences per patient. Uppermost basal and lower apical images comprise the non-LV chamber class

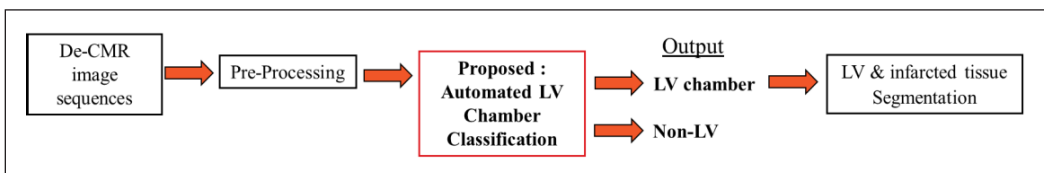


Figure 2. The Proposed automated LV chamber classification in overall workflow for fully automated myocardial infarction diagnosis

features from the input data (Abdullah et al., 2023; Khairandish et al., 2022; Harron et al., 2022). In the cardiac study, Zhang et al. (2016) examined unnecessary CMR images using two distinct 5-layer CNN models by identifying a missing apical or basal slice. In another study, Ho and Kim (2021) explored the effectiveness of transfer learning for CINE CMR images. They evaluated 18 pre-trained Deep CNN models and three models trained from scratch. Among these, the VGG16 model achieved the highest accuracy with 86% across all evaluation categories, suggesting its potential as a suitable choice for cardiac classification. However, no additional study into CNN hyperparameters was presented as a result of those two studies. In contrast to the previous two investigations, which utilized the CINE Cardiac MRI modality, our study employs the De-CMR modality. Although pre-trained models are known for their efficiency and rapid deployment, there is a unique aspect to developing a custom CNN from scratch. By learning from a myriad of different data, pre-trained models can become quite complicated and hard to understand. Conversely, the process of designing a CNN model from scratch offers a straightforward and clear, making it easier to grasp and adaptable to necessary modifications. Moreover, the performance of CNNs can be further enhanced by incorporating additional techniques and optimizations.

Batch normalization is one such technique that has garnered attention in recent years. The batch normalization layer helps reduce dependence on specific weight initializations and acts as a regularizer, preventing overfitting and promoting generalization to unseen data. However, the impact of the batch normalization layer on CNNs varies depending on their arrangement and configurations. Hasani and Khotanlou (2019) investigated the placement of batch normalization in the network using three well-known pre-trained networks on three image datasets (CIFAR10, Cifar100 and Tiny Imaget). Since the results vary for various networks, their study proposed that tests should be conducted on various networks and image datasets to determine the ideal configuration. There is ongoing debate in the field of machine learning regarding the optimal placement of an additional layer in a network to achieve the greatest acceleration in the training process (Garbin et al., 2020; Laurent et al., 2016). Further investigation in this study is motivated by the advantages of the batch normalization layer.

Accordingly, the primary objective of this study is to enhance the performance of our new classification model for segregating images with LV chambers from De-CMR images using the CNN classification model from scratch. To the best of our knowledge, the influence of incorporating a batch normalization layer and its arrangement on the performance of our image classification tasks has not been thoroughly studied and analyzed in the training CNNs. Furthermore, these enhancements form the foundation for the key contributions of our paper:

- **Novel Classification Model:** We present a new shallow convolutional neural network model specifically designed to automate the classification of LV and non-

LV chambers in De-CMR image slices, aiming to improve myocardial infarction assessment.

- **Optimal Network Configuration:** Through extensive experimentation, we identified the best configuration of batch normalization layers and learning rates across different optimizers, ensuring optimal performance in LV chamber classification.
- **Enhanced Workflow for Radiologists:** Our proposed model significantly improves radiologists' workflow by providing an efficient and automated solution, reducing the need for manual selection of LV chamber slices in De-CMR for myocardial infarction diagnosis.

METHODOLOGY

Data Preparation

This research utilized datasets from the De-CMR modality chosen at random from the Radiology Unit of the Imaging Department, Advanced Medical and Dental Institute. Approval from the Human Research Ethics Committee of USM was necessary to access this private dataset. All selected images, originally in Digital Imaging and Communications in Medicine (DICOM) format, were anonymized and then converted to bitmap (bmp) format. To ensure a balanced dataset for each class, the non-LV chamber images, which were fewer in number compared to the LV chamber images, were augmented using geometric transformation techniques. These techniques included rotations of +90, +180, and +270 degrees. A total of 1420 images were used in this study. All experimental network models were trained and validated on 80% (1136 images) (Bichri et al., 2024) of the data using five-fold cross-validation (Hou et al., 2024). This method involves splitting the training data into five folds, using four folds for training and one for validation in each iteration. This process is repeated five times, ensuring all data is used for both training and validation, leading to a more robust estimate of model performance. We reserved the remaining 20% (284 images) of the total dataset to avoid evaluation bias as a separate test set. These unseen images were not included in the training process and were used solely for model test evaluation.

Network Architecture

CNN's most essential layer is the convolution layer, which extracts features. Ghosh et al. (2020) summarize the convolution layer's operating principle. CNN's weights are learned from back-propagation, except for the initial condition when given randomly. The three convolution layers depicted in Figure 3 of our proposed CNN architecture from scratch were generated experimentally, as described in our prior research by Awang Damit et al. (2022). However, no additional experiments or discussions regarding the use of batch

normalization were presented in our previous study. Therefore, the current work aims to fill this gap by focusing on the inclusion of batch normalization in the model and thoroughly investigating its effects through experimental and in-depth discussions.

Certain values, such as the number of layers and filters, were selected as the acceptable accuracy for each dataset due to the limited computational resources. The network was kept simple and reliable to fulfill the next research objective: to hybrid with another network model to automatically segment the infarcted tissue in the LV chamber. MATLAB software was used to specify the network parameters. The proposed model input layer expects input images with a resolution of 227×227 pixels. Kandel and Castelli (2020) state that higher learning rates require bigger batch sizes. Thus, a fixed learning rate of 0.0001, 16 batch size, and the Adam optimizer were used to train the first experiment regarding the presence of batch normalization layer because a greater learning rate is not advised in this study due to an insufficiently large dataset.

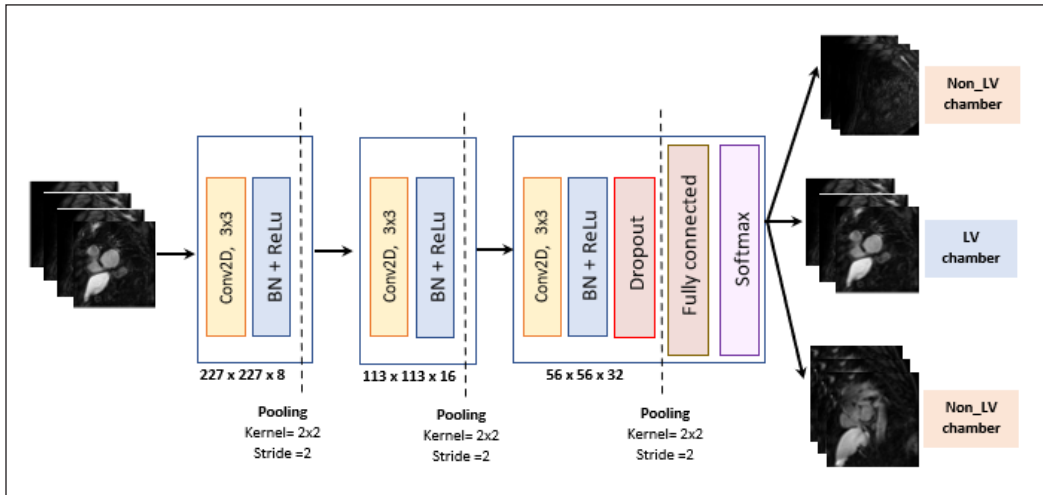


Figure 3. Network architecture for the proposed CNN model

Training Scenario with Batch Normalization

Three different arrangements of stacking the layers in our proposed CNN with the appearance of a batch normalization layer were systematically tested in this work. Figure 4 illustrates these three CNN models, one without batch normalization layer (A1) and the other with different batch normalization layer arrangements. The first arrangement of batch normalization layers was to place them after the convolution layer (A2). In contrast, the second arrangement placed them before the convolution layer, where it will normalize the input (A3). The test dataset was used to generate the final metrics after all models had been trained using the training dataset with the hyperparameters tuned by the validation

dataset. Adam optimizer was adopted as our chosen optimizer with an initial learning rate of 0.0001. The optimum performance model configuration shown in the previous experiment was then examined utilizing three learning rates from two different types of optimizers, Adam and Sgdm (Zohrevand & Imani, 2022). Furthermore, our best-proposed model with the optimal parameter configuration from this experiment was further evaluated against well-known models, including GoogleNet (Szegedy et al., 2015), SqueezeNet (Avanzato & Beritelli, 2023), and AlexNet (Krizhevsky et al., 2017). The same parameter settings and testing datasets were used across all models to ensure a fair comparison and avoid potential biases. The images were resized to match the required input size for each network to adapt these pre-trained models to our task. GoogleNet requires input images of size $224 \times 224 \times 3$, whereas SqueezeNet and AlexNet require $227 \times 227 \times 3$. The final layer of each network was fine-tuned by replacing it with a new layer for the two-class classification task of LV and non-LV chambers.

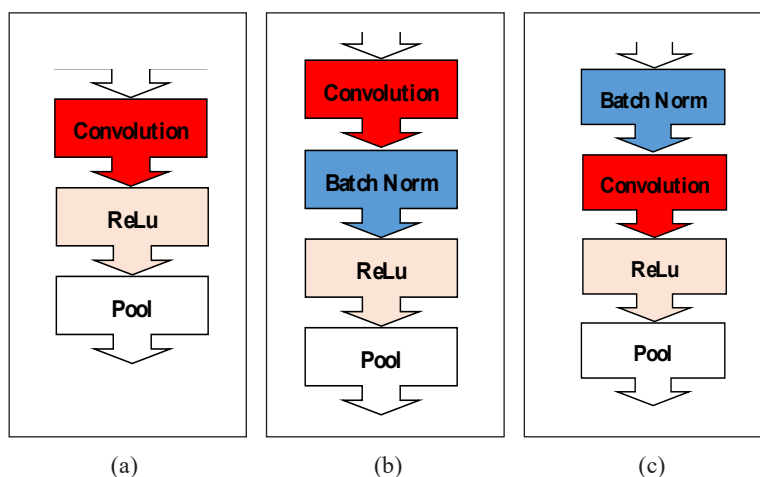


Figure 4. Illustration of the three CNN models: (a) Model A1 without a batch normalization layer, (b) Model A2 with batch normalization after the convolution layer, and (c) Model A3 with batch normalization before the convolution layer

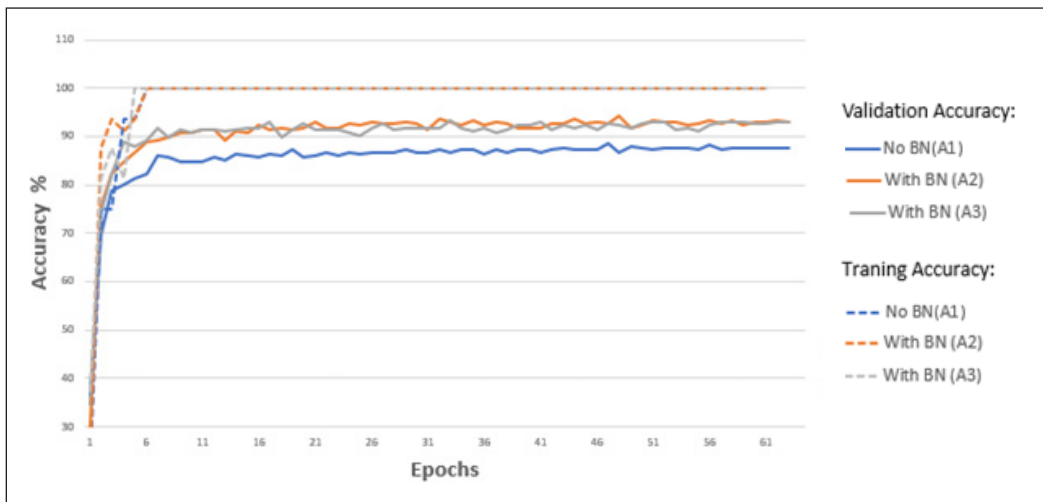
RESULTS

These experiments aimed to select the best layer architecture for the CNN model by utilizing a batch normalization layer for the De-CMR dataset.

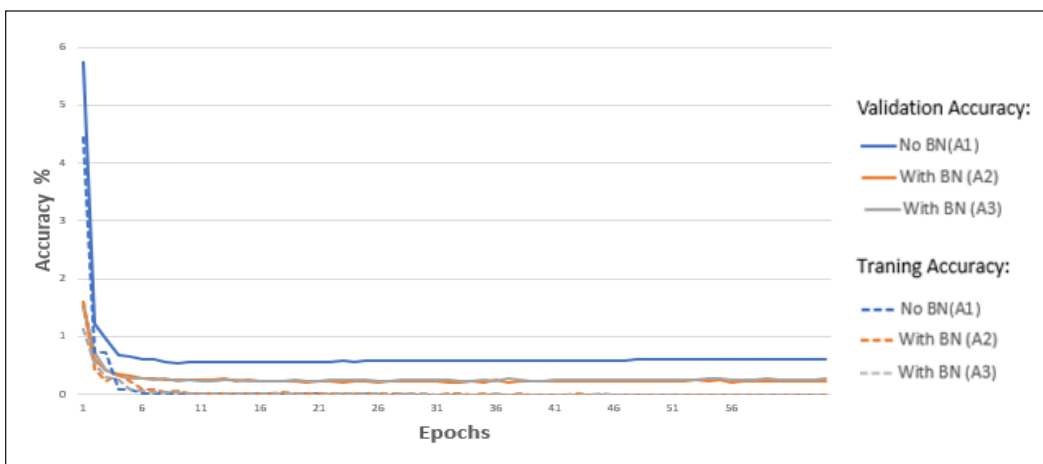
Results of Batch Normalization Implementation

The implications of the three distinct configurations mentioned earlier were compared to average accuracy performance. The model's validation and loss accuracy performance without a batch normalization layer and with two distinct batch normalization

layer arrangements converged in the line graphs of Figures 5(a) and 5(b). The training was stopped when no substantial gain was observed in accuracy after 64 epochs. The steady decrease in loss and consistent increase in accuracy, as depicted in the plots, provide strong evidence that the models were able to learn from the dataset effectively. While the validation accuracy follows a similar trend, none of the models show signs of overfitting. Figures 6(a) and 6(b) provide a detailed view of the convergence curves for training and validation accuracy, emphasizing the initial stages of the training process. The blue line represents accuracy over arrangement A1, while the orange and grey lines represent accuracy over arrangement A2 and A3, respectively. Both models with a batch normalization layer, A2 and A3, demonstrate an improved learning speed performance with a faster training



(a)

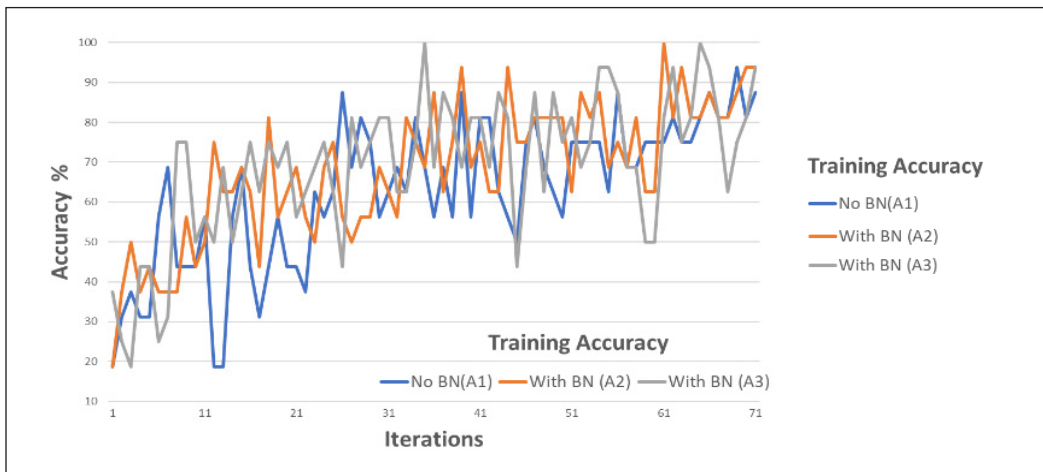


(b)

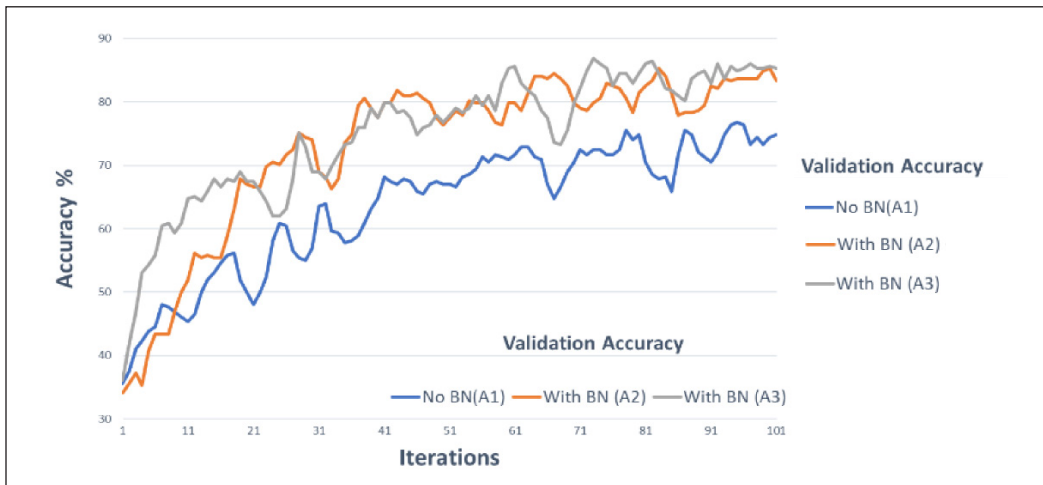
Figure 5. Plots of training and validation (a) accuracy and (b) loss for three CNN models in 64 epochs

and validation convergence curve than model A1. Additionally, model configuration A3 exhibits slightly faster convergence than A2. These results confirm that incorporating batch normalization slightly improves accuracy performance and leads to faster model learning compared to a model without batch normalization.

Table 1 presents the validation and testing accuracy performance of models A1, A2, and A3. Validation accuracy reflects the average testing accuracy achieved during the training process using five-fold cross-validation. In contrast, testing accuracy refers to the model’s performance on a completely new set of images not included in the training process. This metric is crucial for understanding how well the model generalizes to unseen data. All models were trained using a learning rate 0.0001 and the Adam optimizer. Notably, A2



(a)



(b)

Figure 6. Plots of (a) training and (b) validation accuracy for three CNN models on early training convergence

stands out as the highest performer in terms of validation and test accuracy, achieving an exceptional 93.41% and 88.4%, respectively. A3 follows closely in testing accuracy with a slight difference of 1.4%. Conversely, the model without batch normalization, A1, exhibits the lowest performance, with a difference of 5.3% compared to A2.

Further investigating the performance of each model, Table 2 showcases the precision, recall, and F1-score metrics for the above three CNNs model configurations. Overall, both models with batch normalization, A2 and A3, significantly outperform the model without batch normalization, A1, across all three metrics, highlighting the positive impact of batch normalization on the model's ability to accurately classify the left ventricle segment. A2 achieves the highest F1-score (0.8773), indicating a well-balanced performance between precision (0.9291) and recall (0.8310). While A3 exhibits a slightly lower F1-score (0.8614), its precision remains above average (0.9200). These findings suggest that both batch normalization arrangements enhance the model's ability to correctly identify true positives while minimizing false positives, leading to a more accurate classification of the left ventricle segment. Further validation of these findings is provided by the confusion matrices presented in Figure 7, which compares the predicted classifications for all three CNN models (7(a) A1, 7(b) A2, and 7(c) A3) to the actual classifications for the two categories, namely LV and non-LV. It is important to note that the testing set contains an equal number of De-CMR images for both LV and non-LV categories (142 images each, resulting in a total of 284). This ensures a balanced representation of both classes. The first predicted row of each confusion matrix shows the number of correctly identified images: Model A1: 110 LV images and 126 non-LV images, Model A2: 118 LV images and 133 non-LV images, and Model A3: 115 LV images and 132 non-LV images. These values demonstrate that all models correctly identified a significant portion of the images. Notably, Figure 7 also

Table 1

Validation and test accuracy result and comparison of three different batch normalization arrangements with LR=0.0001

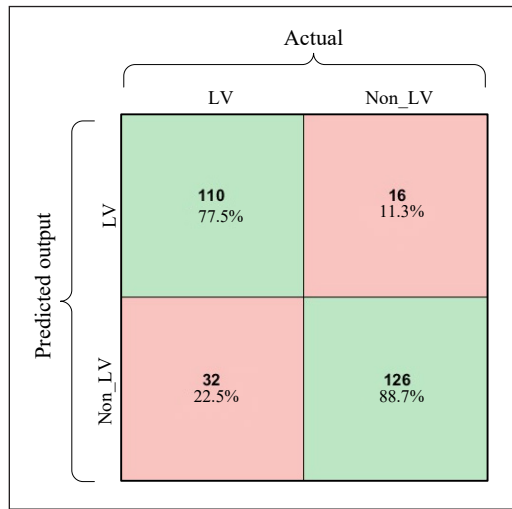
CNN Model	Validation Accuracy (%)	Test Accuracy (%)
A1 (No BN)	87.6	83.1
A2 (With BN)	93.41	88.4
A3 (With BN)	92.64	87

Table 2

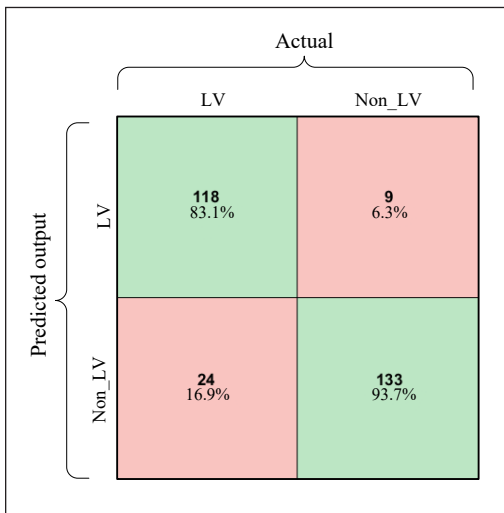
Precision, recall and F1-Score performance of three different batch normalization arrangements with LR=0.0001

CNN Model	Precision	Recall	F1-Score
A1 (No BN)	0.8730	0.7746	0.8209
A2 (With BN)	0.9291	0.8310	0.8773
A3 (With BN)	0.9200	0.8099	0.8614

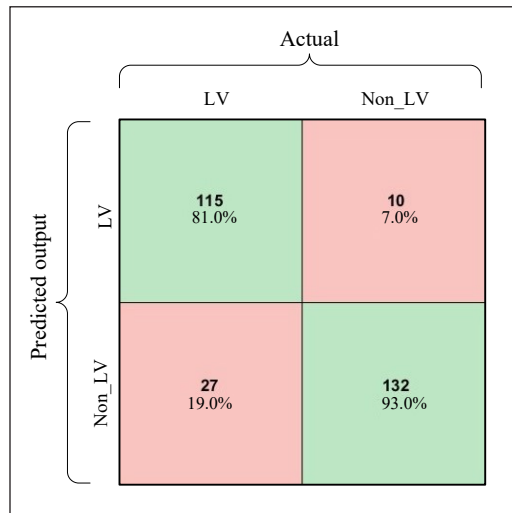
reveals a consistent pattern across all models: the number of false negatives and incorrectly classified positive images is higher than the number of false positives and incorrectly classified negative images. This is also proved by the data shown in the confusion matrix in Figure 7. The True Positives in the confusion matrix represent the number of correctly classified LV chamber images, while the True Negatives represent the correctly classified non-LV chamber images. The LV and non-LV De-CMR images are given equally in the testing set as 142 and 142 give the total of 284 of the testing set. In the first predicted row for all models, 110(77.5%), 118(83.1%) and 115(81%) out of 142 De-CMR images with LV chamber were correctly identified in models A1, A2 and A3, respectively and 126(88.7%), 133(93.7%) and 132(93%) out of 142 De-CMR images with non- LV chamber were correctly identified in model A1, A2 and A3, respectively. These values demonstrate that all models correctly identified a significant percentage of the images. Notably, Figure 7 also reveals a consistent pattern across all models, where the number of false negatives (which are incorrectly classified LV images) is higher than the number of false positives (the incorrectly classified non-LV images). This



(a)



(b)



(c)

Figure 7. Testing confusion matrix for CNN Model (a) A1 (b) A2 and (c) A3

phenomenon can be partially attributed to the anatomical similarity between the utmost apical and basal regions of the LV chamber with the surrounding non-LV image, particularly in cases where the boundaries are unclear or the image quality is poor.

Results of Batch Normalization Implementation in Different Learning Rates

Figure 8 illustrates the impact of incorporating batch normalization and different learning rates on the performance of the proposed CNN models. It presents the accuracy achieved for each model configuration with the Adam and Sgdm optimizers across three different learning rates: 0.0001, 0.001, and 0.01. Across all learning rates and optimizers, models with batch normalization consistently achieve higher accuracy compared to models without batch normalization. This confirms the effectiveness of batch normalization in stabilizing the training process and improving the overall performance of the CNN models. The optimal learning rate appears to be 0.0001 for both Adam and Sgdm optimizers. At this learning rate, models with batch normalization achieve their highest accuracy at 88.4% with Adam and 86.1% with Sgdm. Using higher learning rates as 0.001 and 0.01 generally leads to a decline in accuracy for both models with and without batch normalization. This suggests that the chosen network architecture can be more sensitive to larger learning rates, potentially leading to instability and suboptimal performance. While both Adam and Sgdm optimizers benefit from batch normalization, Adam seems to achieve slightly higher accuracy with batch normalization across all learning rates. This indicates that the Adam optimizer is better suited for this specific network architecture and task.

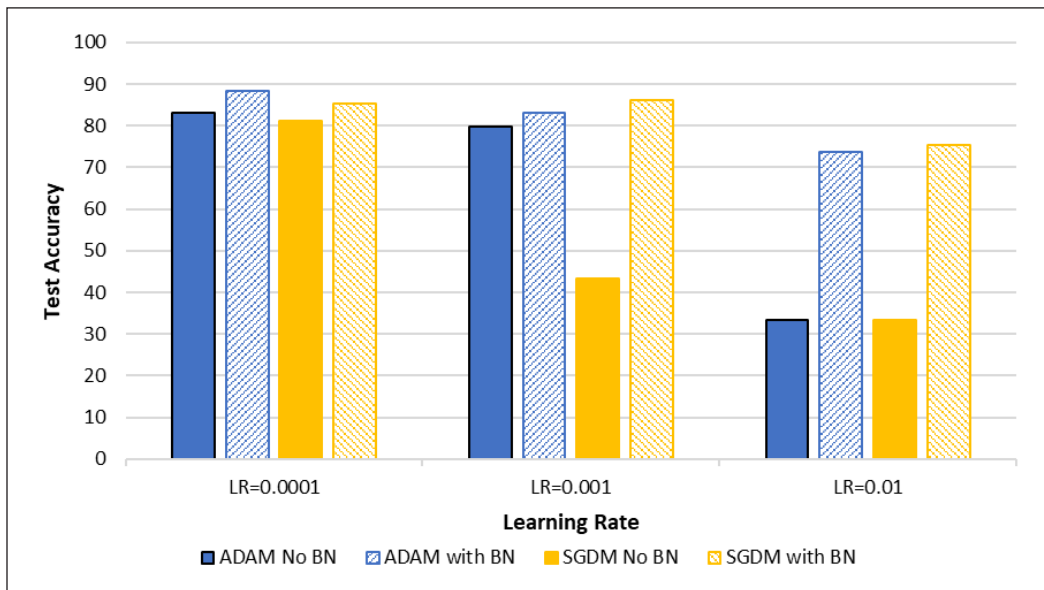


Figure 8. Accuracy performance for test data on Adam and Sgdm optimizers with different learning rates

DISCUSSION

This study investigated the performance of a newly proposed CNN model architecture, specifically focusing on the influence of batch normalization layer placement and learning rate on its ability to automatically classify images containing the LV chamber and non-LV chamber regions in De-CMR modality images. Our results demonstrated that incorporating a batch normalization layer after each convolution led to the highest accuracy compared to models without batch normalization or with batch normalization before the convolution layer. Although arrangement A3 accelerates the learning ability more quickly than arrangement A2, A2 eventually generates higher accuracy than A3. Additionally, experimentation with three different learning rates (0.0001, 0.001, 0.01) and two optimizers (Adam and Sgdm) identified 0.0001 as the optimal learning rate when using the Adam optimizer. Models trained with this lower learning rate demonstrated better generalization compared to those trained with larger rates (0.001 and 0.01), where a notable decline in accuracy was observed due to instability and suboptimal convergence. The lower learning rate allowed for more gradual and stable updates during gradient descent, preventing large oscillations in the loss function, which can occur with higher learning rates. The significant improvement in accuracy observed with batch normalization further highlights its importance. Through its ability to mitigate internal covariate shifts, batch normalization contributes to preventing overfitting by ensuring more consistent gradient updates. This ultimately leads to faster convergence and enhanced generalization performance. While the study focused solely on Adam and Sgdm optimizers, it is important to note that both these optimizers benefit from batch normalization. Exploring other optimization algorithms might reveal further insights. These findings highlight the importance of batch normalization in optimizing CNN architectures to improve accuracy in medical image analysis, leading to a future fully automated diagnosis system.

Based on the investigation, we evaluate our best-proposed model, A2, against AlexNet, SqueezeNet, and GoogleNet, which are well-established architectures. The accuracy metric is used to evaluate the performance of each model. Our proposed model achieves an accuracy of 88.4%, which slightly outperforms AlexNet (87%) but is lower than GoogleNet (92.96%) and SqueezeNet (92.61%) (Table 3). While our model exhibits slightly lower accuracy compared to pre-trained models like SqueezeNet and GoogleNet, it presents significant advantages in terms of simplicity and computational efficiency. Its less complex architecture translates to faster training times and lower resource requirements, making it a more practical choice for deployment in resource-constrained environments. Additionally, the model leverages automated feature extraction, eliminating the need for manual screening, which can be time-consuming. Notably, unlike pre-trained models that require fixed input image sizes, the proposed model offers greater adaptability to different image size datasets and potential future applications without the need for image resizing,

Table 3

Comparison of the proposed CNN with established pre-trained CNNs architectures

Author	CNN Model	Accuracy (%)
This study	A2 (Proposed)	88.4
Krizhevsky et al., 2017	AlexNet	87
Avanzato et al., 2023	SqueezeNet	92.61
Szegedy et al., 2015	GoogleNet	92.96

which can introduce noise and potentially degrade performance. Therefore, its simplicity, efficiency, and flexibility strengths make our proposed model a compelling alternative to pre-trained models, particularly in situations where computational resources are critical.

CONCLUSION AND RECOMMENDATIONS

In this study, we have examined the result of adopting the batch normalization layer in different positions of CNN models for LV chamber and non-LV chamber classification in De-CMR images as one of the pre-processing procedures in myocardial infarction assessment. This study aims to identify the optimal network layer configuration and learning rate combination for De-CMR image classification that maximizes accuracy while maintaining computational efficiency. The results demonstrate that incorporating a batch normalization layer after the convolution layer in arrangement A2 significantly improves the network's accuracy (88.4%) compared to models without batch normalization (83.1%) or with different layer placements. Additionally, the study reveals that using a lower learning rate (0.0001) with the Adam optimizer yields the best performance. While the proposed model achieves competitive accuracy compared to established architectures like AlexNet, this paper suggests more investigation into this model's behavior by increasing the training data volume for the diversity and complexity of medical conditions. Additionally, exploring the effectiveness of other architectures like inception modules, skip connections, or attention mechanisms could lead to further performance improvements. Overall, this study presents a promising initial approach for fully automated myocardial infarction assessment through LV chamber classification using a simple and efficient CNN model.

ACKNOWLEDGMENT

This research was funded by the Ministry of Higher Education through the Fundamental Research Grant Scheme (FRGS) with code FRGS/1/2023/SKK06/UITM/02/12, titled "New convolutional neural networks - autoencoder model with fusion correlation layer for left ventricle classification and scar tissue segmentation in cardiac magnetic resonance images of myocardial infarction disease." Ethical approval was granted on November 22nd, 2022, by the Human Research Ethics Committee of USM (JEPeM), Universiti Sains Malaysia

(USM/JEPeM/21090623). The authors would like to express their gratitude to members of the Advanced Control System and Computing Research Group (ACSCRG), Advanced Rehabilitation Engineering in Diagnostic and Monitoring Research Group (AREDiM), Integrative Pharmacogenomics Institute (iPROMISE) and Centre for Electrical Engineering Studies, Universiti Teknologi MARA, Cawangan Pulau Pinang for their assistance and guidance during the fieldwork. Finally, the authors are grateful to Universiti Teknologi MARA, Cawangan Pulau Pinang, for their immense administrative support.

REFERENCES

- Abdullah, M. F., Sulaiman, S. N., Osman, M. K., Karim, N. K. A., Setumin, S., Isa, I. S., & Ani, A. I. C. (2023). Geometrical feature of lung lesion identification using computed tomography scan images. *Jurnal Teknologi*, 85(2), 149–156. <https://doi.org/10.11113/JURNALTEKNOLOGI.V85.18828>
- Abdullah, M. F., Sulaiman, S. N., Osman, M. K., Karim, N. K. A., Shuaib, I. L., & Alhamdu, M. D. I. (2020). Classification of lung cancer stages from CT scan images using image processing and k-Nearest neighbours. In *2020 11th IEEE Control and System Graduate Research Colloquium (ICSGRC)* (pp. 68–72). IEEE Publication. <https://doi.org/10.1109/ICSGRC49013.2020.9232492>
- Avanzato, R., & Beritelli, F. (2023). Thorax disease classification based on the convolutional network squeezeNet. In *2023 IEEE 12th International Conference on Intelligent Data Acquisition and Advanced Computing Systems: Technology and Applications (IDAACS)* (Vol. 1, pp. 933–937). IEEE Publishing. <https://doi.org/10.1109/IDAACS58523.2023.10348691>.
- Bichri, H., Chergui, A., & Hain, M. (2024). Investigating the impact of train / test split ratio on the performance of pre-trained models with custom datasets. *International Journal of Advanced Computer Science and Applications*, 15(2), 331–339. <https://doi.org/10.14569/IJACSA.2024.0150235>
- Chen, C., Qin, C., Qiu, H., Tarroni, G., Duan, J., Bai, W., & Rueckert, D. (2020). Deep learning for cardiac image segmentation: A review. *Frontiers in Cardiovascular Medicine*, 7, Article 25. <https://doi.org/10.3389/fcvm.2020.00025>
- Damit, D. S. A., Sulaiman, S. N., Osman, M. K., A. Karim, N. K., & Setumin, S. (2022). Classification of left ventricle and non-left ventricle segment for cardiac assessment using deep convolutional neural network. *Journal of Electrical & Electronic Systems Research*, 21, 31–38. <https://doi.org/10.24191/jeesr.v21i1.005>
- Garbin, C., Zhu, X., & Marques, O. (2020). Dropout vs. batch normalization: An empirical study of their impact to deep learning. *Multimedia Tools and Applications*, 79(19), 12777–12815. <https://doi.org/10.1007/s11042-019-08453-9>
- Ghosh, A., Sufian, A., Sultana, F., Chakrabarti, A., & De, D. (2020). Fundamental concepts of convolutional neural network. In V. E. Balas, R. Kumar, & R. Srivastava (Eds.), *Recent Trends and Advances in Artificial Intelligence and Internet of Things* (pp. 519–567). Springer International Publishing. https://doi.org/10.1007/978-3-030-32644-9_36
- Harron, N. A., Sulaiman, S. N., Osman, M. K., Isa, I. S., A. Karim, N. K., & Maruzuki, M. I. F. (2022). Deep learning approach for blur detection of digital breast tomosynthesis images. *Journal of Electrical & Electronic Systems Research*, 21, 39–44. <https://doi.org/10.24191/jeesr.v21i1.006>

- Hasani, M., & Khotanlou, H. (2019). An empirical study on position of the batch normalization layer in convolutional neural networks. In *2019 5th Iranian Conference on Signal Processing and Intelligent Systems (ICSPIS)* (pp. 1-4). IEEE Publishing. <https://doi.org/10.1109/ICSPIS48872.2019.9066113>
- Ho, N., & Kim, Y. C. (2021). Evaluation of transfer learning in deep convolutional neural network models for cardiac short axis slice classification. *Scientific Reports*, *11*(1), Article 1839. <https://doi.org/10.1038/s41598-021-81525-9>
- Hou, R., Lo, J. Y., Marks, J. R., Hwang, E. S., & Grimm, L. J. (2024). Classification performance bias between training and test sets in a limited mammography dataset. *PLOS ONE*, *19*(2), Article e0282402. <https://doi.org/10.1371/journal.pone.0282402>
- Huang, L., Zhao, P., Tang, D., Zhu, T., Han, R., Zhan, C., Liu, W., Zeng, H., Tao, Q., & Xia, L. (2020). Cardiac involvement in patients recovered from COVID-2019 identified using magnetic resonance imaging. *JACC: Cardiovascular Imaging*, *13*(11), 2330–2339. <https://doi.org/10.1016/J.JCMG.2020.05.004>
- Im, D. J., Hong, S. J., Park, E. A., Kim, E. Y., Jo, Y., Kim, J., Park, C. H., Yong, H. S., Lee, J. W., Hur, J. H., Yang, D. H., & Lee, B. Y. (2019). Guidelines for cardiovascular magnetic resonance imaging from the Korean society of cardiovascular imaging - Part 3: Perfusion, delayed enhancement, and T1- and T2 mapping. *Korean Journal of Radiology*, *20*(12), 1562–1582. <https://doi.org/10.3348/kjr.2019.0411>
- Kandel, I., & Castelli, M. (2020). The effect of batch size on the generalizability of the convolutional neural networks on a histopathology dataset. *ICT Express*, *6*(4), 312–315. <https://doi.org/10.1016/j.icte.2020.04.010>
- Karim, R., Bhagirath, P., Claus, P., Housden, R. J., Chen, Z., Karimaghloo, Z., Sohn, H. M., Rodríguez, L. L., Vera, S., Albà, X., Hennemuth, A., Peitgen, H. O., Arbel, T., González Ballester, M. A., Frangi, A. F., Götte, M., Razavi, R., Schaeffter, T., & Rhode, K. (2016). Evaluation of state-of-the-art segmentation algorithms for left ventricle infarct from late Gadolinium enhancement MR images. *Medical Image Analysis*, *30*, 95–107. <https://doi.org/10.1016/j.media.2016.01.004>
- Khairandish, M. O., Sharma, M., Jain, V., Chatterjee, J. M., & Jhanjhi, N. Z. (2022). A hybrid CNN-SVM threshold segmentation approach for tumor detection and classification of MRI brain images. *IRBM*, *43*(4), 290–299. <https://doi.org/10.1016/j.irbm.2021.06.003>
- Krizhevsky, A., Sutskever, I., & Hinton, G. E. (2017). ImageNet classification with deep convolutional neural networks. *Communications of the ACM*, *60*(6), 84–90. <https://doi.org/10.1145/3065386>
- Laurent, C., Pereyra, G., Brakel, P., Zhang, Y., & Bengio, Y. (2016). Batch normalized recurrent neural networks. In *2016 IEEE International Conference on Acoustics, Speech and Signal Processing (ICASSP)* (pp. 2657-2661). IEEE Publishing. <https://doi.org/10.1109/ICASSP.2016.7472159>
- Leong, C. O., Lim, E., Tan, L. K., Aziz, Y. F. A., Sridhar, G. S., Socrates, D., Chee, K. H., Lee, Z. V., & Liew, Y. M. (2019). Segmentation of left ventricle in late gadolinium enhanced MRI through 2D-4D registration for infarct localization in 3D patient-specific left ventricular model. *Magnetic Resonance in Medicine*, *81*(2), 1385–1398. <https://doi.org/10.1002/mrm.27486>
- Li, G., Zhang, W., Jia, D., Rong, J., Yu, Z., & Wu, D. (2023). Epidemic of the SARS-CoV-2 Omicron variant in Shanghai, China in 2022: Transient and persistent effects on Out-of-hospital cardiac arrests. *Resuscitation*, *186*, Article 109722. <https://doi.org/10.1016/j.resuscitation.2023.109722>

- Shaaf, Z. F., Jamil, M. M. A., Ambar, R., Alattab, A. A., Yahya, A. A., & Asiri, Y. (2022). Automatic left ventricle segmentation from short-axis cardiac mri images based on fully convolutional neural network. *Diagnostics*, 12(2), Article 0414. <https://doi.org/10.3390/diagnostics12020414>
- Szegedy, C., Liu, W., Jia, Y., Sermanet, P., Reed, S., Anguelov, D., Erhan, D., Vanhoucke, V., & Rabinovich, A. (2015). Going deeper with convolutions. In *Proceedings of the IEEE Conference on Computer Vision and Pattern Recognition* (pp. 1-9). IEEE Publishing. <https://doi.org/10.1109/CVPR.2015.7298594>
- Toro, A., Bozzani, A., Tavazzi, G., Urtis, M., Giuliani, L., Pizzoccheri, R., Aliberti, F., Fergnani, V., & Arbustini, E. (2021). Long COVID: long-term effects? *European Heart Journal Supplements*, 23, E1–E5. <https://doi.org/10.1093/eurheartj/suab080>
- World Health Organization. (2021). *Cardiovascular Diseases (CVDs)*. World Health Organization. [https://www.who.int/news-room/fact-sheets/detail/cardiovascular-diseases-\(cvds\)](https://www.who.int/news-room/fact-sheets/detail/cardiovascular-diseases-(cvds))
- Zhang, L., Gooya, A., Dong, B., Hua, R., Petersen, S. E., Medrano-Gracia, P., & Frangi, A. F. (2016). Automated quality assessment of cardiac MR images using convolutional neural networks. In S. A. Tsaftaris, A. Gooya, A. F. Frangi, & J. L. Prince (Eds.), *Simulation and Synthesis in Medical Imaging* (pp. 138–145). Springer International Publishing.
- Zohrevand, A., & Imani, Z. (2022). An empirical study of the performance of different optimizers in the deep neural networks. In *2022 International Conference on Machine Vision and Image Processing (MVIP)* (pp. 1-5). IEEE Publishing. <https://doi.org/10.1109/MVIP53647.2022.9738743>
- Zorkafli, M. F., Osman, M. K., Isa, I. S., Ahmad, F., & Sulaiman, S. N. (2019). Classification of cervical cancer using hybrid multi-layered perceptron network trained by genetic algorithm. *Procedia Computer Science*, 163, 494–501. <https://doi.org/10.1016/j.procs.2019.12.132>

Physical Parameters Optimization of Bacterial Cellulose from *Komagataeibacter sucrofermentans*

Siti Noorfathiah Mohd Razin¹, Siti Nurbaya Oslan^{1,2,3} and Noor Dina Muhd Noor^{1,2*}

¹Department of Biochemistry, Faculty of Biotechnology and Biomolecular Sciences, Universiti Putra Malaysia, 43400 UPM, Serdang, Selangor, Malaysia

²Enzyme and Microbial Technology Research Centre (EMTech), Faculty of Biotechnology and Biomolecular Sciences, Universiti Putra Malaysia, 43400 UPM, Serdang, Selangor, Malaysia

³Enzyme Technology and X-ray Crystallography Laboratory, VacBio 5, Institute of Bioscience, Universiti Putra Malaysia, 43400 UPM, Serdang, Selangor, Malaysia

ABSTRACT

Many studies have been concerned with nanocellulose's potential to produce environmentally friendly nanomaterial fibers. Bacterial cellulose has shown superiority over plant cellulose, leading to increased research focus on bacterial cellulose production. Among bacterial species, *Acetobacter*, particularly *Komagataeibacter* (formerly *Gluconacetobacter*), has captured interest due to its enhanced bacterial cellulose (BC) production and strain stability. Optimizing production processes becomes imperative with the growing demand for BC in various industries. This study explores the optimization of physical conditions for BC production using *Komagataeibacter sucrofermentans*. Five parameters—pH, temperature, aeration rate, shaking rate, and surface area, were examined using the One-factor-at-a-time (OFAT) method. This method was selected as it is useful in early-stage optimization to understand the effect of individual factors on BC production. The extracted BC was purified with 4.0 M NaOH solution at 80°C, and wet and dry weights were measured. Analysis via ANOVA determined the significance of each parameter in enhancing BC yield. Optimized conditions from this experiment —pH 5, temperature 20°C, 60% aeration rate,

slow agitation (50 rpm), and large surface area fermentation (63.62 cm²) shown to give better BC production. These findings have substantial implications for enhancing BC production efficiency on an industrial scale.

ARTICLE INFO

Article history:

Received: 21 June 2024

Accepted: 18 November 2024

Published: 07 March 2025

DOI: <https://doi.org/10.47836/pjst.33.2.16>

E-mail addresses:

208117@student.upm.edu.my (Siti Noorfathiah Mohd Razin)

snurbayaoslan@upm.edu.my (Siti Nurbaya Oslan)

dina@upm.edu.my (Noor Dina Muhd Noor)

*Corresponding author

Keywords: Acetobacter, bacterial cellulose, environmental, fiber, industrial, optimization, pollution, polymer

INTRODUCTION

Nowadays, the extensive use of fossil-based chemicals in sectors such as textiles, packaging, medicine, cosmetics, and other contemporary applications has resulted in pollution (Samanta & Das, 2021; Clews, 2016). Thus, utilizing environmentally friendly, renewable, and sustainable materials has gained increasing significance in creating diverse high-value goods with minimal environmental impact (Gupta & Pathak, 2020). Consequently, the search for alternatives has drawn considerable interest from academics and industry stakeholders, as these materials offer a substitute for diminishing non-renewable resources, environmental degradation, global warming, and energy scarcity. In this regard, cellulose, starch, alginate, chitin, chitosan, and gelatine have emerged as promising candidates due to their abundant availability from various sources (Trache, 2018). Among these, cellulose is the most abundant renewable compound derived from the biosphere, present in plants, algae, and certain bacteria (Trache et al., 2020). Bacterial nanocellulose was introduced as a non-toxic material to substitute the hydrocarbon-based material used in many products. The demand for bacterial nanocellulose or bacterial cellulose is increasing in the global market as it can be used in various applications. The United Kingdom has become the largest consumer of nanocellulose, followed by North America. In the Asia Pacific, South Korea, India, and Malaysia have also become countries that have rapidly uptaken this environmentally friendly material (Grand View Research, 2021). Hence, demands for bacterial cellulose across various industries have increased remarkably over the years.

Cellulose is generally found in plants, the main constituent of plant cell walls. It is a polymer composed of D-glucopyranose units linked by β -1,4-glycosidic bonds. Due to intra and intermolecular hydrogen bonds from the hydroxyl group present in cellulose, it forms various crystalline arrangements (Martins et al., 2011; Park et al., 2010). However, certain types of bacteria also can produce cellulose that has the same polymer composition in plants but differs in its characteristics. Some bacteria have the ability to synthesize cellulose by absorbing glucose, which are usually gram-negative bacteria (Swingler et al., 2021). Bacteria such as *Rhizobium*, *Agrobacterium*, *Salmonella*, and *Alcaligenes* are known to exhibit cellulose-producing capabilities. Notably, *Acetobacter*, now referred to as *Komagataeibacter*, is recognized as a prominent cellulose producer (Barja, 2021; da Gama & Dourado, 2018). BC is devoid of lignin, hemicellulose, and pectin; hence, it is considered to have high purity, leading to a higher degree of polymerization and crystallization at 40.6% to 83.4% (Pham & Tran, 2023; Naomi et al., 2020; Moniri et al., 2017). The crystallinity of wood fibers ranges from 55 to 70%, and natural plant fibers range from 60% to 70%, which shows that the crystallinity of cellulose from plants is much lower than BC (Jakob et al., 2022; Petroudy, 2017). These characteristics make BC resistant to wet conditions and have high elasticity and conformability.

Due to its superior characteristics, bacterial cellulose (BC) has become a product of interest to many industrial sectors seeking sustainable materials on par with petrochemicals. Especially in biomedical industries that have an increasing demand for BC materials (Choi et al., 2022). Bacterial cellulose is highly biocompatible, biodegradable, and non-toxic, which makes it a very competent material for pharmaceutical and biomedical industries. Due to its high porosity and ability to prevent microbial infection, it has become interesting and has high potential for biomedical applications. An example of BC application in biomedical is wound dressing. For example, BC is heightened with an antibacterial function that inhibits and suppresses bacterial growth in wound dressing (Volova et al., 2018; Deshpande et al., 2023). Not only that, BC can also be used for drug delivery, regeneration of bone, and as a biosensor (Deshpande et al., 2023). In a review by Bianchet et al. (2020), interest in BC for cosmetic applications has significantly increased over the years. Biotechnology advancements have led to the development of BC sheets tailored for the cosmetics and pharmaceutical industries, including innovations like antioxidant nanocellulose and vitamin B-loaded formulations (Deshpande et al., 2023; Bianchet et al., 2020; Volova et al., 2018). However, BC's potential goes beyond these industries; it is additionally marketable for use in culinary applications, such as packaging. Its thin, porous, reticulated structure efficiently filters out dust, fungi, and microbes, extending the shelf life of food that has been stored. According to Poyrazoğlu et al. (2021), sausages wrapped in BC film have lower microbial loads than those wrapped in cling film or left uncovered, proving that BC film can extend the shelf life of food. Compared to cling wrap made from petrochemicals, the web-like structure of BC provides better filtration against airborne pollutants (Choi et al., 2022; Poyrazoğlu et al., 2021). Furthermore, BC can be used as an organic polymer in the paper and pulp business and as a biotechnological polymer in the fabric industry (Coseri, 2021; Lahiri et al., 2021). Therefore, this demonstrates that BC offers numerous advantages and significantly influences various industries, contributing to the development of economically viable and sustainable materials for the benefit of society.

Physical conditions or the environment of bacteria culture become one of the important factors in the production of BC. It has been known that environmental conditions usually affect the activity of bacteria. Physical conditions such as pH, temperature, aeration rate and agitation rate play some roles in the production of BC. The pH conditions observed in conducted studies revealed that a pH range of 4.5 to 6.0 could efficiently induce the production of BC by several *Acetobacter* species, such as *Acetobacter xylinum* BRC5 and *Acetobacter senegalensis* MA1 (Hasanin et al., 2023; Aswini et al., 2020; Hwang et al., 1999). *Acetobacter* sp. was able to produce acid by converting glucose to gluconic or acetic acid. This resulted in a change in the pH condition of the media, resulting in a decline in pH levels. Although BC production is hindered at the lowest pH level, acid production may yield greater benefits by lowering the initial higher pH level to conditions

favorable for BC production (Victor et al., 2018; Siew, 2012). Thus, maintaining certain pH conditions for the fermentation process is essential to keep the efficient production of BC on an industrial scale.

Temperatures are essential in promoting the growth of bacteria and cellular activities. In a study investigating cellulose production from bacteria isolated from rotten fruit, the highest cellulose yield was observed at a temperature of 30°C, demonstrated by *Glunconacetobacter* sp. RV28, *Pseudomonas* sp. RV14, and *Enterobacter* sp. RV 11. This shows that most bacteria of different species have an optimal temperature of producing cellulose at 30°C (Rangaswamy et al., 2015).

Aeration plays a crucial role in supplying oxygen with the efficient cellular activities of bacteria. Optimal BC production occurs within a medium range of aeration. High BC yields were observed within the range of 3 L/min to 6 L/min aeration, as Krusong et al. (2021) and Shavyrkina et al. (2021) reported. Under low oxygen levels, cellulose production is constrained due to depleted oxygen content, resulting in reduced cellulose production. Conversely, excess oxygen acts as a proton acceptor at higher concentrations, converting glucose to gluconic acid and diverting the production pathway away from cellulose production (Tantratian et al., 2005). Agitated culture is preferred in industrial production as it can be mass-produced, and the process is quick (Lahiri et al., 2021). However, it causes a low degree of polymerization and exhibits a lower crystallinity level than the cellulose produced in static fermentation (Lahiri et al., 2021; Watanabe et al., 2007). It also induces mutant cells into non-cellulose-producing cells, which die due to shear stress (Buldum et al., 2018; Campano et al., 2015). Static culture has a low possibility of mutant cells and better steady production of BC. Nonetheless, static culture has a slower process and limited oxygen supply as the production only occurs on the surface of the liquid area (Ul-Islam et al., 2015).

While many studies have focused on other bacterial cellulose producers, fewer investigations have aimed to optimize conditions for improving BC yield from *K. sucrofermentans*. *Komagataeibacter sucrofermentans* has gained significant interest because of its superior BC production capabilities compared to its predecessor, the *Acetobacter* species. Thus, the primary objective of this study is to evaluate the influence of various physical parameters such as pH, temperature, shaking rates, and aeration on BC production by *K. sucrofermentans*. Using the one-factor-at-a-time (OFAT) approach, the study aims to analyze the effects of these physical conditions on bacterial culturing for enhanced BC production. This approach was chosen because it is useful in early-stage optimization where the effects of all the said parameters need to be understood before moving on to more complex statistical methods like response surface methodology (Tajik et al., 2024; Bhaturiwala et al., 2022). Parameters such as surface area were added to observe how the size of the container may affect BC production.

MATERIALS AND METHODS

The commercialized bacteria strain, *K. sucrofermentans* JCM 9370, was purchased from The American Type Culture Collection (ATCC), Gaithersburg, Maryland. It was grown on a glucose-yeast extract-calcium carbonate (GYC) agar plate prepared by and obtained from the Institute of Bioscience (IBS) Universiti Putra Malaysia, UPM Serdang, Selangor, Malaysia.

Agar and Media Preparation

K. sucrofermentans grew up in Hestrin-Schramm media (HS). HS media contained peptone (2.5 g), yeast extract (2.5 g), disodium hydrogen phosphate (Na_2HPO_4) (1.35 g), citric acid (0.7 g), magnesium sulfate (MgSO_4) (0.6 g), in distilled water (dH_2O) (0.3 L)—additional agar (7.5 g) for agar plate. In preparing HS media, 10% of the glucose solution was prepared separately and autoclaved. All media prepared were autoclaved at 121°C for 15 min. All media were stored in the chiller at 4°C.

Preparation of Inoculum

K. sucrofermentans stock was streaked on an HS agar plate and incubated at 30°C for 4 days. Then, a single colony was inoculated in HS broth and incubated at 30°C, shaking rate at 150 rpm for 3 days. The growth of bacteria was noted with the formation of cellulose in broth with no or less cloudy conditions. A 10% (v/v) inoculum of *K. sucrofermentans* was inoculated to the HS medium for each of the parameters experimented on.

Bacterial Cellulose Culture Using One-factor-at-a-time (OFAT)

Preparation of Different pH for BC Production

Four different pH levels were established for each prepared HS medium—pH 5, pH 6, pH 7, and pH 8 in each flask. Sodium hydroxide (NaOH) was employed to elevate the pH, while hydrochloric acid (HCl) was used to lower it. Each flask was incubated for seven (7) days at 30°C. After seven days, the production was observed.

Preparation of Different Temperatures for BC Production

Four flasks were prepared with HS medium, and the pH was standardized to 5. Inoculum of *K. sucrofermentans* was cultivated into each flask, which was labeled with different temperatures: 20°C, 25°C, 30°C, and 35°C. The flasks were incubated at the temperature labeled for 7 days. After 7 days, the production was harvested and observed.

Agitated Culture Fermentation

Three flasks with HS medium were prepared and labeled with 0 rpm, 50 rpm, 150 rpm and 250 rpm, with pH and temperature standardized to pH 5 and 30°C. They were left incubated for 7 days (Pa'e et al., 2007).

Preparation of Different Aeration Rates for BC Production

Four flasks were prepared with 20%, 40%, 60% and 80% of aeration and labeled according to the percentage of aeration. The aeration of percentage was calculated using Equation 1:

$$\text{Aeration (\%)} = \frac{\text{Volume of flask} - \text{Volume of culture broth}}{\text{Volume of flask}} \times 100\% \quad [1]$$

The pH and temperature were standardized to pH 5 and 30°C, respectively. It was left incubated for 7 days.

Preparation of Different Surface Areas for BC Production

Following the size of the fermentation flasks, different surface areas were prepared. The bottom flasks were measured to determine the area value of each flask, which were 19.63 cm² (50mL flask), 28.27 cm² (250mL flask), 44.18 cm² (500mL flask), and 63.62 cm² (1000mL flask). Each flask was prepared with 20% HS media with pH and temperature standardized to pH 5 and 30°C. It was left incubated for 7 days in static condition.

Purification of Bacterial Cellulose

The bacterial cellulose membrane was harvested from the flask and cleaned with distilled water to remove excess media. Then, it was soaked in 1M NaOH solution for 30 min at 80°C to kill the bacteria and completely remove the cells and medium embedded in it. The BC membrane was left to cool down at room temperature. Then, it was soaked for 3 days with deionized water to further clean the BC sheet from any remaining excess media and bacterial cells on the cellulose fiber (Kiziltas et al., 2015). After 3 days, the extracted BC was dried in an oven at 100°C for 30 minutes.

Measuring of Wet Weight and Dry Weight Cellulose

Harvested BC were immediately weighed, and the reading was recorded as wet weight. After oven-drying, the dry-weight BC was recorded. The wet weight of BC indicates the capacity of water it can hold, resulting in swelling. Dry BC measures the weight of pure cellulose produced (Bodea et al., 2021; Pa'e et al., 2007).

Statistical Analysis

Comparison of BC yields obtained was subjected to One-way analysis of variance (ANOVA) using Microsoft Excel 365. A post-hoc test was done to compare the significance of the value between the means of each parameter (Nagmetova et al., 2020).

RESULTS AND DISCUSSION

The Production of Bacterial Cellulose in Different pH

Figure 1 illustrates BC's wet and dry weight profiles obtained from a seven-day fermentation process conducted in various pH mediums. Among the four levels of pH that were experimented on for the production of BC (pH 5, pH 6, pH 7 and pH 8), pH 5 demonstrated the highest yield in both wet and dry BC, followed by the remaining pH levels.

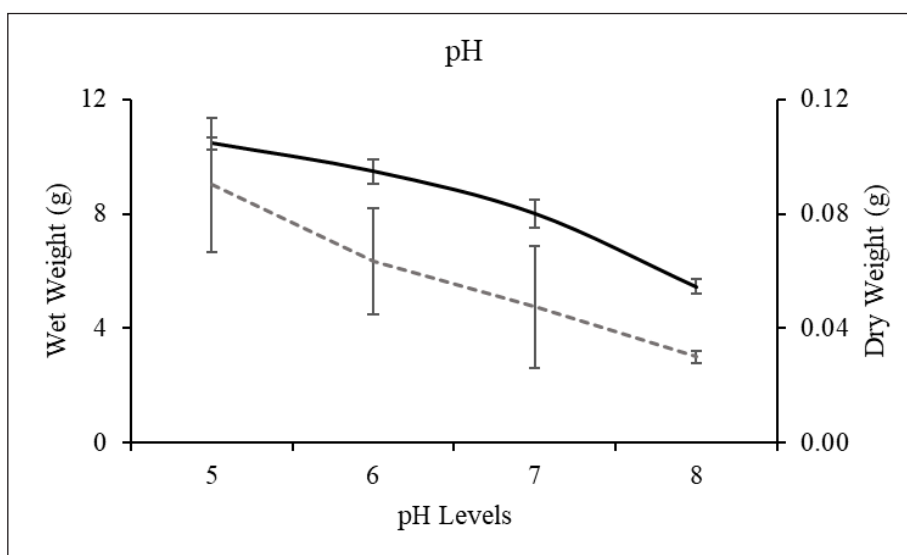


Figure 1. BC production by *K. sucrofermentans* at different pH conditions from pH 5 to 8. The graph shows the weight of BC; The smooth line denotes the wet weight of BC, and the dashed line denotes the dry weight of BC

Acetic acid bacteria efficiently produce cellulose at low pH levels ranging from 5 to 6.5 (Gomes et al., 2018). Referring to the data in Figure 1, *K. sucrofermentans* can efficiently produce BC at pH 5. The weight of BC obtained at pH 5 was approximately 10.5 g for wet BC and 0.09 g for dried BC. As pH increased, BC production was decreased but not entirely inhibited. At pH 8, BC was still produced but exhibited the lowest yield (within the pH range studied), with approximately 5.5 g for wet BC and 0.03 g for dried BC—half of the weight obtained at pH 5. This suggests that higher pH levels are not optimal for achieving high BC production. This was supported by ANOVA statistical analysis

revealing a calculated *p-value* of 0.0006, significantly below the critical threshold (*p-value* < 0.05), suggesting a significant difference in the influence of pH conditions on BC production. Nonetheless, by post-hoc Tukey test, a comparison of mean that has no significant difference is between pH 5 and pH 6 (*q-value* = 0.98 < 1.48, T-value = 1.48) as well as pH 6 and pH 7 (*q-value* = 1.47 < 1.48, T-value = 1.48) This can be seen in Table 1.

The impact of pH on BC production varies depending on whether the cellulose is in its wet or dry form. In wet BC, pH levels significantly influence the production process, with distinct variations observed across different pH values (Table 1). However, in the case of dry BC, post-hoc analysis indicates that pH does not have a significant effect on the formation of the dried membrane. This suggests that while pH plays a critical role during the initial synthesis and hydration stages of BC, its influence diminishes once the cellulose has dried.

A study by Hasanin et al. (2023) also achieved pH 5 to be an optimal condition for producing high BC yields. However, a study by Aswini et al. (2020) reported a high BC yield at pH 4.5. Moreover, after 7 days of fermentation, all culture pH levels were reduced to pH 3, indicating that *K. sucrofermentans* produced acid alongside BC production. It is critical that they utilize glucose and convert it into gluconic acid, thereby reducing pH in the media (Victor et al., 2018). Although this phenomenon contributes to BC production at high pH levels, synthesis of BC is inhibited as the pH reaches 3 (Siew, 2012). Further studies on lower pH values and variations in pH conditions may provide insight into BC production.

The Production of Bacterial Cellulose in Different Temperatures

The weights of wet and dry BC obtained from different temperatures are depicted in Figure 2. Four different temperatures condition was tested on the production of BC, which were 20°C, 25°C, 30°C and 35°C. *Komagataeibacter spp.* can grow and produce BC at temperatures ranging from 28°C to 30°C (Cannazza et al., 2021; Marič et al., 2020).

Table 1
Post hoc Tukey test, comparison between the mean of each pH to the production of BC

Wet BC	k	df	q	T
	4	4	5.757	1.483
pH	$ \bar{x}_1 - \bar{x}_2 $			*Significant diff.
5v6	0.976			q<1.483
5v7	2.448			q>1.483
5v8	5.001			q>1.483
6v7	1.473			q<1.483
6v8	4.026			q>1.483
7v8	2.553			q>1.483
Dry BC	k	df	q	T
	4	4	5.757	0.0745
pH	$ \bar{x}_1 - \bar{x}_2 $			*Significant diff.
5v6	0.0267			q<0.0745
5v7	0.0426			q<0.0745
5v8	0.0601			q<0.0745
6v7	0.0159			q<0.0745
6v8	0.0334			q<0.0745
7v8	0.0175			q<0.0745

*q-value < T-value has no significant difference

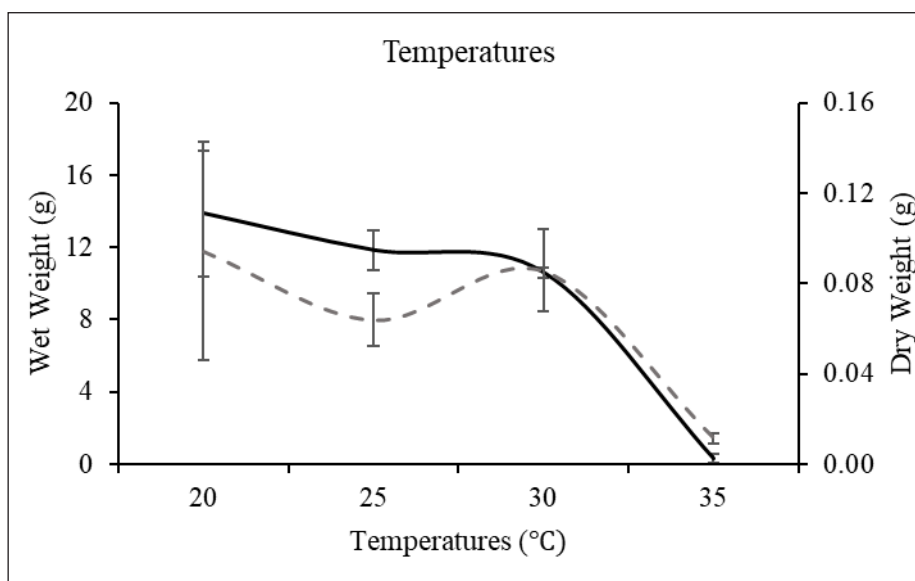


Figure 2. Production of BC by *K. sucrofermentans* in different temperature conditions from 20°C to 30°C. The graph shows the weight of BC; The smooth line denotes the wet weight of BC, and the dashed line denotes the dry weight of BC

The wet weight of BC from 20°C can be observed to be the highest compared to other temperatures (Figure 2). The total weight of wet BC obtained from 20°C culture fermentation was 13.9 g, while the dry BC weight obtained was 0.09 g. Both wet and dry weight BC obtained from 30°C was 10.6 g and 0.08 g, respectively. This finding contradicts previous reports on the influence of temperature conditions on BC production. Reshmy et al. (2021) indicated that the production of BC by *Acetobacter* sp. occurred at 30°C. In a study by Zakaria and Nazeri (2012), the maximum BC from *Acetobacter xylinum* was achieved at 30°C. Most of the conducted studies have also reported that the optimum condition of BC production ranges from 28°C to 30°C (Lahiri et al., 2021). However, a wide error bar was shown at 20°C (Figure 2). This indicates that the data achieved for BC produced at 20°C has less certainty (Cumming et al., 2007). The BC produced at 30°C was the second highest and had a smaller error bar which tells the data have more certainty and the results were less likely to happen by chance (Cumming et al., 2007). This may explain why *K. sucrofermentans* can produce efficiently and consistently at 30°C; however, this new finding can also signify that *K. sucrofermentans* may have different optimal temperature conditions in producing high-yield BC. Further study of BC production by *K. sucrofermentans* at lower temperatures should be done to gain better insight into the effect of temperature on BC production from this strain.

Table 2

Post hoc Tukey test, comparison between the mean of each temperature to the production of BC

Wet BC	k	df	q	T
	4	8	4.529	7.249
Temperature (°C)	$ \bar{x}_1 - \bar{x}_2 $	*Significant diff.		
20v25	2.028	q<7.249		
20v30	3.266	q<7.249		
20v35	13.560	q>7.249		
25v30	1.238	q<7.249		
25v35	11.532	q>7.249		
30v35	10.294	q>7.249		
Dry BC	k	df	q	T
	4	8	4.529	0.0693
Temperature (°C)	$ \bar{x}_1 - \bar{x}_2 $	*Significant diff.		
20v25	0.0306	q<0.0693		
20v30	0.0088	q<0.0693		
20v35	0.0829	q>0.0693		
25v30	0.0218	q<0.0693		
25v35	0.0524	q<0.0693		
30v35	0.0742	q>0.0693		

*q-value < T-value has no significant difference

The post-hoc test reveals a significant difference in BC weight between the lowest temperature (20°C) and the highest temperature (35°C) (Table 2). This implies that large temperature variations substantially impact BC production, with lower temperatures promoting higher yield. Lower temperatures (<20°C) could increase the efficiency of BC production. Nevertheless, the reduction in BC weight observed at 25°C could potentially be linked to fluctuations in temperature occurring within the incubator. Fluctuation of temperature causes physiological stress to the bacteria; hence, it disturbs the cellular activities of the bacteria (Ivancic et al., 2013) and causes *K. sucrofermentans* to produce BC inefficiently.

The Production of Bacterial Cellulose in Different Aeration Rates

Figure 3 displays the wet and dry weight BC harvested after 7 days of fermentation with different aeration. Four aeration rates (20%, 40%, 60%, 80%) were set upon BC production by *K. sucrofermentans*. Maximum BC yield was obtained from fermentation culture with 60% aeration.

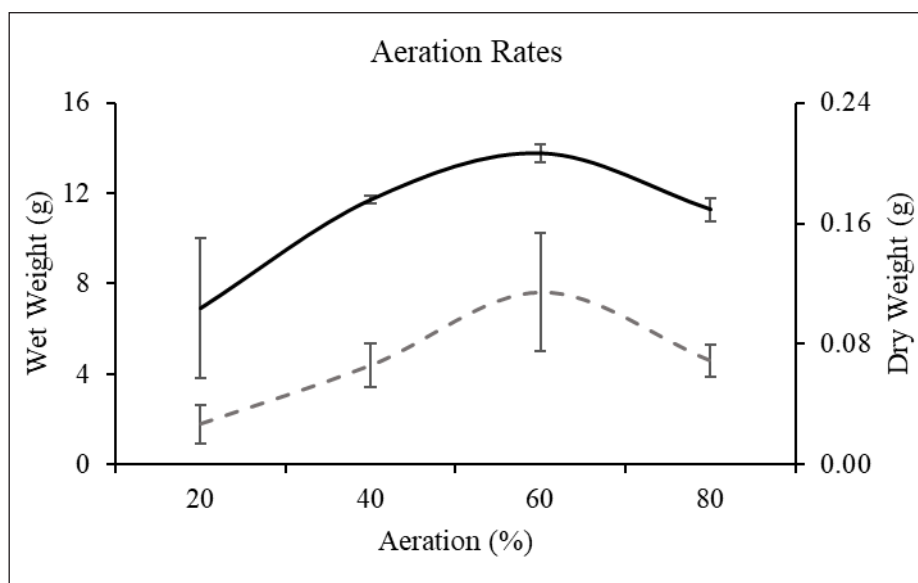


Figure 3. BC production by *K. sucrofermentans* under varying aeration rates ranging from 20% to 80%. The graph shows the weight of BC; The smooth line denotes the wet weight of BC, and the dashed line denotes the dry weight of BC

The highest wet and dry weights obtained from the fermentation culture were at 60% aeration, with approximately 13.7 g and 0.115 g, respectively. In contrast, wet BC obtained from other aeration levels ranged from 6.0 g to 11.7 g, and dry BC ranged from 0.2 g to 0.6 g—both significantly lower than the BC produced with 60% aeration. The production of BC exhibited an increase at 60% aeration but declined as aeration levels increased to 80%.

The aeration rate exhibits the least significant impact, as shown in Table 3. A notable difference in BC production is observed between 20% and 60% aeration, but this effect is primarily evident in wet BC. In contrast, the aeration rate does not have a measurable influence on the characteristics of the BC membrane once it has dried. The lack of significance observed in dry weight may be attributed to the close variance in dry BC between 20%, 40% and 80%, which were close to each other (20%, $\sigma^2 = 0.00017$; 40%, $\sigma^2 = 0.00021$; 80%, $\sigma^2 = 0.00012$). Following the principles outlined in "Understanding Analysis of Variance" by Natoli (2017), the variance within or between factors influences the statistical significance of parameters.

Low aeration reduces efficiency and limits the biosynthesis of BC by *K. sucrofermentans* while excessive aeration can prove detrimental due to oxygen saturation (Shavyrkina et al., 2021). In such instances, surplus oxygen acts as a proton acceptor, converting glucose to gluconic acid, thus reducing cellulose production (Tantratian et al., 2005). Hence, optimizing the balance between media culture and aeration is crucial for enhancing cellulose synthesis and obtaining a higher yield of BC.

Table 3

Post hoc Tukey test, comparison between the mean of each aeration rate to the production of BC

Wet BC	k	df	q	T
	4	4	5.757	6.437
Aeration (%)	$\bar{x}_1 - \bar{x}_2$		*Significant diff.	
20v40	4.783		q<6.437	
20v60	6.838		q>6.437	
20v80	4.357		q<6.437	
40v60	2.055		q<6.437	
40v80	0.426		q<6.437	
60v80	2.481		q<6.437	
Dry BC	k	df	q	T
	4	4	5.757	0.0918
Aeration (%)	$\bar{x}_1 - \bar{x}_2$		*Significant diff.	
20v40	0.0389		q<0.0918	
20v60	0.0876		q<0.0918	
20v80	0.0420		q<0.0918	
40v60	0.0487		q<0.0918	
40v80	0.0031		q<0.0918	
60v80	0.0456		q<0.0918	

*q-value < T-value has no significant difference

The Production of Bacterial Cellulose in Agitated Culture and Static Culture

Agitation was conducted at 50 rpm, 150 rpm, and 250 rpm; however, shaken cultures at 150 rpm and 250 rpm did not yield any BC. A comparison was made between static conditions and cultures shaking at 50 rpm, revealing that shaken cultures produced higher amounts of BC than static cultures (0 rpm) (Figure 4).

The average weight of wet and dry BC obtained from 50 rpm shaken culture was 14.97 g and 0.09 g, respectively. The average weight of wet BC gained from static culture (0rpm) was 10.75 g, while dry BC had an average of 0.07g. These results indicate that BC derived from shaken cultures at 50 rpm exhibits a higher yield compared to that from static cultures, both in wet and dry forms. There was a significant difference between each agitation (wet weight BC; $p=0.00141$, dry weight $p=0.0199$, $p\text{-value}<0.05$). Agitation helps distribute nutrients evenly and supply oxygen efficiently, which improved the synthesis of BC by *K. sucrofermentans* in a 50 rpm shaken culture (Zhou et al., 2018). Static culture has lower production compared to agitated culture due to the limited oxygen supplied to the bacteria (Ul-Islam et al., 2015). This shows that agitated culture can be used to mass-produce bacterial cellulose (Lahiri et al., 2021; Rahman et al., 2021). Nonetheless, as the shaking went higher, the production of BC was inhibited, and an intense cloudy solution

was produced. This results in failing to achieve cellulose for any cellulose above 50 rpm agitation. As Rahman et al. (2021) reported, acetic acid bacteria have more difficulties producing BC in agitated culture. Agitation during fermentation promotes the development of non-producing cellulose mutant cells (Cel-) in response to shear stress, consequently reducing their metabolic performance (Jasme et al., 2022; Raghavendran et al., 2020). A similar observation could be made in the culture of the *K. sucrofermentans* strain at higher shaking rates when it failed to produce cellulose.

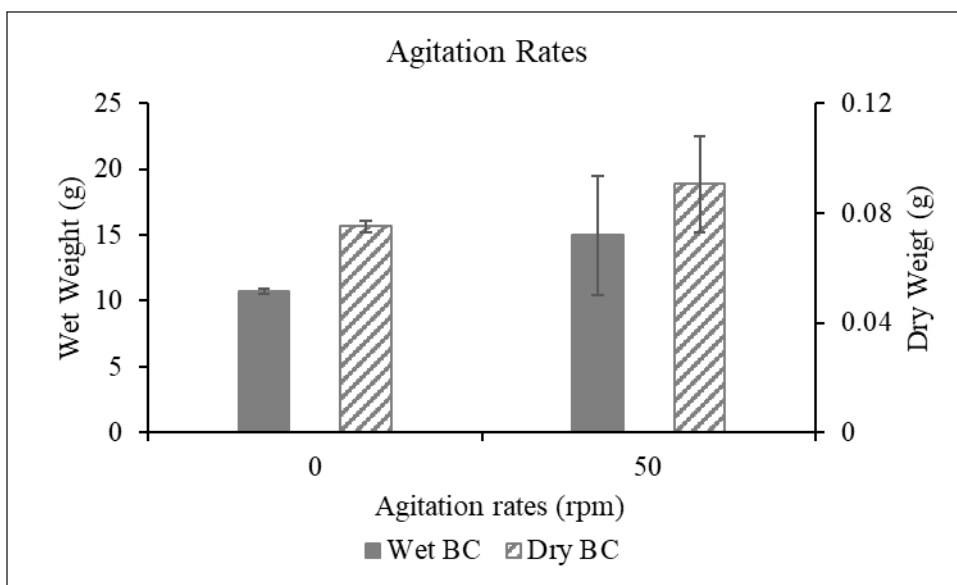


Figure 4. Production of BC by *K. sucrofermentans* in static culture and slow agitated culture. The graph shows the weight of BC; the fill bar graph denotes the wet weight of BC; and the diagonal stripes bar denotes the dry weight of BC

The Production of Bacterial Cellulose in Different Surface Areas

The surface area (SA) parameter was added to observe the effect of different areas on the efficiency of BC production by *K. sucrofermentans*. Larger surface areas yield the highest amount of BC and result in much larger BC membranes compared to other surface areas (Figure 5). The size of BC membranes across different surface areas is detailed in Table 4.

Maximum BC produced was on large SA (63.62 cm²), obtained about 17.61 g of wet BC and 0.14 g of dry BC. Smaller SA (19.63 cm²) yields the lowest BC at about 2.66 g for wet BC and only obtained 0.011 g for dry BC (Figure 5). The size of the BC membrane can be seen differently across the surface areas. The BC membrane was smaller when fermented in 19.63cm². When dried, it shrunk into much smaller pieces, as displayed in Table 4. BC production increases as surface areas increase. Larger surface areas provide more nutrient content and supply more oxygen, which improves the metabolic process of

K. sucrofermentans in producing BC (Abou-Taleb & Galal, 2018; Abusham et al., 2009). This can be seen in Table 4, where the BC membrane in a large surface area (63.63 cm²) exhibits a thicker membrane, looking opaque compared to other surface areas of culture fermentation. The effects on the surface area are highly significant and distinctly varied (Wet BC; $p=0.00047$, Dry BC $p=1.88E-07$; $p<0.05$). This can be seen in Table 5.

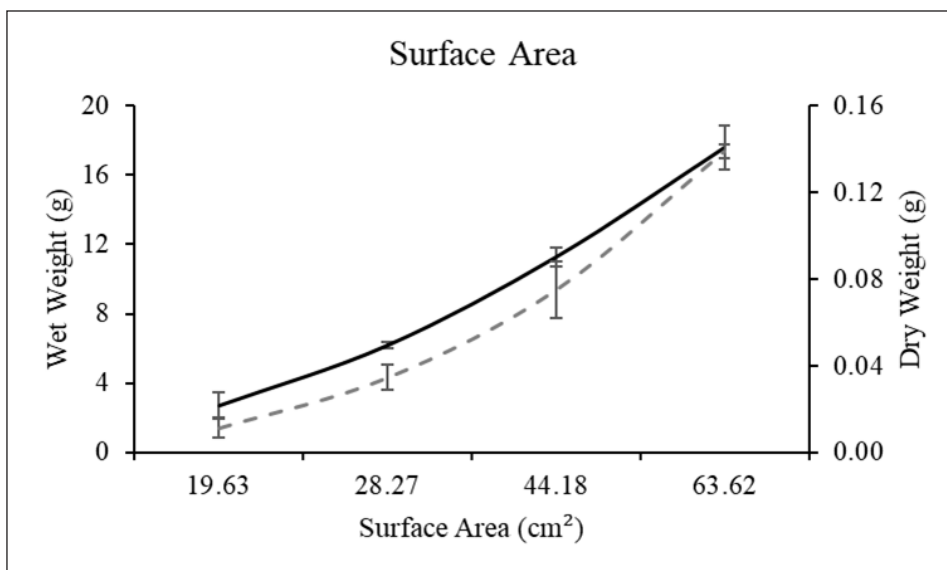
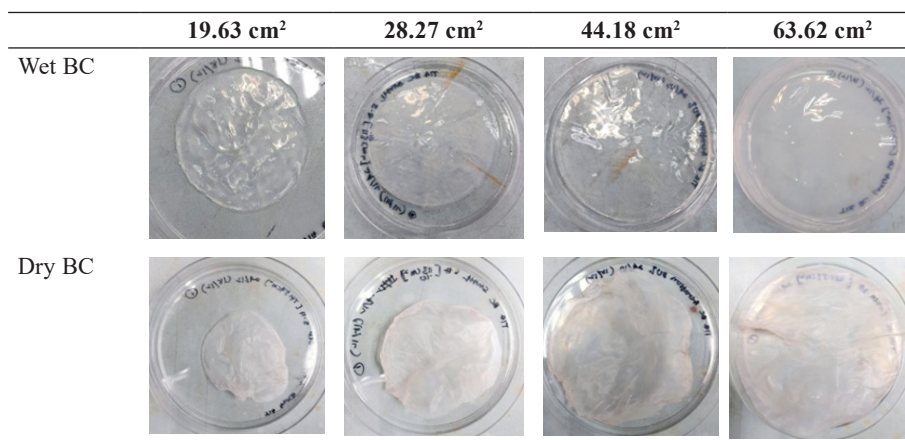


Figure 5. BC production by *K. sucrofermentans* with different surface areas from 19.63 cm² to 63.62 cm². The graph shows the weight of BC; The smooth line denotes the wet weight of BC, and the dashed line denotes the dry weight of BC

Table 4

The wet and dry membranes of BC were harvested from different surface area cultures after 7 days of fermentation



The post-hoc test for surface area revealed a statistically significant difference in cellulose production efficiency for both wet and dry BC. This finding suggests that variations in surface area significantly impact the efficiency of cellulose production by bacteria. This suggests that BC yields vary based on surface areas. Larger surface areas demonstrate greater efficiency in mass-producing BC, providing evidence that this parameter can be further optimized for production on a larger scale in an industrial setting.

Table 5

The Post hoc Tukey test compares the mean of each surface area to the production of BC. $A=19.63 \text{ cm}^2$
 $B=28.27 \text{ cm}^2$ $C= 44.18 \text{ cm}^2$ $D=63.62 \text{ cm}^2$

Wet BC	k	df	q	T
	4	8	4.529	7.094
Surface Area (cm ²)		$ \bar{x}_1 - \bar{x}_2 $		*Significant diff.
AvB		3.497		q<7.094
AvC		11.615		q>7.094
AvD		14.953		q>7.094
BvC		8.118		q>7.094
BvD		11.455		q>7.094
CvD		3.338		q<7.094
Dry BC	k	df	q	T
	4	8	4.529	0.0202
Surface Area (cm ²)		$ \bar{x}_1 - \bar{x}_2 $		*Significant diff.
AvB		0.023		q>0.0202
AvC		0.064		q>0.0202
AvD		0.128		q>0.0202
BvC		0.040		q>0.0202
BvD		0.104		q>0.0202
CvD		0.064		q>0.0202

*q-value < T-value has no significant difference

CONCLUSION

Physical conditions play a vital role in influencing the production of BC. This study examined various parameters to ascertain the optimal conditions for BC production. Based on the maximum yield observed across different parameters, conditions that enhance the synthesis of bacterial cellulose (BC) were identified: pH 5, temperature of 20°C, aeration rates of 60%, shaking rates at 50 rpm, and surface areas ($\geq 63.62 \text{ cm}^2$). Through ANOVA analysis, each parameter was found to significantly influence BC production. The physical parameters influencing BC production are crucial; failing to maintain optimal conditions diminishes bacterial activity, as evidenced by fluctuations in factors like pH and

temperature. As these factors deviate from their optimal ranges, the efficiency of cellulose synthesis declines, which can lead to lower production of cellulose. This important finding on physical characterization has the potential to significantly enhance cellulose production efficiency by *K. sucrofermentans* at an industrial scale.

ACKNOWLEDGEMENT

The invaluable support and resources provided by the Enzyme and Microbial Technology Research Centre (EMTech), Faculty of Biotechnology and Biomolecular Sciences, UPM and the Institute of Bioscience, UPM are deeply appreciated. The authors would like to thank Prof. Emeritus Dato' Dr. Abu Bakar Salleh for the valuable editorial contributions given as an internal reviewer.

REFERENCES

- Abou-Taleb, K. A., & Galal, G. F. (2018). A comparative study between one-factor-at-a-time and minimum runs resolution-IV methods for enhancing the production of polysaccharide by *Stenotrophomonas daejeonensis* and *Pseudomonas geniculata*. *Annals of Agricultural Sciences*, 63(2), 173–180. <https://doi.org/10.1016/j.aosas.2018.11.002>
- Abusham, R. A., Rahman, R. N. Z. R., Salleh, A. B., & Basri, M. (2009). Optimization of physical factors affecting the production of thermo-stable organic solvent-tolerant protease from a newly isolated halo tolerant *Bacillus subtilis* strain rand. *Microbial Cell Factories*, 8, Article 20. <https://doi.org/10.1186/1475-2859-8-20>
- Aswini, K., Gopal, N. O., & Uthandi, S. (2020). Optimized culture conditions for bacterial cellulose production by *Acetobacter senegalensis* MA1. *BMC Biotechnology*, 20(46), 1-16. <https://doi.org/10.1186/s12896-020-00639-6>
- Barja, F. (2021). Bacterial nanocellulose production and biomedical applications. *Journal of Biomedical Research*, 35(4), 310-317. <https://doi.org/10.7555/JBR.35.20210036>
- Bhaturiwala, R., Bagban, M., Mansuri, A., & Modi, H. (2022). Successive approach of medium optimization using one-factor-at-a-time and response surface methodology for improved β -mannanase Production from *Streptomyces* sp. *Bioresource Technology Reports*, 18, Article 101087. <https://doi.org/10.1016/j.biteb.2022.101087>
- Bianchet, R. T., Cubas, A. L. V., Machado, M. M., & Moecke, E. H. S. (2020). Applicability of bacterial cellulose in cosmetics - Bibliometric review. *Biotechnology Reports*, 27, Article e00502. <https://doi.org/10.1016/j.btre.2020.e00502>
- Bodea, I. M., Beteg, F., Pop, C., David, A., Dudescu, M. C., Vilău, C., Stănilă, A., Rotar, A. M., & Cătunescu, G. M. (2021). *Optimization of Moist and Oven-Dried Bacterial Cellulose Production for Functional Properties*. Research Square. <https://doi.org/10.21203/rs.3.rs-203952/v1>
- Buldum, G., Bismarck, A., & Mantalaris, A. (2018). Recombinant biosynthesis of bacterial cellulose in genetically modified *Escherichia coli*. *Bioprocess Biosystems Engineering*, 41, 265-279. <https://doi.org/10.1007/s00449-017-1864-1>

- Campano, C., Balea, A., Blanco, Á., & Negro, C. (2015). Enhancement of the fermentation process and properties of bacterial cellulose: A review. *Cellulose*, 23(1), 57-91. <https://doi.org/10.1007/s10570-015-0802-0>
- Cannazza, P., Rissanen, A. J., Guizelini, D., Losoi, P., Sarlin, E., Romano, D., Santala, V., & Mangayil, R. (2021). Characterization of *Komagataeibacter* isolate reveals new prospects in waste stream valorization for bacterial cellulose production. *Microorganisms*, 9(11), Article 2230. <https://doi.org/10.3390/microorganisms9112230>
- Choi, S. M., Rao, K. M., Zo, S. M., Shin, E. J., & Han, S. S. (2022). Bacterial cellulose and its applications. *Polymers*, 14(6), Article 1080. <https://doi.org/10.3390/polym14061080>
- Clews, R. J. (2016). Fundamentals of the petroleum industry. In R. J. Clews (Ed.), *Project Finance for the International Petroleum Industry* (pp. 83-99). Academic Press. <https://doi.org/10.1016/b978-0-12-800158-5.00005-0>
- Coseri, S. (2021). Insights on cellulose research in the last two decades in Romania. *Polymers*, 13(5), Article 689. <https://doi.org/10.3390/polym13050689>
- Cumming, G., Fidler, F., & Vaux, D. L. (2007). Error bars in experimental biology. *The Journal of Cell Biology*, 177(1), 7–11. <https://doi.org/10.1083/jcb.200611141>
- da Gama, F. M. P., & Dourado, F. (2018). Bacterial nanocellulose: What future? *BioImpacts: BI*, 8(1), 1–3. <https://doi.org/10.15171/bi.2018.01>
- Deshpande, P., Wankar, S., Mahajan, S., Patil, Y., Rajwade, J. M., & Kulkarni, A. (2023). Bacterial cellulose: Natural biomaterial for medical and environmental applications. *Journal of Natural Fibers*, 20(2), Article 2218623. <https://doi.org/10.1080/15440478.2023.2218623>
- Grand View Research. (2021). *Nanocellulose market size, share & trends analysis report by type (cellulose nanofibers, bacterial cellulose, crystalline nanocellulose), by application, by region, and segment forecasts, 2023 - 2030*. Grand View Research. <https://www.grandviewresearch.com/industry-analysis/nanocellulose-market>
- Gomes, R. J., Borges, M. F., Rosa, M. F., Castro-Gómez, R. J. H., & Spinosa, W. A. (2018). Acetic acid bacteria in the food industry: Systematics, characteristics and applications. *Food Technology and Biotechnology*, 56(2), 139–151. <https://doi.org/10.17113/ftb.56.02.18.5593>
- Gupta, S., & Pathak, B. (2020). Mycoremediation of polycyclic aromatic hydrocarbons. In P. Singh, A. Kumar, A. Borthakur (Eds.), *Abatement of Environmental Pollutants: Trends and Strategies* (pp. 127-149). Elsevier. <https://doi.org/10.1016/b978-0-12-818095-2.00006-0>
- Hasanin, M. S., Abdelraof, M., Hashem, A. H., & Saied, H. E. (2023). Sustainable bacterial cellulose production by *Achromobacter* using mango peel waste. *Microbial Cell Factories*, 22, Article 24. <https://doi.org/10.1186/s12934-023-02031-3>
- Hwang, J. W., Yang, Y. K., Hwang, J. K., Pyun, Y. R., & Kim, Y. S. (1999). Effects of pH and dissolved oxygen on cellulose production by *Acetobacter xylinum* BRC5 in agitated culture. *Journal of Bioscience and Bioengineering*, 88(2), 183-188. [https://doi.org/10.1016/s1389-1723\(99\)80199-6](https://doi.org/10.1016/s1389-1723(99)80199-6)

- Ivancic, T., Jamnik, P., & Stopar, D. (2013). Cold shock CSPA and CSPB protein production during periodic temperature cycling in *Escherichia coli*. *BMC Research Notes*, 6, Article 248. <https://doi.org/10.1186/1756-0500-6-248>
- Jakob, M., Mahendran, A. R., Gindl-Altmutter, W., Bliem, P., Konnerth, J., Müller, U., & Veigel, S. (2022). The strength and stiffness of oriented wood and cellulose-fibre materials: A review. *Progress in Materials Science*, 125, Article 100916. <https://doi.org/10.1016/j.pmatsci.2021.100916>
- Jasme, N., Elangovan, J., Yahya, A. M., Noh, N. M. & Bustami, Y. (2022). First report of biocellulose production by an indigenous yeast, *Pichia kudriavzevii* USM-YBP2. *Green Processing and Synthesis*, 11, 458-477. <https://doi.org/10.1515/gps-2022-0023>
- Kiziltas, E. E., Kiziltas, A., & Gardner, D. J. (2015). Synthesis of bacterial cellulose using hot water extracted wood sugars. *Carbohydrate Polymers*, 124, 131-138. <https://doi.org/10.1016/j.carbpol.2015.01.036>
- Krusong, W., Pothimon, R., La China, S., & Thompson, A. K. (2021). Consecutive bacterial cellulose production by luffa sponge enmeshed with cellulose microfibrils of *Acetobacter xylinum* under continuous aeration. *3 Biotech*, 11, Article 6. <https://doi.org/10.1007/s13205-020-02569-8>
- Lahiri, D., Nag, M., Dutta, B., Dey, A., Sarkar, T., Pati, S., Edinur, H. A., Kari, Z. A., Noor, N. H. M., & Ray, R. R. (2021). Bacterial cellulose: Production, characterization, and application as antimicrobial agent. *International Journal of Molecular Sciences*, 22(23), Article 12984. <https://doi.org/10.3390/ijms222312984>
- Marič, L., Cleenwerck, I., Accetto, T., Vandamme, P., & Trček, J. (2020). Description of *Komagataeibacter melaceti* sp. nov. and *Komagataeibacter melomenus* sp. nov. isolated from apple cider vinegar. *Microorganisms*, 8(8), Article 1178. <https://doi.org/10.3390/microorganisms8081178>
- Martins, D. A. B., do Prado, H. F. A., Leite, R. S. R., Ferreira, H., de Souza Moretti, M. M., da Silva, R., & Gomes, E. (2011). Agroindustrial wastes as substrates for microbial enzymes production and source of sugar for bioethanol production. In S. Kumar (Ed.), *Integrated Waste Management – Volume II* (pp. 319-360). InTech. <https://doi.org/10.5772/23377>
- Moniri, M., Moghaddam, A. B., Azizi, S., Rahim, R. A., Ariff, A., Saad, W. Z., Navaderi, M., & Mohamad, R. (2017). Production and status of bacterial cellulose in biomedical engineering. *Nanomaterials*, 7(9), Article 257. <https://doi.org/10.3390/nano7090257>
- Nagmetova, G., Berthold-Pluta, A., Garbowska, M., Kurmanbayev, A., & Stasiak-Róžańska, L. (2020). Antibacterial activity of biocellulose with oregano essential oil against *Cronobacter* Strains. *Polymers*, 12(8), Article 1647. <https://doi.org/10.3390/polym12081647>
- Naomi, R., Idrus, R., & Fauzi, M. B. (2020). Plant- vs. bacterial-derived cellulose for wound healing: A review. *International Journal of Environmental Research and Public Health*, 17(18), Article 6803. <https://doi.org/10.3390/ijerph17186803>
- Natoli, C. (2017). *Understanding Analysis of Variance: Best Practice* (Report No. 29). Scientific Test & Analysis Techniques Center of Excellence.
- Pa'e, N., Hui, C. C., & Muhamad, I. I. (2007, January 4-6). Shaken culture fermentation for production of microbial cellulose from pineapple waste. In *Proceeding of International Conference on Waste to Wealth* (pp. 26-28). Kuala Lumpur, Malaysia.

- Park, S., Baker, J.O., Himmel, M.E., Parilla, P. A., & Johnson, D. K. (2010). Cellulose crystallinity index: Measurement techniques and their impact on interpreting cellulase performance. *Biotechnology Biofuels*, 3, Article 10. <https://doi.org/10.1186/1754-6834-3-10>
- Petroudy, S. R. D. (2017). Physical and mechanical properties of natural fibers. In F. Mizi & F. Feng (Eds.), *Advanced High Strength Natural Fibre Composites in Construction* (pp. 59-83). Woodhead Publishing. <https://doi.org/10.1016/b978-0-08-100411-1.00003-0>
- Pham, T. T., & Tran, T. T. A. (2023). Evaluation of the crystallinity of bacterial cellulose produced from pineapple waste solution by using *Acetobacter xylinum*. *ASEAN Engineering Journal*, 13(2), 81-91. <https://doi.org/10.11113/aej.v13.18868>
- Poyrazoğlu, E., Bıyık, H. H., & Çetin, Ö. (2021). Environmentally friendly bacterial cellulose films for food packaging. *Eurasian Journal of Food Science and Technology*, 5(2), 127-135.
- Raghavendran, V., Asare, E., & Roy, I. (2020). Bacterial cellulose: Biosynthesis, production, and applications. In R. K. Poole (Ed.), *Advances in Microbial Physiology* (pp. 89-138). Academic Press. <https://doi.org/10.1016/bs.ampbs.2020.07.002>
- Rahman, S. S. A., Vaishnavi, T., Vidyasri, G. S., Sathya, K., Priyanka, P., Venkatachalam, P., & Karuppiah, S. (2021). Production of bacterial cellulose using *Gluconacetobacter kombuchae* immobilized on *Luffa aegyptiaca* support. *Scientific Reports*, 11(1), Article 2912. <https://doi.org/10.1038/s41598-021-82596-4>
- Rangaswamy, B. E., Vanitha, K. P., & Hungund, B. S. (2015). Microbial cellulose production from bacteria isolated from rotten fruit. *International Journal of Polymer Science*, 1, Article 280784. <https://doi.org/10.1155/2015/280784>
- Reshmy, R., Philip, E., Thomas, D., Madhavan, A., Sindhu, R., Binod, P., Varjani, S., Awasthi, M. K., & Pandey, A. (2021). Bacterial nanocellulose: Engineering, production, and applications. *Bioengineered*, 12(2), 11463-11483. <https://doi.org/10.1080/21655979.2021.2009753>
- Samanta, C., & Das, R. K. (2021). C3-based petrochemicals: Recent advances in processes and catalysts. In K. K. Pant, K. G. Sanjay & A. Ejaz (Eds.), *Catalysis for Clean Energy and Environmental Sustainability* (pp. 149-204). Springer. https://doi.org/10.1007/978-3-030-65021-6_5
- Shavyrkina, N. A., Skiba, E. A., Kazantseva, A. E., Gladysheva, E. K., Budaeva, V. V., Bychin, N. V., Gismatulina, Y. A., Kashcheyeva, E. I., Mironova, G. F., Korchagina, A. A., Pavlov, I. N., & Sakovich, G. V. (2021). Static culture combined with aeration in biosynthesis of bacterial cellulose. *Polymers*, 13(23), Article 4241. <https://doi.org/10.3390/polym13234241>
- Siew, K. W. (2012). Enhancement of biocellulose production in mixed medium culture. [Undergraduates Project Papers]. Universiti Malaysia Pahang, Malaysia. <http://umpir.ump.edu.my/id/eprint/4481>
- Swingler, S., Gupta, A., Gibson, H., Kowalczyk, M., Heaselgrave, W., & Radecka, I. (2021). Recent advances and applications of bacterial cellulose in biomedicine. *Polymers*, 13(3), Article 412. <https://doi.org/10.3390/polym13030412>
- Tajik, A., Samadlouie, H. R., Farrokhi, A. S., & Ghasemi, A. (2024). Optimization of chemical conditions for metabolites production by *Ganoderma lucidum* using response surface methodology and investigation of antimicrobial as well as anticancer activities. *Frontiers in Microbiology*, 14, Article 1280405. <https://doi.org/10.3389/fmicb.2023.1280405>

- Tantratian, S., Tammarate, P., Krusong, W., Bhattarakosol, P., & Phunsri, A. (2005). Effect of dissolved oxygen on cellulose production by *Acetobacter* sp. *Journal of Scientific Research of Chulalongkorn University*, 30(2), 179-186.
- Trache, D. (2018). Nanocellulose as a promising sustainable material for biomedical applications. *AIMS Materials Science*, 5(2), 201–205. <https://doi.org/10.3934/matricsci.2018.2.201>
- Trache, D., Tarchoun, A. F., Derradji, M., Mehelli, O., Hussin, M. H., & Bessa, W. (2020). Cellulose fibers and nanocrystals: Preparation, characterization, and surface modification. In K. Vineet., G. Praveen, D. Nandita, & R. Shivendu (Eds.), *Functionalized Nanomaterials* (pp.171–190). CRC Press. <https://doi.org/10.1201/9781351021623-11>
- Ul-Islam, M., Khan, S., Ullah, M. W., & Park, J. K. (2015). Bacterial cellulose composites: Synthetic strategies and multiple applications in bio-medical and electro-conductive fields. *Biotechnology Journal*, 10(12), 1847–1861. <https://doi.org/10.1002/biot.201500106>
- Victor, R., Elena, Li., Maria, N., Alena, B., & Mikhail, S. (2018). Cost-effective production of bacterial cellulose using acidic food industry by-products. *Brazilian Journal of Microbiology*, 49, 151-159. <https://doi.org/10.1016/j.bjm.2017.12.012>
- Volova, T. G., Shumilova, A. A., Shidlovskiy, I. P., Nikolaeva, E. D., Sukovatiy, A. G., Vasiliev, A. D., & Shishatskaya, E. I. (2018). Antibacterial properties of films of cellulose composites with silver nanoparticles and antibiotics. *Polymer Testing*, 65, 54-68. <https://doi.org/10.1016/j.polymertesting.2017.10.023>
- Watanabe, A., Morita, S., & Ozaki, Y. (2007). Temperature-dependent changes in hydrogen bonds in cellulose I α studied by infrared spectroscopy in combination with perturbation-correlation moving-window two-dimensional correlation spectroscopy: Comparison with cellulose I β . *Biomacromolecules*, 8(9), 2969-2975. <https://doi.org/10.1021/bm700678u>
- Zakaria, J., & Nazeri, A. (2012, July 10-12). *Optimization of Bacterial Cellulose Production from Pineapple Waste: Effect of Temperature, pH and Concentration*. [Paper presentation]. In Engineering Conference 2012, 5th Engineering Conference, Kuching, Sarawak, Malaysia
- Zhou, Y., Han, L. R., He, H. W., Sang, B., Yu, D. L., Feng, J. T., & Zhang, X. (2018). Effects of agitation, aeration and temperature on production of a novel glycoprotein GP-1 by *Streptomyces kanasensis* ZX01 and scale-up based on volumetric oxygen transfer coefficient. *Molecules*, 23(1), Article 125. <https://doi.org/10.3390/molecules23010125>

Investigation of Partial Discharge Characteristics in Mineral Oil Induced by Dibenzyl Disulfide

Amran Mohd Selva¹, Norhafiz Azis^{1*}, Muhammad Umair Tariq¹,
Mohd Zainal Abidin Ab Kadir¹, Jasronita Jasni¹ and Hidayat Zainuddin²

¹Advanced Lightning, Power and Energy Research Centre (ALPER), Universiti Putra Malaysia, 43400 UPM, Serdang, Selangor, Malaysia

²Faculty of Electrical Engineering, Universiti Teknikal Malaysia Melaka, Durian Tunggal 76100, Melaka, Malaysia

ABSTRACT

In this paper, an experimental study is carried out to investigate the partial discharge (PD) characteristic based on phase-resolved partial discharge (PRPD) and partial discharge inception voltage (PDIV) in mineral oil (MO) in the presence of dibenzyl disulfide (DBDS). MOs with different DBDS concentrations were aged at 150 °C for 5 days. Several parameters of the MO were measured, such as AC breakdown voltage, PDIV, apparent charge, average charge and PD repetition rate based on the needle-sphere, needle-plane and plane-plane electrode configurations. The AC breakdown voltage of aged MO displays a decrement pattern as the concentration of DBDS in the oil increases for all electrode configurations and gap distances. The average apparent charge of aged MO depicts an increment pattern in the presence of DBDS, whereas the PD repetition rate of aged MO displays variations of patterns for all electrode configurations. The PDIV of aged MOs shows an increment pattern at a 10 mm gap distance for all electrode configurations in the presence of DBDS. In contrast, the increment pattern of aged MOs is only observed for plane-plane electrode configuration at a 20 mm gap distance in the presence of DBDS. PDs occur predominantly

at negative peak half-wave between the 3rd to 4th quadrants and are undetectable at positive half-wave in base and aged MO for all electrode configurations.

ARTICLE INFO

Article history:

Received: 30 June 2024

Accepted: 24 December 2024

Published: 07 March 2025

DOI: <https://doi.org/10.47836/pjst.33.2.17>

E-mail addresses:

gs61085@student.upm.edu.my (Amran Mohd Selva)

norhafiz@upm.edu.my (Norhafiz Azis)

gs65418@student.upm.edu.my (Muhammad Umair Tariq)

mzk@upm.edu.my (Mohd Zainal Abidin Ab Kadir)

jas@upm.edu.my (Jasronita Jasni)

hidayat@utem.edu.my (Hidayat Zainuddin)

*Corresponding author

Keywords: Dibenzyl disulfide, partial discharge inception voltage, phased-resolved partial discharge

INTRODUCTION

The threat posed by the formation of corrosive sulphur on the transformer has

gained more attention over the past decades due to the increasing number of failures (Amaro, 2015; Cong et al., 2021; Khiar et al., 2020; Vahidi & Tenbohlen, 2015). Generally, copper conductors can react with sulphur in mineral oil (MO) to form semi-conductive copper sulphide (Cu_2S) on the surface of the copper and insulating paper (eCIGRE, 2009; Yuan et al., 2022). Dibenzyl disulfide (DBDS) is an organic sulphur compound from the disulphide group commonly found in transformer's MO, which is considered a highly corrosive and a major cause of Cu_2S formation (Rehman et al., 2016). Cu_2S deposited on the winding can weaken the strength of the oil–paper insulation, and without mitigation, it can lead to failures (Hu et al., 2016; Yang et al., 2022). Sulphur compounds in the MO are usually present during the refining process of petroleum, which contains a high percentage of sulphur (Jadim et al., 2020; Rehman et al., 2016). The presence of Cu_2S and other corrosive by-products, i.e., copper oxide (Cu_2O), can accelerate the ageing process of oil-paper insulation (Cong et al., 2021). This phenomenon can lead to dielectric strength reduction, dielectric loss increment, and electrical discharge formation in oil-paper insulation due to the migration of Cu_2S (Liao et al., 2015; Yuan et al., 2022).

Dissolved gas analysis (DGA) is a common technique that can be used to analyse the issue related to corrosive sulphur in transformers (Amalanathan et al., 2023; Scatiggio et al., 2011). Other techniques that are used to evaluate the corrosive sulphur in transformer include gas chromatography electron capture detector, Fourier transform infrared spectroscopy, pyrolysis gas chromatography-mass spectrometry and covered conductor deposit (Jadim et al., 2020; Rehman et al., 2017). Fourier transform infrared spectroscopy can effectively detect the concentration of DBDS higher than 1.5% (Cong et al., 2018; Khan & Rajan, 2015). Gas chromatography-mass spectrometry is highly sensitive towards DBDS along with total and mercaptan sulphur. The combination of these techniques with DGA can be useful to understand the migration of DBDS (Toyama et al., 2009). Presently, relevant international test standards can be used to detect the corrosivity in oil, including DIN 51353, ISO 5662, ASTM D1275A, ASTM D1275B and IEC 62535-2008 standards. The corrosiveness of MO can be evaluated based on ASTM D 130/TP 154 standard. However, different standards may lead to different interpretations of the condition of MO (Khiar et al., 2019; Gao et al., 2019). Partial discharge (PD), frequency domain spectroscopy, frequency response analysis, polarisation depolarisation current, and recovery voltage are among alternative methods that can be used to evaluate the corrosive sulphur issue in oil-paper insulation (Bramantyo et al., 2014; Cong et al., 2024; Flora & Rajan, 2016).

The phenomenon of PD in dielectric insulating fluid is inherently random and involves complex interactions with electrical, mechanical and thermal factors (Dixit & Samarasinghe, 2019; Jin et al., 2015). PD events can arise from localised electric field intensification due to the amplitude and waveform of the applied voltage, the distance between electrodes, the configuration of the electrodes, conductor defects, floating particles, bubbles and contaminants in dielectric insulating fluid (Sima et al., 2013). In dielectric

insulating fluid, the PD occurrence is more complex as electrons are unstable, forming and collapsing unpredictably under the influence of the electric field. Consequently, rapid bursts of PD pulses in dielectric insulating fluids can occur with increasing magnitude, which can be challenging to detect. The initiation of discharges in a low-density region of dielectric insulating fluids depends on the availability of electrons. The electrons can trigger an avalanche effect and subsequently streamer occurrence.

Several studies have previously been carried out to examine the impact of moisture and contaminants on the PD properties of MO. These contaminants can exist as either floating conductive or non-conductive particles. Other works also examine the PD due to ageing and oxidation by-products of oil-paper insulation. It is found that these contaminants can affect the PD properties of the MO, although the extent of its impact can vary depending on the voltage level and chemical composition. Previous studies demonstrate that moisture can reduce the PD magnitude at low voltage, which leads to a high partial discharge inception voltage (PDIV) (Liu et al., 2014; Pattanadech & Muhr, 2016). Conversely, at high voltage, the PD magnitude increases with the increment of the moisture. The presence of moisture can significantly affect the PD repetition rate. The PD pattern also shows apparent changes due to the increment of moisture. Another study shows that the PD induced by the bubbles in MO is predominantly concentrated at the negative half-wave (Tang et al., 2018). Additionally, negative PD generally exhibits a higher apparent charge than positive PD, regardless of whether the MO is flowing or stationary.

Generally, depending on their size and concentration, metallic particles can reduce the PDIV. It can also act as an initiation point for discharges and reduce AC breakdown voltage in the MO (Ma et al., 2019). Furthermore, the metallic particle can change PD characteristics and magnitude. Large particles can increase PD magnitude by offering more sites for discharges to initiate, while small particles may have less effect depending on their dispersion and interaction with the electric field. Research has shown that metallic particles can cause different PD patterns and discharge phenomena, impacting the oil-paper insulation's overall condition (Tang et al., 2018).

The main motivation of this study is to investigate the impact of DBDS on the dielectric strength and PD characteristics of MO. The aim of the research is to examine the feasibility of PD as an alternative technique to detect DBDS-induced corrosion in MO. First, the AC breakdown of base and aged MOs at different DBDS concentrations for needle-sphere, needle-plane and plane-plane electrode configurations at 10 mm and 20 mm gap distances are recorded and analysed. Next, the PD magnitude in terms of apparent charge (Q_{IEC}), average charge (Q_{AVG}), PD repetition rate and PDIV in MOs at various DBDS concentrations are compared with the base oil. PRPD of MOs at various DBDS concentrations is acquired for different electrode configurations and gap distances to investigate the shape and PD intensity, $H_n(\varphi)$.

METHODOLOGY

Material Preparation for Thermal Ageing

The overall framework of this experimental study can be seen in Figure 1. A test cell made of perspex with a height, width and depth of 2,200 mm × 100 mm × 100 mm and a volume capacity of 2,200 ml was used to investigate the PD characteristics in MO in the presence of DBDS. For needle-sphere electrode configuration, a needle with a tip radius of 200 μm was used as the high potential electrode, whereas a sphere with a diameter of 12.7 mm was set as the ground electrode. For needle-plane electrode configuration, a needle with a tip radius of 200 μm was used as the high potential electrode, whereas a plane with a diameter of 50 mm was set as the ground electrode. A plane with a 50 mm diameter was used as the high potential and ground electrodes for plane-plane electrode configuration. These configurations are designed to study PD characteristics. The needle-sphere and needle-plane configurations create a concentrated electric field at the needle's tip, intensifying electric field stress and simulating conditions for PD initiation. On the other hand, the plane-plane configuration offers a more uniform electric field, typically used to examine discharge activities under evenly distributed field conditions. The specifications of MO, Kraft paper, and copper conductor used in this experiment can be obtained from Selva et al. (2024). DBDS with 246.39 g/mol was used in this study to induce corrosivity in oil.

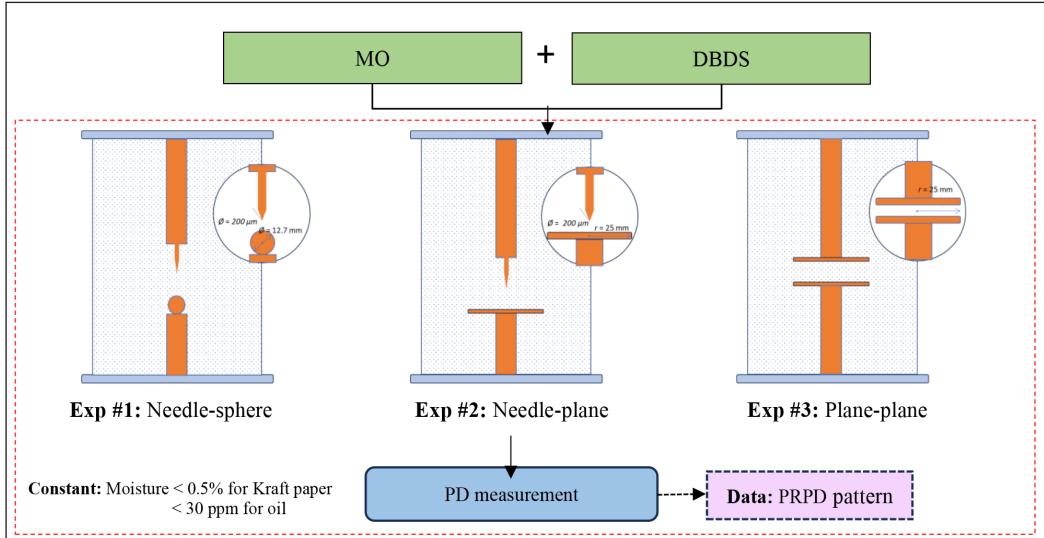


Figure 1. Overall framework of the study

In total, 4 samples were prepared for this experiment to investigate the scenarios described in Table 1. First, the MO was filtered based on a membrane filter with a pore size of 0.25 μm. Next, MO was dried in an air-circulating oven for 96 h at 85°C. Similarly, the

Kraft paper was dried for 48 hours at 105°C. The MO was subjected to nitrogen purging for 20 minutes to further reduce the moisture content. The moisture content of the Kraft paper and MO were determined based on the IEC 60814 standard, whereby the values were 0.1287% and 17 ppm. The copper conductor with height, width and depth of 100 mm × 15 mm × 3 mm was wound with dried Kraft paper with a width of 25 mm width for 10 layers in a half-lap configuration similar to the arrangement in the transformer, where half of the paper was overlapped with the next turn and in direct contact with the copper conductor as shown on Figure 2. DBDS was added to the 1,000 ml of MO at different weights of 1 g, 5 g and 10 g and mixed using a magnetic stirrer to create concentrations of 1,000, 5,000 and 10,000 ppm, respectively, as shown in Table 1. The wrapped copper conductor was then added to the oil with DBDS at room temperature for 12 hours. The samples were then thermally aged under sealed conditions for 5 days at 150°C in an oven with a closed cap to reduce contact with oxygen from the atmosphere.

Table 1
Experimental condition of the study

Experiment	Description	DBDS Weight (g)	DBDS concentration (PPM)	Experimental condition
1	Base MO	0	0	150°C, 5 days
2	Aged MO-DBDS#1	1	1,000	
3	Aged MO-DBDS#2	5	5,000	
4	Aged MO-DBDS#3	10	10,000	

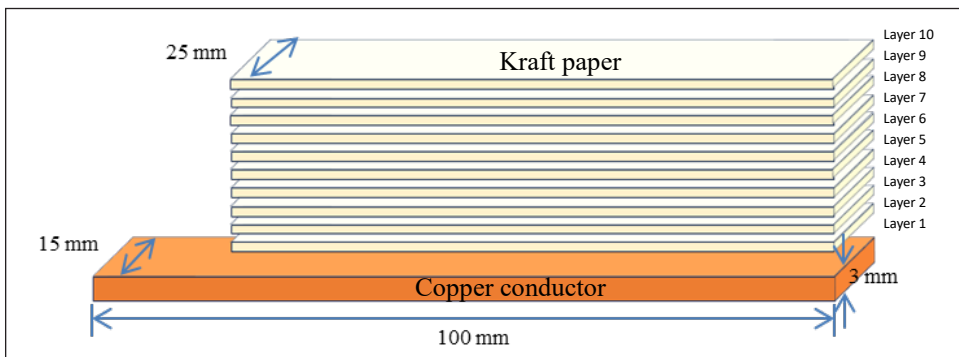


Figure 2. The cross-sectional area of paper-wrapped copper

Experimental Procedure

The test setup for AC breakdown voltage is shown in Figure 3. A PD-free transformer provided AC voltages up to 100 kV at 50 Hz. A protective resistor of 2 kΩ was placed to limit the breakdown current. The gap distances between the electrodes were set at 10 mm

and 20 mm. A small gap results in strong electric fields, which increases the likelihood of PDs, especially around sharp points in needle electrode configuration. This also reduces the voltage required to initiate PDs due to higher field stress. In contrast, a large gap reduces the field intensity and raises the inception voltage (Wang, 2011). These variations help in comparing how concentrated fields in needle-plane and needle-sphere electrode configurations differ from uniform fields in plane-plane electrode configuration, revealing valuable insights into insulation design and discharge characteristics under different conditions. The MO was poured carefully into the test cell and allowed to stand for at least 15 minutes before the voltage was applied. The voltage automatically increased by 1 kV per step until it broke down. The AC breakdown for each type of MO was recorded as a reference for the threshold voltage of PD measurement.

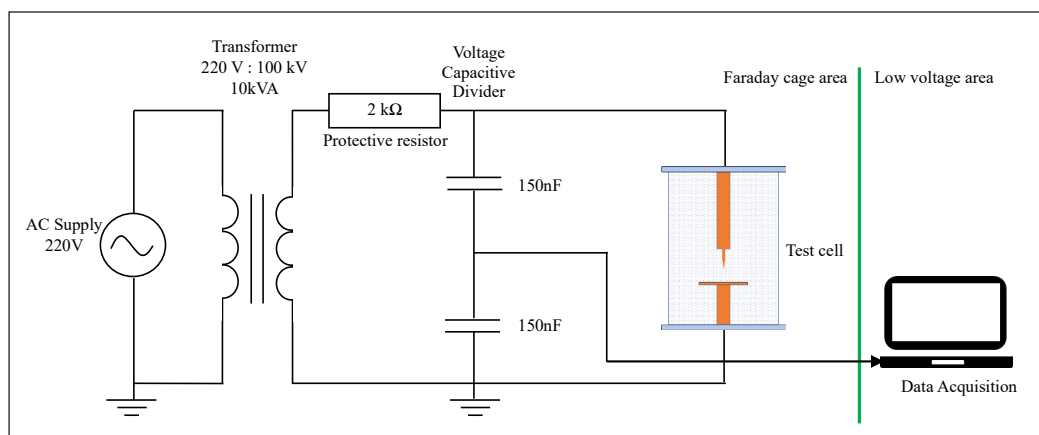


Figure 3. Schematic diagram of AC breakdown measurement

The PD characteristics were acquired through a conventional PD coupling circuit in accordance with IEC 61294 and IEC 60270 standards. The schematic diagram of PD measurement can be seen in Figure 4. A coupling capacitor of 1 nF was used to provide a displacement current. The setup can provide additional information about the test voltage needed for the PRPD analysis. The maximum apparent charge of the background noise was registered at less than 600 fC. The PD detection system was calibrated based on the IEC 60270 standard, where an external charge of 20 pC value was injected into the system, which simulated a PD event, and its amplitude was used as a reference scale. The 70% and 90% AC breakdown voltage for each of the MO samples was used as a reference for the threshold voltage for PD measurement. The step voltage of 1 kV was applied automatically via an AC high voltage controller until it reached the peak voltage, whereby the time interval between each of the voltages was set to 30 s. A wide bandwidth PD detector recorded the PD signals continuously for 1 min once it reached the required voltage. In this study, the

lowest voltage at which the maximum amplitude of PD signals reached 10 pC was defined as the PDIV. The PD charge (q) was determined through the integration of the PD current ($i(t)$) over the PD time interval, as shown in Equation 1.

$$q = \int_{t_1}^{t_2} i(t) dt \quad [1]$$

Here, q represents the charge, $i(t)$ denotes the current, and t_1 and t_2 indicate the start and end times of the discharge pulse, respectively.

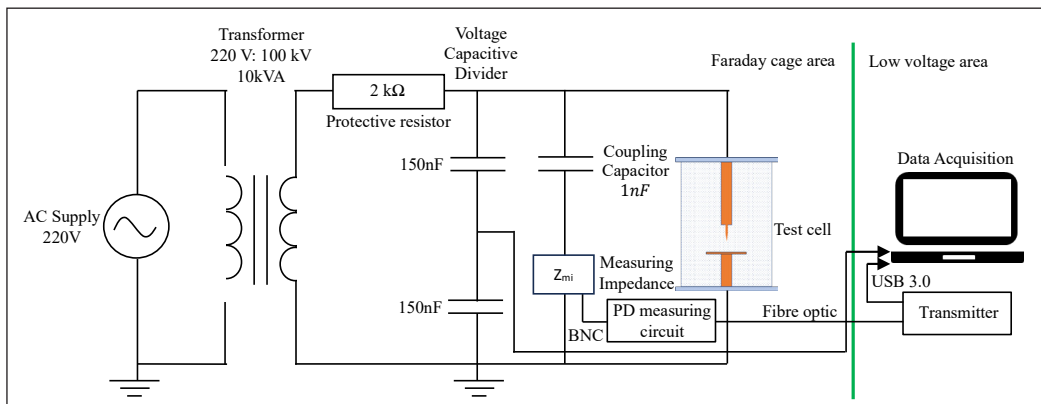


Figure 4. Schematic diagram of partial discharge measurement

RESULTS AND DISCUSSION

Effect of DBDS on AC Breakdown Voltage

The reductions of AC breakdown voltages for aged MO in the presence of DBDS are quite apparent for needle-sphere and needle-plane electrode configurations compared to plane-plane electrode configuration for a 10 mm gap distance, as shown in Figure 5. For all electrode configurations, the highest reduction of AC breakdown voltage is found for aged MO in the presence of a DBDS concentration of 5,000 ppm. The highest percentages of AC breakdown voltage reductions for aged oils under needle-sphere, needle-plane and plane-plane electrode configurations are 42.0%, 33.3% and 8.1%.

The AC breakdown voltage reduction patterns for aged MO at a 20 mm gap distance are quite similar for all electrode configurations in the presence of DBDS, as shown in Figure 6. Similar to the 10 mm gap distance, the AC breakdown voltage reduction of aged MO is the highest at a DBDS concentration of 5,000 ppm. The aged MO in the presence of DBDS experiences the highest percentages of AC breakdown voltage reductions of 21.9%, 17.1% and 18.3% under needle-sphere, needle-plane and plane-plane electrode

configurations. Based on the previous finding by Cong et al. (2018), the addition of DBDS can increase the moisture content in aged MO, which results in the reduction of the AC breakdown voltage and increment of the dielectric loss.

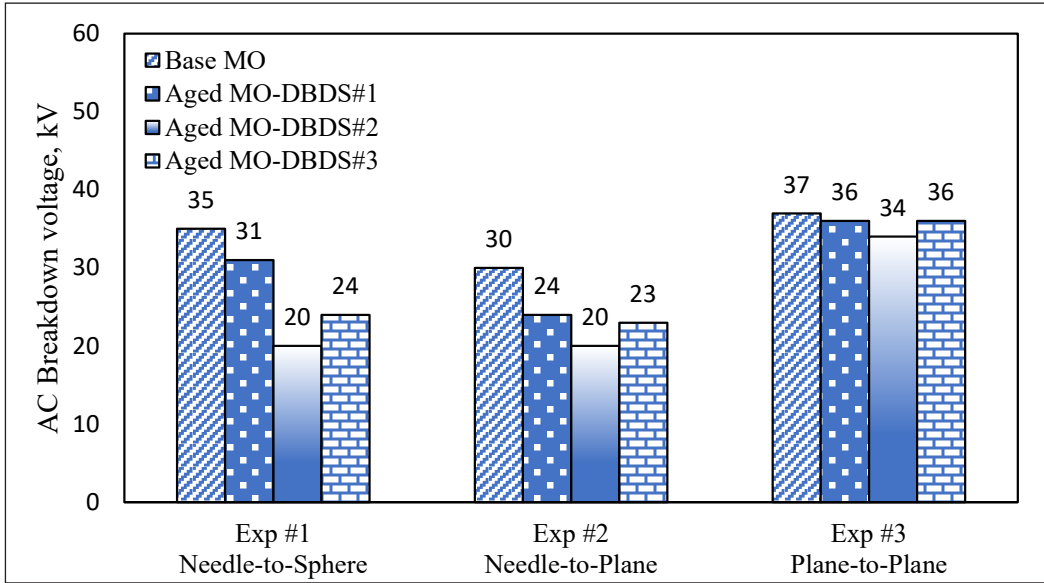


Figure 5. The AC breakdown voltage of MO in the presence of DBDS at a 10 mm gap distance

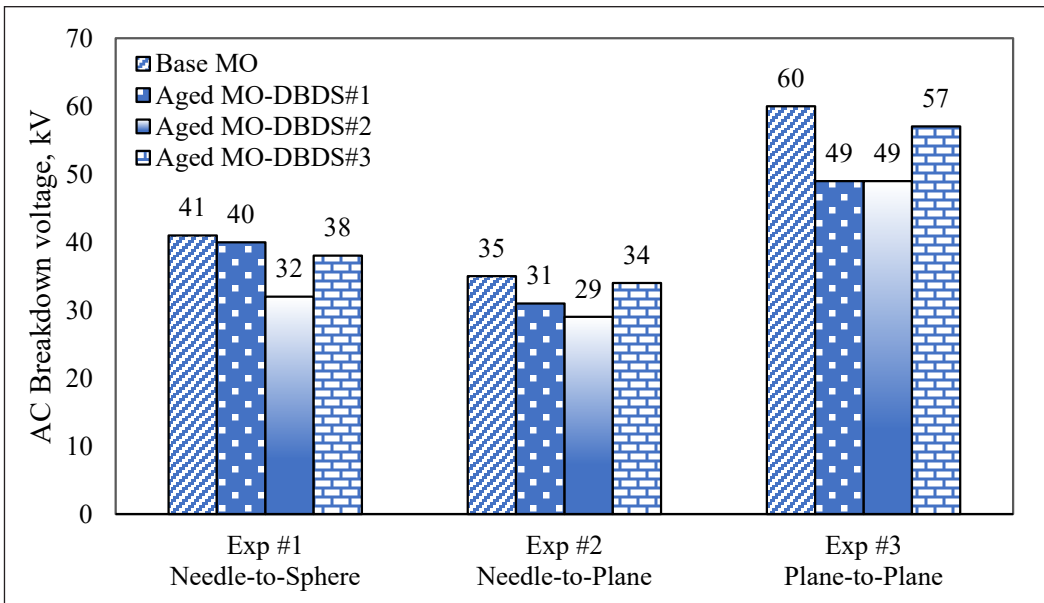


Figure 6. The AC breakdown voltage of MO in the presence of DBDS at a 20 mm gap distance

Effect of DBDS on Partial Discharge Characteristics

The PD apparent charge, average charge and PD repetition rate that are recorded from 70% to 80% of peak voltage for 1-minute intervals are obtained based on the mean of the datasets for base and aged MOs in the presence of DBDS. There is a clear reduction pattern for an apparent charge of aged MO with the increment of DBDS concentration at a 10 mm gap distance for needle-sphere electrode configuration, as shown in Figure 7. The highest reduction percentage for an apparent charge of aged MO is found at a DBDS concentration of 1,000 ppm with 83.5%. The average charge of aged MO shows a slight increment pattern as the DBDS concentration increases. The average charge of aged MO experiences the highest percentage of increment up to 50.2% at DBDS concentrations of 5,000 ppm and 10,000 ppm. The PD repetition rate of aged MO initially decreases to 50.0% as the DBDS concentration increases to 5,000 ppm. As the DBDS concentration increases to 10,000 ppm, the PD repetition rate of aged MO slightly increases.

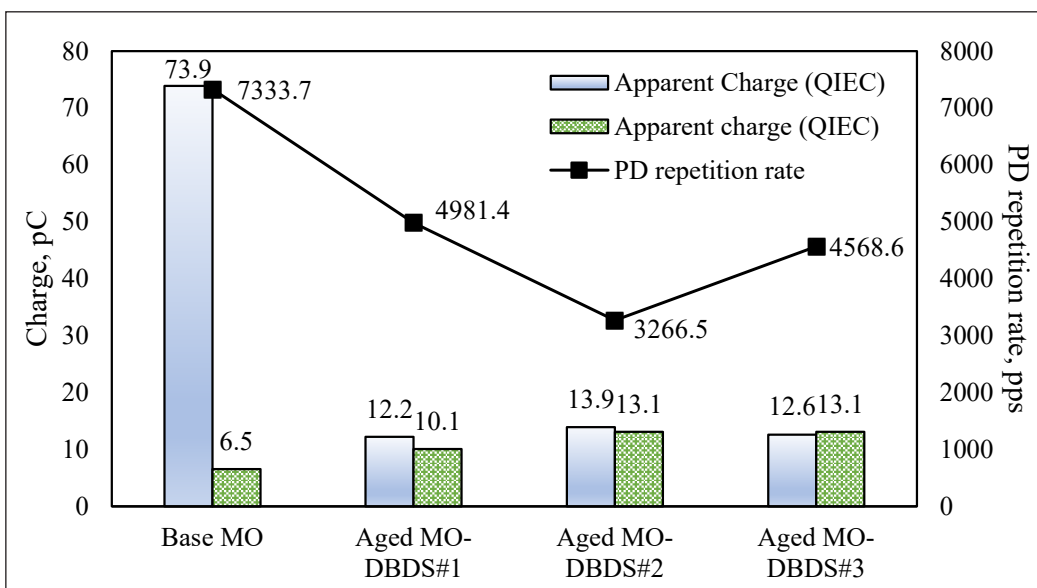


Figure 7. Comparison of the partial discharge characteristics for the base and aged MOs in the presence of DBDS based on needle-sphere electrode configuration at a 10 mm gap distance

At a 20 mm gap distance, the apparent charge of aged MO shows a slight increment pattern as the DBDS concentration increases for needle-sphere electrode configuration, as shown in Figure 8. The highest increment percentage for an apparent charge of aged MO is 53.5% at a DBDS concentration of 10,000 ppm. Similarly, the average charge of aged MO shows a slight increment pattern whereby the highest increment percentage occurs at a DBDS concentration of 10,000 ppm with 61%. The PD repetition rate of aged MO increases steadily with the increment of DBDS concentration, whereby the highest percentage of increment can be up to 40.4% at DBDS concentration of 10,000 ppm.

The skewness and kurtosis were calculated based on Janani et al. (2020). Table 2 shows the skewness and kurtosis of PD apparent charge, average charge, and PD repetition rate for needle-sphere electrode configuration. At a 10 mm gap, the skewness of apparent charge for all MO samples stays low, which indicates consistent symmetry, while kurtosis increases, especially for aged MOs, in the presence of DBDS, which suggests more discharge activity. The average charge shifts from negative to positive skewness as DBDS is introduced, which indicates a change in data symmetry, and the kurtosis slightly peaks for aged MO at a DBDS concentration of 10,000 ppm. The PD repetition rate skewed slightly for aged MOs in the presence of DBDS, with some left-skewed data, and kurtosis increases for aged MOs at DBDS concentrations of 5,000 and 10,000 ppm, respectively, which indicates more irregular distributions.

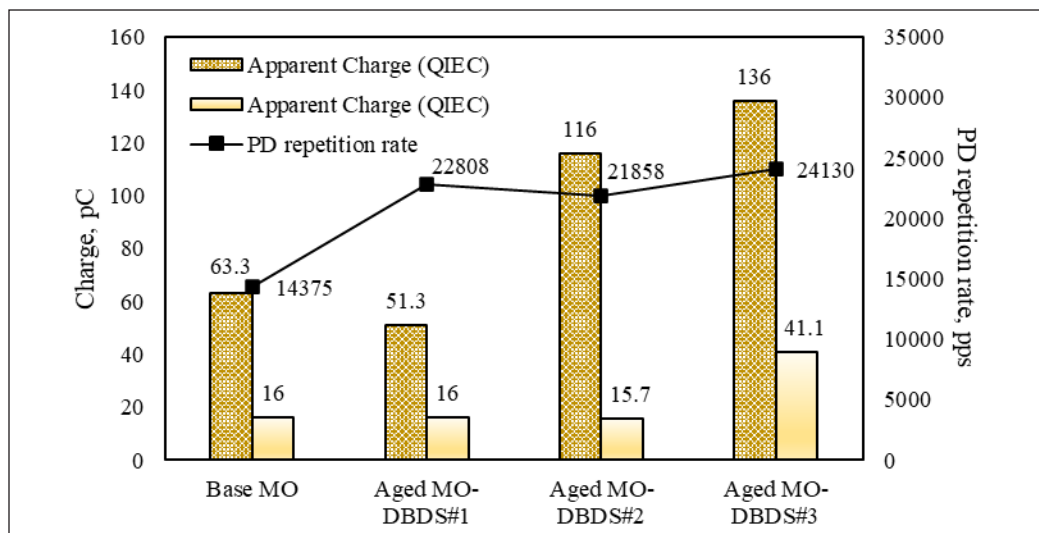


Figure 8. Comparison of the partial discharge characteristics for the base and aged MOs in the presence of DBDS based on needle-sphere electrode configuration at 20 mm gap distance

At a 20 mm gap, the skewness of apparent charge for all MO samples remains low and stable, which indicates minimal effect of the DBDS, while kurtosis peaks for aged MO at DBDS concentration of 1,000 ppm, which suggests more extreme values as compared to other MO samples with high DBDS concentrations. The average charge skewness shifts from left-skewed in base MO to more negative for aged MOs in the presence of DBDS, which shows an increment of the asymmetry, while the kurtosis peaks for aged MO at DBDS concentration of 5,000 ppm, which indicates a concentrated distribution. The PD repetition rate skewness of all MO samples maintained low with minor left-skew, and the kurtosis is high for base MO and peaks for aged MO at a DBDS concentration of 10,000 ppm, which indicates concentrated distributions for both MO samples.

Table 2
Skewness and kurtosis analyses for apparent charge, average charge and partial discharge repetition rate under needle-sphere electrode configuration

Parameter	Apparent charge			Average Charge			PD repetition rate					
	Base MO	Aged MO-DBDS#1	Aged MO-DBDS#2	Base MO	Aged MO-DBDS#1	Aged MO-DBDS#2	Base MO	Aged MO-DBDS#1	Aged MO-DBDS#2	Aged MO-DBDS#3		
Skewness - 10 mm	1.9	1.1	-4.3	5.4	-1.4	-0.3	1.3	2.3	-0.1	0.6	-3.7	-2.7
Kurtosis - 10 mm	6.4	-0.3	18.4	29.7	0.7	-0.9	0.4	4.3	-0.3	-0.6	17.8	13.4
Skewness - 20 mm	6.8	12.7	3.5	1.3	-1.5	-0.2	-2.3	-1.8	-3.5	-0.8	-1.0	-4.6
Kurtosis - 20 mm	55.0	172.5	11.0	2.4	0.8	-0.3	5.1	1.9	14.0	2.9	6.1	26.8

At a 10 mm gap distance, the increment pattern for an apparent charge of aged MO is not apparent as the DBDS concentration increases for needle-plane electrode configuration, as shown in Figure 9. The highest percentage of increment for an apparent charge of aged MO is 7.9% at DBDS concentrations of 5,000 and 10,000 ppm. The average charge of aged MO shows a fluctuation pattern whereby the percentage of differences with base MO varies between 1.9% and 61% as the DBDS concentration increases to 10,000 ppm. The PD repetition rate of aged MO initially decreases as the DBDS concentration increases to 5,000 ppm. It increases to 58.7% as the DBDS concentration increases to 10,000 ppm.

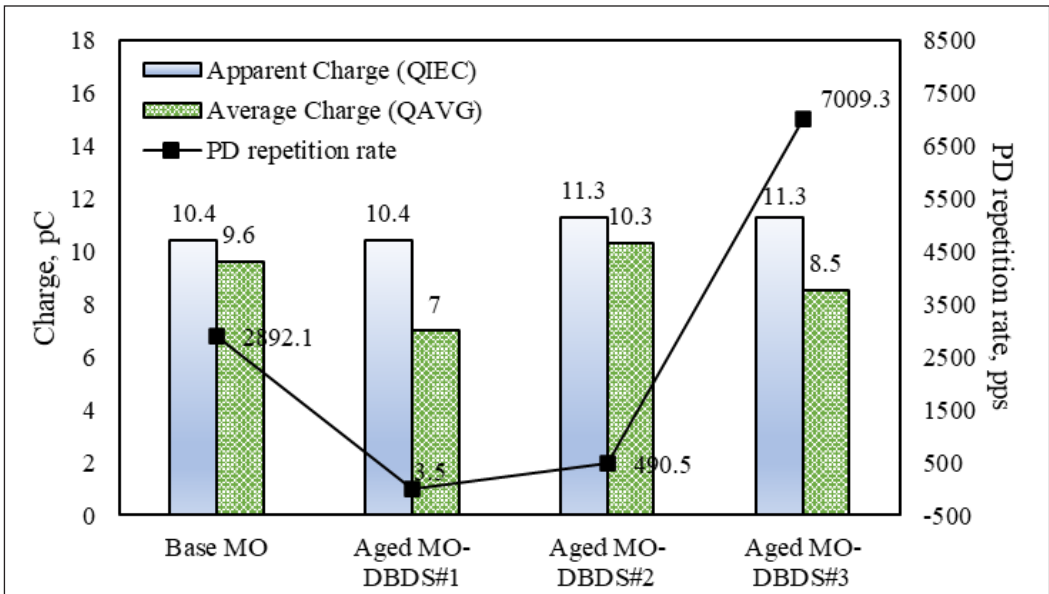


Figure 9. Comparison of the partial discharge characteristics for the base and aged MOs in the presence of DBDS based on needle-plane electrode configuration at a 10 mm gap distance

There is no clear pattern for an apparent charge of aged MO as the DBDS concentration increases at a 20 mm gap distance for needle-plane electrode configuration, as shown in Figure 10. The apparent charge of aged MO maintains close to 12 pC as the DBDS concentration increases by 10,000 ppm. A similar pattern is found for the average charge of aged MO, whereby it slightly increases as the DBDS concentration increases to 1,000 ppm. It decreases to 9.8% as the DBDS concentration increases to 10,000 ppm. There is a clear reduction pattern for the PD repetition rate of aged MO as the DBDS concentration increases at a 10 mm gap distance for needle-sphere electrode configuration. The highest percentage of reduction for PD repetition rate of aged MO is found at DBDS concentration of 1,000 ppm with 84.5%.

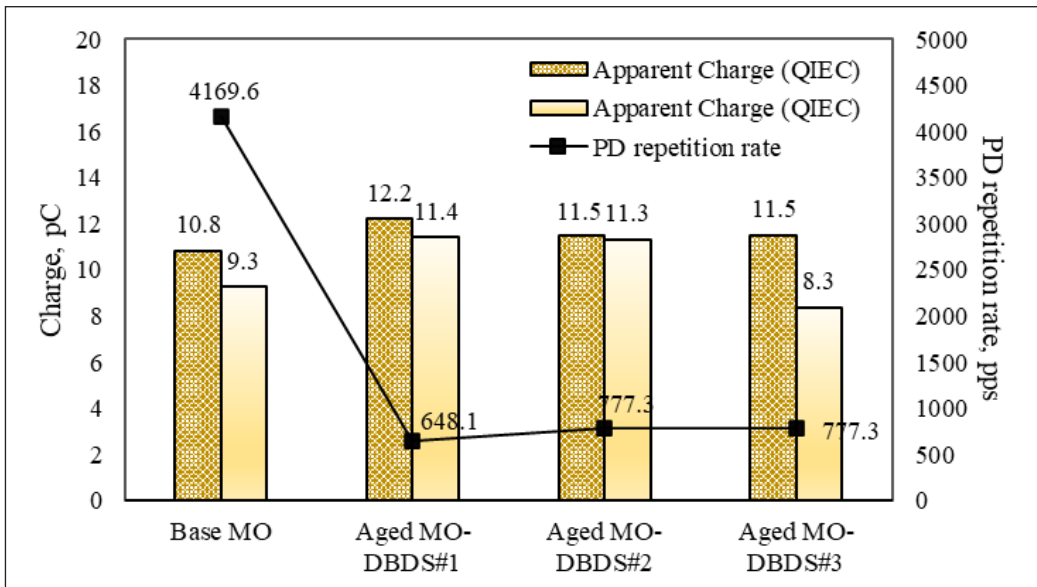


Figure 10. Comparison of the partial discharge characteristics for the base and aged MOs in the presence of DBDS based on needle-plane electrode configuration at 20 mm gap distance

Table 3 shows the skewness and kurtosis of apparent charge, average charge, and PD repetition rate for needle-plane electrode configuration. At a 10 mm gap, the skewness of apparent charges for all MO samples remains low and stable, which indicates consistent symmetry. The kurtosis of MO decreases, indicating a transition from extreme to uniform distributions as the DBDS concentration increases. The skewness of the average charge for all MO samples stays consistent, with base MO slightly left-skewed, while the kurtosis of aged MO decreases as the DBDS concentration increases, which suggests a shift from a peak to a flat distribution. The PD repetition rate skewness for all MO samples remains stable and slightly left-skewed, while the kurtosis for aged MO decreases in a similar pattern as the apparent charge.

At a 20 mm gap, the skewness of apparent charges for all MO samples stays low and consistent, while the kurtosis of aged MO decreases as the DBDS concentration increases to 10,000 ppm, which suggests a more uniform distribution as compared to base MO. The average charge skewness shifted from left-skewed for base MO to right-skewed as the DBDS concentration increased for aged MO, with the kurtosis showing initial peaks and eventually remaining flat as the DBDS concentration increased, which indicates uniform distribution. The PD repetition rate skewness for all MO samples stayed mostly negative, which indicates a right-skewed tendency, with high kurtosis in base MO and aged MO at a DBDS concentration of 5,000 ppm, which suggests extreme data.

Table 3
Skewness and kurtosis analyses for apparent charge, average charge and partial discharge repetition rate under needle-plane electrode configuration

Parameter	Apparent charge			Average Charge			PD repetition rate					
	Base MO	Aged MO- DBDS#1	Aged MO- DBDS#2	Base MO	Aged MO- DBDS#1	Aged MO- DBDS#2	Base MO	Aged MO- DBDS#1	Aged MO- DBDS#2	Aged MO- DBDS#3		
Skewness - 10 mm	16.5	6.5	9.6	5.0	3.7	1.2	-1.3	1.9	-5.7	7.0	-5.2	-4.0
Kurtosis - 10 mm	279.9	43.1	96.1	24.3	13.8	-0.1	0.0	2.1	50.4	48.3	35.9	19.4
Skewness - 20 mm	9.9	6.8	4.8	0.9	-1.8	-1.2	1.4	0.7	-4.4	0.3	-3.1	-2.6
Kurtosis - 20 mm	98.0	45.4	26.9	2.4	1.8	0.2	1.1	-0.9	23.1	-0.6	23.5	10.1

At a 10 mm gap distance, there is no clear pattern for an apparent charge of aged MO as the DBDS concentration increases for plane-plane electrode configuration, as shown in Figure 11. The apparent charge of aged MO fluctuates between 6.1% and 11.5% compared to base MO once the DBDS increases to 10,000 ppm. There is a slight increment pattern for the average charge of aged MO, whereby the highest percentage of increment is 34.7% at a DBDS concentration of 10,000 ppm. The PD repetition rate of aged MO initially decreases to 77.2% as the DBDS concentration increases to 5,000 ppm. It slightly increases as the DBDS concentration increases to 10,000 ppm.

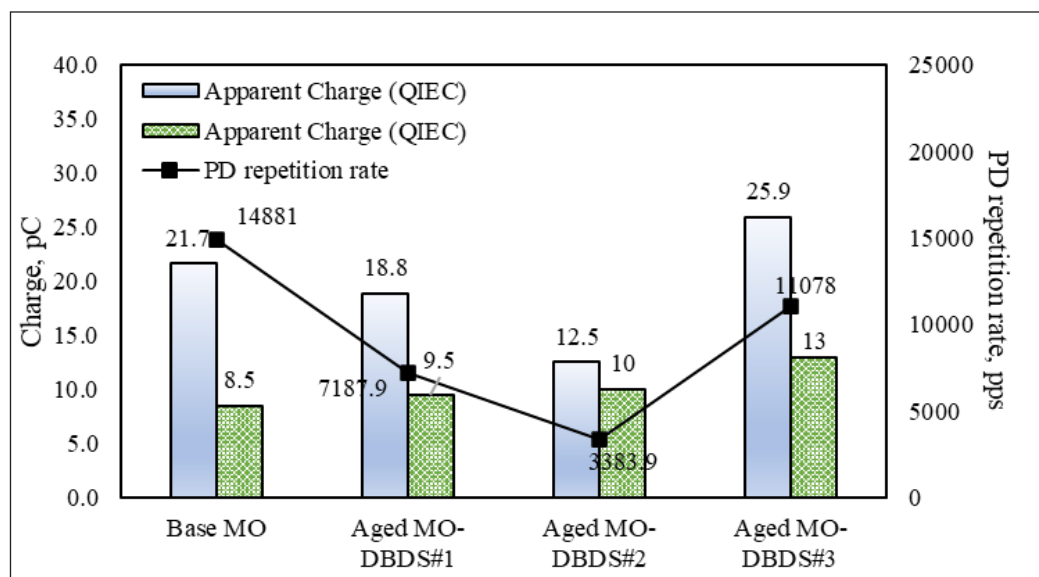


Figure 11. Comparison of the partial discharge characteristics for the base and aged MOs in the presence of DBDS based on plane-plane electrode configuration at 10 mm gap distance

The apparent charge of aged MO shows no clear pattern as the DBDS concentration increases for plane-plane electrode configuration for a 20 mm gap distance, as shown in Figure 12. As the DBDS increases to 10,000 ppm, the apparent charge of aged MO fluctuates between 10.8% and 34.7% compared to base MO. There is no clear pattern for the average charge of aged MO as the DBDS concentration increases. The apparent charge of aged MO maintains close to 20 pC as the DBDS concentration increases by 10,000 ppm. The PD repetition rate of aged MO shows a slight increment pattern whereby the highest increment percentage can be up to 14.8% at a DBDS concentration of 10,000 ppm.

Table 4 summarises the skewness and kurtosis of PD apparent charge, average charge, and PD repetition rate for plane-plane electrode configuration. At a 10 mm gap, the skewness of apparent charge stays for all MO samples consistently low, which indicates uniform data, while kurtosis varies, with peaks for aged MO at DBDS concentrations

of 1,000 ppm and 5,000 ppm and flat distributions in base MO and aged MO at DBDS concentration of 10,000 ppm. The average charge skewness shifts slightly from right- to left-skewed as the DBDS concentration increases, with kurtosis increases for aged MO at a DBDS concentration of 10,000 ppm, which indicates extreme data. The PD repetition rate skewness of all MO samples stays low and slightly positive, with kurtosis increasing for aged MO at a DBDS concentration of 5,000 ppm and decreasing for MO at a DBDS concentration of 10,000 ppm.

At a 20 mm gap, the apparent charge skewness shifts from right-skewed in base MO to nearly symmetrical and left-skewed as the DBDS concentration increases for aged MO. The kurtosis peaks for aged MO at a DBDS concentration of 5,000 ppm DBDS and decreases for aged MO at a DBDS concentration of 10,000 ppm. The average charge starts right skewed in base MO and becomes symmetrical as the DBDS concentration increases for aged MO, with the kurtosis being the highest for base MO and decreasing for aged MOs with DBDS. The PD repetition rate skewness stays slightly negative, while kurtosis is high for base MO and decreases as the DBDS increases, which indicates more uniform distributions. These trends reflect the changes in distribution characteristics.

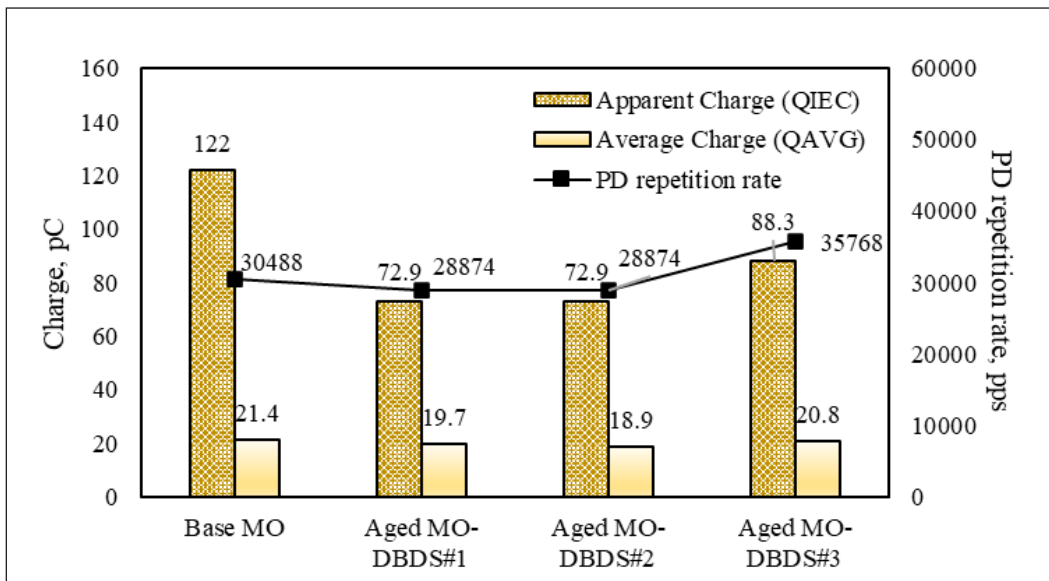


Figure 12. Comparison of the partial discharge characteristics for the base and aged MOs in the presence of DBDS based on plane-plane electrode configuration at 20 mm gap distance

Table 4
Skewness and kurtosis analyses for apparent charge, average charge and partial discharge repetition rate under plane-plane electrode configuration

Parameter	Apparent charge			Average Charge			PD repetition rate					
	Base MO	Aged MO- DBDS#1	Aged MO- DBDS#2	Base MO	Aged MO- DBDS#1	Aged MO- DBDS#2	Base MO	Aged MO- DBDS#1	Aged MO- DBDS#2	Aged MO- DBDS#3		
Skewness - 10 mm	-0.3	-7.8	-6.8	-1.0	-1.0	0.0	-1.1	-2.9	2.5	3.8	3.9	1.0
Kurtosis - 10 mm	-0.6	74.0	46.7	1.1	1.1	-1.3	1.3	6.6	12.0	16.6	20.6	6.0
Skewness - 20 mm	1.5	0.2	-0.7	-0.1	-0.1	-1.5	-1.6	-1.6	-7.3	-3.6	-4.9	-3.7
Kurtosis - 20 mm	0.9	-0.5	0.9	-0.3	-0.3	1.1	1.3	1.2	83.4	14.9	30.3	15.6

The PDIV increment patterns for aged MOs with the increment of DBDS concentration are quite clear for needle-sphere and needle-plane electrode configurations compared to plane-plane electrode configurations at a 10 mm gap distance, as shown in Figure 13. The highest increment of PDIV is found at a DBDS concentration of 10,000 ppm for both electrode configurations. The highest percentages of PDIV increments for aged MO under needle-sphere, needle-plane and plane-plane electrode configurations are 89.0%, 85.7% and 31.5%.

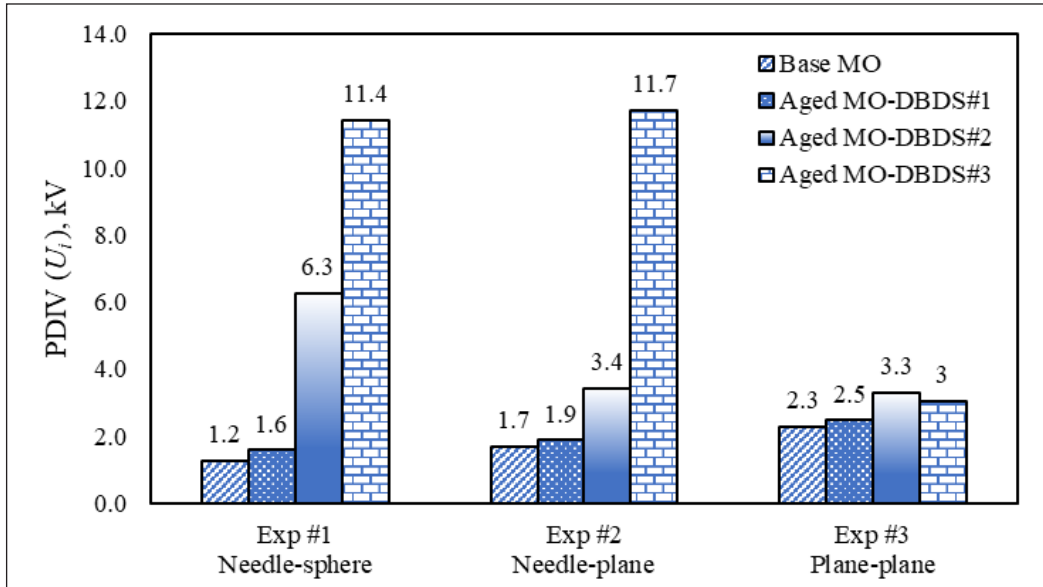


Figure 13. Partial discharge inception voltage, U_i at 10 mm gap distance

The PDIV patterns for aged MO at a 20 mm gap distance are quite similar for all electrode configurations in the presence of DBDS, as shown in Figure 14. For needle-sphere and needle-plane electrode configurations, the PDIVs of aged MOs show a decrement pattern as the DBDS concentration increases to 5,000 ppm. The PDIVs of aged MOs slightly increase at the DBDS concentration of 10,000 ppm. The PDIV of aged MO shows an increment pattern for plane-plane electrode configuration as the DBDS concentration increases. The PDIVs of aged MO for needle-sphere and needle-plane electrode configurations experience the highest reduction of 55.1% and 47.3% at DBDS concentrations of 1,000 ppm and 5,000 ppm. The highest increment of PDIV for aged MO is 31.7% at a DBDS concentration of 5,000 ppm for plane-plane electrode configuration. In conclusion, at both gap distances, the increment pattern of PDIV due to the increment of DBDS concentrations somehow exhibits a similar increment pattern in the presence of moisture as compared to when it is in the dry condition as studied in Jaroszewski and Rakowiecki (2017) and Liu et al. (2014).

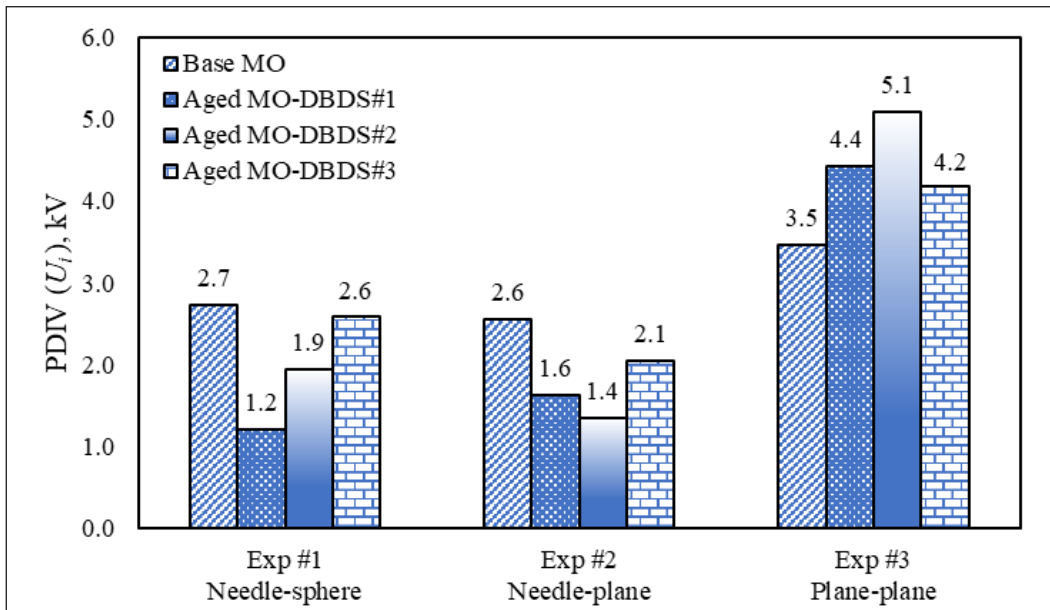


Figure 14. Partial discharge inception voltage, U_i at 20 mm gap distance

At a 10 mm gap distance, it is found that the PDs of aged MO start to initiate in correspondence to negative peak half-wave between 225° and 290° from the 3rd to 4th quadrants and are undetectable at positive half-wave for all electrode configurations as shown in Figures 15 to 17. The patterns of PD intensity, $H_n(\varphi)$ of aged MO, are distributed along apparent charge, Q_{IEC} of 10 pC at all electrode configurations for both base and aged MOs with the increment of DBDS concentrations whereby no obvious shape is observed. However, it is observed that there is an enlargement of the PRPD pattern's shape for aged MO at DBDS concentration of 10,000 ppm under needle-plane and plane-plane electrode configurations, as shown in Figures 16(d) and 17(d), respectively.

At 20 mm gap distance, the PD of aged MO tends to increase predominantly in correspondence to negative peak half-wave between 200° and 315° from 3rd to 4th quadrants and undetectable at positive half-wave for all electrode configurations as shown in Figures 18 to 20. The patterns of PD intensity, $H_n(\varphi)$ for needle-plane electrode configuration, are distributed along the apparent charge, Q_{IEC} , of 10 pC. However, the PD intensity, $H_n(\varphi)$ for needle-sphere and plane-plane electrode configurations are distributed between apparent charge, Q_{IEC} from 5 pC to 100 pC. The asymmetric shape of PRPD patterns for base and aged MOs at different DBDS concentrations in all electrode configurations for both gap distances suggest a Type 5 PRPD pattern due to strong discharge in the negative half-wave and negligible discharges in the positive half-wave. This pattern is often associated with non-conductive cavities in insulation materials like oil or solid dielectrics (eCIGRE, 2017).

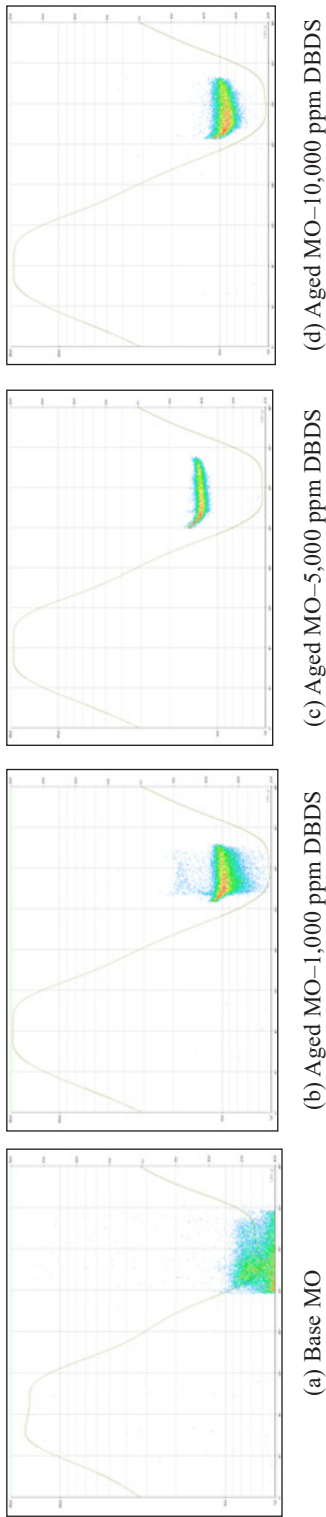


Figure 15. PRPD pattern for needle-sphere electrode configuration at 10 mm gap distance for 250kHz \pm 150kHz (IEC 60270)

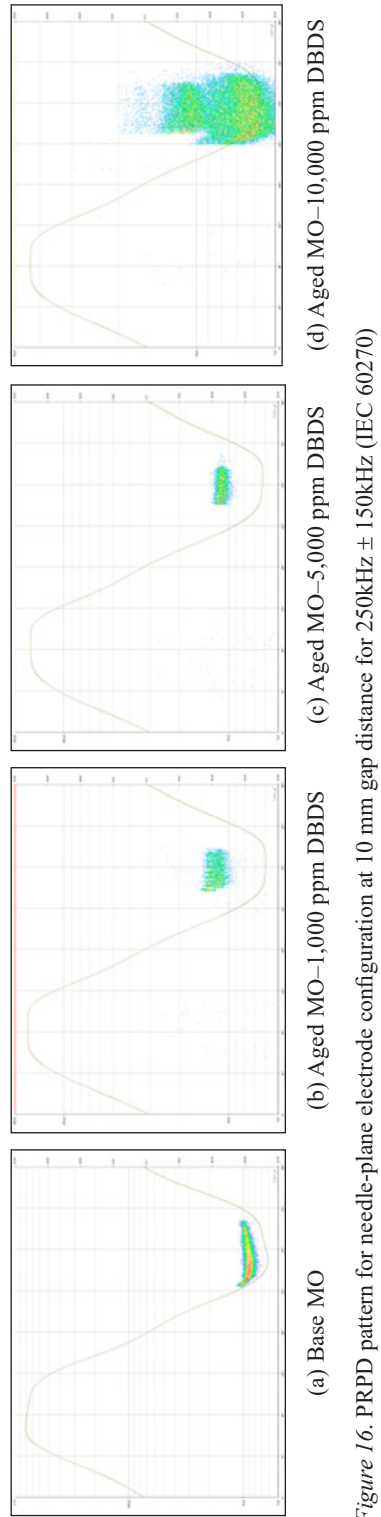


Figure 16. PRPD pattern for needle-plane electrode configuration at 10 mm gap distance for 250kHz \pm 150kHz (IEC 60270)

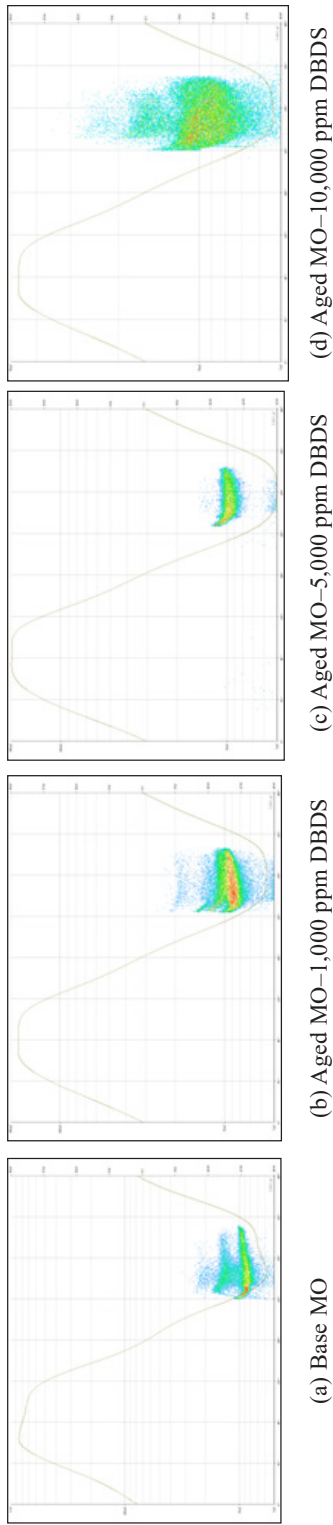


Figure 17. PRPD pattern for plane-plane electrode configuration at 10 mm gap distance for 250kHz \pm 150kHz (IEC 60270)

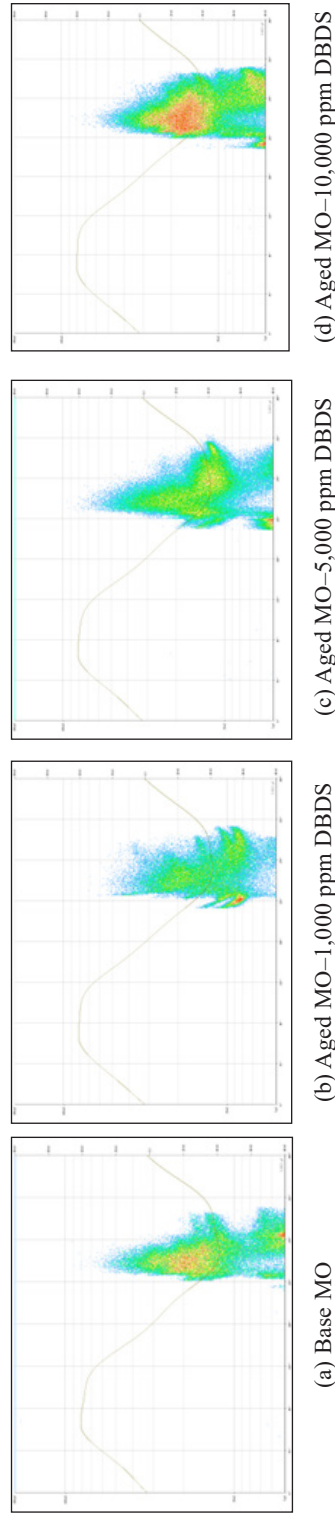


Figure 18. PRPD pattern for needle-sphere electrode configuration at 20 mm gap distance for 250kHz \pm 150kHz (IEC 60270)

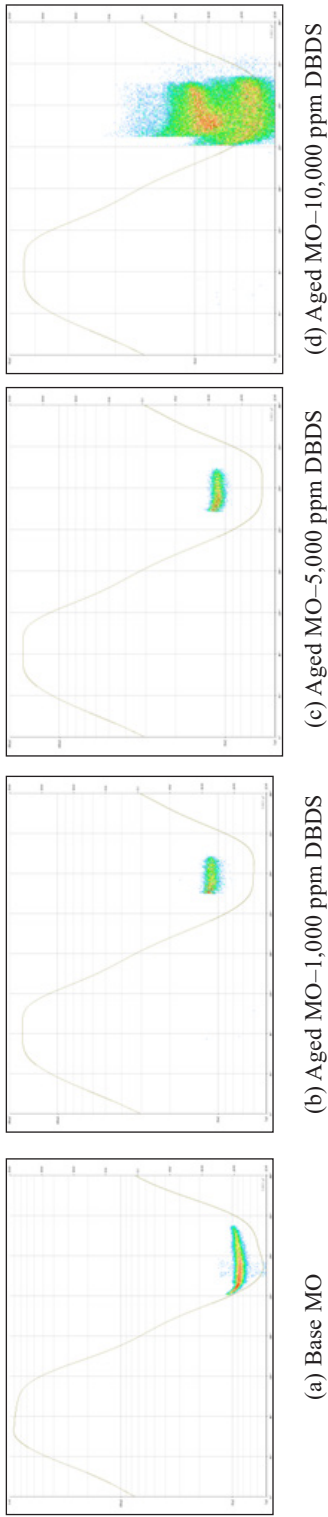


Figure 19. PRPD pattern for needle-plane electrode configuration at 20 mm gap distance for 250kHz \pm 150kHz (IEC 60270)

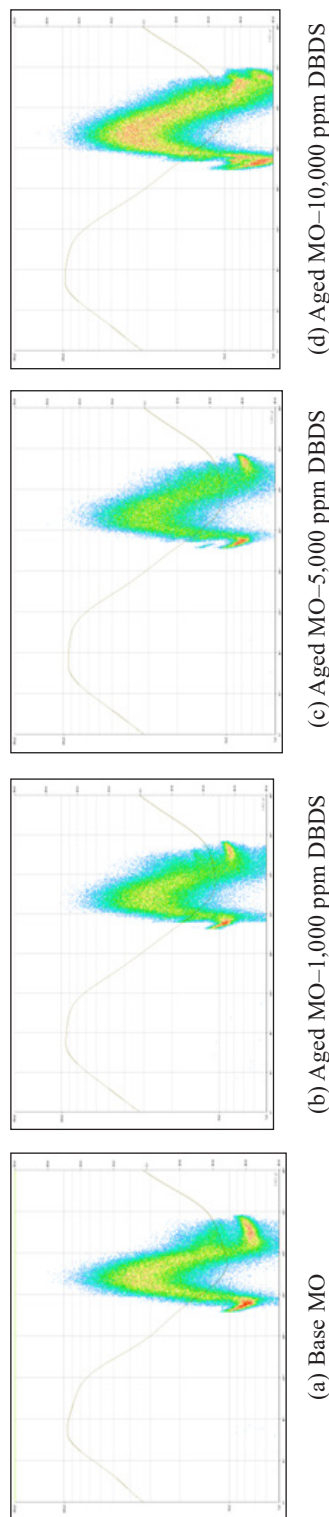


Figure 20. PRPD pattern for plane-plane electrode configuration at 20 mm gap distance for 250kHz \pm 150kHz (IEC 60270)

It is important to observe that the discharge is found to predominantly occur in the negative half-wave for the base and aged MOs as well as dielectric insulating fluids that contain nanoparticles, as investigated by other works (Atiya et al., 2020; Sangineni et al., 2023). During the positive half-wave, the electric field might not be strong enough to cause significant ionisation and discharges. Negative charges accumulate in the defects at the negative half-wave, which provides better conditions for PDs. Positive charges have lower mobility than negative charges. The shape of the electrodes also affects how the electric field is distributed. Electric fields distribute ununiformly for positive half-wave, which leads to low stress near defects, especially for needle-plane electrode configuration. Also, MO with DBDS can behave non-linearly in high electric fields, leading to high discharge in the negative half-wave (Pompili & Bartnikas, 2014; Roslan et al., 2023).

CONCLUSION

The AC breakdown voltages of aged MOs generally show a decrement pattern as the concentration of DBDS increases for all electrode configurations and gap distances. The apparent and average charges of aged MOs show increment patterns as the DBDS concentration increases. The PD repetition rate of aged MO shows fluctuation patterns for all electrode configurations in the presence of DBDS. The data across various electrode configurations and gap distances show that the increment of DBDS concentration in MO can affect the skewness and kurtosis of PD apparent charge, average charge, and PD repetition rate, indicating symmetry and distribution uniformity shifts. The PDIVs of aged MOs show an increment pattern as the DBDS concentration increases for all electrode configurations at a 10 mm gap distance. At a 20 mm gap distance, the increment pattern of PDIVs for aged MOs is found only for plane-plane electrode configuration. It also reveals that the PRPD is asymmetrical for positive and negative half-waves, and discharge mainly concentrates around the negative peak of the applied voltage. The PRPD is undetectable at positive half-wave for both gap distances. The PRPD pattern exhibits a type 5 PD pattern, which indicates non-conducting material, i.e., a cavity without direct contact with the electrode.

ACKNOWLEDGEMENT

This research was funded by Universiti Putra Malaysia, Putra Grant Scheme, Inisiatif Putra Berkumpulan (GP- IPB/2022/9717000).

REFERENCES

- Amalanathan, A. J., Sarathi, R., Zdanowski, M., Vinu, R., & Nadolny, Z. (2023). Review on gassing tendency of different insulating fluids towards transformer applications. *Energies*, 16(1), Article 488. <https://doi.org/10.3390/en16010488>
- Amaro, P. S. (2015). *Corrosive Sulphur in Large Transformers: Impact, Quantification and Detection*. (Doctoral dissertation). Universiti of Southampton, UK. <https://eprints.soton.ac.uk/374902/>

- Atiya, E. G., Mansour, D. E. A., & Izzularab, M. A. (2020). Partial discharge development in oil-based nanofluids: Inception, propagation and time transition. *IEEE Access*, 8, 181028–181035. <https://doi.org/10.1109/ACCESS.2020.3027905>
- Bramantyo, A. P., Ciani, F., Serra, S., Morshuis, P. H. F., Cavallini, A., & Montanari, G. C. (2014). Experimental investigation on the role of corrosive sulphur on the development of partial discharges in power transformers. In *Proceedings of 2014 International Symposium on Electrical Insulating Materials* (pp. 136-139). IEEE Publishing. <https://doi.org/10.1109/ISEIM.2014.6870739>
- Cong, H., Pan, H., Qian, D., Zhao, H., & Li, Q. (2021). Reviews on sulphur corrosion phenomenon of the oil–paper insulating system in mineral oil transformer. *High Voltage*, 6(2), 193-209. <https://doi.org/10.1049/hve.2020.0060>
- Cong, H., Qiao, L., Wang, Y., Hu, X., Su, W., Lian, H., & Li, Q. (2024). Effect of copper sulfide deposition on the partial discharge of oil-paper insulation under plate-plate electrodes. *IEEE Transactions on Dielectrics and Electrical Insulation*, 31(2), 824–833. <https://doi.org/10.1109/TDEI.2023.3332052>
- Cong, H., Zhang, M., & Li, Q. (2018). Study on sulfide distribution in the operating oil of power transformers and its effect on the oil quality. *Applied Sciences*, 8(9), Article 1577. <https://doi.org/10.3390/app8091577>
- Dixit, A., & Samarasinghe, S. (2019). Comparative study of partial discharge (PD) signal characteristics in insulation systems filled with mineral and ester oil. In *2019 IEEE Innovative Smart Grid Technologies-Asia (ISGT Asia)* (pp. 3849-3854). IEEE Publishing. <https://doi.org/10.1109/ISGT-Asia.2019.8880928>
- eCIGRE. (2009). Copper Sulphide in Transformer Insulation. CIGRE. <https://www.e-cigre.org/publications/detail/378-copper-sulphide-in-transformer-insulation.html>
- eCIGRE. (2017). Partial Discharges in Transformers. CIGRE. <https://www.e-cigre.org/publications/detail/676-partial-discharges-in-transformers.html>
- Flora, S. D., & Rajan, J. S. (2016). Assessment of paper-oil insulation under copper corrosion using polarization and depolarization current measurements. *IEEE Transactions on Dielectrics and Electrical Insulation*, 23(3), 1523–1533. <https://doi.org/10.1109/TDEI.2016.005577>
- Gao, S. H., Yang, L. J., & Ding, D. (2019). Corrosion mechanism for copper sulfide formation induced by dibenzyl disulfide in oil-immersed insulation. *IEEE Access*, 7, 23100–23108. <https://doi.org/10.1109/ACCESS.2019.2894125>
- Hu, E., Yang, L., Liao, R. J., Liu, Y., & Yuan, Y. (2016). Effect of an electric field on copper sulphide deposition in oil-impregnated power transformers. *IET Electric Power Applications*, 10(3), 155–160. <https://doi.org/10.1049/iet-epa.2015.0018>
- Jadim, R., Kans, M., Rehman, S., & Alhems, L. M. (2020). A relevant condition monitoring of corrosive sulphur deposition on the windings of oil-filled electrical transformers. *IEEE Transactions on Dielectrics and Electrical Insulation*, 27(5), 1736–1742. <https://doi.org/10.1109/TDEI.2020.008955>
- Janani, H., Shahabi, S., & Kordi, B. (2020). Separation and classification of concurrent partial discharge signals using statistical-based feature analysis. *IEEE Transactions on Dielectrics and Electrical Insulation*, 27(6), 1933–1941. <https://doi.org/10.1109/TDEI.2020.009043>

- Jaroszewski, M., & Rakowiecki, K. (2017). Partial discharge inception voltage in transformer natural ester liquid - Effect of the measurement method in the presence of moisture. *IEEE Transactions on Dielectrics and Electrical Insulation*, 24(4), 2477–2482. <https://doi.org/10.1109/TDEI.2017.005917>
- Jin, H., Morshuis, P., Mor, A. R., Smit, J. J., & Andritsch, T. (2015). Partial discharge behavior of mineral oil based nanofluids. *IEEE Transactions on Dielectrics and Electrical Insulation*, 22(5), 2747–2753. <https://doi.org/10.1109/TDEI.2015.005145>
- Khan, F., & Rajan, J. (2015). Experimental simulation of effects of copper sulphide on insulation system of transformers. *IEEE Transactions on Dielectrics and Electrical Insulation*, 22(1), 571–580. <https://doi.org/10.1109/TDEI.2014.004408>
- Khlar, M. S. A., Brown, R. C. D., & Lewin, P. L. (2019). Sacrificial copper strip sensors for sulfur corrosion detection in transformer oils. *Measurement: Journal of the International Measurement Confederation*, 148, Article 106887. <https://doi.org/10.1016/j.measurement.2019.106887>
- Khlar, M. S. A., Garcia, S., Lewin, P. L., Brown, R. C. D., Pilgrim, J. A., Langley, G. J., & Wilson, G. (2020). On-line quantification of corrosive sulphur content in large autotransformers. *IEEE Transactions on Dielectrics and Electrical Insulation*, 27(6), 1787–1794. <https://doi.org/10.1109/TDEI.2020.008548>
- Liao, R., Hu, E., Yang, L., & Yuan, Y. (2015). Space charge behavior in paper insulation induced by copper sulfide in high-voltage direct current power transformers. *Energies*, 8(8), 8110–8120. <https://doi.org/10.3390/en8088110>
- Liu, Z., Liu, Q., Wang, Z. D., Jarman, P., Krause, C., Smith, P. W. R., & Gyore, A. (2014). Partial discharge behaviour of transformer liquids and the influence of moisture content. In *2014 IEEE 18th international conference on dielectric liquids (ICDL)* (pp. 1-4). IEEE Publishing. <https://doi.org/10.1109/ICDL.2014.6893155>
- Ma, S., Yang, D., Liang, B., & Jin, Y. (2019). Impact of metal particle size on partial discharge characteristics of moving metal particles in transformer oil. *Chemical Physics Letters*, 731, Article 136577. <https://doi.org/10.1016/j.cplett.2019.07.005>
- Pattanadach, N., & Muhr, M. (2016). Partial discharge inception voltage investigation of mineral oil: Effect of electrode configurations and oil conditions. *IEEE Transactions on Dielectrics and Electrical Insulation*, 23(5), 2917–2924. <https://doi.org/10.1109/TDEI.2016.7736853>
- Pompili, M., & Bartnikas, R. (2014). Gas formation in transient cavities undergoing PD pulse burst discharges in transformer oils. *IEEE Transactions on Plasma Science*, 42(6), 1697–1703. <https://doi.org/10.1109/TPS.2014.2317847>
- Rehman, S., Alhems, L. M., Jadim, R., Al Faraj, B. A., Balasubramanian, K. S., Al Mutairi, K. S., Al-Yemni, A. K., Shinde, D. V., & Al-Hsaien, S. A. (2016). Maximum acceptable concentrations of dbds, sulphur mercaptan and optimal concentration of passivators for safe and prolonged operation of power transformers. *IEEE Transactions on Dielectrics and Electrical Insulation*, 23(4), 2438–2442. <https://doi.org/10.1109/TDEI.2016.7556523>
- Rehman, S., Alhems, L. M., Jadim, R., Faraj, B. A. A., Mutairi, K. S. A., & Al-Yemni, A. K. (2017). Experimental investigation of temperature effect on corrosive sulfur formation in transformers. *IEEE Transactions on Dielectrics and Electrical Insulation*, 24(5), 3201–3206. <https://doi.org/10.1109/TDEI.2017.006024>

- Roslan, M. H., Azis, N., Kadir, M. Z. A. A., Jasni, J., & Yousof, M. F. M. (2023). The influence of cavity size and location within insulation paper on the partial discharge activities. *Pertanika Journal of Science and Technology*, 31(6), 2915–2930. <https://doi.org/10.47836/pjst.31.6.15>
- Sangineni, R., Chandrasekaran, T., & Nayak, S. K. (2023). Study of partial discharges in fresh and oxidative aged mineral-natural ester blended oils. *IEEE Transactions on Dielectrics and Electrical Insulation*, 30(5), 2325–2333. <https://doi.org/10.1109/TDEI.2023.3308531>
- Scatiggio, F., Pompili, M., & Bartnikas, R. (2011). Effects of metal deactivator concentration upon the gassing characteristics of transformer oils. *IEEE Transactions on Dielectrics and Electrical Insulation*, 18(3), 701-706. <https://doi.org/10.1109/TDEI.2011.5931055>
- Selva, A. M., Azis, N., Kadir, M. Z. A. A., Jasni, J., Zainuddin, H., & Yousof, M. F. M. (2024). Morphological study on corrosive sulphur development in transformer windings. In *2024 IEEE 4th International Conference in Power Engineering Applications (ICPEA)* (pp. 197-200). IEEE Publishing. <https://doi.org/10.1109/ICPEA60617.2024.10498156>
- Sima, W., Jiang, C., Lewin, P., Yang, Q., & Yuan, T. (2013). Modeling of the partial discharge process in a liquid dielectric: Effect of applied voltage, gap distance, and electrode type. *Energies*, 6(2), 934–952. <https://doi.org/10.3390/en6020934>
- Tang, J., Zhang, Y., Pan, C., Zhuo, R., Wang, D., & Li, X. (2018). Impact of oil velocity on partial discharge characteristics induced by bubbles in transformer oil. *IEEE Transactions on Dielectrics and Electrical Insulation*, 25(5), 1605–1613. <https://doi.org/10.1109/TDEI.2018.006888>
- Toyama, S., Tanimura, J., Yamada, N., Nagao, E., & Amimoto, T. (2009). Highly sensitive detection method of dibenzyl disulfide and the elucidation of the mechanism. *IEEE Transactions on Dielectrics and Electrical Insulation*, 16(2), 509–515. <https://doi.org/10.1109/TDEI.2009.4815186>
- Vahidi, F., & Tenbohlen, S. (2015). *Statistical Failure Analysis of European Substation Transformers*. ResearchGate.
- Wang, X. (2011). *Partial Discharge Behaviours and Breakdown Mechanisms of Ester Transformer Liquids Under AC Stress*. (Doctoral dissertation). University of Manchester, UK. <https://www.escholar.manchester.ac.uk/uk-ac-man-scw:136066>
- Yang, L., Ding, D., Yuan, Y., Gao, S., & Lu, Y. (2022). Influence of contact layer on the sulphur corrosion of copper conductors in power transformers. *High Voltage*, 7(1), 176–184. <https://doi.org/10.1049/hve2.12088>
- Yuan, Y., Gao, X., Zhou, J., Liu, G., Kuang, X., Yang, L., & Liao, R. (2022). A review: Research on corrosive sulphur in electrical power equipment. *High Voltage*, 7(2), 209–221). <https://doi.org/10.1049/hve2.12155>

Review Article

Fulfilling Feed Demands: Industrial Production of *Saccharomyces cerevisiae* as Key Protein Source for Aquaculture, Poultry and Livestock

Zahra Safdari¹, Mohd Khairol Anuar Ariffin^{1*}, Eris Elianddy Supeni¹ and Mohamed Thariq Hameed Sultan^{2,3}

¹Department of Mechanical and Manufacturing Engineering, Faculty of Engineering, Universiti Putra Malaysia, 43400 UPM, Serdang, Selangor, Malaysia

²Laboratory of Biocomposite Technology, Institute of Tropical Forestry and Forest Products (INTROP), Universiti Putra Malaysia, 43400 UPM, Serdang, Selangor, Malaysia

³Aerospace Malaysia Innovation Centre (944751-A), Prime Minister's Department, MIGHT Partnership Hub, 63000 Cyberjaya, Selangor, Malaysia

ABSTRACT

With the world's population expected to grow, addressing global hunger sustainably requires innovative solutions. Utilizing microorganisms in the form of single-cell protein can play a crucial role in enhancing food security by offering a sustainable, efficient, and nutritionally valuable protein source that complements traditional food and feed sources. Yeasts are commonly used for single-cell protein production, and *Saccharomyces cerevisiae* has a profound role in this industry, drawing from its historical significance in baking and brewing. In the feed industry, *S. cerevisiae*, as an effective feed supplement, enhances feed efficiency, animal health, and pathogen control. This review explores various aspects of single-cell protein production, emphasizing *S. cerevisiae*'s nutritional benefits for animal feed as a source of proteins, vitamins, minerals, and fatty acids. Future research should optimize industrial production processes for *S. cerevisiae* to maximize yield and minimize costs.

Keywords: Feed industry, food security, protein production, *Saccharomyces cerevisiae*, single-cell protein

ARTICLE INFO

Article history:

Received: 24 July 2024

Accepted: 18 November 2024

Published: 07 March 2025

DOI: <https://doi.org/10.47836/pjst.33.2.18>

E-mail addresses:

zahraa.safdari8@gmail.com (Zahra Safdari)

khairol@upm.edu.my (Mohd Khairol Anuar Ariffin)

eris@upm.edu.my (Eris Elianddy Supeni)

thariq@upm.edu.my (Mohamed Thariq Hameed Sultan)

*Corresponding author

INTRODUCTION

According to the Global Operational Response Plan 2022 of the World Food Program (WFP) and the Global Hunger Index (GHI) 2023, evidence and statistics

of hunger levels worldwide indicate that food shortages in 2023 were higher than ever before noting that as many as 783 million people were experiencing chronic hunger with the situation expected to worsen in the year 2024 (<https://openknowledge.fao.org/items/c0239a36-7f34-4170-87f7-2fcc179ef064>; <https://www.fao.org/4/y5019e/y5019e00.htm#Contents>; <https://www.fao.org/fishery/en/publication/295155>; von Grebmer et al., 2023). Since 2019, COVID-19 has combined with previous crises across the world, such as conflict, the menace of global recession and climate changes, causing the number of people dealing with acute food insecurity to precipitously rise from 135 million to 345 million (WFP, 2022).

In the definition, food security is the unrestricted access of everyone to food in such a way that it grants them their basic needs. Therefore, taking quick action is needed to prevent an imminent food crisis. In the first place, food insecurity affects diet quality, including the quality of women's and children's diets. Accordingly, it contributes to increasing the risk of child malnutrition as a threat worldwide (<https://openknowledge.fao.org/items/c0239a36-7f34-4170-87f7-2fcc179ef064>). Many studies have reiterated the magnitude of proteins in food security (Pencharz et al., 2016; Allen, 2017; Bai et al., 2021). According to Jach et al. (2022), the global average meat consumption of a person is 43 kg in a year, and about half of the African population suffers from protein deficiency, with meat in their diets only about 10 kg per person annually. It has been predicted that diet-related health costs linked to mortality and non-communicable diseases under current food consumption patterns will exceed USD 1.3 trillion per year by 2030 (<https://openknowledge.fao.org/items/c0239a36-7f34-4170-87f7-2fcc179ef064>).

The production of easily available protein products without adverse effects on human life has been one of the most critical global challenges for many years (Jach et al., 2022). The global population of impoverished individuals and the scarcity of protein-rich food have prompted governments to seek alternatives to traditional costly protein sources like soy meal and fishmeal (Anupama & Ravindra, 2000). In the current situation, single-cell protein (SCP) is one of the most attractive choices as a desirable alternative to the conventional protein components of the diet (Haddish, 2015). Humans have been eating products linked to microbes (bread, cheese, and yogurt) for many years; hence, consuming microbial protein is acceptable and familiar (Kieliszek et al., 2017; Bajić et al., 2022). Microbial proteins are derived from microorganisms, including algae, yeasts (single-celled fungi), filamentous fungi, and bacteria, while yeasts are the most broadly accepted among all (Haddish, 2015). The convenience of using fungi, especially yeasts, for SCP production, in comparison with other microorganisms, is due to their easy propagation using cheap raw materials and simple harvesting, as they have bigger cell sizes and flocculation abilities (Bekatorou et al., 2006). From a sustainability viewpoint, exploiting novel biotechnological solutions, i.e., SCP, is indispensable.

Since waste disposal is financially burdensome, producing microorganisms' biomass, such as yeasts, is commercially viable while effectively contributing to waste management practices (Kieliszek et al., 2020). Yeast also provides other benefits, including higher nitrogen content than algae, more ash content compared to bacteria, rapid biomass production because of shorter growth time, and the capacity to grow in acidic pH conditions (Mohammadi et al., 2016)). These impressive advantages of yeasts for microbial protein production are well-known among world-famous manufacturers (Bekatorou et al., 2006). Bajić et al. (2022) in their paper reported that according to a GFI (Good Food Institute) company database where 88 fermentation companies were entirely focused on alternative proteins, the contribution of such companies rose to ~US\$1.69 B from 2020 to 2021, which is up 285%, representing 60% of the all-time investment. The Transparency Market Research Report (2020) predicted that the SCP market will reach ~US\$ 24.5 M at a CAGR of 9.7% by the end of 2030. The value of the worldwide market for SCP reached US\$13.1 B in 2022 (Koukoumaki et al., 2023; Ye et al., 2024).

In 2020, Vietnam's income from the SCP market was over US\$ 26.7 M, while economic experts estimate that this number will surpass US\$ 69.4 M by 2030 (Transparency Market Research Report, 2020). Pursuing the goal of developing efficient feed formulations for aquaculture, a recent practice in this industry has been the exploration of alternative proteins that promote sustainable further growth. As announced by FAO, the successful Asian countries in the aquaculture industry, such as China, Indonesia, India, Bangladesh, and Vietnam, produce around 50–60% of the total aquaculture production and use SCP as a nutritive and more cost-effective alternative to fishmeal (<https://www.fao.org/fishery/en/publication/295155>). Thus, it is anticipated that these producers will expand the aquaculture industry in the near future, causing a great rise in the SCP market (Transparency Market Research Report, 2020).

A balanced diet is necessary for livestock animals to give them proper nutrients and energy for growth, reproduction, and immunity against infections, leading to a more sustainable and profitable farming system. Therefore, due to its vital attributes, such as containing different micronutrients, SCP has garnered particular interest in the feed industry. The microorganisms applied for SCP production affect the food values and nutritiousness of the products (Bratosin et al., 2021). *Saccharomyces cerevisiae* is a yeast species widely known for being nutritious and edible by humans. It also has a diverse array of uses in multiple industries, including beverage and food production, biofuel manufacturing, and biotechnological products such as enzymes and probiotics (Bekatorou et al., 2006). One of the advantageous characteristics of *S. cerevisiae* is its ability to use plenty of organic compounds, such as agricultural residues and industrial waste, for growth.

This property is substantial because it creates value-added products and establishes a novel pathway for a circular economy (Nyyssölä et al., 2022). One further recent aspect

regarding *S. cerevisiae* that has garnered the attention of researchers and community health participants is the prominent role it can take in the “One Health” concept, from controlling pathogenic microorganisms (in both humans and animals) to leveraging food quality and preserving the environment, due to its unique features. The One Health approach is a collaborative strategy that addresses health issues sustainably through joint efforts of experts across multiple disciplines (animal, human health, and environmental) (Ballet et al., 2023). This review focuses on the single-cell protein as a way out of worldwide protein shortage and its production processes. It also aims to bring up *S. cerevisiae* as one of the most prevalent yeasts in the SCP industry while discussing some critical research demonstrating its unique role in the feed industry.

SINGLE-CELL PROTEIN AS A SUSTAINABLE SOLUTION FOR GLOBAL FOOD INSECURITY

The predicament of world hunger, measured in various indices such as “undernourishment” and “food insecurity,” among other terms, has unfortunately reached a new level of severity. According to the statistics provided by FAO in its 2022 report, between 702 and 828 million people lived in hunger during 2021. Above and beyond, according to this statistic, an increase of 150 million people living in hunger has been observed since the COVID-19 pandemic in 2019 (<https://openknowledge.fao.org/items/c0239a36-7f34-4170-87f7-2fcc179ef064>). Adding to that, according to WFP (2022), a United Nations Sustainable Development Group (UNSDG) member, in 49 countries, as many as 49 million people are staggering on the edge of starvation. The aforementioned statistics reflect the cruciality of addressing world hunger as it affects human life and future generations. Analytical data on adequate nourishment indicates that proteins are the most significant part of the diet, highlighted in a combined study undertaken by WHO, FAO and United Nations University (UNU) referring to proteins as necessary for growth (WHO, 2007). With reference to the expected growth of the world’s population to approximately 9 billion people by 2050, the food demand will increase by 60%, while the predicted value for protein is 40% (Ye et al., 2024). The International Feed Industry Federation has estimated that the production of different animal proteins like beef, dairy, and poultry will double and that fish production will nearly triple this year (IFIF, 2023). Animal protein in all its forms, such as meat, milk, and eggs, has a substantial place in providing macro and micronutrient deficiencies in a healthy human diet worldwide. Whereas the most expensive and essential component in an animal raising system is feed, the animal feed industry is considered a leading player in achieving sustainable food security.

Novel protein sources like SCP, insects and underused plants are among the most important sources that are anticipated to contribute to the future protein nutrition of humans and animals. Anti-nutritional components of many plant species and allergenicity

and biosecurity risks of insect protein, besides questions relating to their digestibility level, are considered the main obstacles before they can become desirable substitutes in human food or as an animal feed ingredient (Salter & Lopez-Viso, 2021). Though SCP is known as a notable source of protein as well as many other vital nutrients, there has been an outstanding rising interest in the consumption of microbial protein in feeding in recent decades. Superiorities such as not being influenced by seasons or climate conditions and being cost-effective and environmentally safe are the most dominant benefits of microbial protein compared with animal and plant proteins (Onyeaka et al., 2022).

SINGLE-CELL PROTEIN

As previously stated, the world's growing population and their increasing requirements for vital nutritional elements, particularly protein sources, represent a critical issue in the coming decades (Raziq et al., 2020). Food security and meat consumption are closely connected as meat remains a primary source of crucial nutrients for a significant proportion of the global population. According to Salazar-López et al. (2022), the preferred source of protein for most consumers is meat products. On the other hand, the dependency of industrial livestock production on human-edible crops makes it fundamentally inefficient. While the land directly utilized for animal housing may not be extensive, a vast amount of arable land is exploited for cultivating the crops that will later serve as animal feed (Stevenson, 2015). To achieve the goal of sustainable food production, competitively priced protein sources, such as microbial protein, can be exploited (Raziq et al., 2020; Salter & Lopez-Viso, 2021). SCP protein sources exhibit remarkable advantages, including significant protein content, a short period of microorganism proliferation, and the capability to be genetically manipulated for desirable content or the degradation of specific raw materials (Kieliszek et al., 2017).

Although the idea of consumption of microbes as a food source for humans and animals may appear to be unacceptable, humans have been using them, either unintentionally or intentionally, as these microscopic organisms are present in bread, fermentative beverages, yogurt, cheese, and soya sauce for thousands of years (Anupama & Ravindra, 2000). Germany in World War I used SCP extracted from *S. cerevisiae* as a replacement for more than half of its important protein sources (Ukaegbu-Obi, 2016; Ye et al., 2024). *Candida utilis* is another yeast species comprising a high amount of exogenous amino acids, which has been applied as a protein source (Kieliszek et al., 2017). In 1968, for the first time, the term single cell protein (SCP) as an alternative to terminologies like microbial protein was introduced by scientists (Sharif et al., 2021). SCP biomass possesses the special attribute of being entirely edible without generating any biowaste like stems, roots or leaves. Since the process of SCP production occurs in a bioreactor with no leakage to the environment and no need for pesticides, the technology has no ecological impact (Bogdahn, 2015). SCP

has been reported to be a good source of protein (30%–80%) and also essential amino acids (threonine, lysine and methionine), minerals, vitamins, lipids, and carbohydrates (Salazar-López et al., 2022).

Microbial protein is employed in many food areas, such as ready-to-serve meals, diet recipes, emulsifying aids, vitamins, and aroma carriers (Suman et al., 2015; Ukaegbu-Obi, 2016). Nowadays, SCP is perceived as part of a healthy diet with respect to their appreciable content of bioactive peptides, proteins, amino acids, fatty acids and pigments, which this complex of valuable biological compounds engages in the process of preventing diet-induced obesity (Patias et al., 2018). Furthermore, many other industries like industrial animal feed, wastewater treatment, paper and leather processing, biofuel, and foam stabilizers benefit from SCP in various ways (Suman et al., 2015; Raziq et al., 2020; Bratosin et al., 2021).

MICROORGANISMS FOR SINGLE-CELL PROTEIN PRODUCTION

SCP is produced from many microorganisms, including algae, yeast, filamentous fungi, and bacteria (Anupama & Ravindra, 2000; Mohammadi et al., 2016; Sharif et al., 2021). The microbial communities should exhibit specific traits like rapid as well as stable growth, high biological value, non-toxicity, non-pathogenicity, and minimal nucleic acid content to be appropriate for SCP production (Zhou et al., 2019). The growth rates of microorganisms exploited in SCP production are as follows: bacteria with 30 min to 2 h, yeast with 40 min to 3 h and algae with 3–6 h. It is apparent that yeast and bacteria can multiply in a very short period of time as it has been reported that in only 5–15 min, they double their population, while this duration for algae and filamentous fungi is 2–4 h (Sharif et al., 2021). More examples of each microbial group are given below.

Algae

Algae have been regarded as an important dietary component for people in central Africa and East Asia (Nyssölä et al., 2022). For example, thousands of years ago, *Spirulina* was harvested from the water by people of the Aztecs near Lake Texcoco in Mexico and near Lake Chad in Africa to be consumed after drying (Costa et al., 2004). Algae species are the source of many vitamins (A, B, C, D and E), proteins and fats. The protein content of algae is 40%–60%, while bile pigments, chlorophyll, mineral salts and fiber are its other biomass contents. In a study, *Pelvetia* was used in cow feed ingredients, which enhanced the milk-yielding capacity (Anupama & Ravindra, 2000). As algae have valuable nutrient contents and can capture solar energy, many algae species (*Soenedesmus*, *Chlorella*, *Coelastrum*, and *Spirulina*) have been exploited for mass cultivation desirably (Raziq et al., 2020). As stated, *Spirulina* has been successfully produced in large quantities and used in dietary supplements and food products. Besides, its usage in the feed industry brings

advantageous features such as giving rise to healthy yolk composition for poultry and coloring fish flesh in aquaculture. Both *Chlorella* and *Spirulina*, with a high protein content of up to 50%–70%, are now marketed as functional foods. These species also increase the food and feed values with their other desirable components, i.e., small peptides, lipids, vitamins, and pigments (Nyyssölä et al., 2022).

Bacteria

The rapid growth, short generation time and high protein content (50–80%) of bacteria make them suitable cases for SCP production. Hence, many bacterial species have been investigated for such applications (Raziq et al., 2020). They also can grow on many types of raw materials and edible substrates like sugars and starches (Sharif et al., 2021). *Alcaligenes* and *Cellulomonas* are the most widely used bacterial species in SCP production (Ukaegbu-Obi, 2016). Two bacterial species with good protein compositions applied in animal feed are *Methylophilus methylotrophus* and *Methylotrophic bacterium*, which have about 2 hours of generation time (Raziq et al., 2020). Photosynthetic Purple Non-Sulphur Bacteria (PNSB) are among the beneficial microorganisms in fish feed with 70%–72% protein content and highly resistant to toxicants. It is noteworthy that its essential amino acids profile is similar to soybean protein (Raziq et al., 2020). The limitations of using bacteria as food include public acceptance, high content of nucleic acid on a dried mass basis and difficulty of harvesting due to its small size (Ukaegbu-Obi, 2016).

Filamentous Fungi

Trichoderma album, *White rot fungi* and *Paecilomyces variolii* are examples of filamentous fungi which serve as SCP sources (Anupama & Ravindra, 2000). In general, the nutritional composition of fungi makes them desirable to use as SCP products. They have mainly 30%–50% protein as well as essential amino acids, vitamins and lipids (Anupama & Ravindra, 2000; Nasserri et al., 2011; Onyeaka et al., 2022). Exploiting fungal species in bioconversion of lignocellulosic waste is one of the recent trends in SCP production (Anupama & Ravindra, 2000). One of the oldest providers of commercial fungus is Quorn, which Marlow Foods (GB) launched in 1985. Quorn products are an example of successful protein production from filamentous fungi (*Fusarium venenatum*) for human consumption (Nyyssölä et al., 2022; Graham & Ledesma-Amaro, 2023).

Yeast

Yeasts are microscopic fungi that metabolize organic substances to harness their required nutrients and energy for reproduction and growth (Walker & Stewart, 2016). The non-pathogenic character of many types of yeasts resulted in their significant role in human

life since antiquity. Yeasts have superior nutritional qualities like high lysine and malic acid contents (Raziq et al., 2020). Another remarkable advantage of yeasts over other microorganisms is their ability to withstand acidic environments (Bogdahn, 2015). They have been used in the feed as supplements since the olden days. It is noteworthy that a considerable portion of the SCP from yeast and other fungi that are used in the feed industry comprises by-products from food and beverage plants as well as biorefineries. In addition, a large number of studies utilize by-products of industrial processes for producing yeast biomass, mostly for investigating their application as feed supplements. These include culturing various yeast species on brewer's spent grain, dairy waste, orange pulp, potato starch processing waste, and many more (Nyssölä et al., 2022).

In a study by Onyeaka et al. (2022), food waste and vegetable products used to culture *S. cerevisiae* and the protein content of the biomass were successfully boosted up to 39.8%. They concluded that the use of these types of waste in SCP production by *S. cerevisiae* reduces expenses linked to waste management while producing beneficial food and feed ingredients. Arous et al. (2016) studied the potential capacity of two discovered yeast species, *Candida pararugosa* BM24 and *Schwanniomyces etchellsii* M2, for degradation of olive mill wastewater for SCP production and reported 35.9% protein content as the maximum yield. In this experiment, the concentration of olive mill wastewater was 75% (v/v), followed by an incubation period of 96-h with an inoculum volume of 5% (v/v) at 30°C. As an instance of problematic industrial by-products, potato wastewater and glycerol were successfully applied by Kurcz et al. (2018) as nutrient sources in *Candida utilis* production, and the protein content of produced SCP was 42%. This yeast is validated as a safe species and has contributed to feed and food supplements for decades (Bekatorou et al., 2006; Bzducha-Wróbel et al., 2018a). Apart from protein, some yeast species have the capability to accumulate lipids in their cells, which has been called Single Cell Oil (SCO), with fatty acid profiles that are similar to those of vegetable oils (Gientka et al., 2017). Gientka et al. (2017) applied a similar industrial waste (deproteinated potato wastewater enhanced by carbon sources, i.e., glycerol) to produce SCO and successfully reached lipid accumulation above 20% in the yeast cells. Another noteworthy feature of yeast is its capability to absorb critical microelements in their cell structure and create stable binding with proteins (bioplexes). These complexes are enriched with metal ions (i.e., selenium), which have medical and veterinary applications (Kieliszek et al., 2017). The versatile yeast *S. cerevisiae* is able to easily ferment available sugar in various types of wastes, i.e., glucose, sucrose, fructose, maltose, galactose, maltotriose, and mannose, into carbon dioxide and ethanol (Walker & Stewart, 2016). Furthermore, it has probiotic properties and is regarded as an effective feed supplement that ameliorates feed utilization, reduces the number of pathogens, and improves animal performance and health (Elghandour et al., 2020).

Saccharomyces cerevisiae

In 1838, for the first time, Meyen named the fermentation yeasts *Saccharomyces* (Boynton & Greig, 2014; Stewart, 2014). Subsequently, another researcher named Hansen pinpointed the specific characteristics of *S. cerevisiae* in 1888 (Boynton & Greig, 2014). The application of fermentation for producing food and beverages can be traced back to as early as 7000 BC in China and 6000 BC and 3000 BC in Iran and Egypt, respectively. Therefore, it is concluded that such fermenting techniques developed from Mesopotamia across the world (Legras et al., 2007). It is remarkable that according to the new genomic confirmations, the canonical bread yeast, *S. cerevisiae*, originated in China before moving west 16–14 tya via the Silk Road (Lahue et al., 2020). One of the recognized capacities of yeasts is producing alcohols with intricate and extended chemical structures along with their derived esters that represent intriguing flavor profiles.

De Almeida Silva Vilela et al. (2020), in their experiments, identified phenylethyl alcohol in selected *S. cerevisiae* strains, which is a highly important alcohol in terms of aroma with a rose-like fragrance. *S. cerevisiae* demonstrates resilience to elevated sugar levels, a quality that is pivotal in its industrial uses (Parapouli et al., 2020). Furthermore, the glycoproteins and polysaccharides of *S. cerevisiae* cell walls provide functional qualities for human and animal bodies (Kieliszek et al., 2017). The European Food Safety Authority acknowledged the Qualified Presumption of Safety (QPS) status of this distinguished yeast, the most widely employed food sector (Moslehi-Jenabian et al., 2010). Except for the fermented products, i.e., bread, cider, and beer, *S. cerevisiae* has species that have been isolated from other sources like soil, fruits and trees. *S. cerevisiae* needs to adapt to unique selection pressures to survive in each of these environments. For over a century, companies such as Cenovis R (Gustav Gerig AG), Marmite R (Unilever and Sanitarium Health Food), and Vegemite R (Bega Cheese Ltd.) have been selling *S. cerevisiae* in the form of yeast extract due to its high protein content and its provision of five essential B vitamins. Among some industrial establishments that employ *Saccharomyces* as the main microorganism in their SCP products, Bega Cheese Ltd., Flint Hills Resources, Shanghai Tramy Green Food Co., and Tangshan Top Bio-Technology Co. can be mentioned (Ritala et al., 2017).

Moreover, the use of *S. cerevisiae* as a model organism in various fields of research ranging from molecular biology to basic genetics is frequently preferable due to a number of its pivotal (Mohammadi et al., 2016). As Stewart (2014) mentions, among eukaryotes, the inner cell structure of *S. cerevisiae* is very close to animals and plants. In addition, there are several other justifications that make this species a valuable tool in a wide range of investigations, including ease of genomic manipulation, which is beneficial in various biotechnological areas from human genetics investigations to testing new drugs and much more (Stewart, 2014; Parapouli et al., 2020). Including a simple unicellular character while demonstrating most of the metabolic pathways and essential cellular activities that

appeared in higher eukaryotes, simplicity of culturing and maintaining in the lab, the possibility of storing viably at -80°C that provides researchers with the feasibility of cross-generational studies, its special economic importance among all other microorganisms, and its application in contagious illnesses studies, specifically prions, ssRNA viruses and dsRNA viruses through explanation of the interactions between them and cellular components (Stewart, 2014; Parapouli et al., 2020). In addition, multiple studies have proven that *S. cerevisiae* exhibits a great tolerance to high sugar levels in the medium, which has an impressive role in its industrial usage (Parapouli et al., 2020). The cellular response system triggered by such conditions contributes to yeast survival by maintaining the robustness and integrity of the cell wall (Bzducha-Wróbel et al., 2018b).

In recent years, significant efforts have been made to modify yeast species in order to enhance the generation of desirable compounds (Kieliszek et al., 2020). Regarding *S. cerevisiae* species, genetic engineering for utilizing targeted substrates, producing high-value chemicals, and boosting stress resistance are among the most attentive studies. A vast area of this research concerns the development of the capability of utilizing lignocellulosic biomass in *S. cerevisiae* production as a cheap and problematic raw material. Lignocellulosic wastes are one of the most abundant agricultural residues, and acid treatments are the common method for their hydrolyzation (Çakar et al., 2012). This approach is not considered attractive due to its high cost and not being in accordance with the environment. Currently, recombinant *S. cerevisiae* strains have been produced for later commercial usage. Production of organic acids such as lactic acid, succinic acid, and 3-hydroxypropionic acid by this genetically engineered *S. cerevisiae* are noteworthy case studies. One of the carbohydrates with a considerable volume in the market is sorbitol, a common sweetener widely applicable in food industries. It has been successfully produced by a mutant of *S. cerevisiae* yeast (Baptista et al., 2021).

As mentioned, demonstrating adequate tolerance to agitated conditions during industrial processes plays an important role in most *S. cerevisiae* applications. Researchers introduced a mutant strain of *S. cerevisiae* that possesses more resistance to such conditions, e.g., higher freeze tolerance (Teunissen et al., 2002). Another aspect that needs to be addressed for sustainable and meaningful yeast production is conducting comprehensive life cycle assessments (LCA) of procedures to perceive their environmental impact compared to traditional protein sources. Life-cycle assessment (LCA) is a useful assessment of a process or product throughout its entire life cycle to analyze its environmental impacts (Ye et al., 2024). As stated by McAuliffe et al. (2023), multiple recent research on life cycle assessment (LCA) has come to the conclusion that animal proteins (especially those from ruminants) have a significant environmental footprint and should be highly limited. Ye et al. (2024) reviewed the latest life-cycle assessments and techno-economic analyses of SCP production by various microorganisms. The raw material used, cultivation methods, and

downstream processing are some of the critical factors that must be confronted for yeast production. At the same time, feedstock upstream treatment seems to be the major obstacle to filamentous fungi and yeast production. The main strategies to overcome this hurdle are co-cultivation and pretreatment, which have been reported to improve process productivity.

In a report prepared by the Norwegian Institute for Sustainability Research (NORSUS), the Life Cycle Assessment (LCA) for yeast production has been documented. According to the data, sugar source, the major proportion of raw material production, had the most significant environmental impact across different groups, followed by ammonia and other materials. They declared that consequences from yeast processing only contributed to a small percentage of climate change, and it was negligible in all other categories. In addition, yeast production had lower environmental impacts when nitrogen source was derived from an organic source, such as wastes from the livestock slaughter process (Møller & Modahl, 2020).

***S. cerevisiae* in Feed Industry**

The industrial application of amino acids in the feed industry dates back to the late 1950s and 1960s, when DL-Methionine was synthesized chemically and used in poultry feed. During the 1960s, L-Lysine was produced through fermentation in Japan (<https://www.fao.org/4/y5019e/y5019e00.htm#Contents>). Apart from these products, in the late 1980s, L-Tryptophan, HCl and L-Threonine were introduced. Decreasing the production costs of each amino acid due to biotechnological advancements has led to the growth of using amino acids in animal feed. It is important to note that amino acids are a key factor in improving feed efficiency. With this respect, there is a notable interest in the expansion of the use of SCP as a natural source of essential and nonessential amino acids among owners of livestock industries. Kieliszek et al. (2017) stated that the well-balanced amino acid profile of SCP yeasts led to outstanding interest in their application.

The obtained SCP from yeast has a relatively low proportion of methionine, but its lysine and threonine contents meet FAO guidelines (Nyyssölä et al., 2022). In their experimental study, Bertasini et al. (2022) discovered that in the single-cell protein produced by *S. cerevisiae*, nearly all amino acid concentrations exceeded those found in the commercial monogastric feed (Table 1). It could be concluded that SCP from *S. cerevisiae* source can be utilized to enhance growth performance and general animal health as well as improve the nutritional quality of the feed.

Another study mentioned that the amino acid profile of SCP from *S. cerevisiae* is similar to that of soya protein. It also contains vitamins such as riboflavin, nicotinic acid, biotin, thiamine, ascorbic acid, pyridoxine, β -carotene, cyanocobalamin, pantothenic acid, atocopherol and folic acid, which maintain a pivotal function in metabolism and health (Bratosin et al., 2021). What makes using yeast (i.e., *S. cerevisiae*) as animal feed superior is

their nutritional quality, together with their history of long-term use without adverse effects (Nasseri et al., 2011). The composition of fresh *S. cerevisiae*, depending on the growth condition and strains are as follows: around 40.6%–58.0% of proteins, 31.55%–45.0% of carbohydrates, 6.5%–9.3% of nitrogen, 5.0%–7.98% of minerals, 4.0%–6.0% of lipids, and different vitamin contents (Bekatorou et al., 2006; Onofre et al., 2017). β -glucans is another advantageous compound identified in *S. cerevisiae* with diverse applications in biotechnology. These polysaccharides are applied as novel nutritional ingredients but are also utilized in the role of antimicrobial and anticancer agents, immunomodulators, oral vaccine carriers, and cosmetics components (Bzducha-Wróbel et al., 2018a). In summary, the most significant effects of *S. cerevisiae* are associated with the above-mentioned valuable nutrients, which ultimately lead to overall animal health by inducing positive effects on gut microbiota and the immune system and acting as a natural antibiotic.

Table 1

Aminoacidic profile of the SCPs (S. cerevisiae) and of monogastric animals (Bertasini et al., 2022)

	Monogastric feed (NRC, 1998)	SCPs
Arginine	34	53
Cysteine	31	23
Hstidine	32	41
Isoleosine	55	70
Leosine	100	87
Lysine	100	100
Methionine	29	26
Phenylalanine + Tyrosine	94	106
Thronine	65	82
Tryptophan	16	18
Valine	65	65

The obvious relationship between animal gut microbiome and their immune status and health has been reported in numerous studies (El-Bab et al., 2022). Thus, understanding the yeast's impact on the animal microbiota could positively contribute to optimizing and enhancing animal health. Wang et al. (2022), in their study on the effects of *S. cerevisiae* supplementation in fattening sheep diet, observed better growth and animal performance in comparison with the controlled groups, particularly well-developed rumen epithelium and microbial flora of rumen. Another investigation on grass carp with %12 *S. cerevisiae* dietary supplementation improved the host's gut microbiota and biochemical parameters (Liu et al., 2018). Overall, the findings of studies on gut microbiome in various animals demonstrate promising effects of *S. cerevisiae* on gut microbiota profile in various hosts.

Table 2 represents the pivotal effects of *S. cerevisiae* supplementation in the diets of different animal species.

Table 2
Effects of S. cerevisiae supplementation in diets of different animal species

<i>S. cerevisiae</i> Doses	Animal Species	Effects	References
(2 kg/ton feed)	Broiler	Increase in the number of gut yeast and lactic acid-fermenting bacteria while causing a reduction of <i>Escherichia coli</i> Enhancement of feed intake and weight gain	(Koç et al., 2010)
0.2%–0.4% diet	Broiler	Modulating the intestinal immune system and microbiology boosts production metrics and enhances feed efficiency	Bortoluzzi et al. (2018)
1–5 g/d	Dairy calves	Regulates both mucosal immune and systemic responses, diminishing clinical disease, occurrence of secondary bacterial infection, and lung pathology	Mahmoud et al. (2020)
28 g/calf/day	Fattening calves	Improvement of body weight reduces feed intake and average feed conversion rate (FCR)	Maamouri and Salem (2022)
5 g/day	Goats	Betterment of intestinal microecology, protein, lactose and fat content enhancement of the milk	Ma et al. (2020)
0.60% of the dry matter (DM) weight of the basal diet	Heat-stressed goats	Higher rumen fermentation, improvement in digestibility factors, increased growth performance	Xue et al. (2020)
0.8 g/kg diet	Fattening lambs	Increase in dry and organic matter, acid detergent fiber digestibility, enhancement of daily gain	Sun et al. (2022)
0.1% (w/w)	New Zealand white (NZW) Rabbit	Higher feed conversion efficiency and body weight, increase in nitrogen utilization	El-Badawi (2017)
11 g/head/day	Horse	Enhancement in intake and digestibility of dry matter, organic matter, neutral detergent fiber and acid detergent fiber	Salem et al. (2016)
4 mg/g of feed dry matter	Horse	Higher fiber digestibility and fermentation	Elghandour et al. (2016)

***S. cerevisiae* in Poultry Feed**

As a cheap and affordable animal protein source, chicken is economically valuable for most societies. Many poultry producers use antibiotics as medicine to prevent diseases or as a

growth enhancer, which has recently caused concerns among chicken consumers about antibiotic residues. In this situation, probiotic or live microbes and spores that develop in the intestine provide their hosts with beneficial properties of their metabolites directly or indirectly, encouraging nutritionists to use them as an alternative to antibiotics (Wulandari & Syahniar, 2018). In poultry nutrition, *S. cerevisiae* attains the position of the most popular probiotic or prebiotic among all yeast species. As in healthy broiler chicken, *S. cerevisiae* improves gut health by balancing the gut microbiome (increasing the multiplication of useful microbes, producing short-chain fatty acids, decreasing intestinal pH, and thus preventing pathogenic proliferation). This is in addition to possessing positive effects on histomorphological parameters and helping to maintain the homeostasis of epithelial cells (Ahiwe et al., 2021). Fanelli et al. (2015) in their study evaluated the effect of live *S. cerevisiae* on *Campylobacter jejuni* and *Salmonella enteritidis* content in broiler chicken and observed a remarkable control of *C. jejuni* as well as preventive effects on *S. enteritidis*. They concluded that *S. cerevisiae* in chicken feed could decrease the contamination of carcasses and prevent human foodborne illnesses.

In addition, *S. cerevisiae* can result in boosting the synthesis and release of pro-inflammatory cytokines from macrophages (Elghandour et al., 2020). Gheisari and Kholeghipour (2006) studied the *S. cerevisiae* effects on blood parameters, growth performance and immune response on 3-days-old male broilers by dietary inclusion of 01, 02 and 03% (w/w) of live *S. cerevisiae* powder and observed daily and final body weight, feed intake, serum high-density lipoprotein level, and antibody titer against influenza disease virus increased. Faria-Oliveira et al. (2013) mentioned the favorable effects of baker's yeast for laying chicken and breeder turkeys. They relate the effects to the rich folic acid content in *S. cerevisiae*, an important vitamin for turkeys and other poultry. As previously noted, *S. cerevisiae* is an excellent source of various vitamins, including biotin. A deficiency in biotin can result in poor hatchability, low egg production and reduced feed conversion. In fact, reproductive improvements in chickens fed by *S. cerevisiae* are connected to the high level of biotin and selenium in yeast, which is more effective than inorganic selenium, which is usually added to their diets. Chollom et al. (2017) declared the nutritional value of *S. cerevisiae*, which could be replaced with soybean in poultry feed as a protein source. They evaluated the amino acid profile of *S. cerevisiae* and identified the presence of essential amino acids, including lysine, threonine, histidine, valine, phenylalanine, leucine, isoleucine, tyrosine, and arginine. In addition, they found nonessential amino acids in the following order: aspartic acid, serine, glycine, glutamic acid, alanine, and proline. Interestingly, it was comparable to the amino acid profile of soybeans. Although tryptophan, cystic acid and methionine were not reported, the content levels were even higher than that of soybean. Izah et al. (2019) evaluated the vitamin content of *S. cerevisiae* cultured in cassava wastewater, and the results (Table 3) showed desirable vitamin content (A, E, D, C, B1, B3 and B12) of *S. cerevisiae* to be used in animal feed.

Table 3

Vitamin content in *S. cerevisiae* biomass cultured in cassava mill effluents (Izah et al., 2019)

Vitamins	Mean ± Standard deviation
Vitamin A, µg/100 g	2280.37 ± 105.85
Vitamin D, mg/100 g	40.73 ± 7.94
Vitamin E, µg/100 g	132.54 ± 14.00
Vitamin C, µg/100 g	6.88 ± 1.62
Vitamin B12, µg/100 g	0.58 ± 0.10
Vitamin B3, mg/100 g	2.62 ± 0.92
Vitamin B1, mg/100 g	1.05 ± 0.21

S. cerevisiae in Aquaculture (Fish Feed)

For both humans and animals, amino acids play a crucial role as intermediates in many metabolic pathways while serving as protein building blocks (Kasozi et al., 2019). Although fishmeal's essential amino acid profile is satisfactory for most species, the growing price has made producers use unbalanced ingredients as alternatives. Therefore, finding a substitute that meets the standard criteria for proteinous feed ingredients seems necessary. On the other hand, the pressure of increasing demand for marine resources doubles the necessity for finding novel protein sources with lower costs, like SCP (Ahmed et al., 2019). *S. cerevisiae* is the most used species in fish farming, demonstrating health-boosting effects (Agboola et al., 2021). Currently, most feeding trials tend to work on shrimp and salmon. In a study, the replacement of soybean meals (up to 24%) and fish meal (from 15% to 24%, depending on the product) with *S. cerevisiae*, *Kluyveromyces marxianus*, and *C. utilis* exhibits satisfactory results for shrimp (Jones et al., 2020). Bertasini et al. (2022) observed that the concentration of almost all amino acids was higher than the required levels for monogastric animals in producing SCP from *S. cerevisiae* using the effluent of the candy production process mixed with agricultural digestate. The only exceptions were leucine and cysteine levels, which were slightly lower. Furthermore, according to the review of literature conducted by Agboola et al. (2021) on selected yeast species of commercial importance for aquafeeds, based on several studies on *S. cerevisiae* from 1997 to 2016, they concluded that the total essential amino acid contents of *S. cerevisiae* are in similar concentration of the requirements for rainbow trout and Atlantic salmon.

S. cerevisiae in Livestock Feed

Alongside increasing interest in the use of *S. cerevisiae* in animal feed, related techniques and technologies need to be examined. In their research, Song et al. (2021) examined the effects of *S. cerevisiae* supplemented into pelleted total mixed rations (TMR) at two proportions of corn in the diet on fattening lambs. This study aims to determine whether the

process of pelleting resulted in *S. cerevisiae* becoming ineffective. The measured parameters were feed digestion, rumen fermentation, animal performance, microbial community, and blood parameters. Their findings indicated that pelleting resulted in dead yeast cells, which improved male lamb growth performance, probably due to improved fiber digestibility regardless of the proportion of corn in the diet. The change in the rumen bacteria and species was also reported. Alugongo et al. (2017) reported that supplementing mature ruminants feed with active live *Saccharomyces* and inactivated cell culture increased the production parameters, altered rumen fermentation and improved nutrient utilization. Interestingly, animals that were exposed to transport stress exhibited better health and growth performance when *S. cerevisiae* was added to their feed. In the process of preparing live *S. cerevisiae* for animal feed, the first step involves introducing live yeast cells into damp cereal grains or grain by-products. The mixture is then partially fermented, followed by a drying process that preserves the enzymes, vitamins and yeast without killing them. Providing a consistent supply of dicarboxylic acids and vitamins while reducing the presence of pathogenic microorganisms such as protozoa and removal of oxygen are among the main benefits of *S. cerevisiae* in ruminants. These effects ultimately result in improved digestion of fibers, increased feed intake and better animal performance (Faria-Oliveira et al., 2013).

According to Alugongo et al. (2017), the weaning process in some animals, such as calves, might be very stressful and even lead to respiratory problems, while supplementing the feed with *S. cerevisiae* can amend the situation as well as help the animal's immune system to reduce the risk of diseases that are intensified in this condition. In particular, it has been reported that *S. cerevisiae* can increase feed efficiency, improve immunity and reduce diarrhea in calves. In field research, the effect of *S. cerevisiae* on lactating Holstein cows and their lactational performance was assessed. All the cows were under heat stress during the experiment. Results of this study indicated that feeding *S. cerevisiae* to cows improved milk yields (1.2 kg/d), with more milk and true protein, and produced solids, not fat (Bruno et al., 2009). Another study by Hiltz et al. (2023) demonstrated that adding *S. cerevisiae* to the feed of dairy cows resulted in an enhancement of milk yield and also an improvement in efficiency at the beginning of lactation.

Substrates for SCP Production by S. cerevisiae

Various substrates have been used for SCP production by cultivating bacteria, algae, filamentous fungi, and yeasts. Some researchers classified them into conventional substrates like fruit and vegetable waste, molasses, whey, straw, starch, distiller's wash and wood and unconventional ones like lignocellulosic biomass, natural gas, methanol, petroleum by-products and ethanol (Bekatorou et al., 2006; Bzducha-Wróbel et al., 2018b). Others categorize the SCP raw materials into different groups, such as various types of waste (fruit waste, molasses, whey, sulfite waste liquor and milk), renewable plant resources (sugar,

cellulose and starch), carbon dioxide, and high-energy resources (natural gas, ethanol, gas oil, n-alkanes, acetic acid and methanol) (Bratosin et al., 2021). In addition, SCP is regarded as an economic by-product of biorefinery processes that enhance their profitability while reducing the burden of waste disposal. As a matter of fact, selling residual biomass in the form of SCP for animal feeding is preferable to selling them as fertilizer (Ritala et al., 2017). According to Koukoumaki et al. (2023), who reviewed the latest progress in SCP production, many by-products from industrial sectors and agricultural wastes, such as residues containing high levels of carbohydrates or a variety of effluents, are considered preferable substrates in terms of sustainability matters.

Generally, various agricultural and industrial wastes represent 20 to 30% of the total production cost (Sharif et al., 2021). A high proportion of by-products is generated during fruit and vegetable processing, such as those from apple processing, which are considered a major environmental problem in many countries. The issue could be managed through an environmentally friendly approach by exploiting yeast species (e.g., *S. cerevisiae*) to produce aromatic compounds that have vast applications in the food industry (Kieliszek et al., 2020). In their experiments, Bzducha-Wróbel et al. (2018a) effectively utilized deproteinated potato juice water to produce *S. cerevisiae* cell wall polysaccharides with biotechnology applications in the food industry. They presented a theory regarding the feasibility of yeast biomass production while enhancing the cell wall polysaccharides. Hence, utilizing various types of waste to produce SCP is considered an interesting strategy as it simultaneously produces food-grade protein for human and animal usage and lowers the waste load and environmental pollution (Kieliszek et al., 2020). In this respect, SCP production techniques are often combined with waste processing and bioremediation practices. In China, technologies related to producing SCP from agricultural or food residues are highly favored, and this country holds the record for the highest number of patent submissions and publications related to SCP (Ribeiro et al., 2023). Their share of patent applications from 2001 to 2016 was up to 70% (Ritala et al., 2017). Besides, the ability of microorganisms to decompose hydrocarbon residues as a source of carbon and energy has been widely exploited to produce SCP (Al-Mehmdi & Al-Rawi, 2019).

Nevertheless, there are specific standards that waste materials must meet to be considered a suitable substrate in SCP production. Some of the important ones include abundant, non-toxic, inexpensive and regenerable. The selection of proper substrate is also important since it has a direct impact on the biomass yield and the productivity of fermentation. Microorganisms react differently to various substrates; thus, for each type of substrate, an appropriate fermentation technique needs to be optimized (Reihani & Khosravi-Darani, 2019). Many of the raw materials for producing SCP need to be hydrolyzed through different techniques (physical, chemical and enzymatic) for better fermentation (Suman et al., 2015; Ukaegbu-Obi, 2016). Furthermore, some microorganisms

need to be provided with extra minerals and vitamins to obtain maximum productivity (Sharif et al., 2021). The yeast *S. cerevisiae* is mainly cultured on beet or cane molasses, which are the major by-products of the sugar industry. The fermentable sugars in molasses are glucose, galactose, sucrose, fructose, and melibiose, with 45%–55% of the substrate while containing approximately 40% (dry mass) of nonfermentable substances. Molasses in SCP production possess advantages such as the absence of fermentation inhibitors and toxic substances, desirable composition, low cost and abundance (Bekatorou et al., 2006).

In SCP production, a major portion of the cost is attributed to the carbon source, while ammonia contributes only 7%–15%; hence, efforts have been made for *S. cerevisiae* propagation from inexpensive carbon sources such as different fruit waste and cheese whey (Reihani & Khosravi-Darani, 2019; Sharif et al., 2021). For instance, cucumber waste and orange peels have been recommended as useful substrates for producing SCP from this yeast (Suman et al., 2015). Shahzad et al. (2024) studied SCP production from vegetable residues (eggplant, tomato, cucumber, and capsicum) by some yeast species. Their experiments revealed that a co-cultivation of *S. cerevisiae* and *Candida tropicalis* indicated the highest protein yield. Starch will only be usable by *S. cerevisiae* after conversion to fermentable sugars, i.e., glucose and maltose. To maintain the cost of the process, simultaneous culture of *S. cerevisiae* with amylolytic fungi such as *Aspergillus* species are common practices in SCP production from starch (Bekatorou et al., 2006). Molitor et al. (2019) designed a two-stage bioprocessing system under aerobic and anaerobic conditions and caught the ammonia in wastewater as a nitrogen source for edible protein production by *S. cerevisiae*, aligned with the needs of a circular economy. They also applied renewable electric power in their system, referring to a power-to-protein (P2P) scheme to produce SCP (Molitor et al., 2019).

SCP Production Process by S. cerevisiae

Technically, SCP is the production of beneficial biomass cells using microorganisms by culturing them on raw materials or different agricultural and industrial wastes (Anupama & Ravindra, 2000). After choosing a suitable substrate, microorganisms such as algae, bacteria, yeasts, and filamentous fungi can be cultivated on it to increase their cell mass (Bratosin et al., 2021). The industrialization of yeast production began when optimized and standardized manufacturing systems replaced handmade processes of producing fermented food and beverages. Since then, millions of tons of yeast biomass have been produced every year, while optimization of the process is continuously monitored to reduce costs and boost productivity. *S. cerevisiae* is cultured through a two-stage fermentation process: batch fermentation and then fed-batch or aerobic metabolism, designed to propagate the cell numbers. The process occurs in bioreactors where the conditions are controlled, such as temperatures kept between 28–30°C, pH levels between 4.5 and 5.0, and oxygenation rates

below 140 mM/L.h. In the initial phase (batch fermentation), high carbon concentration induces hyperosmotic stress in *S. cerevisiae*.

Gradually, the carbon source is consumed along the exponential growth phase, which results in the accumulation of ethanol. This condition exposes the yeast cells to high ethanol concentration as well as nutritional deprivation stress at the end of the process. Under these conditions, *S. cerevisiae* cells switch their metabolism from the fermentative to the oxidative method. If the ethanol concentrations are lower than 0.05%, it is alternatively used as a carbon source (Pereira et al., 2021). Another common method for industrial propagation of *S. cerevisiae* comprises several stages: proliferation through several fermentation processes, harvesting, concentration and/or drying, and packaging (Bekatorou et al., 2006). First, specific *S. cerevisiae* strains from a pure yeast culture are cultivated on an appropriate substrate in the laboratory. Then, the biomass from the laboratory culture is transferred precisely into anaerobic bioreactors. The next stage is *S. cerevisiae* proliferation in fermentation bioreactors operating in anaerobic and fed-batch mode. Using centrifugation, the produced biomass is harvested and utilized for the next steps: fed-batch pitch fermentor and then trade fermentor. The maturation phase includes aerating the contents of the trade bioreactor in the last step. Manufacturers vary in the number of bioreactors, fermentation stages, and sequences. The end product is collected using a rotary vacuum filter or a filter press, with a 27–33% dry cell mass concentration. Appropriate quantities of water, emulsifiers, and cutting oils derived from cottonseed or soybean oil are mixed with *S. cerevisiae* cake to achieve an adequate form for extrusion (Figure 1) (Bekatorou et al., 2006).

A complete setup is required to maintain hygiene and sterile conditions to prevent various types of contamination. This is a recognized occurrence that the SCP process of all types of microorganisms, except algae, requires adequate aeration, which might contain different pathogens (Raziq et al., 2020). The nutritional value of the final SCP product is affected by the methods of harvesting and drying as well as processing techniques (Bratosin et al., 2021). Some researchers have also mentioned further processing stages, such as purification, cell disruption, washing, and protein extraction (Sharif et al., 2021). Generally, the last stage is packaging under a vacuum or nitrogen atmosphere and shipping the product as compressed yeast (Bekatorou et al., 2006).

Regardless of recent promising advancements in SCP production (particularly those from yeast), the primary technologies must be modified for greater improvement in cost efficiency and availability on scale (Ye et al., 2024). In this context, major consideration should focus on optimized utilization of abundant agro-industrial wastes, new process design in line with circular economy principles, exploiting recent innovative automation and control techniques for large-scale production, harnessing genetically manipulated microorganisms for the purpose of degradation of aimed substrates, and novel co-culture

cultivation to enhance efficiency and final product yield. In addition, the results of life cycle assessments (LCA) must be factored into a new fermentation scheme and further development of this technology.

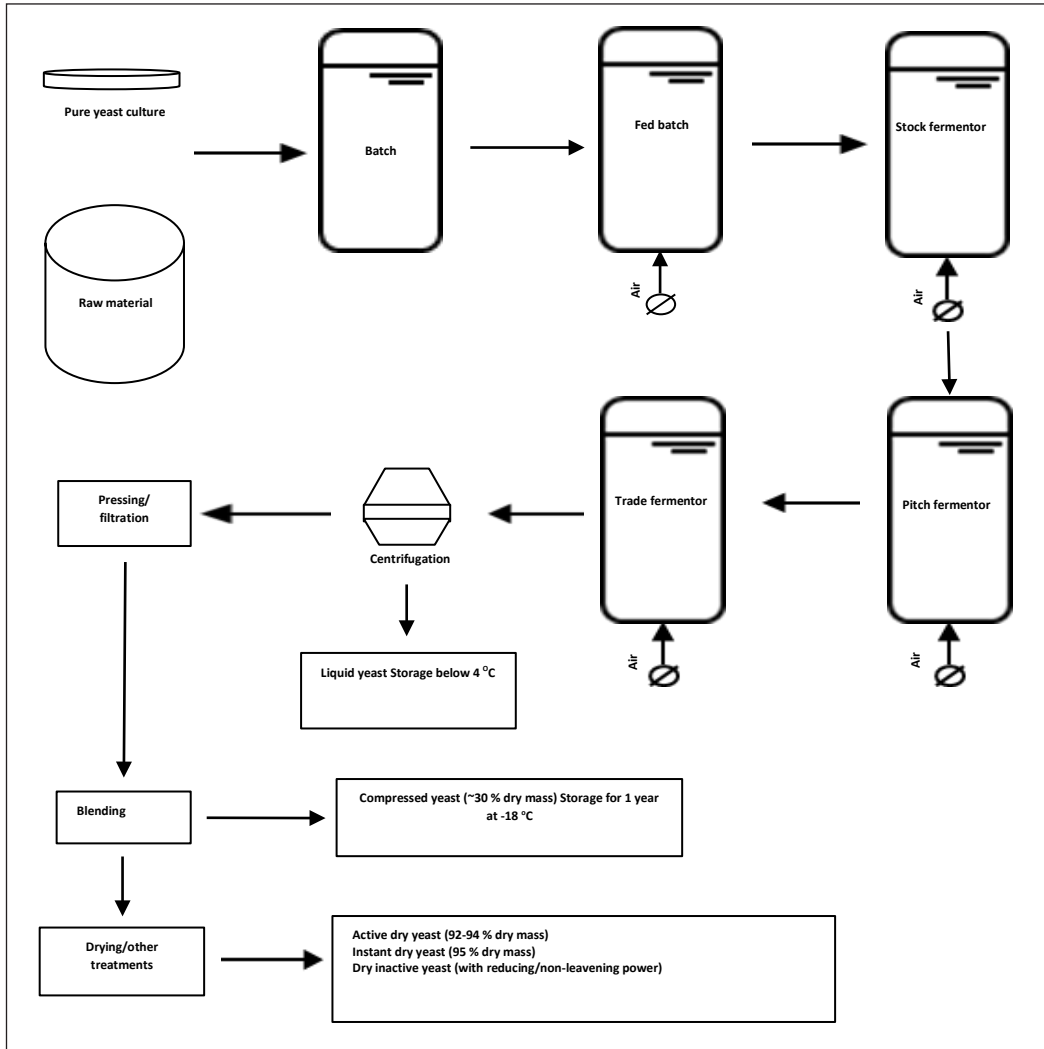


Figure 1. The propagation scheme of a commercial baker's yeast (Bekatorou et al., 2006)

Precision fermentation is one of the newest advances in utilizing recombinant yeast strains to express proteins that have evolved to make particular food-related items accessible (Martin & Chan, 2024). As previously noted, utilizing waste substrates is crucial for any further development of yeast production in the future. One of the main challenges of using lignocellulosic wastes in producing microbial protein is that they need to be hydrolyzed prior to introducing to the main fermentation media (Martin & Chan, 2024). Thanks to the

advancement of genetic engineering, a new modified microbial strain with the capability of lignocellulosic waste hydrolyzation could be generated. Another successful example of employing agro-industry by-products is using potato wastewater for yeast cultivation since it is rich in organic carbon, minerals, amino acids and different proteins (Gientka et al., 2017). The high nucleic acid content of yeast cells is a problematic issue addressed through enzyme, alkali, and heat treatments as one of the newest developments in the downstream processing of yeast production (Martin & Chan, 2024).

Microbial protein production via membrane bioreactors is another recent development in the field that could lead to a prominent contribution to efficient manufacturing. In conclusion, the interdisciplinary approach to SCP production involves combining biotechnology and environmental sciences with chemical engineering to reach an efficient and sustainable production system. While biotechnology advancements enable the optimization of culture conditions, instrumental tools of environmental sciences (e.g., life cycle assessment (LCA) and techno-economic analysis (TEA)) evaluate major impacts of the process and present solutions where required for minimizing ecological effects. The integration of chemical engineering and biotechnology offers innovative final products (e.g., environmentally friendly compounds). Moreover, the synergy between the above-mentioned technologies and agricultural systems further supports SCP production.

CULTIVATION METHODS

Based on the physical state of the nutrient medium, SCP production processes (fermentation process) are categorized into three groups (Gupta et al., 2022):

- Submerged fermentation
- Semisolid fermentation
- Solid state fermentation

Submerged Fermentation

Submerged fermentation is known as a more commonly used method in SCP production (Reihani & Khosravi-Darani, 2019). In this type of fermentation process, the used substrates, which contain the nutrients required for microorganisms' growth, are always in liquid forms. The fermenter tank operates continuously, and the biomass yield is harvested continuously through different techniques. The produced SCP is then filtered or centrifuged and subsequently dried. Due to the heat generation during the whole cultivation process, aeration is required, which is done using a cooling device (Ukaegbu-Obi, 2016; Raziq et al., 2020; Sharif et al., 2021). In addition, stirring the fermentation media is required during the submerged fermentation to provide microorganisms with sufficient oxygen (Ukaegbu-Obi, 2016). The methods for harvesting microbial biomass vary, as yeast and bacteria can

be recovered through centrifugation, while filtration is usually used for filamentous fungi. Recovery of maximum water content is important, especially prior to the final drying stage. This water has valuable soluble nutrients that can be extracted under clean conditions (Ukaegbu-Obi, 2016; Raziq et al., 2020; Sharif et al., 2021).

Semisolid Fermentation

SCP production by semisolid fermentation involves key operations, including preparing proper media with suitable carbon sources, preventing medium and bioreactor contamination, separating the final product, and processing it accordingly. Effective preparation of substrates plays a crucial role in this type of fermentation. This process takes place in a solid state and requires substantial operating costs and capital investments. Many types of carbon sources, such as carbon oxide, gaseous hydrocarbons, methanol, polysaccharides, ethanol, effluents of various breweries, n-alkenes, molasses and other solid substrates, are usable in semisolid fermentation. The cultivation process itself consists of several steps, including multiphase system mixing, stirring, transport of oxygen from gas bubbles to microorganisms through the liquid phase, and finally, heat transfer to the surroundings (Ukaegbu-Obi, 2016; Raziq et al., 2020; Sharif et al., 2021).

Solid State Fermentation

Solid-state fermentation is implemented via various types of bioreactors, process conditions and many microorganism species to produce a variety of value-added products like SCP, enzymes, feeds, organic acids, flavors, B-complex vitamins, and pigments (Ukaegbu-Obi, 2016; Sharif et al., 2021). The process requires substrates in pure solid form, such as rice and wheat bran. The selected substrate is deposited on the flatbeds subsequent to inoculation with microorganisms, and then the substrate is left in a temperature-controlled room for a few days. The optimal yield can be achieved by ensuring that the moisture level is properly maintained at 60%–65% (Ukaegbu-Obi, 2016; Raziq et al., 2020; Sharif et al., 2021). Although submerged fermentation is the common process for producing SCP from yeast and other fungal species, recently, solid-state fermentation has caught the interest of producers. As previously mentioned, this type of fermentation provides solid nutrients and physical support for the culture, resulting in some advantages over the submerged production process, including lower energy requirements and less wastewater production (Nyyssölä et al., 2022).

CONCLUSION

The yeast *S. cerevisiae*, with unique biological characteristics, is among the most prominent microorganisms used in industrial SCP production, and it is regarded as a promising solution to the feed industry for addressing the challenges of sourcing a safe, sustainable,

and competent protein ingredient. Despite the fact that it has been many years since *S. cerevisiae*'s introduction to the feed industry, both traditionally and industrially, there are still several challenges that need to be discussed by the scientific research community in the future. The condition that favors *S. cerevisiae* growth and subsequently improves the techno-economics in the related SCP industry is a case in point. Novel bioprocess designs in the industrial production of *S. cerevisiae* require particular consideration in terms of maximizing biomass yields at low costs. The number of research papers investigating the LCA of *S. cerevisiae* is rather low, while such analyses can lead to an increase in interest in scaling up the related technologies. According to the most recent research under different aerobic and anaerobic conditions, the yeast proteomes and their amino acid profile are not similar. This concept could be more considered in future studies aiming to identify growth conditions focused on targeted results.

In addition to the above-mentioned gaps, some of the key issues to be addressed in future studies are as follows: (1) the effects of *S. cerevisiae* supplementation on growth performance of many non-studied livestock and aquatic animals (2) continuing the use of genetic engineering to enhance the performance of *S. cerevisiae* strains in converting lignocellulosic biomass (3) alleviating the concentration of nucleic acid content of the produced SCP by *S. cerevisiae*. Undeniably, empirical investigations that can assist in providing affordable and feasible solutions for producing protein requirements of feed can eventually help in reducing the burdens of world hunger.

ACKNOWLEDGEMENT

We would like to acknowledge Sahar Sepehr, head of Central Association of Iranian Inventors (CAII), who was pivotal in inspiring and supporting our investigations into the industrial production of *S. cerevisiae*.

REFERENCES

- Agboola, J. O., Øverland, M., Skrede, A., & Hansen, J. Ø. (2021). Yeast as major protein-rich ingredient in aquafeeds: A review of the implications for aquaculture production. *Reviews in Aquaculture*, 13(2), 949-970. <https://doi.org/10.1111/raq.12507>
- Ahiwe, E. U., Dos Santos, T. T., Graham, H., & Iji, P. A. (2021). Can probiotic or prebiotic yeast (*Saccharomyces cerevisiae*) serve as alternatives to in-feed antibiotics for healthy or disease-challenged broiler chickens? A review. *Journal of Applied Poultry Research*, 30(3), Article 100164. <https://doi.org/10.1016/j.japr.2021.100164>
- Ahmed, M., Liang, H., Kasiya, H. C., Ji, K., Ge, X., Ren, M., Liu, B., Zhu, X., & Sun, A. (2019). Complete replacement of fish meal by plant protein ingredients with dietary essential amino acids supplementation for juvenile blunt snout bream (*Megalobrama amblycephala*). *Aquaculture Nutrition*, 25(1), 205-214. <https://doi.org/10.1111/anu.12844>

- Allen, R. C. (2017). Absolute poverty: When necessity displaces desire. *American Economic Review*, 107(12), 3690-3721. <https://doi.org/10.1257/aer.20161080>
- Alugongo, G. M., Xiao, J., Wu, Z., Li, S., Wang, Y., & Cao, Z. (2017). Utilization of yeast of *Saccharomyces cerevisiae* origin in artificially raised calves. *Journal of Animal Science and Biotechnology*, 8, 1-12. <https://doi.org/10.1186/s40104-017-0165-5>
- Anupama, R. P., & Ravindra, P. (2000). Value-added food: Single cell protein. *Biotechnology Advances*, 18(6), 459-479. [https://doi.org/10.1016/S0734-9750\(00\)00045-8](https://doi.org/10.1016/S0734-9750(00)00045-8)
- Arous, F., Azabou, S., Jaouani, A., Zouari-Mechichi, H., Nasri, M., & Mechichi, T. (2016). Biosynthesis of single-cell biomass from olive mill wastewater by newly isolated yeasts. *Environmental Science and Pollution Research*, 23, 6783-6792. DOI: 10.1007/s11356-015-5924-2
- Bai, Y., Alemu, R., Block, S. A., Headey, D., & Masters, W. A. (2021). Cost and affordability of nutritious diets at retail prices: Evidence from 177 countries. *Food Policy*, 99, Article 101983. <https://doi.org/10.1016/j.foodpol.2020.101983>
- Bajić, B., Vučurović, D., Vasić, Đ., Jevtić-Mučibabić, R., & Dodić, S. (2022). Biotechnological production of sustainable microbial proteins from agro-industrial residues and by-products. *Foods*, 12(1), Article 107. <https://doi.org/10.3390/foods12010107>
- Ballet, N., Renaud, S., Roume, H., George, F., Vandekerckove, P., Boyer, M., & Durand-Dubief, M. (2023). *Saccharomyces cerevisiae*: Multifaceted applications in one health and the achievement of sustainable development goals. *Encyclopedia*, 3(2), 602-613. <https://doi.org/10.3390/encyclopedia3020043>
- Baptista, S. L., Costa, C. E., Cunha, J. T., Soares, P. O., & Domingues, L. (2021). Metabolic engineering of *Saccharomyces cerevisiae* for the production of top value chemicals from biorefinery carbohydrates. *Biotechnology Advances*, 47, Article 107697. <https://doi.org/10.1016/j.biotechadv.2021.107697>
- Bekatorou, A., Psarianos, C., & Koutinas, A. A. (2006). Production of food grade yeasts. *Food Technology & Biotechnology*, 44(3), 407-415.
- Bertasini, D., Binati, R. L., Bolzonella, D., & Battista, F. (2022). Single cell proteins production from food processing effluents and digestate. *Chemosphere*, 296, Article 134076. <https://doi.org/10.1016/j.chemosphere.2022.134076>
- Bogdahn, I. (2015). Agriculture-independent, sustainable, fail-safe and efficient food production by autotrophic single-cell protein (No. e1709). *PeerJ PrePrints*. <https://doi.org/10.7287/peerj.preprints.1279v3>
- Bortoluzzi, C., Barbosa, J. G. M., Pereira, R., Fagundes, N. S., Rafael, J. M., & Menten, J. F. M. (2018). Autolyzed yeast (*Saccharomyces cerevisiae*) supplementation improves performance while modulating the intestinal immune-system and microbiology of broiler chickens. *Frontiers in Sustainable Food Systems*, 2, Article 85. <https://doi.org/10.3389/fsufs.2018.00085>
- Boynton, P. J., & Greig, D. (2014). The ecology and evolution of non-domesticated *Saccharomyces* species. *Yeast*, 31(12), 449-462. <https://doi.org/10.1002/yea.3040>
- Bratosin, B. C., Darjan, S., & Vodnar, D. C. (2021). Single cell protein: A potential substitute in human and animal nutrition. *Sustainability*, 13(16), Article 9284. <https://doi.org/10.3390/su13169284>

- Bruno, R. G., Rutigliano, H. M., Cerri, R. L., Robinson, P. H., & Santos, J. E. (2009). Effect of feeding *Saccharomyces cerevisiae* on performance of dairy cows during summer heat stress. *Animal Feed Science and Technology*, *150*(3-4), 175-186. <https://doi.org/10.1016/j.anifeedsci.2008.09.001>
- Bzducha-Wróbel, A., Błażej, S., Kieliszek, M., Pobiega, K., Falana, K., & Janowicz, M. (2018a). Modification of the cell wall structure of *Saccharomyces cerevisiae* strains during cultivation on waste potato juice water and glycerol towards biosynthesis of functional polysaccharides. *Journal of Biotechnology*, *281*, 1-10. <https://doi.org/10.1016/j.jbiotec.2018.06.305>
- Bzducha-Wróbel, A., Pobiega, K., Błażej, S., & Kieliszek, M. (2018b). The scale-up cultivation of *Candida utilis* in waste potato juice water with glycerol affects biomass and β (1, 3)/(1, 6)-glucan characteristic and yield. *Applied Microbiology and Biotechnology*, *102*, 9131-9145. <https://doi.org/10.1007/s00253-018-9357-y>
- Çakar, Z. P., Turanlı-Yıldız, B., Alkım, C., & Yılmaz, Ü. (2012). Evolutionary engineering of *Saccharomyces cerevisiae* for improved industrially important properties. *FEMS Yeast Research*, *12*(2), 171-182. <https://doi.org/10.1111/j.1567-1364.2011.00775.x>
- Chollom, P. F., Agbo, B. E., Doma, D. U., Okojokwu, J. O., & Yisa, A. G. (2017). Nutritional value of spent brewers' yeast (*Saccharomyces cerevisiae*): A potential replacement for soya bean in poultry feed formulation. *Researcher*, *9*(1), 70-74. <https://doi.org/10.7537/marsrsj090117.11>
- Costa, J. A. V., Colla, L. M., & Duarte Filho, P. F. (2004). Improving *Spirulina platensis* biomass yield using a fed-batch process. *Bioresource Technology*, *92*(3), 237-241. <https://doi.org/10.1016/j.biortech.2003.09.013>
- De Almeida Silva Vilela, J., de Figueiredo Vilela, L., Ramos, C. L., & Schwan, R. F. (2020). Physiological and genetic characterization of indigenous *Saccharomyces cerevisiae* for potential use in productions of fermented maize-based-beverages. *Brazilian Journal of Microbiology*, *51*, 1297-1307. <https://doi.org/10.1007/s42770-020-00271-8>
- El-Bab, A. F. F., Saghir, S. A., El-Naser, I. A. A., El-Kheir, S. M. A., Abdel-Kader, M. F., Alruhaimi, R. S., Alqhtani, H. A., Mahmoud, A. M., Naiel, M. A. E., & El-Raghi, A. A. (2022). The effect of dietary *Saccharomyces cerevisiae* on growth performance, oxidative status, and immune response of sea bream (*Sparus aurata*). *Life*, *12*(7), Article 1013. <https://doi.org/10.3390/life12071013>
- El-Badawi, A. Y. (2017). Growth performance of male NZW rabbits fed diets supplemented with beneficial bacteria or live yeast. *Agricultural Engineering International: CIGR Journal*, 220-226. <http://orcid.org/0000-0003-2407-4883>
- Elghandour, M. M. Y., Tan, Z. L., Abu Hafsa, S. H., Adegbeye, M. J., Greiner, R., Ugbo, E. A., Monroy, J. C., & Salem, A. Z. M. (2020). *Saccharomyces cerevisiae* as a probiotic feed additive to non and pseudo-ruminant feeding: A review. *Journal of Applied Microbiology*, *128*(3), 658-674. <https://doi.org/10.1111/jam.14416>
- Elghandour, M. M., Mellado, M., Kholif, A. E., Salem, A. Z., Barbabosa, A., Ballinas, S., Esquivel, A., & Odongo, N. E. (2016). Fecal gas production of ten common horse feeds supplemented with *Saccharomyces cerevisiae*. *Journal of Equine Veterinary Science*, *47*, 1-8. <https://doi.org/10.1016/j.jevs.2016.07.008>
- Fanelli, A., Agazzi, A., Pilotto, A., Bontempo, V., Dell'Orto, V., Caputo, J. M. & Savoini, G. (2015). Prevalence reduction of pathogens in poultry fed with *Saccharomyces cerevisiae*. *Biotechnologie, Agronomie, Societe Et Environnement*, *19*(1), 3-10.

- Faria-Oliveira, F., Puga, S., & Ferreira, C. (2013). Yeast: World's finest chef. In I. Muzzalupo (Ed.), *Food Industry* (pp. 519–547). IntechOpen. <https://doi.org/10.5772/53156>
- Gheisari, A. A., & Kholehipour, B. (2006, September 10-14). Effect of dietary inclusion of live yeast (*Saccharomyces cerevisiae*) on growth performance, immune responses and blood parameters of broiler chickens [Paper Presented]. In Proceedings of the XII European Poultry Conference, Verona, Italia.
- Gientka, I., Kieliszek, M., Jermacz, K., & Błażejczak, S. (2017). Identification and characterization of oleaginous yeast isolated from kefir and its ability to accumulate intracellular fats in deproteinated potato wastewater with different carbon sources. *BioMed Research International*, 2017(1), Article 6061042. <https://doi.org/10.1155/2017/6061042>
- Graham, A. E., & Ledesma-Amaro, R. (2023). The microbial food revolution. *Nature Communications*, 14(1), Article 2231. <https://doi.org/10.1038/s41467-023-37891-1>
- Gupta, K., Bardhan, P., Saikia, D., Rather, M. A., Loying, S., Mandal, M., & Katak, R. (2022). Microbial fermentation: Basic fundamentals and its dynamic prospect in various industrial applications. In P. Verma (Ed.), *Industrial Microbiology and Biotechnology* (pp. 107-128). Springer. https://doi.org/10.1007/978-981-16-5214-1_4
- Haddish, K. (2015). Production of single cell protein from fruit of beles (*Opuntia Ficus-Indica L.*) peels using *Saccharomyces cerevisiae*. *Journal of Microbiology & Experimentation*, 2, Article 00073. <https://doi.org/10.15406/jmen.2015.02.00073>
- Hiltz, R. L., Steelreath, M. R., Degenshein-Woods, M. N., Hung, H. C., Aguilar, A., Nielsen, H., Rezamand, P., & Laarman, A. H. (2023). Effects of *Saccharomyces cerevisiae boulardii* (CNCM I-1079) on feed intake, blood parameters, and production during early lactation. *Journal of Dairy Science*, 106(1), 187-201. <https://doi.org/10.3168/jds.2021-21740>
- IFIF. (2023). *IFIF Annual Report*. International Feed Industry Federation. <https://annualreport.ifif.org/wp-content/uploads/IFIF-Annual-Report-2022-2023-15-03-24.pdf>
- Izah, S. C., Enaregha, E. B., & Epidi, J. O. (2019). Vitamin content of *Saccharomyces cerevisiae* biomass cultured in cassava wastewater. *MOJ Toxicology*, 4(1), 42-45. <https://doi.org/10.15406/mojt.2019.05.00151>
- Jach, M. E., Serefko, A., Ziaja, M., & Kieliszek, M. (2022). Yeast protein as an easily accessible food source. *Metabolites*, 12(1), Article 63. <https://doi.org/10.3390/metabo12010063>
- Jones, S. W., Karpol, A., Friedman, S., Maru, B. T., & Tracy, B. P. (2020). Recent advances in single cell protein use as a feed ingredient in aquaculture. *Current Opinion in Biotechnology*, 61, 189-197. <https://doi.org/10.1016/j.copbio.2019.12.026>
- Kasoz, N., Iwe, G., Sadik, K., Asizua, D., & Namulawa, V. T. (2019). Dietary amino acid requirements of pebbly fish, *Alestes baremoze* (Joannis, 1835) based on whole body amino acid composition. *Aquaculture Reports*, 14, Article 100197. <https://doi.org/10.1016/j.aqrep.2019.100197>
- Kieliszek, M., Kot, A. M., Bzducha-Wróbel, A., Błażejczak, S., Gientka, I., & Kurcz, A. (2017). Biotechnological use of Candida yeasts in the food industry: A review. *Fungal Biology Reviews*, 31(4), 185-198. <https://doi.org/10.1016/j.fbr.2017.06.001>

- Kieliszek, M., Piwowarek, K., Kot, A. M., & Pobięga, K. (2020). The aspects of microbial biomass use in the utilization of selected waste from the agro-food industry. *Open Life Sciences*, *15*(1), 787-796. <https://doi.org/10.1515/biol-2020-0099>
- Koç, F., Samli, H., Okur, A., Ozduven, M., Akyurek, H., & Senkoylu, N. (2010). Effects of *Saccharomyces cerevisiae* and/or mannanoligosaccharide on performance, blood parameters and intestinal microbiota of broiler chicks. *Bulgarian Journal of Agricultural Science*, *16*(5), 643-650.
- Koukoumaki, D. I., Tsouko, E., Papanikolaou, S., Ioannou, Z., Diamantopoulou, P., & Sarris, D. (2023). Recent advances in the production of single cell protein from renewable resources and applications. *Carbon Resources Conversion*, *7*(2), Article 100195. <https://doi.org/10.1016/j.crccon.2023.07.004>
- Kurcz, A., Błażejczak, S., Kot, A. M., Bzducha-Wróbel, A., & Kieliszek, M. (2018). Application of industrial wastes for the production of microbial single-cell protein by fodder yeast *Candida utilis*. *Waste and Biomass Valorization*, *9*, 57-64. <https://doi.org/10.1007/s12649-016-9782-z>
- Lahue, C., Madden, A. A., Dunn, R. R., & Heil, C. S. (2020). History and domestication of *Saccharomyces cerevisiae* in bread baking. *Frontiers in Genetics*, *11*, Article 584718. <https://doi.org/10.3389/fgene.2020.584718>
- Legras, J. L., Merdinoglu, D., Cornuet, J. M., & Karst, F. (2007). Bread, beer and wine: *Saccharomyces cerevisiae* diversity reflects human history. *Molecular Ecology*, *16*(10), 2091-2102. <https://doi.org/10.1111/j.1365-294X.2007.03266.x>
- Liu, H., Li, J., Guo, X., Liang, Y., & Wang, W. (2018). Yeast culture dietary supplementation modulates gut microbiota, growth and biochemical parameters of grass carp. *Microbial Biotechnology*, *11*(3), 551-565. <https://doi.org/10.1111/1751-7915.13261>
- Ma, Z. Z., Cheng, Y. Y., Wang, S. Q., Ge, J. Z., Shi, H. P., & Kou, J. C. (2020). Positive effects of dietary supplementation of three probiotics on milk yield, milk composition and intestinal flora in Sannan dairy goats varied in kind of probiotics. *Journal of animal physiology and animal nutrition*, *104*(1), 44-55. <https://doi.org/10.1111/jpn.13226>
- Maamouri, O., & Salem, M. B. (2022). The effect of live yeast *Saccharomyces cerevisiae* as probiotic supply on growth performance, feed intake, ruminal pH and fermentation in fattening calves. *Veterinary Medicine and Science*, *8*(1), 398-404. <https://doi.org/10.1002/vms3.631>
- Mahmoud, A. H., Slate, J. R., Hong, S., Yoon, I., & McGill, J. L. (2020). Supplementing a *Saccharomyces cerevisiae* fermentation product modulates innate immune function and ameliorates bovine respiratory syncytial virus infection in neonatal calves. *Journal of Animal Science*, *98*(8), Article skaa252. <https://doi.org/10.1093/jas/skaa252>
- Martin, G. J., & Chan, S. (2024). Future production of yeast biomass for sustainable proteins: A critical review. *Sustainable Food Technology*, *2*, 1592-1609. <https://doi.org/10.1039/D4FB00164H>
- McAuliffe, G. A., Takahashi, T., Beal, T., Huppertz, T., Leroy, F., Buttriss, J., Collins, A. L., Drewnowski, A., McLaren, S. J., Ortenzi, F., van der Pols, J. C., van Vliet, S., & Lee, M. R. F. (2023). Protein quality as a complementary functional unit in life cycle assessment (LCA). *The International Journal of Life Cycle Assessment*, *28*(2), 146-155. <https://doi.org/10.1007/s11367-022-02123-z>

- Mohammadi, M., Samadi, S., & Darzi, G. N. (2016). Production of single cell protein from sugarcane bagasse by *Saccharomyces cerevisiae* in tray bioreactor. *International Journal of Engineering*, 29(8), 1029-1036. <https://doi.org/10.5829/idosi.ije.2016.29.08b.01>
- Molitor, B., Mishra, A., & Angenent, L. T. (2019). Power-to-protein: Converting renewable electric power and carbon dioxide into single cell protein with a two-stage bioprocess. *Energy & Environmental Science*, 12(12), 3515-3521. <https://doi.org/10.1039/c9ee02381j>
- Møller, H., & Modahl, I. S. (2020). *Life Cycle Assessment of Yeast from Spruce*. NORSUS. <https://norsus.no/wp-content/uploads/OR-46.20-Life-cycle-assessment-of-yeast-from-spruce-1.pdf>
- Moslehi-Jenabian, S., Pedersen, L. L., & Jespersen, L. (2010). Beneficial effects of probiotic and food borne yeasts on human health. *Nutrients*, 2(4), 449-473. <https://doi.org/10.3390/nu2040449>
- Nasseri, A. T., Rasoul-Amini, S., Morowvat, M. H., & Ghasemi, Y. (2011). Single cell protein: Production and process. *American Journal of Food Technology*, 6(2), 103-116. <https://doi.org/10.3923/ajft.2011.103.116>
- NRC. (1998). *Nutrient requirements of swine* (10th ed.). National Academy Press.
- Nyyssölä, A., Suhonen, A., Ritala, A., & Oksman-Caldentey, K. M. (2022). The role of single cell protein in cellular agriculture. *Current Opinion in Biotechnology*, 75, Article 102686. <https://doi.org/10.1016/j.copbio.2022.102686>
- Onofre, S. B., Bertoldo, I. C., Abatti, D., & Refosco, D. (2017). Chemical composition of the biomass of *Saccharomyces cerevisiae*-(Meyen ex EC Hansen, 1883) yeast obtained from the beer manufacturing process. *International Journal of Advanced Engineering Research and Science*, 5(8), Article 264258. <https://doi.org/10.22161/ijeab/2.2.2>
- Onyeaka, H., Anumudu, C. K., Okpe, C., Okafor, A., Ihenetu, F., Miri, T., Odeyemi, O. A., & Anyogu, A. (2022). Single cell protein for foods and feeds: A review of trends. *The Open Microbiology Journal*, 16(1), Article e187428582206160. <https://doi.org/10.2174/18742858-v16-e2206160>
- Parapouli, M., Vasileiadis, A., Afendra, A. S., & Hatziloukas, E. (2020). *Saccharomyces cerevisiae* and its industrial applications. *AIMS Microbiology*, 6(1), Article 1. DOI: 10.3934/microbiol.2020001
- Patias, L. D., Maroneze, M. M., Siqueira, S. F., de Menezes, C. R., Zepka, L. Q., & Jacob-Lopes, E. (2018). Single-cell protein as a source of biologically active ingredients for the formulation of antiobesity foods. In A. M. Holban & A. M. Grumezescu (Eds.), *Alternative and Replacement Foods* (pp. 317-353). Academic Press. <https://doi.org/10.1016/b978-0-12-811446-9.00011-3>
- Pencharz, P. B., Elango, R., & Wolfe, R. R. (2016). Recent developments in understanding protein needs - How much and what kind should we eat? *Applied Physiology, Nutrition, and Metabolism*, 41(5), 577-580. <https://doi.org/10.1139/apnm-2015-0549>
- Pereira, P. R., Freitas, C. S., & Paschoalin, V. M. (2021). *Saccharomyces cerevisiae* biomass as a source of next-generation food preservatives: Evaluating potential proteins as a source of antimicrobial peptides. *Comprehensive Reviews in Food Science and Food Safety*, 20(5), 4450-4479. <https://doi.org/10.1111/1541-4337.12798>
- Raziq, A., Lateef, M., Ullah, A., Ullah, H., & Khan, M. W. (2020). 02. Single cell protein (SCP) production and potential substrates: A comprehensive review. *Pure and Applied Biology (PAB)*, 9(3), 1743-1754. <http://dx.doi.org/10.19045/bspab.2020.90185>

- Reihani, S. F. S., & Khosravi-Darani, K. (2019). Influencing factors on single-cell protein production by submerged fermentation: A review. *Electronic Journal of Biotechnology*, 37, 34-40. <https://doi.org/10.1016/j.ejbt.2018.11.005>
- Ribeiro, G. O., Rodrigues, L. D. A. P., Santos, T. B. S. D., Alves, J. P. S., Oliveira, R. S., Nery, T. B. R., Barbosa, J. D. V., & Soares, M. B. P. (2023). Innovations and developments in single cell protein: Bibliometric review and patents analysis. *Frontiers in Microbiology*, 13, Article 1093464. <https://doi.org/10.3389/fmicb.2022.1093464>
- Ritala, A., Häkkinen, S. T., Toivari, M., & Wiebe, M. G. (2017). Single cell protein-state-of-the-art, industrial landscape and patents 2001–2016. *Frontiers in Microbiology*, 8, Article 2009. <https://doi.org/10.3389/fmicb.2017.02009>
- Salazar-López, N. J., Barco-Mendoza, G. A., Zuñiga-Martínez, B. S., Domínguez-Avila, J. A., Robles-Sánchez, R. M., Ochoa, M. A. V., & González-Aguilar, G. A. (2022). Single-cell protein production as a strategy to reincorporate food waste and agro by-products back into the processing chain. *Bioengineering*, 9(11), Article 623. <https://doi.org/10.3390/bioengineering9110623>
- Salem, A. Z., Elghandour, M. M., Kholif, A. E., Barbabosa, A., Camacho, L. M., & Odongo, N. E. (2016). Influence of feeding horses a high fiber diet with or without live yeast cultures supplementation on feed intake, nutrient digestion, blood chemistry, fecal coliform count, and in vitro fecal fermentation. *Journal of Equine Veterinary Science*, 39, 12-19. <https://doi.org/10.1016/j.jevs.2015.08.020>
- Salter, A. M., & Lopez-Viso, C. (2021). Role of novel protein sources in sustainably meeting future global requirements. *Proceedings of the Nutrition Society*, 80(2), 186-194. <https://doi.org/10.1017/s0029665121000513>
- Shahzad, H. M. A., Asim, Z., Mahmoud, K. A., Abdelhadi, O. M., Almomani, F., & Rasool, K. (2024). Optimizing cultural conditions and pretreatment for high-value single-cell protein from vegetable waste. *Process Safety and Environmental Protection*, 189, 685-692. <https://doi.org/10.1016/j.psep.2024.06.139>
- Sharif, M., Zafar, M. H., Aqib, A. I., Saeed, M., Farag, M. R., & Alagawany, M. (2021). Single cell protein: Sources, mechanism of production, nutritional value and its uses in aquaculture nutrition. *Aquaculture*, 531, Article 735885. <https://doi.org/10.1016/j.aquaculture.2020.735885>
- Song, B., Wu, T., You, P., Wang, H., Burke, J. L., Kang, K., Yu, W., Wang, M., Li, B., He, Y., Huo, Q., Li, C., Tian, W., Li, R., Li, J., Wang, C., & Sun, X. (2021). Dietary supplementation of yeast culture into pelleted total mixed rations improves the growth performance of fattening lambs. *Frontiers in Veterinary Science*, 8, Article 657816. <https://doi.org/10.3389/fvets.2021.657816>
- Stevenson, P. J. (2015). *Industrial Livestock Production: The Twin Myths of Efficiency and Necessity*. Compassion in World Farming. <https://www.ciwf.com/media/7425974/industrial-livestock-production-the-twin-myths-of-efficiency-and-necessity.pdf>
- Stewart, G. G. (2014). *Saccharomyces* | *Saccharomyces cerevisiae*. In C. A. Batt & M. L. Tortorello (Eds.), *Encyclopedia of Food Microbiology* (pp. 309-315). Academic Press. <https://doi.org/10.1016/B978-0-12-384730-0.00292-5>
- Suman, G., Nupur, M., Anuradha, S., & Pradeep, B. (2015). Single cell protein production: A review. *International Journal of Current Microbiology and Applied Sciences*, 4(9), 251-262.

- Sun, X., Wang, H., You, P., Pacheco, D., Wang, M., Wu, T., Song, B., kang, K., Li, Y., Li, B., He, Y., Huo, Q., Li, C., Tian, W., Li, R., Li, J., Wang, C., You, M., Cai, Q., & Wubulayin, B. (2022). Agglomerated live yeast (*Saccharomyces cerevisiae*) supplemented to pelleted total mixed rations improves the growth performance of fattening lambs. *Livestock Science*, 258, Article 104855. <https://doi.org/10.1016/j.livsci.2022.104855>
- Teunissen, A., Dumortier, F., Gorwa, M. F., Bauer, J., Tanghe, A., Loiez, A., Smet, P., Van Dijck, P., & Thevelein, J. M. (2002). Isolation and characterization of a freeze-tolerant diploid derivative of an industrial baker's yeast strain and its use in frozen doughs. *Applied and Environmental Microbiology*, 68(10), 4780-4787. <https://doi.org/10.1128/AEM.68.10.4780-4787.2002>
- Transparency Market Research Report. (2020). *Single Cell Protein Market*. <https://www.transparencymarketresearch.com/single-cell-protein-market.html>
- Ukaegbu-Obi, K. M. (2016). Single cell protein: A resort to global protein challenge and waste management. *Journal of Microbiology & Microbial Technology*, 1(1), Article 5. <https://doi.org/10.13188/2474-4530.1000006>
- von Grebmer, K., Bernstein, J., Wiemers, M., Reiner, L., Bachmeier, M., Hanano, A., Chéilleachair, R. N., Foley, C., Sheehan, T., Gitter, S., Larocque, G., & Fritschel, H. (2023). *2023 Global Hunger Index: The Power of Youth in Shaping Food Systems*. Coherent Digital. <https://www.globalhungerindex.org/pdf/en/2023.pdf>
- Walker, G. M., & Stewart, G. G. (2016). *Saccharomyces cerevisiae* in the production of fermented beverages. *Beverages*, 2(4), Article 30. <https://doi.org/10.3390/beverages2040030>
- Wang, J., Zhao, G., Zhuang, Y., Chai, J., & Zhang, N. (2022). Yeast (*Saccharomyces cerevisiae*) culture promotes the performance of fattening sheep by enhancing nutrients digestibility and rumen development. *Fermentation*, 8(12), Article 719. <https://doi.org/10.3390/fermentation8120719>
- WFP. (2022). *WFP Global Operational Response Plan 2022 Update #5*. World Food Programme https://docs.wfp.org/api/documents/WFP-0000140306/download/?_ga=2.103844736.180123984.1668594359-14562101.1665048913
- WHO. (2007). *Protein and Amino Acid Requirements in Human Nutrition (Vol. 935)*. World Health Organization. https://iris.who.int/bitstream/handle/10665/43411/WHO_TRS_935_eng.pdf
- Wulandari, S., & Syahniar, T. M. (2018). The effect of adding probiotic *Saccharomyces cerevisiae* on dietary antibiotic-free on production performance and intestinal lactic acid bacteria growth of broiler chicken. In *IOP Conference Series: Earth and Environmental Science* (Vol. 207, No. 1, p. 012034). IOP Publishing. <https://doi.org/10.1088/1755-1315/207/1/012034>
- Xue, L., Zhou, S., Wang, D., Zhang, F., Li, J., & Cai, L. (2022). The low dose of *Saccharomyces cerevisiae* is beneficial for rumen fermentation (both *in vivo* and *in vitro*) and the growth performance of heat-stressed goats. *Microorganisms*, 10(10), Article 1877. <https://doi.org/10.3390/microorganisms10101877>
- Ye, L., Bogicevic, B., Bolten, C. J., & Wittmann, C. (2024). Single-cell protein: Overcoming technological and biological challenges towards improved industrialization. *Current Opinion in Biotechnology*, 88, Article 103171. <https://doi.org/10.1016/j.copbio.2024.103171>
- Zhou, Y. M., Chen, Y. P., Guo, J. S., Shen, Y., Yan, P., & Yang, J. X. (2019). Recycling of orange waste for single cell protein production and the synergistic and antagonistic effects on production quality. *Journal of Cleaner Production*, 213, 384-392. <https://doi.org/10.1016/j.jclepro.2018.12.168>

Virus Particle Dispersion and Infection Risk Assessment in Aircraft Cabins: A CFD Approach

Mohd Syakirin Rusdi¹, Di Fey Way², Mohd Sharizal Abdul Aziz¹, Farzad Ismail²
and Mohammad Hafifi Hafiz Ishak^{2*}

¹*School of Mechanical Engineering, Universiti Sains Malaysia, Engineering Campus, 14300 Nibong Tebal, Seberang Perai Selatan, Penang, Malaysia*

²*School of Aerospace Engineering, Universiti Sains Malaysia, Engineering Campus, 14300 Nibong Tebal, Seberang Perai Selatan, Penang, Malaysia*

ABSTRACT

The work employed computational fluid dynamics to model virus-carrying particle transport mechanisms in a low-cost carrier passenger cabin. The study investigated the effect of virus source location and particle size on particle dynamics and infection risk. The infection risk assessment was conducted based on particle deposition onto surfaces such as passenger bodies and seats. The study found that the direction and velocity magnitude of the airflow in the cabin were almost symmetric about the aisle, with some asymmetry in the velocity magnitude observed due to the coughing passenger's location. Most particles in the cabin were found to be either deposited onto surfaces or removed through the ventilation system within 10 minutes. The study also found that the particle deposition and removal dynamics were strongly affected by the particle source location and the particle size due to the proximity to different surfaces depending on the source location and the propagation distance of the particles, which depends on the gravitational effect based on the size of the particles. The propagation of the particles was found to be mostly contained within the row of the source and two rows in front of the source throughout the 10 minutes. The infection risk assessment indicated a higher risk for passengers seated in the column directly in front of the virus source and for passengers seated on the same side of the aisle as the virus source.

ARTICLE INFO

Article history:

Received: 6 August 2024

Accepted: 24 December 2024

Published: 07 March 2025

DOI: <https://doi.org/10.47836/pjst.33.2.19>

E-mail addresses:

syakirin@usm.my (Mohd Syakirin Rusdi)

dfusm98@gmail.com (Di Fey Way)

msharizal@usm.my (Mohd Sharizal Abdul Aziz)

aefarzad@usm.my (Farzad Ismail)

mhafifhafiz@usm.my (Mohammad Hafifi Hafiz Ishak)

*Corresponding author

Keywords: Airflow dynamics, computational fluid dynamics (CFD), contaminant transport analysis

INTRODUCTION

Since 2019, the coronavirus disease (COVID-19) has brought about a global pandemic, leading to worldwide health,

safety, and economic crises. The highly infectious COVID-19 was identified to be caused by the severe acute respiratory syndrome coronavirus 2 (SARS-CoV-2), which is the same family of viruses that led to the SARS outbreak between 2002-2004. Initial responses to stop the spread of COVID-19 led to worldwide border restrictions and local movement restrictions. The global economy suffered a huge blow due to these restrictions. The civil aviation industry is one of, if not the most affected sectors globally due to a shortage in international air travel demands. Several studies, including those by Rahman et al. (2020) and Dube (2023), have thoroughly examined the extent of these disruptions. These works underscore the pandemic's unprecedented effects on civil aviation, a sector that continues to grapple with recovery amidst ongoing uncertainties.

The accuracy of Computational Fluid Dynamic (CFD) simulations on particle transport has been validated by comparing them with the results of experimental methods in various studies. For instance, Yan et al. (2009) demonstrated a comparison between experimental and CFD investigation on particle transport mechanisms in a Boeing 767 cabin. They indicated that CFD simulations provided more detailed information that could not be observed or evaluated through experimental setups due to sensor and equipment setup inaccuracy and technological limitations. Zhang et al. (2009) compared experimental and numerical investigations of the airflow and particle transport in a twin-aisle cabin. They concluded that the numerical results of the particle concentration distribution quantitatively agreed with experimental results, but there are some significant differences in the airflow distribution due to the inaccurate measurement of the flow boundary condition from the air supply diffusers. Liu et al. (2013) evaluated the turbulence models in predicting air distribution in aircraft cabins by comparing them with experimental data. They showed that the RNG k- ϵ , Large eddy simulation (LES) and Detached eddy simulation (DES) turbulence models show satisfactory agreement with the experimental data with small discrepancies in terms of relative accuracy, but the RNG k- ϵ model was 20 times more efficient in terms of computing time. Q. Wang et al. (2022) evaluated the performance of CFD simulations by comparing the simulation results to actual in-flight transmission studies of 2 long haul flights, including London to Hanoi and Singapore to Hangzhou. They were able to accurately predict 84.2% of the infection in the London to Hanoi flight, and they also found that talking was one of the main methods of spreading COVID-19 in the Singapore to Hangzhou flight. They concluded that face masks are important in preventing the spread of COVID-19 in aircraft passenger cabins.

Multiple studies highlight the significance of seating proximity in SARS-CoV-2 transmission on aircraft. Luo et al. (2023) found that passengers seated within two rows of an infected individual had a higher risk of infection due to short-range airborne transmission, similar to influenza A(H1N1). Schijven et al. (2023) reinforced this, noting that infection risk decreases with distance from the source, supporting the need for measures

like pre-boarding testing and mask-wearing. Aircraft ventilation systems also play a key role. Hui et al. (2023) found that SARS-CoV-2 is less stable on aircraft surfaces, and regular cleaning combined with ventilation effectively reduces transmission. Similarly, Dietrich et al. (2021) showed that vacant middle seats could reduce exposure by up to 57%.

Mask-wearing and surface disinfection further reduce exposure, as Bennett et al. (2022) reported that universal masking decreases exposure by 62% and, combined with distancing, offers greater protection. Additionally, antiviral surface coatings, while effective, require frequent maintenance to remain useful (Hui et al., 2023). Airborne particle behavior in the respiratory system and air filtration are also factors in transmission control (Le Guellec et al., 2023). Khoa et al. (2023) showed how particles deposit in the respiratory tract, which is critical for understanding infection risks. Studies by Lee et al. (2023) and Li et al. (2023) highlighted the role of air filtration in reducing viral loads and particle concentrations, reducing transmission risk. Inhalation is the dominant route of short-range virus transmission, as shown by Chen et al. (2023), emphasizing the importance of ventilation and masking.

Research has long focused on understanding the transmission dynamics of infectious pathogens in enclosed spaces like hospital rooms, classrooms, and aircraft cabins. Morawska et al. (2022) studied respiratory particle behavior and its implications for infection control. Silva et al. (2022) reviewed droplet emission dynamics in public transport, highlighting the role of ventilation and the environment in mitigating airborne infections. Li et al. (2021) conducted an experimental study in a 6-row aircraft cabin mock-up, simulating particle emission from a masked passenger, though these investigations face challenges due to the technical and cost demands.

Most studies focus on long-haul aircraft (e.g., Boeing 700, Airbus A300) because longer flights increase infection risk (Gupta et al., 2020; Chen et al., 2021). However, as global air travel recovers, there is growing demand for short-haul flights, particularly within Europe and Southeast Asia, where low-cost carriers dominate due to affordability and shorter travel times (IATA, 2022). These carriers operate smaller single-aisle aircraft with high passenger density, increasing the risk of airborne infection due to limited social distancing. This underscores the need for studies on virus transmission in low-cost carrier cabins to develop effective mitigation strategies and boost public confidence in air travel.

The primary focus of this study is on understanding how virus source location and particle size affect particle dynamics and the associated infection risk within a low-cost carrier airline cabin. The study modeled particles expelled through coughing and assessed infection risk based on particle deposition on surfaces, including passenger bodies and seats. The research provides insights into how particle size and source location influence the deposition and removal of virus-carrying particles in aircraft cabins.

METHODOLOGY

Physical Model and Computational Domain

The passenger cabin chosen for this study was modeled after the ATR 72-600 aircraft. The cabin geometry was based on dimensions data available from ATR aircraft, as shown in Figure 1. The ATR 72-600 passenger has a standard 72-seat configuration with a 29" (740 mm) seat pitch. This study measured the seat pitch between the back end of the seat headrests. The cabin model only included a single section of the passenger cabin with six rows of seats to reduce the scale of the model and increase computational efficiency.

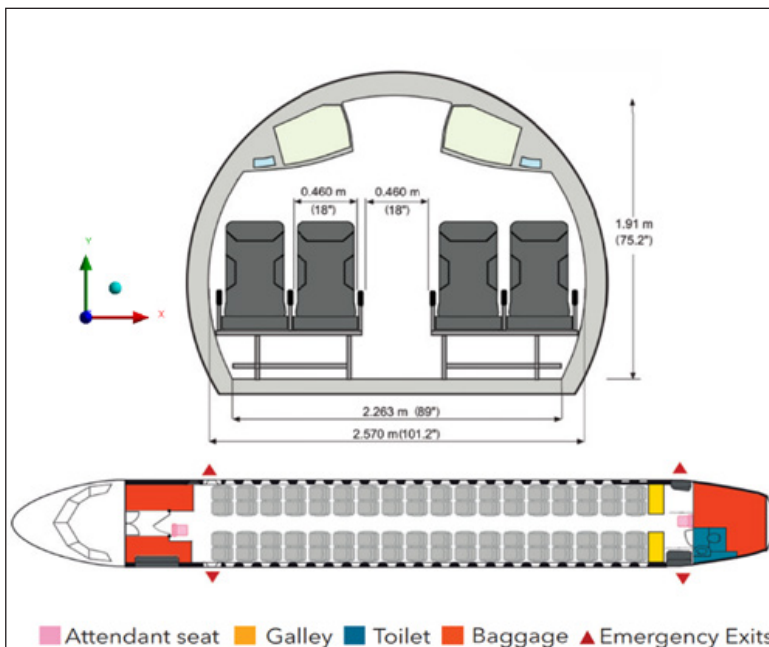


Figure 1. Cross section of ATR 72-600 passenger cabin with dimensions

The cabin interior was modeled according to dimensions available from the ATR aircraft factsheet for the ATR 72-600, as shown in Figure 1. The dimensions of detailed geometry, such as around the stow bins, are modeled by tracing a sketch to scale in Figure 1. The inlet (50mm) and outlet (100mm) of the cabin ventilation system are labeled in yellow and red circles, respectively, in Figure 2. The total length of the cabin was 5 m.

The dimensions of the manikin are modeled by referring to an anthropometric study on Malaysians by Karmegam et al. (2011), which characterized the average dimensions of Malaysians with different ethnicities. The manikin is modeled after the anthropometric data of Chinese females aged 18 to 24 years old. The dimensions of the manikin are summarized in Table 1. The manikin model has an approximate 122 cm seated height with

43 cm shoulder width. A mouth surface is included to be simulated as the source of the expiratory particles. All passengers on board are assumed to have similar dimensions and are always seated in an upright position.

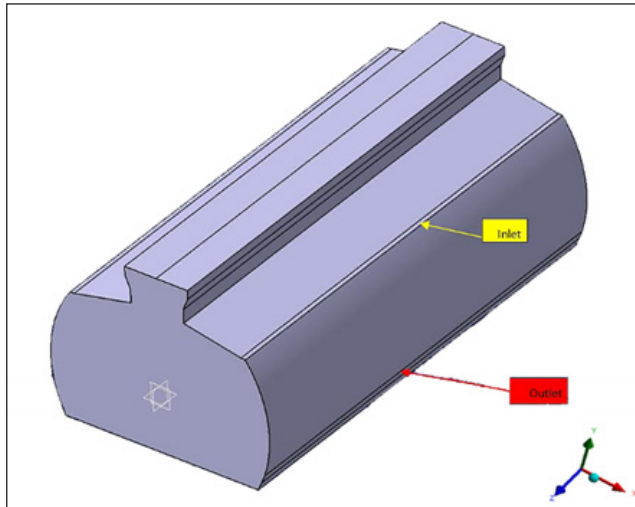


Figure 2. Full Cabin interior solid body

Table 1
Dimensions to model the human manikin (Karmegam et al., 2011)

Anthropometric Component	Dimensions (mm)
Head Height	180
Head Width	140
Abdominal Depth	180
Shoulder Height	540
Hand Breadth	70
Elbow Grip Length	336
Thigh Thickness	130
Popliteal Height	393
Buttock Popliteal Length	449
Buttock Knee Length	551

The modeled components are assembled into a 6-row configuration with a 29" (740 mm) seat pitch. The full cabin has four columns of seats with a single aisle in between, which can accommodate 24 passengers. The final assembly is presented in Figure 3. The model assumed full passenger capacity, with all 24 seats filled with passengers seated upright and stationary throughout the study. The seat numbering used in this study is shown in Figure 4.

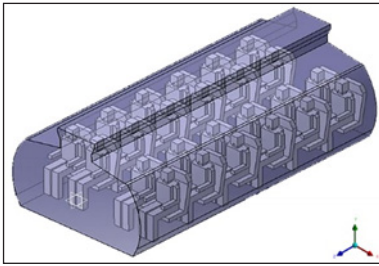


Figure 3. Full cabin assembly

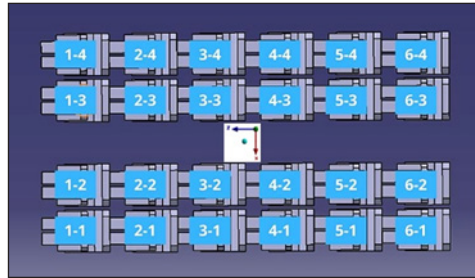


Figure 4. Numbering convention for passenger seat position from the top view

Governing Equations

The flow herein satisfies the incompressible Navier-Stokes (NS) equation with turbulent flow and is solved through the Reynolds-Averaged Navier-Stokes (RANS) equations. Using Einstein's notation in Cartesian coordinates, the continuity is given by Equations 1 and 2.

$$\frac{\partial u_i}{\partial x_i} = 0, \tag{1}$$

where u_i denotes the fluid velocity in index form. The momentum equation is

$$\frac{\partial (u_i u_j)}{\partial x_j} = -\frac{1}{\rho} \frac{\partial P}{\partial x_i} + g_i + \nu \frac{\partial}{\partial x_j} \left(\frac{\partial u_i}{\partial x_j} + \frac{\partial u_j}{\partial x_i} \right) \tag{2}$$

where P represents the pressure on the fluids, g_i denotes the gravitational field strength, acting only in the negative y -direction, and the shear stress tensor accounts for the viscous effects on the fluids. The viscosity ν includes physical and eddy viscosities, calculated using the k - ϵ model.

Turbulence Kinetic Energy, k and Specific Dissipation Rate, ω is given by Equations 3 and 4:

$$\frac{\partial}{\partial t} (\rho k) + \frac{\partial}{\partial x_i} (\rho k u_i) = \frac{\partial}{\partial x_j} \left(\Gamma_k \frac{\partial k}{\partial x_j} \right) + \tilde{G}_k - Y_k + S_k, \tag{3}$$

$$\frac{\partial}{\partial t} (\rho \omega) + \frac{\partial}{\partial x_i} (\rho \omega u_i) = \frac{\partial}{\partial x_j} \left(\Gamma_\omega \frac{\partial \omega}{\partial x_j} \right) + G_\omega - Y_\omega + D_\omega + S_\omega \tag{4}$$

where Γ_k and Γ_ω are effective diffusivities of k and ω respectively, \tilde{G}_k is the generation of turbulence kinetic energy due to mean velocity gradients, G_ω is the generation of ω , Y_k and Y_ω are dissipation of k and ω respectively, S_k and S_ω are user-defined source terms, and D_ω is the cross-diffusion term.

The continuous phase solver for turbulence modeling was assumed to be steady-state and pressure-based for incompressible flow. Gravitational acceleration in the negative direction of Y was considered, and the simulation was assumed to be in an isothermal domain, neglecting the effects of heat transfer. The RNG k - ϵ turbulence model was chosen to model the airflow within the cabin. The suitability of the RNG k - ϵ turbulence model to predict the airflow in an isothermal cabin was verified by Liu et al. (2013). The working fluid within the domain was air with density (1.1116 kg/m^3) and viscosity ($1.74645 \times 10^{-5} \text{ kg/m-s}$).

The air supply for the ventilation system follows recommendations from ASHRAE (2018) for air quality in commercial aircraft. The recommended air supply was 20 cfm per passenger, and for 24 passengers, the total air supply was 480 cfm or approximately $0.2265 \text{ m}^3/\text{s}$. Considering the inlet has a surface area of 0.25 m^2 , the velocity of the inlet obtained from the air supply flow rate would be 0.9061 m/s . A study examining airflow through ceiling air ventilation in aircraft by Pang et al. (2018) demonstrated that a small angle helped better airflow distribution in confined environments. Furthermore, a study by C. Wang et al. (2022) demonstrated that variations in air supply angles significantly affect airflow distribution in narrow-body aircraft cabins, where small angles (0° – 20°) enhance airflow efficiency and passenger comfort. Another study by Talaat et al. (2021), which focuses on airflow in a Boeing 737, found that small angles effectively enhanced airflow and reduced aerosol transmission, supporting the use of smaller angles for optimal performance. Additionally, Shi et al. (2020) examined the impact of air supply positions and angles on cabin thermal comfort, concluding that small angles (5° – 30°) improve airflow distribution, particularly for passenger comfort in aircraft cabins. Based on these findings, the 5° angle of the inlet is chosen in accordance with best practices for airflow optimization in regional passenger aircraft. The velocity inlet boundary condition for the ventilation supply was 0.9027 m/s in the horizontal direction of the aisle, respectively, and 0.0790 in the vertical upwards direction.

The mouth surface of the infected passenger also had a velocity inlet boundary of 2.22 m/s , which corresponded to an exhalation of 20 l/min through a 0.00015 m^2 mouth surface. The turbulence intensity and viscosity ratio for the inlet boundaries were left to the default values of 5% and 10%, respectively. The ventilation exhaust was designated an outlet boundary condition with 89 kPa , corresponding to the pressurized cabin at an altitude of approximately 1000 m . Like the inlet boundary, the backflow turbulence intensity and backflow turbulence viscosity ratio for the outlet boundary were also left at 5% and 10%,

respectively. The manikin, seat and cabin wall surfaces were also designated as stationary, with no-slip wall boundary conditions.

Table 2 summarizes the solution methods, including the pressure-velocity coupling scheme and discretization methods. The solver was then initialized using the hybrid method. Lastly, the calculation was run for 2500 iterations until convergence was observed on either the residuals or the outlet velocity monitors.

Table 2
Solution methods in Fluent

Pressure Velocity Coupling	
Scheme	SIMPLE
Gradient	Least Squares Cell-Based
Pressure	Second Order
Momentum	Second Order Upwind
Turbulent Kinetic Energy	Second Order Upwind
Turbulent Dissipation Rate	Second Order Upwind

The discrete phase solver was assumed to be in a transient state, and the discrete phase model with unsteady particle tracking was activated in ANSYS FLUENT v2023. The interaction with the continuous phase option was disabled for a one-way coupling between the continuous and discrete phases. The tracking parameters, including the maximum number of steps and length scale, were specified as 500000 steps and 6 m, respectively.

Monodisperse simulations for different particle sizes were carried out independently because the cubic scaling of spherical particle mass with diameter can affect mass-based distribution when conducting polydisperse particle simulations. Each simulation will have one injection with a uniform particle size, which means four independent simulations with 4 different particle sizes conducted for each seating position case. The particles are assumed to be spherical since the dominant mode for particle transport was momentum diffusivity. The Discrete Random Walk Model is adopted to provide more realistic and diffusive particle trajectories. Particle sizes for each simulation are uniform with 1 μm , 2 μm , 8 μm , and 15.9 μm , respectively. The particle sizes were obtained from the distribution mode size and maximum droplet size determined by Yang et al. (2007) and shown in Table 3.

Lastly, the discrete phase boundary conditions were set up where the inlets and outlets are specified as escape boundary conditions while the walls, including seats, cabin walls, and passenger surfaces, are specified as trap boundary conditions for the deposition of droplets. The particle track will end after the particle has been removed through an escape boundary or deposited on a trap boundary. Finally, the calculation was run for 1200 time steps with a step size of 0.5 seconds, which corresponded to a 10-minute simulation. After the calculation, the particle track data were obtained and extracted for further analysis.

Table 3

Parcel mass and total mass flow rate for each particle size (Yang et al., 2007)

Particle Size (μm)	Parcel Mass (kg)	Total Mass Flow Rate (kg/s)
1	5.235e-16	1.047e-10
2	4.200e-15	8.400e-10
8	2.681e-13	5.632e-8
15.9	2.105e-12	4.209e-7

Grid Independence Test

In this research, Grid Independence Tests (GIT) were used to develop optimal numerical models. The GIT was conducted by solving a simple flow in the cabin by using the RNG k- ϵ model. The number of mesh elements was increased by decreasing the mesh element size. Two points monitoring the flow velocity located at the outlet are used as reference values for comparison. The hybrid mesh was used to create four different grids. The super fine grid comprises 6.66 million elements, the fine grid has approximately 4.56 million elements, the medium grid contains 3.27 million elements, and the coarse grid includes 1.19 million elements. Figure 5 shows a decreasing trend of flow velocity at outlet velocity reference points as the number of mesh elements increased. Considering the significant increase in the number of mesh elements, from 3.27 million to 6.16 million, the marginal differences between these results were only 6.7% and 3.07%. However, due to the significant increase in computational time required of approximately 10 hours with less significant results improvement. Therefore, the mesh with 3.27 million elements was selected as the optimal mesh for this study.

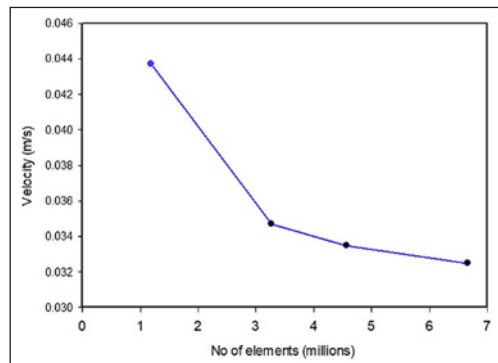


Figure 5. Grid Independence Test Results

CFD Code Validation

It is crucial to compare the current numerical model with previous experimental studies to ensure accurate results. Therefore, a validation study was conducted using the numerical results reported by Talaat et al. (2021), who carried out a similar study in a single-aisle aircraft cabin with three columns of passenger seats. Our study's numerical setup and conditions were identical to those used in the validation to ensure consistency and accuracy. The airflow velocity vector and contour plots from the study are shown in Figure 6. The

vector plot revealed a consistent airflow pattern: air is supplied from the inlet, flows along the cabin walls toward the aisle, and then shifts downward at the aisle section. Further analysis is done by plotting velocity values along the centerline of the cabin, as depicted in Figure 7. The comparison reveals a good agreement between the simulation and experimental data on the front face. There is an average discrepancy of 7.19% between the numerical results reported by Talaat et al. (2021) and current simulation results for velocity contour. These findings indicate the effectiveness of the RANS model in accurately simulating airflow for ventilation phenomena.

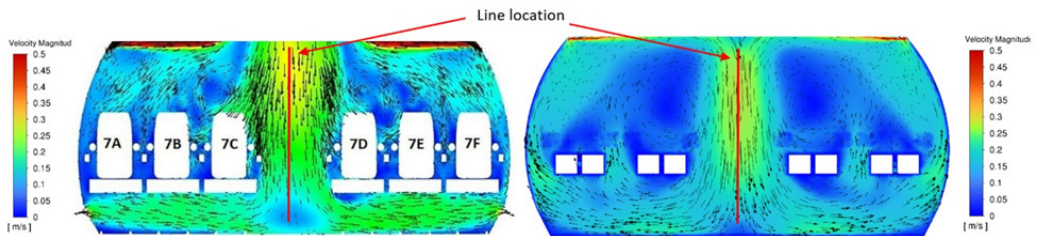


Figure 6. Velocity vector and contour plot. (a) Talaat et al., (2021) and (b) this study

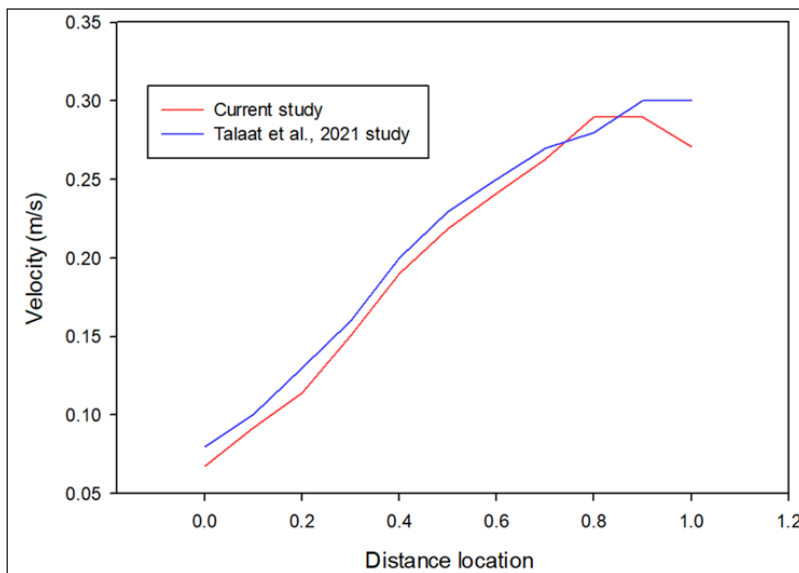


Figure 7. Comparison velocity value along the centerline between Talaat et al. (2021) and this study

RESULTS AND DISCUSSION

The cabin airflow is primarily driven by the ventilation system and influenced by the geometry of passengers, seats, and cabin walls. Figures 8(a) and 8(b) show velocity vectors and contours in the x-y plane for cases where the infected passenger is seated near the aisle

(4-3) and the window (4-4), respectively. In both cases, airflow follows a similar pattern: air enters from the inlet, flows upwards along the upper cabin walls, then moves downwards into the aisle, circulating under the seats toward the exhaust outlets. The downward flow at the aisle splits laterally towards the passenger section, forming a circulation that flows toward the cabin walls without crossing the aisle.

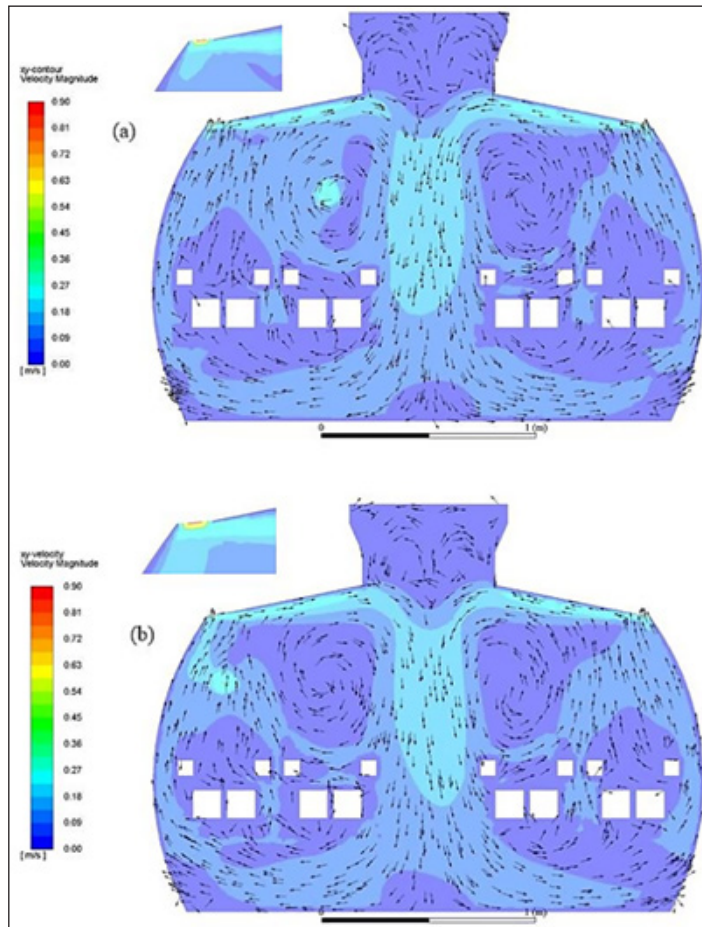


Figure 8. Airflow velocity vector and contour at x-y plane with the infected passenger seated near the (a) aisle (4-3) and (b) window (4-4)

The velocity contours in Figures 8(a) and 8(b) indicate the highest velocity at the ventilation inlet, with velocities decreasing as airflow moves toward the cabin walls, aisle, and exhaust outlets. High-velocity spots depend on the infected passenger's position. Although the velocity distribution is mostly symmetrical, slight asymmetries occur around the passenger section due to different seating positions and the infected passenger exhaling. The overall symmetry results from idealized conditions, assuming uniform passenger geometry and ignoring heat transfer effects on airflow.

Effect Of Infected Passenger Seating Position on Particle Dynamics

The seating position will follow the numbering convention presented in Figure 4. The infected passenger will either be seated near the aisle at seat 4-3 or near the window at seat 4-4. The distribution of 1 μm particles for different infected passenger seats 4-3 and 4-4 with respect to time was presented in Figures 9 and 10, respectively. In 600 seconds, both figures show that the distribution of 1 μm particles is mostly contained within the row of the infected passenger and two rows in front. Both figures also show that after 20 seconds, the particles started to propagate towards the other side of the aisle. At 600 seconds, almost all the particles were either trapped on surfaces or removed through the ventilation system, with only a few particles left trapped within the cabin.

Table 4 highlights the impact of passenger position on particle deposition and removal. Surface deposition is 13.7% higher when particles are released near the aisle (4-3) compared to the window (4-4), while removal is 12.6% higher near the window. Particle depositions on passenger bodies and seats are 3.4% and 27.3% higher near the aisle, but cabin walls show 17% more deposition near the window. Ventilation inlet removal is 15.8% higher near the window, while exhaust outlet removal is 2.1% higher near the aisle. The differences between the particle deposition and removal percentage when released from near the aisle (4-3) and from near the window (4-4) are due to the proximity distance to the surfaces. The

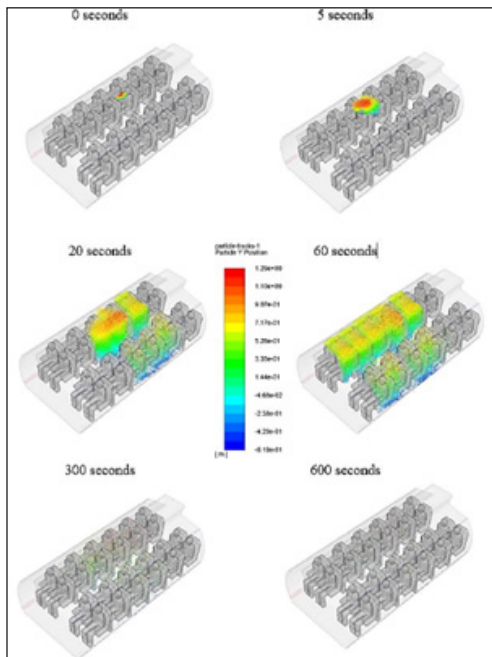


Figure 9. Distribution of 1 μm particles exhaled from seat 4-3 with respect to time

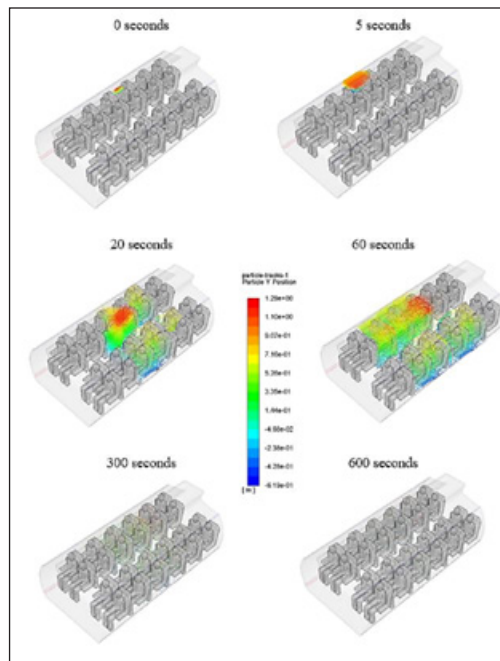


Figure 10. Distribution of 1 μm particles exhaled from seats 4-4 with respect to time

infected passenger seated near the window is much closer to the cabin walls and the inlet than the passenger seated near the aisle. The study by Li et al. (2021) aligns with current findings, which also emphasize the role of seating position and airflow in determining particle deposition and removal. The current study focuses on the effects of seating position near the aisle versus near the window, as well as the detailed quantitative comparison of particle deposition percentages based on these positions. This contributes to a more granular understanding of how different cabin zones and surfaces impact particle behavior.

Table 4

Comparison of particle deposition and removal based on different infected passenger seat positions

Particle Destination		Passenger Seat Position		Difference (%)
		Aisle (4-3)	Window (4-4)	
Deposited (%)	Cabin wall	20.461	37.467	17.006
	Passenger body	31.968	28.584	3.384
	Passenger seats	46.256	18.945	27.311
	Total	98.685	84.996	13.689
Removed (%)	Inlet	5.478	21.234	15.756
	Outlet	6.919	3.776	2.143
	Total	11.397	25.01	12.613

Effect Of Infected Passenger Seating Position on Infection Risk

Particle distribution is mainly confined to the infected passenger's row and the two rows in front. More particles are deposited in the third row (directly in front of the source) than in the fourth row (where the source is). Less deposition occurs on the opposite side of the aisle and back of the source. The aisle seat (4-3) consistently has a higher particle fraction, increasing infection risk, likely due to airflow circulation moving particles toward the cabin walls and reaching 4-3 first. Similar patterns are seen in the second row, with higher deposition at seats 2-3. Overall, infection risk is higher for passengers in front of the source and on the same side of the aisle. The finding is consistent with findings of past studies by To et al. (2009), in which particles expelled by a cough could move forward to the row of seats ahead of the source and lateral air movements influenced the dispersion of these aerosols. This aligns with the result where there was a higher particle deposition on the surfaces in the row directly in front of the particle source.

Effect of Particle Size on Infection Risk

Figure 12 shows the distribution of particle deposition fractions on various seat positions depending on the particle size released from the aisle seat (4-3). The observations from Figure 12 show an agreement with the observations discussed in Figure 11, where the particle deposition has the highest fraction on the seat directly in front of the source (2-3

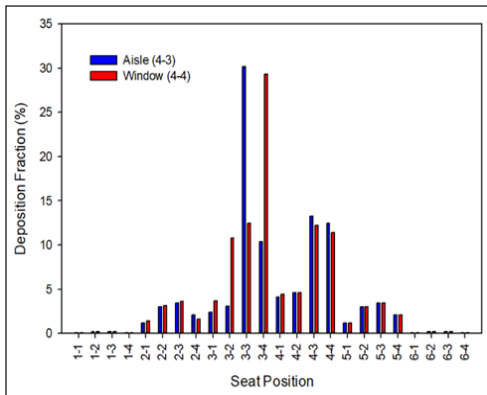


Figure 11. Particle deposition fraction distribution on various seat positions depends on the position of particle release

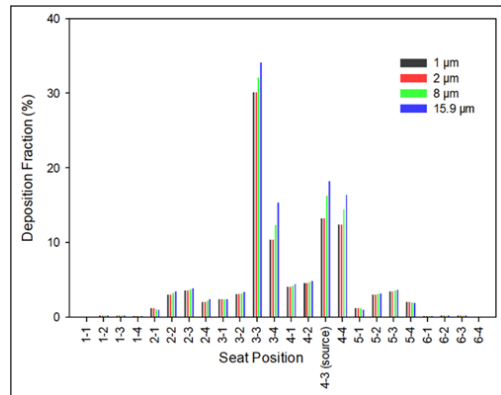


Figure 12. Particle deposition fraction distribution on various seat positions depending on the particle size

and 3-3) and at the location of the source (4-4) compared to other seats of the same row. The deposition is also higher on the same side of the aisle as the source than on the other side of the aisle. As the particle size increases, the deposition fraction also increases at the seat of the particle source (4-3) and the seats directly in front of the source (2-3 and 3-3). On the other hand, the deposition fraction decreases at other seats on the same row as the particle size increases. This could be due to the shorter distance to the surfaces directly in front of the source (2-3 and 3-3) than other lateral seats of the same row. The larger the particle size, the smaller the propagation distance of the particle, resulting in a higher risk of short-range transmission. In summary, the seats directly in front of the source (2-3 and 3-3) and at the source (4-3) have the highest risk of infection, and the risk increases when larger particles are present. Although the risk of infection of passengers seated on other seats of the same row will also increase with the presence of larger particles due to the increase in particle number, the increase of risk is not as high as the seats directly in front of the source (2-3 and 3-3) as there are fewer particles deposited on other seats of the same row compared to the seats directly in front of the source.

Effect of Particle Size on Particle Dynamics

Figure 13 illustrates the correlation between particle size affecting their deposition and removal in an aircraft cabin. Generally, particles are more likely to deposit on surfaces than to be removed via ventilation. Specifically, the highest deposition occurs on passenger seats, followed by passenger bodies and cabin walls. Conversely, the fraction removed through ventilation inlets and outlets is lowest, with larger particles showing a consistent decrease in removal efficiency and an increase in deposition on surfaces. Notably, particles of 8 µm show a slight reduction in seat deposition compared to 1 µm and 15.9 µm particles, likely due to their tendency to be redirected towards cabin walls.

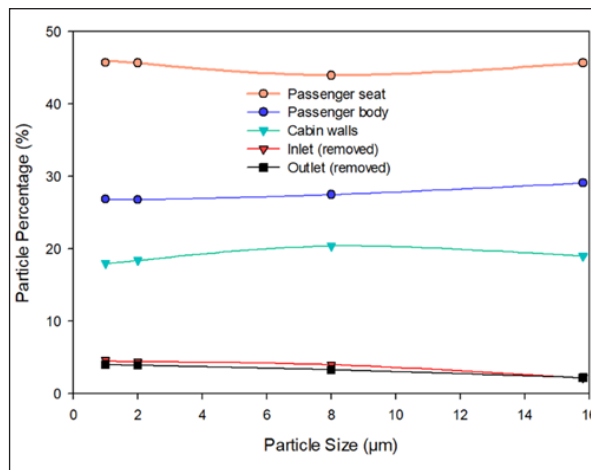


Figure 13. Effect of particle size on particle fate released from aisle seats 4-3

Larger particles have greater mass, enhancing gravitational effects and limiting their travel distance, thus increasing surface deposition risk. This indicates a higher risk of short-range transmission with larger particles. Wang et al. (2011) support these findings, noting that surface deposition exceeds removal through ventilation. These results highlight the importance of tailored cleaning and filtration strategies based on particle size and deposition patterns.

CONCLUSION

The study presented in this paper used computational fluid dynamics (CFD) to investigate virus transmission mechanics in an ATR 72-600 passenger cabin. The results indicated high symmetry in flow directions on both sides of the aisle, with higher velocities near the ventilation inlets, cabin walls, aisle sections, and under seats. The velocity was mostly symmetrical about the aisle, with minor asymmetry near the infected passenger. Particle dynamics, influenced solely by airflow, showed that particle deposition was higher when expelled from the aisle seat compared to the window seat. Surface deposition increases by 13.7% when particles are released near the aisle (4-3) compared to the window (4-4), whereas removal through ventilation is 12.6% higher near the window. Depositions on passenger bodies and seats are 3.4% and 27.3% greater near the aisle, respectively, while deposition on cabin walls is 17% higher near the window. Ventilation inlet removal is 15.8% more effective near the window, whereas exhaust outlet removal is 2.1% higher near the aisle. Conversely, particle removal via the ventilation system was higher for particles released from the window seat. This difference was attributed to the relative proximity of the window seat to cabin walls and ventilation inlets. Particles of 8 µm exhibit a slight

decrease in deposition on seats compared to 1 μm and 15.9 μm particles, likely because they tend to be redirected toward the cabin walls. Larger particles exhibited increased deposition due to gravitational effects, suggesting a higher short-range transmission risk. Based on surface contamination, the infection risk assessment showed a higher risk for seats in front of the infected passenger and on the same side of the aisle. Larger particles increased the infection risk in front of the infected passenger, though the effect was less pronounced for passengers seated in the same row. This study highlights the complex interplay between particle size, seating position, and airflow in determining viral transmission risk in aircraft cabins.

ACKNOWLEDGEMENTS

This work was supported by the Ministry of Higher Education (MoHE) Malaysia for the Fundamental Research Grant Scheme with Project Code: FRGS/1/2022/TK10/USM/03/11

REFERENCES

- ASHRAE. (2018). *Air Quality within Commercial Aircraft*. American Society of Heating, Refrigerating and Air-Conditioning Engineers. https://www.ashrae.org/file%20library/technical%20resources/standards%20and%20guidelines/standards%20addenda/161_2018_g_20231130.pdf
- Bennett, J., Mahmoud, S., Dietrich, W. L., Jones, B., & Hosni, M. (2022). Evaluating vacant middle seats and masks as Coronavirus exposure reduction strategies in aircraft cabins using particle tracer experiments and computational fluid dynamics simulations. *Engineering Reports*, 5(4), Article e12582. <https://doi.org/10.1002/eng2.12582>
- Chen, Q., Qin, S., & Liu, H. (2021). Airflow and virus transmission in aircraft cabins: CFD simulations and risk analysis. *Building and Environment*, 188, 107-121. <https://doi.org/10.1016/j.buildenv.2020.107121>
- Chen, W., Liu, L., Hang, J., & Li, Y. (2023). Predominance of inhalation route in short-range transmission of respiratory viruses: Investigation based on computational fluid dynamics. In *Building Simulation* (Vol. 16, No. 5, pp. 765-780). Tsinghua University Press. <https://doi.org/10.1007/s12273-023-00000-0>
- Dietrich, W. L., Bennett, J., Jones, B., & Hosni, M. (2021). Laboratory modeling of SARS-CoV-2 exposure reduction through physically distanced seating in aircraft cabins using bacteriophage aerosol. *Morbidity and Mortality Weekly Report*, 70, 595-599. <https://doi.org/10.15585/mmwr.mm7016e1>
- Dube, K. (2023). Emerging from the COVID-19 pandemic: Aviation recovery, challenges, and opportunities. *Aerospace*, 10(1), Article 19. <https://doi.org/10.3390/aerospace10010019>
- Gupta, J. K., Lin, C. H., & Chen, Q. (2020). Risk assessment of airborne infectious diseases in aircraft cabins. *Indoor Air*, 21(1), 3-9. <https://doi.org/10.1111/j.1600-0668.2010.00683.x>
- Hui, K. P., Chin, A., Ehret, J., Ng, K., Peiris, M., Poon, L. L. M., Wong, K. H. M., Chan, M., Hosegood, I., & Nicholls, J. (2023). Stability of SARS-CoV-2 on commercial aircraft interior surfaces with implications for effective control measures. *International Journal of Environmental Research and Public Health*, 20(16), Article 6598. <https://doi.org/10.3390/ijerph20166598>

- IATA. (2022). *Annual Review 2022*. International Air Transport Association. <https://www.iata.org/contentassets/c81222d96c9a4e0bb4ff6ced0126f0bb/annual-review-2022.pdf>
- Karmegam, K., Sapuan, S. M., Ismail, M. Y., Ismail, N., Shamsul Bahri, M. T., Shuib, S., Mohana, G. K., Seetha, P., TamilMoli, P., & Hanapi, M. J. (2011). Anthropometric study among adults of different ethnicity in Malaysia. *International Journal of Physical Sciences*, 6(4), 777–788.
- Khoa, N. D., Li, S., Phuong, N. L., Kuga, K., Yabuuchi, H., & Yokota, H. (2023). Computational fluid-particle dynamics modeling of ultrafine to coarse particles deposition in the human respiratory system, down to the terminal bronchiole. *Computer Methods and Programs in Biomedicine*, 237, Article 107589. <https://doi.org/10.1016/j.cmpb.2023.107687>
- Le Guellec, S., Pardessus, J., Bodier-Montagutelli, E., Vecellio, L., de Monte, M., Feteanu, D., Tewes, F., Couet, W., Vecellio, L., & Diot, P. (2023). Administration of bacteriophages via nebulization during mechanical ventilation: *In vitro* study and lung deposition in macaques. *Viruses*, 15(3), Article 602. <https://doi.org/10.3390/v15010047>
- Lee, L. Y. Y., Landry, S. A., Jamriska, M., Subedi, D., McGain, F., & Johnson, G. R. (2023). Quantifying the reduction of airborne infectious viral load using a ventilated patient hood. *Journal of Hospital Infection*, 136, 110–117. <https://doi.org/10.1016/j.jhin.2023.103115>
- Li, L., Pope, Z. C., Son, Y., Eilts, S. M., & Hogan Jr., C. J. (2023). Effects of portable air filtration on submicrometer- and micrometer-sized particle deposition and concentration in a naturally ventilated skilled nursing facility. *Building and Environment*, 240, Article 110454. <https://doi.org/10.1016/j.buildenv.2023.109211>
- Li, X., Zhang, T., Fan, M., Liu, M., Chang, D., Wei, Z., Lin, C. H., Ji, S., Liu, J., Shen, S., & Long, Z. (2021). Experimental evaluation of particle exposure at different seats in a single-aisle aircraft cabin. *Building and Environment*, 202, Article 108049. <https://doi.org/10.1016/j.buildenv.2021.108049>
- Liu, W., Wen, J., Lin, C. H., Liu, J., Long, Z., & Chen, Q. (2013). Evaluation of various categories of turbulence models for predicting air distribution in an airliner cabin. *Building and Environment*, 65, 118–131. <https://doi.org/10.1016/j.buildenv.2013.03.023>
- Luo, Y., Li, Y., Xiao, S., & Lei, H. (2023). Comparative analysis of inflight transmission of SARS-CoV-2, influenza, and SARS-CoV-1. *Epidemiology and Infection*, 151, Article e111. <https://doi.org/10.1017/S0950268823001012>
- Morawska, L., Buonanno, G., Mikszewski, A., & Stabile, L. (2022). The physics of respiratory particle generation, fate in the air, and inhalation. *Nature Reviews Physics*, 4(9), 723–734. <https://doi.org/10.1038/s42254-022-00506-7>
- Pang, Y., Smith, J., & Lee, R. (2018). Optimization of air distribution modes for civil aircraft cabins using CFD. *Journal of Aircraft Engineering and Aerospace Technology*, 90(4), 123–135. <https://doi.org/10.1108/JAAET-10-2018-0025>
- Rahman, N. A. A., Rahim, S. A., Ahmad, M. F., & Hafizuddin-Syah, B. A. M. (2020). Exploring Covid-19 pandemic: Its impact on the global aviation industry and the key strategy. *International Journal of Advanced Science and Technology*, 29(6), 1829–1836.

- Schijven, J., van Veen, T., Delmaar, C., Kos, J., Vermeulen, L., Roosien, R., Verhoeven, F., Schipper, M., Peerlings, B., Duizer, E., Derei, J., Lammen, W., Bartels, O., van der Ven, H., Maas, R., & de Roda Husman, A. M. (2023). Quantitative microbial risk assessment of contracting COVID-19 derived from measured and simulated aerosol particle transmission in aircraft cabins. *Environmental Health Perspectives*, 131(8), Article 087011. <https://doi.org/10.1289/EHP11495>
- Shi, X., Chao, D., Zhang, Y., & Zhao, H. (2020). The study of air supply ways effects on the aircraft cabin thermal environment. In R. Wang, Z. Chen, W. Zhang, & Q. Zhu (Eds.), *Proceedings of the 11th International Conference on Modelling, Identification and Control (ICMIC2019)* (Vol. 582, pp. 123-131). Springer. https://doi.org/10.1007/978-981-15-0474-7_12
- Silva, P. G., Branco, P. T. B. S., Soares, R. R. G., Mesquita, J. R., & Sousa, S. I. V. (2022). SARS-CoV-2 in indoor environments and the impact of ventilation. *Building and Environment*, 219, Article 109224. <https://doi.org/10.1016/j.buildenv.2022.109224>
- Talaat, K., Abuhegazy, M., Mahfoze, O. A., Anderoglu, O., & Poroseva, S. V. (2021). Simulation of aerosol transmission on a Boeing 737 airplane with intervention measures for COVID-19 mitigation. *Physics of Fluids*, 33(3), Article 033312. <https://doi.org/10.1063/5.0040849>
- To, G. N. S., Wan, M., Chao, C., Fang, L., & Melikov, A. (2009). Experimental study of dispersion and deposition of expiratory aerosols in aircraft cabins and impact on infectious disease transmission. *Aerosol Science and Technology*, 43(5), 466-485. <https://doi.org/10.1080/02786820902736658>
- Wang, C., Zhang, J., Chao, J., Yang, C., & Chen, H. (2022). Evaluation of dynamic airflow structures in a single-aisle aircraft cabin mockup based on numerical simulation. *Indoor and Built Environment*, 31(2), 398–413. <https://doi.org/10.1177/1420326X21992094>
- Wang, Q., Gu, J., & An, T. (2022). The emission and dynamics of droplets from human expiratory activities and COVID-19 transmission in public transport system: A review. *Building and Environment*, 219, Article 109224. <https://doi.org/10.1016/j.buildenv.2022.109224>
- Wang, M., Lin, C. H., & Chen, Q. (2011). Determination of particle deposition in enclosed spaces by detached Eddy simulation with the Lagrangian method. *Atmospheric Environment*, 45(29), 5376-5384. <https://doi.org/10.1016/j.atmosenv.2011.06.042>
- Yan, W., Zhang, Y., Sun, Y., & Li, D. (2009). Experimental and CFD study of unsteady airborne pollutant transport within an aircraft cabin mock-up. *Building and Environment*, 44(1), 34–43. <https://doi.org/10.1016/j.buildenv.2008.01.012>
- Yang, S., Lee, G. W. M., Chen, C. M., Wu, C. C., & Yu, K. P. (2007). The size and concentration of droplets generated by coughing in human subjects. *Journal of Aerosol Medicine: The Official Journal of the International Society for Aerosols in Medicine*, 20(4), 484–494. <https://doi.org/10.1089/jam.2007.0610>
- Zhang, Z., Chen, X., Mazumdar, S., Zhang, T., & Chen, Q. (2009). Experimental and numerical investigation of airflow and contaminant transport in an airliner cabin mockup. *Building and Environment*, 44(1), 85–94. <https://doi.org/10.1016/j.buildenv.2008.01.012>

Public Awareness and Performance Assessment of Communal Grease Traps in Klang Valley, Malaysia

Theban Arumugam, Priyadarshini Ravindran, Shafreeza Sobri*, Salmiaton Ali and Mus'ab Abdul Razak

Department of Chemical and Environmental Engineering, Faculty of Engineering, Universiti Putra Malaysia, 43400 UPM, Serdang, Selangor, Malaysia

ABSTRACT

The presence of fat, oil and grease (FOG) in wastewater has become an alarming concern worldwide, and Malaysia is no exception. FOG that escapes into the sewer system can cause sewer network blockages and overflow, contamination of water bodies and inefficient sewerage treatment plant processes, which will harm the ecosystem. This paper aims to investigate the level of awareness and current practices on FOG management among food operators and management staff in selected hotels and shopping malls in Klang Valley, Malaysia. Analysis revealed that most respondents (81.2%) had perceived awareness of FOG, and 76.2% were aware of FOG management and practices on their premises. Although awareness levels for both management and operators are high, in reality, they have not been translated into practice. This is evident from investigating the effectiveness of the existing communal grease trap design by analyzing the effluent samples. The highest levels of biochemical oxygen demand (BOD) for hotel and shopping mall effluents were 9000 mg/L and 13000 mg/L, respectively, while chemical oxygen demand (COD) values in the effluent range from 30000 to 93000 mg/L. The oil and grease (O&G) and total suspended solids

(TSS) values in the effluent were in the range of 50000-85000 mg/L and 10,000-72,000 mg/L, respectively. All tested parameters were well above the permissible limit based on Malaysia's Water Services Industry (Prohibited Effluent) Regulations 2021 (Regulation 4). This concludes that the communal grease traps investigated in this study are ineffective and most likely allow non-permissible effluent into the environment.

ARTICLE INFO

Article history:

Received: 27 August 2024

Accepted: 24 December 2024

Published: 07 March 2025

DOI: <https://doi.org/10.47836/pjst.33.2.20>

E-mail addresses:

gs61649@student.upm.edu.my (Theban Arumugam)

gs60628@student.upm.edu.my (Priyadarshini Ravindran)

shafreeza@upm.edu.my (Shafreeza Sobri)

mie@upm.edu.my (Salmiaton Ali)

musab@upm.edu.my (Mus'ab Abdul Razak)

*Corresponding author

Keywords: Awareness, communal grease trap, fat, oil and grease (FOG), management

INTRODUCTION

Fat, oil, and grease (FOG) are harmful to the existing sewer network regardless of the origin of its source (Wallace et al., 2017). For this reason, legislation ensuring that effective FOG management is in place by food service operators is now being heavily enforced worldwide. In the Southeast Asian region, Thailand and Indonesia have emphasized the installation of grease traps for any food service establishment due to the potential of discharging significant amounts of FOG deposition in the sewer system. Malaysia, Brunei and Singapore have imposed strict regulations on installing grease traps to limit the discharge of FOG that is less than 50 to 100 mg/L into the sewer lines (Tang et al., 2024). In 2021, Malaysia introduced the Water Services Industry (Prohibited Effluent) Regulations 2021, which stipulated that no person is permitted to discharge any prohibited effluent, including discharges containing pollutants such as oil and grease, to a public sewage system or treatment plant without the approval of the National Water Services Commission (SPAN). Table 1 shows the discharge limit specified under the Water Services Industry (Prohibited Effluent) Regulations 2021.

Table 1

Discharge limit specified under Water Services Industry (Prohibited Effluent) Regulations 2021

Item	Parameter	Unit	Limit
1.	Temperature	°C	40
2.	pH	-	6.0 – 9.0
3.	Biological Oxygen Demand (BOD)	mg/L	250
4.	Suspended Solids (SS)	mg/L	300
5.	Chemical Oxygen Demand (COD)	mg/L	500
6.	Total Nitrogen (TN)	mg/L	50
7.	Ammoniacal Nitrogen (AMN)	mg/L	30
8.	Total Phosphorus (TP)	mg/L	10
9.	Oil and Grease (O&G)	mg/L	50

A grease trap is the most common and economical solution to intercept the FOG and, therefore, reduces the amount that enters the main sewers, which can cause inconvenience to the authorities, contractors, end users and the public such as blocked sewer pipelines, overflowing manholes, and flooding of walkways, roads and public amenities (Nieuwenhuis et al., 2018). Grease traps work on the basic principle of gravity, where FOG floats on water and solid particles sink (Aziz, 2010). Baffles within the trap slow the inflow of wastewater from the kitchen sinks. This encourages a settlement period where the separation of fats, oils, grease, water and solid food particles occur within the unit. A trap on the inlet prevents FOG from flowing directly through the unit, with the FOG retained within the unit with food particles, allowing cleaner water to flow through. The retained waste will build up over time and requires regular service and removal of waste for disposal (Aziz et al., 2011).

Today, most pipelines from commercial kitchens, such as floor traps and pot wash areas that use dishwashing detergent, are connected to the sink wastewater pipeline carrying FOG. If the purity of the wastewater or effluent is questionable, the grease trap will be deemed unfit or ineffective (Chinwetkitvanich & Ektaku, 2020).

The fact that FOG is considered accountable for 50–70% of sewer blockages worldwide triggers questions about the claimed efficacy of grease traps in retaining 50%–90% of FOG (Sultana et al., 2022). The consultants usually determine the dimension of the grease trap during the design phase based on kitchen capacity and usage factors. The unprecedented pipeline modifications and unplanned increased usage contribute to the ineffectiveness of the grease trap, which is designed for a specific population or person equivalent. The uncontrolled flow of effluent more than often forces the FOG from the first chamber to the next and subsequently to the grease trap outlet, thus escaping the trap. This is often related to the unexpected increase in usage compared to the expected volume during the design phase. Over time, modifications to the pipeline due to additional sinks, cooking stations, and new pipelines have also contributed to the increased flow of FOG. In addition, the maintenance of grease traps by emptying, cleaning, and disposing of the collected FOG in a timely manner influences the grease traps' efficiency (He et al., 2017; Sultana et al., 2022). Current monitoring of the grease traps is done manually based on historical data with poor closed-loop inspection and improvements, thus resulting in overflows, spillages and, in some cases, blockages causing backflow (Wallace et al., 2017; Ali et al., 2022). The cost of clearance, the acute and complex treatment requirements, and the potential for environmental pollution and health risks during sewer overflows make this issue a concern.

Studies have shown that grease trap efficiency is influenced by volatile influent flow that impacts the hydraulic residence times and physical and chemical characteristics of the FOG, such as pH, chemical oxygen demand, dissolved oxygen, biological oxygen demand, total solids and depth of FOG layer. Understanding the physicochemical properties of the FOG, as well as the discharge characteristics, will help in the successful control of FOG deposition. Tang et al. (2024) conducted several site investigations at different food service establishments in Kuching, Sarawak. A significant difference in solid and dissolved constituents was discovered between the inlet and outlet chambers of the grease traps, indicating that the baffle wall could affect the separation mechanism. Ahmad et al. (2023) characterized the restaurant wastewater collected from a central grease interceptor situated at UTM Residensi, Kuala Lumpur. It was found that the COD, BOD and FOG values were 9948, 3170, and 1640 mg/l, respectively, well above the permitted discharge standards given by the Department of Environment, Malaysia.

On top of design standards, inspection and enforcement, one of the key elements in the FOG program is public awareness directed at reducing the amount of FOG discharged from food establishments and ensuring those handling the FOG waste are properly trained

(Wallace et al., 2017). Ultimately, awareness among food establishment operators on the grease trap installation and maintenance determines the success or failure of FOG management. Collin et al. (2023) investigated the awareness of and experiences with FOG by those working within food service establishments. Findings demonstrate that awareness of issues caused by FOG in sewer networks is independent of job role or position and that most respondents (74%) are acquainted with the impacts of poor FOG management.

Understanding the objectives of FOG management and its impact on the environment will help ensure that the waste is handled correctly from its origin until disposal. However, this is only viable when the standard operating procedures are governed by strict legislation to ensure compliance. In the United Kingdom, Water UK, in collaboration with several agencies, has established a guidance document to advise food establishments on the need to keep FOG out of drains and sewers (Water UK, 2017). Singapore's 2019 Code of Practice on Sewerage and Sanitary Works incorporates guidelines on the sizing of grease traps for all establishments that handle food, including restaurants, coffee shops and hawker centers (PUB, 2017). In Malaysia, the Ministry of Local Government Development has established a guideline stipulating the recommended design, installation, operation and maintenance of grease traps (KPKT, 2017). The existing law requires evidence of grease trap installation during business license applications or renewal with the local authorities. However, improvements must be made to the guidelines to include specific volumes and dimensions of the grease traps, as well as monitoring the cleaning schedule and frequency to avoid noncompliance.

This study investigated communal grease traps in 14 premises in Klang Valley, Malaysia, comprising hotels and shopping malls. Hotels have multiple kitchens working around the clock to cater to major events such as parties, weddings, company dinners, and room service. On the other hand, shopping malls have shared communal grease traps due to the high number of food and beverage eateries operating within the premises. Both hotels and shopping malls require significant manpower resources to ensure operations continue without disruption. Furthermore, they need to be properly trained to comply with standard operating procedures (SOP) to ensure standardization in food preparation, cleaning and waste management, particularly FOG.

While food service establishments are often assumed to be the major source of FOG deposits in the sewer, their contribution to the problem has not been thoroughly investigated. This research aims to (1) investigate the current practices and level of awareness of FOG management among food operators and management staff in selected hotels and shopping malls through questionnaire distribution and (2) quantify the discharge characteristics of the grease trap to assess the effectiveness of existing communal grease trap design. Samples were collected before and after passing through the grease traps and analyzed based on the following parameters: biochemical oxygen demand (BOD), chemical oxygen demand

(COD), dissolved oxygen (DO), oil and grease (O&G), total suspended solids (TSS) and pH. The investigation was carried out to determine if these parameters comply with the permitted discharge standards given by the Department of Environment, Malaysia.-The information gathered from this study may be the basis for redesigning the grease trap or developing a sustainable and smart grease trap to reduce and mitigate discharges of FOG.

METHODOLOGY

Premises

The study focuses on 14 premises in Klang Valley, divided into two categories: shopping malls and hotels. Seven hotels and seven shopping malls were selected. For confidentiality reasons, the hotels and shopping malls are denoted as H and S, respectively. All the grease traps at the respective premises have relatively similar frequency in terms of usage, size and maintenance. Details related to hotel and restaurant operating information are described in Tables 2 and 3.

Table 2
Hotel operating information

Hotel	Number of kitchens	Kitchen cooking frequency	Hotel rating	Number of grease traps	Grease trap size (GPM)	Frequency of service (per month)
H1	6	Minimum 3	5	8	500	4
H2	7	meals per day	5	3	500	1
H3	5		5	2	500	8
H4	4		5	4	500	4
H5	3		4	2	500	4
H6	2		5	1	500	1
H7	1		3	1	500	2

Table 3
Shopping mall operating information

Shopping malls	Number of F&B	Kitchen cooking frequency	Number of grease traps	Grease trap size (GPM)	Frequency of service (per month)
S1	10	Continuously	10	250	2
S2	30	from 10 am to	6	250	4
S3	25	9 pm	17	250	1
S4	5		2	250	1
S5	30		3	250	2
S6	56		21	250	2
S7	3		3	250	2

Instrument

The questionnaire was constructed based on expert consultation and an intensive literature review. Data collection was carried out by sharing questionnaires through Google Forms and face-to-face interviews with the respondents. The first section of the questionnaire included demography surveys on age, educational level, job categories, and premises location. The second section covered awareness questions regarding FOG management. Current practices of FOG management at the premises were assessed in the third part of the instrument. Upon data collection, descriptive analysis in SPSS was used.

This survey used a nominal scale to gather the respondents' basic demographic information. The data required to understand awareness and practices were gathered using a 5-point Likert Scale ranging from (1) Strongly Disagree to (5) Strongly Agree. The questionnaire has gone through a process of validity and reliability testing. A pilot test was conducted to determine the questionnaire's reliability and ensure that the overall structure of the survey was in no way ambiguous. Cronbach's Alpha was found to be 0.84 and 0.81 for Sections 2 and 3, respectively. It is stated that a survey construct has a high level of reliability when the Alpha coefficient of the reliability test in the survey falls within the range of 0.7 and 0.9 (Straub et al., 2004).

Sampling

Wastewater samples were collected from the premises during the weekly maintenance of the grease traps by a local service provider. Two samples were taken from each grease trap; influent samples were collected from the second chamber, where most of the FOG remained, while effluent samples were obtained from the final chamber before exiting into the sewer network. All samples were taken during the morning hours between 12:00 am and 3:00 am, and the sampling procedure was consistent throughout the study. The composite samples were collected using a 1-liter plastic bottle, a 500 mL plastic bottle preserved with sulphuric acid and a 1-liter glass bottle preserved with hydrochloric acid. Any foreign materials and rubbish found were discarded before samples were sent to an accredited lab to test for pH, biochemical oxygen demand (BOD), chemical oxygen demand (COD), dissolved oxygen (DO), oil and grease (O&G) and total suspended solids (TSS). Figure 1 summarizes the research activities involved in this work.

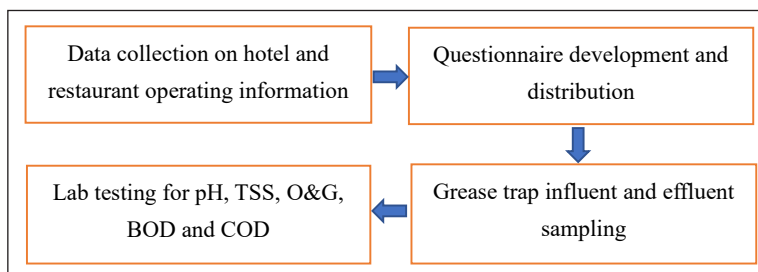


Figure 1. Flowchart of research activities

RESULT AND DISCUSSIONS

Analysis of Public Awareness

A total of 336 respondents were involved in the survey to evaluate FOG management practices and levels of awareness in the pre-determined premises. Table 4 shows the demographic analysis of the respondents.

Table 4
Demographic of respondents

Demographic	Population (n)	Percentage (%)
Types of premises		
Hotels	175	52.1
Shopping malls	161	47.9
Categories of respondents		
Food operators	207	61.6
Administration	129	38.4
Level of education		
Malaysian Certificate of Education (<i>Sijil Pelajaran Malaysia (SPM)</i>)	81	24.1
Diploma	132	39.3
Degree	117	34.8
Masters	6	1.8

175 respondents (52.1%) work in the hotel industry, while 161 (47.9%) were shopping mall employees. Further breakdown amongst the respondents shows that 38.4% (129 respondents) are from the management, whereas 61.6% (207 respondents) are food operators. Management refers to supervisors and those working in an office environment, whereas operators are those working in the kitchen or dealing directly with customers. A huge difference in the breakdown can be noticed as there are generally a small number of people in the management team per venue. In contrast, food operators at any single premises would be on the higher side due to the number of kitchens per venue.

It was found that most respondents are diploma (39.3%) and degree (34.8%) holders, and only 6 are Master's degree holders. Upon further investigation among the diploma holders, 35.6% were at a management level, and 64.4% were food operators. Through verbal communication, it was deduced that a high number of food operators were diploma holders working part-time jobs while awaiting further education. In management, it can be commended that those with a diploma were able to work rank and file to reach a management level. Among the degree holders, 68.4% were at a management level, and 31.6% were food operators. The degree holders could be working as part-time food operators to earn extra income or while waiting for a permanent job offer. 100% of Master's degree holders were from the management level. Figure 2 shows the level of education among the management

team and food operators. It can be concluded that most management teams hold a degree or at least a diploma, while the food operators are school leavers with a secondary school certificate or diploma holder.

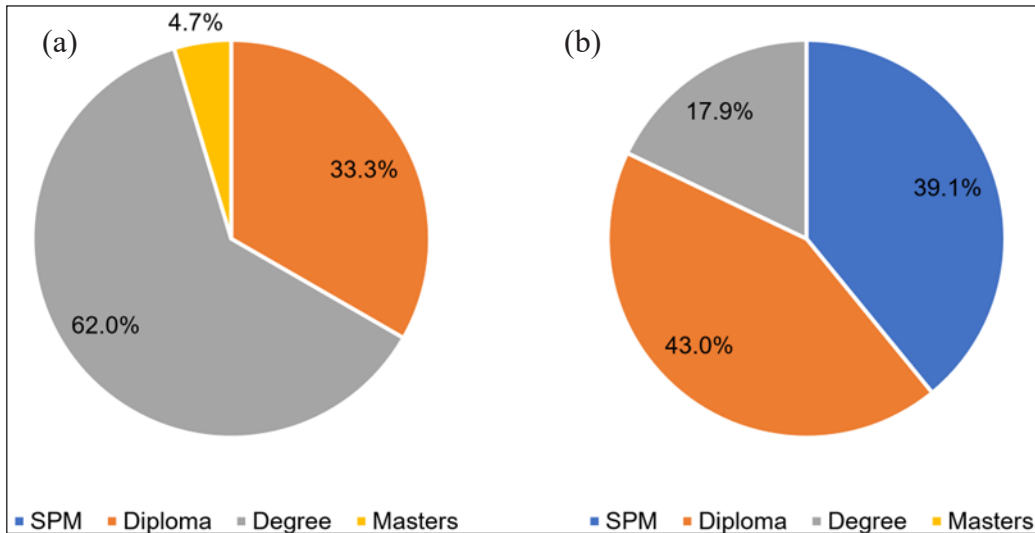


Figure 2. Level of education among the respondents: a) management, b) food operators

Successful control and management of FOG is largely dependent on public awareness and a clear understanding of its impact on the environment. Table 5 shows respondent’s awareness of FOG in general. The survey revealed that 85% of the respondents understood that FOG is a by-product of food preparation and production and that food service establishments are a significant source of FOG. Although 14% of the respondents are uncertain about the substance, all respondents are well aware that their premises are producing FOG.

Waste cooking oil (WCO) consists of oils and fats used for cooking or frying in the food processing industry, food handling businesses, and households. Although both WCO and FOG are by-products from food establishments, collecting WCO is much easier and can be recycled to make soap, lubricants, candles, animal and pet feed as well as renewable energy (Awogbemi et al., 2021). Considering that WCO has become a valuable commodity and may constitute a great proportion of FOG, respondents were enquired on the difference between WCO and FOG. 81.6% were aware of the difference and understood that pouring WCO down the kitchen sink and into the drain is detrimental to the environment. *The Star* has reported that in 2016, Klang Municipal Council spent almost RM6 million to remove clogging caused by hardened cooking oil in drains (Edward, 2016).

Drainage systems in food processing facilities can experience a build-up of FOG. When FOG is allowed to go down the drain, it solidifies, reducing and preventing water

flow in drains and sewer pipes, causing sewage backups and overflows, leading to property damage, environmental problems, and other health hazards (Owolabi et al., 2022). This survey revealed that 83.1% of the respondents agree that FOG is a potential environmental threat if disposed of inappropriately. However, only 67.6% knew that the Housing and Local Government Ministry made it a requirement since 2005 for all food premises to install, maintain and desludge grease trap systems to obtain or renew business licenses. Under the present guidelines, restaurant operators must clean and dislodge a grease inceptor installed at their premises once every two weeks. The remaining respondents were unaware of any rules or regulations imposed by the government.

Table 5
Respondent's awareness of FOG

Awareness	Population, n (total 336)				
	Strongly agree	Agree	Neither agree nor disagree	Disagree	Strongly disagree
FOGs are by-products from food preparation and production	276 (82.1%)	10 (3.0%)	3 (0.9%)	47 (14.0%)	0
FOG is produced in the premise	322 (95.8%)	14 (4.2%)	0	0	0
FOG differs from WCO (waste cooking oil)	260 (77.4%)	14 (4.2%)	2 (0.6%)	60 (17.9%)	0
FOG has a negative impact on the environment	261 (77.7%)	18 (5.4%)	20 (6.0%)	37 (11.0%)	0
Rules and regulations exist related to FOG	219 (65.2%)	8 (2.4%)	25 (7.4%)	84 (25.0%)	0

The median was calculated for the data set, and it was found that 81.2% of the total respondents perceived awareness of FOG, and 18.5% can be considered neutral. Only 0.3% of respondents had very limited knowledge of FOG. Crosstabulation between the median and categories of respondents found that 98.44% of the management personnel have an awareness of FOG, compared to 70.53% among the food operators.

FOG management is vital to running an efficient, hygienic and compliant kitchen. Typically, a grease trap is used as a receptacle into which wastewater containing FOG flows before entering a drainage system. From Table 6, all respondents reported that their premises installed individual grease traps and that FOG produced at their premises was channeled to these grease traps and subsequently to a communal grease trap. However, a small number of businesses chose to pour FOG into containers and dispose of it in the bin once it had hardened, as reported by six respondents. Also, 6% of the respondents admitted that their premises flushed the FOG down the drains and sinks and into the sewer system. This may cause sanitary sewer overflows, which are clogs in the collection systems, that

can potentially result in raw sewage being released into communities, causing potentially dangerous health conditions (Owolabi et al., 2022). Although the numbers are not alarming, food establishments should make conscious efforts to dispose of FOG safely. There are a plethora of ways restaurants and eateries can stop FOG from going down the drain and into the sewer. Even making small changes, such as wiping down plates and pans with paper towels, can make a huge difference in washing areas of kitchens, where blockages frequently occur in the sink units.

The types of cleaning agents most commonly used in commercial kitchens are detergents, degreasers, abrasives and acids. Detergents are usually neutral chemicals with pH 6-8 and contain surfactants to break up dirt or soil for easy washing. Degreasers remove grease from surfaces such as oven tops and counters, while abrasives are usually used to clean floors, pots and pans. Acids are the most powerful type of cleaning agent and are usually used to clean drains and sinks in the kitchen as well as descaling the dishwashers. From this survey, 96.7% of total respondents agreed to use the stated chemicals in their premises. The use of acids and alkaline can potentially cause damage to the pipes as well as alter the constituents of the FOG. Detergents in background water increase the production of calcium-based saponified solids that may clog sewer lines and eventually cause sanitary sewer overflows (Iasmin et al., 2016). The use of detergents and sanitizers may also affect the emulsification characteristics, such as the droplet size of FOG discharges, and thus impact the separation ability in the grease trap (Sello, 2021).

Table 6
Respondent's awareness of FOG management in the premise

Awareness	Population, n (total 336)				
	Strongly agree	Agree	Neither agree nor disagree	Disagree	Strongly disagree
The presence of a grease trap in the premise	316 (94.0%)	20 (6.0%)	0	0	0
FOG is channeled directly to the grease trap	316 (94.0%)	20 (6.0%)	0	0	0
FOG is discarded into the dustbin	0	6 (1.8%)	19 (5.7%)	311 (92.6%)	0
FOG is flushed into the sewer line	0	20 (6.0%)	18 (5.4%)	298 (88.7%)	0
Chemicals are used as cleaning materials in the kitchen	293 (87.2%)	32 (9.5%)	11 (3.3%)	0	0

Based on the median, 76.2% of the respondents perceived awareness of FOG management in their premises. Crosstabulation between the median and categories

of respondents found that 85.3% of management respondents understood good FOG management practices, whereas only 70.5% of food operators practiced good FOG management.

Performance Evaluation of Communal Grease Trap

Restaurants and the food processing industry are the main sources of FOG; therefore, it is important that the grease traps used at these establishments are effective in removing the substance from wastewater before entering the sewer system. Ensuring that grease traps are properly installed and, most importantly, properly maintained is challenging. Poorly maintained and low capacity of grease traps will allow FOG to flow into the sewer pipes, causing the build-up of fatberg. A fatberg is a coagulated mass of congealed grease and non-biodegradable matter found in sewers and drains that cause extensive damage to drainage systems (Abdullah, 2021).

The principal constituents of concern for restaurant wastewater are its organic strength (BOD and COD), particulate loading (TSS), and oil and grease (O&G). The strength of the wastewater is affected by many factors, including cuisine type, kitchen capacity, grease trap size and FOG management practices (Gurd et al., 2019). Ultimately, the effluent from food establishments must meet certain discharge limits before entering the public sewer system.

Figures 3 and 4 show the BOD and COD values for communal grease traps at selected hotels and shopping malls for both influent and effluent streams. As evident from Figure 3, all premises have exceeded the allowable BOD discharge limit of 250 mg/L. Unexpectedly, BOD values of the effluent for most premises were found to increase from the influent values, which indicated that the effluent was contaminated with high organic loading. Only one hotel premise, H1, was able to remove 40% of BOD compared to four shopping malls (S4, S5, S6 and S7) that were able to remove as low as 3% to 75% of BOD. Figure 4 shows similar observations for COD where concentrations at the effluent were higher than the influent and exceeded the permissible limit of 500 mg/L. The highest level of COD for hotel effluent was almost 30000 mg/L, while for shopping malls, soar to 93000 mg/L. Although some communal grease traps at the shopping malls (S4, S5, S6 and S7) were able to treat between 5% to 62% of COD, the final effluent still did not meet the discharge requirement. This indicates that the grease traps did not work as anticipated.

It has been reported that grease traps are capable of removing up to 80% of FOG from the influent. However, little evidence was presented for BOD and COD removal. A study by the United States Environmental Protection Agency (U.S. EPA) reported that the grease trap unit was able to remove 26%–65% of BOD, 40%–80% of TSS and 70%–80% of FOG, while a laboratory scale study proved that grease traps can remove 50%–80% of BOD and TSS (U.S. EPA, 2012; Wongthanate et al., 2014). The incapability of grease traps to treat BOD and COD usually stems from a lack of timely servicing and poor maintenance. A

regular grease trap cleaning schedule prevents FOG from building up and ensures that the trap continues to operate effectively. Also, the inadequate size of the grease trap may cause insufficient retention time for organic/inorganic matter breakdown, leading to significant variations of BOD and COD.

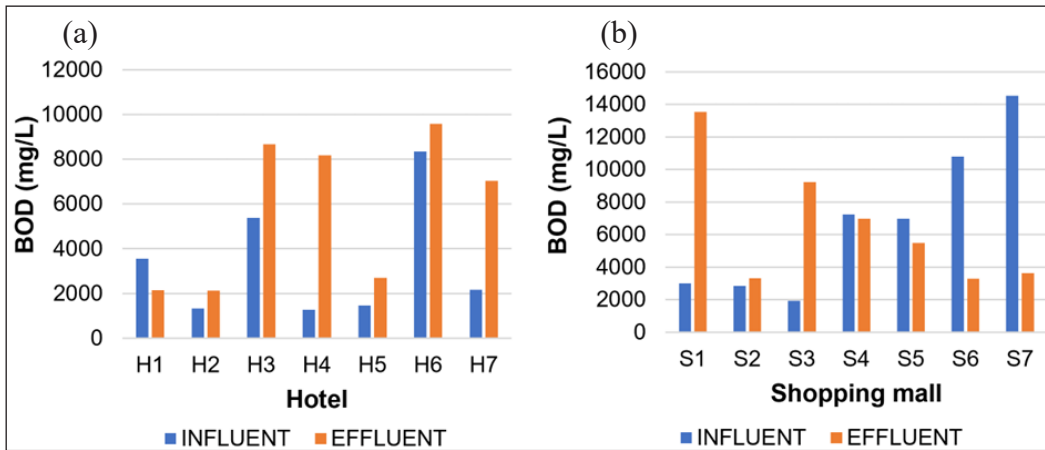


Figure 3. BOD results for communal grease traps at (a) hotels and (b) shopping malls

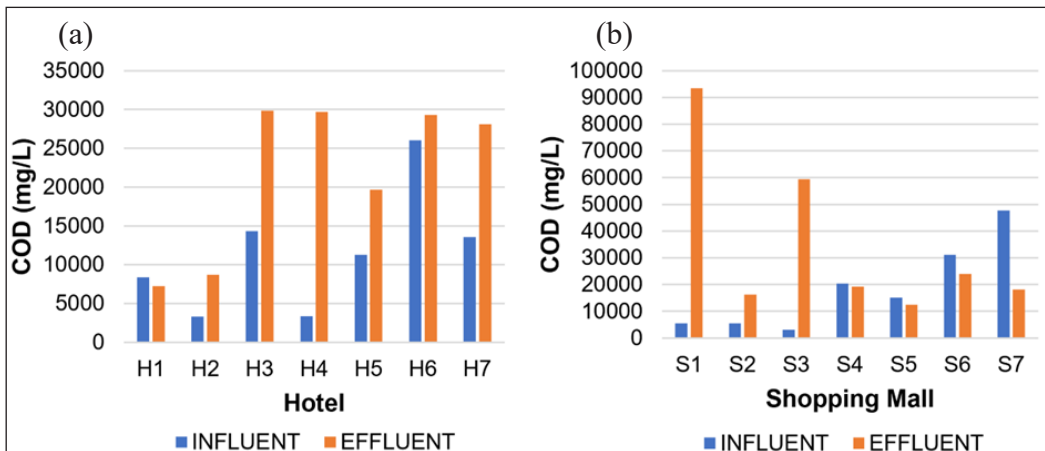


Figure 4. COD results for communal grease traps at (a) hotels and (b) shopping malls

High COD in water indicates greater levels of oxidizable organic matter and, consequently, a lower amount of DO. All hotels and shopping malls depict a DO reading of less than 1 mg/L before and after the grease trap, which indicates a symptom of excessive contamination. Low dissolved oxygen may result from high water temperature and suspended solids. It is well known that food premises use hot water together with acidic cleaning agents to clean utensils and the kitchen at the end of the operation. When

there is a rise in effluent temperature due to the discarded hot water during the cleaning process, the suspended solids will absorb the heat and decrease the DO levels (Musalib et al., 2015). Also, hot water holds less DO compared to cold water (Bozorg-Haddad et al., 2021). The presence of O&G in the grease trap forms an impenetrable layer above the effluent surface. This decreases interaction in the open air and thus reduces the DO level in the effluent. Grease traps are usually situated in secluded areas of the hotel and shopping mall premises due to bad odor and unexpected backflow or flooding. It is usually not in an open area with adequate air circulation, thus reducing the opportunity for any sort of sunlight, natural aeration or ventilation.

As presented in Figure 5, all premises have exceeded the allowable discharge limit of 50 mg/L for O&G. Three of the hotel premises (H1, H3 and H4) were able to reduce the O&G content between 39% to 65%, and three of the shopping malls (S3, S4 and S6) were able to remove 25%–83% of the O&G. The rest of the grease traps in both hotels and shopping malls showed an increment of O&G content in the effluent. Ideally, the O&G content should be reduced when subjected to an efficient working condition of the grease trap, as it would stay afloat in the first and second chambers. FOG is derived from many organic non-polar compound food sources with a density of approximately 0.863–0.926 g/cm³ (Wallace et al., 2017; Ali et al., 2022), while water is a polar solvent which has a density of 1.000 g/cm³. Hence, density and polarity contribute towards the floating of FOG over water. Issues occur when high water temperatures are used for washing and cleaning in the kitchen. The heating of oils causes FOG to liquefy, emulsify and react with other organic compounds, thus changing the chemical composition of FOG and its polarity.

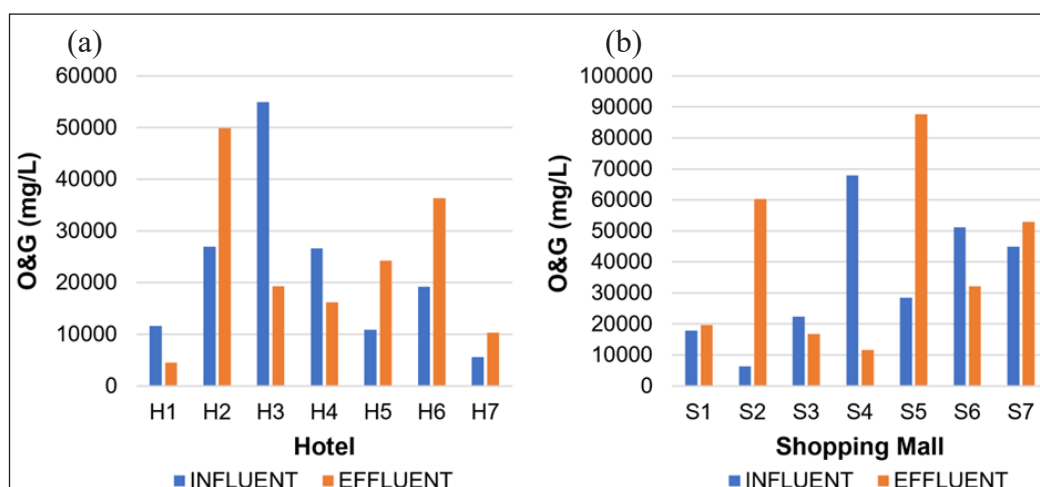


Figure 5. O&G results for communal grease traps at (a) hotels and (b) shopping malls

Compared to hotel premises, the shopping malls are bigger in size; for this reason, the content and quantity of the O&G differs greatly between the two premises. The quality of the effluent also differs depending on the type of grease traps used in the premises and the frequency of service. The type of grease trap plays a vital role in ensuring that the O&G is retained in the first and second chambers while the water exits the grease trap through the outlet pipe. In this study, hotel H2 has been in the industry for 40 years and operates with concrete-based grease traps with only two chambers. The baffles are worn out, and the concept of O&G retaining them in the first chamber is almost impossible. The baffle in the grease trap is the integral component that serves to slow down the flow of water and lengthen the detention time to maximize the separation of the FOG and settling of the solids (Hendrasarie & Maria, 2021). The failure of the grease trap is clearly depicted in the O&G effluent value, which increased significantly by almost 84.7%. Similarly, hotel H5 has an increased O&G effluent value of almost 122.3% as it uses a two-chamber grease trap of insufficient size.

Be it a hotel or a shopping mall, items discarded into the kitchen sink vary from cooking oil to organic materials such as food waste, raw materials, meats, margarine and flour. The pipelines carry this waste through its channel to the respective grease traps. High grease loads, emulsified grease, and fast flow volume have caused FOG to bypass the grease trap and discharge in the effluents. Grease traps with a higher frequency of service will have O&G concentrated in the first and second chambers, whilst the third chamber would only contain clouded water with minimal oil traces floating. In comparison with grease traps that are serviced monthly or bi-monthly, traces of O&G will be evident in all three chambers and can be seen flowing out via the outlet as well when agitated. With timely service, the O&G will be removed, and the process will stay efficient.

High TSS values in the effluent are often related to excessive solids generation due to an increase in BOD loading. Figure 6 shows that the TSS values in the effluent for both hotels and shopping malls range from 10,000 mg/L to 72,000 mg/L. Grease traps at the shopping malls S4, S5, S6 and S7 could reduce 39%–88% of the TSS, while a very low removal rate was observed for hotel grease traps (H3 and H7). The high flow rate of the influence was found to affect the TSS removal, although the same could not be said for BOD and FOG removal.

Solids in the grease trap may originate from different areas of the premise. In some premises, the kitchen pipelines are shared amongst floor traps, stove areas, food preparation areas, sink pipelines, and dishwashers, which end up in the grease trap. Apart from the organic compound, other materials are discarded into the pipeline that contributes to the significant level of TSS in hotels and shopping malls, such as cleaning the kitchen flooring, which results in dirt, sand, and even sometimes gravel-washed into the pipeline. Another important factor to consider is that the grease trap main pipeline is usually made of cast iron

or PVC pipes. Over time, cast iron pipes tend to corrode due to the use of acidic cleaning agents and the rodding process that scrapes the inner layer of the pipe and releases metal particles. As the effluent passes through these pipes, the above residues join the affluent and end in the grease traps, which was the case with hotels H3, H6 and H7 and shopping malls S4, S6 and S7.

At the grease trap itself, there were signs of damage due to wear and tear and evidence of corrosion, which further contributed to the increment of TSS values in the effluent stream. Furthermore, if the grease traps are made of old traditional concrete design, they are more likely to have sand, silt, and gravel residue in the grease trap, as in the case of hotel H2. Also, the grease traps are usually located in the basement or car park areas, with significant amounts of sand, silt, dried leaves and dirt escaping into the grease traps due to vehicle movement. Although the grease traps are covered, the contractors will lift the lid during scheduled servicing, which causes these elements to fall into the traps.

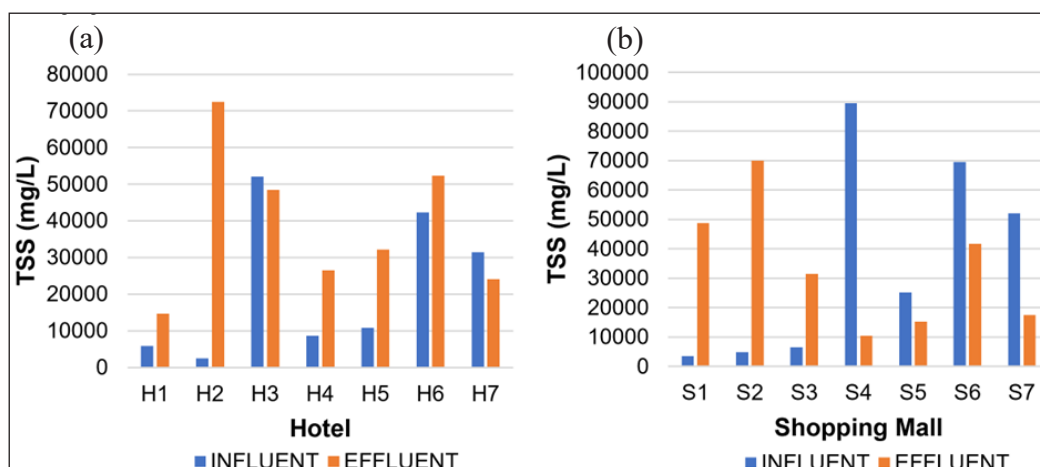


Figure 6. TSS results for communal grease traps at (a) hotels and (b) shopping malls

The permitted pH value of effluent in the sewer network is between pH 6.0 to 9.0. As shown in Figure 7, all hotels and shopping malls recorded a pH value of less than 6.0, which is acidic and not permissible to be discharged into the sewer network. FOG in the grease trap will begin to float as the influent cools down, after which it will start to break down by hydrolysis, where the fatty acids are released. The decrease in pH value is a result of the release of a significant volume of free fatty acids (FFA), which eventually will cause corrosion inside the grease trap (Husain et al., 2014). Also, food operators in hotels and shopping malls are usually instructed to wash and discard all wastewater via the sink, which connects to the floor trap pipeline. By the same token, during closing hours, the workstations, food preparation tables, floors and sinks are washed down using cleaning agents, which are commonly acidic.

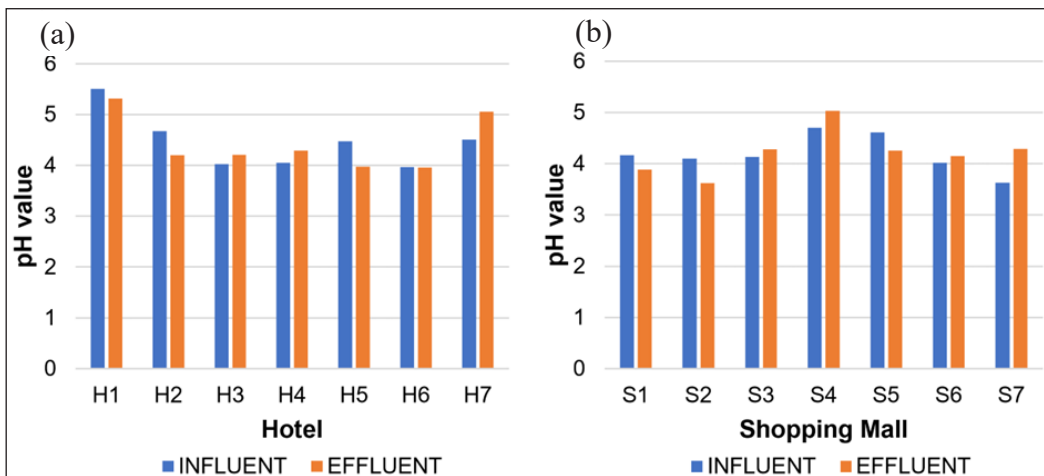


Figure 7. pH values for communal grease traps at (a) hotel and (b) shopping malls

An improper discard of organic food wastes into the pipeline will end up in the first chamber basket. Depending on the frequency of service, this food waste will remain in the grease trap basket and begin to decompose. Organic matter, such as vegetables and meat products, contains carbon elements, which will be released into the effluent during decomposition. Due to the instability of these organic compounds and their ability to be easily oxidized, carbon dioxide will be produced. As a result, the dissolved carbon content will increase the hydrogen ions, causing the pH value to decrease, denoting its acidity.

In addition, certain kitchens and floor traps may experience the gargling effect or slow exit as foreign materials may build up or harden FOG, which reduces the pipe's clearance for a smooth effluent flow out. At this point, it is a common practice in hotels and shopping malls to pour acid-based FOG cutters into these floor traps to help them clear the line. This is a quick fix in practice that helps hotel, and shopping mall kitchen operators expedite the cleaning process. Another factor that causes an increase in effluent acidity is the dumping of cleaning agents into the grease trap by unauthorized personnel. The housekeeping personnel are usually scheduled to clean the grease trap area as it is commonly used as temporary storage. The housekeepers dumped the leftover solutions into the grease traps for convenience during the cleaning process using acidic detergents and cleaning agents.

CONCLUSION

Awareness among those working within food service establishments determines the success or failure of the FOG management initiatives. In this work, we reported that 81.2% of the respondents had a perceived understanding of FOG, while 76.2% possessed an awareness of how it is managed within their premises. The awareness level is independent of job

position; however, a vast majority of the respondents who work in management are more acquainted with the knowledge of FOG and its management compared to the operators. Further investigation of the communal grease traps at selected hotels and shopping malls revealed that none of the effluent parameters met the permissible discharge level stipulated in the Water Services Industry (Prohibited Effluent) Regulations 2021 (Regulation 4). The highest level of O&G for hotel and shopping mall effluents were 50000 mg/L and 85000 mg/L, respectively, while TSS values in the effluent range from 10,000 mg/L to 72,000 mg/L. This important finding demonstrates poor design, maintenance, and monitoring of the grease traps by the premises owner and local authorities. Further work will be focusing on upgrading the conventional grease trap to a smart grease trap with sensor incorporation that will enable accurate level measurements and an effective alarm system to indicate the user and contractor for maintenance services.

ACKNOWLEDGEMENT

This work was financially supported by Geran Universiti Putra Malaysia (Project code: GP-IPS/2023/9743500).

REFERENCES

- Abdullah, N. I. (2018). *Grease Trap Helps to Prevent Environmental Problems*. Federation of Malaysian Consumers Associations. <https://www.fomca.org.my/v1/index.php/fomca-di-pentas-media/fomca-di-pentas-media-2018/268-grease-trap-helps-to-prevent-environmental-problems>
- Ahmad, I., Abdullah, N., Koji, I., Yuzir, A., Ahmad, M. D., Rachmadona, N., Al-Dailami, A., Show, P. L., & Khoo, K. S. (2023). Micro and macro analysis of restaurant wastewater containing fat, oil, grease (FOG): An approach based on prevention, control, and sustainable management. *Chemosphere*, 325, Article 138236. <https://doi.org/10.1016/j.chemosphere.2023.138236>
- Ali, M. A. H., Talib, S. H. A., & Hashim, S. I. N. S. (2022). The combination of a previous kitchen waste grease trap for fat, oil, and grease for pre-treatment. *Journal of Advancement in Environmental Solution and Resource Recovery* 2(2), 37–43.
- Awogbemi, O., Von Kallon, D. V., Aigbodion, V. S., & Panda, S. (2021). Advances in biotechnological applications of waste cooking oil. *Case Studies in Chemical and Environmental Engineering*, 4, Article 100158. <https://doi.org/10.1016/j.cscee.2021.100158>
- Aziz, T. N. (2010). *Analysis of Grease Abatement Devices and the Measurement of Fat, Oil, and Grease in Food Service Establishment Waste Streams*. (PhD dissertation). North Carolina State University, USA. <http://www.lib.ncsu.edu/resolver/1840.16/4395>
- Aziz, T. N., Holt, L. M., Keener, K. M., Groninger, J. W., & Ducoste, J. J. (2011). Performance of grease abatement devices for removal of fat, oil, and grease. *Journal of Environmental Engineering* 137(1), 84–92. [https://doi.org/10.1061/\(ASCE\)EE.1943-7870.0000295](https://doi.org/10.1061/(ASCE)EE.1943-7870.0000295)

- Bozorg-Haddad, O., Delpasand, M., & Loáiciga, H. A. (2021). Water quality, hygiene, and health. In O. Bozorg-Haddad (Ed.), *Economical, Political, and Social Issues in Water Resources* (pp. 217-257). Elsevier. <https://doi.org/10.1016/B978-0-323-90567-1.00008-5>
- Chinwetkitvanich, S., & Ektaku, P. (2020). Reality in package on-site grease trap performance: Success and failure in fog removal. *GEOMATE Journal*, 18(67), 156-161.
- Collin, T., Cunningham, R., MacAdam, J., Villa, R., Jefferson, B., & Jeffrey, P. (2023). Towards a risk ranking for improved management of discharges of fats, oils, and greases (FOG) from food outlets. *H2Open Journal*, 6(1), 29-39. <https://doi.org/10.2166/h2oj.2023.056>
- Edward, R. (2016, December 7). MPK Spent Close to RM6mil to Remove Hardened Cooking Oil from Drains. *The Star*. <https://www.thestar.com.my/metro/community/2016/12/07/expensive-mess-to-clean-mpk-spent-close-to-rm6mil-to-remove-hardened-cooking-oil-from-drains/>
- Gurd, C., Jefferson, B., & Villa, R. (2019). Characterisation of food service establishment wastewater and its implication for treatment. *Journal of Environmental Management*, 252, Article 109657. <https://doi.org/10.1016/j.jenvman.2019.109657>
- He, X., de los Reyes, F. L., & Ducoste, J. J. (2017). A critical review of fat, oil, and grease (FOG) in sewer collection systems: Challenges and control. *Critical Reviews in Environmental Science and Technology* 47(13), 1191–1217. <https://doi.org/10.1080/10643389.2017.1382282>
- Hendrasarie, N., & Maria, S. H. (2021). Combining grease trap and *Moringa oleifera* as adsorbent to treat wastewater restaurant. *South African Journal of Chemical Engineering*, 37, 196-205. <https://doi.org/10.1016/j.sajce.2021.05.004>
- Husain, I. A. F., Alkhatib, M. F., Jammi, M. S., Mirghani, M. E. S., Zainudin, Z. B., & Hoda, A. (2014). Problems, control, and treatment of fat, oil, and grease (FOG): A review. *Journal of Oleo Science* 63(8), 747–752. <https://doi.org/10.5650/jos.ess13182>
- Iasmin, M., Dean, L. O., & Ducoste, J. J. (2016). Quantifying fat, oil, and grease deposit formation kinetics. *Water Research*, 88, 786-795. <https://doi.org/10.1016/j.watres.2015.11.009>
- KPKT. (2017). *Garis Panduan Pemasangan Perangkap Minyak di Premis Makanan di Kawasan Pihak Berkuasa Tempatan* [Guidelines for the Installation of Grease Traps in Food Premises under the Local Authorities Area]. Kementerian Perumahan dan Kerajaan Tempatan. https://mpkulai.gov.my/wp-content/uploads/2024/05/garis_panduan_pemasangan_perangkap_minyak_di_premis_makanan_di_kawasan_pihak_pbt_kpkt.pdf
- Mutalib, N. A. A., Karim, O. A., & Mustafa, A. D. (2015). The water quality study and sources of pollution in Alur Ilmu, UKM. *Malaysian Journal of Analytical Sciences*, 19(5), 1137-1146.
- Nieuwenhuis, E., Post, J., Duinmeijer, A., Langeveld, J., & Clemens, F. (2018). Statistical modelling of fat, oil and grease (FOG) deposits in wastewater pump sumps. *Water research*, 135, 155-167. <https://doi.org/10.1016/j.watres.2018.02.026>
- Owolabi, T. A., Mohandes, S. R., & Zayed, T. (2022). Investigating the impact of sewer overflow on the environment: A comprehensive literature review paper. *Journal of Environmental Management*, 301, Article 113810. <https://doi.org/10.1016/j.jenvman.2021.113810>

- PUB. (2017). *Code of Practice on Sewerage and Sanitary Works*. Public Utilities Board. <https://www.pub.gov.sg/-/media/PUB/PDF/Compliance/Used-Water/GreaseTrap/COPSSW2nded2019.pdf>
- Sello, M. (2021). Wastewater fats oils and grease characterisation, removal and uses. A review. *Environmental Science: An Indian Journal* 17(10), Article 200.
- Straub, D., Boudreau, M. C., & Gefen, D. (2004). Validation guidelines for IS positivist research. *Communications of the Association for Information Systems*, 13, 380-427. <https://doi.org/10.17705/1CAIS.01324>
- Sultana, N., Roddick, F., Gao, L., Guo, M., & Pramanik, B. K. (2022). Understanding the properties of fat, oil, and grease and their removal using grease interceptors. *Water Research*, 225, Article 119141. <https://doi.org/10.1016/j.watres.2022.119141>
- Tang, L. Y., Wong, N. H., Am Chieng, T., Kiu, A. K. J., Choo, C. S., Li, Y., Tan, C. P., Yaser, A. Z., Khaerudini, D. S., Chen, G. H., & Sunarso, J. (2024). Physicochemical characteristics of grease-trap wastewater with different potential mechanisms of FOG solid formation, separation, and accumulation inside grease traps. *Water Research*, 256, Article 121607. <https://doi.org/10.1016/j.watres.2024.121607>
- U.S.EPA. (2012). *Design Manual: Onsite Wastewater Treatment and Disposal System*. United States Environmental Protection Agency. https://www.epa.gov/sites/default/files/2015-06/documents/2004_07_07_septics_septic_2002_osdm_all.pdf
- Wallace, T., Gibbons, D., O'Dwyer, M., & Curran, T. P. (2017). International evolution of fat, oil and grease (FOG) waste management - A review. *Journal of Environmental Management* 187, 424–435. <https://doi.org/10.1016/j.jenvman.2016.11.003>
- Water UK. (2017). *Disposal of Fats, Oils, Grease and Food Waste - Best Management Practice for Catering Outlets*. Water UK. <https://www.aquariusgroup.co.uk/wp-content/uploads/2018/03/Disposal-of-Fats-Oils-Grease-and-Food-Fats.pdf>
- Wongthanate, J., Mapracha, N., Prapagdee, B., & Arunlertaree, C. (2014). Efficiency of modified grease trap for domestic wastewater treatment. *The Journal of Industrial Technology*, 10(2), 10-22.

Hydrogenolysis of Glycerol to Propanediols over Ni supported on MgO Catalyst

Maryam Shakur*, Maryum Irshad and Muhammad Sajjad Haider

Department of Chemical Engineering, University of Engineering & Technology, Lahore 54890, Pakistan

ABSTRACT

A Ni/MgO catalyst was used to undergo hydrogenolysis of glycerol, a byproduct of biodiesel synthesis, in the aqueous phase at different nickel loadings (10–40% by weight). The wet impregnation-prepared catalysts were characterized by XRD, SEM, TPR, and BET methods and showed strong metal-support interaction, good Ni dispersion, and high surface area, respectively. The catalytic activity in a batch reactor was measured at 220°C, 3 MPa hydrogen pressure, and 20 hours of reaction time. Glycerol conversion exhibited an increasing trend with Ni loading in the following sequence: 10%Ni/MgO < 20%Ni/MgO < 30%Ni/MgO < 40%Ni/MgO. The 20%Ni/MgO catalyst yielded the highest 1,2-propanediol (1,2-PDO) production, with a subsequent decrease observed at higher Ni loadings. In particular, the 20%Ni/MgO catalyst produced a 74% total glycerol conversion and a 76% selectivity toward 1,2-PDO. The optimal reaction conditions were then ascertained by examining the effects of temperature (200–240°C), glycerol content (5%–30% by weight), hydrogen pressure (3–5 MPa), and reaction time (6–25 hours) on the activity of the 20%Ni/MgO catalyst.

Keywords: Biomass; catalysis; glycerol; green economy; hydrogenolysis; Ni/MgO

ARTICLE INFO

Article history:

Received: 13 September 2024

Accepted: 16 January 2025

Published: 07 March 2025

DOI: <https://doi.org/10.47836/pjst.33.2.21>

E-mail addresses:

maryamshakur@hotmail.com (Maryam Shakur)

irshadmm@mail.uc.edu (Maryum Irshad)

sajjadhaider51272@gmail.com (Muhammad Sajjad Haider)

*Corresponding author

INTRODUCTION

Prices have increased, and carbon emissions have increased because of the growing demand for and decreased availability of fossil fuels. Biofuel production offers a crucial alternative to meet energy needs and reduce the carbon footprint (Quispe et al., 2013). Biodiesel, a sustainable fossil fuel alternative, produces significant glycerol byproducts (Gonzalez-Garay et al., 2017). Increasing biodiesel production has boosted

glycerol supply, posing challenges. Converting excess glycerol into valuable chemicals like propanediols and acrolein can improve biodiesel economics (Sun et al., 2016).

Glycerol hydrogenolysis via catalysis can be directed towards the yield of several alcohols, among which the two most relevant are 1,2-propanediol (1,2-PDO) and 1,3-propanediol (1,3-PDO). 1,2-Propanediol finds usage in the medicine and tobacco sectors. Other important areas for its use are in the manufacture of antifreeze additives, paints, cosmetics and polymers (Bagheri et al., 2015; Nakagawa & Tomishige, 2011). Historically, a petrochemical method that involved the hydration of propylene oxide and hydroperoxide made from propylene or chlorohydrin obtained from oil has been used to create 1,2-PDO (Tendam & Hanefeld, 2011). However, these procedures are both environmentally detrimental and costly (Kumar et al., 2020).

Glycerol hydrogenolysis, in which hydrogen cleaves the C–C and C–O bonds in glycerol, provides a more economical as well as ecologically sound way to produce 1,2-PDO. Along with lower amounts of alcohols, including methanol, ethanol, and ethylene glycol, the process yields a variety of compounds, such as 1,2-propanediol, 1,3-propanediol, acetol, 1-propanol, and 2-propanol (Wang et al., 2019). The catalyst's nature, metal-support interaction, and particle size significantly influence the reaction mechanism and product selectivity. Glycerol hydrogenolysis is generally understood to occur in two steps: Glycerol is hydrogenated after dehydration to create an intermediate to the final product (Vasiliadou & Lemonidou, 2015).

Numerous heterogeneous catalysts have been investigated for glycerol hydrogenolysis. These include those based on noble metals like Pt (Dolsiririttigul et al., 2023), W (Numpilai et al., 2021), Pd and Ru (Salgado et al., 2021), Rh (Wang et al., 2013), Ag (Rekha et al., 2017), and Au (Checa et al., 2012), as well as those based on transition metals like Ni (Azri et al., 2021) Cu (Raju et al., 2020; Wu et al., 2021; Xia et al., 2012; Zhou et al., 2010) and Co (Cai, Song et al., 2018). Wang et al. (2013) investigated a range of metal nanoparticles, about 2 nm in size, supported on m-ZrO₂ for the hydrogenolysis of glycerol, including Ru, Rh, Pt, and Pd. The findings showed that the turnover rates were Ru > Rh > Pt > Pd in that order. On the other hand, Pd > Pt > Rh > Ru was the sequence in which the selectivity ratio for the cleavage of C–O to C–C bonds dropped.

Noble metals are too costly for the industrial manufacture of 1,2-PDO despite being efficient and selective in the manufacture of propanediol. The development of catalysts based on first-row transition metals, which are significantly less expensive than second—and third-row noble metals, is advantageous for improving the economic viability of glycerol hydrogenolysis.

Several elements from the d-block, such as Cu, Ni, Co, and Zn, have been studied by researchers as possible catalysts for glycerol hydrogenolysis. Cu-dolomite catalyst has been shown to be effective by Azri et al. (2020), who achieved total glycerol conversion with

92.2% selectivity toward 1,2-PDO at low temperature and pressure. Strong acid sites and low-temperature reduction were identified as critical factors influencing the reaction. The catalyst was stable after five successive reaction cycles, exhibiting 95% conversion and 84% selectivity towards 1,2-PDO. The good activity and selectivity of Cu nanoparticles based on ZnO against propylene glycol was shown by Wang and Liu (2014). Propylene glycol was shown to be produced as a result of the interaction between the metal and support. On the zinc oxide surface, glycerol first experienced dehydration, which produced acetol. Acetol was then hydrogenated on the Cu sites, resulting in the creation of 1,2-PDO. Conversely, when Cu was supported on a basic material such as MgO, the reaction mechanism was altered (Balaraju et al., 2012)

Ni is widely used in industrial catalytic processes, including steam reforming of methane (Rogers et al., 2016; Ross et al., 1978), methane decomposition (Rivas et al., 2008) and glycerol reforming (Seretis & Tsiakaras, 2016). Ni is a good contender for the creation of a less expensive catalyst than Pd- and Pt-based ones since it shares a group in the periodic table with Pd and Pt and frequently displays similar chemistry. Glycerol hydrogenolysis has been thoroughly researched using Ni-based catalysts. Van Ryneveld et al. (2011) evaluated the Ni catalyst's performance in a fixed-bed reactor running at 4 and 7.5 MPa pressures and temperatures between 230 and 320°C. Silica and alumina served as the catalysts' supports. Ni/SiO₂ achieved a glycerol conversion of 99%, while Ni/Al₂O₃ reached 96%. Higher density of active Ni sites and improved reducibility from weaker metal-support interactions were the causes of Ni/SiO₂'s superior conversion. However, Ni/Al₂O₃ showed higher selectivity (80%) toward 1,2-PDO in contrast with Ni/SiO₂ (71%) due to the alumina surface's higher concentration of sites containing strong acids.

Reaction activity and selectivity toward 1,2-PDO are improved when the catalyst surface has adequate basic and/or acidic sites (Vasiliadou & Lemonidou, 2015). Mg, Al, Zn, and silica were added to a Ni catalyst supported on CeO₂ to maximize its selectivity toward 1,2-PDO and ethanol. The selectivity toward 1,2-PDO and ethanol was 68% and 9%, respectively, after Mg was added as a promoter on Ni/CeO₂. This work sheds important light on the effects of attaching a basic promoter to an amphoteric support. The addition of zinc and magnesium increased the number of basic sites, increasing the hydrogenolysis activity in terms of conversion and selectivity, according to the study's findings. Menchavez et al. (2017) suggest that the selectivity of the final product is largely dependent on the basicity of the catalyst.

The utilization of monometallic Ni catalysts for glycerol hydrogenolysis has primarily focused on acidic and amphoteric supports, with comparatively limited research available on monometallic Ni catalysts supported on basic materials. Nonetheless, studies on sorbitol hydrogenolysis have looked at the use of Ni/MgO catalysts, showing that, when the same conditions are met, these catalysts have better activity and selectivity than Cu/MgO and

Co/MgO catalysts. Ni/MgO demonstrated a liquid-phase carbon recovery of 91%, sorbitol conversion of 57%, and 33.5% selectivity toward 1,2-PDO at 473 K and 6 MPa of hydrogen pressure. In contrast, when Raney Ni was tested without support under the same operating conditions, both the activity and selectivity toward propanediols were notably lower, highlighting the synergistic role of Ni in conjunction with the MgO support in reaching a high level of selectivity and conversion. Notably, the Raney Ni catalyst also led to a notable rise in the production of gaseous byproducts, suggesting deep hydrogenolysis (X. Wang et al., 2015). In another study investigating sorbitol hydrogenolysis over Ni/MgO, Chen et al. (2013) demonstrated that harsher reaction conditions led to deep degradation and produced more byproducts but increased the overall sorbitol conversion.

The synthesis, characteristics, and catalytic efficiency of many Ni/MgO catalysts with varying Ni loadings are covered in this work. The wet impregnation method was used to manufacture the catalysts and determine how the morphology of the catalysts affected their catalytic performance. XRD, SEM, TPR, and BET tests were used to evaluate them. 20%Ni/MgO catalyst produced the best yield of 1,2-PDO, according to preliminary studies done at a fixed temperature, hydrogen pressure, glycerol feed concentration, and reaction duration. Next, to ascertain the ideal reaction conditions for the chosen 20%Ni/MgO catalyst, a thorough investigation was conducted into the effects of the temperature, hydrogen pressure, feed concentration of glycerol, and reaction time.

MATERIALS AND METHODS

Materials

Nickel nitrate hexahydrate (>98%) was purchased from BDH Chemicals, UK. Glycerol (>99.9%), ethylene glycol (>99.9%), and 1,2-PDO (>99%) were purchased from Fisher Scientific, USA. Methanol (>99.8%), 1-propanol (>99.5%), and 2-propanol (>99.5%) were purchased from Sigma-Aldrich, USA. Merck in Germany was the supplier of ethanol (>99%). Daejung Chemicals, located in South Korea, provided 1-butanol (>99%) and 1,3-PDO (>99%). Acetonitrile (>99.9%) was purchased from Honeywell, USA. Acetol (95%) was purchased from Alfa Aesar, USA. Nitrogen (99.999%) and hydrogen (99.999%) cylinders were purchased from Fine Gas Company, Pakistan. Without any additional purification, all compounds were utilized just as supplied.

Catalyst Preparation

The Ni/MgO catalysts were prepared with different Ni loadings (10%–40% by weight) using the wet impregnation method. To prepare a certain amount of catalyst with 10% Ni loading, 0.496 g of $\text{Ni}(\text{NO}_3)_2 \cdot 6\text{H}_2\text{O}$ was dissolved in deionized water. After that, this solution was combined with commercially available MgO and agitated for three hours at 50°C. The wet catalyst was dried overnight in an oven (Memmert, Germany) at 110 °C.

The dry catalyst was calcined for three hours at 500 °C in a tube furnace (Carbolite Gero, UK) with static air. The calcined catalyst was stored in air-tight glass bottles in a desiccator. Prior to use in the reactor, the catalyst was reduced in the tube furnace under hydrogen flow (50 mL/min) at 500 °C for 3 hours.

Catalyst Characterization

The calcined catalysts were characterized by X-ray diffraction (XRD) using a D8 DISCOVER X-ray diffractometer (Bruker, Germany). Cu-K α radiation ($\lambda = 0.15418$ nm) was installed in the apparatus, and a scintillation detector running at room temperature, 40 kV, and 40 mA was used. The powder samples were scanned at a pace of 1.4 seconds per step, with an increment of 0.04° from 20° to 85° (2 θ). The phase was identified by comparing the XRD spectrum with the JCPDS data cards.

A Quantachrome® ASiQwin™ gas adsorption device (Quantachrome Instruments, USA) was used to study nitrogen adsorption at -196 °C. The powder samples were degassed at 250°C for 3 hours under a secondary vacuum before the nitrogen adsorption test at P/P₀ = 0.3. The samples' surface areas were determined using the BET equation.

A Quantachrome® Autosorb iQ chemisorption analyzer (Quantachrome Instruments, USA) was used to perform the H₂-TPR (temperature-programmed reduction with hydrogen) examination of the catalysts. The catalyst sample (100 mg) was purged in helium flow for one hour prior to the TPR experiment. The TPR study was then performed with a linear heating rate of 10 K/min while hydrogen was flowing from 353 K to 1173 K. A thermal conductivity detector was used to track the amount of hydrogen consumed (TCD).

SEM (scanning electron microscopy) was used to investigate the catalyst shape and particle distribution using an Evo LS10 scanning electron microscope (Zeiss, Germany).

Catalyst Performance Evaluation

A benchtop stainless steel autoclave reactor (Parr 4566, Parr Instruments, USA) was used for the catalyst performance evaluation. The reactor had a capacity of 300 mL and was equipped with temperature and pressure sensors and a mechanical stirrer. Figure 1 displays the layout of the setup for the experiment.

A typical experiment involved adding 1 g of freshly reduced catalyst to the reactor after adding 100 mL of feed solution (10 weight percent glycerol in water). The reactor was sealed and purged with high-purity nitrogen at least five times to get rid of any air within. In the same manner, hydrogen was added in place of nitrogen. Prior to initiating the experiment, the reactor was examined for leaks for two hours after being pressurized with hydrogen to the required pressure of 3–5 MPa. With the Parr 4848 Reactor Controller (Parr Instruments, USA), the temperature (200–240°C) and stirring rate (500 rpm) were automatically adjusted.

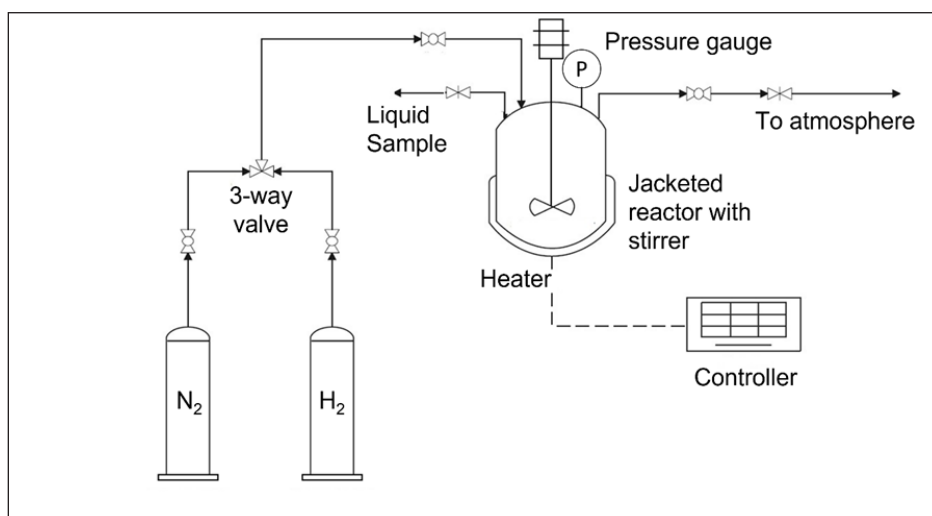


Figure 1. Reactor setup for catalyst evaluation

After the appropriate reaction time had passed (6–25 h), the reactor was quenched by being plunged into an ice bath, and samples of the liquid and gaseous products were collected through the respective sampling ports. The catalyst in the liquid sample was removed by filtration followed by centrifugation at 10,000 rpm for 10 min. All experiments were run in duplicate on different batches of catalysts.

Analysis of Reaction Products

Liquid samples were analyzed by the Shimadzu GC-2014 gas chromatograph (Shimadzu, Japan), which was equipped with an AOC-20i autoinjector, FID, and the HP-Innowax capillary column (30 m × 0.25 mm × 0.25 μm); 1-butanol was used as the internal standard, acetonitrile as the dilution solvent, and nitrogen as the carrier gas. A temperature schedule of injection at 45°C, hold for 4 min, rise to 180°C at 5°C/min and hold for 14 min. Injector temperature: 250°C, detector temperature: 280°C, column flow rate 0.75 mL/min, split ratio 1:50, injection volume 1 μL. Calibration curves were built up for glycerol, 1,2-PDO, 1,3-PDO, 1-propanol, 2-propanol, acetol, ethylene glycol, ethanol and methanol (4 points, $R_2 > 0.9995$). All samples were run twice on the gas chromatograph; the average result is reported here.

The breakdown of glycerol also produces trace amounts of gaseous products. The gaseous samples were examined using a Chromatec Crystal 9000 gas chromatograph (Chromatec, Russia), and the results showed the presence of CO₂, CH₄, and CO in trace levels. However, the composition of the gaseous samples was not quantified.

The overall glycerol conversion, X_{Gly} , was calculated using Equation 1:

$$X_{\text{Gly}} [\%] = \frac{n_{\text{Gly,in}} - n_{\text{Gly,out}}}{n_{\text{Gly,in}}} \times 100 \quad [1]$$

where $n_{\text{Gly,in}}$ and $n_{\text{Gly,out}}$ represent the total moles of glycerol in the reactor both prior to and following the experiment. The selectivity to any specific product, S_i , was calculated using Equations 2 (Ramesh et al., 2022):

$$S_i [\%] = \frac{\text{carbon moles of product } i \text{ produced}}{\text{carbon moles of all products}} \times 100 \quad [2]$$

RESULTS AND DISCUSSION

Catalyst Characterization

The crystalline phases of the MgO support and the Ni/MgO catalysts were investigated using X-ray diffraction. To provide an equitable comparison of these data, we have only offset these diffractograms' intensities (Figure 2) rather than rescaling them. Discrete diffraction peaks for the MgO powder at 2θ angles of 36.9° , 42.9° , 62.3° , and 74.7° demonstrate the presence of well-defined MgO crystallites in the support material. Diffraction peaks at 2θ angles of 37.3° , 43.3° , and 79.4° correspond to the crystal planes of NiO(111), NiO(200), and NiO(222) for the Ni/MgO catalysts, respectively. The diffraction peaks corresponding to MgO and NiO are distinctly resolved and can be observed as clearly separated in the XRD pattern. To further emphasize this distinction, a zoomed-in snapshot of the relevant regions of the diffraction pattern has been included in Figure 2. In the case of the Ni/MgO catalysts, these peaks increase in intensity upon increasing the Ni concentration of the catalyst, which again indicates the increased formation of NiO species on the catalytic surface. Interestingly, the diffractograms of Ni/MgO catalysts also present evidence that the catalysts contain a MgNiO_2 phase evidenced by diffraction peaks which are somewhat higher at 2θ angles than those of NiO and MgO (Chuanming et al., 2006; Nakayama et al., 1997). Furthermore, the MgNiO_2 peaks at roughly 43° and 62° gradually move toward larger 2θ angles as the catalyst's Ni concentration increases. The trends seen in the peak shift are in line with previous research and can be attributed to a greater degree of Mg substitution with Ni in the catalyst structure (Chen et al., 2013). Overall, the presence of the MgNiO_2 phase, along with the shifting diffraction peaks, indicates strong metal-support interaction.

Hydrogen consumption analysis of Ni/MgO catalysts was conducted using H_2 -TPR studies. The results revealed three distinct reduction peaks observed at around 440 K, 600 K, and 1050 K (Figure 3). According to the literature (Shi et al., 2009; Usman & Daud, 2016), these peaks represent weak, medium-strong, and strong interactions between MgO and NiO. Thus, a low reduction temperature of 440 K indicates that NiO present on the

catalyst surface is weakly bound and, hence, easily reducible. Strong interaction between NiO and the support MgO restricts the reduction of Ni, and the reduction temperature rises.

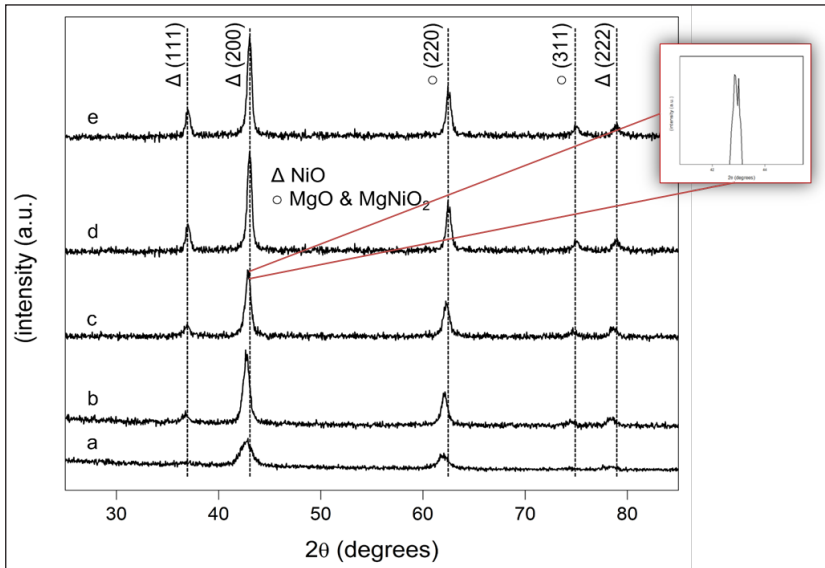


Figure 2. XRD spectra of Ni/MgO catalysts: (a) MgO, (b) 10%Ni/MgO, (c) 20%Ni/MgO, (d) 30%Ni/MgO, (e) 40%Ni/MgO

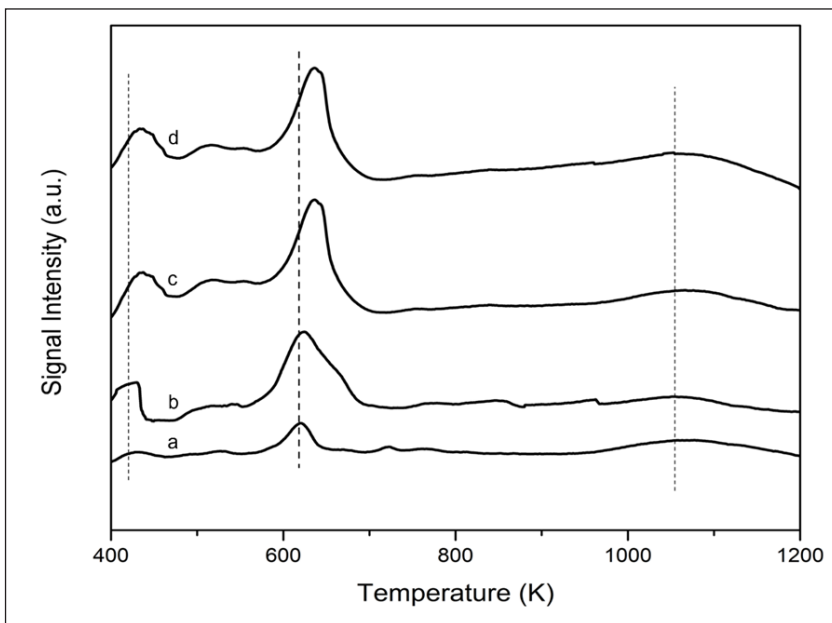


Figure 3. H₂-TPR curves for Ni/MgO catalysts: (a) 10%Ni/MgO, (b) 20%Ni/MgO, (c) 30%Ni/MgO, (d) 40%Ni/MgO

At higher Ni loadings (30%–40%), the H₂-TPR curves show minimal variation around the reduction peaks at 440 K and 600 K. However, increasing nickel loading makes the reduction peak near 1050 K more noticeable. Catalysts with elevated Ni loadings (30%–40%) display reduced hydrogen consumption across all temperatures, further indicating a stronger interaction of Ni and MgO, potentially leading to the formation of MgNiO₂ solid solution, as confirmed by the XRD analysis.

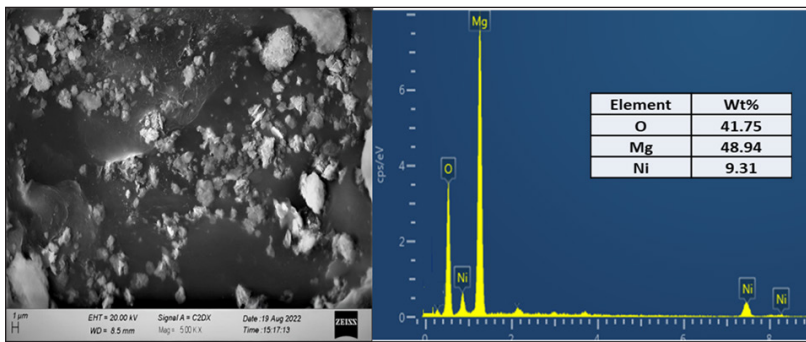
SEM-EDX images show that at low Ni loading, Ni distribution on the catalyst support is relatively homogenous (Figure 4). However, as the Ni content is increased, Ni particles have a noticeable agglomeration, which is particularly prominent for the 40%Ni/MgO catalyst (Figure 4d). This is consistent with the XRD analysis and can be explained by the increased formation of the MgNiO₂ solid solution at high Ni loading (Echegoyen et al., 2007). Overall, the catalyst with 20% Ni loading appears to have the best surface dispersion of Ni among all synthesized catalysts. Additionally, the EDX analysis for all four catalysts, along with the weight percentages of Ni and Mg prior to the reduction process, is presented in Figure 4. The EDX results demonstrate a clear increase in Ni content as the Ni loading progressively increases.

The results of the BET analysis reflect a similar trend, as presented in Table 1. The surface area and pore volume of the MgO support are comparatively high. However, applying a tiny amount of Ni (10% loading) to the support reduces its pore volume and surface area to about half its original value. This is frequently observed in catalysts that have been prepared by wet impregnation and is explained by the Ni particles blocking the pores of the catalyst. Further additions of Ni loading further reduce the catalyst surface area and pore volume. This agrees with a progressive increase in the dimensions of the Ni particles and an accompanying rise in the pore-blocking effect. This effect is most pronounced for the 40%Ni/MgO catalyst, as expected from the corresponding XRD and SEM analyses.

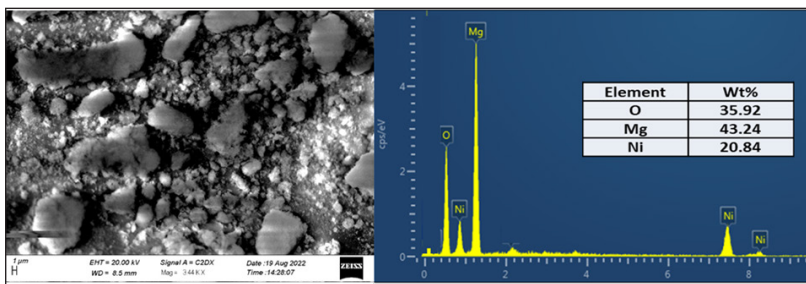
Table 1
Catalyst surface area and pore volume from BET analysis

Catalyst	Surface Area [m ² /g]	Pore volume* [×10 ⁻² cm ³ /g]
MgO	172.57	8.54
10%Ni/MgO	78.26	3.92
20%Ni/MgO	71.30	3.31
30%Ni/MgO	56.07	2.79
40%Ni/MgO	29.22	1.46

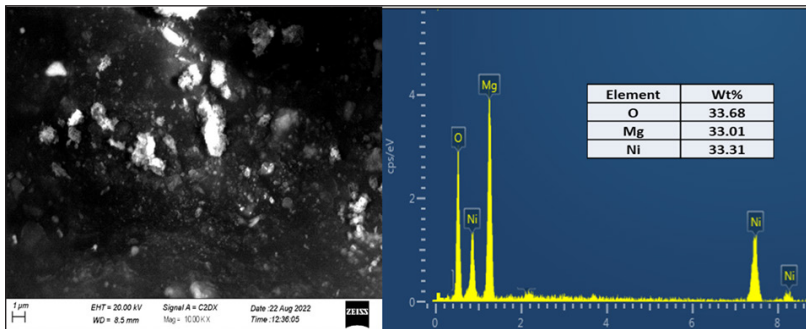
*The pore volume of the catalysts was calculated using a relative pressure (P/P₀) of 0.3



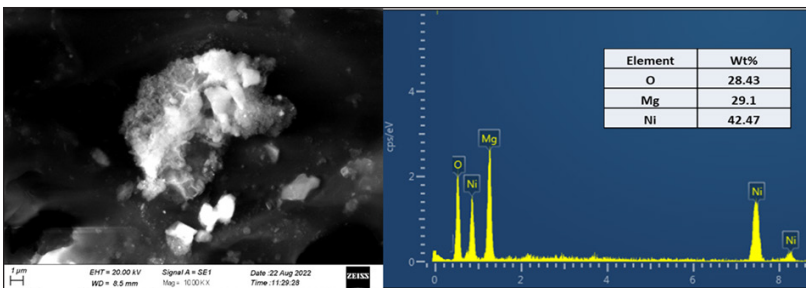
(a)



(b)



(c)



(d)

Figure 4. SEM-EDX images of Ni/MgO catalysts: (a) 10%Ni/MgO, (b) 20%Ni/MgO, (c) 30%Ni/MgO, (d) 40%Ni/MgO Catalyst Performance Evaluation

In the first blank experiment, the hydrogenolysis of glycerol was studied in the absence of a catalyst. The reaction conditions included 10 wt.% glycerol in water, 220°C temperature, 3 MPa hydrogen pressure, and 20 hours reaction time. No conversion of glycerol was observed at the end of the experiment. We conclude that the hydrogenolysis reaction cannot proceed spontaneously under these reaction conditions. In the second blank experiment, the hydrogenolysis was carried out under the same reaction conditions but in the presence of MgO support without any Ni metal added to it. A very low conversion of glycerol (<3%) was obtained, and no 1,2-PDO was detected in the liquid mixture. We conclude from this that MgO alone has little influence on the decrease in the energy activation of glycerol hydrogenolysis.

Significantly higher glycerol conversion was recorded when the glycerol hydrogenolysis was performed in the presence of Ni/MgO catalyst under identical reaction conditions. The liquid product mixture mainly consisted of 1,2-PDO, 2-propanol and unconverted glycerol. In addition, in minor quantities, ethylene glycol, methanol, acetol, 1-propanol, and ethanol were present.

Table 2

Effect of Ni loading on the conversion of glycerol (10 wt.% glycerol solution, 220°C temperature, 3 MPa hydrogen pressure, 20 hours reaction time)

Catalyst	Glycerol Conversion [%]	Selectivity [%] ^a				
		1,2-PDO	2-Propanol	Ethylene Glycol	Methanol	Others ^b
Blank	-	-	-	-	-	-
MgO	<3%	-	-	-	-	-
10%Ni/MgO	47.3	80	9	5	5	2
20%Ni/MgO	74.2	76	13	7	3	2
30%Ni/MgO	80.6	67	19	7	5	2
40%Ni/MgO	87.9	65	21	9	4	2

^aThe calculated selectivity has been rounded to the nearest integer

^bOthers include acetol (detected in all experiments, 0.4%–2%), 1-propanol (detected in all experiments, 0.3–0.8%), and ethanol (detected in some experiments, ~0.1%)

Table 2 also shows that while increasing the Ni loading from 10% to 20%, the conversion of glycerol increased significantly from 47% to 74%, whereas the selectivity of 1,2-PDO remained almost the same, with a marginal decrease from 80% to 76%. Further increasing the Ni loading to 40%, the glycerol conversion further increased to 88%, whereas the selectivity of 1,2-PDO decreased gradually to 65%. All of them provided a general trend where the conversion of glycerol was in the order of 10%Ni/MgO < 20%Ni/MgO < 30%Ni/MgO < 40%Ni/MgO, whereas selectivity to 1,2-PDO was in the order of 10%Ni/MgO > 20%Ni/MgO > 30%Ni/MgO > 40%Ni/MgO. While the conversion of glycerol

increases, there is a distinct increase in the production of 2-propanol. This is normal because, under these reaction conditions, 1,2-PDO may further undergo hydrogenolysis into 2-propanol (Wang et al., 2022). Another important observation is the consistent increase in the production of cracking products, ethylene glycol and methanol, at high Ni loading. This is in accordance with earlier research that demonstrated Ni is an effective catalyst for C–C bond breakage (Davda et al., 2005; El Doukkali et al., 2020). The 20%Ni/MgO catalyst generally showed the best balance of glycerol conversion and 1,2-PDO selectivity since it had a high surface area and good Ni dispersion, as evidenced by the catalyst characterization tests.

A comparison of the catalysts created in this investigation with those documented in the literature is shown in Table 3. The present review demonstrates that the Ni/MgO catalysts developed in this work have comparable amounts of glycerol conversion and 1,2-PDO selectivity. Coupled with their low cost and the relative ease of synthesis using well-established techniques, this makes them a suitable candidate for further evaluation and optimization of reaction conditions.

Table 3

Comparison of glycerol conversion and 1,2-PDO selectivity over several Ni-based catalysts tested under batch conditions

Catalyst	Experimental Conditions T [°C]/P [MPa]/Reaction time [h]/ Feed Conc. [wt.%]	Glycerol Conversion [%]	1,2-PDO Selectivity [%]	Reference
Ni/C	200°C/1.4 MPa/24 h/80%	39.8	68.6	Dasari et al. (2005)
Ni/SiO ₂ -Al ₂ O ₃	200°C/1.4 MPa/24 h/80%	45.1	64.5	Dasari et al. (2005)
Ni/HDT	220°C/ 3.4 MPa/24 h/60%	47.8	100	Lopez et al. (2019)
Ni/NaX	200°C/6 MPa/10 h/25%	94.5	72.1	Zhao et al. (2010)
Co/MgO	200°C/2 MPa/9 h/10%	44.8	42.2	Guo et al. (2009)
Ni/MgO	220°C/3 MPa/20 h/10%	74.2	76	This work

Reaction Mechanism

Three different mechanisms have been proposed for glycerol hydrogenolysis over supported metal catalysts. These consist of the direct hydrogenolysis mechanism, the dehydration–hydrogenation mechanism, and the dehydrogenation–dehydration–hydrogenation mechanism (Y. Wang et al., 2015). The product distribution analysis shows that a quantifiable amount of acetol is present in all experiments (Table 2). Glycerol is dehydrated to produce acetol (Figure 5). This process takes place on sites that are either very acidic or basic, such as MgO (Kinage et al., 2010; Stošić et al., 2012; Velasquez et al.,

2014). Acetol is then hydrogenated on metallic Ni sites to produce 1,2-PDO. According to Gandarias et al. (2010), these data align with the dehydration–hydrogenation mechanism. We note here that dehydration of glycerol can involve either the terminal –OH group (resulting in acetol) or the middle –OH group (resulting in 3-hydroxypropionaldehyde). Hydrogenation of 3-hydroxypropionaldehyde produces 1,3-PDO, which was not detected in any experiment. Based on Ni/MgO catalysts, we deduce that the terminal –OH group is important for the early dehydration of glycerol.

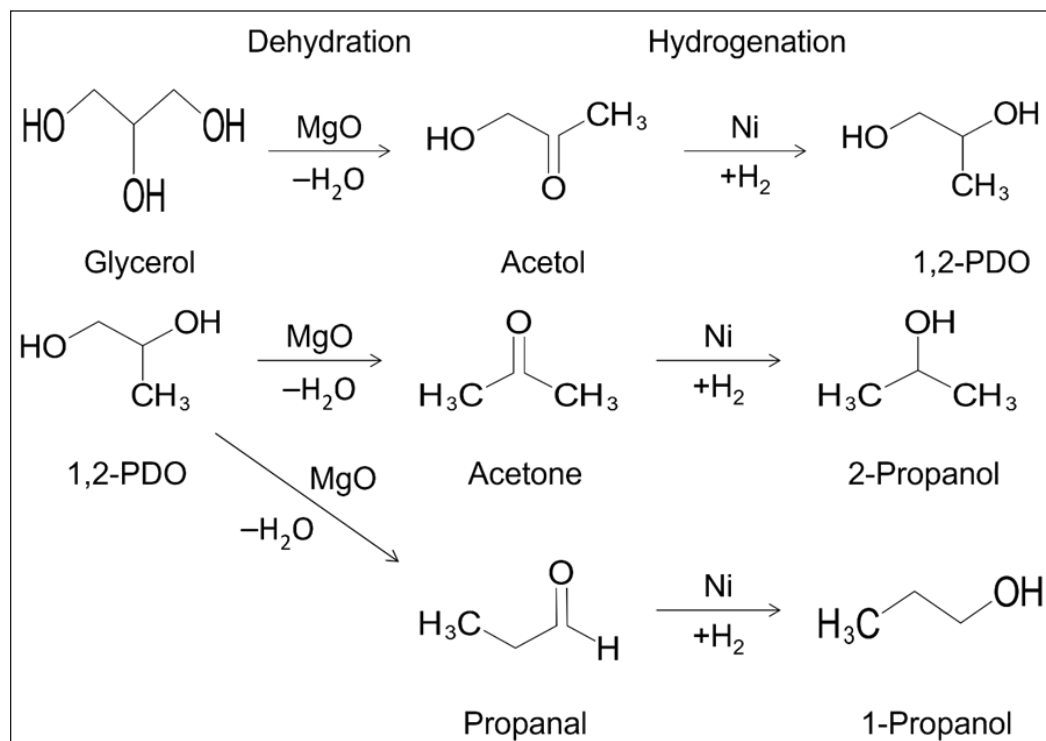


Figure 5. Proposed reaction pathway for the hydrogenolysis of glycerol

On the other hand, the dehydrogenation–dehydration–hydrogenation mechanism goes through glyceraldehyde and pyruvaldehyde intermediates. We note here that no significant peak in any chromatogram was left unquantified. Furthermore, considering the excellent hydrogenation activity of Ni and the hydrogen-rich reaction atmosphere, the initial dehydrogenation of glycerol is highly unlikely to occur, effectively shutting down this reaction pathway.

Because glycerol and 1,2-PDO have similar molecular structures, deep hydrogenolysis is possible under these reaction conditions. Dehydration of 1,2-PDO through the terminal—OH group produces acetone, which is then hydrogenated to produce 2-propanol. On the other hand, dehydration of 1,2-PDO through the mid-chain –OH group forms

propionaldehyde (propanol), which subsequently undergoes hydrogenation to 1-propanol. As shown in Table 2, the selectivity to 2-propanol is always many times higher than that to 1-propanol. We conclude that the dehydration of 1,2-PDO also predominantly proceeds through the terminal –OH group. Further hydrogenolysis of 1- and 2-propanol would produce propane, which was not detected in any experiment.

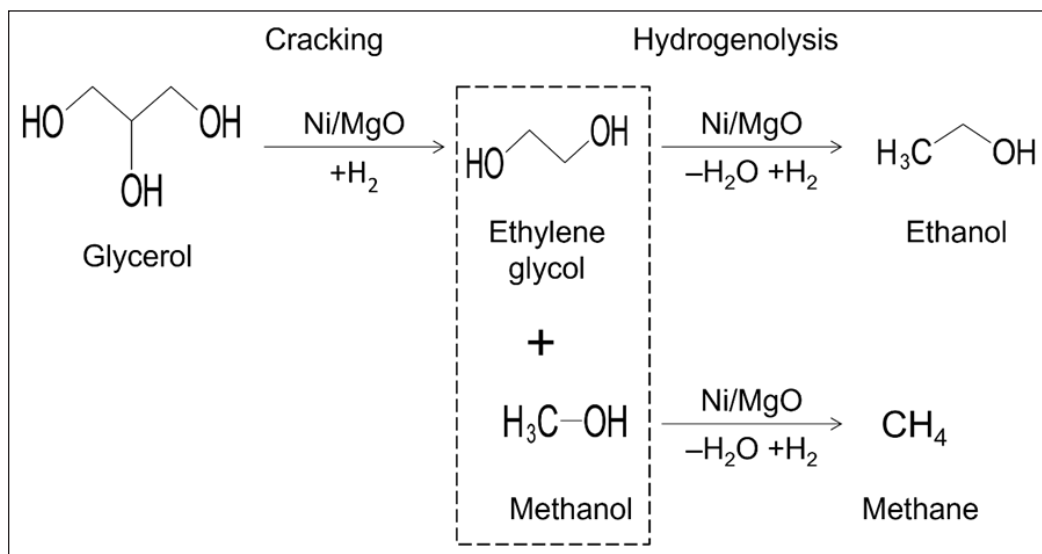


Figure 6. Possible cracking reactions during the hydrogenolysis of glycerol

Cleavage of C–C bonds in glycerol presents another selectivity challenge. Figure 6 illustrates how glycerol splits into a hydrogen-rich environment to create methanol and ethylene glycol. Both these products were present in quantifiable amounts in all experiments. Further hydrogenolysis of ethylene glycol and methanol produces ethanol and methane, respectively. These products were detected only in small quantities.

Likewise, Table 2 demonstrates that when Ni loading increases, the production of byproducts increases. This is observed both in terms of deep hydrogenolysis and cracking pathways, consistent with previous studies (Wolosiak-Hnat et al., 2013). We conclude that under these reaction conditions, glycerol conversion proceeds primarily through hydrogenolysis, with undesired reactions presenting serious selectivity challenges at high Ni loading.

Effect of Reaction Conditions

The 20%Ni/MgO catalyst produced the highest yield of 1,2-PDO through a combination of good glycerol conversion and high selectivity toward 1,2-PDO. It was chosen for additional research to examine the impact of reaction circumstances.

Effect of Temperature

To investigate the effect of temperature on the hydrogenolysis of glycerol, a 20% Ni/MgO catalyst was utilized, and the reaction temperature was changed from 200°C to 240°C. Other reaction conditions were kept fixed, including 10 wt.% glycerol feed, 3 MPa hydrogen pressure, and 20 hours of reaction time. The findings showed that the selectivity of 1,2-PDO and glycerol conversion are both significantly influenced by the reaction temperature (Figure 7). The glycerol conversion rises gradually with increasing reaction temperature, reaching 100% at 240°C from 61% at 200°C. Selectivity for 1,2-PDO has a reverse trend, progressively declining from 82% at 200°C to barely 60% at 240°C. Additionally, there is a noticeable rise in the generation of propanols, with 2-propanol production rising from 9% at 200°C to 24% at 240°C and 1-propanol production rising from 0% at 200°C to 4% at 240°C. From that, we can also infer that higher temperatures increase the glycerol conversion because of an increase in the reaction rate constant since, under such conditions, the hydrogenolysis reaction is not equilibrium-limited.

On the other hand, such excessive hydrogenolysis, 2-PDO at elevated temperatures to produce more propanol, causes a decrease in 1,2-PDO. Higher temperatures promote glycerol cracking and reforming over Ni-based catalysts (Mondal & Biswas, 2022), resulting in lower total liquid phase carbon recovery, indicating an increase in the creation of gaseous substances.

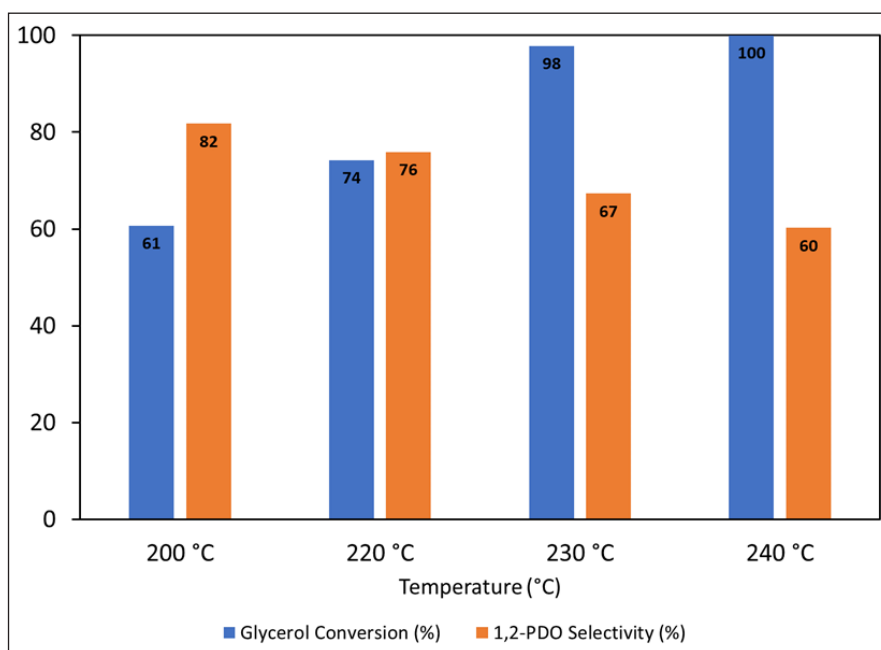


Figure 7. Effect of temperature on the hydrogenolysis of glycerol (20%Ni/MgO catalyst, 10 wt.% glycerol solution, 3.0 MPa hydrogen pressure, 20 hours reaction time)

Effect of Glycerol Concentration

To study the influence of feed concentration, the glycerol concentration of the feed solution varied from 5 weight percent to 30 weight percent in the hydrogenolysis of glycerol over the catalyst of 20%Ni/MgO. The reaction temperature was held constant at 220°C, the hydrogen pressure was kept invariant at 3 MPa, and the reaction time was kept constant at 20 hours. It is evident from the results that the glycerol conversion decreased from 100% in the case of a relatively dilute feed solution of 5 wt% to only 44% in the case of a concentrated feed solution of 30 wt% (Figure 8). This would, therefore, suggest that the concentration of the feed is of particular importance regarding glycerol conversion. This limit in the number of active Ni sites available, even for far larger amounts of glycerol molecules present in the reaction mixture, provides the basis for the observed decrease in conversion at higher glycerol concentrations. Another possible explanation, though not investigated in this study, is the possibility of increased mass transfer resistance around catalyst particles due to increased viscosity of the reaction mixture at higher glycerol concentrations (Cai, Pan et al., 2018; Cai et al., 2016).

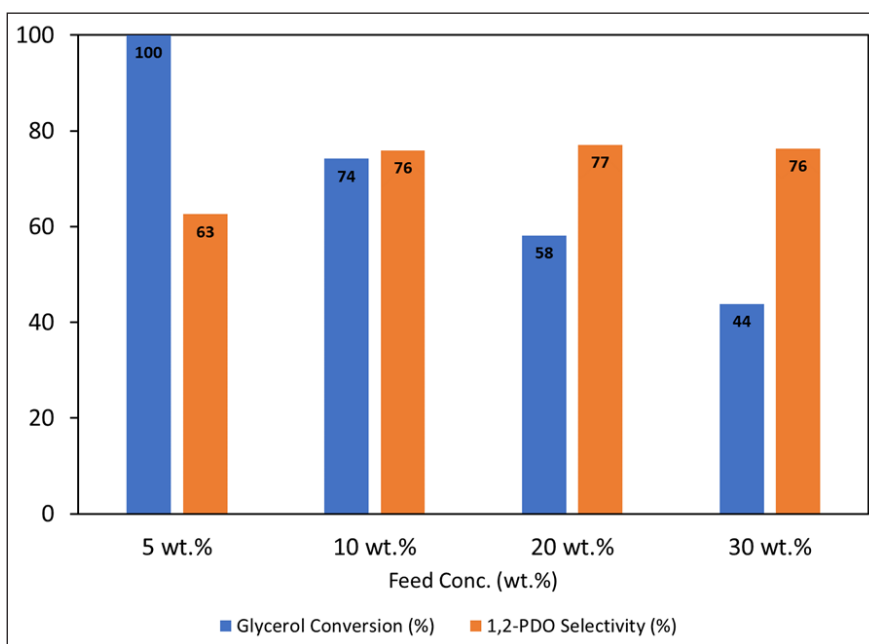


Figure 8. Effect of feed concentration on the hydrogenolysis of glycerol (20%Ni/MgO catalyst, 220°C temperature, 3.0 MPa hydrogen pressure, 20 hours reaction time)

The selectivity towards 1,2-PDO reached as high as 76% in the case of a 10 wt.% feed solution and remained almost constant at this level when the glycerol concentration of the feed solution was increased further to 20 wt.% and 30 wt.%. In these cases, 2-propanol

production also remained almost constant in the range of 10%–12%. This perfectly aligns with the previously reported behavior of Ru and Ni-based catalysts (Alhanash et al., 2008; Yu et al., 2010)—only the feed solution of 5 wt.% showed a considerably lower 1,2-PDO selectivity of 63% and increased production of 2-propanol as high as 23%. From these results, we conclude that beyond the complete conversion of glycerol, the reaction of hydrogenolysis of 1,2-PDO continues and, as such, is responsible for the decrease of 1,2-PDO selectivity observed towards the end of the test.

Effect of Reaction Time

Using a 20%Ni/MgO catalyst, reaction periods ranging from 6 to 25 hours were employed to investigate the impact of reaction length on glycerol hydrogenolysis. Other reaction parameters that were held constant were the feeding of 10% glycerol, the reaction temperature of 220°C, and the hydrogen pressure of 3 MPa. The results show that the glycerol conversion steadily increases for longer reaction times, rising from 64% after 6 hours to 84% after 25 hours (Figure 9). The 1,2-PDO selectivity does, however, significantly decrease with extended reaction periods, indicating that longer reaction times cause deeper hydrogenolysis, which ultimately results in the undesirable destruction of 1,2-PDO. Overall, a reaction time of 12–20 hours is reasonable under these reaction conditions.

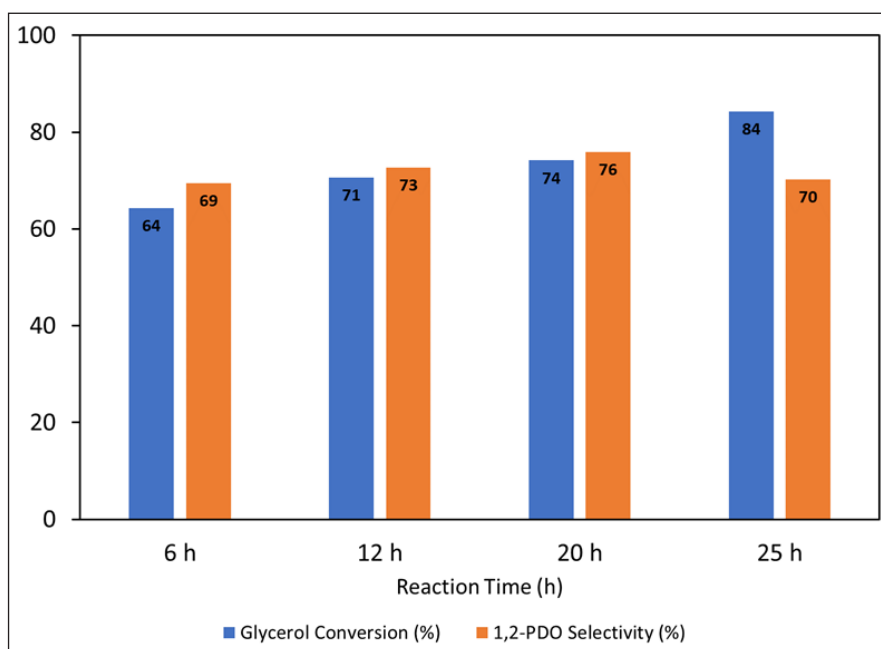


Figure 9. Effect of reaction time on the hydrogenolysis of glycerol (20%Ni/MgO catalyst, 10 wt.% glycerol solution, 220°C temperature, 3.0 MPa hydrogen pressure)

Effect of Pressure

The total hydrogen pressure was changed from 3 MPa to 5 MPa to investigate the effect of pressure on the hydrogenolysis of glycerol using the 20%Ni/MgO catalyst. A 10-weight percent glycerol feed, a reaction temperature of 220°C, and a 20-hour reaction duration were further predetermined reaction parameters. According to the data (Figure 10), glycerol conversion increased steadily at greater pressures. At 3 MPa hydrogen pressure, the acetol concentration in the final mixture drops significantly to less than 0.4%, but the 1,2-PDO selectivity stays relatively stable at 76%–78%. Higher gas phase hydrogen pressure causes hydrogen to dissolve more readily in the liquid reaction mixture. This increased availability of hydrogen near the catalyst facilitates rapid hydrogenation of acetol and, hence, a slight increase in the production of 1,2-PDO over acetol.

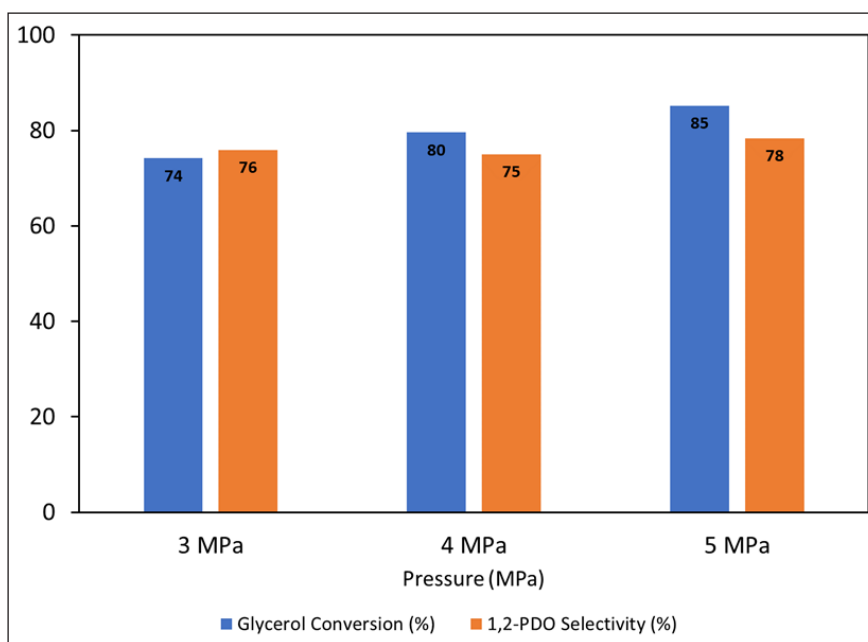


Figure 10. Effect of pressure on the hydrogenolysis of glycerol (20%Ni/MgO catalyst, 10 wt.% glycerol solution, 220°C temperature, 20 hours reaction time)

We highlight that in terms of cost-effectiveness, the aim should be to achieve the desired level of glycerol hydrogenolysis at lower operating pressures to reduce equipment costs. Considering the relatively small gain in glycerol conversion by increasing the total pressure but a potentially significant increase in equipment cost, a hydrogen pressure of 3–4 MPa is recommended.

CONCLUSION

The current work concentrated on synthesizing and characterizing Ni/MgO catalysts made with different Ni loadings using the wet impregnation approach. Under specific reaction circumstances (20 hours of reaction time, 220°C temperature, 3 MPa hydrogen pressure, and 10% weight percent glycerol solution in water), the catalyst with 20% Ni loading (20%Ni/MgO) demonstrated a strong combination of activity and selectivity. This catalyst showed a 76% selectivity toward 1,2-PDO and a 74% glycerol conversion. The catalyst's remarkable performance can be attributed to its small particle size, optimal metal-support interaction, and good Ni concentration and dispersion. It was discovered that the main chemical pathway involved the hydrogenation of acetol to 1,2-PDO after glycerol was dehydrated to acetol. Side reactions, including C-C bond breakage and extra 1,2-PDO hydrogenolysis, were more prevalent when reaction times were extended and Ni loadings were high. Several reaction conditions were subsequently analyzed, and the results indicated that they significantly affected the glycerol conversion and the selectivity of 1,2-PDO. It was discovered that the ideal values for temperature, pressure, feed concentration, and reaction time were 220°C, 3 MPa, 10 weight percent glycerol concentration, and 20 hours, respectively. Due to these conditions, a reasonable trade-off between 1,2-PDO selectivity and glycerol conversion could be reached, highlighting the importance of carefully controlling the reaction conditions to maximize the desired product's yield.

Overall, this work's results advance our knowledge of the hydrogenolysis process using Ni/MgO catalysts. The developed catalyst and optimized reaction conditions provide valuable insights for future research and potential industrial applications in glycerol conversion processes.

ACKNOWLEDGEMENTS

The Higher Education Commission of Pakistan provided financial support (grant number NRPU-9360) to the authors, which they sincerely acknowledge. M.S. also thanks the Higher Education Commission of Pakistan for funding assistance the Indigenous PhD Fellowships for 5000 Scholars (Phase II) program provides.

REFERENCES

- Alhanash, A., Kozhevnikova, E. F., & Kozhevnikov, I. V. (2008). Hydrogenolysis of glycerol to propanediol over Ru: Polyoxometalate bifunctional catalyst. *Catalysis Letters*, *120*, 307–311. <https://doi.org/10.1007/s10562-007-9286-3>
- Azri, N., Irmawati, R., Nda-Umar, U. I., Saiman, M. I., & Taufiq-Yap, Y. H. (2021). Promotional effect of transition metals (Cu, Ni, Co, Fe, Zn)-supported on dolomite for hydrogenolysis of glycerol into 1,2-propanediol. *Arabian Journal of Chemistry*, *14*(4), Article 103047. <https://doi.org/10.1016/j.arabjc.2021.103047>

- Bagheri, S., Julkapli, N. M., & Yehye, W. A. (2015). Catalytic conversion of biodiesel derived raw glycerol to value added products. *Renewable and Sustainable Energy Reviews*, *41*, 113–127. <https://doi.org/10.1016/j.rser.2014.08.031>
- Balaraju, M., Jagadeeswaraiiah, K., Prasad, P. S. S., & Lingaiah, N. (2012). Catalytic hydrogenolysis of biodiesel derived glycerol to 1,2-propanediol over Cu-MgO catalysts. *Catalysis Science and Technology*, *2*, 1967–1976. <https://doi.org/10.1039/C2CY20059G>
- Cai, F., Pan, D., Ibrahim, J. J., Zhang, J., & Xiao, G. (2018). Hydrogenolysis of glycerol over supported bimetallic Ni/Cu catalysts with and without external hydrogen addition in a fixed-bed flow reactor. *Applied Catalysis A: General*, *564*, 172–182. <https://doi.org/10.1016/j.apcata.2018.07.029>
- Cai, F., Song, X., Wu, Y., Zhang, J., & Xiao, G. (2018). Selective hydrogenolysis of glycerol over acid-modified Co-Al catalysts in a fixed-bed flow reactor. *ACS Sustainable Chemistry and Engineering*, *6*(1), 110–118. <https://doi.org/10.1021/acssuschemeng.7b01233>
- Cai, F., Zhu, W., & Xiao, G. (2016). Promoting effect of zirconium oxide on Cu-Al₂O₃ catalyst for the hydrogenolysis of glycerol to 1,2-propanediol. *Catalysis Science and Technology*, *6*, 4889–4900. <https://doi.org/10.1039/C6CY00085A>
- Checa, M., Auneau, F., Hidalgo-Carrillo, J., Marinas, A., Marinas, J. M., Pinel, C., & Urbano, F. J. (2012). Catalytic transformation of glycerol on several metal systems supported on ZnO. *Catalysis Today*, *196*(1), 91–100. <https://doi.org/10.1016/j.cattod.2012.02.036>
- Chen, X., Wang, X., Yao, S., & Mu, X. (2013). Hydrogenolysis of biomass-derived sorbitol to glycols and glycerol over Ni-MgO catalysts. *Catalysis Communications*, *39*, 86–89. <https://doi.org/10.1016/j.catcom.2013.05.012>
- Chuanming, L., Donghua, C., Wanjun, T., & Yuhua, P. (2006). Synthesis of MgNi₂O₃ and kinetics of thermal decomposition of the oxalate precursor. *Journal of Analytical and Applied Pyrolysis*, *75*(2), 240–244. <https://doi.org/10.1016/j.jaap.2005.06.007>
- Davda, R. R., Shabaker, J. W., Huber, G. W., Cortright, R. D., & Dumesic, J. A. (2005). A review of catalytic issues and process conditions for renewable hydrogen and alkanes by aqueous-phase reforming of oxygenated hydrocarbons over supported metal catalysts. *Applied Catalysis B: Environmental*, *56*(1-2), 171–186. <https://doi.org/10.1016/j.apcatb.2004.04.027>
- Dasari, M. A., Kiatsimkul, P. P., Sutterlin, W. R., & Suppes, G. J. (2005). Low-pressure hydrogenolysis of glycerol to propylene glycol. *Applied Catalysis A: General*, *281*, 225–231. <https://doi.org/10.1016/j.apcata.2004.11.033>
- Dolsirittigul, N., Numpilai, T., Wattanakit, C., Seubsai, A., Faungnawakij, K., Cheng, C. K., Vo, D. V. N., Nijpanich, S., Chanlek, N., & Witoon, T. (2023). Structure-activity relationships of Pt-WO_x/Al₂O₃ prepared with different W contents and pretreatment conditions for glycerol conversion to 1,3-propanediol. *Topics in Catalysis*, *66*(1–4), 205–222. <https://doi.org/10.1007/S11244-022-01753-9/METRICS>
- Echegoyen, Y., Suelves, I., Lázaro, M. J., Sanjuán, M. L., & Moliner, R. (2007). Thermo catalytic decomposition of methane over Ni-Mg and Ni-Cu-Mg catalysts. Effect of catalyst preparation method. *Applied Catalysis A: General*, *333*, 229–237. <https://doi.org/10.1016/j.apcata.2007.09.012>

- El Doukkali, M., Iriondo, A., & Gandarias, I. (2020). Enhanced catalytic upgrading of glycerol into high value-added H₂ and propanediols: Recent developments and future perspectives. *Molecular Catalysis*, 490, Article 110928. <https://doi.org/10.1016/j.mcat.2020.110928>
- Gandarias, I., Arias, P. L., Requies, J., Güemez, M. B., & Fierro, J. L. G. (2010). Hydrogenolysis of glycerol to propanediols over a Pt/ASA catalyst: The role of acid and metal sites on product selectivity and the reaction mechanism. *Applied Catalysis B: Environmental*, 97(1–2), 248–256. <https://doi.org/10.1016/j.apcatb.2010.04.008>
- Gonzalez-Garay, A., Gonzalez-Miquel, M., & Guillen-Gosalbez, G. (2017). High-value propylene glycol from low-value biodiesel glycerol: A techno-economic and environmental assessment under uncertainty. *ACS Sustainable Chemistry and Engineering*, 5, 5723–5732. <https://doi.org/10.1021/acssuschemeng.7b00286>
- Guo, X., Li, Y., Shi, R., Liu, Q., Zhan, E., & Shen, W. (2009). Co/MgO catalysts for hydrogenolysis of glycerol to 1, 2-propanediol. *Applied Catalysis A: General*, 371, 108–113. <https://doi.org/10.1016/j.apcata.2009.09.037>
- Kinage, A. K., Upare, P. P., Kasinathan, P., Hwang, Y. K., & Chang, J. S. (2010). Selective conversion of glycerol to acetol over sodium-doped metal oxide catalysts. *Catalysis Communications*, 11(7), 620–623. <https://doi.org/10.1016/j.catcom.2010.01.008>
- Kumar, P., Shah, A. K., Lee, J. H., Park, Y. H., & Štangar, U. L. (2020). Selective hydrogenolysis of glycerol over bifunctional copper-magnesium-supported catalysts for propanediol synthesis. *Industrial and Engineering Chemistry Research*, 59, 6506–6516. <https://doi.org/10.1021/acs.iecr.9b06978>
- López, A., Aragón, J. A., Hernández-Cortez, J. G., Mosqueira, M. L., & Martínez-Palou, R. (2019). Study of hydrotalcite-supported transition metals as catalysts for crude glycerol hydrogenolysis. *Molecular Catalysis*, 468, 9–18. <https://doi.org/10.1016/j.mcat.2019.02.008>
- Menchavez, R. N., Morra, M. J., & He, B. B. (2017). Glycerol hydrogenolysis using a Ni/Ce-Mg catalyst for improved ethanol and 1,2-propanediol selectivities. *Canadian Journal of Chemical Engineering*, 95(7), 1332–1339. <https://doi.org/10.1002/cjce.22779>
- Mondal, S., & Biswas, P. (2022). Conversion of bio-glycerol to propylene glycol over basic oxides (MgO, La₂O₃, MgO-La₂O₃, CaO, and BaO₂) supported Cu–Zn bimetallic catalyst: A reaction kinetic study. *Environmental Technology & Innovation*, 27, Article 102367. <https://doi.org/10.1016/j.eti.2022.102367>
- Nakagawa, Y., & Tomishige, K. (2011). Heterogeneous catalysis of the glycerol hydrogenolysis. *Catalysis Science & Technology*, 1(2), 179–190. <https://doi.org/10.1039/C0CY00054J>
- Numpilai, T., Cheng, C. K., Seubsai, A., Faungnawakij, K., Limtrakul, J., & Witoon, T. (2021). Sustainable utilization of waste glycerol for 1,3-propanediol production over Pt/WO_x/Al₂O₃ catalysts: Effects of catalyst pore sizes and optimization of synthesis conditions. *Environmental Pollution*, 272, Article 116029. <https://doi.org/10.1016/J.ENVPOL.2020.116029>
- Nakayama, T., Ichikuni, N., Sato, S., & Nozaki, F. (1997). Ni/Mgo catalyst prepared using citric acid for hydrogenation of carbon dioxide. *Applied Catalysis A: General*, 158(1–2), 185–199. [https://doi.org/10.1016/S0926-860X\(96\)00399-7](https://doi.org/10.1016/S0926-860X(96)00399-7)

- Quispe, C. A. G., Coronado, C. J. R., & Carvalho, J. A. (2013). Glycerol: Production, consumption, prices, characterization and new trends in combustion. *Renewable and Sustainable Energy Reviews*, *27*, 475–493. <https://doi.org/10.1016/j.rser.2013.06.017>
- Ramesh, A., Ali, B. M., Manigandan, R., Da, C. T., & Nguyen-Le, M. T. (2022). Hydrogenolysis of glycerol to 1, 2-propanediol on MgO/Ni₃C catalysts fabricated by a solid-state thermal synthesis. *Molecular Catalysis*, *525*, Article 112358. <https://doi.org/10.1016/j.mcat.2022.112358>
- Rivas, M. E., Hori, C. E., Fierro, J. L. G., Goldwasser, M. R., & Griboval-Constant, A. (2008). H₂ production from CH₄ decomposition: Regeneration capability and performance of nickel and rhodium oxide catalysts. *Journal of Power Sources*, *184*, 265–275. <https://doi.org/10.1016/j.jpowsour.2008.06.002>
- Rogers, J. L., Mangarella, M. C., D'Amico, A. D., Gallagher, J. R., Dutzer, M. R., Stavitski, E., Miller, J. T., & Sievers, C. (2016). Differences in the nature of active sites for methane dry reforming and methane steam reforming over nickel aluminate catalysts. *ACS Catalysis*, *6*, 5873–5886. <https://doi.org/10.1021/acscatal.6b01133>
- Ross, J. R. H., Steel, M. C. F., & Zeini-Isfahani, A. (1978). Evidence for the participation of surface nickel aluminate sites in the steam reforming of methane over nickel/alumina catalysts. *Journal of Catalysis*, *52*, 280–290. [https://doi.org/10.1016/0021-9517\(78\)90142-2](https://doi.org/10.1016/0021-9517(78)90142-2)
- Raju, N., Rekha, V., Abhishek, B., Kumar, P. M., Sumana, C., & Lingaiah, N. (2020). Studies on continuous selective hydrogenolysis of glycerol over supported Cu-Co bimetallic catalysts. *New Journal of Chemistry*, *44*(7), 3122–3128. <https://doi.org/10.1039/c9nj04945b>
- Rekha, V., Raju, N., Sumana, C., & Lingaiah, N. (2017). Continuous hydrogenolysis of glycerol to 1,2-Propanediol over Bi-metallic Ni–Ag supported on γ -Al₂O₃ catalysts. *Catalysis Letters*, *147*(6), 1441–1452. <https://doi.org/10.1007/s10562-017-2052-2>
- Salgado, A. L. P., Araújo, F. C., Soares, A. V. H., Xing, Y., & Passos, F. B. (2021). Glycerol hydrogenolysis over Ru-Cu bimetallic catalysts supported on modified zirconias. *Applied Catalysis A: General*, *626*, Article 118359. <https://doi.org/10.1016/j.apcata.2021.118359>
- Stošić, D., Bennici, S., Sirotnin, S., Calais, C., Couturier, J. L., Dubois, J. L., Travert, A., & Auroux, A. (2012). Glycerol dehydration over calcium phosphate catalysts: Effect of acidic-basic features on catalytic performance. *Applied Catalysis A: General*, *447–448*, 124–134. <https://doi.org/10.1016/j.apcata.2012.09.029>
- Seretis, A., & Tsiakaras, P. (2016). Hydrogenolysis of glycerol to propylene glycol by in situ produced hydrogen from aqueous phase reforming of glycerol over SiO₂-Al₂O₃ supported nickel catalyst. *Fuel Processing Technology*, *142*, 135–146. <https://doi.org/10.1016/j.fuproc.2015.10.013>
- Shi, Q., Liu, C., & Chen, W. (2009). Hydrogen production from steam reforming of ethanol over Ni/MgO-CeO₂ catalyst at low temperature. *Journal of Rare Earths*, *27*, 948–954. [http://dx.doi.org/10.1016/S1002-0721\(08\)60368-3](http://dx.doi.org/10.1016/S1002-0721(08)60368-3)
- Sun, D., Yamada, Y., Sato, S., & Ueda, W. (2016). Glycerol hydrogenolysis into useful C₃ chemicals. *Applied Catalysis B: Environmental*, *193*, 75–92. <https://doi.org/10.1016/j.apcatb.2016.04.013>
- Tendam, J., & Hanefeld, U. (2011). Renewable chemicals: Dehydroxylation of glycerol and polyols. *ChemSusChem*, *4*, 1017–1034. <https://doi.org/10.1002/cssc.201100162>

- Usman, M., & Daud, W. M. A. W. (2016). An investigation on the influence of catalyst composition, calcination and reduction temperatures on Ni/MgO catalyst for dry reforming of methane. *RSC Advances*, 6, 91603–91616. <https://doi.org/10.1039/C6RA15256B>
- Vasiliadou, E. S., & Lemonidou, A. A. (2015). Glycerol transformation to value added C₃ diols: Reaction mechanism, kinetic, and engineering aspects. *Wiley Interdisciplinary Reviews: Energy and Environment*, 4, 486–520. <https://doi.org/10.1002/wene.159>
- van Ryneveld, E., Mahomed, A. S., van Heerden, P. S., Green, M. J., & Friedrich, H. B. (2011). A catalytic route to lower alcohols from glycerol using Ni-supported catalysts. *Green Chemistry*, 13(7), 1819–1827. <https://doi.org/10.1039/c0gc00839g>
- Velasquez, M., Santamaria, A., & Batiot-Dupeyrat, C. (2014). Selective conversion of glycerol to hydroxyacetone in gas phase over La₂CuO₄ catalyst. *Applied Catalysis B: Environmental*, 160–161(1), 606–613. <https://doi.org/10.1016/j.apcatb.2014.06.006>
- Wang, S., Yin, K., Zhang, Y., & Liu, H. (2013). Glycerol hydrogenolysis to propylene glycol and ethylene glycol on zirconia supported noble metal catalysts. *ACS Catalysis*, 3(9), 2112–2121. <https://doi.org/10.1021/cs400486z>
- Wang, S., & Liu, H. (2014). Selective hydrogenolysis of glycerol to propylene glycol on hydroxycarbonate-derived Cu-ZnO-Al₂O₃ catalysts. *Cuihua Xuebao/Chinese Journal of Catalysis*, 35(5), 631–643. [https://doi.org/10.1016/s1872-2067\(14\)60094-2](https://doi.org/10.1016/s1872-2067(14)60094-2)
- Wang, X., Liu, X., Xu, Y., Peng, G., Cao, Q., & Mu, X. (2015). Sorbitol hydrogenolysis to glycerol and glycols over M-MgO (M = Ni, Co, Cu) nanocomposite: A comparative study of active metals. *Cuihua Xuebao/Chinese Journal of Catalysis*, 36(9), 1614–1622. [https://doi.org/10.1016/S1872-2067\(15\)60928-7](https://doi.org/10.1016/S1872-2067(15)60928-7)
- Wang, Y., Zhou, J., & Guo, X. (2015). Catalytic hydrogenolysis of glycerol to propanediols: A review. *RSC Advances* (5, 91, 74611–74628). <https://doi.org/10.1039/c5ra11957j>
- Wang, Y., Xiao, Y., & Xiao, G. (2019). Sustainable value-added C₃ chemicals from glycerol transformations: A mini review for heterogeneous catalytic processes. *Chinese Journal of Chemical Engineering*, 27(7), 1536–1542. <https://doi.org/10.1016/j.cjche.2019.03.001>
- Wu, K., Dou, B., Zhang, H., Liu, D., Chen, H., & Xu, Y. (2021). Effect of impurities of CH₃OH, CH₃COOH, and KOH on aqueous phase reforming of glycerol over mesoporous Ni–Cu/CeO₂ catalyst. *Journal of the Energy Institute*, 99, 198–208. <https://doi.org/10.1016/j.joei.2021.09.009>
- Wang, J., Wang, M., Li, X., Gu, X., Kong, P., Wang, R., Ke, X., Yu, G., & Zheng, Z. (2022). Bidentate ligand modification strategy on supported Ni nanoparticles for photocatalytic selective hydrogenation of alkynes. *Applied Catalysis B: Environmental*, 313, Article 121449. <https://doi.org/10.1016/j.apcatb.2022.121449>
- Wolosiak-Hnat, A., Milchert, E., & Grzmil, B. (2013). Influence of Parameters on Glycerol Hydrogenolysis over a Cu/Al₂O₃ Catalyst. *Chemical Engineering & Technology*, 36, 411–418. <https://doi.org/10.1002/ceat.201200549>
- Xia, S., Nie, R., Lu, X., Wang, L., Chen, P., & Hou, Z. (2012). Hydrogenolysis of glycerol over Cu_{0.4}/Zn_{5.6-x}MgxAl₂O_{8.6} catalysts: The role of basicity and hydrogen spillover. *Journal of Catalysis*, 296, 1–11. <https://doi.org/10.1016/j.jcat.2012.08.007>

- Yu, W., Zhao, J., Ma, H., Miao, H., Song, Q., & Xu, J. (2010). Aqueous hydrogenolysis of glycerol over Ni-Ce/AC catalyst: Promoting effect of Ce on catalytic performance. *Applied Catalysis A: General*, *383*, 73–78. <https://doi.org/10.1016/j.apcata.2010.05.023>
- Zhou, J., Guo, L., Guo, X., Mao, J., & Zhang, S. (2010). Selective hydrogenolysis of glycerol to propanediols on supported Cu-containing bimetallic catalysts. *Green Chemistry*, *12*(10), 1835–1843. <https://doi.org/10.1039/c0gc00058b>
- Zhao, J., Yu, W., Chen, C., Miao, H., Ma, H., & Xu, J. (2010). Ni/NaX: A bifunctional efficient catalyst for selective hydrogenolysis of glycerol. *Catalysis Letters*, *134*, 184–189. <https://doi.org/10.1007/s10562-009-0208-4>

Random Forest Model for Software Build Time Prediction on CI/CD Pipeline

Wen Han Seow¹, Chia Yean Lim^{1*} and Sau Loong Ang²

¹School of Computer Sciences, Universiti Sains Malaysia, 11800, Minden, Pulau Pinang, Malaysia

²Department of Computing and Information Technology, Tunku Abdul Rahman University of Management and Technology, Penang Branch, 11200, Tanjung Bungah, Pulau Pinang, Malaysia

ABSTRACT

In the fast-paced world of software engineering, Continuous Integration/Continuous Delivery (CI/CD) pipelines are essential to deliver software builds continuously. However, the varying time taken for software builds to complete on these pipelines can challenge scheduling software delivery and impact productivity. To the best of researchers' knowledge, machine learning techniques have never been used to predict software build time in the CI/CD pipeline. This research attempted to apply data science and machine learning techniques, including linear regression (LR), support vector regressor (SVR), random forest regressor (RFR), and XGBoost regressor, to predict software build completion time to address this research gap. Past build events were used as a dataset to train and identify the best-performing model by evaluating the time a software build takes to complete. Different factors contributing to software build time on the CI/CD pipeline were also analyzed to identify opportunities for improvement. This research found that the random forest (RF) model achieved the best and outstanding performance of 14.306 in mean squared error (MSE). This model could be deployed to provide completion time estimates for software builds, enabling better code delivery scheduling. This research also suggested opportunities for improvement in the CI/CD pipeline by discovering major factors causing high build time in the CI/CD pipeline that engineers could rectify to reduce software build time in the CI/CD pipeline.

Keywords: CI/CD, machine learning, random forest, regression, software engineering

ARTICLE INFO

Article history:

Received: 30 October 2023

Accepted: 3 October 2024

Published: 21 February 2025

DOI: <https://doi.org/10.47836/pjst.33.2.22>

E-mail addresses:

seowwenhan@student.usm.my (Wen Han Seow)

cylim@usm.my (Chia Yean Lim)

angsl@tarc.edu.my (Sau Loong Ang)

*Corresponding author

INTRODUCTION

Continuous Integration/Continuous Delivery (CI/CD) is a method of frequently delivering applications or software by introducing automation into the stages of software development (Red Hat, 2023). In

short, new software codes submitted by the software engineers will go through a pipeline consisting of several stages of processes defined with steps to be tested and built, then proceed to deployment into the production environment. This method was widely used in software development companies of all sizes.

At this point in time, CI/CD is no longer a stranger to the software engineering field and has been widely adapted into the software development process across companies and industries. Benefits such as ensuring code quality, delivering codes faster with accelerated release rate, simplified rollback and cost reduction are among the top reasons companies adopt CI/CD (Silverthorne, 2022). In a study aimed at investigating how CI/CD adoption can impact open-source repositories hosted on GitLab and GitHub, it was found that adoption of CI/CD enhanced commit velocity by 141.19% in more than 12,000 repositories (Fairbanks et al., 2023).

A survey conducted by JetBrains showed the importance of CI/CD. 44% of the participants confirmed regular usage of CI/CD tools, and a significant 22% of them even adopted a new CI/CD tool within the past year (Bedrina, 2023). Since the usage of the CI word back in 1991, CI/CD has evolved from a relatively niche practice into an industry standard (Snyk, 2020).

In software development companies, the developer productivity (DevProd) team often aims to enhance the overall software development process and environment for all software engineers. Factors such as software tools and their configurations, development environments, cloud services like Amazon Web Services (AWS) and most importantly, the CI/CD framework could affect the software's build time in their own way (Amazon Web Services, 2023). With the size of an established technology company, more and more software engineers would join the company, and the number of software products would grow daily. There is no doubt a pressing need to improve the productivity of software engineers by streamlining their daily jobs.

There have always been issues in the availability and reliability of CI/CD service, and the unsatisfactory performance of software build time on the CI/CD pipeline has led to concern among the DevProd team and software engineers in the software development company. Software engineers in the company approach the DevProd team regularly for support and troubleshooting problems during their daily software engineering work. The DevProd team has also continuously made an effort to improve the quality of service of the CI/CD pipeline to benefit the company's software production efficiency. Hence, the continuous effort to find ways to further optimize the CI/CD quality of service is never-ending.

It was discovered that data science techniques can be used to eradicate the existing software build time issues in the CI/CD pipeline. In a multi-national software development company, the DevProd team has collected the data and logs of software build events for a long period. Information such as *time start*, *time end*, *region*, and *operating system* were

collected and archived on data platforms for data-keeping purposes. With the dataset being stored and kept unused, the company now sees a chance to use it well. Data science techniques can be applied to the dataset for further analysis, achieving the goal of providing a better software development experience for the company. To the best knowledge of literature searching, no prior research was conducted on applying machine learning (ML) methods on CI/CD pipelines to predict software build time and analyze the major factors causing high software build time.

This research was conducted by applying several data science techniques to find out the causes behind the CI/CD pipeline's flaky service quality while utilizing the dataset to train a machine learning model that predicts the estimated time taken by a software build. Data analysis efforts were carried out to look for factors behind the unusually long software build time and availability issues of the CI/CD service. Supervised machine learning methods like regression can be applied to predict the estimated time the software build takes to complete. It not only saves software engineers time by giving them an expectation of time for their software build to complete in the CI/CD pipeline but also enables software engineers to plan their tasks better by hand. When it comes to urgent bug fixes and patches where deployments are expected to happen as soon as possible, the estimated build time will be helpful for the software team to anticipate the successful build to go live on production.

With the predicted output of the machine learning model on the estimated time taken of software build, anomaly build events that end prematurely or take extended time will be detected and then reported to the DevProd team. The team could immediately look after the CI/CD pipeline and respond when anomalies happen. A variety of reasons could lead to CI/CD pipeline issues and out-of-ordinary software build times. However, these issues could be investigated and rectified swiftly if identified instantly. The research hopes not only to benefit the DevProd team and the software company but also to discover and study the possibility of applying data science and machine learning techniques to the hard-to-reach areas of software build data on the CI/CD pipeline. It is crucial to software development productivity because it would greatly reduce engineering effort, money, and time.

Literature Review

Continuous Integration (CI) and Continuous Delivery (CD)

Continuous Integration (CI) is a software development practice where the software engineers merge new codes into the remote code repository (such as GitHub) regularly; the automated builds and tests are running in a usually cloud-hosted CI pipeline instead of the software engineer's local development environment (Amazon, 2023). CI saves the software engineer's effort and time by running the software builds and tests over the centralized pipeline, where the CI pipeline is usually the single source of truth on whether the build has passed the tests and is good to go for deployment into production.

Continuous Delivery (CD) is the process where new software codes are automatically built, tested and released into production continuously (Amazon, 2023). It is important to ensure the code changes are fit for going into the production environment with the help of a series of automated software tests. The stages of the CI/CD process are shown in Figure 1.

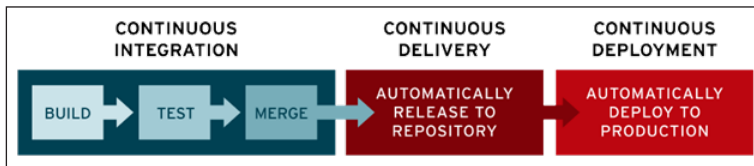


Figure 1. Stages of CI/CD Process (Red Hat, 2023)

When the DevProd team has already integrated the CI/CD pipeline by involving a wide range of AWS services and other Software as a Service (SaaS) products such as Buildkite, project development will be easier after understanding how the products interact with the CI/CD pipeline that has been serving the company's software engineers.

Contrary to what most believe, the build time of software impacts a software developer's productivity more than most people would imagine. By accurately providing the estimated build time, developers could have better control over their time planning and organizing their tasks based on the predicted build time of software on the CI/CD pipeline. For example, the developer may go for a lunch break when the build is predicted to take around an hour. When the build is expected to take 5 minutes, the developer may proceed to check the emails or go for a quick code review. The essence is to come up with a build time prediction that is accurate enough for developers to gain control of time and optimize the tasks in their hands (Jaspan & Green, 2023). Ultimately, it brings more efficiency into daily tasks by reducing time wasted waiting for the software build to be completed or time spent on miscellaneous tasks when the software build has already been completed.

Google conducted an in-house experiment to measure how the improvement of software build time affects developer satisfaction (Jaspan & Green, 2023). In the experiment group, developers were equipped with performant machines that outperformed the control group machines by a modest 15%. The results of the experiment have shown that developers managed to achieve higher self-reported productivity and higher self-reported velocity in their work. Developers in the experiment group also measured a greater satisfaction level than the control group. It is a concrete example of how faster build time could bring benefits to developers and the company.

CI/CD pipelines are not easy to troubleshoot. The time taken for software to build on a CI/CD pipeline could fluctuate due to many factors, including machine specification, agent availability, and CI/CD pipeline configurations. Engineers spend much time daily discovering the reasons that have caused inconsistency or even a spike in software build

time on the CI/CD pipeline. The action taken to remedy the issue may not always be the best action to resolve the issue. It is challenging to quickly come up with the right solution to fix the slow-performing CI/CD pipeline. While there are no existing machine learning methods to help in the prediction of the CI/CD pipeline build time and discovering the factors affecting the build time, the effort to optimize the build time is always based on conventional and traditional methods such as expert knowledge, software engineer's best guessing, or finding similar solution from online sources. The current methods are illustrated in Table 1.

Table 1
Comparison between current methods of debugging CI/CD pipeline

Current Method	Methodology	Weakness
Expert knowledge	Experts will diagnose the issue based on experience and domain knowledge	Highly dependent on having an experienced expert with deep domain knowledge
Engineer's guessing	Engineers debug based on their guessing and experience	Guessing may be inconsistent and unreliable
Finding solutions from online Sources	Engineers look for possible solutions from online sources, such as forums, to fix the issue	It is time-consuming to look for solutions from different sources Unreliable and unverified answers can waste time

Memory Bottleneck in Compile-time

In a study by Cahoon (2002) on compile-time analysis based on the programming language Java, he found that memory hierarchy in modern architecture is among the major performance bottlenecks in compile-time. However, when the software build and software compilation happens on the CI/CD pipeline rather than the software engineer's local development machine, the local development machine's performance does not matter anymore. It is acceptable for the software engineers to have a relatively weaker machine since the software is expected to be built and pass the automated tests on the remote CI/CD pipeline. The CI/CD pipeline is the centralized location and the single source of truth to ensure the software build is fit for going into production. This means that improving the performance of the CI/CD pipeline will reduce the software build time for the software engineers, triggering a build in the pipeline. It shows that investing effort in optimizing the CI/CD pipeline is worthwhile.

Machine Learning Techniques for CI/CD Prediction

This research explored various machine learning (ML) techniques such as random forest (RF), XGBoost (XGB), gradient boosting (GB), k-nearest neighbor (KNN), support vector regressor (SVR), which the characteristics and performance of the techniques are believed

to be suitable in the CI/CD prediction's context. Kaliappan et al. (2021) have compared the performance of the above ML models in their study by evaluating them on the prediction of the COVID-19 reproduction rate. The research used common evaluation metrics such as mean absolute error (MAE), mean squared error (MSE), root mean squared error (RMSE), determination coefficient (R^2), relative absolute error (RAE), and root relative squared error (RRSE) to benchmark the performance of the ML model in regression task. The comparison result is shown in Table 2.

Table 2
Performance comparison between ML models in a Regression task

Performance Metrics	RF	XGB	GB	KNN	SVR
MAE	0.020	0.019	0.021	0.019	0.077
MSE	0.001	0.002	0.002	0.002	0.007
RMSE	0.038	0.041	0.041	0.041	0.085
R-Squared	0.976	0.973	0.973	0.973	0.884
RAE	0.106	0.102	0.112	0.102	0.404
RRSE	0.154	0.166	0.164	0.165	0.341

*Source: Kaliappan et al. (2021)

As shown in Table 2, RF and XGBoost performed very well against the other ML models used in the study. RF achieved the best MSE, RMSE, R-Squared and RRSE, while XGBoost achieved the best MAE and RAE. RF and XGBoost are very popular ML models used in machine learning tasks. They are also ensemble ML methods that consider multiple ML models to produce a final prediction output that is generally more accurate than a single ML model.

Based on the analysis of Kaliappan et al.'s (2021) findings, RF and XGBoost are believed to be the ideal models to be used in the study because of their strong performance. Meanwhile, this study would also adopt other simple regression models, such as linear regression (LR) and support vector regression (SVR), to benchmark the performance with the two suggested ML models.

Related Work on Applying Machine Learning to DevOps Processes

The research conducted by Battina (2021) was identical to this research because it applied machine learning techniques to optimize the DevOps processes. Several machine learning techniques were studied to apply them to DevOps processes for better software quality. The author stated that dataset inputs, which are outputs from Git and Jenkins, can provide insight into the software delivery process. The anomalies of large code volumes and long build times in the data can be identified using machine learning models. The said study

has a certain level of similarity to this research in the sense of performing prediction on software build time with a dataset of build event logs. This research brings confidence and proves the feasibility of delivering a solution that detects anomaly software build events in a CI/CD pipeline by comparing the instance with the prediction.

In another similar research, the authors proposed applying machine learning techniques to find defects in the CI/CD pipeline (Lazzarinetti et al., 2021). Attributes from software code version control include *commits* (author, commit message, date), *changes in commit* (added lines, deleted lines), and *sonar measures* (line of codes in the commit), which were used to identify the defects in the CI/CD pipeline. Albeit the slight difference in research methodology where the said research measures the software code version control attributes while this research uses attributes of the software build event on CI/CD pipeline, it shows there were prior efforts on experimenting with machine learning techniques on CI/CD pipelines with the same goal to improve the productivity of software engineers.

Related Work on Predicting Continuous Integration Build Failures with Evolutionary Search

Saidani et al. (2020) have conducted research to predict build failures on continuous integration by using evolutionary search. The research used a novel search-based approach based on multi-objective genetic programming (MOGP) instead of machine learning or deep learning. A model was built to predict whether the CI build will succeed or fail. The research was conducted with a benchmark of 56,019 builds from 10 large-scale software projects running on the Travis CI build system (Saidani et al., 2020). As a result, the author found that the method mentioned achieved a statistically better result than the models developed with machine learning techniques.

The main differences between the research conducted by Saidani et al. (2020) and this research are the features used and the prediction outcome. In the former, the researcher was trained on attributes specific to the files and codes changed in the commit, such as *change size*, *file changes*, and *committer experience*. In this research, the features used were the CI/CD pipeline attributes as well as the time when the commit is pushed to the pipeline. The target of the prediction is different as well. The former tries to predict whether the CI build will pass or fail, while this research predicts the time taken for the software build to complete in the CI/CD pipeline.

Literature Review Discussion

At the time of writing, no research papers and reports were found on the Internet or in research databases with the exact same objective: to predict the software build time on the CI/CD pipeline with machine learning. This research is considered relatively unique because it lacks other research to be benchmarked and compared against.

It is firmly believed that this research will be impactful and stir inspiration in the software development industry. Software engineers and technical leaders could benefit from their daily work of software development by applying the ML model to predict software build time on CI/CD pipeline and perform data analysis to root cause CI/CD pipeline issues, ultimately bringing better productivity in software development.

Without other research to compare with, this research should be conducted with a proper methodology and evaluated with correct judgment based on the research context and business requirements.

MATERIALS AND METHODS

Research Framework

Figure 2 shows the components of the research framework conducted in this research. The software development process could be illustrated in four areas: (1) development environment, (2) CI/CD Pipeline, (3) CI/CD prediction, and (4) production environment. The four areas are described in Table 3.

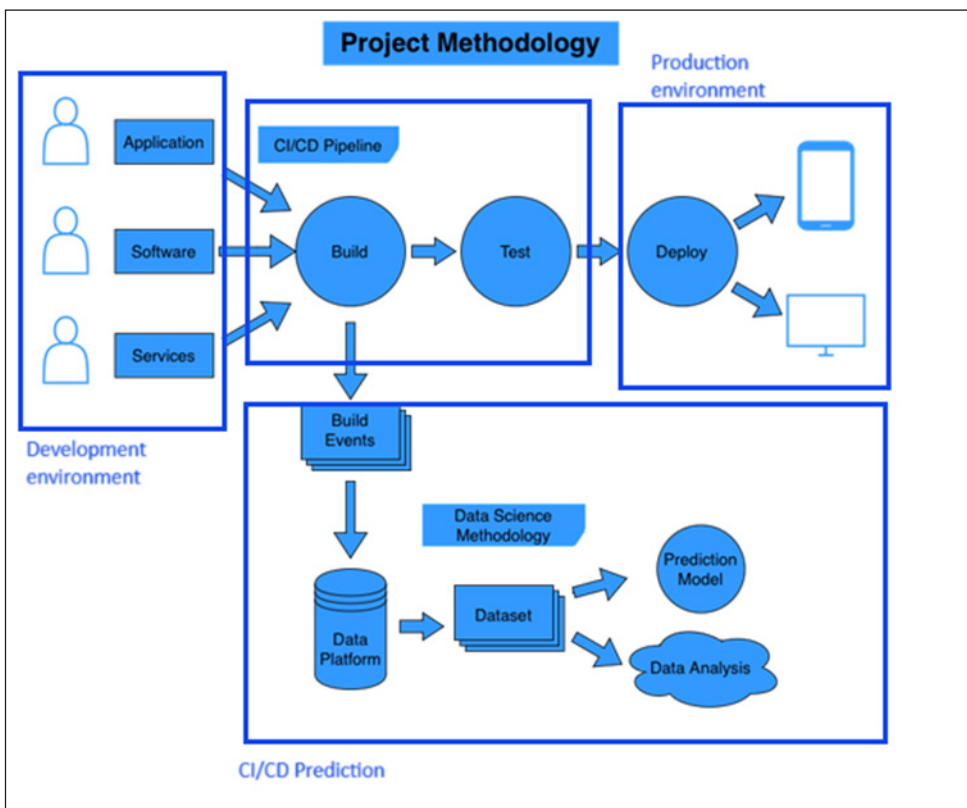


Figure 2. Research framework

Table 3
Description of research framework's components

Component	Description
Development environment	It is the environment where software engineers build applications and software codes locally. The finished codes will be pushed to the remote repository and version control system for further perusal.
CI/CD pipeline	It tracks the remote repositories and checks the status of new codes constantly "pushed." Auto build process will take place whenever new "commits" are available on the remote repository. Unit tests or integration tests come next after a successful build.
CI/CD prediction	The collected build event dataset is used to conduct software build time prediction using data science techniques.
Production environment	It is the environment where the successfully built and tested codes are deployed. New changes for the webpage can be rolled out immediately to the live environment. New web API services can be published to the production environment easily and efficiently with minimal to no server downtime.

Experiment Setting and Machine

Model selection and training were also solely conducted on the local machine, which performed very promisingly. The machine used is an Apple MacBook Pro 16 equipped with an Apple M1 Pro as the central processing unit (CPU) and 32GB of random access memory (RAM).

The biggest training dataset used in this project is around 800MB in CSV file form. The historical data was collected from a multi-national software development company. With the dataset loaded and preprocessed into Jupyter Notebook for model training, the machine handled the training without any hint of stress and completed the training within a few minutes. Considering the scale of the project's dataset, it is an acceptable performance for this project.

Research Methodology

This research adopted the cross-industry standard process for data mining (CRISP-DM), an industry-proven data science methodology, to organize data science projects. The sequence of the phases (Figure 3) may not be strict, and most projects may move back and forth between them when deemed necessary (IBM, 2021).

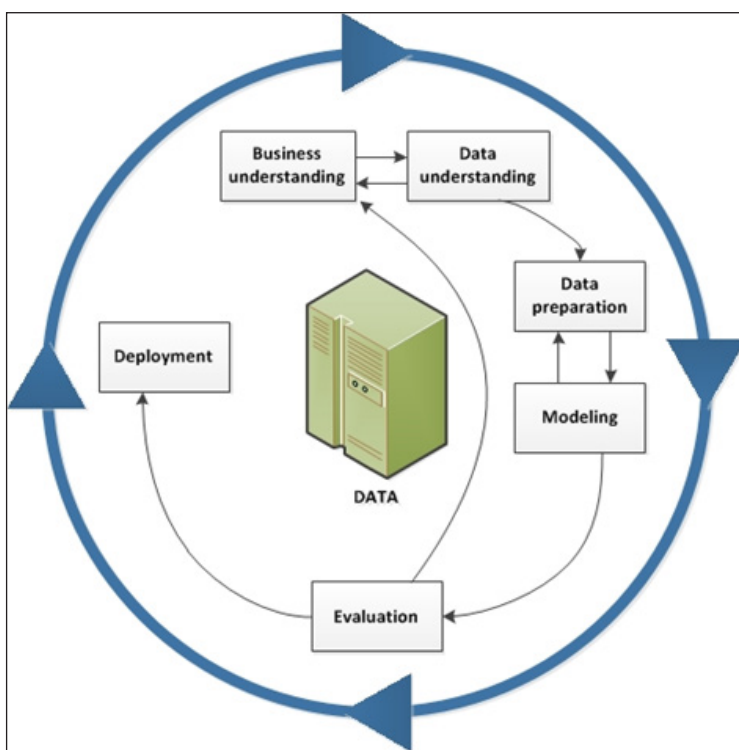


Figure 3. CRISP-DM methodology (IBM, 2021)

The first step in this research was to understand the business requirements and the available dataset. The Research acknowledges that the company's DevProd team was encountering inconsistent software build time on the CI/CD pipeline and would like to resolve this issue. The research has proposed adopting ML models, training the ML models with the build event dataset to predict CI/CD pipeline software build time, and further data analysis of the root causes of high software build time.

Next, the dataset needs to be prepared before the modeling step. Several steps, such as feature selection, feature encoding, and feature engineering, were performed to train the ML model.

With several ML models in mind, this research evaluated the ML models' performance on this preprocessed dataset. Mean squared error (MSE) was chosen as the evaluation metric because it is a common metric used to benchmark ML models in regression tasks. It averaged out the positive and negative differences by squaring the values. According to Hodson et al. (2021), mean squared error (MSE) is an ideal performance benchmark because of its link to the concept of cross-entropy from information theory. An ML model with a low MSE score is considered a good ML model, whereas a perfect ML model would have a perfect score of 0 in MSE.

After picking the best ML model, it will be tested with deployment. Depending on the scenario, the ML model might be tested on a test project to experiment with its performance and results. Further adjustments to the ML model and project setup can be made at this point.

Steps to Conduct Build Time Prediction with Data Science Techniques

Step 1: Feature Selection

Feature selection is the process of choosing the best features for the model under investigation (Rosidi, 2023). According to Rosidi (2023), correlated features that would cause multicollinearity and high computational power caused by too many features in a dataset were among the reasons why feature selection is crucial to a machine learning model.

The original dataset is a CSV file generated by a Python script specifically written to preprocess the dataset file format exported by Splunk. The dataset has 79 columns. The required features are selected based on the domain expert's knowledge of the dataset. For example, it is logical to remove the feature *git_commit_id* since a Git commit ID that looks like "070dcfee" will not make any sense to the machine learning model since it is generated without bringing any meaning or significance other than uniquely identifying the specific Git commit. Many other features in the original dataset carrying unmeaningful values, such as randomized character strings, null values, and irrelevant values, were also removed because they would not provide useful information for model training. Finally, 13 columns (features) were selected as the prediction variables.

Step 2: Feature Encoding

Feature encoding is the step to transform features with string values, usually into numerical values comprehensible by machine learning models. It can be done manually by providing a mapping of values in the form of a data structure or by using data science libraries to automate the process when it comes to features with a high number of distinct values.

Several feature encoding methods were used to transform the variables into the right format for the prediction process. A simple encoding process is adapted to store the mapping value for month and day, such as by declaring a Python Dictionary variable. In the case of features with a large number of unique values, label encoding was used to transform the relevant feature from categorical string labels into number labels by using the scikit-learn library method called *LabelEncoder*.

Step 3: Feature Engineering

The feature engineering technique creates useful features not in the original dataset and potentially improves the machine learning model's performance. In this case, the variable *time_taken_min* is created by calculating the time difference between existing features

end_time and *start_time* to be this machine learning project's target variable (output). The new variable generated with feature engineering is added to the existing 13 variables chosen from the feature selection step to form 14 columns (features), as shown in Figure 4, to be used as the prediction model's variables.

```

... <class 'pandas.core.frame.DataFrame'>
Int64Index: 13325 entries, 5 to 70935
Data columns (total 14 columns):
 #   Column                Non-Null Count  Dtype
---  -
 0   date_hour             13325 non-null  int64
 1   date_mday             13325 non-null  int64
 2   date_minute          13325 non-null  int64
 3   date_month           13325 non-null  int64
 4   date_second          13325 non-null  int64
 5   date_wday            13325 non-null  int64
 6   date_year            13325 non-null  int64
 7   detail.build.state   13325 non-null  int64
 8   detail.job.exit_status 13325 non-null  float64
 9   detail.job.passed    13325 non-null  int64
10   detail-type          13325 non-null  int64
11   detail.pipeline.repo 13325 non-null  int64
12   time_taken_min       13325 non-null  float64
13   is_weekend           13325 non-null  int64
dtypes: float64(2), int64(12)
memory usage: 1.5 MB

```

Figure 4. A snippet of dataset columns after feature selection and engineering steps

Step 4: Identifying Relevant Machine Learning Models

According to the famous no-free-lunch theorem (NFL), the researchers cannot formally ground their conviction that some machine learning models are more sensible than others (Sterkenburg & Grünwald, 2021). Machine learning models have varying behaviors in different datasets, and the performance of the models is not guaranteed to be the same in all situations. Hence, there is a need to test the waters by trying out several machine-learning models to find the most suitable model for this dataset.

The project first conducted experiments with simpler machine learning models such as linear regression (LR) and support vector regression (SVR) to get a glimpse into how these models would perform against the baseline benchmark. The experiments' results were unsatisfactory compared to the baseline benchmark.

Therefore, more complex machine learning models, such as RF, multilayer perceptron regressor and XGBoost, were added to the experiment list to see if the complex model would achieve better performance than the simpler model. The results of each machine-learning experiment are shown in Table 4.

Table 4
Result of experiments with different machine learning models

Model Name	MSE
Baseline-dummy	299.36
Linear regression	293.50
Support vector regressor	308.49
Random forest	260.73
Multilayer perceptron regressor	278.91
XGBoost regressor	275.76

Table 4 shows that the more complex machine learning models, such as XGBoost regressor and multilayer perceptron regressor, have performed better than the baseline benchmark, linear regression, and support vector regressor by achieving lower MSE scores. However, they are less outstanding in comparison to the RF model because the model has achieved the best result with the lowest MSE score out of all models. As such, the RF model would be used to perform the software build time prediction.

RESULTS AND DISCUSSIONS

Experiment Set Up

The experiment was conducted with two datasets with different instances (Table 5) to explore whether the number of instances affects the prediction model's performance. Both datasets underwent the same data preprocessing methods and were trained using the same machine learning, the random forest (RF) model. For a small dataset, 70% of the data was used for training, while the other 30% was used for testing. The dataset is retrieved from Splunk with 1 week's worth of data for the build event dataset. As for the big dataset, 5-fold cross-validation was used to validate the model. The dataset was retrieved from AWS CloudWatch, which had 1 month's worth of data for the build event dataset. The number of features used in the big dataset was reduced to 8 from 14 in the small dataset by removing irrelevant features that scored zero in feature importance, deduced from the RF model trained on the small dataset.

Table 5
Comparison of small and large datasets

Dataset	Small Dataset	Big Dataset
Size of data frame	2394	44344
Number of features	14	8
Number of instances	171	5543

The prediction of software build time on the CI/CD pipeline was made using the trained RF model to perform prediction on a new data instance.

For example, the trained RF model will give a new data instance with the same set of features. Since the RF model was trained on the dataset with the same set of features, it will be able to provide a prediction for the new data instance after “learning” from the training dataset.

Table 6 shows the result of the software build prediction with an RF model with small and big datasets. The RF model’s performance in the smaller dataset is highly assuring and outperformed by the dummy regressor, which is used as the baseline for comparison in this experiment. On the other hand, the RF model with a big dataset did not outperform the baseline dummy regressor too much (less than 1.0) as previously expected.

Table 6
Prediction result comparison for small and big datasets

Dataset	Model	MSE	RMSE
Small dataset	Dummy regressor	53.232	7.296
	RF model	14.306	3.782
Big dataset	Dummy regressor	19.008	4.360
	RF model	16.642	4.079

Discussion on Result

The experiment showed that the RF model performed better when using a small dataset than a big dataset. There could be several possible reasons for the not-so-good performance of a big dataset. Firstly, the dataset might have a high variance. Secondly, the dataset might be imbalanced. Thirdly, more features could be required for the big dataset to produce more accurate prediction output. Fourthly, the repository that was used might have glitches in the build time in the dataset.

Considering the outstanding performance of the RF model over the dummy regressor in the small dataset, it is believed that the result of the RF model that was trained in this research was significant. With the RMSE score of 3.782 achieved in the small dataset, where the feature unit is in minutes, the model’s prediction is only 3.782 minutes away from the actual result on average. In a dataset with software build, events take 20 minutes to 1 hour. The RMSE score of 3.782 achieved by the RF model is considered outstanding in this business context.

While it is fine to conduct software build time prediction with a small dataset at a time by using a dataset with build data for a shorter period, with the latest trend analysis, the RF model is the ideal machine learning model to be used on this software build dataset for software build time prediction.

Direct comparison of this research with other existing research is unavailable because this research is unique as far as the researchers' best effort of literature search. However, it is important to note that the result achieved by the RF model is reassuring and gives confidence in the technique of applying ML models to predict CI/CD pipeline software build time and provide further analysis using the model trained to give better suggestions on root cause leading to slow CI/CD pipeline performance, in comparison to using the traditional and unstructured methods as discussed in Table 1.

Impact of Research in the Real World

The RF model has been deployed in a small-scale project's CI/CD pipeline for testing and observing its performance. After deploying the model on the testing project's CI/CD pipeline, the team has observed a similar performance of MSE score with the RF model trained. The RF model is able to predict software build time on the CI/CD pipeline, which is relatively close to the actual software build time on the pipeline.

Due to the limited scope of the test environment and dataset involved, the major factor that affects the software build time on the CI/CD pipeline the most is the start time. It seems that in this environment and scope, the start time, especially the hour it started, will impact the most on how much time it will take to finish the software build on the CI/CD pipeline.

This is explainable because although software building might happen frequently within a certain hour, the busy CI/CD pipeline might not have enough agents and hardware resources to perform the software build requests in a timely manner. Ultimately, this leads to a longer waiting time and, thus, a longer software building time.

It is hoped that this research will inspire software engineers, CI/CD engineers and technical leaders to adopt ML techniques into their infrastructure and technology stack. This will improve software development productivity by providing accurate software build completion time. It will also decrease CI/CD pipeline downtime coupled with performance improvement with the help of data analysis and machine learning techniques to debug issues.

Adopting the technique proposed in this research will save time and provide a higher accuracy of troubleshooting on the CI/CD pipeline. These will all lead to a lesser downtime of CI/CD pipelines with higher performance. Engineers will also better understand the factors leading to depriving performance of the CI/CD pipeline. The monetary costs of the computing infrastructures will be saved for the above-mentioned reasons. Faster software shipping speed thanks to the efficient CI/CD pipeline enables speedy business software delivery. A healthy and efficient CI/CD pipeline would improve the recovery crisis of website downtime.

CONCLUSION

This research explored the machine learning model to predict software build time with various sizes of datasets. Five machine learning models, linear regression, support vector regressor, random forest, multilayer perceptron regressor, and XGBoost regressor, were experimented with to find the best prediction model to predict software build time with the selected 14 features. The experiment showed that the RF model with a small dataset in this research experiment is the best model for software build time prediction.

Without prior research on this specific subject matter, this research has uniquely provided an approach to adopting data science and ML techniques in the CI/CD pipeline to predict the software build time-based on a dataset of past software build events. Data analysis could be done with the help of the trained model to further analyze and debug the performance issues in the CI/CD pipeline.

In an ideal world, developers would not only wish to reduce their software build time optimally but also get an accurate prediction of their software build time. It enables the developers to perform at a higher level of productivity and brings more satisfaction to their daily jobs. This brings us to the goal of this research: discovering the feasibility of applying machine learning and data analysis to help predict the software build time, as well as discovering major factors that could lead to better-optimized software build time.

FUTURE WORK

The first possible improvement that came to mind was introducing more features to the dataset. The project dataset did not have several good candidates for features such as agent (a virtual agent that runs jobs), waiting time, and instance startup time (time for virtual machines to boot into usable state). They would certainly bring more information and insight into the study and help better analyze how other factors could also contribute to a higher build time. By taking more meaningful dataset features into account, bottlenecks can be identified to help bring improvement for a faster build time. The machine learning model also gains robustness with more relevant features in the training dataset.

Another future work that would take the project idea to a further step is to train a generalized machine learning model. The RF model was trained in very specific variables in the current project. Only one single code repository and specific CI/CD pipeline configuration were included in this project dataset. The model is expected to not perform well universally outside the specific features or variables it was trained on. The ideal machine learning model should have the ability to cater to changes, such as predicting across different code repositories and adding extra steps into the CI/CD pipeline. These are indeed ambitious targets for the project and require an immense amount of expert knowledge with a deep understanding of the domain. An enormous amount of data collection, analysis

and research into the CI/CD pipeline is required to deliver this seemingly bold yet highly rewarding improvement.

ACKNOWLEDGEMENT

The authors thank Universiti Sains Malaysia for funding this paper's publication.

REFERENCES

- Amazon Web Services. (2023). *Practicing continuous integration and continuous delivery on AWS*. AWS. <https://docs.aws.amazon.com/pdfs/whitepapers/latest/practicing-continuous-integration-continuous-delivery/practicing-continuous-integration-continuous-delivery.pdf>
- Battina, D. S. (2021). The challenges and mitigation strategies of using devops during software development. *International Journal of Creative Research Thoughts (IJCRT)*, 9(1), 4760–4765.
- Bedrina, O. (2023, August 7). *Best continuous integration tools for 2023 – Survey results*. JetBrains Blog. <https://blog.jetbrains.com/teamcity/2023/07/best-ci-tools/>
- Cahoon, B. D. (2002). *Effective compile-time analysis for data prefetching in Java* [Doctoral dissertation, University of Massachusetts Amherst]. University of Massachusetts Amherst. <https://www.cs.utexas.edu/users/mckinley/papers/cahoon-thesis.pdf>
- Fairbanks, J., Tharigonda, A., & Eisty, N. U. (2023, May 23-25). *Analyzing the effects of CI/CD on open source repositories in github and gitlab*. [Paper presentation]. IEEE/ACIS 21st International Conference on Software Engineering Research, Management and Applications (SERA), Orlando, Florida. <https://doi.org/10.1109/sera57763.2023.10197778>
- Hodson, T. O., Over, T. M., & Foks, S. S. (2021). Mean squared error, deconstructed. *Journal of Advances in Modeling Earth Systems*, 13(12), Article e2021MS002681. <https://doi.org/10.1029/2021ms002681>
- IBM. (2021, August 17). *CRISP-DM help overview*. IBM. <https://www.ibm.com/docs/en/spss-modeler/saas?topic=dm-crisp-help-overview>
- Jaspan, C., & Green, C. (2023). developer productivity for humans, part 4: Build latency, predictability, and developer productivity. *IEEE Software*, 40(4), 25–29. <https://doi.org/10.1109/ms.2023.3275268>
- Kaliappan, J., Srinivasan, K., Mian Qaisar, S., Sundararajan, K., Chang, C. Y., & C, S. (2021). Performance evaluation of regression models for the prediction of the COVID-19 reproduction rate. *Frontiers in Public Health*, 9, Article 729795. <https://doi.org/10.3389/fpubh.2021.729795>
- Lazzarinetti, G., Massarenti, N., Sgrò, F., & Salafia, A. (2021, November 30). *A machine learning based framework for continuous defect prediction in CI/CD pipelines*. [Paper presentation]. Proceedings of the Italian Workshop on Artificial Intelligence and Applications for Business and Industries (AIABI), Milan, Italy.
- Red Hat. (2023, December 12). *What is CI/CD?*. Red Hat. <https://www.redhat.com/en/topics/devops/what-is-ci-cd>

- Rosidi, N. (2023, June 6). *Advanced feature selection techniques for machine learning models*. KDnuggets. <https://www.kdnuggets.com/2023/06/advanced-feature-selection-techniques-machine-learning-models.html>
- Saidani, I., Ouni, A., Chouchen, M., & Mkaouer, M. W. (2020). Predicting continuous integration build failures using evolutionary search. *Information and Software Technology*, 128, Article 106392. <https://doi.org/10.1016/j.infsof.2020.106392>
- Silverthorne, V. (2022, February 15). *10 Reasons why your business needs CI/CD*. GitLab. <https://about.gitlab.com/blog/2022/02/15/ten-reasons-why-your-business-needs-ci-cd/>
- Snyk. (2020, October 1). *What is CI/CD? CI/CD Pipeline and Tools Explained*. Snyk. <https://snyk.io/learn/what-is-ci-cd-pipeline-and-tools-explained/>
- Sterkenburg, T. F., & Grünwald, P. D. (2021). The no-free-lunch theorems of supervised learning. *Synthese*, 199(3), 9979–10015. <https://doi.org/10.1007/s11229-021-03233-1>

A Novel Approach to Evaluating HEMA Polymer Gel Dosimeters Using Molecular Vibrational Features

Muhammad Alhassan^{1,2*}, Azhar Abdul Rahman¹, Iskandar Shahrin Mustafa¹, Mohd Zahri Abdul Aziz³, Mohd Zakir Kassim³, Mohammed Salem Abdullah Bagahezel³, Habib Ahmad Ibrahim¹ and Kabiru Alhaji Bala¹

¹*School of Physics, Universiti Sains Malaysia, Main Campus, Pulau Pinang, Malaysia*

²*Department of Physics, Federal University Dutsin-Ma, 821101 Katsina State, Nigeria*

³*Department of Biomedical Imaging, Advanced Medical and Dental Institute, Universiti Sains Malaysia, Bandar Putra Bertam, 13200 Kepala Batas, Pulau Pinang, Malaysia*

ABSTRACT

A polymer Gel Dosimeter (PGD) provides essential three-dimensional (3D) radiation dose distribution for the radiotherapy planning system (TPS). This study investigates the use of infrared absorption spectrum as a novel and more cost-effective alternative to Magnetic Resonance Imaging (MRI), Nuclear Magnetic Resonance (NMR), and Optical Computed Tomography (Optical CT) for reading out PGDs. The PGDs were fabricated using 2-Hydroxyethyl methacrylate (HEMA), maltose, N'N, methylene(bis)acrylamide (Bis), gelatin, deionized water (DI Water), and Tetrakis (hydroxymethyl) phosphonium chloride (THPC), and were irradiated using a Linear Accelerator (LINAC) within the range of 0–30 Gy. The possibility of translating molecular vibrational frequency, amplitude, and energy of vibration into absorbed dose was explored by analyzing the absorption spectra in the near-infrared region (NIR) with wavelengths between 750–1100 nm. The findings reveal that

these vibrational properties can be employed to interpret irradiated PGDs. Furthermore, an increase in maltose concentration within the 0–520 mM range widens the linear dose range and enhances sensitivity. The PGDs exhibit temporal stability up to 7 days post-irradiation, and the span of their response remains relatively unaffected by scanning temperature. In conclusion, NIR spectroscopy offers a cost-effective method for interpreting PGDs, potentially improving the affordability and efficiency of PGD dosimetry in clinical radiotherapy. This holds particularly promising for less developed countries, aligning with the

ARTICLE INFO

Article history:

Received: 30 October 2023

Accepted: 3 October 2024

Published: 21 February 2025

DOI: <https://doi.org/10.47836/pjst.33.2.23>

E-mail addresses:

amuhammad@fudutsinma.edu.ng/amuhammad@student.usm.my (Muhammad Alhassan)

arazhar@usm.my (Azhar Abdul Rahman)

iskandarshah@usm.my (Iskandar Shahrin Mustafa)

mohdzahri@usm.my (Mohd Zahri Abdul Aziz)

mohdzakir@usm.my (Mohd Zakir Kassim)

msbagahezel@student.usm.my (Mohammed Salem Abdullah Bagahezel)

habibahmadibrahim@student.usm.my (Habib Ahmad Ibrahim)

kabala@student.usm.my (Kabiru Alhaji Bala)

*Corresponding author

sustainable development goal (SDG) of ensuring affordable healthcare for all. We finally recommend further research into translating the molecular vibrational parameters into 3D images.

Keywords: HEMA, infrared absorption spectrum, maltose additive, polymer gel dosimeter, saccharide additive

INTRODUCTION

Radiotherapy is a medical technique involving collective responsibilities among radiation oncologists, medical physicists, radiographers, and radiation technologists to eliminate cancerous cells in the human body using ionizing radiation. It becomes increasingly crucial with rising cancer incidences (Jaszczak et al., 2020). There are two common types of radiotherapy: internal radiotherapy or brachytherapy, which involves placing sealed radioisotopes near or inside the tumor (Shukor et al., 2022), and external beam radiotherapy, irradiating the tumor from outside the body. Precision in dosage prescription is paramount in radiotherapy, necessitating careful planning to ensure the target volume receives the proper dose without harming surrounding healthy tissues. As such, the need for a tool that could measure the dose distribution in a 3D manner arises (Kozicki et al., 2020). PGD is a tool made from hydrogels such as gelatin within which monomer is uniformly distributed and readily polymerizes on irradiation and is proven capable of measuring complex 3D radiation dose distribution with high precision and spatial resolution (Adliene et al., 2020; Jaszczak et al., 2020; Rabaeh et al., 2021; Shih et al., 2022).

On irradiation, radiation-induced polymerization occurs as a function of the absorbed dose in such a way that the level of polymerization could thereafter be translated into the absorbed dose (Mustaqim et al., 2020; Shih et al., 2022). Various physical and chemical changes in PGDs – such as shifts in transverse relaxation rate (R_2) during MRI, relaxation times during NMR, and optical appearances via optical CT scanning (OCS) could be translated into absorbed dose (Adliene et al., 2020; Jaszczak et al., 2020), alongside UV-visible spectrophotometry (UV-Vis) revealing optical changes and electronic transitions (Ishak et al., 2015), changes in CT number in x-ray CT scanning (Javaheri et al., 2020), and changes in speed of sound during Ultrasound scanning (Javaheri et al., 2020). Recent advancements utilize angular modulation, plasmonic sensors, and reflection intensity changes during Polarization-Sensitive Optical Coherence Tomography (PS-OCT) for evaluating polymerization (Adliene et al., 2020; Shih et al., 2022), with future predictions involving electrical impedance tomography (EIT), photoacoustic, and diffuse optical tomography (DOT) for PGD readouts (Deene, 2022). However, these techniques often rely on specialized machinery, posing obstacles to the realization of the sustainable development goal of providing comprehensive healthcare, especially in less developed countries.

Our present work pioneers translating molecular vibration-related changes in near infrared (NIR) absorption spectra into absorbed doses. The advantages of NIR spectroscopy

are the availability of infrared (IR) Spectrophotometer or Vis-IR spectrophotometer in most laboratories for identification of chemical substances, it is non-destructive, and is a fast technique compared to others (Masithoh et al., 2023; Zapata et al., 2021) and nowadays, some manufacturers such as Shimadzu, Japan manufactures UV-Vis spectrophotometers with extended energy range to NIR region and could be used to obtain absorption spectra and transmittance spectra of a sample within 200-1100 nm wavelength range. The utilization of UV-Vis spectrophotometer for PGD readout could be considered a better option due to its availability and cost-effectiveness (Lotfy et al., 2017).

The use of IR as a PGD readout technique hinges on the fact that irradiation-induced polymerization and crosslinking within the PGD lead to changes in molecular bonds (Deene, 2022), subsequently influencing the spectral position, bandwidth, and peak. These changes signify modifications in molecular vibration amplitude, frequency, and energy.

When a PGD is exposed to electromagnetic radiation (e.m. waves), three types of interactions can occur: (1) changes in rotational energy levels of molecules (this requires the least energy, typically at longer wavelengths), (2) changes in vibrational energy levels (this requires moderate energy, often happening in the NIR, and (3) electronic transitions (this requires the most energy, occurring at ultraviolet or visible wavelengths). While NIR is primarily associated with vibrational spectroscopy, it can also encompass electronic and rotational spectroscopies (Ozaki, 2021; Zapata et al., 2021). The spectral bands observed in the NIR are mostly due to functional groups containing hydrogen atoms, such as OH, CH, and NH, which are also present in this study's constituents of the PGDs.

In existing literature, IR spectrophotometers are employed in chemistry, biochemistry, biology, and material sciences to obtain transmittance or reflectance spectra within the 780–2500 nm range. These spectra are then translated into molecular vibrations for qualitative and quantitative analyses, determining the presence or concentration of specific materials, bonds, or functional groups in a sample (Darwish & Darwish, 2022; Pratiwi et al., 2022; Renner & Fritz, 2020; Zapata et al., 2021).

The scope of this study is limited to evaluating radiation-induced changes linked to molecular vibrations in the PGDs. Consequently, a single prominent absorption band within the NIR range is chosen to establish a connection between molecular vibrational changes and the absorbed dose that causes these changes. The limitation of this work and the usage of NIR for dose evaluation is the limited penetrability of IR, which might restrict its application in large PGD phantoms. Also, the shapes and sizes of sample holders in the present UV-Vis-IR spectrophotometers might restrict the evaluation of PGDs in humanoid phantoms.

This study aims to produce PGD using the less toxic monomer HEMA with a maltose additive. Subsequently, these PGDs will be irradiated with X-rays from a LINAC, and the vibrational parameters will be translated into absorbed doses.

MATERIALS AND METHOD

Gel Preparation

Four PGDs with varying maltose concentrations were prepared using the following components: DI Water (89.0%), gelatin (Type B, 225 g bloom) (6.0%), HEMA (2.7%), Bis (2.0%), and THPC (0.2%). All reagents except DI Water were obtained from Sigma-Aldrich, Germany. DI water was produced in the lab using the Arium® Pro water system machine.

The PGDs were prepared under normal atmospheric (normoxic) conditions (Nezhad et al., 2021). Throughout the PGDs' preparation, a hot plate with an integrated magnetic bar stirrer was used to facilitate the heating and stirring of the mixture. The PGDs were prepared by first heating DI water to 48°C to enable full dissolution of Bis. Following the addition of Bis, gelatin was added. The heating knob was switched off while the stirring continued to allow the mixture to cool. When the mixture became clear and transparent and cooled to 35°C, maltose was added, followed by HEMA and THPC at 27°C to avoid premature polymerization. The sequential addition of the components and the corresponding temperatures are outlined in Figure 1.

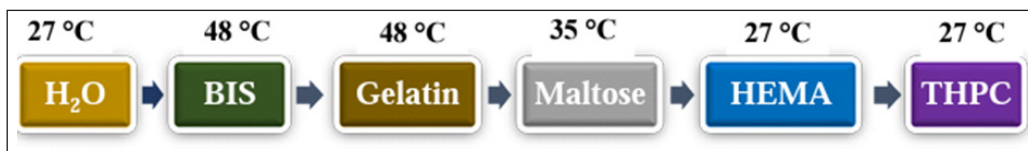


Figure 1. Preparation of PGD with the Sequential addition of its components

Following the addition of the last component, the PGDs' formulation was stirred for over 15 minutes at room temperature to ensure uniformity within the gel matrix. The mixture was then transferred to 4.5 cm³ Perspex cuvettes with a 1.0 cm path length, tightly sealed with parafilm to prevent oxygen penetration, and placed in a refrigerator maintained at 4-6°C for gelation. These dosimeters are named here 'HEMAMAL' as an acronym for 'HEMA dosimeter + MALTOSE'; they are labeled as HEMAMAL1, HEMAMAL2, HEMAMAL3, and HEMAMAL4, corresponding to maltose concentrations of 0 mM, 80 mM, 230 mM, and 520 mM, respectively.

Irradiation

The PGDs were irradiated on the third day after manufacturing using an Elekta LINAC with a photon energy of 6 MV. The samples were positioned on a water phantom 5 cm thick and beneath another water phantom 1.5 cm thick, maintaining a source-surface distance (SSD) of 100 cm. This setup was within a 10 × 10 cm² field of view (FoV) in the isocenter. As mentioned elsewhere, the water phantom ensures uniform radiation distribution among

the PGDs, facilitates radiation build-up effects, and maintains scattering conditions (Al-jarrah et al., 2016).

The four batches of the PGD were irradiated to 5, 10, 15, 20, 25, and 30 Gy, while one PGD from each batch was left unirradiated (control sample). The arrangement for sample irradiation is illustrated in Figure 2.

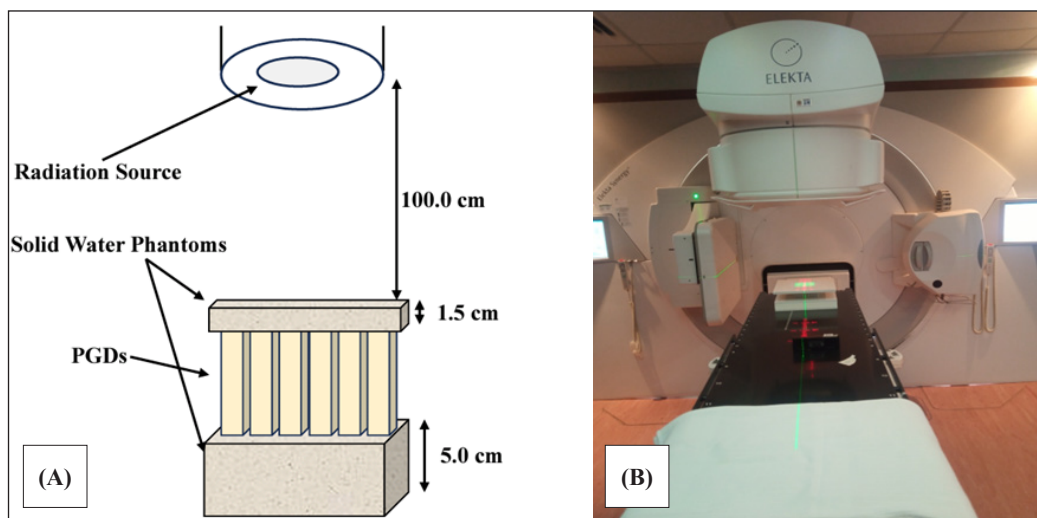


Figure 2. The visualization of irradiation setup with (A) The schematic diagram of the irradiation procedure and (B) Placement of PGDs at the isocenter of radiation FoV with the help of a laser beam

Dose Readout

The Shimadzu UV-1800 is a UV-Vis Spectrophotometer designed to scan samples across ultraviolet (UV), visible (Vis), and certain IR wavelengths. It can provide both absorption and transmittance spectra. Prior to the scanning process, the machine was allowed to warm up and complete initializations. Subsequently, it was configured for absorbance mode within the wavelength range of 750–1100 nm, a portion of the NIR spectrum (Ozaki, 2021). The scanning interval was set to be 1 nm at a medium scan speed, and the range of absorbance was 0.00–4.00. A Perspex cuvette almost full of DI water was used as the reference sample, and baseline correction was performed. The PGDs were scanned while maintaining the room temperature at $22.0 \pm 0.5^\circ\text{C}$ with the help of an air-conditioning system while the doors and windows remained closed.

In this study, we employed three principles to translate molecular vibrations into absorbed doses.

1. Relationship between Vibrational Amplitude and Concentration:

This principle is rooted in Beer Lambert's law, which states the direct proportion between absorbance and concentration of the measured component (Equation 1):

$$A = \epsilon lc \quad [1]$$

Where A represents peak absorbance or band intensity/amplitude, ϵ is the absorptivity, l is the optical path length, and c is the concentration (Darwish & Darwish, 2022; Pratiwi et al., 2022). In our case, concentration signifies polymerization levels and reflects the absorbed dose. Accordingly, we plotted graphs depicting changes in absorbance (ΔA) and peak absorbance (A_p) against absorbed dose.

2. Relationship between Absorbed Energy and Spectral Bandwidth:

Heightened polymerization necessitates greater energy to induce molecular vibrations from lower to higher energy states. This results from structural changes, viscosity changes, and changes in molecular conformity (Darwish & Darwish, 2022; Deene, 2004; Ishak et al., 2015). Energy and vibrational frequency are correlated through Equation 2:

$$E = h\nu \quad [2]$$

Where E is quantized energy, h is Planck's constant, and ν is the frequency (Abdel-Ghany et al., 2020; Ishak et al., 2015). If absorbed energy ΔE leads to an electronic transition or sets molecules into vibration, Equation 2 can be expanded to relate the energy to the absorbance bandwidth, as shown in Equation 3:

$$\Delta E = h(\nu_f - \nu_i) = hc \left(\frac{\Delta\lambda}{\lambda_f \lambda_i} \right) \quad [3]$$

Where $\nu_i = \frac{c}{\lambda_i}$ and $\nu_f = \frac{c}{\lambda_f}$ are initial and final vibrational frequencies before and after energy absorption, and $\Delta\lambda$ is the bandwidth or the difference between λ_i and λ_f in cm. We plotted bandwidth against absorbed dose to capture this relationship.

3. Relationship between Energy and Molecular Frequency/Wave Number:

Equations 2 and 3 establish energy, vibration frequency, and wavelength connections. At λ_{max} , energy aligns with wave number ($\tilde{\nu}$) as shown in Equation 4:

$$E = hc\tilde{\nu} \quad [4]$$

Where $\tilde{\nu} = \frac{1}{\lambda_{max}}$ is the wave number and is measured in cm^{-1} .

Equation 5 defines the wave number for a harmonic oscillator, which is connected to the force constant of the molecular bonds and reduced mass.

$$\tilde{\nu} = \frac{1}{2\pi} \sqrt{\frac{k}{\mu}} \quad [5]$$

Where k represents the force constant in Ncm^{-1} , and μ is reduced mass in kg (Darwish & Darwish, 2022; Ozaki, 2021). In our case, varying polymerization levels and crosslinking lead to different concentrations of double bonds and functional groups within the irradiated polymer matrix. Consequently, different k and μ values emerge. Functional groups were also noted to influence PGD sensitivity to radiation (Deene, 2004). We plotted wavenumbers against absorbed dose to reflect this connection.

RESULT AND DISCUSSION

Absorption Spectra

The irradiated PGDs were scanned using a UV-Vis-IR spectrophotometer capable of covering a portion of the NIR spectrum. The dose evaluation was based on absorption spectra within the 750–1100 nm range, which are depicted in Figure 3.

The absorption spectra in Figure 3 (A)-(E) reveal distinct peak positions (λ_{max}) among the four PGDs. It is attributed to the influence of the maltose additive. This λ_{max} shift is also evident within each batch of PGDs irradiated at varying energies. This intra-batch shift is attributed to differing levels of polymerization and crosslinking, which impact molecular bond vibrations and can be correlated with absorbed doses causing polymerization and crosslinking. Figure 3(E), with an expanded view in 3(F), illustrates bandwidths of absorption spectra for HEMAMAL4 PGDs irradiated at 5, 10, 15, 20, 25, and 30 Gy doses. Bandwidths are measured at half peak absorbance ($\frac{1}{2}A_p$) for each spectrum. The accompanying table in Figure 3(F) indicates that bandwidth increases with an increase in absorbed dose.

Results in Figure 3(A)-(E) reveal the presence of multiple absorption bands with varying heights and widths attributed to diverse functional groups like OH, CH, and NH in dosimeter constituent components (Ozaki, 2021). These findings align with our expectation of λ_{max} shifting to higher energy (shorter wavelength) due to increased concentration of specific components, consistent with Beer Lambert's Law (Equation 1). These observations indicate the effect of absorbed dose on parameters associated with spectral height and width (Darwish & Darwish, 2022).

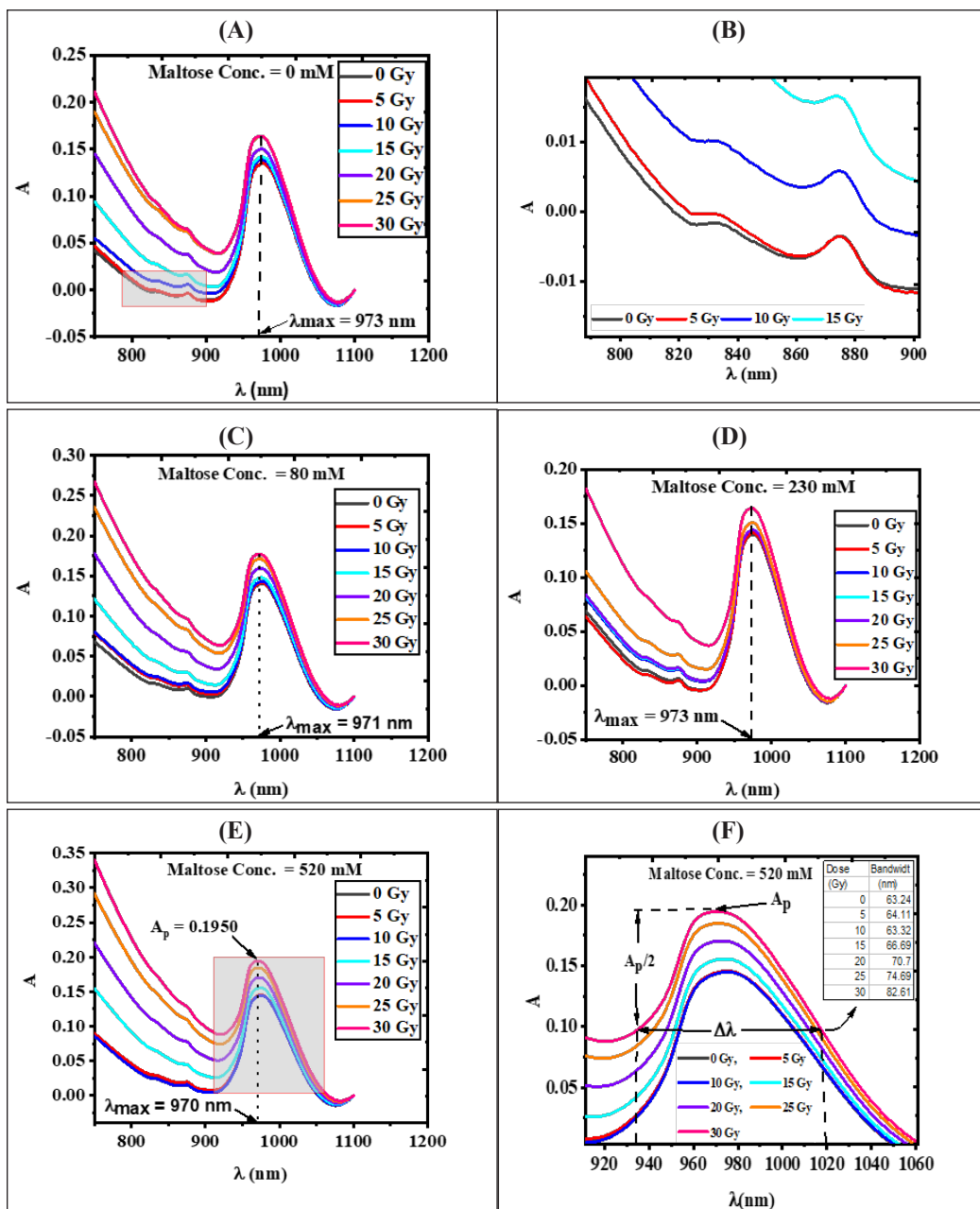


Figure 3. The absorption spectra of four PGDs (A) HEMAMAL1, (B) an enlarged portion of (A) as indicated by the arrow, (C) HEMAMAL2, (D) HEMAMAL3, (E) HEMAMAL4, and (F) an enlarged portion of (E) showing the bandwidth of HEMAMAL4, irradiated to 0-30 Gy

Dose-response

The dose-response, represented by (1) change in absorbance (ΔA), (2) peak absorbance (A_p), (3) bandwidth ($\Delta\lambda$), and (4) wave number ($\tilde{\nu}$), was plotted against the absorbed dose. The resulting graphs are displayed in Figure 4.

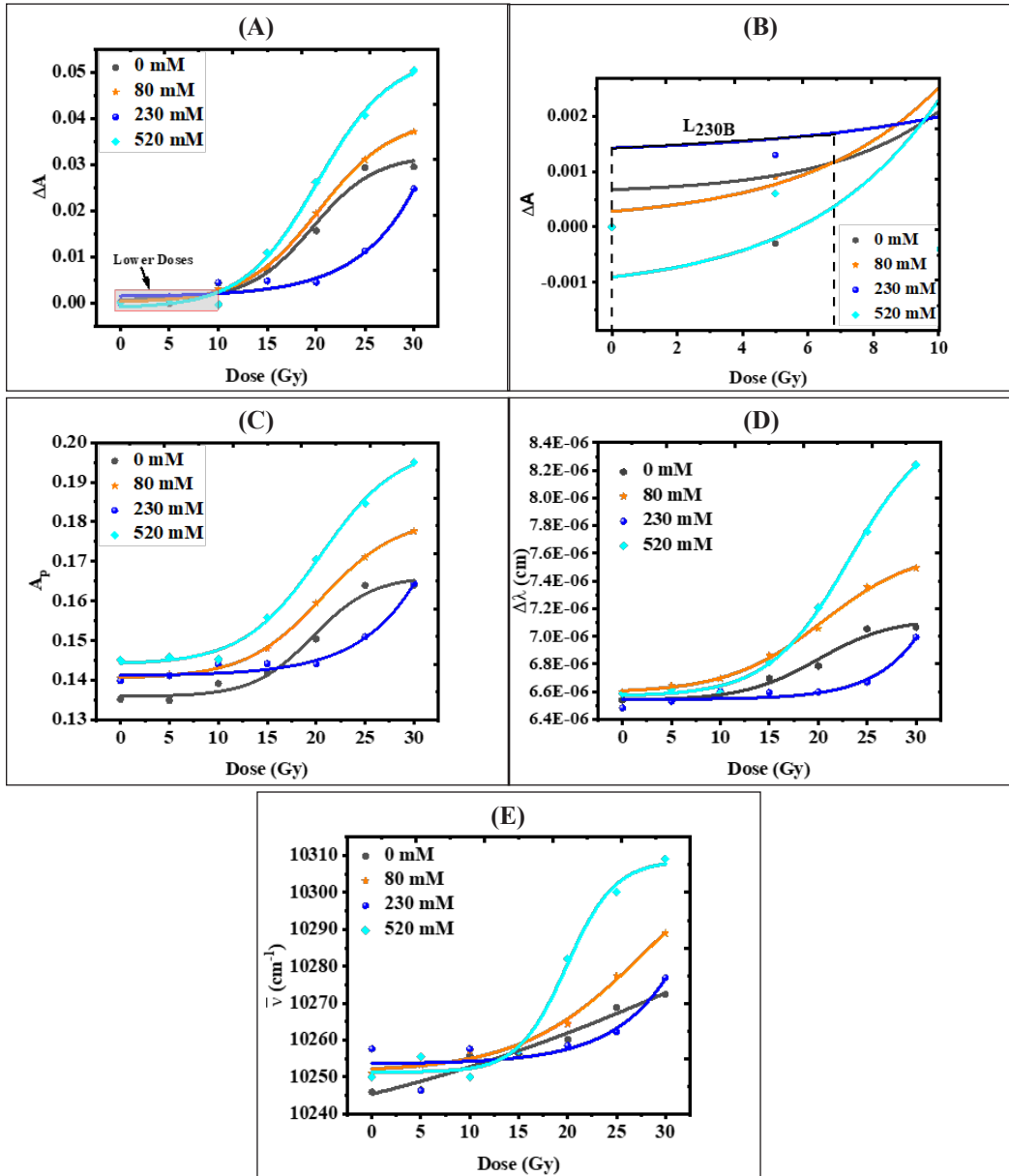


Figure 4. The relationship between the absorbed dose and the measured responses is (A) change in absorbance, (C) peak absorbance, (D) bandwidth, and (E) wave number. (B) is an enlarged portion of the lower dose region shown in (A)

The curves in Figure 4 (A)–(E) depict dose-response patterns for the four PGDs under investigation. These curves were fitted to sigmoidal dose-response curves and can be described mathematically using Hill's Equation, represented by Equation 6.

$$y = A_1 + \frac{A_1 + A_2}{1 + 10^{(\log_x 0 - x)p}} \quad [6]$$

In this equation, y represents the measured response, x represents the dose, A_1 and A_2 denote the lower and upper response limits, and p indicates the slope measured at the steepest point ($x = \log_x 0$, and $y = \frac{A_1 + A_2}{2}$) (Gadagkar & Call, 2015).

The findings in Figure 4(A)–(E) demonstrate gradual response increments at lower doses, followed by more substantial and linear increments at higher doses. As the dose approaches 30 Gy, the response tends to slow again. These graphs highlight that the lower dose range, the extent of the linear region, and the point where responses slow down a second time vary with the response type and the amount of maltose present in each dosimeter. For instance, the linear dose ranges for HEMAMAL1, HEMAMAL2, HEMAMAL3, and HEMAMAL4 are approximately 14.80–24.60 Gy, 14.20–25.70 Gy, 27.00–30.00 Gy, and 14.20 Gy–25.80 Gy, respectively. Comprehensive ranges for all PGDs based on the four different response types used in this study, along with the correlation coefficient (R^2) for each, are presented in Table 1.

The nonlinearity observed in the response of PGDs at lower doses compared to higher doses is attributed to a mechanism that remains not fully understood (Adliene et al., 2020). However, it is suggested that inhibitors such as oxygen could form peroxide radicals, which can potentially terminate the polymerization reaction at lower doses. In contrast, the polymerizing system has a higher viscosity at higher doses, facilitating interactions between growing polymer chains. This impedes termination by inhibitors and results in a steeper response (Deene, 2004). Nevertheless, linearity can still be achieved at lower doses, as illustrated in Figure 4(A), the magnified section in 4(B), and 4(C)–(D), where HEMAMAL3 exhibits linear dose-response within the 0–6 Gy range. However, the gradient is comparatively lower than at higher doses (Deene, 2004).

Similar cases to this observation have been documented in the literature. For instance, the Fricke-xylenol orange (FXO) gel dosimeter, evaluated using Optical CT, displays linearity within the 1–8 Gy range and becomes sublinear for doses below or above this interval (Nezhad & Geraily, 2022). BANG PGD, as manufactured by Farajollahi et al. (1999), also demonstrates a linear region up to 10 Gy (Nezhad & Geraily, 2022). In our study, the linear regions of the dosimeters start from doses around 13.6 Gy, with varying ranges of linearity spanning 2.7–30 Gy, as detailed in Table 1. This variation arises from differences in maltose content within each PGD and the specific response type being measured. Such observations are unsurprising, as reported linear dose ranges

in existing literature are dependent upon PGD's composition, irradiation techniques, and scanning techniques. For example, the PAMPSGAT PGD prepared from 2-Acrylamido-2-MethylPropane Sulfonic acid (AMPS), and scanned via MRI, exhibits a linear dose range within 10–40 Gy (Rashidi et al., 2020). Similarly, NIBMAGAT, synthesized from N-(Isobutoxymethyl) acrylamide monomer and evaluated through UV-Vis readout and NMR, demonstrates linearity within 5–20 Gy, with a linear range of 15 Gy (Lotfy et al., 2017). VIPAR dosimeter, evaluated by Kipouros et al. (2001), is reported to maintain linearity up to 40 Gy (Nezhad & Geraily, 2022).

Table 1

The linearity and correlation coefficients of fitting to the sigmoidal dose-response curve of the four PGDs under study, with different types of responses, are shown

Type of Response	Maltose Conc. (mM)	D ₁ (Gy)	D ₂ (Gy)	Linearity (Gy)	R ²
ΔA	0	14.80	24.60	9.80	0.9840
	80	14.20	25.70	11.50	0.9997
	230	27.00	30.00	3.00	0.9792
	520	14.20	25.80	11.60	0.9957
A _p	0	15.20	24.20	9.00	0.9834
	80	15.30	25.70	10.40	1.0000
	230	25.70	30.00	4.30	0.9817
	520	14.70	26.00	11.30	0.9964
$\Delta\lambda$	0	14.20	26.70	12.50	0.9792
	80	13.60	27.80	14.20	0.9953
	230	27.00	30.00	3.00	0.9489
	520	17.30	28.10	10.80	0.9840
$\tilde{\nu}$	0	0.00	30.00	30.00	0.9643
	80	19.30	30.00	10.70	0.9920
	230	27.30	30.00	2.70	0.8253
	520	16.00	24.10	8.40	0.9616

D₁ = beginning of the linear dose region, D₂ = end of the linear dose region, and R² = correlation coefficient

Unlike other PGDs, HEMAMAL1, depicted in Figure 4(E), demonstrates fitting to both sigmoidal dose-response curve (R² = 0.9643) and linear curve (R² = 0.9578) within the 0–30 Gy range, based on changes in bandwidth. It displays a gradient of 0.9152 cmGy⁻¹. Similarly, the VIPET dosimeter was reported to exhibit wide linearity up to 30 Gy before saturation, based on R₂-dose response (Watanabe et al., 2022).

The outcomes in Table 1 show the broadening of the linear region with increasing maltose concentration, except for HEMAMAL3, based on changes in absorbance and peak absorbance responses. This reveals maltose's ability to enhance HEMA PGD's linear

range. The effect of maltose concentration in elevating peak absorbance and shifting λ_{\max} at doses of 5, 10, 15, 20, 25, and 30 Gy is depicted in Figure 5(A) and (B), respectively.

Combining the curves in Figure 4(A)-(E) with Table 1 reveals a robust correlation between absorbed dose and change in absorbance (ΔA) ($R^2 = 0.9840, 0.9997, 0.9792,$ and 0.9957 for HEMAMAL1, HEMAMAL2, HEMAMAL3, and HEMAMAL4 respectively). Similarly, correlations are evident for peak absorbance ($R^2 = 0.9834, 1.0000, 0.9817,$ and 0.9964), bandwidth ($R^2 = 0.9792, 0.9953, 0.9489,$ and 0.9840), and wave number ($R^2 = 0.9643, 0.9920, 0.8253,$ and 0.9616). The bandwidth ($\Delta\lambda$) signifies the energy range of molecular vibration, as shown in Equation 3, while the wave number ($\tilde{\nu}$) represents molecular vibration frequency, as illustrated in Equations 2–4. These correlations hint at the potential utilization of various energy aspects of molecular vibration (spectral bandwidth), intensity/amplitude (peak absorbance), and frequency (wave number) for translating into absorbed doses.

Effect of Maltose Concentration on Radiation Dose Response

Maltose concentration is observed to impact the response of the studied PGDs, as evident in Figures 4(A)—(E) and Table 1. The impact across varying absorbed dose levels is illustrated in Figures 5(A) and 5(B) based on peak absorbance (A_p) and λ_{\max} , respectively.

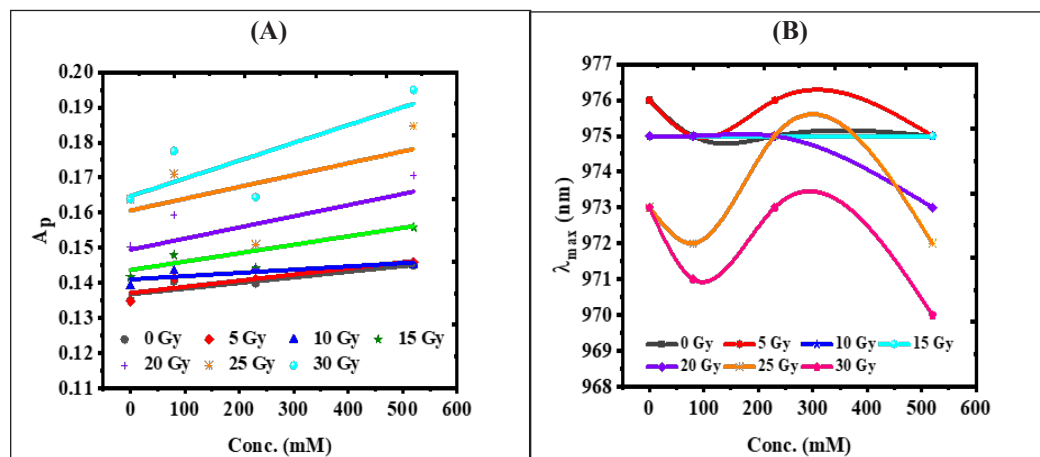


Figure 5. The effect of maltose concentration (A) to increase the peak absorbance and (B) to shift the λ_{\max} for absorbed doses of 5, 10, 15, 20, 25, and 30 Gy

An increase in A_p and a decrease in λ_{\max} serve as indicators of increased polymerization within the PGD. The overlap between the curves for 10 Gy and 15 Gy and the curve for 0 Gy, as observed in Figure 5(B), can, therefore, suggest a deceleration in polymerization when the absorbed dose exceeds 5 Gy until 15 Gy, beyond which there is a resurgence in polymerization rate, as evident from the curves for 20 Gy, 25 Gy, and 30 Gy.

Sensitivity

Sensitivity is a key characteristic of PGDs that reflects their ability to respond to radiation. It is determined by the ratio of the change in response to the change in dose, represented by the slope of the linear portion of the fitting curve (Bahrami et al., 2021; Deene, 2004). The sensitivities of four PGDs, namely HEMAMAL1, HEMAMAL2, HEMAMAL3, and HEMAMAL4, sharing the same composition except for maltose concentrations irradiated within the 0-30 Gy range, are illustrated in Figure 6 based on changes in absorbance, bandwidth, peak absorbance, and wave number.

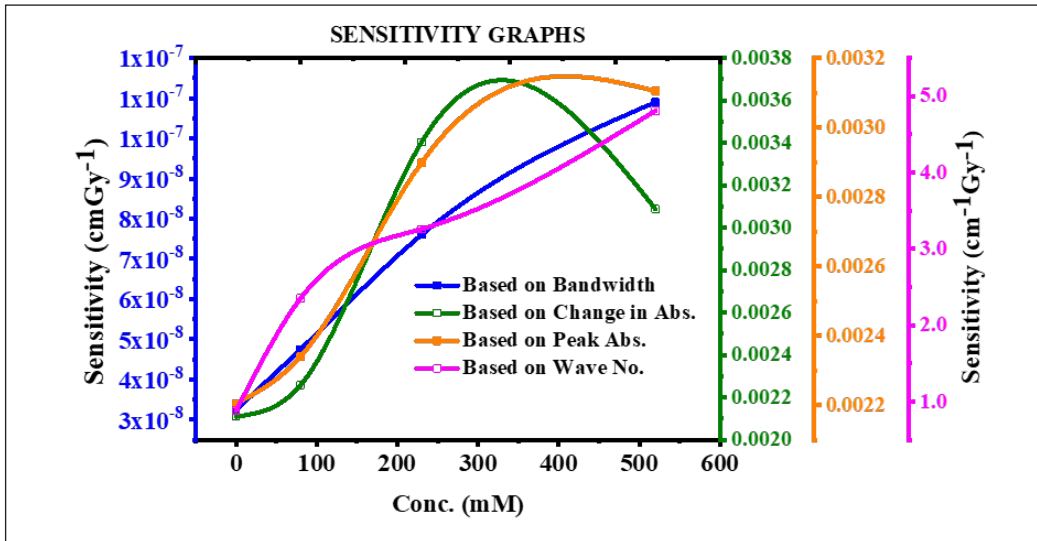


Figure 6. The sensitivity of HEMA PGDs as a function of maltose concentration is based on various measured responses

The findings in Figure 6 reveal an increase in sensitivity with rising maltose concentration. Notably, sensitivities differ across various response types, each carrying its own unit. For bandwidth measured in cm, sensitivity is expressed as cm Gy⁻¹. In terms of bandwidth, sensitivity increases with maltose concentration up to 520 mM. Sensitivity calculated based on wave number (measured in cm⁻¹) is also expressed in cm⁻¹Gy⁻¹. In this context, wave number sensitivity gradually increases within 100-200 mM and a more substantial increase or steeper curve within maltose concentrations of 0-100 mM and 200-520 mM.

Sensitivities based on peak absorbance and change in absorbance are derived from the slope of Beer Lambert's law in equation 1, and they share the unit (cm⁻¹Gy⁻¹). These two responses reveal sensitivities reaching peak values of 0.0037 cm⁻¹Gy⁻¹ at 329 mM and 0.0032 cm⁻¹Gy⁻¹ at 406 mM for change in absorbance and peak absorbance responses,

respectively, after which they begin to decline. In parallel, we are concurrently pursuing research to determine the optimal maltose concentration for HEMA PGD, utilizing the UV-Vis readout technique and exploring various options for baseline correction and reference samples.

This outcome underscores the dependence of the sensitivity of PGDs on the composition of their components and the readout technique employed. In a previous study, NIBMAGAT gel dosimeters irradiated within the 0-30 Gy range exhibited a sensitivity of $0.016 \text{ cm}^{-1}\text{Gy}^{-1}$ based on UV-Vis readout and $0.0775 \text{ s}^{-1}\text{Gy}^{-1}$ based on NMR (Lotfy et al., 2017). Notably, sensitivity based on UV-Vis can also vary for the same dosimeter, depending on the λ_{max} . As an example, the sensitivity of HEMATAG PGD, composed of HEMA as the monomer, was reported as 0.017, 0.015, 0.013, 0.011, and $0.006 \text{ cm}^{-1}\text{Gy}^{-1}$ at $\lambda_{\text{max}} = 500, 550, 600, 650, \text{ and } 700 \text{ nm}$ respectively (Ishak et al., 2015).

Temporal Stability

A study on the stability of PGD responses after irradiation reveals the continuation of polymerization for several hours. It is attributed to the net flux of fresh monomers from regions of low dose to regions of high dose, where they react with long-living polymer radicals in that region. It can also result from auto-polymerization of monomers or structural changes in the gel matrix. However, this effect is unwanted as it could lead to overestimating the absorbed dose (Aliasgharzadeh et al., 2022; Deene, 2004). The temporal stability of HEMAMAL2 was evaluated and is presented in Figure 7.

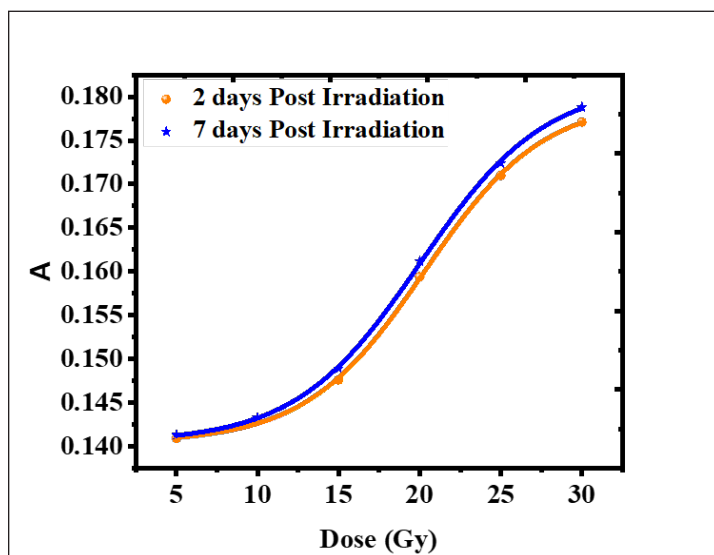


Figure 7. The response of HEMAMAL2 scanned 2 days and 7 days after irradiation

Figure 7 depicts the response curves of HEMAMAL2 scanned 2 days and 7 days post irradiation. These two curves are compared based on the parameters A_1 , A_2 , $\log_x 0$, and p , which describe the sigmoidal dose-response curve given in Equation 6. The comparison results are presented in Table 2.

Table 2

Comparison between the various parameters of HEMAMAL2 scanned 2 days and 7 days post-irradiation

Post Irrad.	A_1	A_2	$\text{Log}_x 0$	p ($\text{cm}^{-1}\text{Gy}^{-1}$)	R^2
2 days	0.1404	0.1796	20.3020 ± 0.17	0.1291 ± 0.01	0.9998
7 days	0.1405	0.1815	20.0347 ± 0.20	0.1134 ± 0.01	0.9995
Dev.]	0.0001	0.0019	0.2673	0.0057	
%Dev.	0.0712%	1.0579%	1.3166%	4.7859%	

Post Irrad. = Post irradiation time, Dev. = deviation, and %Dev. = Percentage deviation

Table 2 shows that the change in absorbance scanned 7 days post-irradiation deviated from its response 2 days post-irradiation by approximately 0.07% in A_1 , 1.1% in A_2 , 1.3% in $\log_x 0$, and 4.8% in p . The standard errors in A_1 and A_2 are in the order of 10^{-4} and are thus considered negligible. This outcome is consistent with temporal stability up to 8 days post-irradiation based on transverse relaxation rate (R_2) and optical absorbance readout techniques reported in another study (Lotfy et al., 2017). Similar stability was observed in the PAKAG PGD 7 days post-irradiation (Rashidi et al., 2020).

Temperature Independence

Temperature can significantly impact the response of irradiated PGDs. This effect may stem from a decrease in viscosity as temperature rises (Deene, 2004). The impact of scanning temperature on HEMAMAL2's response was assessed at two distinct temperatures: 22°C and 25°C, as illustrated in Figure 8.

The two curves in Figure 8 are comparable based on values like A_1 , A_2 , $\log_x 0$, p , and R^2 , provided in Table 3.

Table 3

Comparison between the response of HEMAMAL2 scanned at 22°C and at 25°C

Scan. Temp.	A_1	A_2	$\text{Log}_x 0$	p ($\text{cm}^{-1}\text{Gy}^{-1}$)	R^2
22°C	0.1288	0.1678	17.6639 ± 4.6892	0.0872 ± 0.1063	0.9267
25°C	0.1312	0.1670	16.0286 ± 4.8687	0.1099 ± 0.1731	0.8680
Dev.]	0.0024	0.0008	1.6353	0.0227	
% Dev.	1.8634%	0.4768%	9.2579%	26.0321%	

Scan. Temp. = Scanning Temperature

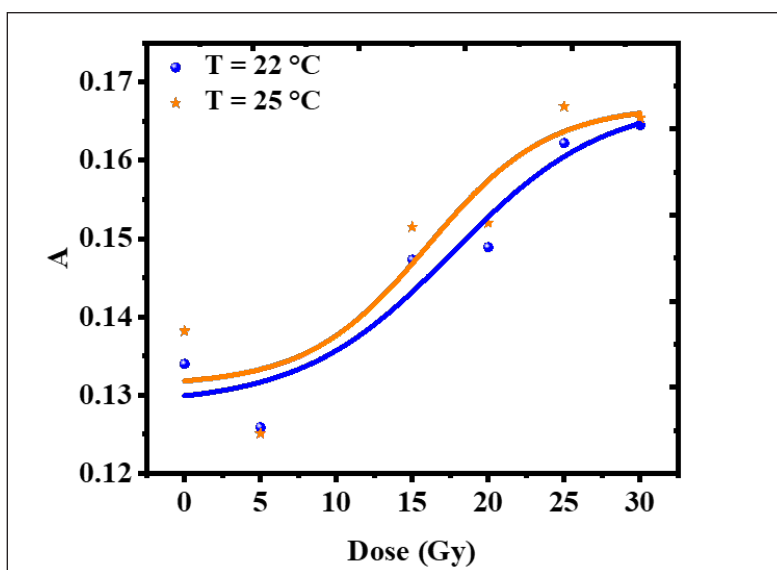


Figure 8. The sigmoidal dose-response curves of HEMAMAL2 scanned at 22°C and 25°C based on absorbance

The examination of Table 3 reveals differences in the lower and upper asymptotes A_1 and A_2 at 22°C and 25°C, which are approximately 1.9% and 0.5%, respectively. The SE values for A_1 and A_2 are 10^{-3} and thus not deemed significant. It suggests relative stability in the span of the dosimeter's response at both temperatures. This finding aligns with the stability observed in the PASSAG gel dosimeter's response, as measured by R_2 when scanned within the temperature ranges of 15°C–18°C and 20°C–24°C (Aliasgharzadeh et al., 2022).

However, the sensitivity (p) at 25°C deviates by $0.0227 \text{ cm}^{-1}\text{Gy}^{-1}$ (approximately 26.0%) from that at 22°C. This discrepancy can be attributed to the shifting back of the steepest point on the curve to lower dose by 1.6 Gy when scanned at 25°C compared to 22°C, owing to the nature of the Hill's curve. This shift likely arises from structural change or increased mobility of the polymerized and crosslinking molecules at higher temperatures, as this significantly affects the PGD's dose response (Deene, 2004).

Applicability of NIR for PGD Evaluation in Clinical Settings and Future Research

NIR spectroscopy can practically be employed for PGD evaluation in clinical settings by installing a high-quality UV-Vis-IR spectrophotometer with a sample holder suitable for various shapes and sizes of phantoms. Some manufacturers have recently provided two or more sample holders that can be substituted for various shapes and sizes. The device shall be accurately calibrated, evaluated and standardized for consistent dose evaluation.

Future research on translating molecular vibrational parameters into 3D images could involve inventing NIR spectral analysis software and algorithms to be integrated into imaging devices or real-time displays that can correlate molecular vibrational changes with the absorbed dose to map 3D dose distribution. Although this could be more complex than ordinary UV-Vis-IR spectroscopy, it might be less time-consuming and more cost-effective.

CONCLUSION

HEMA-based PGDs with maltose additive were fabricated, irradiated within the 0–30 Gy range, and subsequently scanned using a UV-Vis-IR spectrophotometer spanning 750–1100 nm. The outcomes demonstrated the feasibility of translating molecular vibrational frequency, amplitude/intensity, and vibration energy into absorbed doses. The linear dose range and sensitivity expanded as maltose concentration increased. The PGDs' response remained stable for up to 7 days post-irradiation, and this stability was relatively unaffected by scanning temperature. In conclusion, IR spectroscopy presents a potentially more cost-effective means of reading HEMA PGDs. Furthermore, the addition of maltose within the range of 0–520 mM exhibited the capacity to enhance both sensitivity and linear dose responses of the PGDs. These findings promise to enhance the affordability of radiotherapy procedures for underserved populations while bolstering the efficiency of PGD dosimetry in clinical radiotherapy. We finally recommend further research into translating the molecular vibrational parameters into 3D images.

ACKNOWLEDGEMENT

We appreciate the account of the Postgraduate Grant, School of Physics, USM (No Akaun: 308.AIFIZIK.415403) for financial support to purchase reagents. We also extend our gratitude to the technical assistance provided by the Department of Biomedical Imaging, Advanced Medical and Dental Institute, USM, Mr. Mohd Rizal Mohammad Rodin, and Mr. Hazhar Hassan, both from the School of Physics, USM.

REFERENCES

- Abdel-Ghany, A. M., Abu-Khadra, A. S., & Sadeq, M. S. (2020). Influence of Fe cations on the structural and optical properties of alkali-alkaline borate glasses. *Journal of Non-Crystalline Solids*, 548, Article 120320. <https://doi.org/10.1016/j.jnoncrysol.2020.120320>
- Adliene, D., Urbonavicius, B. G., Laurikaitiene, J., & Puiso, J. (2020). New application of polymer gels in medical radiation dosimetry: Plasmonic sensors. *Radiation Physics and Chemistry*, 168, Article 108609. <https://doi.org/10.1016/j.radphyschem.2019.108609>
- Al-Jarrah, A. M., Rahman, A. A., Shahrim, I., Razak, N. N. A. N. A., Ababneh, B., & Tousi, E. T. (2016). Effect of inorganic salts and glucose additives on dose–response, melting point and mass density of genipin gel dosimeters. *Physica Medica*, 32(1), 36–41. <https://doi.org/10.1016/j.ejmp.2015.09.003>

- Aliasgharzadeh, A., Anaraki, V., Khoramian, D., Ghorbani, M., & Farhood, B. (2022). The impact of various amounts of fabricating components on the response of PASSAG polymer gel dosimeter: An optimization study. *Radiation Physics and Chemistry*, 190, Article 109804. <https://doi.org/10.1016/j.radphyschem.2021.109804>
- Bahrami, F., Abtahi, S. M. M., Sardari, D., & Bakhshandeh, M. (2021). Investigation of a modified radiochromic genipin-gel dosimeter: Dosimetric characteristics and radiological properties. *Journal of Radioanalytical and Nuclear Chemistry*, 328(1), 19–31. <https://doi.org/10.1007/s10967-021-07635-w>
- Darwish, S. M., & Darwish, I. M. (2022). Spectroscopic investigation of tau protein conformational changes by static magnetic field exposure. *Journal of Physics Communications*, 6(7), Article 075004. <https://doi.org/10.1088/2399-6528/ac7d3a>
- Deene, Y. D. (2022). Radiation dosimetry by use of radiosensitive hydrogels and polymers: Mechanisms, state-of-the-art and perspective from 3D to 4D. *Gels*, 8(9), Article 599. <https://doi.org/10.3390/gels8090599>
- Deene, Y. D. (2004). Essential characteristics of polymer gel dosimeters. *Journal of Physics: Conference Series*, 3, 34–57. <https://doi.org/10.1088/1742-6596/3/1/006>
- Farajollahi, A. R., Bonnett, D. E., Ratcliffe, A. J., Aukett, R. J., & Mills, J. A. (1999). An investigation into the use of polymer gel dosimetry in low dose rate brachytherapy. *The British Journal of Radiology*, 72(863), 1085–1092. <https://doi.org/10.1259/bjr.72.863.10700826>
- Gadagkar, S. R., & Call, G. B. (2015). Computational tools for fitting the hill equation to dose-response curves. *Journal of Pharmacological and Toxicological Methods*, 71, 68–76. <https://doi.org/10.1016/j.vascn.2014.08.006>
- Ishak, S. A., Iskandar, S. M., & Rahman, A. A. (2015). Sensitivity of HEMATEG induced by radiation dose in the diagnostic X-Ray energy range. *Advanced Materials Research*, 1087, 267–271. <https://doi.org/10.4028/www.scientific.net/AMR.1087.267>
- Jaszczak, M., Maras, P., & Kozicki, M. (2020). Characterization of a new N-vinylpyrrolidone-containing polymer gel dosimeter with Pluronic F-127 gel matrix. *Radiation Physics and Chemistry*, 177, Article 109125. <https://doi.org/10.1016/j.radphyschem.2020.109125>
- Javaheri, N., Yarahmadi, M., Refaei, A., & Aghamohammadi, A. (2020). Improvement of sensitivity of X-ray CT reading method for polymer gel in radiation therapy. *Reports of Practical Oncology & Radiotherapy*, 25(1), 100–103. <https://doi.org/10.1016/j.rpor.2019.12.017>
- Kipouros, P., Pappas, E., Baras, P., Hatzipanayoti, D., Karaiskos, P., Sakelliou, L., Sandilos, P., & Seimenis, I. (2001). Wide dynamic dose range of VIPAR polymer gel dosimetry. *Physics in Medicine and Biology*, 46(8), 2143–2159. <https://doi.org/10.1088/0031-9155/46/8/308>
- Kozicki, M., Berg, A., Maras, P., Jaszczak, M., & Dudek, M. (2020). Clinical radiotherapy application of N-vinylpyrrolidone-containing 3D polymer gel dosimeters with remote external MR-reading. *Physica Medica*, 69, 134–146. <https://doi.org/10.1016/j.ejmp.2019.11.014>
- Lotfy, S., Basfar, A. A., Mofteh, B., & Al-Moussa, A. A. (2017). Comparative study of nuclear magnetic resonance and UV-visible spectroscopy dose-response of polymer gel based on N-(Isobutoxymethyl) acrylamide. *Nuclear Instruments and Methods in Physics Research, Section B: Beam Interactions with Materials and Atoms*, 413, 42–50. <https://doi.org/10.1016/j.nimb.2017.09.033>

- Masithoh, R. E., Pahlawan, M. F. R., Saputri, D. A. S., & Abadi, F. R. (2023). Visible-near-infrared spectroscopy and chemometrics for authentication detection of organic soybean flour. *Pertanika Journal of Science and Technology*, 31(2), 671–688. <https://doi.org/10.47836/pjst.31.2.03>
- Mustaqim, A. S., Yahaya, N. Z., Razak, N. N. A., & Zin, H. (2020). The dose enhancement of MAGAT gel dosimeter doped with zinc oxide at 6 MV photon beam. *Radiation Physics and Chemistry*, 172, Article 108739. <https://doi.org/10.1016/j.radphyschem.2020.108739>
- Nezhad, Z. A., & Geraily, G. (2022). A review study on application of gel dosimeters in low energy radiation dosimetry. *Applied Radiation and Isotopes*, 179, Article 110015. <https://doi.org/10.1016/j.apradiso.2021.110015>
- Nezhad, Z. A., Geraily, G., Parwaie, W., & Zohari, S. (2021). A novel investigation of the effect of different concentrations of methacrylic acid on the dose response of MAGAT gel dosimeter in intraoperative radiotherapy. *Radiation Physics and Chemistry*, 179, Article 109214. <https://doi.org/10.1016/j.radphyschem.2020.109214>
- Ozaki, Y. (2021). Infrared spectroscopy—mid-infrared, near-infrared, and far-infrared/terahertz spectroscopy. *Analytical Sciences*, 37(9), 1193–1212. <https://doi.org/10.2116/analsci.20R008>
- Pratiwi, R. A., Bayu, A., & Nandiyanto, D. (2022). How to read and interpret UV-VIS spectrophotometric results in determining the structure of chemical compounds. *Indonesian Journal of Educational Research and Technology*, 2(1), 1–20. <https://doi.org/10.17509/xxxx.vxix>
- Rabaeh, K. A., Hammoudeh, I. M. E., Oglat, A. A., Eyadeh, M. M., Abdel-Qader, A. J., Aldweri, F. M., & Awad, S. I. (2021). Polymer gel containing N,N'-methylene-bis-acrylamide (BIS) as a single monomer for radiotherapy dosimetry. *Radiation Physics and Chemistry*, 187, Article 109522. <https://doi.org/10.1016/j.radphyschem.2021.109522>
- Rashidi, A., Abtahi, S. M. M., Saeedzadeh, E., & Akbari, M. E. (2020). A new formulation of polymer gel dosimeter with reduced toxicity: Dosimetric characteristics and radiological properties. *Zeitschrift Für Medizinische Physik*, 30(3), 185–193. <https://doi.org/10.1016/j.zemedi.2020.02.002>
- Renner, I. E., & Fritz, V. A. (2020). Using near-infrared reflectance spectroscopy (NIRS) to predict glucobrassicin concentrations in cabbage and brussels sprout leaf tissue. *Plant Methods*, 16(1), Article 136. <https://doi.org/10.1186/s13007-020-00681-7>
- Shih, T. Y., Chen, W. T., Kuo, W. C., & Wu, J. (2022). Application of polarization-sensitive optical coherence tomography in measurement of gel dosimeters. *Journal of Medical and Biological Engineering*, 42(5), 621–629. <https://doi.org/10.1007/s40846-022-00711-w>
- Shukor, N. S. A., Musarudin, M., Abdullah, R., & Aziz, M. Z. A/ (2022). Dose distribution of ¹⁹²Ir HDR brachytherapy source measurement using gafchromic® EBT3 film dosimeter and TLD-100H. *Pertanika Journal of Science and Technology*, 30(1), 691–708. <https://doi.org/10.47836/pjst.30.1.37>
- Watanabe, Y., Maeyama, T., Mizukami, S., Tachibana, H., Terazaki, T., Takei, H., Muraishi, H., Gomi, T., & Hayashi, S. I. (2022). Verification of dose distribution in high dose-rate brachytherapy for cervical cancer using a normoxic N-vinylpyrrolidone polymer gel dosimeter. *Journal of Radiation Research*, 63(6), 838–848. <https://doi.org/10.1093/jrr/rrac053>

Zapata, F., López-Fernández, A., Ortega-Ojeda, F., Quintanilla, G., García-Ruiz, C., & Montalvo, G. (2021).
Introducing ATR-FTIR spectroscopy through analysis of acetaminophen drugs: Practical lessons for
interdisciplinary and progressive learning for undergraduate students. *Journal of Chemical Education*,
98(8), 2675–2686. <https://doi.org/10.1021/acs.jchemed.0c01231>

The Impact of Hydrocarbon R290 Refrigerant on Air Conditioner Performance and Environmental Sustainability

Ferdinand Ng Siek Khai^{1,2} and Nurul Sabihah Zakaria^{1*}

¹*School of Distance Education, Universiti Sains Malaysia (USM), 11800 Minden, Pulau Pinang, Malaysia*

²*Ener-Save Green Air Conditioner Sdn Bhd, 29A, Jalan Ronggeng 11, Taman Skudai, Johor Bahru, 81300 Johor, Malaysia*

ABSTRACT

This study addresses the critical need for environmentally friendly refrigerants in residential air conditioning systems and explores the advantages of hydrocarbon R290 as an alternative to synthetic options. Given the indispensability of air conditioning for human comfort, the shift towards eco-friendly refrigerants becomes paramount. This research aims to demonstrate the superiority of natural refrigerants, particularly hydrocarbon R290, over conventional synthetic alternatives in air conditioning. Through a comparison of two similar air conditioners charged with R290 and R22 refrigerants, the study evaluates their performance and environmental implications. The initial phase involves a thorough analysis of hydrocarbon R290's physical properties and compatibility with synthetic refrigerants. The findings underscore its remarkable compatibility, directly replacing the environmentally harmful Hydrochlorofluorocarbon R22 refrigerant. Practical experiments and theoretical pressure-enthalpy chart analyses establish that R290-equipped air conditioners significantly enhance the coefficient of performance (COP). In practical applications, COP sees a 21.74% boost, while theoretical analysis indicates a 7.33% increase. Furthermore, adopting R290 contributes to a 17.5% reduction in CO₂ emissions through reduced power consumption. Environmental sustainability is a pivotal aspect of refrigerant evaluation; the study furnishes compelling evidence favouring hydrocarbon R290. The research demonstrates that R290 is approximately 1,383 times more environmentally friendly than R22 in terms of global warming potential and refrigerant mass. Safety, a paramount concern in adopting new refrigerants, is also

addressed. R290's mass charge aligns with international standards, and its concentration remains 17.37% below the lower flammability limit, ensuring secure usage in confined spaces.

Keywords: Hydrocarbon R290, air conditioner, coefficient of performance, global warming potential, environmental sustainability, natural refrigerant

ARTICLE INFO

Article history:

Received: 30 October 2023

Accepted: 3 October 2024

Published: 21 February 2025

DOI: <https://doi.org/10.47836/pjst.33.2.24>

E-mail addresses:

skng@ener-save.biz (Ferdinand Ng Siek Khai)

nurulsabihah@usm.my (Nurul Sabihah Zakaria)

*Corresponding author

INTRODUCTION

Global issues such as the energy crisis, the ozone-depleting threat, the impact of global warming and climate change require more public attention. How are these pressing issues interrelated to the heating, ventilation and air conditioning (HVAC) industry?

In the earlier stage of phasing out ozone-depleting substances, most appliances were replaced by non-ozone-depleting refrigerants, mainly formulated by fluorinated gases (F-gases), specifically hydrofluorocarbon (HFC), as an alternative to ozone-depleting refrigerants. However, Europe considers these F-gases powerful greenhouse gases (European Commission, 2022). As a result, some European countries have opted to switch from HFCs to other superior refrigerants or natural refrigerants.

The Kigali Amendment to the United Nations (UN) Montreal Protocol is another effort to reduce global temperature after the success of the UN Montreal Protocol program. It aims to continue addressing the climate change problem by eliminating powerful greenhouse gases and, if faithfully implemented, could control the full rise of 0.5 degrees Celsius in global temperature by the end of the century (United Nations Climate Change, 2016) (2100).

Malaysia ratified the Kigali Amendment to the UN Montreal Protocol on 21 October 2020 (Ministry of Environment and Water, 2020). As a result, Malaysia is obligated to phase down the high global warming HFCs based on the Malaysian Baseline. The first phase down of 10% is scheduled for 2029, with a further 20% of the balance from the baseline allowed for essential uses by 2045.

The hydrocarbon R290 refrigerant is highly flammable, but it is suitable for use as a conversion option for existing R22 refrigerant air conditioners without requiring major retrofitting of the existing system. The primary and only challenge with hydrocarbon refrigerants is their high flammability. However, this concern can be addressed through refrigerant mass charge control, and the HVAC design must comply with international A3-class refrigerant safety standards. Even though the hydrocarbon refrigerant air conditioners require such a safety design, the manufacturing cost is not significantly affected because the compressor is built with explosion-proof mild steel, the copper tubes are sparkless, and the system operates under an oxygen-free circuit. Moreover, the cost of natural refrigerants is much lower than that of synthetic refrigerants. The molecular mass of hydrocarbon R290 refrigerant is lighter than that of existing R22 refrigerant. However, it has a similar volumetric charge, which can further reduce the compressor power consumption and enhance lifespan.

Synthetic refrigerants are widely used in the market but significantly impact global warming. They are super greenhouse gases. These synthetic refrigerants also contribute to the pollution of freshwater sources through trifluoroacetate (TFA) in the atmosphere (Rusyanto, 2021). As scientists have reported, TFA is a chemical compound generated by the latest invented synthetic refrigerants known as hydrofluoric-olefins (HFOs).

Figure 1 shows global greenhouse gas emissions by variable types of gases. The source is the Intergovernmental Panel on Climate Change (IPCC) (2014), based on global emissions from 2010 (EPA, n.d.).

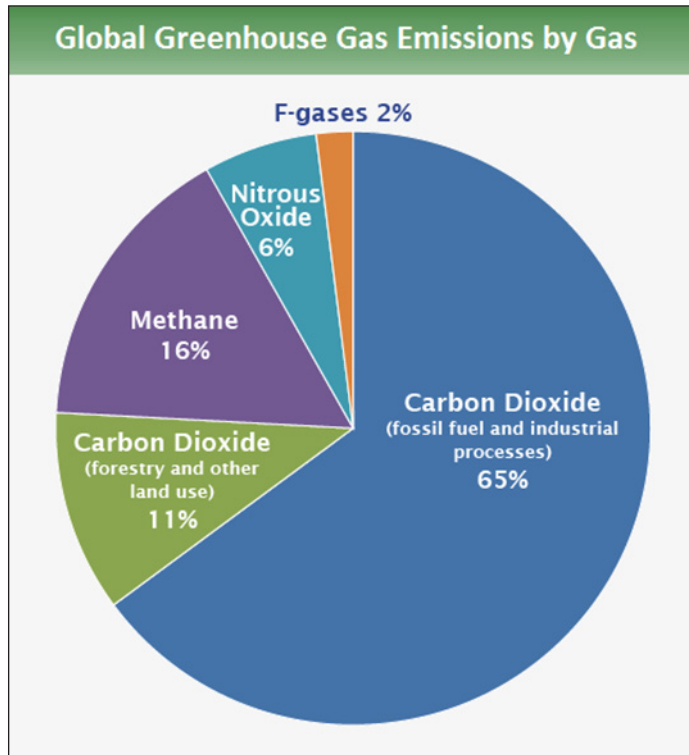


Figure 1. Global greenhouse gas emissions

The air conditioner industry is phasing out the ozone-depleting refrigerants and replacing them with newer alternatives. However, most of the refrigerants used today are high global warming substances. Surprisingly, just two per cent of F-gas refrigerants are the main contributors to Global Warming Source. The impact of this 2% from the F-gases can be significant. On the other hand, if natural refrigerants replace these refrigerants, the reduction in global warming could be substantial and beneficial for mankind. According to the Sustainable Energy Development Authority (SEDA) Malaysia’s 2016 energy and CO₂ emissions report, Peninsular Malaysia’s CO₂ emission coefficient rate is 0.639 kg per kWh of electrical usage (SEDA Malaysia, 2019).

As air conditioning systems have become essential for human comfort, the transition to eco-friendly refrigerants is becoming increasingly important. This research aims to demonstrate the superiority of natural refrigerants, specifically hydrocarbon R290, over traditional synthetic refrigerants in air conditioning applications.

MATERIALS AND METHODS

Preliminary prototype setups are required for a system with R290 refrigerant, and the other unit is charged with R22 Refrigerant for data findings and studying. Instruments to measure the temperature, pressure, airflow and electrical parameters are installed on the prototypes. The important part of prototype setup is ensuring the systems are free from leakage problems. Any faults should be rectified before being charged with refrigerant. Prototypes are vacuumed thoroughly and charged with R290 and R22 refrigerant, respectively. Once the systems have been completely functionally tested, the results will be observed and fine-tuned to meet the required discharge pressure, suction pressure, temperature, air flow rate and power consumption. Neither system should be undercharged nor overcharged with refrigerant. The data findings will further plot the pressure-enthalpy chart and compute the obtained cooling capacity. Subsequently, other related results will be derived via recorded raw data such as refrigerant mass flow, work done during compression, electrical power, CO₂ equivalent emissions and coefficient of performance.

The thermodynamic properties and compatibility study were obtained from the “Ener-Save Hydrocarbon Refrigerants Training Manual” (Ng, 2021). This information is essential to identify whether the existing domestic air conditioner is suitable for conversion into a Hydrocarbon natural refrigerant system or whether any modification is required to retrofit it.

Table 1 contains the basic information related to refrigerants’ physical and chemical properties and related information on R290 refrigerant and R22 refrigerant. R290 refrigerant is an organic natural refrigerant; it is propane hydrocarbon with a chemical compound of C₃H₈, and the R22 refrigerant is a synthetic refrigerant with a chemical compound of hydrochlorofluorocarbon (CHClF₂). The R290 refrigerant is an environmentally friendly refrigerant with zero ozone-depleting potential and negligible global warming potential compared to the R22 refrigerant. The atmospheric life of R290 refrigerant is much shorter than that of R22 refrigerant, making it less harmful to the environment.

While the boiling point of R290 refrigerant is approximately the same as that of R22 refrigerant, due to its lower molecular weight, R290 refrigerant appears to be lighter than R22 refrigerant. The R290 refrigerant also has a higher heat absorption value than the R22 refrigerant, attributed to its latent heat of vaporization value at its boiling point.

Mineral oil is the compressor lubricant oil compatible with R290 and R22 refrigerants. This compatibility enables the conversion of existing R22 refrigerant domestic air conditioners to R290 refrigerant, in addition to the general compatibility with other elastomeric materials.

According to the safety classification from ASHRAE Standard 34, refrigerants are categorized into different safety classes based on their chemical characteristics (ASHRAE, 2022). R290 refrigerant is classified as A3 due to its lower toxicity and high flammability. On the other hand, the R22 refrigerant is classified as an A1 refrigerant with lower toxicity and non-flammability.

Table 1

Physical properties, chemical properties, and related information of R290 refrigerant and R22 refrigerant

Descriptions	Column of Comparison	
Refrigerant Type	R290	R22
Chemical Type	HC (Hydrocarbon)	HCFC (Hydrochloro- fluorocarbon)
Global Warming Potential (GWP), CO ₂ = 1, 100 years basis	3	1,810
Ozone Depleting Potential (ODP)	0	0.055
Atmospheric Life	< 1 year	12 years
Boiling Point (°C)	-42	-41
Molecular Weight,	44.1 g/mol	86.5 g/mol
Latent Heat of Vaporisation @ Boiling Point kJ/kg	426	233
Compressor Lubricant Oils	Mineral or Synthetic Oil	Mineral Oil Only
ASHRAE Standard 34 Refrigerant Safety Classification	A3 Lower toxicity, highly flammable	A1 Lower toxicity, Non-flammable
Leak Detection Method	Hydrocarbon	Halide
Autoignition (°C)	480	NA
Lower Flammability Limit (LFL), kg/m ³	0.038	NA
Toxic Thermal Decomposition	None	Phosgene Gas

The air conditioning system consists of four major components that correspond to the Carnot refrigeration cycle (Cengel & Boles, 2015). These components include the expansion valve for the adiabatic expansion process, the evaporator coil for the isothermal expansion process, the compressor for the adiabatic compression process, and the outdoor condenser coil for the isothermal compression process. This closed-loop cycle uses refrigerant as a heat transfer medium, absorbing heat from the indoor area of the house and releasing it to the outdoor environment. It represents the typical usage of an air conditioner in hot climate countries.

Practically all the different types of refrigerants have different enthalpy properties. Equation 1 gives the relationship of enthalpy, h .

$$h = E_{\text{int}} + pv \quad [1]$$

Where E_{int} is the total internal energy

Pressure-enthalpy charts will be plotted based on the actual performance of the prototype setup to simplify the determination of the work done for air conditioners using different refrigerants. This setup includes an R290 refrigerant air conditioner with pressure gauges, temperature displays, and a similar setup charged with R22 refrigerant. Figure 3 describes the plotting of the pressure-enthalpy chart; the temperatures and pressures are obtainable parameters from the prototype setup. The compressor drives the whole system as a main driver. Thus, the intention to determine the air conditioner’s coefficient of performance will focus on the compression process as it will consume external energy to perform work internally. Even though the condenser fan motor and evaporative fan motor are used to transfer internal heat from the system out to the outdoor environment and from the external heat source of the indoor house to the internal refrigeration system, respectively, the energy of such fan motor is lesser than the energy consumed by the compressor. Therefore, the main focus of the study on the theoretical performance will be narrowed to the compression process, and the formula to obtain the work done during the compression of refrigerant is as Equation 2.

$$Q_c = m_R \times (h_2 - h_1) \tag{2}$$

Where m_R is the mass flow of refrigerant

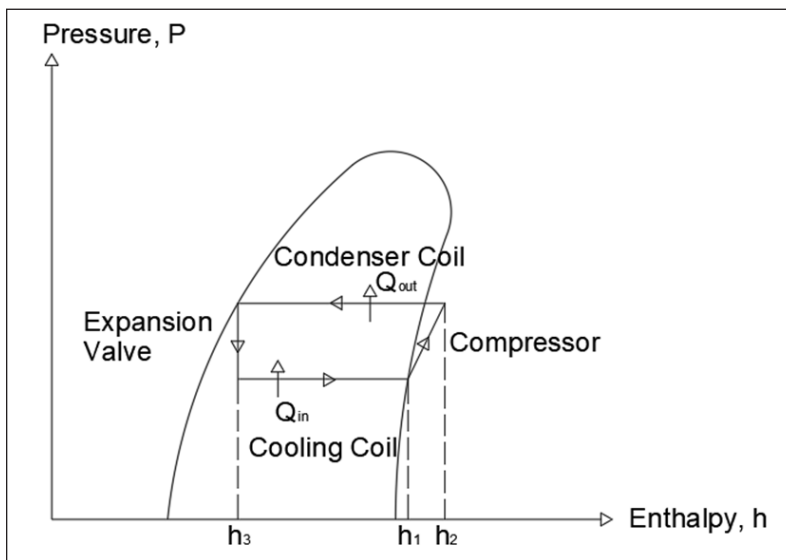


Figure 2. Pressure: Enthalpy diagram of the refrigeration system and the components involved

Ultimately, the coefficient of refrigerant performance in the system between natural R290 refrigerant and synthetic R22 refrigerant will be compared and calculated.

Firstly, the refrigerating effect per kg, R_E , can be obtained from Equation 3 before calculating the mass flow of refrigerant.

$$R_E = h_1 - h_3 \quad [3]$$

After finding the RE value, Equation 4 shows the refrigerant's mass flow, m_R . The cooling capacity is the actual cooling performance of the air conditioner's evaporative blower.

$$m_R = \text{cooling capacity} / R_E$$

Thus,

$$m_R = \text{cooling capacity} / (h_1 - h_3) \quad [4]$$

and

The work done during refrigerant compression, Q_c (Equation 5), is the interesting part of identifying the work done on the air conditioner's compressor, as it is the main driver of the closed-loop thermodynamic process.

$$Q_c = m_R \times (h_2 - h_1) \quad [5]$$

Nevertheless, the theoretical coefficient of performance (COP) for the refrigerant can be obtained from Equation 6.

$$COP = (h_1 - h_3) / (h_2 - h_1) \quad [6]$$

Classically, the cooling capacity was calculated using the imperial unit in most applications; certain conversions are required to identify whether the calculated value matches within the range of design or not. Such as:

$$1 \text{ Watt} = 3.412 \text{ btu/hour (Cooling Capacity)} = 1 \text{ Joule/s}$$

$$1 \text{ horsepower (hp)} = 741 \text{ Watt (Electrical Power)}$$

$$12,000 \text{ btu/hour} = 1 \text{ refrigeration ton (RT)}$$

Practically, the higher the specific power value, the lower the air conditioner's coefficient of performance. Higher specific power means the air conditioning system consumes more energy to produce a refrigeration ton of cooling. The specific power could be obtained from Equation 7.

$$\text{Specific Power} = \frac{\text{Electrical Power}}{\text{Refrigeration Ton}} \quad [7]$$

COP is always inversely proportional to a specific power, as shown in Equation 8.

$$\text{COP} = 12 / (\text{Specific Power} \times 3.412) \quad [8]$$

Specific heat at constant pressure (C_p) is required to raise the temperature of a unit mass of gas by one degree Celsius at constant atmospheric pressure (Khurmi & Gupta, 2008).

Total heat energy, Q , is equal to the mass of air multiplied by its specific heat at constant pressure with the differential temperature obtained, as shown in Equation 9.

$$Q = m C_p (T_{in} - T_{out}) \quad [9]$$

Where T_{in} enters air temperature (data collection from prototype), and T_{out} leaves air temperature (data collection from prototype). Hence, if the thermodynamic takes place, the derivation of heat energy Q is the cooling capacity from the evaporator and is derived in Equation 10.

$$\text{Cooling capacity, } dQ/dt = (m/dt) C_p (T_{in} - T_{out}) \quad [10]$$

Where the m/dt is the mass flow rate of air or M_f .

The mass of air is given by Equation 11.

$$\text{Mass of air, } m = \text{density of air} \times \text{volume of air} \quad [11]$$

However, the airflow from the evaporative blower is a dynamic property. The airflow rate from the evaporative blower must be measured to get the mass flow rate of air. Equation 12 is the formula to find the mass flow rate of air.

$$M_f = \text{density of air (kg/m}^3) \times \text{air flow rate (m}^3/\text{s)} \quad [12]$$

Therefore, the air conditioner's final and simplified cooling capacity can be estimated using Equation 13.

$$\text{Cooling capacity} = M_f \times C_p (T_{in} - T_{out}) \quad [13]$$

Figures 3 and 4 show a complete prototype setup with a temperature sensor, pressure gauge, power logger and air flow meter. One of the air conditioners is charged with 240 grams of R290 refrigerant, and the other is charged with 550 grams of R22 refrigerant for virtual comparison and data finding. Both systems switch on for approximately thirty minutes to achieve stabilisation before performing data collection.



Figure 3. Complete indoor evaporator blower setup with measurement gadget



Figure 4. Complete outdoor compression condenser unit setup with measurement gadget

Never forget to conduct the Hydrocarbon conversion according to the standard operating procedure (SOP) because the R290 refrigerant is hydrocarbon and highly flammable. Table 2 is the practical SOP for conducting the R290 refrigerant conversion in the R22 domestic air conditioner.

Table 2
Standard of procedure for R290 conversion

Working procedures	Instructions
Step 1	Perform a leak test after setting up the air conditioner system
Step 2	Estimate equivalent HC charge—Use conversion rate of R22 to R290
Step 3	Check the maximum practical charge limit and consult the MS2678:2017
Step 4	Ensure all tools and working areas are safe from fire hazards and prepare a fire extinguisher.
Step 5	Identify all potential sources of ignition that are out of range
Step 6	Vacuum the air conditioner system thoroughly
Step 7	Using the refrigerant mass charge method to charge in the estimated R290 refrigerant
Step 8	Put a temporary flammable zone at the drop-in working area
Step 9	Apply relevant system marking with a warning sign
Step 10	Switch on the air conditioner and fine-tune the system

The steps to identify the maximum allowable hydrocarbon refrigerant charge in a specific room are outlined in the standard, defined by the installation location. It is recommended that the Malaysian Standard MS 2678:2017 (MS2678 Working Group, 2017) be consulted, where the relevant charge size shall not be more than 20% LFL of hydrocarbon refrigerant charge. If the facility is below ground level, the maximum charge would be 1kg in all circumstances, but not more than 20% LFL of hydrocarbon refrigerants charge.

Equation 14 calculates the maximum hydrocarbon charge size per sealed system in a specific machinery room. Therefore, the gas leak will not trigger the ignition level five times lower than the LFL level. In all circumstances, the leakage event will not occur catastrophically in more than one compressor.

$$m_r = 0.20 \times (\text{LFL}) \times v_{\text{room}} \quad [14]$$

Where,

LFL = lower flammability limit of refrigerant (kg/m³) from Table 1,

v_{room} = room volume (m³)

m_r = refrigerant mass (kg)

RESULTS AND DISCUSSIONS

The study uses the “ELIWELL” IDPlus974 Thermostat for temperature display. It is a dual sensor system consisting of temperature probes 1 (Pb1) and 2 (Pb2), as shown in Figure 5. The study uses the common air ambient temperature (Figure 6) and water medium temperature (Figure 7) to cross-check the sensible detection reading on temperature probes and both temperature displays and to determine the accuracy of both temperature detections. The temperature reading was observed and recorded in Table 3.

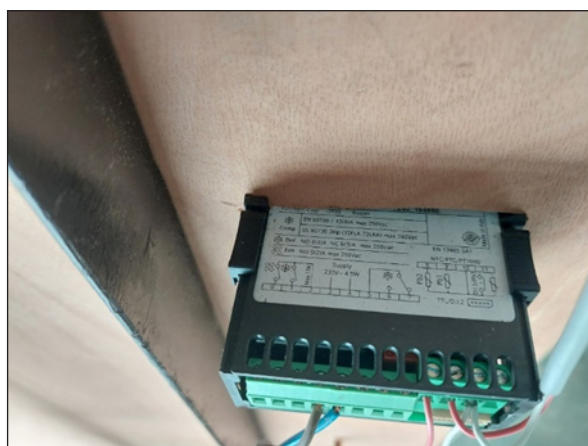


Figure 5. “ELIWELL” IDPlus974 Thermostat Schematic Diagram and Wiring Termination

Table 3

Temperature reading of the Pb1 and Pb2 in ambient air temperature and water medium temperature

Medium of Calibration	Probe 1, Pb1		Probe 2, Pb2	
	AC01 (R290)	AC02 (R22)	AC01 (R290)	AC02 (R22)
In Ambient Air (30/03/23, 10.05am)	30.2 °C	30.2 °C	30.1 °C	29.8 °C
In Water Medium (Trial 1, 30/03/23, 10.13 am)	29.4 °C	29.4 °C	29.3 °C	28.8 °C
In Water Medium (Trial 2, 30/03/23, 10.40 am)	29.4 °C	29.4 °C	29.3 °C	28.8 °C



Figure 6. Temperature sensor calibration check in ambient air



Figure 7. Temperature sensor calibration check in water medium

The temperature reading from the Probe 1 sensor is similar, either displayed from AC01 or AC02; thus, Pb1 is used as the main temperature sensor to observe the leaving air temperature. However, the Pb2 from AC01 is less than 0.1°C. Therefore, a +0.1°C calibration adjustment is required from the thermostat, but the AC02's Pb2 is required to adjust +0.4°C to match the actual reading from the thermostat installed at AC02. The calibrations of the temperature reading will be hereafter.

Both air conditioners operated for approximately thirty minutes to keep the refrigeration cycle steady. The raw data are recorded in Table 4. The R290 refrigerants are natural organic compounds, and the R22 refrigerant is synthetic.

Table 4
Air conditioners' operating parameter

Descriptions	R290 Refrigerant Air Conditioner AC01	R22 Refrigerant Air Conditioner AC02
Refrigerant Mass Charge in 9,000 btu/hr air conditioner	240 grams	550 grams
Suction Pressure in 9,000 btu/hr air conditioner	6.0 Bar/ 0.60 MPa	6.0Bar/ 0.60 MPa
Discharge Pressure in 9,000 btu/hr air conditioner	16 Bar/ 1.6 MPa	18 Bar/ 1.8 MPa
A/C Temperature Set Point (°C)	25	25
Entering Air Temperature °C, T_{in} (Calibrated)	31.5 + 0.1 = 31.6	31.2 + 0.4 = 31.6
Leaving Air Temperature °C, T_{out}	22.8	22.6
Evaporator Blower, airflow speed, m/s	4.3	4.2
Instant Voltage Reading, V	235.9	236.3
Instant Current Reading, A	3.21	3.92
Power Supply Frequency, Hz	50.1	50.0
Instant Real Power, kW	0.735	0.893
Instant Power Factor, PF	0.970	0.965
Instant Reactive Power, kVar	0.186	0.244

Referring to Table 4, the refrigerant mass charge for the R290 refrigerant air conditioner is 240 grams, while for the R22 refrigerant air conditioner, it is 550 grams. It demonstrates that the refrigerant used in the R290 air conditioner is 56.36% lighter than the R22 refrigerant. The R290 system operates at a low head pressure of approximately 1.6 MPa, despite having a similar suction pressure of 0.6 MPa for both systems. The combination of low head pressure and lighter molecular weight contributes to a reduction in compressor torque power. These characteristics further explain the ability of R290 to enhance energy savings, as the compressor requires less energy to operate the air conditioning system.

The conversion to R290 and the use of R290 refrigerant in R22 domestic air conditioners comply with safety standards. A typical 9,000 BTU/hr air conditioner is installed in a

36-cubic-meter room (3m × 4m × 3mH). The concentration of R290 refrigerant from a 9,000 BTU/hr air conditioner in the room is determined by dividing the refrigerant mass charge per sealed system by the room volume. In the case of a 9,000 BTU/hr R290 air conditioner in a room of 36 cubic meters, the concentration is 0.0066 kg/m³ in the event of refrigerant leakage. This concentration adheres to the standard that does not exceed 500g and is less than 20% of the lower flammability limit (LFL) charge limit. In fact, it is 17.37% lower than the LFL charge limit.

Cooling Capacity of R290 Air Conditioner and R22 Air Conditioner

The air conditioners were set to a temperature set point of 25°C. The set point does not affect the constant airflow temperature of the indoor evaporator since the testing site is open to the outdoor ambient air. The outdoor ambient temperature thoroughly influences the indoor temperature, thus consistently maintaining the entering air temperature above the set point. As a result, the compressor operates at a 100% load.

From the Equation 13, cooling capacity = $M_f \times C_p (T_{in} - T_{out})$

Specific heat of air at constant pressure, $C_p = 1.000 \text{ kJ/kg} \cdot ^\circ\text{C}$

Density of air at 25°C, $\rho = 1.1839 \text{ kg/m}^3$

M_f can be obtained from Equation 15; the cooling capacity is calculated separately for the R290 and R22 systems. The airflow rate of the evaporator blower is V_f .

$$V_f(\text{m}^3/\text{s}) = L \times H \times \text{air-flow speed (m/s)} \quad [15]$$

L = length of evaporator blower = 0.675m

H = height of evaporator blower = 0.080m

The airflow speed is recorded in Table 4

Cooling Capacity of R290 System

The system converted to R290 refrigerant is not working 100% to the designed cooling capacity. Calculating the actual cooling capacity is required to identify the air conditioner's performance. Thus, the parameters required to calculate the cooling capacity are taken from the data collections.

The R290 refrigerant air conditioner is currently operating at 8,254.0 BTU/hr, which is 8.29%, slightly below the designed specification of 9,000 BTU/hr. The cooling capacity falls within an acceptable range, meeting the criteria of being within plus or minus 10% of the 9,000 BTU/hr design.

Cooling Capacity R22 System

The R22 refrigerant system is not working 100% to the designed cooling capacity. Calculating the cooling capacity is required to notify the conditioner’s performance air. Thus, the parameters required to calculate the cooling capacity are taken from the data collections.

The R22 refrigerant air conditioner is currently operating at 8,245.4 BTU/hr, which is 8.38%, slightly below the designed specification of 9,000 BTU/hr. The cooling capacity falls within an acceptable range, meeting the criteria of being within plus or minus 10% of the 9,000 BTU/hr design.

Refrigeration Cycle State Analysis

Figure 8 illustrates the operation flow of a refrigeration cycle involving pressure measures. It will then plot the ideal refrigeration cycle in a pressure-enthalpy (p-h) chart. Table 5 summarizes the data found in the p-h chart for every state.

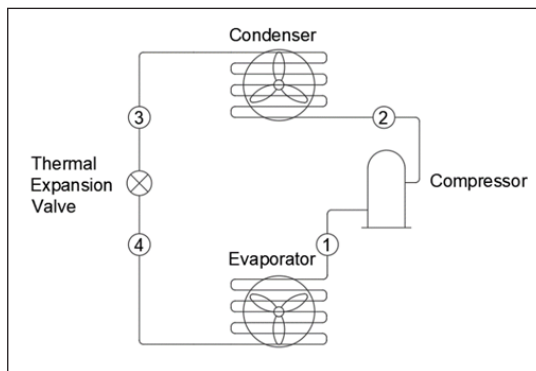


Figure 8. The simple refrigeration cycle diagram involves processes in states 1, 2, 3 and 4. It is a closed-loop cycle from state 1 to state 4 and back to state 1

Table 5
Ideal refrigeration cycle state and data finding summary

Descriptions	State 1	State 2	State 3	State 4
R290 Refrigerant Cycle	$p_1 = 6.0 \text{ Bar}/0.60\text{MPa}$ $T_1 = 13.46^\circ\text{C}$ $h_1 = 479\text{kJ/kg}$	$p_2 = 16 \text{ Bar}/1.60\text{Mpa}$ $T_2 = 49.68 \text{ }^\circ\text{C}$ $h_2 = 529\text{kJ/kg}$	$p_3 = p_2$ $T_3 = (T_2 - \text{Subcooling})$ $h_3 = h_4 = 228\text{kJ/kg}$	$p_4 = p_1$ $T_4 = (T_1 - \text{Superheat})$ $h_4 = h_3 = 228\text{kJ/kg}$
R22 Refrigerant Cycle	$p_1 = 6.0 \text{ Bar}/0.60\text{Mpa}$ $T_1 = 10.98^\circ\text{C}$ $h_1 = 407\text{kJ/kg}$	$p_2 = 18\text{Bar}/1.80\text{Mpa}$ $T_2 = 49.06 \text{ }^\circ\text{C}$ $h_2 = 438\text{kJ/kg}$	$p_3 = p_2$ $T_3 = (T_2 - \text{Subcooling})$ $h_3 = h_4 = 262\text{kJ/kg}$	$p_4 = p_1$ $T_4 = (T_1 - \text{Superheat})$ $h_4 = h_3 = 262\text{kJ/kg}$

Mass Flow of Refrigerant, Work Done and COP

From the pressure-enthalpy chart plotted in Figures 9 and 10, the refrigerating effect per kg could be obtained from Equation 3.

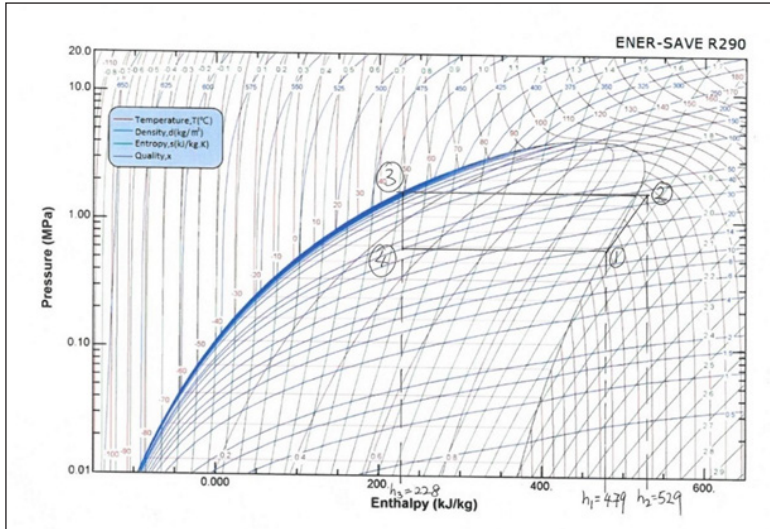


Figure 9. Pressure-enthalpy plotting of R290 air refrigeration system

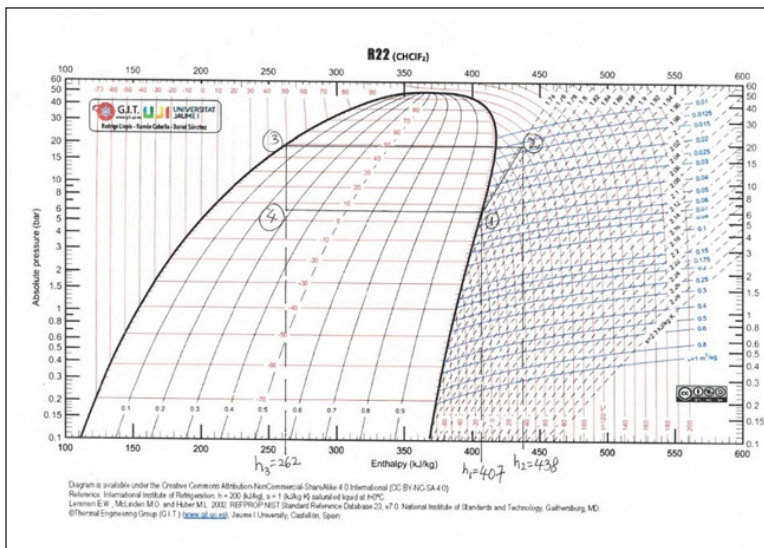


Figure 10. Pressure-enthalpy plotting of the R22 refrigeration system

The mass flow of the refrigerant, m_R , can be obtained from Equation 4. The whole process relies on the compressor's external power. Therefore, the work done during the

compression cycle is significant in identifying the performance of the refrigeration cycle, as the other states' work was merely the same. Work done during refrigerant compression can be obtained from Equation 5; subsequently, the coefficient of performance, COP, can be calculated from Equation 6. The work done on the compression cycle and refrigeration COP are calculated and shown in Table 6.

Table 6
Work done on compression cycle and refrigeration COP in theory

Refrigerant Type	Work Done During Compression Cycle	COP
R290	482 Watt	5.020
R22	517 Watt	4.677

Apparently, the R290 system draws less power for the compression cycle if compared to the R22 system. Furthermore, the COP of the R290 refrigeration cycle shows a 7.33% increase in the R22 system in the theoretical approach.

Energy Saving Verification and System COP in Practical Case Study

Electrical data collection and observation were conducted concurrently. The practical operating comparison is based on each air conditioner's operating power and cooling performance.

From Table 4, the R290 refrigerant air conditioner consumes instantaneous real power at 0.735 kW with a cooling capacity of 0.688 refrigeration tonnage (RT). The specific power value effectively illustrates its efficiency in terms of how much electrical power is used to generate one RT of cooling capacity. The specific power can be derived using Equation 7. In this study, the specific power of the R290 refrigerant air conditioner is calculated to be 1.068 kW/RT, while the specific power of the R22 refrigerant air conditioner is 1.300 kW/RT. Based on specific power, the R290 refrigerant air conditioner is 17.85% more efficient than the existing R22 refrigerant air conditioner.

From the specific power obtained, the COP in practical operation could be derived from Equation 8. Hence, the COP of an R290 refrigerant air conditioner in practical operation is 3.293, and the COP of an R22 refrigerant air conditioner in practical operation is 2.705. It shows a 21.74% increase in COP after converting to R290 natural refrigerant.

In conjunction with the Malaysian Department of Environment program and based on the SEDA 2016 report, the CO₂ equivalent emissions per hour of air conditioner power consumption are calculated by multiplying the total power consumption per hour by Peninsular Malaysia's CO₂ emission coefficient rate of 0.639 kg per kWh of electrical usage. Thus, the R290 refrigerant air conditioner would produce 0.509 kg of CO₂ equivalent emissions per usage hour (0.735 kW × 1 hr × 0.639 kg/kWh). In comparison, the R22

refrigerant air conditioner would produce 0.617 kg of CO₂ equivalent emissions per usage hour ($0.893 \text{ kW} \times 1 \text{ hr} \times 0.639 \text{ kg/kWh}$). The CO₂ emissions equivalent produced by the R290 air conditioner are 17.5% lower than those produced by the R22 refrigerant air conditioner. The R290 refrigerant air conditioner is more energy efficient.

Lastly, the direct impact of refrigerants on global warming is determined by multiplying the amount of refrigerant mass charge per air conditioner by the refrigerant's GWP. The direct CO₂ equivalent for R290 refrigerant equals 240 grams multiplied by three (R290 refrigerant has a GWP of 3). For R22 refrigerant, the direct CO₂ equivalent equals 550 grams multiplied by 1810 (as R22 refrigerant has a GWP of 1810). The release of R290 refrigerant from a 9,000 BTU/hr air conditioner will result in a CO₂ equivalent impact of 0.72 kg. Releasing R22 refrigerant from a 9,000 BTU/hr air conditioner will result in a CO₂ equivalent impact of 995.50 kg. Therefore, the R290 refrigerant air conditioner is 1,383 times more environmentally friendly than the R22 refrigerant air conditioner.

CONCLUSION

The hydrocarbon (HC) R290 refrigerant exhibits a lower molecular weight and the highest latent heat of vaporization at its boiling point. It is compatible with both mineral compressor oil and synthetic compressor oils. The lower molecular weight reduces the torsion power required by the compressor, while the higher latent heat of vaporization aids in absorbing more heat within the R290 refrigerant. The compatibility with both compressor oils allows R290 to be effectively converted for use in existing domestic air conditioners. This approach offers an economical solution to address environmental concerns related to transitioning from ozone-depleting and global-warming refrigerants to natural refrigerants. Remarkably, the results of using R290 refrigerant in existing R22 air conditioners indicate a 17.69% reduction in instantaneous power consumption.

From a technical perspective, the hydrocarbon R290 refrigerant enhances the air conditioner's coefficient of performance (COP) by 21.74% in practical terms and by 7.33% in theoretical analysis based on the pressure-enthalpy chart. This increase in COP leads to energy savings through reduced power consumption by the R290 air conditioner.

In terms of environmental impact and global warming, adopting the natural refrigerant R290 in domestic air conditioners significantly reduces the impact to 720 grams CO₂ equivalent for each R290 system conversion, given its GWP of 3. It starkly contrasts the 995.5 kilograms CO₂ equivalent emitted by an R22 system with a GWP of 1810. It equates to a 1,383 times reduction in CO₂ equivalent released into the environment over one day when an air conditioner is disposed of in a garbage disposal area.

Safety is paramount when adopting new refrigerants, and we assess the safety aspects of R290. The HC air conditioner's safety compliance, verified through refrigerant mass charge safety verification, and the application of the R290 natural refrigerant air

conditioner have been confirmed. The system's flammability is five times lower than the lower flammability limit (LFL) of R290, making it safe for household use and compliant with international standards. However, certain safety precautions are essential to educate users and installers, such as avoiding installation of the R290 system near ignition sources. Electrical components need to be switched to solid-state components; for instance, glass-type fuses are recommended to be replaced with ceramic types on the printed circuit board. Overcoming flammability concerns involves adopting good practices and designs.

Furthermore, to mitigate carbon emissions through the use of HC in domestic air conditioners, refrigerants like synthetic R22 need to be recovered into empty cylinders for recycling, reclamation, and reuse. According to Table 4, each R290 conversion from an existing R22 system (9000 BTU/hr) can directly reduce CO₂ equivalent impact by 994.78 kg due to the refrigerant's global warming potential, making it 1,383 times greener. The projected reduction in carbon dioxide from electricity savings is estimated at about 17.5%, potentially leading to a reduction of up to 0.108 kg of CO₂ emissions per hour of usage for each air conditioner.

Considering the scenario of converting 200,000 units of R22 air conditioners to R290 natural refrigerant instead of replacing them with other high global warming type air conditioners, it could result in a reduction of up to 198.956 million kg of CO₂ equivalent from refrigerant direct impact and 21,600 kg of CO₂ reduction per hour of electricity usage. Environmental sustainability is a critical factor in evaluating refrigerants, and our study presents compelling evidence in favour of hydrocarbon R290. By adopting natural refrigerants, we have the potential to mitigate climate change by reducing the usage of high global warming substances found in traditional synthetic refrigerants. Embracing this change on a larger scale could substantially impact the environment and help address the challenges of global warming.

ACKNOWLEDGEMENT

The author thanks Ener-Save Green Air Conditioner Sdn Bhd for providing facilities, tools and equipment during this research.

REFERENCES

- ASHRAE. (2022). *ASHRAE refrigerant designations*. ASHRAE. <https://www.ashrae.org/technical-resources/standards-and-guidelines/ashrae-refrigerant-designations>
- Cengel, Y., & Boles, M. (2015). *Thermodynamics an engineering approach* (8th ed.). McGraw-Hill Education.
- EPA. (n.d.). *Global Greenhouse gases emissions data*. United States Environmental Protection Agency. <https://www.epa.gov/ghgemissions/global-greenhouse-gas-emissions-data>
- European Commission. (2022). *Climate action*. European Commission. https://climate.ec.europa.eu/eu-action/fluorinated-greenhouse-gases/overview_en

- Khurmi, R. S., & Gupta, J. K. (2008). *A textbook of refrigeration and air conditioning*. (4th ed.). S. Chand Publishing.
- Ministry of Natural Resources and Environmental Sustainability. <https://www.doe.gov.my/en/2021/10/26/malaysia-committed-to-the-protection-of-the-ozone-layer-and-the-earths-climate-through-the-ratification-of-the-kigali-amendment-under-the-montreal-protocol/>
- MS2678 Working Group. (2017). *Malaysian Standard MS 2678:2017, Flammable refrigerant system – Code of practice*. Department of Standards Malaysia.
- Ng, F. (2021). *Ener-save hydrocarbon refrigerants training manual*. Ener-Save Sdn Bhd.
- Rusyanto, P. (2021). *Environmental impact of HFO refrigerants & alternatives for the future*. Open Access Government Team. <https://www.openaccessgovernment.org/hfo-refrigerants/112698/>
- SEDA Malaysia. (2019). *CO₂ Avoidance*. Sustainable Energy Development Authority (SEDA) Malaysia. <https://www.seda.gov.my/statistics-monitoring/co2-avoidance/>
- United Nations Climate Change. (2016). *28th meeting of the parties to the Montreal protocol*. United Nations Climate Change. https://unfccc.int/news/28th-meeting-parties-montreal-protocol?gclid=EAIaIQobChMIpe6y2qaw_wIVx6GWCh1abgmlEAAAYASAAEgJFMPD_BwE

Dynamic Vibration Absorber (DVA) Using Combined Piecewise and Magnetic Stiffness Mechanism

Wan Muhammad Amir¹, Roszaidi Ramlan^{1*}, Mohd Nazim Abdul Rahman¹,
Azma Putra Azis², Abd Rahman Dullah¹ and Kok Swee Leong³

¹Faculty of Mechanical Technology and Engineering, Universiti Teknikal Malaysia Melaka, 76100, Durian Tunggal, Melaka, Malaysia

²School of Civil and Mechanical Engineering, Faculty of Science and Engineering, Curtin University, Curtin Perth, Kent Street, Bentley, Western Australia 6102, Australia

³Faculty of Electronic and Computer Technology and Engineering, Universiti Teknikal Malaysia Melaka, 76100, Durian Tunggal, Melaka, Malaysia

ABSTRACT

Linear dynamic vibration absorber (DVA) efficiently suppresses the structural vibration within the 3 dB amplitude frequency bandwidth. Beyond this bandwidth, it may not be effective in suppressing the vibration. In fact, if not properly tuned, it may increase the vibration of the structure. This study examines a DVA mechanism incorporating a unique piecewise and magnetic stiffness combination. By integrating these two types of stiffness, the DVA operates in nonlinear modes, improving its ability to dampen vibrations over a wider frequency range. The positioning of limit blocks and the gap between magnets allows precise control over the level of nonlinearity for each mode, namely, hardening, softening and combined modes. Quasi-static measurements were conducted to analyse the static characteristics of the device for each mode. Dynamic measurements were conducted to analyse the device's dynamic performance in deflection-frequency characteristics, providing insights into the device's response across a frequency range (10 Hz to 50 Hz) for each mode. This evaluation helped assess the proposed mechanism's ability as a DVA to mitigate vibrations with varying frequencies. The measurement results from the three modes were compared. While hardening and softening modes proved to be able to widen the bandwidth, the combined mode was

the most effective one in widening the bandwidth as its operation covers both operating regions of softening and hardening modes. The decrease in the multi-stable solution frequency region ensures that the NDVA operates with a larger amplitude in the vibration suppression region more favourably.

ARTICLE INFO

Article history:

Received: 6 March 2024

Accepted: 21 October 2024

Published: 21 February 2025

DOI: <https://doi.org/10.47836/pjst.33.2.25>

E-mail addresses:

amir9firdaus@gmail.com (Wan Muhammad Amir)

roszaidi@utem.edu.my (Roszaidi Ramlan)

nazim@utem.edu.my (Mohd Nazim Abdul Rahman)

Azmaputra.Azis@curtin.edu.au (Azma Putra)

abdrahman@utem.edu.my (Abd Rahman Dullah)

sweeleong@utem.edu.my (Kok Swee Leong)

*Corresponding author

Keywords: Hardening stiffness, nonlinear dynamic vibration absorber, piecewise stiffness, softening stiffness

INTRODUCTION

Vibration control is paramount in maintaining the stability of structures and machinery. Passive control strategies, specifically dynamic vibration absorbers (DVAs), have shown remarkable effectiveness in achieving this goal.

The fundamental principle of linear DVAs revolves around designing an absorber with a natural frequency that coincides with the primary structure's resonance frequency, as shown in Figure 1. When these two frequencies match, the vibration of the primary structure will be suppressed, leaving the linear DVA to continue vibrating to counter the motion of the primary structure. The vibration suppression bandwidth of the primary structure $\Delta\Omega_t$ shown in Figures 2 and 3 depends on the dynamic characteristics of the linear DVA, i.e. the half-power bandwidth of the DVA. However, these linear DVAs face limitations due to their restricted operational bandwidth, which prevents them from effectively functioning when dealing with applications with varying frequencies. The linear DVA must be constantly re-tuned to match the primary structure's resonance frequency to stay effective. Typically, the stiffness will be re-tuned instead of the mass. Constant re-tuning can be made in several ways. They are active (Kassem et al., 2020), adaptive (Guo et al., 2022; Komatsuzaki et al., 2016) and passive tuning (Cheng et al., 2022). Although active and adaptive tuning often results in better performance, the requirement of an external system as part of the tuning mechanism may not be favourable in some applications. On the other hand, passive tuning may perform less but is always chosen due to its simplicity and the absence of an external tuning system.

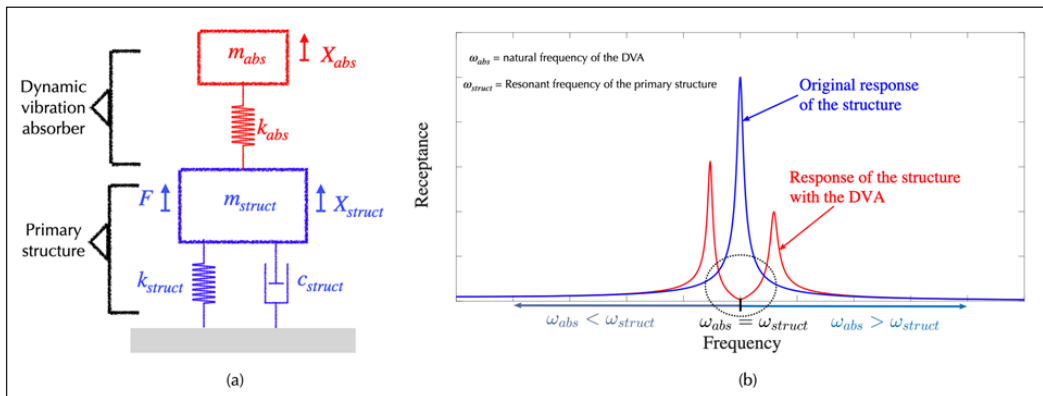


Figure 1. Quasi-static Measurement Setup (a) mass-spring-damper model of the primary structure and the dynamic vibration absorber (DVA), and (b) Frequency of the response function (receptance) of the primary structure with and without the DVA indicating the tuned response ($\omega_{abs} = \omega_{struct}$) and the mistuned response ($\omega_{abs} < \omega_{struct}$, $\omega_{abs} > \omega_{struct}$)

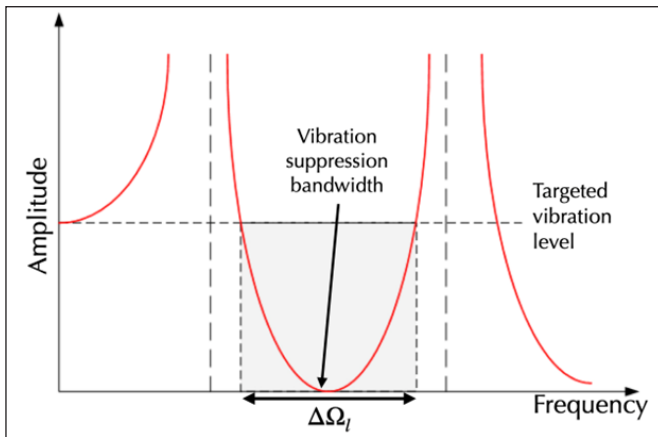


Figure 2. A magnified view of the vibration suppression bandwidth is shown in Figure 1(b) around $\omega_{abs} = \omega_{struct}$

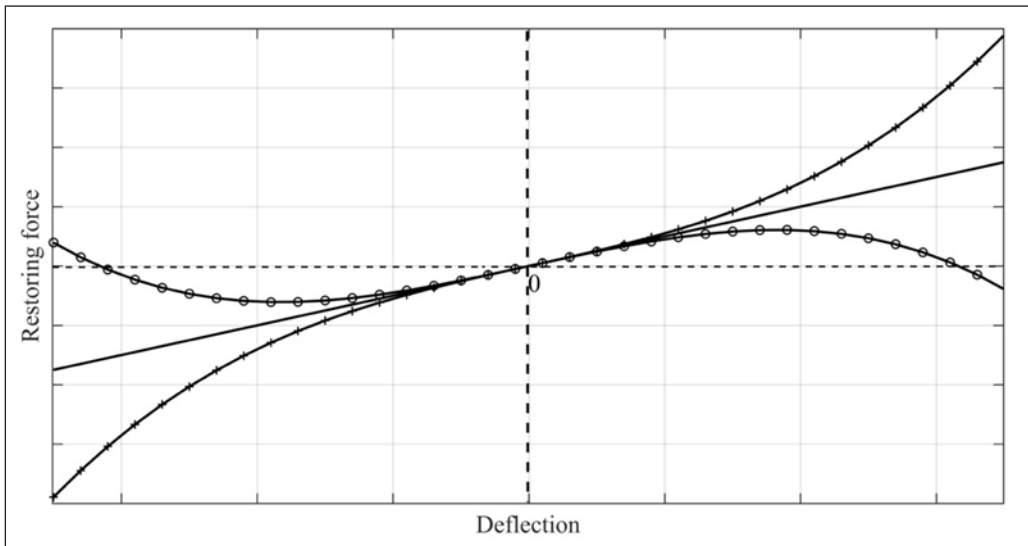


Figure 3. Restoring force versus tip deflection for different modes of stiffness (linear stiffness [solid line], softening stiffness [solid line with circle], hardening stiffness [solid line with plus sign])

The Duffing oscillator transforms the traditional linear system into a nonlinear system, enhancing its capabilities through stiffness adjustments to overcome the need for constant re-tuning (Brennan et al., 2008; Sun & Nagarajaiah, 2019). In the beginning, the primary research on the application of the Duffing oscillator was on vibration-based energy harvesting before embarking on the vibration mitigation application. These two applications benefit from the same system and can be used interchangeably. However, they may be referred to as energy harvesting devices and dynamic vibration absorbers, respectively.

The first aims to harvest energy from the system's motion, and the second is to suppress the vibration of the primary structure as it vibrates. In some applications, both purposes are combined (Kakou et al., 2024).

Numerous researchers have explored nonlinear stiffness mechanisms (Gatti et al., 2019; Li & Cui, 2017; Ramlan et al., 2010), particularly in energy harvesting systems, for their potential to cover a broader frequency spectrum and efficiently capture energy. Usually, two types of nonlinear stiffness mechanisms have been proposed. They are softening (Low et al., 2020; Wang et al., 2020) and hardening (Huang et al., 2021; Sun et al., 2013) stiffness.

The softening system consists of a stiffness which softens as the deflection increases, as shown in Figure 3. It leads to a left-skewed frequency response, as shown in Figure 4. On the other hand, the stiffness of the hardening system hardens with the deflection, thus leading to a right-skewed frequency response. Unlike linear stiffness, the restoring force-deflection characteristics of softening and hardening stiffness no longer satisfy Hooke's law. Hence, DVAs are often termed nonlinear dynamic vibration absorbers (NDVA) when they operate with softening or hardening stiffness. Both the hardening and the softening system frequency responses vary much slower with respect to the frequency compared to the linear system. This slower rate results in the wider half-power bandwidth, $\Delta\Omega_{NH}$ and $\Delta\Omega_{NS}$, respectively.

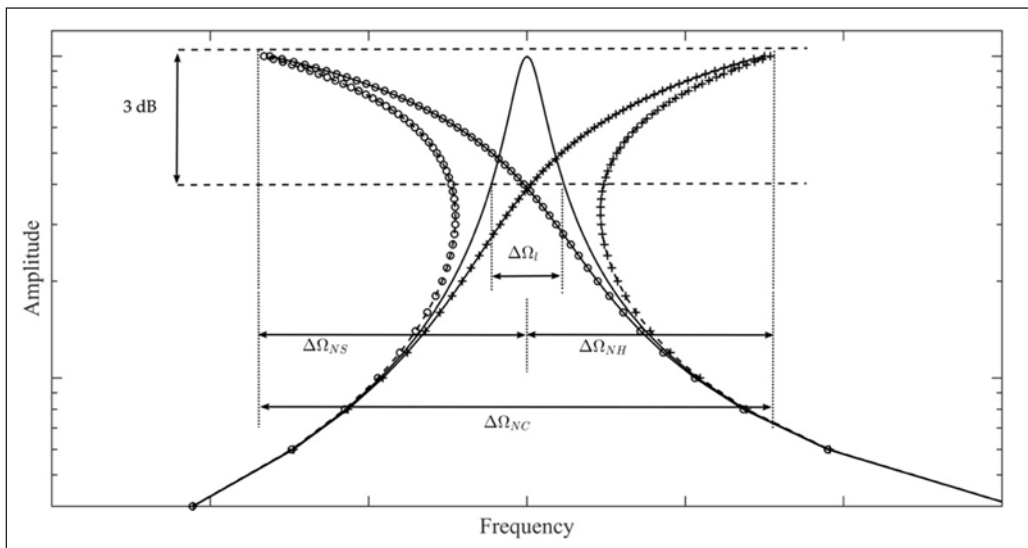


Figure 4. The frequency response function of the respective stiffness modes showing their half-power bandwidth, i.e. linear mode ($\Delta\Omega_L$), hardening mode ($\Delta\Omega_{NH}$), softening mode ($\Delta\Omega_{NS}$) and combined mode [hardening + softening] ($\Delta\Omega_{NC}$)

The softening and hardening stiffness can be realised by having magnetic stiffness in attractive and repulsive modes, respectively. The stiffness can be adjusted by altering the

gap between the magnets (Rezaei et al., 2024). In addition, the hardening stiffness can also be realised using a constrained motion (Shui & Wang, 2018; Jin et al., 2022), which is very similar to the piecewise-linear stiffness mechanism. A nonlinear gas-spring hardening mechanism is used to mitigate the vibration of large structures such as buildings (Rong et al., 2023).

Currently, the two nonlinear stiffness mechanisms have been used independently in the application of vibration absorption, i.e. softening (Wang et al., 2020) and hardening (Dou et al., 2023; Jin et al., 2022; Mustaffer et al., 2020). This paper introduces a novel approach to vibration mitigation through a unique DVA design that combines softening and hardening mechanisms in one device. Combining softening and hardening modes in one system aims to widen the effective vibration suppression bandwidth $\Delta\Omega_{NC}$ even wider than the bandwidth of individual modes. The absorber's ability to operate on hardening and softening stiffness makes it adaptable to various frequency-changing applications, even better than the individual NDVA. Experimental assessments were conducted to evaluate the static and dynamic properties of the absorber and validate its feasibility. However, the study's scope is limited to the absorber's frequency response since the vibration suppression bandwidth depends on the half-power bandwidth of the DVA. Thus, the performance of the absorber is qualitatively determined from the half-power bandwidth of the absorber's response rather than from the suppression bandwidth of the vibrating structure's response.

METHODS

Configuration of DVA and Operating Principle

Figure 5 shows the schematic of the proposed NDVA mechanism, which combines softening and hardening mechanisms. The mechanism consists of a cantilevered beam with a tip mass. It will give the linear natural frequency of the NDVA, which is given by

$$\omega_n = \sqrt{\frac{3EI}{mL^3}} \quad [1]$$

where E is Young's Modulus, I is the second moment of area, m is the tip mass, and L is the length of the beam. A limit block is placed on each side of the beam. The beam hardens as it touches the limit block, resulting in hardening stiffness. The limit block's horizontal X and vertical Y distance can be altered. Two stationary and an oscillating magnet produce lateral stiffness, which softens the stiffness of the beam. The stiffness can be altered by varying the gap G . In this study, individual and combined modes were investigated to justify the benefits of the combined mode.

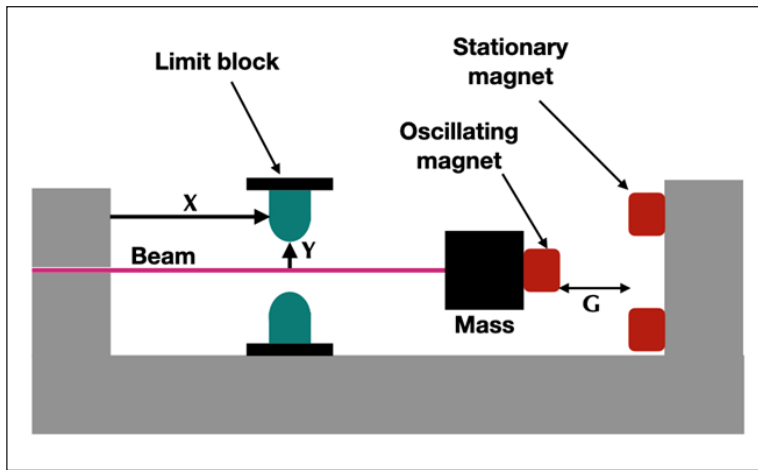


Figure 5. Proposed configurations to generate hardening and softening stiffness by combining the linear stiffness from the beam, piecewise-linear stiffness from the constrained motion and the nonlinear magnetic stiffness

Figure 6 illustrates four distinctive modes of the fabricated dynamic vibration absorber (DVA) system used in the study. At the same time, Table 1 presents the parameters involved in characterising the property of each DVA mode. In particular, Figure 6(a) presents the linear mode configuration, showcasing a cantilever beam paired with a seismic tip mass. The essence of this mode lies in its simplicity, embodying the fundamental principle of DVA operation, i.e. matching its linear natural frequency to the resonance frequency of the structure. For this type of configuration, the length of the beam is usually altered instead of the mass to vary the natural frequency in Equation 1.

Figure 6(b) then delves into the hardening mode, which introduces an intriguing shift in dynamic characteristics. This alteration is achieved by manipulating two tuning parameters, i.e., the horizontal distance X and the vertical distance Y of the limit block. These adjustments noticeably influence the system's behaviour, allowing the ability to tune the absorber's response to specific frequency ranges. However, in this study, only the horizontal distance X was varied, as in Table 1, while the vertical distance Y was kept constant at 1 mm.

Table 1
Adjustable parameters for each DVA mode

DVA Mode	Adjustable Parameters (mm)		
	X	Y	G
Linear	-	-	-
	10	1	-
Hardening	20	1	-
	30	1	-
Softening	-	-	1
	-	-	2
	-	-	3
Combined Mode	10	1	1
	20	1	1
	30	1	1

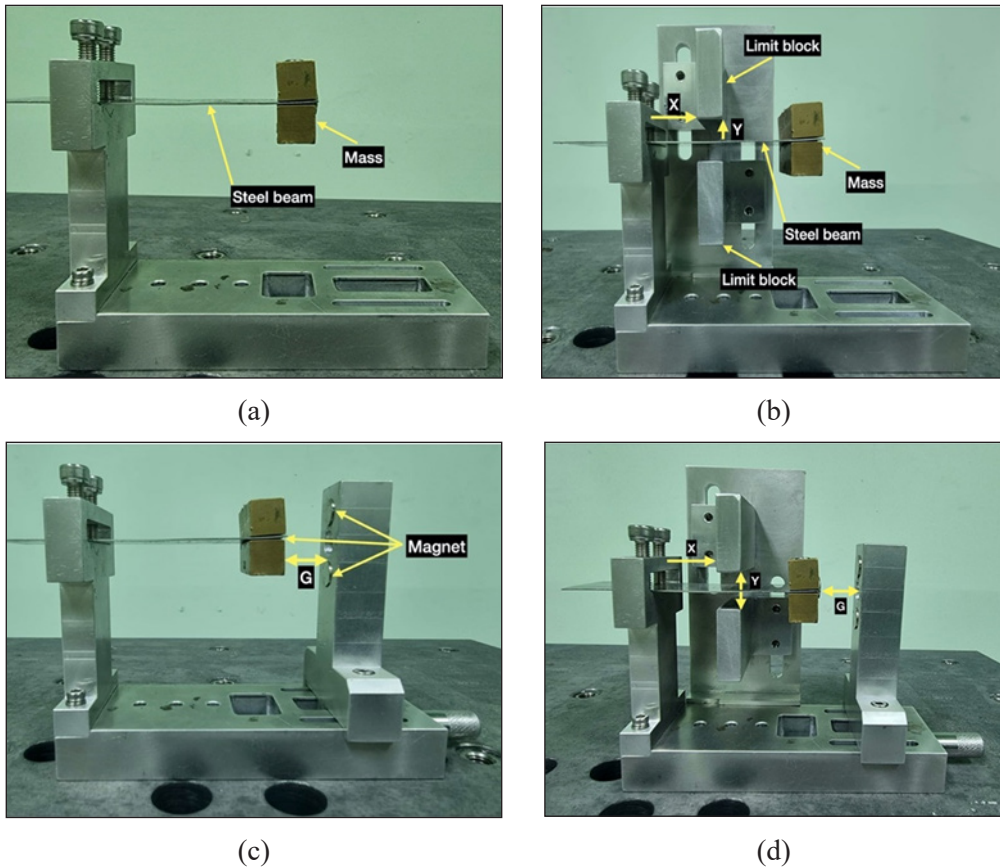


Figure 6. DVA Device in different modes: (a) linear, (b) hardening, (c) softening and (d) combined modes (Dimension of the steel beam: Length = 70 mm, Thickness = 0.1 mm, Width = 26 mm and seismic mass = 48 g)

Moving forward, Figure 6(c) unveils the softening mode, which depends on the gap G separating repulsive magnets in addition to the existing cantilevered beam and tip mass. Here, the DVA's dynamic characteristics depend on the gap G . This mode introduces negative stiffness, effectively reducing the overall stiffness.

The culmination of these nonlinear modes is illustrated in Figure 6(d), where a combined configuration is presented. This mode introduces an array of adjustable parameters: X , Y and G in one device. The combination of these parameters enables the device to either harden or soften the overall stiffness of the system. This adaptive nature allows for tailored responses to applications with varying frequency.

Each DVA mode presented in Figure 6 was characterised statically and dynamically using the adjustable parameters in Table 1. The aim was to investigate the feasibility of the combined mode rather than to compare each mode extensively.

Quasi-static Measurement

Figure 7 shows the setup for the quasi-static measurements. The NDVA tip mass was excited by the TIRA S51140 electrodynamic shaker at a low frequency, around 1 Hz.

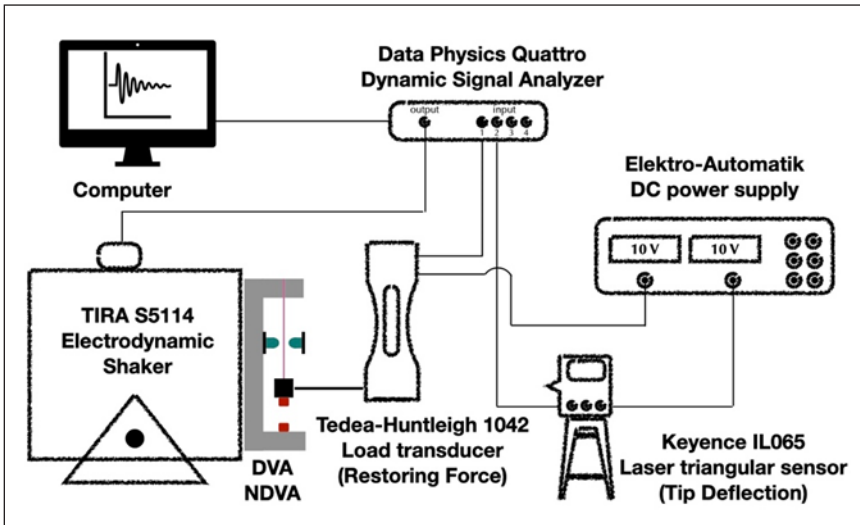


Figure 7. Quasi-static measurement setup

The outcomes of this experiment consist of two key parameters: deflection of the tip mass and restoring force of the beam. A Keyence IL-065 laser triangulation sensor and a Tedeia-huntleigh 1042 load cell were used to measure the deflection of the tip mass and the restoring force of the beam, respectively. The data from the laser sensor and the load cell were recorded using a Data Physics Quattro Dynamic Signal Analyser. These measurements provide an early insight into each configuration's stiffness linearity and nonlinearity.

Dynamic Measurement

The dynamic measurement setup is shown in Figure 8. The NDVA was placed and excited on an ETS L215M electrodynamic shaker. The Vibration Research Medallion II shaker controller was utilised to maintain the excitation level. During measurement, the absorber was subjected to harmonic excitation within a frequency range from 10 to 50 Hz. The nonlinearity requires the device to be excited in an ascending frequency sweep (10 to 50 Hz) and a descending frequency sweep (50 to 10 Hz) with identical frequency increments. The input displacement was maintained at 1 mm (pk-pk) at a sweep rate of 30 Hz/s, controlled by the feedback signal from the input accelerometer.

The acceleration of the tip mass that represents the output and the input acceleration were measured using Dytran 3225F1 accelerometers. Subsequently, the results from the

measurements were used to construct the frequency response curve in the form of the deflection of the tip mass against the excitation frequency. The sweep-up and sweep-down responses are plotted together in one graph. The deflection-frequency response curves provide a comprehensive understanding of the characteristics of each configuration across frequencies. This exploration allows for insightful observations regarding how the DVA's dynamic characteristics evolve in response to changing parameters, shedding light on the efficacy and adaptability of the proposed design.

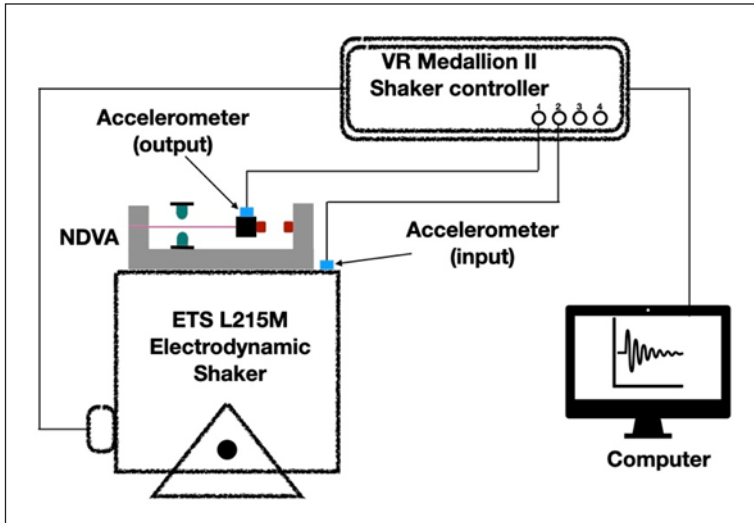
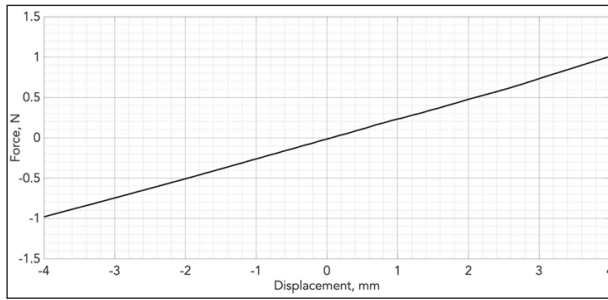


Figure 8. Dynamic measurement setup

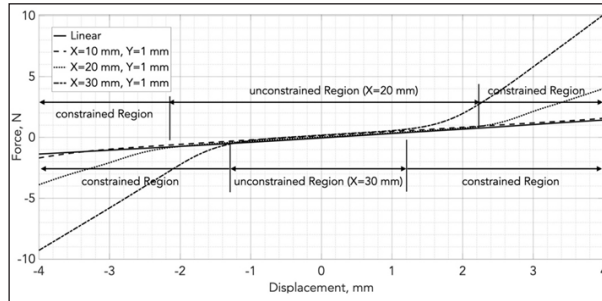
RESULTS AND DISCUSSIONS

Figure 9 presents comprehensive quasi-static behaviours exhibited by the device across different modes of operation. In the linear mode, as shown in Figure 9 (a), the force-deflection graph highlights a direct and linear correlation between the restoring force of the beam and the deflection of the tip mass. This linear relationship signifies that as the restoring force of the beam increases, the deflection follows proportionately, resulting in a constant stiffness. However, this holds only when the beam remains within its elastic deformation range, governed by the principles of Hooke's law.

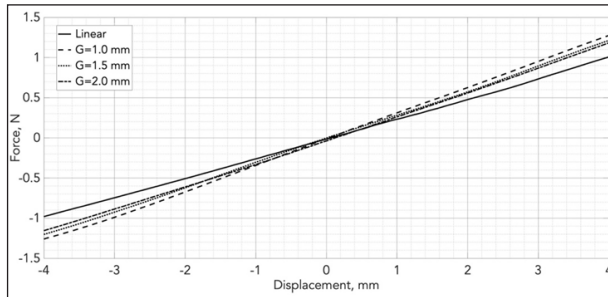
Moving to Figure 9 (b), the force-deflection graph from the hardening mode shows different force-deflection characteristics in two distinct regions, i.e., constrained and unconstrained. The unconstrained region depicts a linear behaviour similar to the linear configuration in Figure 9(a), where the deflection and force relationship remains proportionate. In this region, the motion of the beam was not constrained by the limit blocks. On the other hand, the constrained region reveals a departure from linearity due to



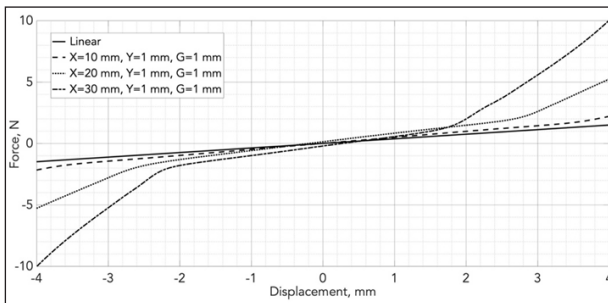
(a)



(b)



(c)



(d)

Figure 9. The quasi-static response of the DVA for (a) linear, (b) hardening, (c) softening, and (d) combined modes

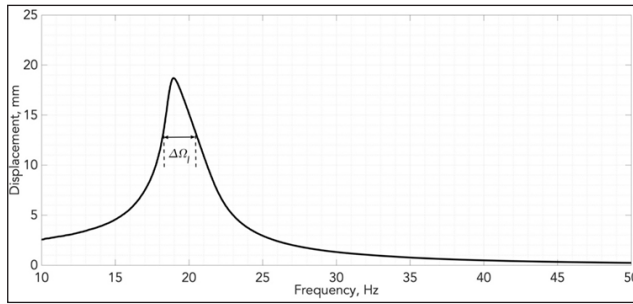
the restricted motion of the beam by the limit blocks, as shown in Figure 6(b). This motion restriction triggers a shift into nonlinear characteristics. Notably, the constrained region increases with the horizontal distance X , inducing a larger degree of hardening nonlinearity.

Figure 9 (c) shows the quasi-static measurement results for the softening mode. In this mode, the overall stiffness comprises the stiffness from the beam and the magnetic stiffness from the repulsive magnets. Interestingly, altering the distance between the magnets impacts the overall linear stiffness (around the equilibrium position) and the nonlinear stiffness (around the maximum deflection). A decrease in gap G increases the linear stiffness and softens the nonlinear stiffness. The behaviour might not be visible in the quasi-static measurement yet but will be visible in the dynamic measurement in the later discussion.

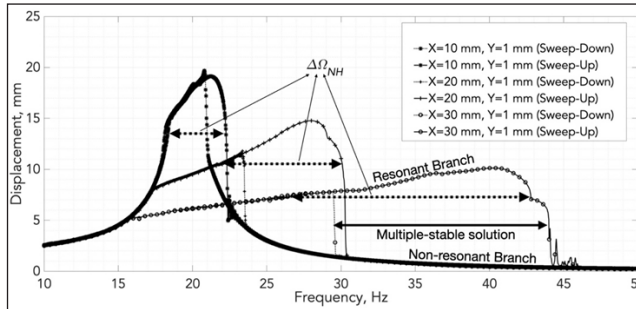
Figure 9 (d) combines these modes, i.e. hardening and softening, into one device. In this case, the force-deflection graph captures the combined effects of the two modes. In the constrained region, the hardening mode prevails, reflecting nonlinearity due to the motion restriction by the limit blocks. Conversely, in the unconstrained region, the magnetic stiffness dictates the linear stiffness around the equilibrium position. The linear stiffness is no longer constant in the unconstrained region, i.e. as a hardening mode in Figure 9(b), due to the influence of the magnetic stiffness.

Figure 10 portrays the dynamic responses of different DVA modes under sweep-up and sweep-down harmonic excitation. The linear mode in Figure 10(a) produces a similar response in sweep-up and sweep-down excitations due to the monotonic nature of the linear response. The adequate frequency bandwidth of the linear mode DVA in suppressing the vibration is closely related to its half-power bandwidth frequency, as denoted by $\Delta\omega$. The inclusion of the limit blocks hardens the overall stiffness of the system, as indicated by the right skewness of the dynamic response in Figure 10(b). The frequency sweep-up response follows the resonant branch (larger amplitude). In comparison, the frequency sweep-down response (smaller amplitude) follows the non-resonant branch—the slow rate of amplitude change against the frequency on the resonant branch results in a wider bandwidth. The bandwidth is related to the size of the constrained region shown in Figure 9(b), i.e. the larger the constrained region, the larger the bandwidth. Increasing the horizontal distance X can realise a large, constrained region. However, the nonlinearity induces a multi-stable solution region in which the response can either be on the resonant or non-resonant branches. The initial conditions solely determine the type of response in this region. The response must be on the resonant branch for the DVA application to provide a large counterforce to the vibrating structure for a wide frequency range. Operating on the non-resonant branch is less effective for a DVA application. In practice, however, the bandwidth can be less than the one presented in Figure 10(b) due to the interchanging response between the two branches.

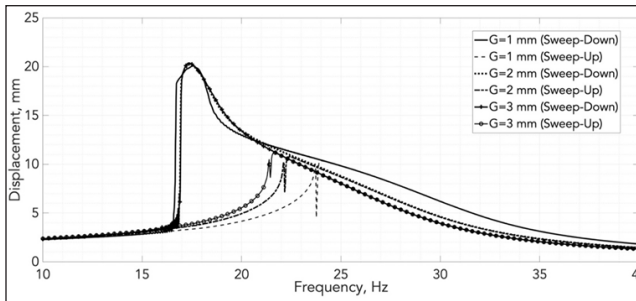
The inclusion of double repulsive magnets, on the other hand, softens the stiffness, which skews the dynamic response to the left, as shown in Figure 10(c). The half-power



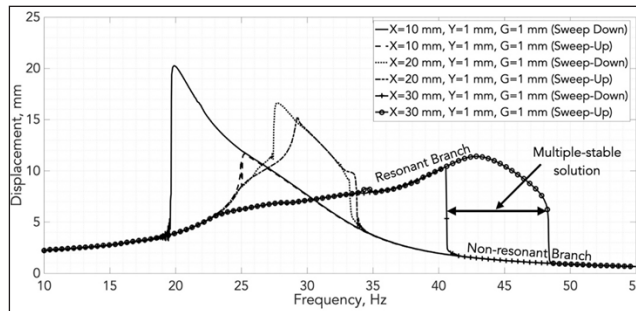
(a)



(b)



(c)



(d)

Figure 10. The dynamic response of the DVA for (a) linear, (b) hardening, (c) softening, and (d) combined modes

bandwidth is still greater than the linear mode but less than the hardening mode. Similar to the hardening mode, the response of the softening mode is also made up of two branches, i.e. resonant and non-resonant. As in the previous mode, the existence of these branches results in the multi-stable solution regions. Based on Figure 10(c), the multi-stable solution region increases with the decrease in the gap G .

Figure 10(d) shows the dynamic response of the combined mode, which combines hardening and softening modes in one device. The response of the combined mode can be tuned accordingly by adjusting X , Y and G . Due to the combined adjustable parameters, the response may behave similarly to softening or hardening modes. As discussed in the quasi-static results, the magnetic stiffness dictates the response characteristics considering the same X and Y parameters as in the hardening mode. The softening magnetic stiffness overpowers the hardening stiffness due to the restricted motion for small, constrained regions, i.e. small X , resulting in a softening-like response.

On the other hand, as the constrained region gets larger, i.e. large X , the hardening stiffness dictates the response, producing a hardening-like response. During the dynamic characterisation with X set at 20 mm, Y at 1 mm, and G at 1 mm, the sweep-up and sweep-down processes produced nearly identical patterns. It suggests that the system can exhibit a near-linear behaviour in both sweep directions at specific positions. The combined mode might be more beneficial as a DVA due to the smaller multi-stable solution region when both modes are positioned at the same distance from the limit blocks, specifically X at 30 mm, focusing on the hardening-like response. The smaller multi-stable solution region ensures that the response is on the resonant branch, thus enhancing its ability to suppress the vibration effectively. In addition, a variety of dynamic characteristics of the DVA can be altered to suit the target vibration to be suppressed.

CONCLUSION

Existing hardening and softening mechanisms prove their ability to widen the half-power bandwidth better than the traditional linear mechanism by skewing the frequency response of the DVA to the right or left, respectively. The study presented here shows that integrating hardening and softening stiffness into the design results in a remarkable expansion of the operational bandwidth of dynamic vibration absorbers (DVAs). By adjusting the tuning parameters X , Y and G , the effective frequency region of the DVA can be altered using only one device instead of two individual nonlinear mode DVAs. Its bandwidth-widening ability and ease of tunability may benefit vibration mitigation in broadband excitation applications such as pipe vibration due to flow turbulence and variation in the input flow rate. The combined mode DVA also shows a reduction in the multi-stable solution region, which addresses possible drawbacks of the hardening mode DVA. A smaller multi-stable solution region minimises the likelihood of the response engaging with the non-resonant

branch, thereby enhancing the effectiveness and reliability of the system. Although the combined mode outperforms the individual modes, its performance depends on the actual suppression bandwidth, which may require independent tuning of X , Y and G .

While the hardening mode using piecewise-linear stiffness responds well to the alteration of tuning parameters, the sensitivity of the tuning mechanism of the softening mode can be improved. It can be done by either using stronger magnets or adjusting the vertical distance of the stationary magnets. The scope of investigating the performance of the NDVA to mitigate the vibration of the primary structure shall not be limited to harmonic excitation and shall be expanded to random excitation.

ACKNOWLEDGEMENT

The project is funded by the Ministry of Higher Education Malaysia through the Fundamental Research Grant Scheme (FRGS), No. FRGS/1/2020/FKM-CARE/ F00433. The authors would also like to acknowledge the support from Universiti Teknikal Malaysia Melaka (UTeM)

REFERENCES

- Brennan, M. J., Kovacic, I., Carrella, A., & Waters, T. P. (2008). On the jump-up and jump-down frequencies of the Duffing oscillator. *Journal of Sound and Vibration*, 318(4–5), 1250–1261. <https://doi.org/10.1016/J.JSV.2008.04.032>
- Cheng, Y., Peng, Z., Wen, H., Song, H., & Cui, Z. (2022). Design of multi-mode low-frequency vibration suppressor based on dynamic vibration absorption principle. *International Journal of Acoustics and Vibration*. 27(3), 265-275. <https://doi.org/10.20855/ijav.2022.27.31870>
- Dou, J., Yao, H., Cao, Y., & Wang, Z. (2023). Permanent magnet based nonlinear energy sink for torsional vibration suppression of rotor systems. *International Journal of Non-Linear Mechanics*, 149, Article 104321. <https://doi.org/10.1016/j.ijnonlinmec.2022.104321>.
- Gatti, G., Brennan, M. J., & Tang, B. (2019). Some diverse examples of exploiting the beneficial effects of geometric stiffness nonlinearity. *Mechanical Systems and Signal Processing*, 125, 4–20. <https://doi.org/10.1016/J.YMSSP.2018.08.024>
- Guo, X., Zhu, Y., Qu, Y., & Cao, D. (2022). Design and experiment of an adaptive dynamic vibration absorber with smart leaf springs. *Applied Mathematics and Mechanics*, 43(10), 1485-1502. <https://doi.org/10.1007/s10483-022-2905-6>
- Huang, H., Yuan, Z., & Liu, W. (2021). Design strategy for optimising the bandwidth of the hardening vibration generator with customised response. *Sensors and Actuators A: Physical*, 332, Article 113197. <https://doi.org/10.1016/J.SNA.2021.113197>
- Jin, Y., Liu, K., Xiong, L., & Tang, L. (2022). A non-traditional variant nonlinear energy sink for vibration suppression and energy harvesting. *Mechanical Systems and Signal Processing*. 181, Article 109479. <https://doi.org/10.1016/j.ymssp.2022.109479>.

- Kakou, P., Gupta, S. K., & Barry, O. (2024). A nonlinear analysis of a *Duffing oscillator* with a nonlinear electromagnetic vibration absorber–inserter for concurrent vibration mitigation and energy harvesting. *Nonlinear Dynamics*, *112*(8), 5847–5862. <https://doi.org/10.1007/s11071-023-09163-6>
- Kassem, M., Yang, Z., Gu, Y., Wang, W., & Safwat, E. (2020). Active dynamic vibration absorber for flutter suppression. *Journal of Sound and Vibration*, *469*, Article 115110. <https://doi.org/10.1016/j.jsv.2019.115110>
- Komatsuzaki, T., Inoue, T., & Terashima, O. (2016). Broadband vibration control of a structure by using a magnetorheological elastomer-based tuned dynamic absorber. *Mechatronics*, *40*, 128–136. <https://doi.org/10.1016/j.mechatronics.2016.09.006>
- Li, L., & Cui, P. (2017). Novel design approach of a nonlinear tuned mass damper with duffing stiffness. *Journal of Engineering Mechanics*, *143*(4), Article 04017004. [https://doi.org/10.1061/\(asce\)em.1943-7889.0001229](https://doi.org/10.1061/(asce)em.1943-7889.0001229)
- Low, P., Ramlan, R., Ghani, H. A., & Muhammad, N. S. (2020). Experimental analysis on the transduction coefficient of a nonlinear electromagnetic energy harvesting device with softening stiffness. *International Journal of Automotive and Mechanical Engineering*, *7*(2), 7816–7831. <https://doi.org/10.15282/ijame.17.2.2020.01.0582>
- Mustaffer, M. H., Ramlan, R., Nazim, M., Rahman, A., & Putra, A. (2020). Experimental characterisation and performance of dynamic vibration absorber with tunable piecewise-linear stiffness. *Journal of the Brazilian Society of Mechanical Sciences and Engineering*, *42*(3), Article 355. <https://doi.org/10.1007/s40430-020-02435-x>
- Ramlan, R., Brennan, M. J., Mace, B. R., & Kovacic, I. (2010). Potential benefits of a nonlinear stiffness in an energy harvesting device. *Nonlinear Dynamics*, *59*(4), 545–558. <https://doi.org/10.1007/s11071-009-9561-5>
- Rezaei, M., Talebitooti, R., Liao, W. H., & Friswell, M. I. (2024). A comparative study on vibration suppression and energy harvesting via mono-, bi-, and tri-stable piezoelectric nonlinear energy sinks. *Nonlinear Dynamics*, *112*(13), 10871–10910. <https://doi.org/10.1007/s11071-024-09562-3>
- Rong, K., Lu, Z., Zhang, J., Zhou, M., & Huang, W. (2023). Nonlinear gas-spring DVA for seismic response control: Experiment and numerical simulation, *Engineering Structures*, *283*, Article 115940. <https://doi.org/10.1016/j.engstruct.2023.115940>.
- Shui, X., & Wang, S. (2018). Investigation on a mechanical vibration absorber with tunable piecewise-linear stiffness. *Mechanical Systems and Signal Processing*, *100*, 330–343. <https://doi.org/10.1016/J.YMSSP.2017.05.046>
- Sun, C., Eason, R. P., Nagarajaiah, S., & Dick, A. J. (2013). Hardening *Düffing oscillator* attenuation using a nonlinear TMD, a semi-active TMD and multiple TMD. *Journal of Sound and Vibration*, *332*(4), 674–686. <https://doi.org/10.1016/j.jsv.2012.10.016>
- Sun, C., & Nagarajaiah, S. (2019). Study of a novel adaptive passive stiffness device and its application for seismic protection. *Journal of Sound and Vibration*, *443*, 559–575. <https://doi.org/10.1016/j.jsv.2018.12.015>

Wang, X., Wu, H., & Yang, B. (2020). Nonlinear multi-modal energy harvester and vibration absorber using magnetic softening spring. *Journal of Sound and Vibration*, 476, Article 115332. <https://doi.org/10.1016/j.jsv.2020.115332>

REFEREES FOR THE PERTANIKA JOURNAL OF SCIENCE & TECHNOLOGY

Vol. 33 (2) MAR. 2025

The Editorial Board of the Pertanika Journal of Science and Technology wishes to thank the following:

Abdullah Hisam Omar
UTM, Malaysia

Ghasan Fahim Huseien
NUS, Singapore

Mohamad Zhafran Hussin
UiTM, Malaysia

Adnan Ibrahim
UKM, Malaysia

Helena V. G. Navas
FCT NOVA, Portugal

Mohd Na'im Abdullah
UPM, Malaysia

Ahmad Shukri Abu Hasim
UPNM, Malaysia

Hu Li
GZU, China

Mohd Ridhwan Adam
USM, Malaysia

Ahmad Taufek Abdul Rahman
UiTM, Malaysia

James S. Bennett
CDC, Ohio

Mohsen Sheikholeslami
BNUT, Iran

Ahmed Abtan Al-Jumaili
Tikrit University, Iraq

Jasmina Khaw Yen Min
UTAR, Malaysia

Muhammad Wajid Ullah
UJS, China

Aimi Salihah Abdul Nasir
(UNIMAP, Malaysia)

Juan Carlos Chavarria-
Hernandez
CICY, Mexico

Narendra Khatri
MIT, India

Alaa Abdulhady Jaber
University of Technology, Iraq

Junaid Ali Reshi
AMU, India

Neeraj Priyadarshi
JISCE, India

Ali Hajnayeb
SCU, Iraq

Khairul Hamimah Abas
UTM, Malaysia

Nikolay Hinov
Technical University, Bulgaria

Bo Hsiao
Yunke University, Taiwan

Khor Chu Yee
UNIMAP, Malaysia

Noor Hafizah Amer
UPNM, Malaysia

Dayang Azra Awang Mat
UNIMAS, Malaysia

Lim Jun Wei
UTP, Malaysia

Nor Hasanah Abdul Shukor Lim
UTM, Malaysia

Eric Tzyy Jiann Chong
UMS, Malaysia

Lindah Roziani Jamru
UMS, Malaysia

Norizah Kamarudin
UPM, Malaysia

Erzam Marlisah
UPM, Malaysia

Marek Kieliszek
(Warsaw University, Poland)

Nur Rashid Mat Nuri
UTEM, Malaysia

Farshid Keynia
GUAT, Iran

Mazhar Iqbal
UAF, Pakistan

Nur Syakina Jamali
UPM, Malaysia

Fathin Ayuni Azizan
UNIMAP, Malaysia

Mohamad Adzhar Md Zawawi
USM, Malaysia

Ojo Joseph Sunday
FUTA, Nigeria

Ooi Boon Yaik
UTAR, Malaysia

See Kok Fong
USM, Malaysia

Thongthai Witoon
KU, Thailand

Rajkishor Kumar
VIT, India

Shalyda Md Shaarani
UMP, Malaysia

Wan Mariam Wan Muda
UMT, Malaysia

Ramadhansyah Putra Jaya
UMPISA, Malaysia

Simon A. Kondrat
Loughborough University, UK

Zulkarnain Ahmad Noorden
UTM, Malaysia

Ramli Dollah
UMS, Malaysia

Song Yang
GZU, China

Zulkarnain Hassan
UNIMAP, Malaysia

Ratna Suffhiyanni Omar
UKM, Malaysia

Syed Zulqadar Hassan
UCP, Pakistan

Ravi Pratap Singh
NITKKR, India

Tan Tse Guan
UMK, Malaysia

BNUT – Babol Noshirvani University of Technology
CDC – Centers for Disease Control and Prevention
CICY – Yucatan Scientific Research Center
FCT/NOVA – NOVA School of Science and Technology
FUTA – Federal University of Technology Akure
GUAT – Graduate University of Advanced Technology
GZU – Guizhou University
JISCE – JIS College of Engineering
KU – Kasetsart University
MIT – Manipal Institute of Technology
NITKKR – National Institute of Technology Kurukshetra
SCU – Shahid Chamran University
UAF – University of Agriculture
UCP – University of Central Punjab
UiTM – Universiti Teknologi MARA Malaysia
UJS – Jiangsu University

UKM – Universiti Kebangsaan Malaysia
UMK – Universiti Malaysia Kelantan
UMP – Universiti Malaysia Pahang
UMPISA – Universiti Malaysia Pahang Al-Sultan Abdullah
UMS – Universiti Malaysia Sabah
UMT – Universiti Malaysia Terengganu
UNIMAP – Universiti Malaysia Perlis
UNIMAS – Universiti Malaysia Sarawak
UPM – Universiti Putra Malaysia
UPNM – Universiti Pertahanan Nasional Malaysia
USM – Universiti Sains Malaysia
UTAR – Universiti Tun Abdul Rahman
UTEM – Universiti Teknikal Malaysia Melaka
UTM – Universiti Teknologi Malaysia
UTP – Universiti Teknologi PETRONAS
VIT – Vellore Institute of Technology

While every effort has been made to include a complete list of referees for the period stated above, however if any name(s) have been omitted unintentionally or spelt incorrectly, please notify the Chief Executive Editor, *Pertanika* Journals at executive_editor.pertanika@upm.edu.my

Any inclusion or exclusion of name(s) on this page does not commit the *Pertanika* Editorial Office, nor the UPM Press or the university to provide any liability for whatsoever reason.

The Impact of Hydrocarbon R290 Refrigerant on Air Conditioner Performance and Environmental Sustainability 1069
Ferdinand Ng Siek Khai and Nurul Sabihah Zakaria

Selected paper from The 9th International Conference and Exhibition on Sustainable Energy and Advanced Material 2023 (ICE-SEAM 2023)

Dynamic Vibration Absorber (DVA) Using Combined Piecewise and Magnetic Stiffness Mechanism 1089
Wan Muhammad Amir, Roszaidi Ramlan, Mohd Nazim Abdul Rahman, Azma Putra Azis, Abd Rahman Dullah and Kok Swee Leong

Physical Parameters Optimization of Bacterial Cellulose from <i>Komagataeibacter sucrofermentans</i> <i>Siti Noorfathiah Mohd Razin, Siti Nurbaya Oslan and Noor Dina Muhd Noor</i>	893
Investigation of Partial Discharge Characteristics in Mineral Oil Induced by Dibenzyl Disulfide <i>Amran Mohd Selva, Norhafiz Azis, Muhammad Umair Tariq, Mohd Zainal Abidin Ab Kadir, Jasronita Jasni and Hidayat Zainuddin</i>	913
<i>Review Article</i>	
Fulfilling Feed Demands: Industrial Production of <i>Saccharomyces cerevisiae</i> as Key Protein Source for Aquaculture, Poultry and Livestock <i>Zahra Safdari, Mohd Khairol Anuar Ariffin, Eris Elianddy Supeni and Mohamed Thariq Hameed Sultan</i>	939
Virus Particle Dispersion and Infection Risk Assessment in Aircraft Cabins: A CFD Approach <i>Mohd Syakirin Rusdi, Di Fey Way, Mohd Sharizal Abdul Aziz, Farzad Ismail and Mohammad Hafifi Hafiz Ishak</i>	969
Public Awareness and Performance Assessment of Communal Grease Traps in Klang Valley, Malaysia <i>Theban Arumugam, Priyadarshini Ravindran, Shafreeza Sobri, Salmiaton Ali and Mus'ab Abdul Razak</i>	987
Hydrogenolysis of Glycerol to Propanediols over Ni supported on MgO Catalyst <i>Maryam Shakur, Maryum Irshad and Muhammad Sajjad Haider</i>	1007
Selected papers from The 11th International Conference on Multidisciplinary Research 2023 (iCMR 2023)	
Random Forest Model for Software Build Time Prediction on CI/CD Pipeline <i>Wen Han Seow, Chia Yean Lim and Sau Loong Ang</i>	1031
A Novel Approach to Evaluating HEMA Polymer Gel Dosimeters Using Molecular Vibrational Features <i>Muhammad Alhassan, Azhar Abdul Rahman, Iskandar Shahrin Mustafa, Mohd Zahri Abdul Aziz, Mohd Zakir Kassim, Mohammed Salem Abdullah Bagahezel, Habib Ahmad Ibrahim and Kabiru Alhaji Bala</i>	1049

Performance of High-volume Carbide Lime Mortar Under Accelerated <i>CO₂ Curing Followed by Postconditioning Treatments</i> <i>Adrina Rosseira A. Talip, Nur Hafizah A. Khalid and Abdul Rahman Mohd Sam</i>	677
<i>Review Article</i>	
An Overview of the 5G Patent Landscape <i>Mohammad Sadegh Naghipour and Zulhasni Abdul Rahim</i>	693
Effective Vibration-Based Anomaly Detection in Water Pump Operation Using Arduino Microcontroller <i>Azahar Mohd, Khairil Anas Md Rezali, Sharafiz Abdul Rahim, Mohammad Yazdi Harmin, Abdul Murad Zainal Abidin and Mohamad Fikri Mohamad Yunus</i>	725
Temperature-corrected Performance Ratio of Grid-Connected Photovoltaic System: Tropical versus Continental Climate <i>Siti Nor Nakhirah Ibrahim, Hedzlin Zainuddin and Shahril Irwan Sulaiman</i>	745
<i>Review Article</i>	
Machine Learning Applications in Multiplayer Online Battle Arena Esports—A Systematic Review <i>Ahmad Alif Kamal, Mohd. Asyraf Mansor, Liyana Truna, Norhunaini Mohd. Shaipullah and Nor Hafizie Habib Sultan</i>	765
Estimation of Mangrove Gross Primary Productivity Using Sentinel-2 Imagery Data: A Case Study in Ujung Pangkah East Java, Indonesia <i>Zainul Hidayah, Abd Rahman As-Syakur, Herlambang Aulia Rachman, Linda Sri Rahayu Romadhoni and Martiwi Diah Setiawati</i>	799
Stock Trend Prediction Using Multi-attention Network on Domain- specific and Domain-general Features in News Headline <i>Phaik Ching Soon, Tien-Ping Tan, Huah Yong Chan and Keng Hoon Gan</i>	823
<i>Review Article</i>	
Recent Advances in Nickel Catalysts for Deoxygenation of Triglycerides and Fatty Acids: A Review <i>Syazwani Mahmud Puzi, Khairuddin Md Isa, Farizul Hafiz Kasim, Tuan Amran Tuan Abdullah, Mohd. Aizudin Abd. Aziz and Nur Amira Fatimah Bashari</i>	845
Better Network Optimization Through Batch Normalization in Left Ventricle Chamber Classification <i>Dayang Suhaida Awang Damit, Siti Noraini Sulaiman, Muhammad Khusairi Osman, Noor Khairiah A Karim and Samsul Setumin</i>	875

Pertanika Journal of Science & Technology

Vol. 33 (2) Mar. 2025

Content

Foreword	i
<i>Luqman Chuah Abdullah</i>	
A Study of Different Antenna Models on the Performance of UAV-Based LoRa Communication Network Using Taguchi and ANOVA Methods	557
<i>Mohamad Hazwan Mohd Ghazali, Kelvin Teoh and Wan Rahiman</i>	
Numerical Analysis of Solar Pavement Collector for Malaysian Environment	579
<i>Nurul Aqilah Razeman, Zarina Itam, Salmia Beddu, Muhammad Imran Najeeb, Nazirul Mubin Zahari, Daud Mohammad, Mohd Hafiz Zawawi, Agusril Syamsir and Norizham Abdul Razak</i>	
Determination of Optimal Water Requirement for Sweet Corn Crop Based on Meteorological Data and Plant Growth Parameters	599
<i>Noorellimia Mat Toridi, Muhammad Maleq Isqandar Nor Jalal, Aimrun Wayayok and Mohamed Azwan Mohamed Zawawi</i>	
A Study on the Impact of Chamber Size, Configuration, Environmental Factors and Maximum Power Point Tracking (MPPT) Integration on Microbial Fuel Cell Voltage	625
<i>Siti Kudnie Sahari, Nashley Ursula Mundi Ujai, Thommy Thomas, Ibrahim Yakub, Marini Sawawi, Lilik Hasanah, Abdul Rahman Kram, Zaidi Embong, Kasumawati Lias, Annie Joseph, Kho Lee Chin and Sharifah Masniah Wan Masra</i>	
Simulation of Solar Charge Controller Module with Current Backflow Protection	639
<i>Aimi Dalila Azhar, Weng Ho Yew, Akmal Zaini Arsad, Azrul Ghazali, Fazrena Azlee Hamid and Ahmad Wafi Mahmood Zuhdi</i>	
Leveraging Computational Model Approach in Understanding Infectious Disease: A Case Study in Sabah, Malaysia	653
<i>Siti Sarah Mohd Isnan, Ahmad Fikri Abdullah, Abdul Rashid Mohamed Shariff, Iskandar Ishak, Sharifah Norkhadijah Syed Ismail, Doria Tai and Maheshwara Rao Appanan</i>	



Pertanika Editorial Office, Journal Division,
Putra Science Park,
1st Floor, IDEA Tower II,
UPM-MTDC Center,
Universiti Putra Malaysia,
43400 UPM Serdang,
Selangor Darul Ehsan
Malaysia

<http://www.pertanika.upm.edu.my>
Email: executive_editor.pertanika@upm.edu.my
Tel. No.: +603- 9769 1622

PENERBIT
UPM
UNIVERSITI PUTRA MALAYSIA
PRESS

<http://penerbit.upm.edu.my>
Email: penerbit@upm.edu.my
Tel. No.: +603- 9769 8855

